

Spin-Crossover Iron Complexes Bearing Alkyl Chain Substituents

Iurii Galadzhun

Submitted in accordance with the requirements for the degree of
Doctor of Philosophy

The University of Leeds

School of Chemistry

May, 2019

The candidate confirms that the work submitted is his own, except where work which has formed part of jointly authored publications has been included, and that appropriate credit has been given where reference has been made to the work of others.

Two papers containing work from this PhD thesis have been published at the time of writing, which contains results from Chapters 2 and 3. Although I contributed to the preparation of these manuscripts, the final versions were completed by my supervisor Prof Malcolm Halcrow, who is also the corresponding author on all the papers. The description of these results in Chapters 2 and 3 is not directly reproduced from the papers.

The references are:

Five 2,6-Di(pyrazol-1-yl)pyridine-4-carboxylate Esters, and the Spin States of their Iron(II) Complexes. Galadzhun, I.; Kulmaczewski, R. and Halcrow, M.A. *Magnetochem.* **2019**, 5, 9.

2,6-Bis(pyrazol-1-yl)pyridine-4-carboxylate Esters with Alkyl Chain Substituents and Their Iron(II) Complexes. Galadzhun, I.; Kulmaczewski, R.; Cespedes, O.; Yamada, M.; Yoshinari, N.; Konno, T. and Halcrow, M.A. *Inorg. Chem.* **2018**, 57 (21), 13761-13771.

This copy has been supplied on the understanding that it is copyright material and that no quotation from the thesis may be published without proper acknowledgement.

The right of Iurii Galadzhun to be identified as Author of this work has been asserted by him in accordance with the Copyright, Designs and Patents Act 1988.

Acknowledgements

First and foremost, I would like to thank Prof Malcolm Halcrow for giving me the opportunity to undertake this PhD project, for all his excellent supervision during the time I have been here, and for his valuable advices and help with solving challenging crystal structures, as well as for the opportunity to experience working with Diamond Light Source and to attend the International Coordination Chemistry Conference in Japan. Also, I would like to thank him for all the efforts he put into publishing the research discussed in thesis, especially for writing up the Inorganic Chemistry paper, which together with the supporting information has as much as 87 pages.

I would like to thank the technical staff, including Mrs Tanya Marinko-Covell and Mr Stephen Boyer for running elemental analyses, Mr Simon Barrett and Dr Mark Howard for their help with NMR spectra, Dr Stuart Warriner for keeping the MS machine running smoothly, Dr Christopher Pask for his training and help with collecting and solving X-ray crystal structures, and Mr Algy Kazlaucius for promptly running DSC and TGA measurements. Thanks Diamond Light Source for providing an opportunity for our group to collect crystal structures of our samples at their facility.

Also, I would like to thank Dr Rafal Kulmaczewski, Namrah Shahid, and Izar Capel Berdiell for running SQUID measurements. Thanks to Kay Burrows, and to especially Izar Capel Berdiell, who collected some crystal structures for my research at the Diamond Light Source. Thanks Dr Rafal Kulmaczewski, Izar Capel Berdiell, and Dr Matthew Allison for helpful practical advices. Thanks Dr Stephen Gorman, Felix Janeway, Dr Nimesh Mistry, and Prof Dmitry Shalashilin for excellent demonstrating supervision during their classes.

I would like to thank all past and present members of the Halcrow and McGowan groups, with whom we shared the 1.25 office: Ahmed Ahmed, Dr Cecilia Madzivire-Penduka, Dr Heba Abdelgawad, Dr Laura Gandhi, , Pablo Carames Mendez, and Dr Sam Greatorex for their help and support.

Thanks to the Willans and Hardie group members for occasionally borrowing us some liquid nitrogen, and for their fun company during the Christmas meals. Thanks to the Postgraduate Chemical Society for organizing fun events and retreats.

Special thanks to my parents, brother and friends for their loving support.

Abstract

This thesis concerns synthesis, magnetic and mesogenic properties of novel iron(II) complexes based on 2,6-bis(pyrazol-1-yl)pyridine derivatives, with short and long alkyl chains on the pyrazolyl or pyridyl rings.

Chapter 1 is an introduction to the spin crossover and liquid crystal phenomena. Using significant literature examples, it outlines: their discovery and physical origin; the interplay between spin crossover and long alkyl chains; the factors that affect spin crossover; and progress towards their practical application.

Chapter 2 describes a family of 2,6-bis(pyrazol-1-yl)pyridine derivatives with no long alkyl chain substituents, and explores the effect of small structural differences on their spin crossover.

Chapter 3 presents two series of 2,6-bis(pyrazol-1-yl)pyridine derivatives with long alkyl chains bound to the pyridyl ring, and investigates the effect of the alkyl chain length on spin crossover and phase transitions in their iron(II) complexes.

Chapter 4 discusses four series of 2,6-bis(pyrazol-1-yl)pyridine derivatives with long alkyl chains on the pyrazolyl rings. Mono- and disubstituted examples bearing saturated and unsaturated substituents are included. An unusual spin crossover exhibited by some of the complexes is described.

Chapter 5 details some asymmetric 2,6-bis(pyrazol-1-yl)pyridine and isomeric 2-(1H-pyrazol-1-yl)-6-(triazolyl)pyridine derivatives. It includes a study of a coordination polymer formed from one of these ligands, using crystallography and magnetic measurements.

Chapter 6 is an account of all the synthetic procedures used in this work, the standard characterisation of the new products, and the instrumentation used for the analyses.

Table of Contents

Acknowledgements	iii
Abstract	iv
Table of Contents	v
List of Tables	xiv
List of Figures	xvi
List of Abbreviations	xxvi
Colour Scheme for Crystal Structures	xxviii
Chapter 1 Introduction	1
1.1 Spin crossover phenomenon.....	2
1.1.1 Introduction to the SCO effect	2
1.1.2 Types of SCO switching	4
1.1.3 Metal ions that can undergo SCO	4
1.1.4 Influence of the lattice solvent and counterion on SCO.....	5
1.1.5 The LIESST effect.....	6
1.1.6 Detection methods for SCO	7
1.1.7 Possible applications for SCO	8
1.2 Liquid crystals	9
1.2.1 Liquid crystal phase overview	9
1.2.2 Intermediate LC phases	10
1.2.3 Langmuir-Blodgett films.....	12
1.3 Spin-crossover liquid crystals.....	12
1.4 Spin-crossover metal complexes bearing alkyl chains	15
1.5 Project aims	19
List of References	20
Chapter 2 Bis(pyrazol-1-yl)pyridine derivatives with no long alkyl chains, and their iron(II) complexes	29
2.1 Introduction	30
2.2 Ligand synthesis	30
2.2.1 L1 - 2,6-dibromo pyridine-4-carboxylic acid.....	30
2.2.2 L2 - 2,6-di(1H-pyrazole-1'-yl)pyridine-4-carboxylic acid	31
2.2.3 L3, L4 - 3,4-dimethoxyphenyl (2,6-di-1H-pyrazole-1-yl)pyridine-4-carboxylate, and 4-methoxyphenyl (2,6-di-1H-pyrazole-1-yl)pyridine-4-carboxylate	32

2.2.4 L5, L6 - 3,4-dihydroxyphenyl (2,6-di-1H-pyrazole-1-yl)pyridine-4-carboxylate, and 4-hydroxyphenyl (2,6-di-1H-pyrazole-1-yl)pyridine-4-carboxylate	32
2.2.5 L7 - 1,4-Bis[2,6-di(1H-pyrazole-1'-yl)pyridine-4-carboxylate]benzene	33
2.2.6 L8, L9, L10 - 3,4-dimethoxy benzyl(2,6-di-1H-pyrazole-1-yl)pyridine-4-carboxylate, 4-methoxy benzyl(2,6-di-1H-pyrazole-1-yl)pyridine-4-carboxylate, and benzyl(2,6-di-1H-pyrazole-1-yl)pyridine-4-carboxylate	34
2.3 Iron(II) complex synthesis	34
2.4 XRD.....	35
2.4.1 Crystal structures of the ligands	35
L2, L3, L4, L5, and L6	35
L7	37
L8, L9, L10	38
2.4.2 Crystal structures of iron complexes	39
[Fe(L3) ₂][BF ₄] ₂ , [Fe(L4) ₂][BF ₄] ₂ , [Fe(L5) ₂][BF ₄] ₂ , [Fe(L6) ₂][BF ₄] ₂ ,	39
[Fe(L8) ₂][BF ₄] ₂ , [Fe(L9) ₂][BF ₄] ₂ , and [Fe(L10) ₂][BF ₄] ₂	44
2.5 SQUID.....	46
2.5.1 [Fe(L3) ₂][BF ₄] ₂ , [Fe(L4) ₂][BF ₄] ₂ , [Fe(L5) ₂][BF ₄] ₂ , and [Fe(L6) ₂][BF ₄] ₂	46
2.5.2 [Fe(L8) ₂][BF ₄] ₂ , [Fe(L9) ₂][BF ₄] ₂ , and [Fe(L10) ₂][BF ₄] ₂	48
2.6 Distortion parameters for the XRD crystal structures	51
2.6.1 Introduction to distortion parameters	51
2.6.2 Distortion parameters for the structures, for which SQUID has been measured	52
2.6.3 Distortion parameters for the structures, for which SQUID hasn't been measured	56
2.7 Powder Patterns.....	56
2.7.1 [Fe(L3) ₂][BF ₄] ₂ , [Fe(L4) ₂][BF ₄] ₂ , [Fe(L5) ₂][BF ₄] ₂ , and [Fe(L6) ₂][BF ₄] ₂	56
2.7.2 [Fe(L7) ₂][BF ₄] ₂ , [Fe(L8) ₂][BF ₄] ₂ , and [Fe(L9) ₂][BF ₄] ₂	57
2.8 Evans method NMR	59
2.9 Paramagnetic NMR	59
2.10 Conclusions for Chapter 2.....	61
List of References	62

Chapter 3 Pyridine-substituted bis(pyrazol-1-yl)pyridine derivatives with long alkyl chains, and their iron(II) complexes.....	64
3.1 Introduction	65
3.2 Ligands synthesis.....	65
3.2.1 L11Cx - alkyl (2,6-di-1H-pyrazol-1-yl)pyridine-4-carboxylates	65
3.2.4 L12Cx - 4-alkyloxyphenols	67
3.2.5 L13Cx - 4-(alkyl)phenyl 2,6-di-1H-pyrazol-1-ylisonicotinates.....	68
3.3 Iron(II) complex synthesis	69
3.4 Crystal structures	70
3.4.1 Crystal structures of the ligands	71
L11Cx.....	71
L12Cx.....	72
L13Cx.....	73
3.4.2 Crystal structures of iron complexes	74
[Fe(L11Cx) ₂][BF ₄] ₂	74
[Fe(L13Cx) ₂][BF ₄] ₂	74
3.5 Distortion parameters	77
3.6 SQUID.....	77
3.6.1 [Fe(L11Cx) ₂][BF ₄] ₂	77
3.5.2 [Fe(L13Cx) ₂][BF ₄] ₂	79
3.7 DSC and TGA	81
3.7.1 Ligands.....	81
L11Cx.....	81
L13Cx.....	83
3.7.2 Iron(II) complexes	84
[Fe(L11Cx) ₂][BF ₄] ₂	84
[Fe(L13Cx) ₂][BF ₄] ₂	88
3.8 VT photographs.....	92
3.9 Powder patterns	95
3.9.1 Ligands.....	95
L11Cx.....	95
L13Cx.....	96
3.9.2 Iron(II) complexes	96
[Fe(L11Cx) ₂][BF ₄] ₂	96

[Fe(L13Cx) ₂][BF ₄] ₂	97
3.10 Magnetic properties in solution.....	110
Evans method NMR	110
Paramagnetic NMR	110
3.11 Conclusions.....	113
List of References	115
Chapter 4 Pyrazole-substituted bis(pyrazol-1-yl)pyridine derivatives with long alkyl chains, and their iron(II) complexes.....	118
4.1 Introduction	119
4.2 Ligands synthesis.....	119
4.2.1 L14, L15, L16 – the precursors	119
4.2.2 L17CxM – unsaturated mono-substituted ligands	121
4.2.3 L17CxD – unsaturated di-substituted ligands.....	122
4.2.4 L18CxM – saturated mono-substituted ligands	124
4.2.5 L18CxD – saturated di-substituted ligands.....	126
4.3 Iron(II) complex synthesis	127
4.4 XRD Crystal Structures	128
4.4.1 Ligand crystal structures	128
Precursor ligands: L14, L15, L16	128
Unsaturated ligands: L17CxM and L17CxD	129
Saturated ligands: L18CxM and L18CxD	132
4.4.2 Iron complex crystal structures.....	133
Iron complexes of precursor ligands:	133
Iron complexes of long alkyl chain ligands: Fe(L17C18M) ₂ [BF ₄] ₂ , [Fe(L18C12M) ₂][BF ₄] ₂ , [Fe(L18C16M) ₂][BF ₄] ₂ , and [Fe(L18C18M) ₂][BF ₄] ₂	134
4.5 Distortion parameters.....	136
4.6 Powder diffraction.....	138
4.6.1 Ligands.....	138
4.6.2 Iron complexes	139
4.7 SQUID.....	142
[Fe(L17CxM) ₂][BF ₄] ₂	142
[Fe(L17CxD) ₂][BF ₄] ₂	143
[Fe(L18CxM) ₂][BF ₄] ₂	144
[Fe(L18CxD) ₂][BF ₄] ₂	146
[Fe(L16) ₂][BF ₄] ₂	147

4.8 DSC.....	148
4.8.1 Ligands.....	148
L17CxM.....	148
L17CxD	149
L18CxM.....	150
L18CxD	151
4.8.2 Iron complexes.....	153
[Fe(L17CxM) ₂][BF ₄] ₂	153
[Fe(L17CxD) ₂][BF ₄] ₂	155
[Fe(L18CxM) ₂][BF ₄] ₂	157
[Fe(L18CxD) ₂][BF ₄] ₂	159
4.9 VT images	161
4.10 Evans method NMR	163
4.11 Paramagnetic NMR	163
Iron complexes of precursor ligands	163
[Fe(L17CxM) ₂][BF ₄] ₂	164
[Fe(L17CxD) ₂][BF ₄] ₂	164
[Fe(L18CxM) ₂][BF ₄] ₂	165
[Fe(L18CxD) ₂][BF ₄] ₂	166
4.12 Conclusions.....	166
List of References	168
Chapter 5 Asymmetric ligands with no long alkyl chains, and their iron(II) complexes	169
5.1 Introduction	170
5.2 Ligand synthesis	171
L19 – Two isomers of 2-(1H-pyrazol-1-yl)-6-(1H -1,2,3-triazol-1-yl)pyridine.....	171
L20 – 2-(1H-pyrazol-1-yl)-6-(1H -1,2,4-triazol-1-yl)pyridine.....	172
L21 – 2-(4-(Ethylcarboxy)pyrazol-1-yl)-6-(1H-pyrazol-1-yl)pyridine.....	173
5.3 Iron complex synthesis.....	174
[Fe(L21) ₂][BF ₄] ₂	174
[Fe(L20) ₂][Fe(L20) ₂ (H ₂ O) ₂][BF ₄] ₄ ·MeNO ₂ ·H ₂ O	174
5.4 Paramagnetic NMR	175
[Fe(L21) ₂][BF ₄] ₂	175
5.5 XRD crystal structures and distortion parameters	176

Ligands.....	176
Iron complexes.....	177
[Fe(L20) ₂][Fe(L20) ₂ (H ₂ O) ₂][BF ₄] ₄ ·MeNO ₂ ·H ₂ O	177
5.6 SQUID.....	181
[Fe(L20) ₂][Fe(L20) ₂ (H ₂ O) ₂][BF ₄] ₄ ·MeNO ₂ ·H ₂ O	181
[Fe(L21) ₂][BF ₄] ₂	182
5.7 Conclusions.....	183
List of References	184
Chapter 6 Experimental	185
6.1 General Experimental Considerations.....	186
6.1.1 Analytical techniques used.....	186
6.1.2 Obtaining single crystals for XRD crystallography.....	187
6.1.3 Simulating powder patterns.....	187
6.1.4 Calculating T _{1/2} from SQUID magnetic susceptibility graphs	188
6.1.5 DSC measurements.....	188
6.1.6 Labelling schemes for NMR assignment for each chapter	188
6.2 Chapter 2 - Bis(pyrazol-1-yl)pyridine derivatives with no long alkyl chains, and their iron(II) complexes	189
6.2.1 L1 - 2,6-dibromo pyridine-4-carboxylic acid.....	189
6.2.2 L2 - 2,6-di(1H-pyrazole-1'-yl)pyridine-4-carboxylic acid ...	190
6.2.3 L3 - 3,4-dimethoxyphenyl (2,6-di-1H-pyrazole-1- yl)pyridine-4-carboxylate	190
6.2.4 L4 - 4-methoxyphenyl (2,6-di-1H-pyrazole-1- yl)pyridine-4-carboxylate	191
6.2.5 L5 - 3,4-dihydroxyphenyl (2,6-di-1H-pyrazole-1- yl)pyridine-4-carboxylate	192
6.2.6 L6 - 4-hydroxyphenyl (2,6-di-1H-pyrazole-1-yl)pyridine- 4-carboxylate.....	193
6.2.7 L7 - 1,4-di(2,6-di(1H-pyrazol-1'-yl)pyridine-4- carboxy)benzene.....	193
6.2.8 L8 - 3,4-methoxybenzyl (2,6-di-1H-pyrazol-1- yl)pyridine-4-carboxylate	194
6.2.9 L9 - 4-methoxybenzyl (2,6-di-1H-pyrazol-1-yl)pyridine- 4-carboxylate.....	195
6.2.10 L10 - benzyl (2,6-di-1H-pyrazol-1-yl)pyridine-4- carboxylate.....	195
6.2.11 Iron(II) complexes from chapter 2	196

6.3 Chapter 3 - Pyridine-substituted bis(pyrazol-1-yl)pyridine derivatives with long alkyl chains, and their iron(II) complexes	199
6.3.1 L11Cx - alkyl (2,6-di-1H-pyrazol-1-yl)pyridine-4-carboxylates	200
L11C6 - hexyl (2,6-di-1H-pyrazol-1-yl)pyridine-4-carboxylate.....	200
L11C12 - dodecyl (2,6-di-1H-pyrazol-1-yl)pyridine-4-carboxylate.....	200
L11C14 - tetradecyl (2,6-di-1H-pyrazol-1-yl)pyridine-4-carboxylate.....	201
L11C16 - hexadecyl (2,6-di-1H-pyrazol-1-yl)pyridine-4-carboxylate.....	202
L11C18 - octadecyl (2,6-di-1H-pyrazol-1-yl)pyridine-4-carboxylate.....	202
6.3.2 L12CxM and L12CxM - 4-alkyloxyphenols and 1,4-bis(alkyloxy)benzenes	203
L12C6	203
L12C12	204
L12C14	205
L12C16	205
L12C18	206
6.3.3 L13Cx - 4-(alkyl)phenyl 2,6-di-1H-pyrazol-1-ylisonicotinates.....	207
L13C6	207
L13C12	208
L13C14	208
L13C16	209
L13C18	209
6.3.4 [Fe(L11Cx) ₂][BF ₄] ₂	210
[Fe(L11C6) ₂][BF ₄] ₂	210
[Fe(L11C12) ₂][BF ₄] ₂	211
[Fe(L11C14) ₂][BF ₄] ₂	211
[Fe(L11C16) ₂][BF ₄] ₂	211
[Fe(L11C18) ₂][BF ₄] ₂ ·2.5H ₂ O.....	212
6.3.5 [Fe(L13Cx) ₂][BF ₄] ₂	212
[Fe(L13C6) ₂][BF ₄] ₂	213
[Fe(L13C12) ₂][BF ₄] ₂	213

	[Fe(L13C14) ₂][BF ₄] ₂	213
	[Fe(L13C16) ₂][BF ₄] ₂	214
	[Fe(L13C18) ₂][BF ₄] ₂	214
6.4	Pyrazole-substituted bis(pyrazol-1-yl)pyridine derivatives with long alkyl chains, and their iron(II) complexes	215
6.4.1	L14, L15, L16 – the precursors	215
	L14 - 2-Fluoro-6-(1 <i>H</i> -pyrazol-1-yl)pyridine	215
	L15 - 2,6-Bis(4-iodo-1 <i>H</i> -pyrazol-1-yl)pyridine.....	216
	L16 - 2-(4-iodo-1 <i>H</i> -pyrazol-1-yl)-6-(1 <i>H</i> -pyrazol-1- yl)pyridine.....	216
6.4.2	L17C _x M - 2-(4-alkyl-1-yn-1-yl-1 <i>H</i> -pyrazol-1-yl)-6-(1 <i>H</i> - pyrazol-1-yl)pyridines	217
	L17C12M	217
	L17C14M	218
	L17C16M	219
	L17C18M	219
6.4.3	L17C _x D - 2,6-bis(4-alk-1-yn-1-yl-1 <i>H</i> -pyrazol-1- yl)pyridines	220
	L17C12D	220
	L17C14D	221
	L17C16D	221
6.4.4	L18C _x M - 2-(4-alk-1 <i>H</i> -pyrazol-1-yl)-6-(1 <i>H</i> -pyrazol-1- yl)pyridines	222
	L18C12M	222
	L18C14M	223
	L18C16M	223
	L18C18M	224
6.4.5	L18C _x D - 2-(4-alk-1 <i>H</i> -pyrazol-1-yl)-6-(1 <i>H</i> -pyrazol-1- yl)pyridines	224
	L18C12D	224
	L18C14D	225
	L18C16D	225
6.4.6	Iron(II) complexes	226
	[Fe(L16) ₂][BF ₄] ₂	226
	[Fe(L17C _x M) ₂][BF ₄] ₂	227
	[Fe(L17C12M) ₂][BF ₄] ₂	227
	[Fe(L17C14M) ₂][BF ₄] ₂	227

[Fe(L17C16M) ₂][BF ₄] ₂	228
[Fe(L17C18M) ₂][BF ₄] ₂	228
[Fe(L17CxM) ₂][BF ₄] ₂	228
[Fe(L17C12D) ₂][BF ₄] ₂	228
[Fe(L17C14D) ₂][BF ₄] ₂	229
[Fe(L17C16D) ₂][BF ₄] ₂	229
[Fe(L18CxM) ₂][BF ₄] ₂	229
[Fe(L18C12M) ₂][BF ₄] ₂	230
[Fe(L18C14M) ₂][BF ₄] ₂	230
[Fe(L18C16M) ₂][BF ₄] ₂	230
[Fe(L18C18M) ₂][BF ₄] ₂	231
[Fe(L18CxM) ₂][BF ₄] ₂	231
[Fe(L18C12D) ₂][BF ₄] ₂	231
[Fe(L18C14D) ₂][BF ₄] ₂	232
[Fe(L18C16D) ₂][BF ₄] ₂	232
6.5 Asymmetric ligands with no long alkyl chains, and iron(II) complexes.....	233
6.5.1 L19 - 2-(1H-pyrazol-1-yl)-6-(1H-1,2,3-triazol-1- yl)pyridine.....	233
6.5.2 L20 - 2-(1H-pyrazol-1-yl)-6-(1H-1,2,4-triazol-1- yl)pyridine.....	233
6.5.3 L21 - 2-(4-(ethylcarboxy)pyrazol-1-yl)-6-(1H-pyrazol-1- yl)pyridine.....	234
6.5.4 [Fe(L20) ₂][Fe(L20) ₂ (H ₂ O) ₂][BF ₄] ₄ ·MeNO ₂ ·H ₂ O.....	235
6.5.5 [Fe(L21) ₂][BF ₄] ₂	235
List of References.....	236
Appendix A Crystallographic Tables.....	237

List of Tables

Table 2.1 XRD structures, collected for different solvates of [Fe(L3) ₂][BF ₄] ₂ , [Fe(L4) ₂][BF ₄] ₂ , [Fe(L5) ₂][BF ₄] ₂ , [Fe(L6) ₂][BF ₄] ₂ , [Fe(L8) ₂][BF ₄] ₂ , [Fe(L9) ₂][BF ₄] ₂ , and [Fe(L10) ₂][BF ₄] ₂	40
Table 2.2 Comparison of the unit cells for the two polymorphs of [Fe(L3) ₂][BF ₄] ₂ ·2MeNO ₂	41
Table 2.3 Comparison of the unit cells for [Fe(L4) ₂][BF ₄] ₂ grown from different solvents	42
Table 2.4 Comparison of the unit cells of [Fe(L8) ₂][BF ₄] ₂ , [Fe(L9) ₂][BF ₄] ₂ , and [Fe(L10) ₂][BF ₄] ₂	45
Table 2.5 Typical values of the distortion parameters for iron(II) complexes of bpp derivatives ^{6,7}	52
Table 2.6 Percentage of [Fe(L6) ₂][BF ₄] ₂ ·0.5H ₂ O switched to HS at different temperatures, based on average Fe-N bond length	53
Table 2.7 Percentage of [Fe(L6) ₂][BF ₄] ₂ ·0.5H ₂ O switched to HS at different temperatures, based on the volume of the coordination octahedron	53
Table 2.8 The distortion parameters of [Fe(L3) ₂][BF ₄] ₂ ·2MeNO ₂ and [Fe(L4) ₂][BF ₄] ₂	54
Table 2.9 The distortion parameters of the [Fe(L5) ₂][BF ₄] ₂ and [Fe(L6) ₂][BF ₄] ₂ ·0.5H ₂ O	54
Table 2.10 The distortion parameters of [Fe(L6) ₂][BF ₄] ₂ ·0.5H ₂ O	55
Table 2.11 The distortion parameters of the crystal structures [Fe(L8) ₂][BF ₄] ₂ ·0.5MeCN, [Fe(L9) ₂][BF ₄] ₂ ·1.5MeCN, and [Fe(L10) ₂][BF ₄] ₂ ·1.5MeCN	55
Table 2.12 The distortion parameters of the crystal structures of [Fe(L3) ₂][BF ₄] ₂ ·2MeCN·3H ₂ O, and [Fe(L3) ₂][BF ₄] ₂ ·2MeNO ₂ yellow polymorph	56
Table 3.1 Crystal structures from Chapter 3	70
Table 3.2 Unit cells of L11C12, L11C14, L12C12M and L12C14M	73
Table 3.3 Unit cells of L13C12M and L13C14M	74
Table 3.4 Unit cells of [Fe(L11C6) ₂][BF ₄] ₂ ·2H ₂ O, [Fe(L13C6) ₂][BF ₄] ₂ ·H ₂ O, [Fe(L13C14) ₂][BF ₄] ₂ ·2MeCN, and [Fe(L13C16) ₂][BF ₄] ₂ ·H ₂ O	75
Table 3.5 The distortion parameters for the crystal structures of [Fe(L11C6) ₂][BF ₄] ₂ ·2H ₂ O, [Fe(L13C6) ₂][BF ₄] ₂ ·H ₂ O, [Fe(L13C14) ₂][BF ₄] ₂ ·2MeCN, and [Fe(L13C16) ₂][BF ₄] ₂ ·H ₂ O	77
Table 3.6 Assigning lattice solvents to [Fe(L11Cx) ₂][BF ₄] ₂ based on TGA, CHN and XRD	85

Table 3.7 Assigning lattice solvents to $[\text{Fe}(\text{L13Cx})_2][\text{BF}_4]_2$ based on TGA, CHN and XRD	89
Table 4.1 ^1H NMR spectra comparison for L17C14M and L18C14M	125
Table 4.2 ^{13}C NMR spectra comparison for L17C14M and L18C14M	126
Table 4.3 Unit cells of L17C12D, L17C16D, L17C12M, L18C12M, and L18C14M	130
Table 4.4 Unit cells of $[\text{Fe}(\text{L17C18M})_2][\text{BF}_4]_2$, $[\text{Fe}(\text{L18C12M})_2][\text{BF}_4]_2$, $[\text{Fe}(\text{L18C16M})_2][\text{BF}_4]_2$, and $[\text{Fe}(\text{L18C18M})_2][\text{BF}_4]_2$	136
Table 4.5 Distortion parameters of the iron complexes from chapter 4	137
Table 4.6 The distortion parameters for the crystal structures of $[\text{Fe}(\text{L16})_2][\text{ClO}_4]_2 \cdot 2\text{MeCN}$ and $[\text{Fe}(\text{L18C16M})_2][\text{BF}_4]_2$	137
Table 5.1 Unit cells of L19 and L20	177
Table 5.2 Solvent content in crystal structures of $[\text{Fe}(\text{L20})_2][\text{Fe}(\text{L20})_2(\text{H}_2\text{O})_2][\text{BF}_4]_4 \cdot \text{MeNO}_2 \cdot n\text{H}_2\text{O}$ at different temperatures based on crystal structures	177
Table 5.3 Unit cell parameters for five crystal structures of $[\text{Fe}(\text{L20})_2][\text{Fe}(\text{L20})_2(\text{H}_2\text{O})_2][\text{BF}_4]_4 \cdot \text{MeNO}_2 \cdot n\text{H}_2\text{O}$	179
Table 5.4 Comparison of the octahedral volumes around the two iron centres in crystal structures of $[\text{Fe}(\text{L20})_2][\text{Fe}(\text{L20})_2(\text{H}_2\text{O})_2][\text{BF}_4]_4 \cdot \text{MeNO}_2 \cdot \text{H}_2\text{O}$ at different temperatures	180
Table 5.5 Comparison of Fe-N bond lengths for the two iron centres in crystal structures of $[\text{Fe}(\text{L20})_2][\text{Fe}(\text{L20})_2(\text{H}_2\text{O})_2][\text{BF}_4]_4 \cdot \text{MeNO}_2 \cdot \text{H}_2\text{O}$ at different temperatures	180

List of Figures

Fig. 1.1 Number of research articles containing concept “spin crossover” per each year from 1970 till 2018, according to SciFinder ³	2
Fig. 1.2 Low Spin to High Spin transition of Fe ²⁺ ion in octahedral ligand field	3
Fig. 1.3 Chemical structures of some tridentate ligand cores mentioned in this chapter: bpp - 2,6-bis(pyrazol-1-yl)pyridine, try - 2,2';6',2"-terpyridine, and dpt - 2,4-dipyrazolyl-1,3,5-triazine	3
Fig. 1.4 The five elements that can form homonuclear SCO complexes	3
Fig. 1.5 Types of SCO in solid state: A – gradual, B – abrupt, C – with hysteresis, D – with steps, E – incomplete ³⁰	5
Fig. 1.6 Photo-switchable system obtained by Oshio <i>et al.</i>	7
Fig. 1.7 Schematic representation of the main mesophases of rod-like molecules	10
Fig. 1.8 Schematic representation of the main mesophases of disc-like molecules	10
Fig. 1.9 Calamitic (rod-like) liquid crystal molecule structure and its physical model (left) vs discotic (disc-like) liquid crystal and its physical model (right) ⁶⁷	11
Fig. 1.10 Differential Scanning Calorimetry of octyloxy-cyanobiphenyl at the 1°C/min rate ⁶⁹	12
Fig. 1.11 Chemical structure of 4-hexadecyloxy-N-(2-pyridinylmethylene) -benzenamine [Fe(bzimpy) ₂ (NCS) ₂]	13
Fig. 1.12 Chemical structures of the bzimpy derivatives ligands: A – 2,6-bis(benzimidazol-2'-yl)-4-hexadecyloxy pyridine, and B – 2,6-bis(N-hexadecylbenzimidazol-2'-yl)pyridine	13
Fig. 1.13 Structures of the tripod iron complexes obtained by Real <i>et al.</i> ...	14
Fig. 1.14 Series of SCO coordination polymers, obtained by Aida <i>et al.</i>	14
Fig. 1.15 Coordination polymer with long alkyl chain counterions	15
Fig. 1.16 Long alkyl chain SCO complexes, obtained by Gutlich <i>et al.</i>	15
Fig. 1.17 SCO complexes with alkyl chains, obtained by Weber <i>et al.</i>	16
Fig. 1.18 A N4-hexadecyl-3,5-di(2-pyridyl)-4H1,2,4-triazole	16
Fig. 1.19 The influence of the bridging ligand on the SCO properties of Fe ²⁺ 1D coordination polymers	17
Fig. 1.20 Magnetic tristability observed by Clerac <i>et al.</i>	17
Fig. 1.21 SCO series obtained by Albrecht <i>et al.</i>	18
Fig. 1.22 Dendrimeres reported by: A – Gutlich, ⁸⁵ B – Aida, Schluter ⁸⁶	18

Fig. 1.23 SCO Co ²⁺ complex with a lipophilic glutamate counterion.....	19
Fig. 2.1. The list of the ligands, discussed in chapter 2. The bpp core is highlighted in blue	30
Fig. 2.2. Synthesis of 2,6-dibromo pyridine-4-carboxylic acid	30
Fig. 2.3. Synthesis of 2,6-di(1H-pyrazole-1'-yl)pyridine-4-carboxylic acid	31
Fig. 2.4. Comparison of ¹ H NMRs of the two forms of 2,6-di(1H-pyrazole-1'-yl)pyridine-4-carboxylic acid, measured in DMSO-D ₆	31
Fig. 2.5. Synthesis of L3 and L4	32
Fig. 2.6. Synthesis of L5 and L6	32
Fig. 2.7. Synthesis of L7	33
Fig. 2.8 ¹ H NMR of L7 in DMSO-D ₆ : full view and an expansion	33
Fig. 2.9. Synthesis of L8, L9, L10	34
Fig. 2.10 General scheme for obtaining iron(II) complexes in chapter 2	35
Fig. 2.11 Crystal structure of L2 and its packing diagram from the view, parallel to the [010] vector	36
Fig. 2.13 Crystal structure of L3 and its packing diagram from the view, parallel to the [010] vector	36
Fig. 2.12 Crystal structure of L4 and its packing diagram from the view, parallel to the [010] vector	36
Fig. 2.14 Crystal structure of L6 and its packing diagram from the view, parallel to the [010] vector	37
Fig. 2.15 Crystal structure of the ligand L7 and its packing diagram from the view, parallel to the vector [001].....	37
Fig. 2.16 Crystal structure of L8·0.5MeCN and its packing diagram from the view, parallel to the [100] vector.....	38
Fig. 2.17 Crystal structure of L9 and its packing diagram from the view, parallel to the [010] vector	38
Fig. 2.18 Crystal structure of L10 and its packing diagram from the view, parallel to the [100] vector.....	39
Fig. 2.19 Packing for the [Fe(L3) ₂][BF ₄] ₂ ·2MeNO ₂ : red polymorph (left) and the yellow polymorph (right)	41
Fig. 2.20 Crystal structure of [Fe(L4) ₂][BF ₄] ₂ at 120K, and its packing diagram from the view, parallel to the [010] vector	42
Fig. 2.21 Crystal structure of [Fe(L5) ₂][BF ₄] ₂ at 120K, and its packing diagram from the view, parallel to the [100] vector.....	43
Fig. 2.22 Crystal structure of [Fe(L6) ₂][BF ₄] ₂ ·0.5H ₂ O at 250K, and its packing diagram from the view, parallel to the [100] vector	43
Fig. 2.23 Crystal structure of [Fe(L8) ₂][BF ₄] ₂ ·0.25MeCN, and its packing diagram from the view, parallel to the [100] vector.....	44

Fig. 2.24 Crystal structure of $[\text{Fe}(\text{L9})_2][\text{BF}_4]_2 \cdot 1.5\text{MeCN}$, and its packing diagram from the view, parallel to the $[010]$ vector.....	46
Fig. 2.25 Crystal structure of $[\text{Fe}(\text{L10})_2][\text{BF}_4]_2 \cdot 1.5\text{MeCN}$, and its packing diagram from the view, parallel to the $[100]$ vector.....	46
Fig. 2.26 Variable temperature magnetic susceptibility of $[\text{Fe}(\text{L3})_2][\text{BF}_4]_2 \cdot 2\text{MeNO}_2$ yellow polymorph, and $[\text{Fe}(\text{L4})_2][\text{BF}_4]_2$	47
Fig. 2.27 Variable temperature magnetic susceptibility of $[\text{Fe}(\text{L5})_2][\text{BF}_4]_2$ and $[\text{Fe}(\text{L6})_2][\text{BF}_4]_2 \cdot 0.5\text{H}_2\text{O}$	48
Fig. 2.28 Variable temperature magnetic susceptibility of $[\text{Fe}(\text{L8})_2][\text{BF}_4]_2 \cdot \text{Me}_2\text{CO} \cdot 0.25\text{H}_2\text{O}$, $[\text{Fe}(\text{L9})_2][\text{BF}_4]_2 \cdot 0.5\text{Me}_2\text{CO}$, and $[\text{Fe}(\text{L10})_2][\text{BF}_4]_2 \cdot \frac{2}{3}\text{Me}_2\text{CO}$	49
Fig. 2.29 Variable temperature magnetic susceptibility of $[\text{Fe}(\text{L9})_2][\text{BF}_4]_2 \cdot 1.5\text{MeCN}$	49
Fig. 2.30 Variable temperature magnetic susceptibility of $[\text{Fe}(\text{L10})_2][\text{BF}_4]_2 \cdot 1.5\text{MeCN}$	50
Fig. 2.31 Typical labelling of the Fe and N atoms in an iron(II) complex of a bpp derivative, used in the distortion parameters calculations.....	51
Fig. 2.32 Collected and simulated powder patterns of $[\text{Fe}(\text{L3})_2][\text{BF}_4]_2 \cdot 2\text{MeNO}_2$, $[\text{Fe}(\text{L4})_2][\text{BF}_4]_2$, $[\text{Fe}(\text{L5})_2][\text{BF}_4]_2$, and $[\text{Fe}(\text{L6})_2][\text{BF}_4]_2 \cdot \text{Me}_2\text{CO}$	57
Fig. 2.33 Collected and simulated powder patterns of $[\text{Fe}(\text{L8})_2][\text{BF}_4]_2 \cdot 0.25\text{MeCN}$, $[\text{Fe}(\text{L9})_2][\text{BF}_4]_2 \cdot 1.5\text{MeCN}$, and $[\text{Fe}(\text{L10})_2][\text{BF}_4]_2 \cdot 1.5\text{MeCN}$	58
Fig. 2.34 Collected and simulated powder patterns of $[\text{Fe}(\text{L8})_2][\text{BF}_4]_2 \cdot \text{Me}_2\text{CO} \cdot 0.25\text{H}_2\text{O}$, $[\text{Fe}(\text{L9})_2][\text{BF}_4]_2 \cdot 0.5\text{Me}_2\text{CO}$, and $[\text{Fe}(\text{L10})_2][\text{BF}_4]_2 \cdot \frac{2}{3}\text{Me}_2\text{CO}$	58
Fig. 2.35 Evans method NMRs of $[\text{Fe}(\text{L3})_2][\text{BF}_4]_2$, $[\text{Fe}(\text{L4})_2][\text{BF}_4]_2$, $[\text{Fe}(\text{L5})_2][\text{BF}_4]_2$, and $[\text{Fe}(\text{L6})_2][\text{BF}_4]_2$, measured in MeCN-D_3	59
Fig. 2.36 Paramagnetic NMR of $[\text{Fe}(\text{L3})_2][\text{BF}_4]_2$, measured in MeCN-D_3	60
Fig. 2.37 Paramagnetic NMR of $[\text{Fe}(\text{L8})_2][\text{BF}_4]_2$, measured in MeCN-D_3	60
Fig. 3.1. The ligands, discussed in the chapter 3.....	65
Fig. 3.2. Synthesis of L11C6, L11C12, L11C14, L11C16, and L11C18.....	65
Fig. 3.3. ^1H NMR of L11C14 in CDCl_3 , typical for all L11Cx ligands.....	66
Fig. 3.4. ^{13}C NMR of L11C14 in CDCl_3 : full view and an expansion.....	66
Fig. 3.5 Synthesis of L12C6, L12C12, L12C14, L12C16, and L12C18.....	67
Fig. 3.6. ^1H NMR of L12C14 in CDCl_3 , typical for all L12Cx ligands.....	67
Fig. 3.7. ^{13}C NMR of L12C14 in CDCl_3 : full view and an expansion.....	67
Fig. 3.8 Synthesis of 4-(alkyl)phenyl 2,6-di-1H-pyrazol-1-ylisonicotinates.....	68
Fig. 3.9. ^1H NMR of L13C14 in CDCl_3 , typical for all L13Cx ligands.....	69

Fig. 3.10. ^{13}C NMR of L13C14 in CDCl_3 : full view and an expansion.....	69
Fig. 3.11. General scheme for obtaining iron(II) complexes in chapter 3	69
Table 3.1 Crystal structures from chapter 3	70
Fig. 3.12. Chemical formula, crystal structure, and packing diagram from the view, parallel to the [010] vector, for the DCC intermediate	71
Fig. 3.13. Crystal structure of L11C12 and its packing diagram from the view, parallel to the [010] vector.....	72
Fig. 3.14. Crystal structure of L12C12M and its packing diagram from the view, parallel to the [010] vector.....	72
Fig. 3.15. Crystal structure of L13C12 and its packing diagram from the view, parallel to the [001] vector.....	73
Fig. 3.16. Crystal structure of $[\text{Fe}(\text{L11C6})_2][\text{BF}_4]\cdot 2\text{H}_2\text{O}$ and its packing diagram from the view, parallel to the [001] vector.....	74
Fig. 3.17. Crystal structure of $[\text{Fe}(\text{L13C6})_2][\text{BF}_4]\cdot \text{H}_2\text{O}$ and its packing diagram from the view, parallel to the [100] vector.....	75
Fig. 3.18. Crystal structure of $[\text{Fe}(\text{L13C14})_2][\text{BF}_4]\cdot 2\text{MeCN}$ and its packing diagram from the view, parallel to the [100] vector	76
Fig. 3.19. Crystal structure of $[\text{Fe}(\text{L13C16})_2][\text{BF}_4]\cdot \text{H}_2\text{O}$ and its packing diagram from the view, parallel to the [010] vector.....	76
Fig. 3.20 Variable temperature magnetic susceptibility of $[\text{Fe}(\text{L11C6})_2][\text{BF}_4]_2\cdot 2\text{H}_2\text{O}$, $[\text{Fe}(\text{L11C12})_2][\text{BF}_4]_2\cdot 0.25\text{Me}_2\text{CO}$, and $[\text{Fe}(\text{L11C16})_2][\text{BF}_4]_2$	78
Fig. 3.21 Variable temperature magnetic susceptibility of $[\text{Fe}(\text{L11C14})_2][\text{BF}_4]_2$, showing hysteresis	78
Fig. 3.22 Variable temperature magnetic susceptibility of $[\text{Fe}(\text{L11C18})_2][\text{BF}_4]_2$: annealed at 170°C vs the fresh sample.....	79
Fig. 3.23 Variable temperature magnetic susceptibility of $[\text{Fe}(\text{L13C6})_2]$ $[\text{BF}_4]_2\cdot \text{H}_2\text{O}$, $[\text{Fe}(\text{L13C14})_2][\text{BF}_4]_2\cdot \text{H}_2\text{O}$, $[\text{Fe}(\text{L13C18})_2][\text{BF}_4]_2\cdot 1.4\text{H}_2\text{O}$, and the two measurements of $[\text{Fe}(\text{L13C12})_2][\text{BF}_4]_2$	80
Fig. 3.24 Variable temperature magnetic susceptibility of $[\text{Fe}(\text{L13C16})_2][\text{BF}_4]_2\cdot 1.6\text{H}_2\text{O}$: annealed at 170°C vs the fresh sample	80
Fig. 3.25. DSC of L11C6	81
Fig. 3.26. DSC of L11C14	82
Fig. 3.27. DSC of L11C18	82
Fig. 3.28. TGA of L11C6, L11C12, L11C14, L11C16, and L11C18	82
Fig. 3.29. DSC of L13C6, which is typical for the L13Cx series	83
Fig. 3.30. DSC of L13C12, not similar to the other L13Cx ligands	83
Fig. 3.31. TGA of L13C6, L13C12, L13C14, L13C16, and L13C18	84

Fig. 3.33. DSC of $[\text{Fe}(\text{L11C12})_2][\text{BF}_4]_2 \cdot 0.25\text{Me}_2\text{CO}$	86
Fig. 3.34. DSC of $[\text{Fe}(\text{L11C14})_2][\text{BF}_4]_2$	87
Fig. 3.35. DSC of $[\text{Fe}(\text{L11C16})_2][\text{BF}_4]_2$, showing annealing.....	87
Fig. 3.36. DSC of $[\text{Fe}(\text{L11C16})_2][\text{BF}_4]_2$	87
Fig. 3.37. DSC of $[\text{Fe}(\text{L11C18})_2][\text{BF}_4]_2$	88
Fig. 3.38. TGA of $[\text{Fe}(\text{L11C6})_2][\text{BF}_4]_2 \cdot 2\text{H}_2\text{O}$, $[\text{Fe}(\text{L11C12})_2][\text{BF}_4]_2 \cdot 0.25\text{Me}_2\text{CO}$, $[\text{Fe}(\text{L11C14})_2][\text{BF}_4]_2$, $[\text{Fe}(\text{L11C16})_2][\text{BF}_4]_2$, and $[\text{Fe}(\text{L11C18})_2][\text{BF}_4]_2$	88
Fig. 3.39. DSC of $[\text{Fe}(\text{L13C6})_2][\text{BF}_4]_2 \cdot \text{H}_2\text{O}$	90
Fig. 3.40. DSC of $[\text{Fe}(\text{L13C12})_2][\text{BF}_4]_2$	90
Fig. 3.41. DSC of $[\text{Fe}(\text{L13C14})_2][\text{BF}_4]_2 \cdot \text{H}_2\text{O}$	91
Fig. 3.42. DSC of $[\text{Fe}(\text{L13C16})_2][\text{BF}_4]_2 \cdot 1.6\text{H}_2\text{O}$	91
Fig. 3.43. DSC of $[\text{Fe}(\text{L13C18})_2][\text{BF}_4]_2 \cdot 1.4\text{H}_2\text{O}$	91
Fig. 3.44. TGA of $[\text{Fe}(\text{L13C6})_2][\text{BF}_4]_2 \cdot \text{H}_2\text{O}$, $[\text{Fe}(\text{L13C12})_2][\text{BF}_4]_2$, $[\text{Fe}(\text{L13C14})_2][\text{BF}_4]_2 \cdot \text{H}_2\text{O}$, $[\text{Fe}(\text{L13C16})_2][\text{BF}_4]_2 \cdot 1.6\text{H}_2\text{O}$, and $[\text{Fe}(\text{L13C18})_2][\text{BF}_4]_2 \cdot 1.4\text{H}_2\text{O}$	92
Fig. 3.45. Changes in appearance of $[\text{Fe}(\text{L13Cx})_2][\text{BF}_4]_2$ iron complexes series with heating from room temperature to 170°C	93
Fig. 3.46. Changes in appearance of $[\text{Fe}(\text{L11Cx})_2][\text{BF}_4]_2$ iron complexes series with heating from room temperature to 170°C	94
Fig. 3.47. Collected and simulated powder patterns of L11Cx ligands	95
Fig. 3.48. Collected and simulated powder patterns of L13Cx ligands	96
Fig. 3.49. Powder patterns of $[\text{Fe}(\text{L11C6})_2][\text{BF}_4]_2 \cdot 2\text{H}_2\text{O}$, $[\text{Fe}(\text{L11C12})_2][\text{BF}_4]_2 \cdot 0.25\text{Me}_2\text{CO}$, $[\text{Fe}(\text{L11C14})_2][\text{BF}_4]_2$, and $[\text{Fe}(\text{L11C16})_2][\text{BF}_4]_2$, collected at room temperature, 100°C , 170°C , and, where available, simulated powder patterns.....	98
Fig. 3.50. Powder patterns of $[\text{Fe}(\text{L13C6})_2][\text{BF}_4]_2 \cdot \text{H}_2\text{O}$, $[\text{Fe}(\text{L13C12})_2][\text{BF}_4]_2$, $[\text{Fe}(\text{L13C14})_2][\text{BF}_4]_2 \cdot \text{H}_2\text{O}$, and $[\text{Fe}(\text{L13C16})_2][\text{BF}_4]_2 \cdot 1.6\text{H}_2\text{O}$, collected at room temperature, 100°C , 170°C , and, where available, simulated powder patterns.....	99
Fig. 3.51. Powder patterns of $[\text{Fe}(\text{L11C18})_2][\text{BF}_4]_2$, and $[\text{Fe}(\text{L13C18})_2][\text{BF}_4]_2 \cdot 1.4\text{H}_2\text{O}$ collected at room temperature, 100°C , and 170°C	100
Fig. 3.52. Evans method NMRs of $[\text{Fe}(\text{L11C16})_2][\text{BF}_4]_2$ and $[\text{Fe}(\text{L13C16})_2][\text{BF}_4]_2$, measured in MeCN-D ₃ :CDCl ₃ 1:1 mixture	110
Fig. 3.53. Paramagnetic NMR of $[\text{Fe}(\text{L11C16})_2][\text{BF}_4]_2$, measured in MeCN-D ₃ , typical for $[\text{Fe}(\text{L11Cx})_2][\text{BF}_4]_2$ series.....	111
Fig. 3.54. Paramagnetic ¹ H NMR of $[\text{Fe}(\text{L13C16})_2][\text{BF}_4]_2$, measured in MeCN-D ₃ , typical for $[\text{Fe}(\text{L11Cx})_2][\text{BF}_4]_2$ series.....	111
Fig. 3.55. Paramagnetic ¹ H NMR of $[\text{Fe}(\text{L13C16})_2][\text{BF}_4]_2$, measured in MeCN-D ₃ :CDCl ₃ 1:1 mixture, typical for $[\text{Fe}(\text{L13Cx})_2][\text{BF}_4]_2$ series ..	112

Fig. 3.56. Paramagnetic ^1H NMR of $[\text{Fe}(\text{L13C12})_2][\text{BF}_4]_2$, measured in MeCN-D ₃ :CDCl ₃ 1:1 mixture.....	112
Fig. 4.1 The list of ligands discussed in chapter 4.....	119
Fig. 4.2 Synthesis of 2,6-bis(4-iodo-1H-pyrazol-1-yl)pyridine L15.....	120
Fig. 4.3 Synthesis of 2-fluoro-6-(1H-pyrazol-1-yl)pyridine L14.....	120
Fig. 4.4 Synthesis of 2-(3-iodo-1H-pyrazol-1-yl)-6-(1H-pyrazol-1-yl)pyridine L16.....	120
Fig. 4.5 ^{13}C NMR of L14 2-fluoro-6-(1H-pyrazol-1-yl)pyridine, measured in CDCl ₃ , showing doubling of certain peaks.....	120
Fig. 4.6 ^{19}F NMR of L14 2-fluoro-6-(1H-pyrazol-1-yl)pyridine, measured in CDCl ₃	120
Fig. 4.7 Synthesis of L17CxM ligands.....	121
Fig. 4.8 ^1H NMR of L17C14M with expansion, measured in CDCl ₃ , typical for L17CxM ligands series.....	122
Fig. 4.9 ^{13}C NMR of L17C14M with expansion, measured in CDCl ₃ , typical for L17CxM ligand series.....	122
Fig. 4.10 Synthesis of L17CxD ligands.....	122
Fig. 4.11 ^1H NMR of L15, measured in CDCl ₃	123
Fig. 4.12 ^1H NMR of L17C14D in CDCl ₃ , typical for L17CxD ligand series.....	123
Fig. 4.13 ^{13}C NMR of L17C14D with expansion, measured in CDCl ₃ , typical for L17CxD ligand series.....	124
Fig. 4.14 Synthesis of L18CxM ligands.....	124
Fig. 4.15 ^1H NMR of L18C14M with expansions, measured in CDCl ₃ , typical for L18CxM series.....	125
Fig. 4.16 ^{13}C NMR of L18C14M with expansion, measured in CDCl ₃ , typical for L18CxM series.....	126
Fig. 4.18 Synthesis of L18CxD ligands.....	126
Fig. 4.19 ^1H NMR of L18C14D with expansions, measured in CDCl ₃ , typical for L18CxD series.....	127
Fig. 4.20 ^{13}C NMR of L18C14D with expansion, measured in CDCl ₃ , typical for L18CxD series.....	127
Fig. 4.21 General scheme for obtaining iron(II) complexes in chapter 4 ...	128
Fig. 4.22 Crystal structure of L14 and its packing diagram from the view, parallel to the [100] vector.....	129
Fig. 4.23 Crystal structure of L15 and its packing diagram from the view, parallel to the [010] vector.....	129
Fig. 4.24 Crystal structure of L16 and its packing diagram from the view, parallel to the [010] vector.....	129

Fig. 4.25 Crystal structure of L17C12D and its packing diagram from the view, parallel to the [010] vector.....	131
Fig. 4.26 Crystal structure of L17C16D and its packing diagram from the view, parallel to the [010] vector.....	131
Fig. 4.27 Crystal structure of L17C12M and its packing diagram from the view, parallel to the [010] vector.....	132
Fig. 4.28 Crystal structure of L18C12M and its packing diagram from the view, parallel to the [100] vector.....	132
Fig. 4.29 Crystal structure of L18C14M and its packing diagram from the view, parallel to the [100] vector.....	133
Fig. 4.30 Crystal structure of $[\text{Fe}(\text{L16})_2][\text{ClO}_4]_2 \cdot 2\text{MeCN}$, collected at 120K, and its packing diagram from the view, parallel to the [010] vector	134
Fig. 4.31 Crystal structure of $[\text{Fe}(\text{L17C18M})_2][\text{BF}_4]_2$, and its packing diagram from the view, parallel to the [010] vector.....	135
Fig. 4.32 Crystal structure of $[\text{Fe}(\text{L18C12M})_2][\text{BF}_4]_2$, and its packing diagram from the view, parallel to the [010] vector.....	135
Fig. 4.33 Crystal structure of $[\text{Fe}(\text{L18C16M})_2][\text{BF}_4]_2$, collected at 120K, and its packing diagram from the view, parallel to the [010] vector ...	135
Fig. 4.34 Crystal structure of $[\text{Fe}(\text{L18C18M})_2][\text{BF}_4]_2$, and its packing diagram from the view, parallel to the [010] vector.....	135
Fig. 4.34 Collected and simulated powder patterns of L17CxM ligands....	138
Fig. 4.35 Collected and simulated powder patterns of L17CxM ligands	138
Fig. 4.36 Collected and simulated powder patterns of L18CxM ligands....	139
Fig. 4.37 Collected and simulated powder patterns of L18CxM ligands	139
Fig. 4.38 Powder pattern of $[\text{Fe}(\text{L18C16M})_2][\text{BF}_4]_2$	139
Fig. 4.39 Collected and simulated powder patterns of $[\text{Fe}(\text{L17CxM})_2][\text{BF}_4]_2$	140
Fig. 4.40 Powder patterns of $[\text{Fe}(\text{L17CxD})_2][\text{BF}_4]_2$	140
Fig. 4.41 Powder patterns of $[\text{Fe}(\text{L18CxM})_2][\text{BF}_4]_2$: fresh samples, annealed at 170°C, and simulated from crystal structures	141
Fig. 4.42 Powder patterns of $[\text{Fe}(\text{L18CxD})_2][\text{BF}_4]_2$	141
Fig. 4.43 SQUID magnetic susceptibility measurements for $[\text{Fe}(\text{L17C12M})_2][\text{BF}_4]_2$, $[\text{Fe}(\text{L17C14M})_2][\text{BF}_4]_2$, and $[\text{Fe}(\text{L17C16M})_2][\text{BF}_4]_2$	142
Fig. 4.44 SQUID magnetic susceptibility measurements for $[\text{Fe}(\text{L17C18M})_2][\text{BF}_4]_2$	143
Fig. 4.45 SQUID magnetic susceptibility measurements for $[\text{Fe}(\text{L17CxD})_2][\text{BF}_4]_2$ iron complexes series	143
Fig. 4.47 SQUID magnetic susceptibility measurements for $[\text{Fe}(\text{L18C14M})_2][\text{BF}_4]_2$ and $[\text{Fe}(\text{L18C18M})_2][\text{BF}_4]_2$	144

Fig. 4.48 SQUID magnetic susceptibility measurements for [Fe(L17C16M) ₂][BF ₄] ₂	145
Fig. 4.49 SQUID magnetic susceptibility measurements for [Fe(L18C12D) ₂][BF ₄] ₂	146
Fig. 4.50 SQUID magnetic susceptibility measurements for [Fe(L18C14D) ₂][BF ₄] ₂	146
Fig. 4.51 SQUID magnetic susceptibility measurements for [Fe(L18C16D) ₂][BF ₄] ₂ and [Fe(L16) ₂][BF ₄] ₂	147
Fig. 4.52 DSC of L17C16M, typical for the L17CxM series	148
Fig. 4.53 DSC of L17C12M, different from the other L17CxM ligands	148
Fig. 4.54 TGA of the L17CxM ligand series.....	149
Fig. 4.55 DSC of the L17C14D, typical for the L17CxM series	149
Fig. 4.56 TGA of the L17CxM ligand series	150
Fig. 4.57 DSC of L18C12M, different from the other L18CxM ligands	150
Fig. 4.58 DSC of L18C14M, typical for the L18CxM series	151
Fig. 4.59 TGA of the L18CxM ligand series.....	151
Fig. 4.60 DSC of L18C12D, typical for the L18CxM series	152
Fig. 4.61 DSC of L18C12D showing annealing upon heating above 250°C	152
Fig. 4.62 TGA of the L18CxM ligand series	152
Fig. 4.63 DSC of [Fe(L17C12M) ₂][BF ₄] ₂	154
Fig. 4.64 DSC of [Fe(L17C14M) ₂][BF ₄] ₂	154
Fig. 4.65 DSC of [Fe(L17C16M) ₂][BF ₄] ₂	154
Fig. 4.66 DSC of [Fe(L17C18M) ₂][BF ₄] ₂	155
Fig. 4.67 TGA of the [Fe(L17CxM) ₂][BF ₄] ₂ series iron complexes	155
Fig. 4.68 DSC of [Fe(L17C12D) ₂][BF ₄] ₂	156
Fig. 4.69 DSC of [Fe(L17C14D) ₂][BF ₄] ₂	156
Fig. 4.70 DSC of [Fe(L17C16D) ₂][BF ₄] ₂	157
Fig. 4.71 TGA of the [Fe(L17CxM) ₂][BF ₄] ₂ series iron complexes	157
Fig. 4.72 DSC of [Fe(L18C12M) ₂][BF ₄] ₂	158
Fig. 4.73 DSC of [Fe(L18C14M) ₂][BF ₄] ₂	158
Fig. 4.74 DSC of [Fe(L18C16M) ₂][BF ₄] ₂	158
Fig. 4.75 DSC of [Fe(L18C18M) ₂][BF ₄] ₂	159
Fig. 4.76 TGA of the [Fe(L18CxM) ₂][BF ₄] ₂ series iron complexes	159
Fig. 4.78 DSC of [Fe(L18C14D) ₂][BF ₄] ₂	160
Fig. 4.79 DSC of [Fe(L18C16D) ₂][BF ₄] ₂	161
Fig. 4.80 TGA of the [Fe(L18CxM) ₂][BF ₄] ₂ series iron complexes	161

Fig. 4.81 The photographs of [(L18CxM) ₂ Fe][BF ₄] ₂ iron complexes, as they are being heated from room temperature to 170°C	162
Fig. 4.82 Evans method NMR of [Fe(L18C16M) ₂][BF ₄] ₂ , measured in Me ₂ CO-D ₆	163
Fig. 4.83 Paramagnetic NMR of [Fe(L16) ₂][BF ₄] ₂ , with extension, identical to [Fe(L16) ₂][ClO ₄] ₂ , collected in MeCN-D ₃	164
Fig. 4.84 Paramagnetic NMR of [Fe(L17C12M) ₂][BF ₄] ₂ , with extension, typical for [Fe(L17CxM) ₂][BF ₄] ₂ series, collected in CDCl ₃	164
Fig. 4.85 Paramagnetic NMR of [Fe(L17C14D) ₂][BF ₄] ₂ , with extension, typical for [Fe(L17CxD) ₂][BF ₄] ₂ series, collected in CDCl ₃ /MeCN-D ₃ 1:1 mixture.....	165
Fig. 4.86 Paramagnetic NMR of [Fe(L18C14M) ₂][BF ₄] ₂ , with extension, typical for [Fe(L18CxM) ₂][BF ₄] ₂ series, collected in MeCN-D ₃	165
Fig. 4.87 Paramagnetic NMR of [Fe(L18C14D) ₂][BF ₄] ₂ , with extension, typical for [Fe(L18CxD) ₂][BF ₄] ₂ series, collected in MeCN-D ₃	166
Fig. 5.1 An asymmetric ligand, obtained by Chandrasekar <i>et al.</i> , and its magnetic behaviour ¹	170
Fig. 5.2 List of the ligands discussed in chapter 5.....	170
Fig. 5.3 Synthesis of 2-(1H-pyrazol-1-yl)-6-(1H -1,2,3-triazol-1-yl)pyridine L19.....	171
Fig. 5.4 ¹ H NMR of the L19-A and L19-B 1:1 mixture with expansion, measured in CDCl ₃ . The peaks from L19-B are highlighted in yellow.	171
Fig. 5.5 Synthesis of 2-(1H-pyrazol-1-yl)-6-(1H -1,2,4-triazol-1-yl)pyridine L20.....	172
Fig. 5.6 ¹ H NMR of L20 with expansion, measured in CDCl ₃	172
Fig. 5.7 ¹³ C NMR of L20 with expansion, measured in CDCl ₃	172
Fig. 5.8 Synthesis of 2-(4-(ethylcarboxy)pyrazol-1-yl)-6-(1H-pyrazol-1-yl)pyridine L21.....	173
Fig. 5.9 ¹ H NMR of L21 with expansion, measured in CDCl ₃ . The pyridine ring spiting signals are highlighted with dots for clarity: Py H4 – red, Py H3 – blue, Py H5 – black.....	173
Fig. 5.10 ¹³ C NMR of L21, measured in CDCl ₃	174
Fig. 5.11 Synthesis of [Fe(L21) ₂][BF ₄] ₂	174
Fig. 5.12 The structure of the coordination polymer [Fe(L20) ₂][Fe(L20) ₂ (H ₂ O) ₂][BF ₄] ₄ ·MeNO ₂ ·H ₂ O.....	175
Fig. 5.13 Paramagnetic ¹ H NMR of [Fe(L21) ₂][BF ₄] ₂ with extension, measured in MeCN-D ₃	176
Fig. 5.14 Crystal structure of L19, and its packing diagram from the view, parallel to the [100] vector.....	176

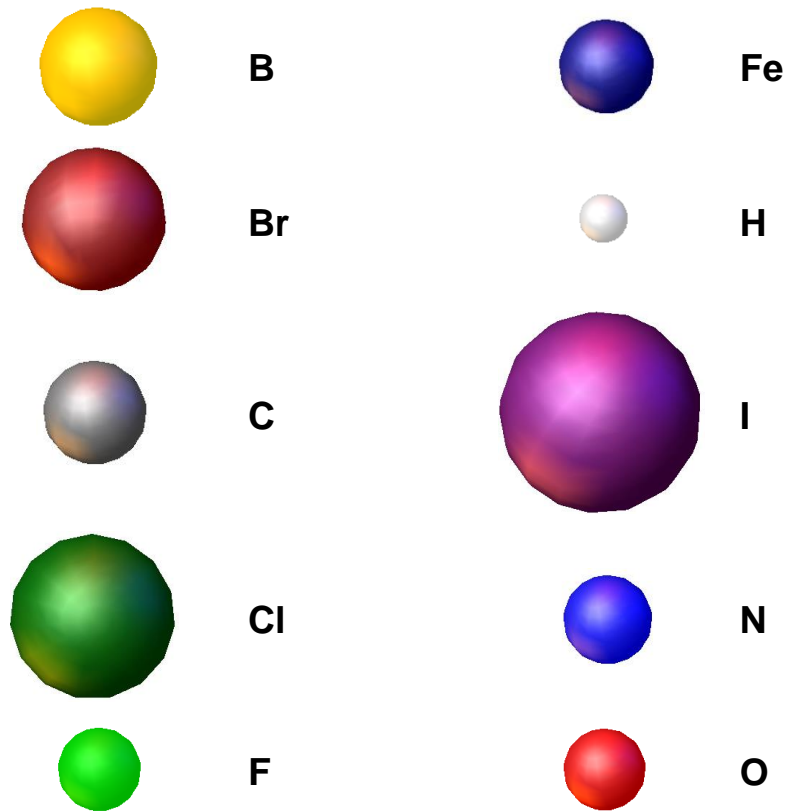
Fig. 5.15 Crystal structure of L20, and its packing diagram from the view, parallel to the [010] vector.....	176
Fig. 5.16 Asymmetric unit of coordination polymer S2 with labelling	178
Fig. 5.17 Fragment of the crystal structure of coordination polymer S2, from the view parallel to the [010] vector. Counterions and lattice solvents are omitted for clarity.....	178
Fig. 5.18 SQUID magnetic susceptibility measurements a the coordination polymer [Fe(L20) ₂][Fe(L20) ₂ (H ₂ O) ₂][BF ₄] ₄ ·MeNO ₂ ·H ₂ O	181
Fig. 5.19 Some of the long alkyl chain SCO complexes, obtained by Gutlich <i>et al.</i> and their magnetic behaviour ⁴	182
Fig. 5.20 SQUID magnetic susceptibility measurements for [Fe(L21) ₂][BF ₄] ₂	182
Fig. 6.1. Labelling scheme for Chapters 2 and 3.....	189
Fig. 6.2 Labelling Scheme for the ligands in the Chapters 4 and 5	215

List of Abbreviations

Å	Angstrom, 10^{-10} m
Ak	Alkyl
BP	Boiling point
bpp	2,6-Bis[pyrazol-1-yl]pyridine
br s	Broad singlet
Bzimpy	2,6-Di(1H-benzo[d]imidazol-2-yl)pyridine
ca.	Circa, approximately
CHN	Elemental analysis for carbon, hydrogen and nitrogen
d	Days
d	Doublet
DCC	N,N-dicyclohexyl carbodiimide
DCM	Dichloromethane
dd	Doublet of doublets
dec.	Decomposing
deion.	Deionized
DFT	Density functional theory
Diglyme	Diethylene glycol dimethyl ether
DMAP	Dimethylaminopyridine
DMF	N,N-dimethylformamide
DMSO	Dimethylsulfoxide
DSC	Differential Scanning Calorimetry
eq.	Equivalent
Et	Ethyl
Et ₃ N	Triethylamine
h	Hours
HMBC	Heteronuclear Multiple-Bond Correlation spectroscopy
HMQC	Heteronuclear Multiple-Quantum Correlation
HR-ESI MS	High-Resolution Electrospray Ionization Mass Spectrometry
HS	High spin
Htrz	1,2,4-1H-triazole
iPr ₂ O	Diisopropyl ether
IR	Infrared
LCD	Liquid Crystal Display
LIESST	Light-Induced Excited Spin-State Trapping
LS	Low spin
m	Multiplet

m.p.	Melting point
Me	Methyl
MeCN	Acetonitrile
MeNO ₂	Nitromethane
MeOH	Methanol
mins	Minutes
MLCT	Metal-to-Ligand Charge Transfer
MP	Melting point
MS	Mass spectrum
m/z	Mass/charge ratio for an ion in mass spectrometry
NMR	Nuclear Magnetic Resonance
p	Pentet
Ph	Phenyl
pH	Potential of hydrogen
PPMA	Poly(methyl methacrylate)
PXRD	Powder X-ray diffraction
Py	Pyridine
Pz	1H-Pyrazole
rt	Room temperature
s	Singlet
SCO	Spin crossover
SQUID	Superconducting Quantum Interference Device
t	Triplet
T _{1/2}	Spin-transition temperature midpoint
Tf	Triflate, CF ₃ SO ₃ ⁻
TGA	Thermogravimetric analysis
THF	Tetrahydrofuran
TMS	Tetramethylsilane
trz	1,2,4-Triazole
UV	Ultra violet
vs	Versus, against
XRD	X-ray diffraction
δ	NMR chemical shift

Colour Scheme for Crystal Structures



Chapter 1

Introduction

1.1 Spin crossover phenomenon

1.1.1 Introduction to the SCO effect

Since its discovery in 1931 by Cambi *et al.*,^{1,2} spin crossover (SCO) has received much interest and has been extensively researched (Fig. 1.1).³

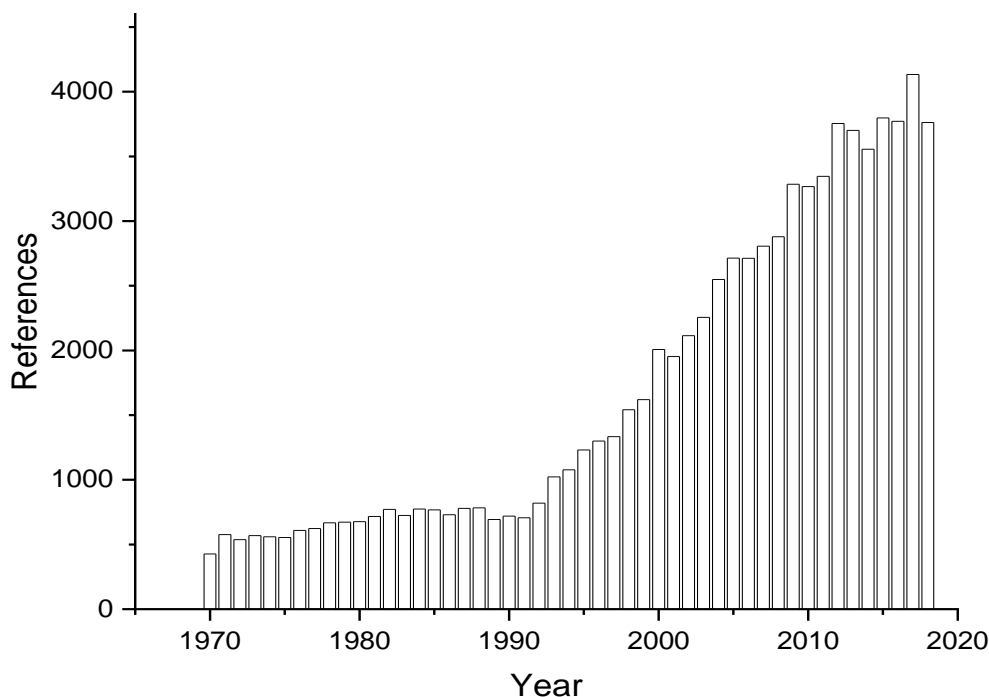


Fig. 1.1 Number of research articles containing concept “spin crossover” per each year from 1970 till 2018, according to SciFinder³

An abrupt drop in the magnetic susceptibility of certain Fe(III) complexes upon cooling was initially explained by a change in the bond type from covalent to ionic,⁴ but Orgel first suggested the correct explanation.^{5,6} According to the Crystal Field Theory, formation of the coordinate bond between the ligand and the metal ion breaks the degeneracy of the d-orbitals.⁷ Strong-field ligands (e.g. CO) produce a bigger gap between the d-orbitals, and therefore favours the low spin (LS) state, while weak-field ligands (e.g. I⁻) produce low splitting energy and high spin (HS) complexes. The gap between the d orbitals is called the splitting energy (Δ), or “10Dq”.⁸ The splitting energy depends on both the ligand and the metal ion. When Δ is between 10,000 cm^{-1} and 23,000 cm^{-1} , the metal complex may switch between high and low spin or, in other words, undergo SCO. SCO is impossible outside of this splitting energy range.⁶

In an octahedral ligand field the t_{2g} orbitals are non-bonding, while the e_g orbitals are anti-bonding and therefore higher in energy (Fig. 1.2). Because of this, the same metal complex in the HS and LS states has different metal-

ligand bond lengths, and therefore different splitting energies, with $\Delta_{LS}/\Delta_{HS} \approx 1.75$. As LS metal complexes have a larger gap between the t_{2g} and e_g orbitals, they also absorb light at higher frequencies.⁹ Iron(II) complexes have different electric conductivity in HS and LS, which is usually lower in HS state.¹⁰

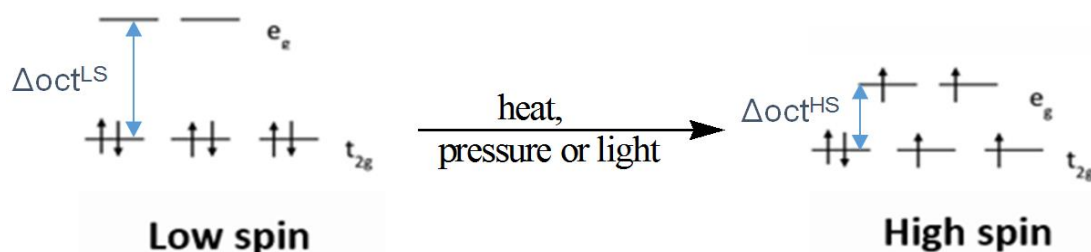


Fig. 1.2 Low Spin to High Spin transition of Fe^{2+} ion in octahedral ligand field

Usually SCO is induced by changing the temperature, but it can also be caused by pressure changes, application of light, a magnetic field or X-rays.¹¹ Bidentate SCO complexes are very common, and tri-, tetra-¹² and polydentates are also quite common, but SCO complexes with solely monodentate¹³ ligands are rarer.¹⁴ This thesis is focused on derivatives of 2,6-bis(pyrazol-1-yl)pyridine, or bpp, which is a very popular tridentate ligand core for spin crossover, and is related to terpyridine, or tpy (Fig. 1.3).

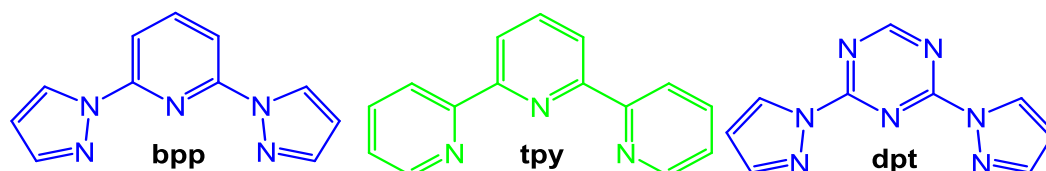


Fig. 1.3 Chemical structures of some tridentate ligand cores mentioned in this chapter: **bpp** - 2,6-bis(pyrazol-1-yl)pyridine, **try** - 2,2';6',2''-terpyridine, and **dpt** - 2,4-dipyrazolyl-1,3,5-triazine

1.1.2 Metal ions that can undergo SCO

SCO is known only for complexes of five metals (Fig. 1.4): Fe^{2+} , Fe^{3+} , Co^{2+} , Co^{3+} , Mn^{2+} , Mn^{3+} , Cr^{2+} , and Ni^{2+} .¹⁵⁻¹⁷

21	22	23	24	25	26	27	28	29	30
Sc	Ti	V	Cr	Mn	Fe	Co	Ni	Cu	Zn
Scandium	Titanium	Vanadium	Chromium	Manganese	Iron	Cobalt	Nickel	Copper	Zinc
44.956	47.867	50.942	51.996	54.938	55.845	58.933	58.693	63.546	65.38

Fig. 1.4 The five elements that can form homonuclear SCO complexes

For example, Zhang *et al.* obtained Mn^{3+} SCO complexes with axially-compressed octahedral geometry, heavy counterions and $T_{1/2}$ at ca 220 K. The originally used Mn^{2+} was oxidized to Mn^{3+} during complex formation.¹⁸ The same author also obtained another series of Mn^{3+} SCO complexes in a axially-compressed octahedral geometry with more abrupt switching.¹⁹

Boskovic *et al.* obtained terpyridine-based SCO coordinational polymers with Co^{2+} .²⁰ Larkworthy *et al.* obtained a Cr^{2+} SCO complex that switches abruptly at ca 170 K.²¹ Homma and Ishida obtained Ni^{2+} complexes, which exhibit gradual SCO with $T_{1/2}$ around 170 K.²²

In the literature there are also examples of **heteronuclear SCO complexes**. They may even contain metal centres that cannot undergo SCO. For example, Bousseksou *et al.* obtained $[\text{Fe}_{1-x}\text{Zn}_x(\text{Htrz})_2(\text{trz})](\text{BF}_4)$ SCO complexes that combine Fe^{2+} and Zn^{2+} ions. Replacing SCO-active Fe^{2+} centres with inactive Zn^{2+} ions led to lowering of the $T_{1/2}$ and broadening of the switching temperature range due to loss of cooperativity. The materials with Fe centres, and the ones with some Fe centres replaced by Zn atoms were isostructural in most cases.¹⁰ There are examples of SCO complexes that combine ions of the same metal in different oxidation states, both of which undergo the switching; such compounds are called mixed-valence complexes. For example, Oshio *et al.* obtained a tetranuclear SCO complex, containing both Fe^{2+} and Fe^{3+} .²³ The other metal in a heteronuclear SCO complex can be also introduced via the counterion, for example, a SCO complex obtained by same author contains Fe^{2+} and Ni^{2+} , where Ni is a part of the counterion.²⁴

Most studied are Fe^{2+} SCO complexes – about 90% of the reported SCO complexes contain Fe^{2+} .⁶ The first SCO Fe^{2+} complex was reported by König and Madeja in 1966.²⁵ In its low-spin state Fe^{2+} is completely diamagnetic, and in the high-spin state it is paramagnetic (Fig. 1.2), which makes it easier to detect its SCO.²⁶ The transition between these states is usually accompanied by a strong colour change. The complexes with Fe^{2+} in the low-spin state are strongly coloured but, on changing to the high-spin state, they usually become pale or colourless.²⁷ SCO is also accompanied by changes to ligand-metal bond lengths. When changing from LS to HS, the ligand-metal bond length in Fe^{2+} complexes increases by ca 10%.²⁸ The Fe-N bond length in bbp ligands (Fig. 1.3) is typically ca. 1.9 Å for LS, and ca 2.2 Å for HS.²⁹ SCO can occur in metal complexes with more than one metal centre. SCO is known for di-, tri-, tetra-, penta-, hexa-, and octanuclear Fe^{2+} complexes.³⁰

1.1.3 Types of SCO switching

The percentage of the molecules that are HS and LS at a given temperature can be measured by different techniques (see below), but the most useful and widely-used are magnetic moment vs temperature graphs, obtained by SQUID magnetometer for solid state SCO, and by Evans method NMR for

solutions. The path that the SCO follows can be very different: gradual, abrupt, with hysteresis, with multiple steps, or incomplete (Fig. 1.5).³¹

In solution SCO is always gradual, and often incomplete inside the liquid range of the solvent (Fig. 1.5 – A and E). In the solid state SCO can be either gradual, as in solution, or abrupt. Abrupt SCO, which is required for practical application, can be achieved in materials with stronger cooperativity.³¹ The greater the structural difference between the HS and LS states a compound has, the more abrupt SCO it undergoes.³²

Some SCO curves can show hysteresis (Fig. 1.5 - C), and in rare cases SCO can occur in multiple steps (Fig. 1.5 - D). For example, a mixed-metal SCO complex $[\text{Fe}(\text{bpp})_2]^{2+}[\text{Ni}(\text{mnt})_2]_2 \cdot \text{MeNO}_2$ undergoes a SCO with three additional steps.²³ A helical supramolecular iron(II) SCO complex obtained by Hannon *et al.* underwent a two-step switching, but only for the perchlorate salt. The salts with other counterions exhibited a regular one-step SCO.³³

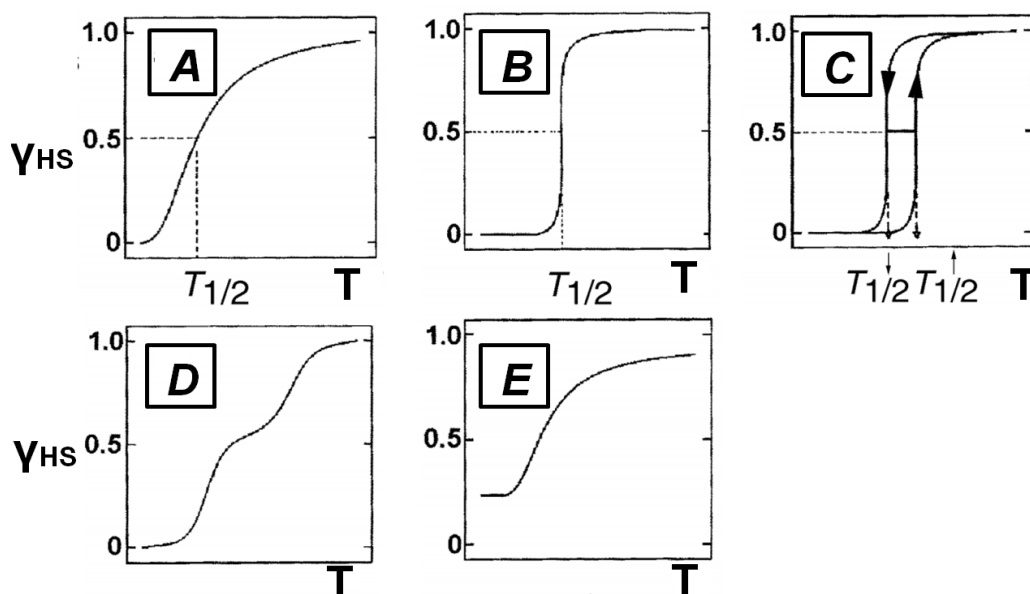


Fig. 1.5 Types of SCO in solid state: A – gradual, B – abrupt, C – with hysteresis, D – with steps, E – incomplete³⁰

1.1.4 Influence of the lattice solvent and counterion on SCO

Even a small change in the ligand geometry can dramatically affect the spin state of its metal complexes. For example, Halcrow *et al.* obtained a series of 2,4-dipyrazolyl-1,3,5-triazine derivatives (Fig. 1.3), and their Fe^{2+} complexes. Unlike many other similar tridentate ligands, which all form SCO complexes with Fe^{2+} , the iron complexes with this ligand series all were HS. This fact can be explained by a subtle change in the ligand's geometry which narrowed the chelate bite angle by ca 1° . This increased the distance between the chelating nitrogens and the d-orbitals of the iron centre, which

lowered the ligand field and the splitting energy, that made the HS state more energetically favourable.³⁴ The strong effect of the ligand geometry distortions on spin crossover should be taken into account when designing SCO materials with specific properties for practical applications.³⁵

Weak intermolecular interactions, such as π - π stacking, play a key role in cooperativity of an SCO behaviour.^{36,37} For example, Vela *et al.* has shown that iron(II) complex of a bpp derivative can undergo an abrupt spin crossover at ca 170 K when there is one acetone in the crystal lattice, whereas having two propylene carbonate molecules per one iron complex molecule makes it stay LS above 300 K. Also, they have shown using DFT, that solvent-solvent interactions promote the LS state by forming propylene carbonate dimers.³⁸ The temperature at which an iron complex exhibits SCO can change by as much as a 100 K from having a different solvent in the lattice.³⁹ An example of a pronounced effect of the lattice solvent on SCO was observed in Chapter 2 of this thesis (Fig. 2.28 and 2.31).

Real *et al.* studied Co(II) 4-terpyridone complexes with $[\text{BF}_4]^-$, $[\text{SiF}_6]^{2-}$, NCS^- , I^- , $[\text{PF}_6]^-$, $[\text{NO}_3]^-$ as counterion, all of which were crystallized from methanol. Co(II) complexes with $[\text{PF}_6]^-$, $[\text{SiF}_6]^{2-}$ were HS, NCS^- , I^- were LS, and $[\text{BF}_4]^-$, $[\text{SiF}_6]^{2-}$, $[\text{NO}_3]^-$ exhibited SCO with $T_{1/2}$ from 100 to 400 K, therefore the counterion can dramatically affect spin crossover in solid state.^{27,40} Hannon *et al.* showed that SCO in the same helical Fe^{2+} complex is strongly influenced by the counterion.³⁴ Brooker *et al.* in their review article showed many examples of SCO in polynuclear iron(II) complexes that heavily depends on both the lattice solvent and the counterion.²⁹ Song *et al.* showed that a Mn^{3+} complex that they obtained undergoes SCO with a $T_{1/2}$ ca 230 K higher when with $[\text{Ni}(\text{mnt})_2]^{2-}$ as a counterion, than with ClO_4^- .¹⁸ Brooker *et al.* obtained seven diiron(II) complexes that vary only by the counterion, which showed that the counterion dramatically affects the lattice packing and the SCO behaviour.⁴¹ A series of Co(II) complexes with a lipophilic counterion, obtained by Hayami *et al.*, all showed very gradual SCO switching.⁴²

1.1.5 The LIESST effect

Light-Induced Excited-State Spin Trapping, or LIESST, was first observed in mid-eighties.² Many SCO compounds can be switched from LS into a metastable HS state by irradiating with the light of the frequency that matches the charge transfer absorption energy. In such case system crosses from the singlet LS to a pentet HS state; and the metal complex may remain in that metastable HS state almost indefinitely,³⁰ as long as it is kept

at cryogenic temperatures.⁴³ LS molecules can be switched to a metastable HS state with a green light laser irradiation at ca 514 nm,⁴⁴ and the reverse switching, from HS to LS, can be achieved with red light laser irradiation at ca 820 nm.^{44,45} As was shown by Hauser *et al.*, the HS to LS LIESST effect can also be achieved by red light irradiation at ca 980 nm.^{46,47}

Oshio *et al.* achieved a controlled stepwise switching of the two iron centres in a tetranuclear mix-valence iron SCO complex (Fig. 1.6) using different frequency lasers.³³

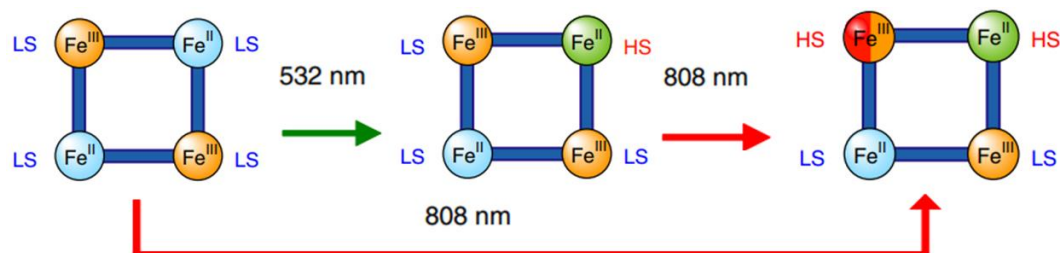


Fig. 1.6 Photo-switchable system obtained by Oshio *et al.*

1.1.6 Detection methods for SCO

SCO can be detected in solution by Evans method NMR, paramagnetic ¹H NMR and UV-VIS spectroscopy. In the solid state SCO can be detected using crystallography, by measuring the metal-ligand bond length and other distortion parameters;⁴⁸ by comparing PXRD patterns taken at different temperatures; by detecting the SCO transition with DSC; by Mössbauer spectroscopy; by UV-VIS spectroscopy;³¹ and, most importantly, by measuring the magnetic susceptibility.

Magnetic susceptibility (χ) is a physical unit which describes quantitatively the interaction between the studied material and magnetic field. In this regard all materials can be divided into three categories: diamagnetic, paramagnetic and ferromagnetic. Diamagnetic substances when put into an external magnetic field produce a very weak internal magnetic field, which opposes the applied magnetic field. For diamagnetic materials the magnetic susceptibility is negative. Paramagnetic substances produce an internal magnetic field in the same direction and proportional to the applied field. Ferromagnetic substances produce very strong magnetic field, often a few times stronger than the original one, pointing the same direction as the original magnetic field. This ferromagnetic field is retained when the external magnetic field is removed.⁴⁹

The oldest technique used for the magnetic susceptibility measurement is the Gouy method: the sample is weighed on a very sensitive balance in the

presence and absence of a magnetic field. The difference in the two measurements is used in the equation to calculate the magnetic susceptibility.⁵⁰ Later the Evans balance, an improved version of the Gouy method, was developed, which allows to samples as small as 50 mg to be studied.⁵¹ The most modern and precise technique for magnetic susceptibility measurement is using Superconducting Quantum Interference Device, or SQUID. During the SQUID measurement the sample is moved up and down in the pick-up coil, which is connected to a Josephson Junction, that consists of two superconductors, separated by a thin insulator. Because of the quantum tunnelling effect, the electrons may pass through the insulator. Even a small change in the magnetic flux through the pick-up coil affects the phase difference between the two superconducting coils, which affects the voltage through the Josephson Junctions. This voltage is then amplified and measured by a voltmeter. Therefore, a SQUID can convert magnetic flux into an electric voltage. The main use of SQUIDs is for biological studies and for diagnostic in medicine.²⁸

The magnetic moment (μ) is not measured directly, but is calculated from the magnetic susceptibility using the equation $\mu_{\text{ef}} = 2.828(\chi_{\text{A}}T)^{1/2}$, where μ_{ef} is the magnetic moment in Bohr Magnetons, χ_{A} is the molar magnetic susceptibility with diamagnetic corrections, and T is the temperature in K.⁵¹ Even if the sample stays HS below 50 K, XT value may decrease at such low temperatures due to zero-field splitting.⁵²

1.1.7 Possible applications for SCO

SCO compounds may potentially be used in molecular electronics, displays manufacturing and data storage.⁵³ SCO occurs in nanoseconds in individual molecules, and switching both from HS to LS and from LS to HS can be induced by application of light. These two features make SCO compounds promising materials for information storage.^{15,54} Also, understanding interactions between a ligand and metal ion is important for bioinorganic chemistry and for base-metal catalysis.⁵⁵ For example, mononuclear iron(IV)-oxo non-heme enzymes which are common in nature, particularly in plant organisms, always contain a HS iron, although the reason for this remains unclear, as similar to them biomimetic enzymes with the iron in LS showed comparable activity.⁵⁶ Spin crossover has also been detected in natural systems, in a number of heme derivatives, where it can play an important role in controlling biological functions.^{31,57}

Study of SCO may help development of single molecule magnets, and different types of functional materials, such as superconducting ceramics.⁵⁸

Liquid crystals with SCO properties, just like any other metal-containing liquid crystals, can align in a much weaker magnetic field much stronger than ordinary diamagnetic liquid crystals.⁵⁹ To have practical application a SCO complex must have the following qualities: a room-temperature working range, full reversibility, low addressing power, and chemical stability.⁵³

Because SCO is associated with molecular volume change, it could be used for development for molecular machines.⁶⁰ Bousseksou *et al.* achieved a tuneable actuation on microscopic scale, using thermal SCO in a bilayer cantilever of a PMMA/[Fe(trz)(Htrz)₂](BF₄) composite deposited on the surface of polymer doped with Ag nanoparticles (PMMA stands for poly(methyl methacrylate)).⁶¹ Besides thermal switching, the same results were achieved using modulated current. In both cases the prototype device showed repeatable and tunable actuation with both large displacements (several mm) and large force (several mN).⁶²

1.2 Liquid crystals

1.2.1 Liquid crystal phase overview

Liquid Crystals (LCs), or mesogens, are materials that in a certain temperature range can exhibit both the properties of liquids, such as molecular mobility and fluidity, and the properties of crystalline state; namely optical and electrical anisotropy. A substance can stay in a liquid crystalline state only in a certain temperature range - between its melting and clearing points.⁶³ Liquid crystals were discovered in 1888 by observing the melting of cholesteryl benzoate, which has two melting points: at 145.5°C it melts into a cloudy liquid, with crystals seen under microscope, and 178.5°C it turns into transparent liquid. Liquid crystals can be thermotropic and lyotropic. Thermotropic liquid crystals exist in a certain temperature range between the solid and liquid state, while lyotropic liquid crystals can exist in a certain range of concentration of the amphiphilic molecules in a solvent.⁶³

Nowadays LCs are broadly researched, and they find application mostly in the LCD screen industry, as the optical properties of some LC systems depend on a magnetic field. Also, LCs are used in many other, more niche areas, such as elastomer actuators, liquid crystal functionalized polymers, and nanoparticle organization using liquid crystals.⁶⁴ LCs can be used in sensors,⁴⁵ and in biosensors.⁶⁵

A molecule is likely to exhibit liquid crystalline behavior if it: has an anisotropic shape, for example if it is elongated,⁶⁶ has a rigid core and

several long flexible groups such as alkyl chains, has strongly polarizable groups⁶², and contains flat substituents, such as benzene rings.⁶⁶ A purely inorganic lyotropic mesogen has been reported, which contains the extended cluster anion Mo_3Se_3^- .⁶⁷

1.2.2 Intermediate LC phases

As a substance with liquid crystalline properties goes from liquid to solid state, it passes through many intermediate phases, called mesophases. The most important of them are: Isotropic (liquid) \rightarrow nematic \rightarrow cholesteric \rightarrow smectic \rightarrow crystalline state (solid) (Fig. 1.7 and 1.8).⁶⁸

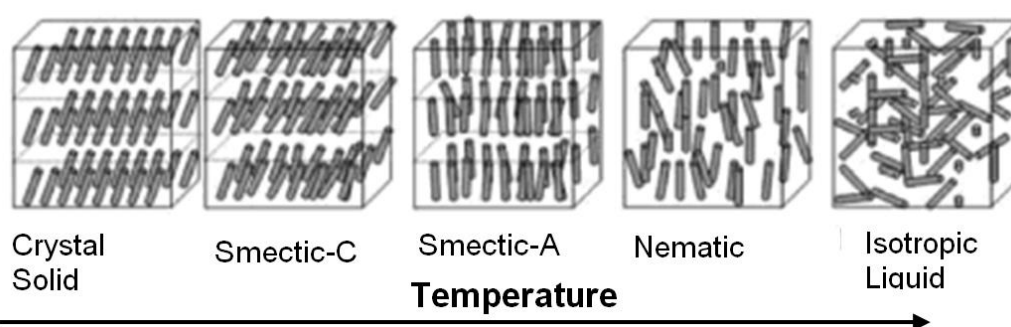


Fig. 1.7 Schematic representation of the main mesophases of rod-like molecules

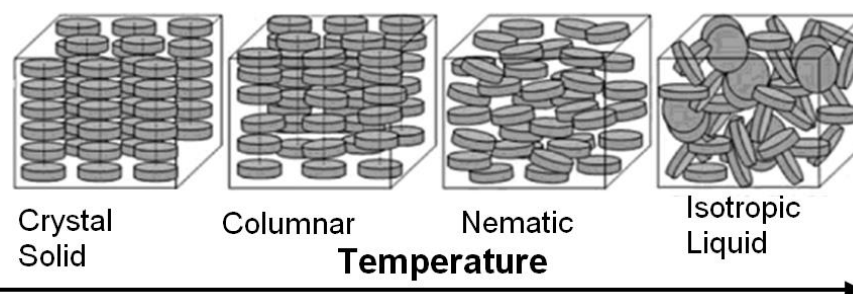


Fig. 1.8 Schematic representation of the main mesophases of disc-like molecules

Molecules in liquid crystalline substances are oriented the same way – parallel to the axis, called the director. In the liquid state the molecules are oriented randomly. The average value of the angle between the molecules in liquid crystal and the director is called theta (θ). It can be used to calculate the order parameter S , using the formula: $S = 0.5 \cdot \langle 3 \cdot \cos^2(\theta) - 1 \rangle$, where the wedge brackets denote the average value. A perfect crystal would have an order parameter equal to 1.⁶⁸

The liquid crystalline state is common for molecules of anisotropic shape. The most common molecular shapes for formation of liquid crystals are rod-shaped and disk-shaped (Fig. 1.9).⁶⁹

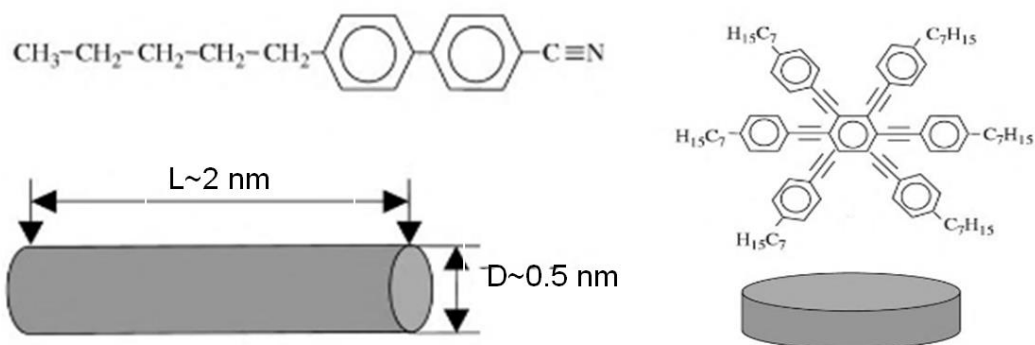


Fig. 1.9 Calamitic (rod-like) liquid crystal molecule structure and its physical model (left) vs discotic (disc-like) liquid crystal and its physical model (right)⁶⁷

The nematic liquid crystal phase is the least ordered mesophase. In nematic phases molecules have no positional order but tend to point in the same direction, along the director. The word “nematic” came from the Greek word “νήμα”, which means “thread”. In nematic phase the molecules are oriented along the director in long “threads”, which however are not ordered with respect to each other.

In a smectic mesophase molecules maintain the orientational order of nematics, but besides this they align themselves in layers or planes. The word smectic came from the Latin word "smecticus", which means “soap”. Most compounds have more than one smectic mesophase.⁶⁸ There are known twelve different smectic phases.

The cholesteric (also called chiral nematic) liquid crystal phase usually consists of chiral molecules, which, due to presence of both enantiomers, can't pack close to each other, and therefore align at a slight angle to each other. This leads to formation of a structure, which can be described as a stack of very thin two-dimensional layers, each of which has order as in nematic phase, and the director of each new layer in the stack is slightly turned, forming a continuous helical pattern.

The columnar mesophase can be formed only by disk-like molecules. It is formed by stacking the discotic molecules into columns. Different arrangements of the molecules within the columns, and the arrangement of the columns with respect of each other lead to additional mesophases.⁶⁹

To study phase transitions in liquid crystals, Differential Scanning Calorimetry, or DSC, is often used. The solid to LC (crystalline to smectic phase) and LC to liquid (nematic to isotropic) transitions are much more distinct than the transitions between the LC mesophases (smectic to nematic) (Fig. 1.10).⁶⁹

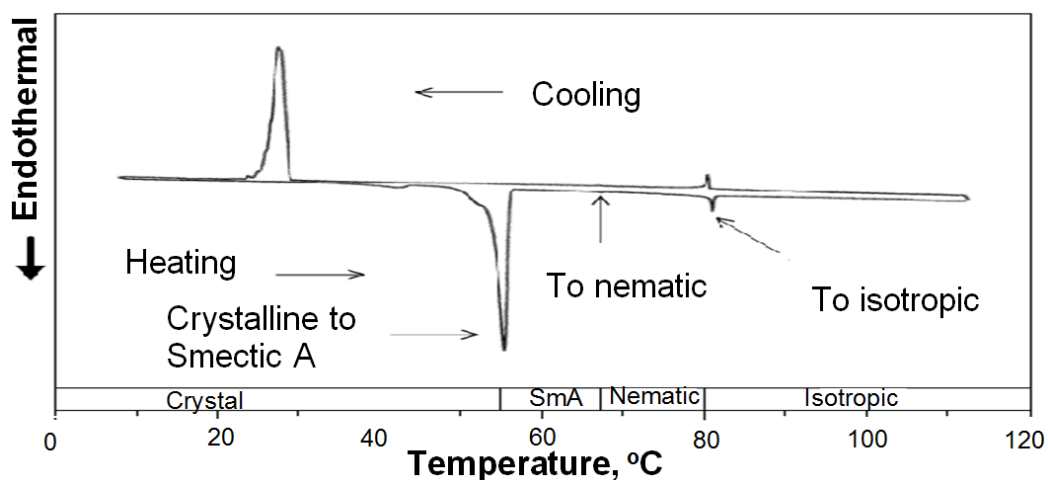


Fig. 1.10 Differential Scanning Calorimetry of octyloxy-cyanobiphenyl at the 1°C/min rate⁶⁹

1.2.3 Langmuir-Blodgett films

A Langmuir film is an organized monolayer of amphiphilic molecules that forms at a liquid/gas interface. These molecules can spontaneously orient themselves at a liquid/gas interface with the hydrophilic head pointing towards the aqueous phase, and hydrophobic tails oriented towards the air or a hydrophobic phase.⁷⁰

A Langmuir film deposited on a solid substrate is called a Langmuir-Blodgett film. Pressure is applied using a moveable barrier in a Langmuir trough to increase the two-dimensional film concentration and obtain a highly ordered two-dimensional film. This film may be prepared also from a mix of different amphiphilic molecules. Multiple layers of Langmuir-Blodgett films can be deposited on a surface by repeating the cycle.⁷⁰

1.3 Spin-crossover liquid crystals

Metallomesogens are broadly researched and are interesting because they may combine the properties associated with metal atoms, such as magnetism, conductivity, bright colour and dichroism, with the properties of mesogens, e.g. order, easy processability, fluidity, etc.⁷¹ The use of metallomesogens in LC displays is hindrance by the fact that they often have high viscosity and conductivity, which increases the magnetic field strength required to switch their orientation and therefore optical properties.⁷² However, they may be used in spatial light modulators, and in information storage and transfer devices.⁷³

Maeda *et al.* obtained a series of nine Fe²⁺ complexes, which combine SCO and the LIESST effect, and five of which also form a LC phase (Fig. 1.11).⁵²

The complexes were studied by SQUID, Mossbauer spectra, DSC, X-ray powder diffraction (PXRD) and optical polarized microscopy using the hot-stage experiment. The temperature range of the mesophase formation obtained by DSC and PXRD corresponded to each other. The compounds that do not exhibit mesophase transition ($n = 6, 8, 10, 22$) exhibit SCO at lower temperatures than the ones that form liquid crystals ($n = 12, 14, 16, 18, 20$) (Fig. 1.11).⁵²

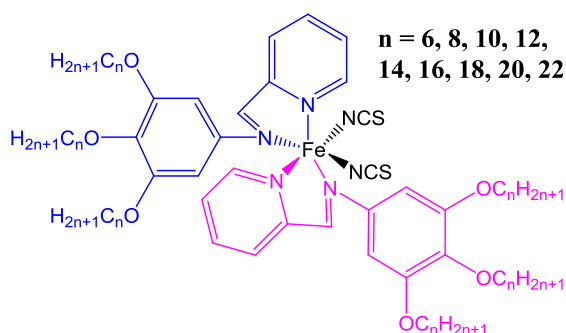


Fig. 1.11 Chemical structure of 4-hexadecyloxy-N-(2-pyridinylmethylene) - benzenamine $[\text{Fe}(\text{bzimpy})_2(\text{NCS})_2]$

The same researcher also obtained another iron(II) complex series that combines liquid crystalline and spin-crossover properties. Both of these ligands (Fig. 1.12) form complexes that have liquid crystalline properties, however only complex of ligand A exhibits spin crossover.⁵⁹

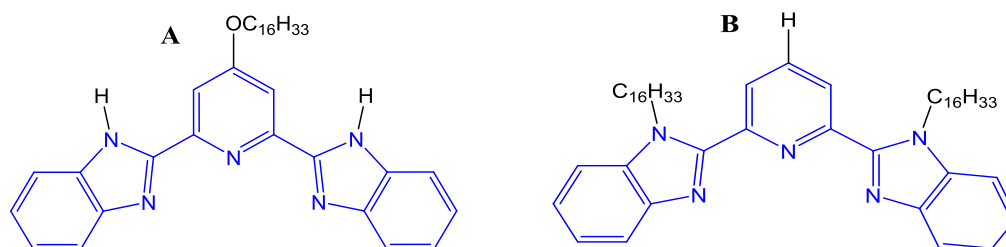


Fig. 1.12 Chemical structures of the **bzimpy** derivatives ligands: A – 2,6-bis(benzimidazol-2'-yl)-4-hexadecyloxy-pyridine, and B – 2,6-bis(N-hexadecylbenzimidazol-2'-yl)pyridine

Hayami *et al.* obtained three similar iron(II) complexes, but with branched long alkyl chain substituents. The iron complex with one branched alkyl chain exhibited a gradual SCO, while the one with three branched alkyl chains showed an abrupt switching, caused by a crystal-mesophase transition which coincided with the SCO and increased the cooperativity.⁷⁴ Based on this it may be concluded that the branched alkyl chain iron complexes are more inclined towards cooperative effects between metal complexes and linear long alkyl chains.

Real *et al.* obtained a series of tripod ligands with short and long alkyl chains, and their Fe^{2+} complexes (Fig. 1.13), which exhibit thermal SCO and form a smectic LC phase. The long alkyl chain complexes switch more gradually than the short alkyl chain ones; and in a form of a thin film they showed more gradual SCO than in solid state. The compounds A and B showed similar SCO behaviour, with compounds B having more abrupt switching (Fig. 1.13), while the compound C remained HS.⁷⁵

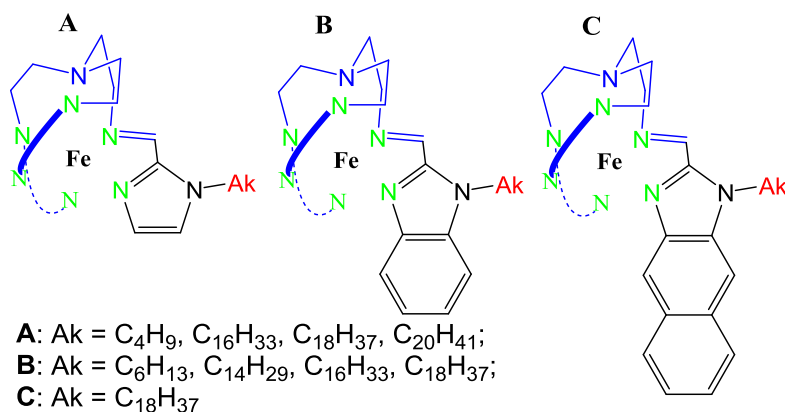


Fig. 1.13 Structures of the tripod iron complexes obtained by Real *et al.*

Aida *et al.* obtained a series of Fe^{2+} long alkyl chain triazole 1D coordination polymers which all undergo SCO. Abrupt switching was achieved for the twelve- and sixteen-carbon chain complexes, because their mesophase transitions coincide with the SCO (Fig. 1.14).⁷⁶

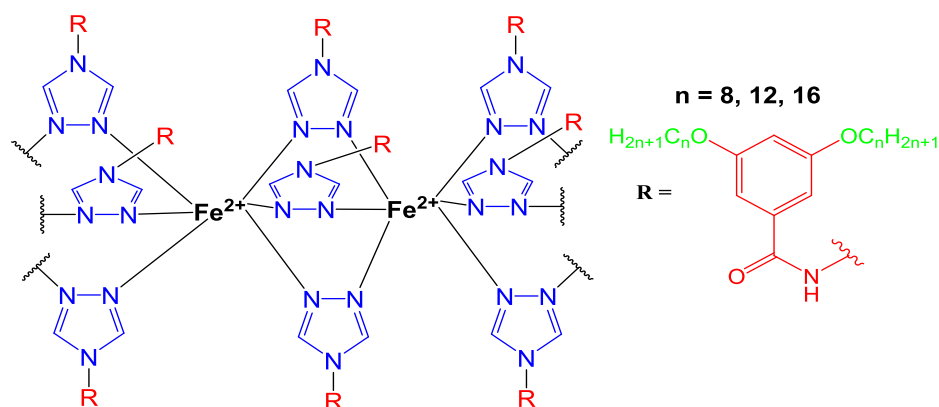


Fig. 1.14 Series of SCO coordination polymers, obtained by Aida *et al.*

Kurth *et al.* obtained a Fe^{2+} coordination polymer, and introduced long alkyl chains into it using dihexadecyl phosphate as an amphiphilic counterion (Fig. 1.15). The phase transition caused distortion around the metal iron and a decrease in the splitting energy between the d-orbitals, which induced a reversible transition from LS to HS state. The obtained compound was successfully deposited as a Langmuir-Blodgett multilayer, which is good for its potential practical application.⁷⁷

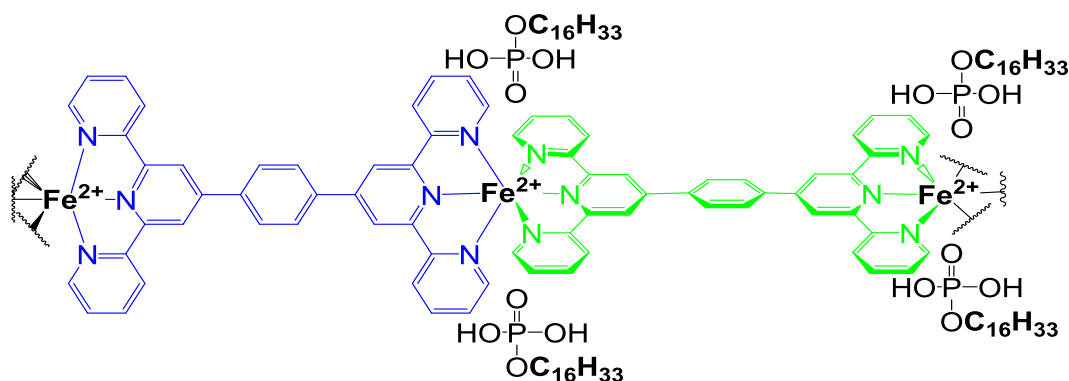
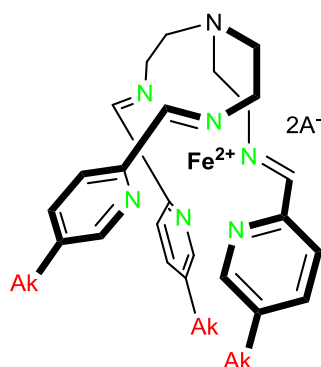


Fig. 1.15 Coordination polymer with long alkyl chain counterions

Usually, when a phase transition coincides with SCO, the switching becomes more abrupt. However, there are some exceptions. For example, Gutlich *et al.* obtained a few series of Fe^{2+} complexes with different substituents, counterions, and lattice solvent contents (Fig. 1.16). Four of them showed a mesophase formation at the same temperature range with SCO, without significantly affecting the SCO transition, which is very unusual. These four compounds include: all three of the different alkyl chain lengths iron complexes with Cl^- counterion, and the eighteen carbon chain compound with the F^- counterion, each containing 3.5 lattice water molecules. Noteworthy is the strong effect of the lattice solvent content on the SCO in these compounds, as the same compounds with 3.5, 0.5, and no water molecules showed completely different magnetic behaviour.⁷⁸



Ak = $\text{C}_{16}\text{H}_{33}$, $\text{C}_{18}\text{H}_{37}$, $\text{C}_{20}\text{H}_{41}$
 $\text{A}^- = \text{Cl}^-$, ClO_4^- , F^- , Br^- , I^-

Fig. 1.16 Long alkyl chain SCO complexes, obtained by Gutlich *et al.*

1.4 Spin-crossover metal complexes bearing alkyl chains

Weber *et al.* obtained iron(II) complexes that differ only by the alkyl chain length (Fig. 1.17 - A). All of them showed the same SCO behaviour in solution, but in the solid state their SQUID curves looked significantly different: the eight-carbon chain ligand showed abrupt switching with a 4 K hysteresis and $T_{1/2}$ at ca 182 K, the twelve-carbon one showed a gradual,

stepwise and incomplete SCO, while the sixteen-carbon iron complexes showed a full switching with a ca 23 K hysteresis and the $T_{1/2}$ of 222 and 245 K.⁷⁹ Therefore the alkyl chain length affects the cooperativity and packing.⁷⁹ The same author obtained a series of short alkyl chain iron(II) complexes with a similar ligand (Fig. 1.17). These didn't show a lipid-bilayer-like packing, which means that eight carbon chains in this case were too short to induce that arrangement. All of them showed a gradual SCO, comparable to the switching in the solution, which may be explained by low cooperativity due to missing lipid-bilayer-like packing.⁸⁰

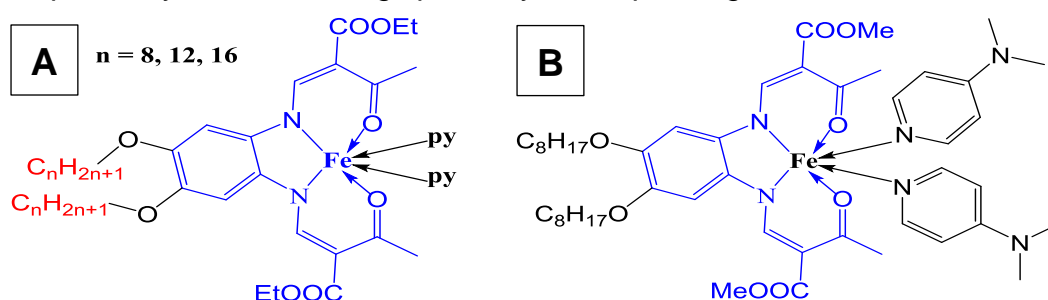


Fig. 1.17 SCO complexes with alkyl chains, obtained by Weber *et al.*

Introducing long alkyl chains into SCO complexes, besides increasing their cooperativity, can help to deposit them on a surface as a thin film. For example, Brooker *et al.* obtained a sixteen-carbon chain Fe^{2+} complex that exhibits SCO around room temperature and can form Langmuir–Blodgett film at an air–water interface. This is good for its potential practical application in devices that can operate at room temperature without need for additional heating or cooling (Fig. 1.18).⁸¹



Fig. 1.18 A N4-hexadecyl-3,5-di(2-pyridyl)-4H1,2,4-triazole

Weber *et al.* also investigated the effect of the long alkyl chains on cooperativity for bipyridines. The magnetic measurements and crystal structures of the three Fe^{2+} SCO complexes with different length of alkyl chain spacers showed the correlation between the alkyl chain length, the system's flexibility, and consequently the cooperativity (Fig. 1.19).⁸²

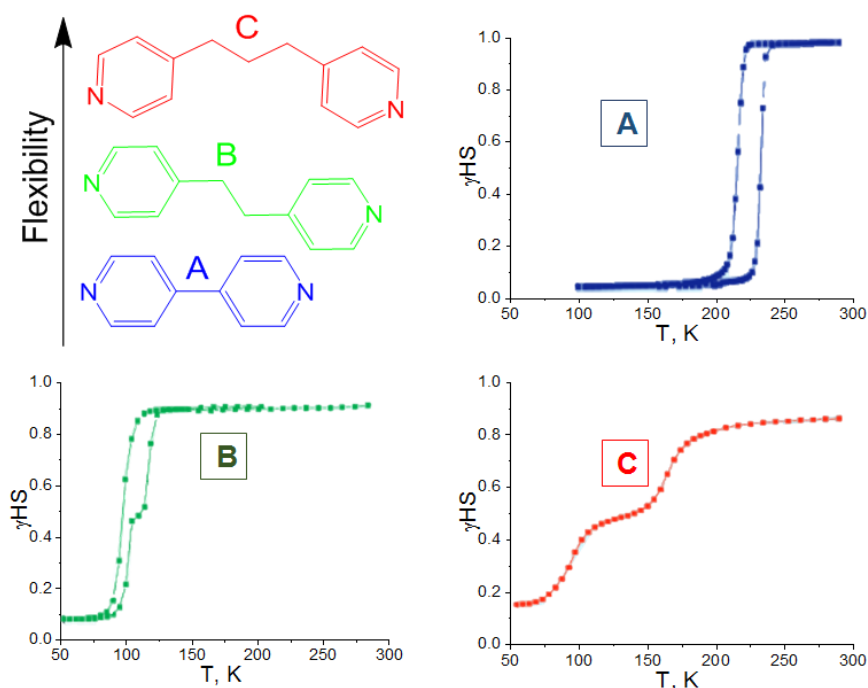


Fig. 1.19 The influence of the bridging ligand on the SCO properties of Fe²⁺ 1D coordination polymers

Clerac *et al.* obtained a long alkyl chain Fe²⁺ complex with interesting properties, such as a wide abrupt hysteresis at room temperature, and formation of an additional ordered HS-LS phase upon cooling, which causes an additional small hysteresis loop on the magnetic susceptibility curve (Fig. 1.20). This transition arises from the symmetry breaking from monoclinic into orthorhombic space group. The bent geometry of this SCO complex causes a strain near the iron centre. When it undergoes SCO transition, the distortion in the core are magnified by the long alkyl chains, which causes huge deformation of the crystal packing and symmetry breaking. This is the first example in the literature, of magnetic tristability caused by coincidence of SCO and symmetry breaking.⁸³

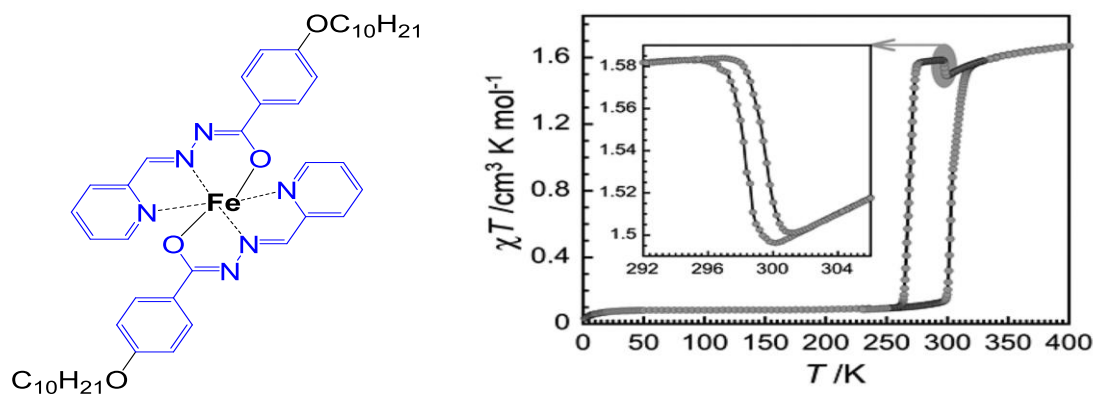
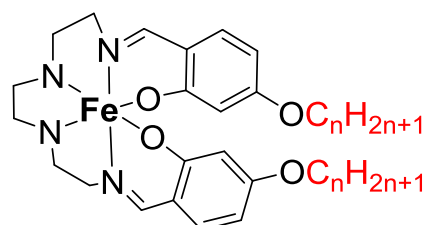


Fig. 1.20 Magnetic tristability observed by Clerac *et al.*

Albrecht *et al.* obtained a series of Fe³⁺ complexes with alkyl chains (Fig. 1.21). Unlike the other members of this series, the iron complex with eighteen carbon chain showed an unusually abrupt SCO in solution, which can be explained by its self-assembly in solution. This quite abrupt SCO can be easily observed by eye or UV-VIS spectroscopy, as when the compound is HS the solution is red, and it is dark-blue when the molecules switch to LS.⁸⁴



n = 6, 8, 18

Fig. 1.21 SCO series obtained by Albrecht *et al.*

Another interesting area of research that often involves long alkyl chain ligands is dendrimers. Dendrimers are materials with densely packed regularly branched substituents. They usually have a good solubility for such large structures, which makes them promising materials for obtaining soluble SCO polymers.⁶² Gutlich *et al.* obtained a series of Fe²⁺ dendrimeres (Fig. 1.22 – A1, A2),⁸⁵ and Schluter *et al.* obtained similar, even more branched iron complexes (Fig. 1.22 – B1, B2).⁸⁵ The compounds **A1** and **B1** shown SCO switching at ca 200 K, while the compounds with long alkyl chains **A2** and **B2** shown incomplete switching above 300 K.^{85,86,87}

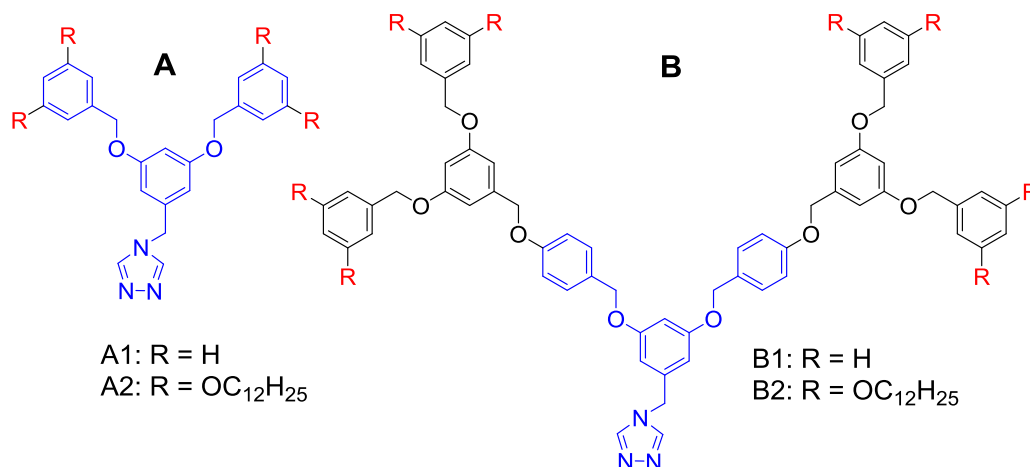


Fig. 1.22 Dendrimeres reported by: **A** – Gutlich,⁸⁵ **B** – Aida, Schluter⁸⁶

Long alkyl chains may be introduced to a SCO complex not only via the ligand, but also through the counterion. For example, Hayami *et al.* obtained a series of long alkyl chain Co²⁺ complexes with a lipophilic glutamate counterion (Fig. 1.23), which all exhibited a very gradual SCO switching.⁴²

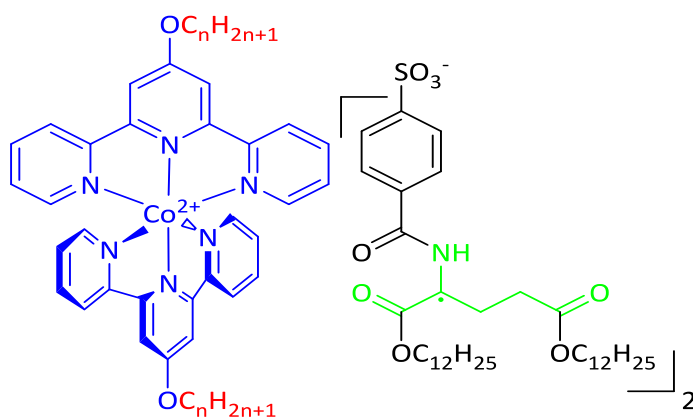


Fig. 1.23 SCO Co²⁺ complex with a lipophilic glutamate counterion

It may be concluded from many of the literature examples, that the presence of long alkyl chains may increase the cooperativity due to the lipid-bilayer-like packing,⁸⁰ and therefore make SCO more abrupt in a solid state. However, in some cases introducing long alkyl chain can make the switching incomplete and more gradual.⁷⁹ Symmetry breaking⁸³ and mesophase transitions⁸³ that coincide with SCO make it more abrupt, but in some rare cases they can coincide without affecting each other.⁷⁸ SCO in solution is normally very gradual, but in rare cases the presence of long alkyl chains can induce self-assembly of the dissolved molecules, and therefore make the switching much more abrupt.⁸⁴

1.5 Project aims

Since the discovery of SCO in 1931,^{1,2} many different metal centres and ligand SCO systems were obtained and studied.⁴⁸ Lately, the multifunctional materials which combine SCO with other functions were receiving much attention in the literature.⁸⁸ This includes nanoparticles,⁸⁹ chiral molecules,^{90,91} liquid crystals,⁹² thin films or gels,⁹³ which can undergo SCO. Development of these materials is an important step towards practical application of spin-crossover materials.⁷⁸

The aim of this project is to obtain series of long alkyl chain Fe²⁺ complexes based on a well-established spin-crossover backbone 2,6-bis(pyrazol-1-yl)pyridine or bpp (Fig. 1.3), functionalized with long alkyl chains at various positions, and to study the influence of the alkyl chain position and length on the SCO transition. Comparison of the switching in solution and in solid together with crystal structure analysis can reveal the effect of the alkyl chains on the cooperativity, packing and SCO.⁸⁰ If some of the compounds exhibit a mesophase formation, the interplay between the phase transition and spin crossover may also be studied.⁵²

List of References

1. Cambi, L. and Gagnasso, A. Iron dithiocarbamates and nitrosodithiocarbamates. *Atti. Accad. Naz. Lincei.* **1931**, *15*, 329-335.
2. Cambi, L. and Szegö L. Über die magnetische Susceptibilität der komplexen Verbindungen. *Ber. Deutsch. Chem. Gesell.* **1931**, *64*, 167.
3. *SciFinder*. Chemical Abstracts Service, accessed 4/4/2019 <https://scifinder.cas.org>
4. Coryell, C.D.; Stitt F. and Pauling, L. *J. Am. Chem. Soc.* **1937**, *59*, 633-642.
5. Orgel, L. E. *10th Chemical Conference*, Brussels. **1956**, 289.
6. Shatruk, M. Spin Crossover in Transition Metal Complexes. ICMM-2012 conference presentation. Orlando, USA. **2012**. <http://obelix.physik.uni-bielefeld.de/~schnack/molmag/material/ICMM-2012-tutorial-Michael-Shatruk.pdf>
7. Bethe, H.A. Zur Theorie des Durchgangs schneller Korpuskularstrahlen durch Materie. *Ann. Physik.* **1929**, *3*, 325-329.
8. O'Donnell Offenhartz, P. On the Calculation of $10Dq$. *J. Am. Chem. Soc.* **1969**, *91*, 5699-5704.
9. Hauser, A. Ligand Field Theoretical Considerations. *Adv. Polym. Sci.* **2004**, *233*, 49-58.
10. Lefter, C.; Tricard, S.; Peng, H; Molna G.; Salmon, L.; Demont, P.; Rotaru, A. and Bousseksou, A. Metal Substitution Effects on the Charge Transport and Spin Crossover Properties of $[\text{Fe}_{1-x}\text{Zn}_x(\text{Htrz})_2(\text{trz})](\text{BF}_4)$. *J. Phys. Chem. C.* **2015**, *119*, 8522-8529.
11. Gutlich, P. and Goodwin, H. A. *Spin Crossover in Transition Metal Compounds I*. Springer-Verlag, Berlin-Heidelberg. **2004**.
12. Costa, J.S.; Lappalainen, K.; de Ruiter, G.; Quesada, M.; Tang, J.; Mutikainen, L.; Turpeinen, U.; Grunert, C.M.; Gutlich, P.; Lazar, H.Z; Letard, J.F.; Gamez, P. and Reedijk, J. Remarkable Steric Effects and Influence of Monodentate Axial Ligands L on the Spin-Crossover Properties of trans- $[\text{Fe}^{\text{II}}(\text{N}_4 \text{ ligand})\text{L}]$ Complexes. *Inorg. Chem.* **2007**, *46*, 4079-4089.
13. Müller, E. W.; Ensling, J.; Spiering, H.; Gütlich, P. High-Spin Low-Spin Transition in Hexacoordinate Complexes of Iron(II) with Monodentate 1-

- Alkyltetrazole Ligands: A Variable-Temperature Mossbauer, Magnetic Susceptibility, and Far-Infrared Studv. *Inorg. Chem.* **1983**, *22*, 2074-2078.
14. Nakamoto, K. *Advances in the Chemistry of Coordination Compounds*. Macmillan: New York. **1961**, 437.
 15. Koudriavtsev, A. B. and Linert, W. Spin crossover—An unusual chemical equilibrium. *J. Struct. Chem.* **2010**, *51*, 335-365.
 16. Abdullah, N.; Noor, N. L. M.; Nordin, A. R.; Halcrow, M. A.; MacFarlane, D. R.; Lazar, M. A.; Pringle, J. M.; Bruce, D. W.; Donnio, B. and Heinrich, B. Spin-crossover, mesomorphic and thermoelectrical properties of cobalt(II) complexes with alkylated N³-Schiff bases. *J. Mater. Chem.* **2015**, *3*, 2491-2499.
 17. Gütllich, P. and Goodwin, H. A. *Spin Crossover in Transition Metal Compounds II*. Springer, Berlin-Heidelberg. **2004**, 49-62.
 18. Liu, L.; Liang, S.; Di, X. and Zhang, J. A manganese(III) complex that exhibits spin crossover behaviour. *Inorg. Chem. Commun.* **2008**, *11*, 783-786.
 19. Chen, Y.; Cao, F.; Wei, R.-M.; Zhang, Y., Zhang, Y.-Q. and Song, Y. Spin-crossover phenomena of the mononuclear Mn^{III} complex tuned by metal dithiolene counteranions. *Dalton Trans.* **2014**, *43*, 3783-3791.
 20. Drath, O.; Gable R.W.; Moubaraki, B.; Murray, K.S. and Boskovic, C. Synthesis and properties of cobalt(II) coordination polymers linked by 4'-(4-pyridyl)-2,2':6',2''-terpyridine. *Polyhedron.* **2018**, *151*, 323-329.
 21. Halepoto, D.M.; Holt, D.G.L.; Larkworthy, L.F.; Povey, D.C. and Smith, G.W. Spin crossover in chromium(II) complexes. *Polyhedron.* **1989**, *8*, 1821-1822.
 22. Homma, Y. and Ishida, T. A New S = 0 ⇌ S = 2 "Spin-Crossover" Scenario Found in a Nickel(II) Bis(nitroxide) System. *Chem. Mater.* **2018**, *30*, 1835-1838.
 23. Matsumoto, T.; Newton, G.N.; Shiga, T.; Hayami, S.; Matsui, Y.; Okamoto, H.; Kumai, R.; Murakami, Y. and Oshio, H. Programmable spin-state switching in a mixed-valence spin-crossover iron grid. *Nat. Commun.* **2014**, *5*, 3865.

24. Nihei, M.; Tahira, H.; Takahashi, N.; Otake, Y.; Yamamura, Y.; Saito, K. and Oshio H. Multiple Bistability and Tristability with Dual Spin-State Conversions in $[\text{Fe}(\text{dpp})_2][\text{Ni}(\text{mnt})_2]_2 \cdot \text{MeNO}_2$. *J. Am. Chem. Soc.* **2010**, *132*, 3553–3560.
25. König, E. and Madeja, K. Unusual Magnetic Behaviour of Some Iron(II)-Bis- (1 10-phenanthroline) Complexes. *Chem. Commun.* **1966**, 61-62.
26. Hayami, S.; Motokawa, N.; Shuto, A.; Masuhara, N.; Someya, T.; Ogawa, Y.; Inoue K. and Maeda, Y. Photoinduced Spin Transition for Iron(II) Compounds with Liquid-Crystal Properties. *Inorg. Chem.* **2007**, *46*, 1789-1794.
27. Halcrow, M. A. The foundation of modern spin-crossover. *Chem. Comm.* **2013**, *49*, 10890-10892.
28. Sternickel, K. and Braginski, A. I. Biomagnetism using SQUIDs: status and perspectives. *Supercond. Sci. Technol.* **2006**, *19*, S160.
29. Halcrow, M. A. Iron(II) complexes of 2,6-di(pyrazol-1-yl)pyridines – a versatile system for spin-crossover research. *Coord. Chem. Rev.* **2009**, *253*, 2493–2514.
30. Hogue, R.W.; Singh, S. and Brooker, S. Spin crossover in discrete polynuclear iron(II) complexes. *Chem. Soc. Rev.* **2018**, *47*, 7303-7338.
31. Gütllich, P.; Garcia, Y. and Goodwin, H.A. Spin crossover phenomena in Fe(II) complexes. *Chem. Soc. Rev.* **2000**, *29*, 419-427.
32. Elhaïk, J.; Kilner, C.A. and Halcrow M.A. Insight into Structure:Function Relationships in a Molecular SpinCrossover Crystal, from a Related Weakly Cooperative Compound. *Eur. J. Inorg. Chem.* **2014**, *26*, 4250 – 4253.
33. Tuna, E.; Lees, M.R.; Clarkson, G.J. and Hannon, G. Readily Prepared Metallo-Supramolecular Triple Helicates Designed to Exhibit Spin-Crossover Behaviour. *J. Chem. – Eur. J.* **2004**, *10*, 5737 -5750.
34. Berdiell, I.C.; Kulmaczewski, R. and Halcrow, M.A. Iron(II) Complexes of 2,4-Dipyrazolyl-1,3,5-triazine Derivatives—The Influence of Ligand Geometry on Metal Ion Spin State. *Inorg. Chem.* **2017**, *56*, 8817–8828.
35. Swart, M. and Costas, M. *Spin States in Biochemistry and Inorganic Chemistry: Influence on Structure and Reactivity*. John Wiley & Sons: Chichester, UK. **2016**, 465.

36. Takahashi, K.; Cui, H.; Kobayashi, H.; Einaga, Y. and Sato., O. The Light-induced Excited Spin State Trapping Effect on Ni(dmit)₂ Salt with an Fe(III) Spin-crossover Cation: [Fe(qsal)₂][Ni(dmit)₂]-2CH₃CN. *Chem. Lett.* **2005**, *34*, 1240-1241.
37. Takahashi, K.; Mori, H.; Kobayashi, H. and Sato, O. Mechanism of reversible spin transition with a thermal hysteresis loop in [FeIII(qsal)₂][Ni(dmise)₂]-2CH₃CN: Selenium analogue of the precursor of an Fe(III) spin-crossover molecular conducting system. *Polyhedron.* **2009**, *28*, 1776-1781.
38. Fumanal, M.; Jiménez-Grávalos, F.; Ribas-Arino, J. and Vela, S. Lattice-Solvent Effects in the Spin-Crossover of an Fe(II)-Based Material. The Key Role of Intermolecular Interactions between Solvent Molecules. *Inorg. Chem.* **2017**, *56*(8), 4474-4483.
39. Galadzhun, I.; Kulmaczewski, R.; Halcrow, M.A. Five 2,6-Di(pyrazol-1-yl)pyridine-4-carboxylate Esters, and the Spin States of their Iron(II) Complexes. *Magnetochem.* **2019**, *5*, 9.
40. Galet, A.; Gaspar, A.B.; Muñoz, M.C. and Real, J.A. Influence of the Counterion and the Solvent Molecules in the Spin Crossover System [Co(4-terpyridone)₂]X_p·nH₂O. *Inorg. Chem.* **2006**, *45*(11), 4413-4422.
41. Kitchen, J.A.; White, N.G.; Jameson, G.N.L.; Tallon, J.L. and Brooker, S. Effect of Counteranion X on the Spin Crossover Properties of a Family of Diiron(II) Triazole Complexes [FeII₂(PMAT)₂](X)₄. *Inorg. Chem.* **2011**, *50*, 4586-4597.
42. Akiyoshi, R.; Kuroiwa, K.; Amolegbe, S.A.; Nakaya, M.; Ohtani, R.; Nakamura, M.; Lindoyd, L.F. and Hayami, S. Supramolecular architectures self-assembled using long chain alkylated spin crossover cobalt(II) compounds. *Chem. Commun.* **2017**, *53*, 4685-4687.
43. Decurtins, S.; Gütllich, P.; Hasselbach, K.M.; Hauser, A. and Spiering, H. Light-Induced Excited-Spin-State Trapping in Iron(II) Spin-Crossover Systems. Optical Spectroscopic and Magnetic Susceptibility Study. *Inorg. Chem.* **1985**, *24*, 2174-2178.
44. Hayami, S.; Gu, Z.-Z.; Shiro, M.; Einaga, Y.; Fujishima, A. and Sato, O. First Observation of Light-Induced Excited Spin State Trapping for an Iron(III) Complex. *J. Am. Chem. Soc.* **2000**, *122*, 7126–712.

45. Poganiuch, P.; Decurtins, S. and Giitlich, P. Thermal- and Light-Induced Spin Transition in $[\text{Fe}(\text{mtz})_6](\text{BF}_4)_2$: First Successful Formation of a Metastable Low-Spin State by Irradiation with Light at Low Temperatures. *J. Am. Chem. Soc.* **1990**, *112*, 3270-3278.
46. Gutlich, P.; Hauser, A. and Spiering, H. Thermal and Optical Switching of Iron(II) Complexes. *Angew. Chem. Int. Ed. Engl.* **1994**, *33*, 2024-2054.
47. Liu, H.; Fujishima, A. and Sato, O. Photoinduced magnetic memory effect in an iron(II) spin-crossover complex. *Appl. Phys. Lett.* **2004**, *85*, 2295-2297.
48. Cook, L.J.K., Kulmaczewski, R., Cespedes, O. and Halcrow, M.A. Different Spin-State Behaviors in Isostructural Solvates of a Molecular Iron(II) Complex. *Chemistry – A European Journal*. 2016, **22**(5), pp.1789-1799.
49. Nave, C.R. Magnetic Properties of Solids. *HyperPhysics*, accessed 31/03/2019
<http://hyperphysics.phy-astr.gsu.edu/hbase/solids/magpr.html>
50. Saunderson, A. A permanent magnet Gouy balance. *Phys. Educ.* **1968**, *3*, 272
51. Lufaso, M. Magnetic susceptibility measurements of transition metal containing compounds. *University of North Florida Web Site*, accessed 05/04/2016 <https://www.unf.edu/~michael.lufaso/chem3610L/inorganiclabexp8.pdf>
52. Hayami, S.; Motokawa, N.; Shuto, A.; Masuhara, N.; Someya, T.; Ogawa, Y.; Inoue, K. and Maeda, Y. *Inorg. Chem.* **2007**, *46*, 1789-1794.
53. Létard, J.-F.; Guionneau, P. and Goux-Capes, L. Towards Spin Crossover Applications. *Spin Crossover in Transition Metal Compounds III*. Springer, Berlin-Heidelberg. **2004**, 221-249
54. Kahn, O. and Martinez, C. J. Spin-Transition Polymers: From Molecular Materials Toward Memory Devices. *Science*. **1998**, *279*, 44-48
55. Ye, S.; Geng, C.Y.; Shaik, S. and Neese, F. Electronic structure analysis of multistate reactivity in transition metal catalyzed reactions: the case of C-H bond activation by non-heme iron(IV)-oxo cores. *Phys. Chem. Chem. Phys.* **2013**, *15*, 8017-8030.

56. Nam, W.; Lee, Y.-M. and Fukuzumi, S. Tuning Reactivity and Mechanism in Oxidation Reactions by Mononuclear Nonheme Iron(IV)-Oxo Complexes. *Acc. Chem. Res.* **2014**, *47*, 1146–1154.
57. Scheidt, W.R. and Reed, C.A. Spin-State/Stereochemical Relationships in Iron Porphyrins: Implications for the Hemoproteins. *Chem. Rev.* **1981**, *81*, 543-555.
58. Halcrow, M. A. Jahn–Teller distortions in transition metal compounds, and their importance in functional molecular and inorganic materials *Chem. Soc. Rev.* **2013**, *42*, 1784-1795.
59. Hayami, S.; Motokawa, N.; Shuto, A.; Moriyama, R.; Masuhara, N.; Inoue, K. and Maeda, Y. Spin-crossover iron(II) compounds with liquid-crystal properties. *Polyhedron.* **2007**, *26*, 2375-2380.
60. Hong Li, H.; Peng, H. Recent advances in self-assembly of spin crossover materials and their applications. *Curr. Opin. Colloid Interface Sci.* **2018**, *35*, 9–16.
61. Gural'skiy, A.L.; Quintero, C.M.; Costa, J.S.; Demon, P.; Molnár G.; Salmon, L.;Shepherd, H.J. and Bousseksou, A. Spin crossover composite materials for electrothermomechanical actuators. *J. Mater. Chem. C.* **2014**, *2*, 2949-2955.
62. Gaspar, A. B. and Seredyuk, M. Spin crossover in soft matter. *Coordin. Chem. Rev.* **2014**, *268*, 41-58.
63. Huang, Y. and Gu, Y. Factors affecting the structure of lyotropic liquid crystals and the correlation between structure and drug diffusion. *RSC Adv.* **2018**, *8*, 6978-6987.
64. Lagerwall, J. P.F and Scalia G. A new era for liquid crystal research: Applications of liquid crystals in soft matter nano-, bio- and microtechnology. *Curr. Appl. Phys.* **2012**, *12*,1387-1412.
65. Chen, C.-H. and Yang, K.-L. Detection and quantification of DNA adsorbed on solid surfaces by using liquid crystals. *Langmuir.* **2010**, *26* (3), 1427-1430.
66. Andrienko, D. *Introduction to liquid crystals*, International Max Planck Research School, Bad Marienberg. **2006**.
67. Sonin, A. S. Inorganic lyotropic liquid crystals. *J. Mater. Chem.* **1998**, *8*, 2557-2574.

68. Wu, S.-T. and Yang, D.-K. *Fundamentals of Liquid Crystal Devices*. John Wiley & Sons. **2006**.
69. Gordon, M. *Liquid Crystal Polymers I*. Springer. **1984**
70. Edwards, G.A.; Bergren, A.J. and Porter, M.D. Chemically Modified Electrodes. *Handbook of Electrochemistry*. Elsevier Science. **2007**, 295-327.
71. Gaspar, A.B.; Seredyuk, M. and Gütllich, P. Spin crossover in metallomesogens. *Coord. Chem. Rev.* **2009**, 253, 2399-2413.
72. Giménez, R.; Lydon, D.P. and Serrano, J.L. Metallomesogens: a promise or a fact? *Curr. Opin. Solid State Mater. Sci.* **2002**, 6, 527-535.
73. Chisholm, M.H. Metallomesogens: Synthesis, Properties and Applications. *J. Am. Chem. Soc.* **1997**, 119 (1), 255-256.
74. Lee, Y.H.; Ohta, A.; Yamamoto, Y.; Komatsu, Y.; Kato, K.; Shimizu, T.; Shinoda, H. and Hayami, S. Iron(II) spin crossover complexes with branched long alkyl chain. *Polyhedron*. **2011**, 30, 3001-3005.
75. Seredyuk, M.; Carmen Muñ, M. C.; Ksenofontov, V.; Gütllich, P.; Galyametdinov, Y. and Real, J.A. Spin Crossover Star-Shaped Metallomesogens of Iron(II). *Inorg. Chem.* **2014**, 53, 8442-8454.
76. Fujigaya, T.; Jiang, D.-L. and Aida, T. Switching of Spin States Triggered by a Phase Transition: Spin-Crossover Properties of Self-Assembled Soc. **2003**, 48, 14690-14691.
77. Bodenthin, Y.; Pietsch, U.; Mohwald, H. and Kurth, D. G. Inducing Spin Crossover in Metallo-supramolecular Polyelectrolytes through an Amphiphilic Phase Transition. *J. Am. Chem. Soc.* **2005**, 127, 3110-3114.
78. Seredyuk, M.; Gaspar, A. B.; Ksenofontov, V.; Galyametdinov, Y.; Kusz, J. and Gutlich, P. Does the Solid-Liquid Crystal Phase Transition Provoke the Spin-State Change in Spin-Crossover Metallomesogens? *J. Am. Chem. Soc.* **2008**, 130, 1431-1439
79. Schlamp, S.; Thoma, P. and Weber, B. New Octahedral, Head-Tail Iron(II) Complexes with Spin Crossover Properties. *Eur. J. Inorg. Chem.* **2012**, 2759-2768.

80. Schlamp, S.; Dankhoff, K. and Weber, B. Amphiphilic iron(II) complexes with short alkyl chains – crystal packing and spin transition properties. *New J. Chem.* **2014**, *38*, 1965-1972.
81. Kitchen, J.A.; White, N.G.; Gandolfi, C.; Albrecht, M.; Jameson, G.N.L.; Tallond, J.L. and Brooker, S. Room-temperature spin crossover and Langmuir–Blodgett film formation of an iron(II) triazole complex featuring a long alkyl chain substituent: the tail that wags the dog. *Chem. Commun.* **2010**, *46*, 6464–6466.
82. Bauer, W.; Scherer, W.; Altmannshofer, S. and Weber, B. Two-Step versus One-Step Spin Transitions in Iron(II) 1D Chain Compounds. *Eur. J. Inorg. Chem.* **2011**, 2803-2818.
83. Rosario-Amorin, D.; Dechambenoit, P.; Bentaleb, A.; Rouzieres, M.; Mathoniere, C. and Clerac, R. Multistability at Room Temperature in a Bent-Shaped Spin-Crossover Complex Decorated with Long Alkyl Chains. *J. Am. Chem. Soc.* **2018**, *140*, 98–101.
84. Gandolfi, C.; Moitzi, C.; Schurtenberger, P.; Morgan, G.C. and Albrecht, M. Improved Cooperativity of Spin-Labile Iron(III) Centers by Self-Assembly in Solution. *J. Am. Chem. Soc.* **2008**, *130*, 14434–14435.
85. Wei, Y.L.; Sonar, P.; Grunert, M.; Kusz, J.; Schlüter, D. and Gütlich, P. Iron(II) Spin-Transition Complexes with Dendritic Ligands, Part II. *Eur. J. Inorg. Chem.* **2010**, 3930–3941.
86. Sonar, P.; Grunert, C.M.; Wei, Y.L.; Kusz, J.; Gütlich and P.; Schluter, A.D. Iron(II) Spin Transition Complexes with Dendritic Ligands, Part I. *Eur. J. Inorg. Chem.* **2008**, 1613-1622.
87. Fujigaya, T.; Jiang, D.L. and Aida, T. Spin-Crossover Dendrimers: Generation Number-Dependent Cooperativity for Thermal Spin Transition. *J. Am. Chem. Soc.* **2005**, *127*, 5484-5489.
88. Halcrow, M. A. *Spin-Crossover Materials*. John Wiley & Sons Ltd, Oxford, UK. **2013**.
89. Galan-Mascaros, J. R.; Coronado, E.; Forment-Aliaga, A.; Monrabal-Capilla, M.; Pinilla-Cienfuegos, E. and Ceolin, M. Tuning Size and Thermal Hysteresis in Bistable Spin Crossover Nanoparticles. *Inorg. Chem.* **2010**, *49*, 5706-5714.

90. Liu, W.; Bao, X.; Mao, L.-L.; Tucek, J.; Zboril, R.; Liu, J.-L.; Guo, F.-S.; Nia, Z.P. and Tong, M.-L. A chiral spin crossover metal-organic framework. *Chem. Commun.* **2014**, 50, 4059-4061.
91. Burrows, K.E.; McGrath, S.E.; Kulmaczewski, R.; Cespedes, O. Barrett, S.A. and Halcrow, M.A. Spin States of Homochiral and Heterochiral Isomers of $[\text{Fe}(\text{PyBox})_2]^{2+}$ Derivatives. *Chem. Eur.J.* **2017**, 23, 9067-9075.
92. Kuroiwa, K. Supramolecular Control of Spin Crossover Phenomena Using Various Amphiphiles. *Inorganics.* **2017**, 5, 1-17.
93. Grondin, P.; Roubeau, O.; Castro, M.; Saadaoui, H.; Colin, A. and Clerac, R. Multifunctional Gels from Polymeric Spin-Crossover Metallo-Gelators. *Langmuir.* **2010**, 26, 5184–5195.

Chapter 2

**Bis(pyrazol-1-yl)pyridine derivatives with no long alkyl
chains, and their iron(II) complexes**

2.1 Introduction

This chapter contains information about novel ligands based on 2,6-bis(pyrazol-1-yl)pyridine bpp (Fig. 2.1), and their iron(II) complexes, which have no long alkyl chains, and therefore are unlikely to form liquid crystals. However, they are interesting in respect of the effect of ligand structure on spin crossover, and the effect of the alkyl chain length, when compared with the corresponding iron(II) complexes from Chapter 3.

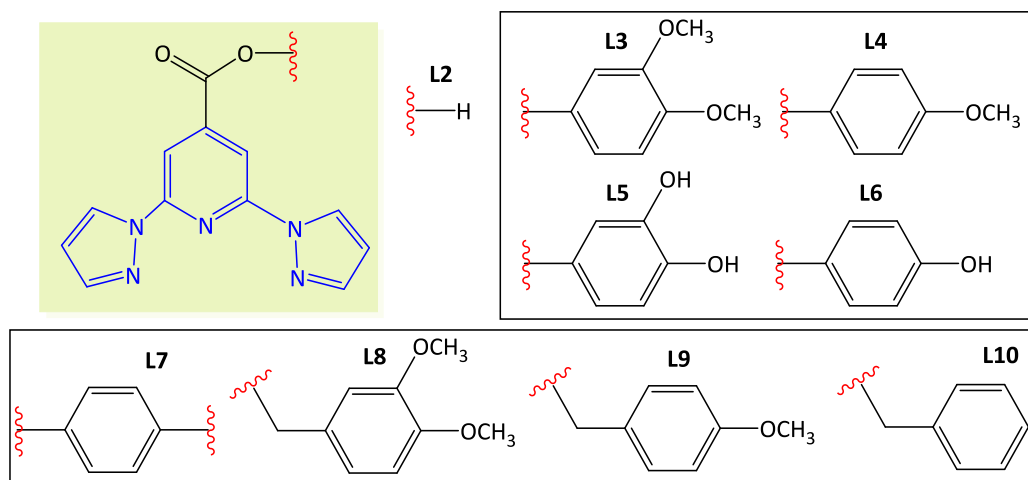


Fig. 2.1. The list of the ligands, discussed in Chapter 2. The **bpp** core is highlighted in blue

2.2 Ligand synthesis

The first two steps of the synthesis below afforded **L2**, which then was used as a precursor for the seven ligands with no long alkyl chains (Fig. 2.1), discussed below in this chapter, as well as for a poorly soluble ligand **L7**, for which no iron complexes were obtained, and for two novel ligands series, **L11C** and **L12C**, with different alkyl chain lengths, which are discussed in Chapter 3.

2.2.1 L1 - 2,6-dibromo pyridine-4-carboxylic acid

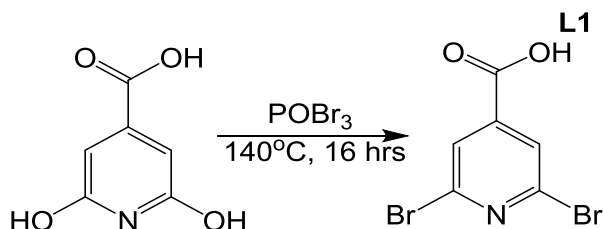


Fig. 2.2. Synthesis of 2,6-dibromo pyridine-4-carboxylic acid

The first step of this synthesis (Fig. 2.2) was performed according to a procedure reported by Beierlein *et al.*¹. Some quantity of insoluble glass-like

impurity formed during this reaction, which was separated piece by piece using tweezers. It appears that if the reaction mixture is heated quickly, the amount of the above-mentioned by-product is reduced.

2.2.2 L2 - 2,6-di(1H-pyrazole-1'-yl)pyridine-4-carboxylic acid

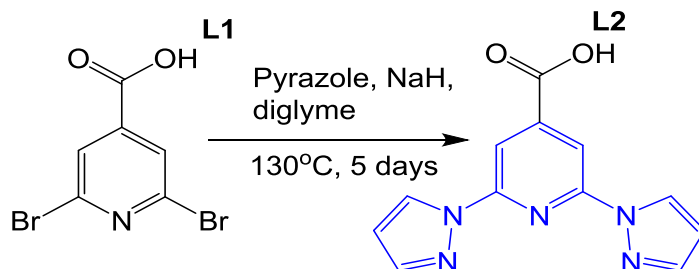


Fig. 2.3. Synthesis of 2,6-di(1H-pyrazole-1'-yl)pyridine-4-carboxylic acid

L2 was obtained according to the procedure, reported by Cook *et al.*² (Fig. 2.3). This compound is soluble in water at alkali pH, but precipitates when the solution is acidified. When obtaining L2 from the solution, a two forms of it, with slightly different ¹H NMR shifts were collected: A and B (Fig. 2.4). If sufficiently acidified, the form A turns into form B.

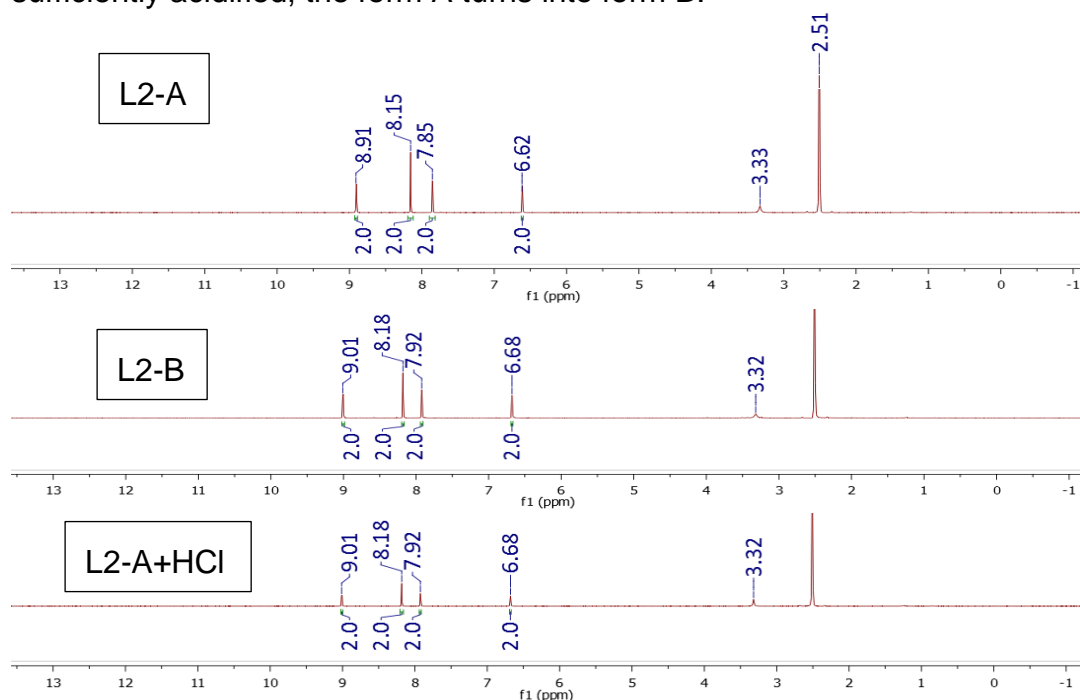


Fig. 2.4. Comparison of ¹H NMRs of the two forms of 2,6-di(1H-pyrazole-1'-yl)pyridine-4-carboxylic acid, measured in DMSO-D6

The transition between the A and the B forms was tracked by ¹H NMR only, and ¹³C NMR has been collected only for the form B. As a quite low pH, around pH 3, is required to convert the form A into B, the two forms must differ from each other by the protonation of the COOH group rather than by

the protonation of the pyridyl nitrogen. Therefore, the form A must have a formula bpp-COO^- , and form B shall be bpp-COOH .

2.2.3 L3, L4 - 3,4-dimethoxyphenyl (2,6-di-1H-pyrazole-1-yl)pyridine-4-carboxylate, and 4-methoxyphenyl (2,6-di-1H-pyrazole-1-yl)pyridine-4-carboxylate

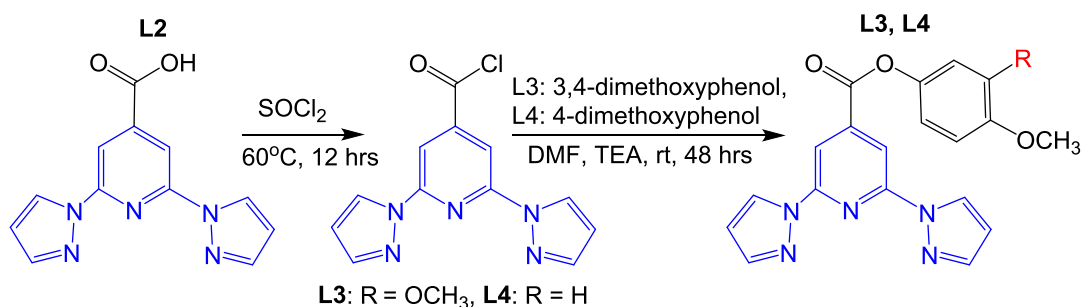


Fig. 2.5. Synthesis of **L3** and **L4**

All attempts to analyse the intermediate acyl chloride were unsuccessful, as it hydrolyses readily.

Out of the two esterification methods³ that were tested: using thionyl chloride, and using DCC as a coupling agent, the second reaction is faster and more convenient (Fig. 2.9). However it is important to use fresh DCC, and to store DCC in a fridge, otherwise the synthesis may fail.

2.2.4 L5, L6 - 3,4-dihydroxyphenyl (2,6-di-1H-pyrazole-1-yl)pyridine-4-carboxylate, and 4-hydroxyphenyl (2,6-di-1H-pyrazole-1-yl)pyridine-4-carboxylate

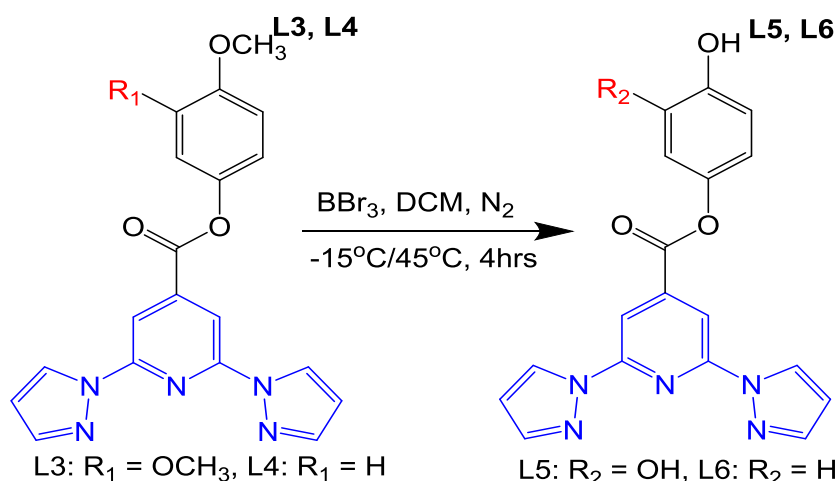


Fig. 2.6. Synthesis of **L5** and **L6**

Ligands **L3** and **L4** were demethylated using boron tribromide,² which turned them into **L5** and **L6** correspondingly (Fig. 2.6). This reaction yielded a mixture of two precipitates - a white and a red one, which were filtered off from the reaction mixture and physically separated. Each precipitate was

separately washed with water, dried on the filter, and then washed with DCM and recrystallized from acetone. After this purification both the red and the white precipitates turned into greyish-white powders, which were confirmed to be the same compound by ^1H NMR.

2.2.5 L7 - 1,4-Bis[2,6-di(1H-pyrazole-1'-yl)pyridine-4-carboxylate]benzene

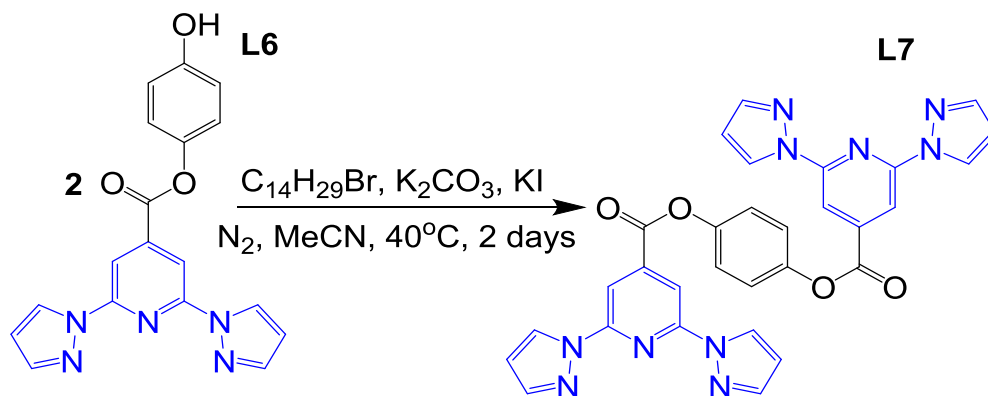


Fig. 2.7. Synthesis of L7

Attempts to attach a long alkyl chain to L6 led to formation of the ligand L7 (Fig 2.7). The product was very poorly soluble in any of the common solvents, so only ^1H NMR (Fig. 2.8) and a crystal structure (Fig. 2.15) were collected for this ligand.

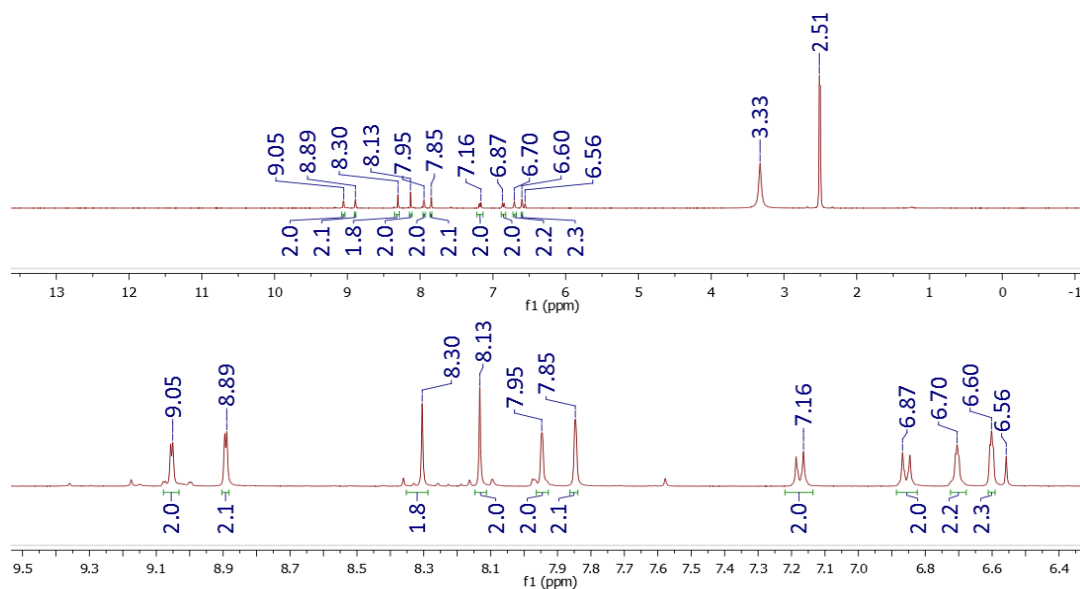


Fig. 2.8 ^1H NMR of L7 in $\text{DMSO}-d_6$: full view and an expansion

2.2.6 L8, L9, L10 - 3,4-dimethoxy benzyl(2,6-di-1H-pyrazole-1-yl)pyridine-4-carboxylate, 4-methoxy benzyl(2,6-di-1H-pyrazole-1-yl)pyridine-4-carboxylate, and benzyl(2,6-di-1H-pyrazole-1-yl)pyridine-4-carboxylate

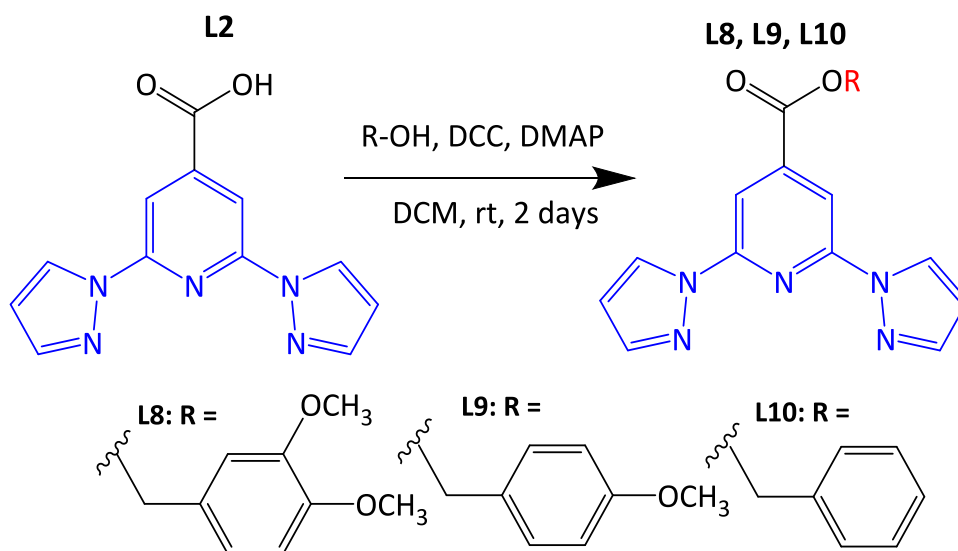


Fig. 2.9. Synthesis of **L8, L9, L10**

3,4-Dimethoxy benzyl(2,6-di-1H-pyrazole-1-yl)pyridine-4-carboxylate **L8**, 4-methoxy benzyl(2,6-di-1H-pyrazole-1-yl)pyridine-4-carboxylate **L9**, and benzyl(2,6-di-1H-pyrazole-1-yl)pyridine-4-carboxylate **L10** were all synthesized using the same esterification reaction protocol, during which the coupling agent, N,N'-dicyclohexylcarbodiimide (DCC) turns into dicyclohexylurea (DCU). The latter is notoriously hard to remove. DCU is much more soluble in cold MeCN than the ligands, and it was possible to obtain a clean ligand **L8** by recrystallization from MeCN, however **L9** and **L10** required column chromatography for complete purification.

2.3 Iron(II) complex synthesis

L1 is not suitable for forming spin crossover iron complexes, the iron(II) complex of **L2** has been reported before², and **L7** was too insoluble to carry out the complexation reaction. For all the other listed above ligands, iron(II) complexes were obtained and studied (Fig. 2.10).

It is known that the structure of the ligand, the counterion⁴ and the lattice solvent⁵ affect spin crossover in solid state, and as trying all of the possible combinations of counterion and crystallization solvent for each ligand would be too much work, the BF_4^- was used as a counterion throughout this thesis. Keeping the same solvent for crystallization with each different ligand was

more difficult, as different ligands have different solubilities, and sometimes growing single crystals for XRD might take many tries to succeed. In general, the lattice solvent was either MeCN or acetone for ligands with no long alkyl chains, and a DCE-acetone mixture for the ligands with long alkyl chains.

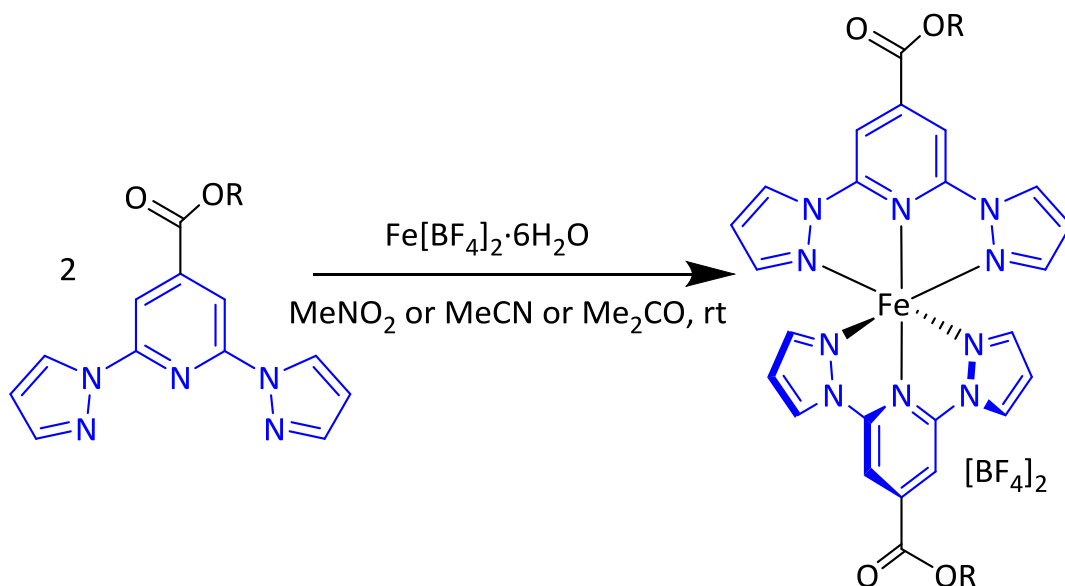


Fig. 2.10 General scheme for obtaining iron(II) complexes in Chapter 2

2.4 XRD

2.4.1 Crystal structures of the ligands

L2, L3, L4, L5, and L6

In this ligand series crystal structures were obtained for each ligand, except **L5**, despite multiple attempts to obtain crystallographic quality crystals of it. All ligands in this series crystallized with no lattice solvent.

L2 molecules stack on top of each other, and form hydrogen bonding between the COOH hydrogen and the N5 nitrogen of the molecule from the neighbouring stack. The second molecule, mentioned above, in turn, bonds with its COOH hydrogen of the molecule directly above the first molecule. This means that, rather than forming the clusters of two molecules, hydrogen bonded to each other reciprocally, this ligand forms long polymeric hydrogen bonded structures, which connect parallel stacks together (Fig 2.11).

In **L4** packing, both bpp and phenyl rings pile in parallel stacks (Fig. 2.12), while **L3** and **L6** pack, so the bpp parts of the molecules stack parallel to each other, with every other bpp turned at ca 96° for **L6** (Fig. 2.14) and ca 109° for **L3** (Fig. 2.13). In this case every other phenyl ring sticks in different direction, so they do not overlap.

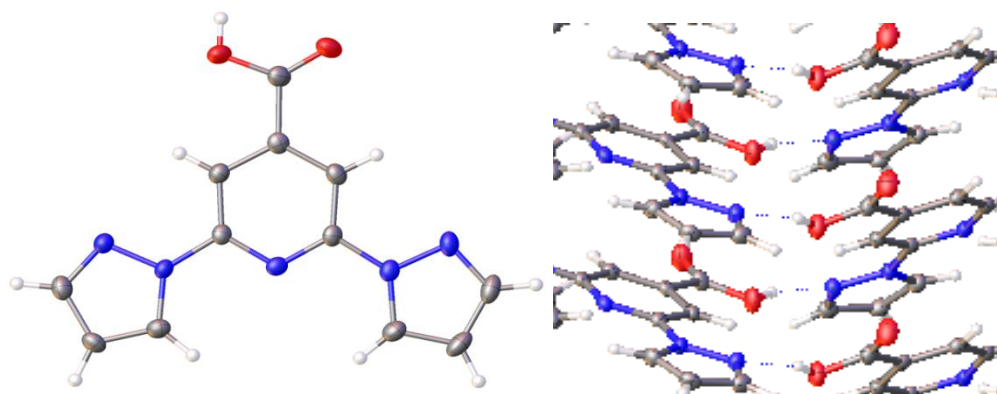


Fig. 2.11 Crystal structure of **L2** and its packing diagram from the view, parallel to the [010] vector

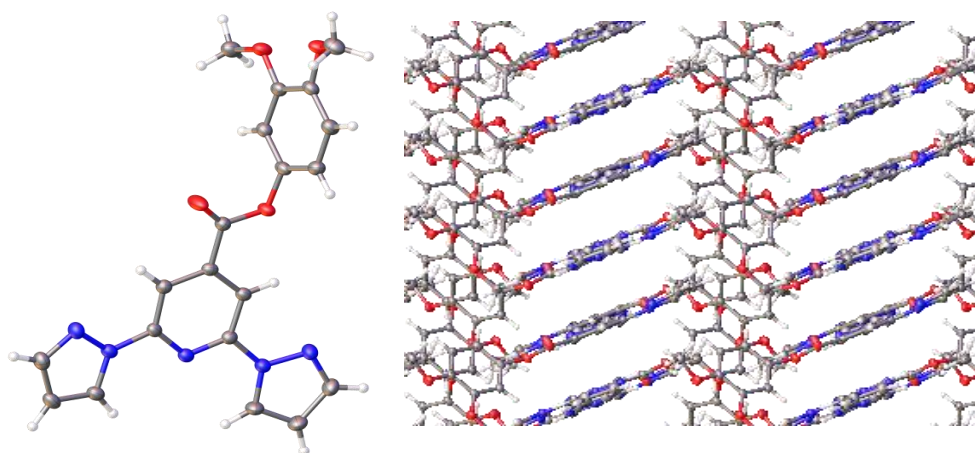


Fig. 2.12 Crystal structure of **L3** and its packing diagram from the view, parallel to the [010] vector

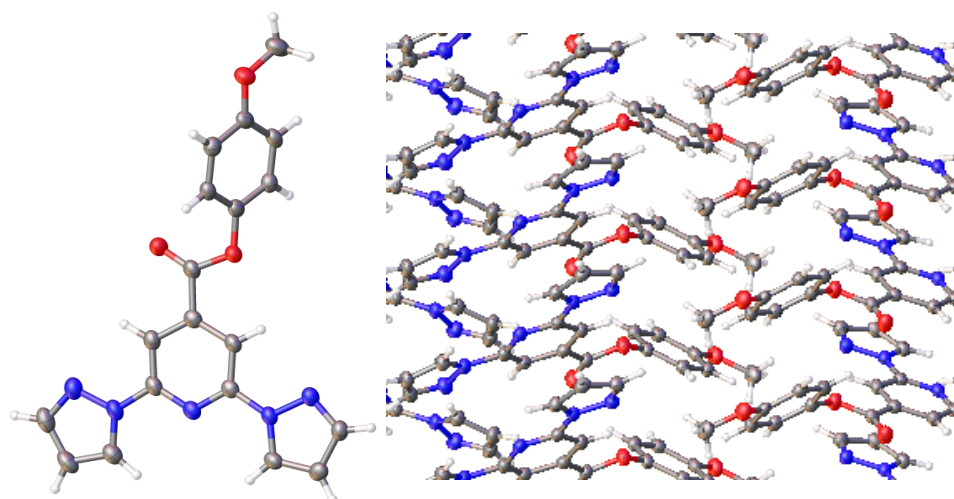


Fig. 2.13 Crystal structure of **L4** and its packing diagram from the view, parallel to the [010] vector

L6 forms a hydrogen bond between the Ph-OH hydrogen and the N5 from the neighbouring molecule, and the ligand molecules are connected with hydrogen bonding in long zig-zag threads. **L3**, **L4**, **L5** and **L6**, all crystallized with one ligand molecule per asymmetric unit, e.g. $Z' = 1$.

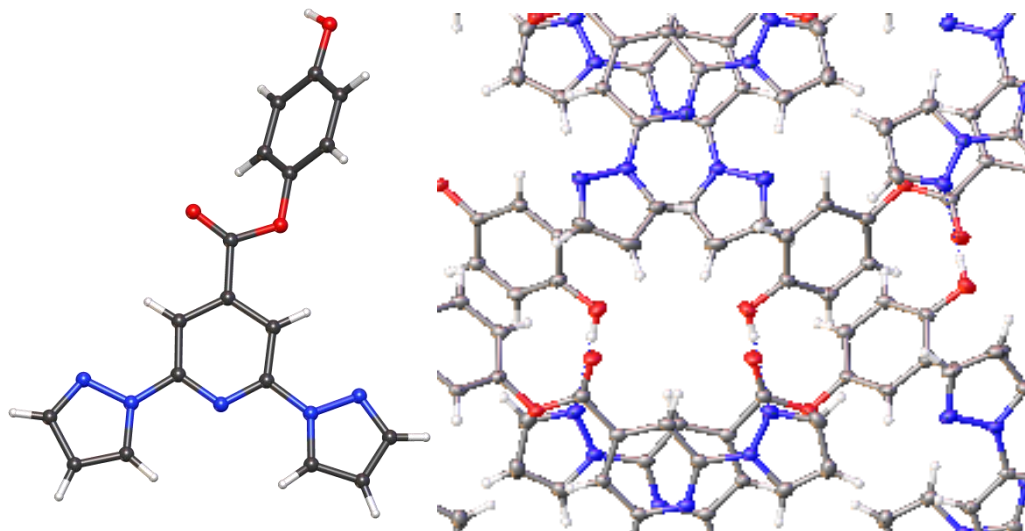


Fig. 2.14 Crystal structure of **L6** and its packing diagram from the view, parallel to the [010] vector

L7

Poorly soluble needle crystals of the ligand **L7**, that formed from the reaction mixture, were of diffraction quality, which allowed to collect the crystal structure from one of them (Fig 2.15). The molecules of **L7** pack in the lattice, so the the bpp fragments of the molecules stack on top each other, same as the phenyl rings (Fig 2.15). For **L7** there is half a molecule in the asymmetric unit, i.e. $Z' = 0.5$.

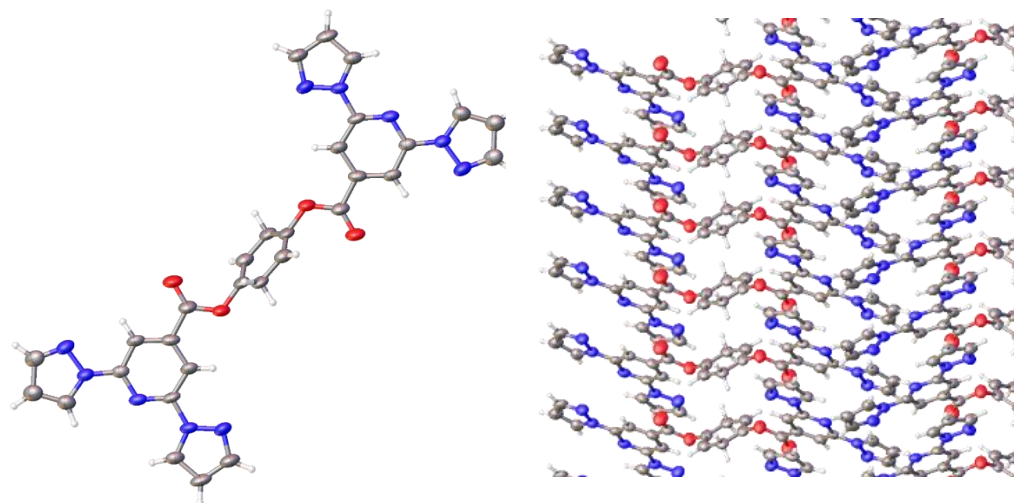


Fig. 2.15 Crystal structure of the ligand **L7** and its packing diagram from the view, parallel to the vector [001]

L8, L9, L10

The crystals of the ligands **L8**, **L9**, and **L10** were collected at the Diamond Light Source. **L8**·0.5MeCN has two ligand molecules and one MeCN molecule per asymmetric unit, while **L9** (Fig. 2.17) has one and **L10** (Fig. 2.18) has two ligand molecules per asymmetric unit, and no lattice solvent.

The molecules of **L8**·0.5MeCN are packed the way that the phenyl rings are facing each other, but not forming π - π stacking, and MeCN molecules are located in the gaps between them (Fig. 2.16). The molecules of **L10** are packed more tightly than **L8**, probably because **L10** has no methoxy groups and lattice solvent.

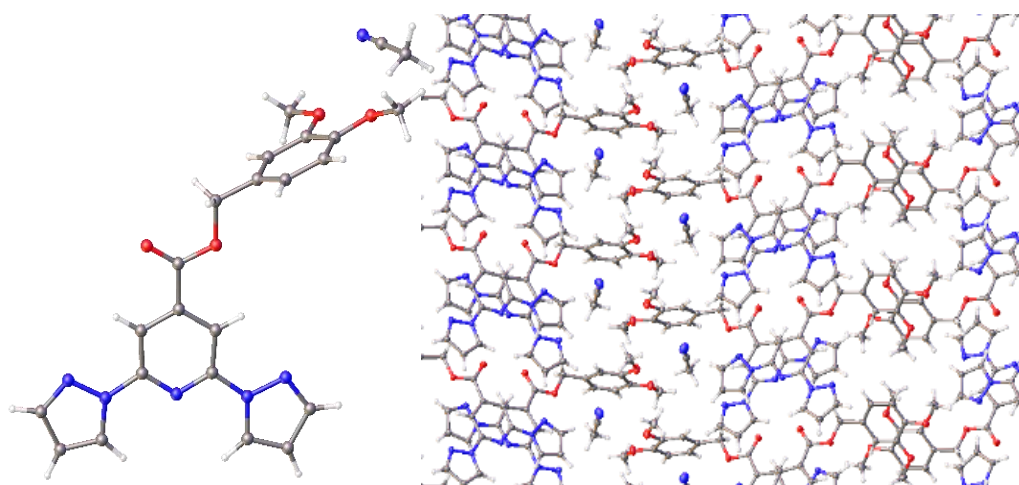


Fig. 2.16 Crystal structure of **L8**·0.5MeCN and its packing diagram from the view, parallel to the [100] vector

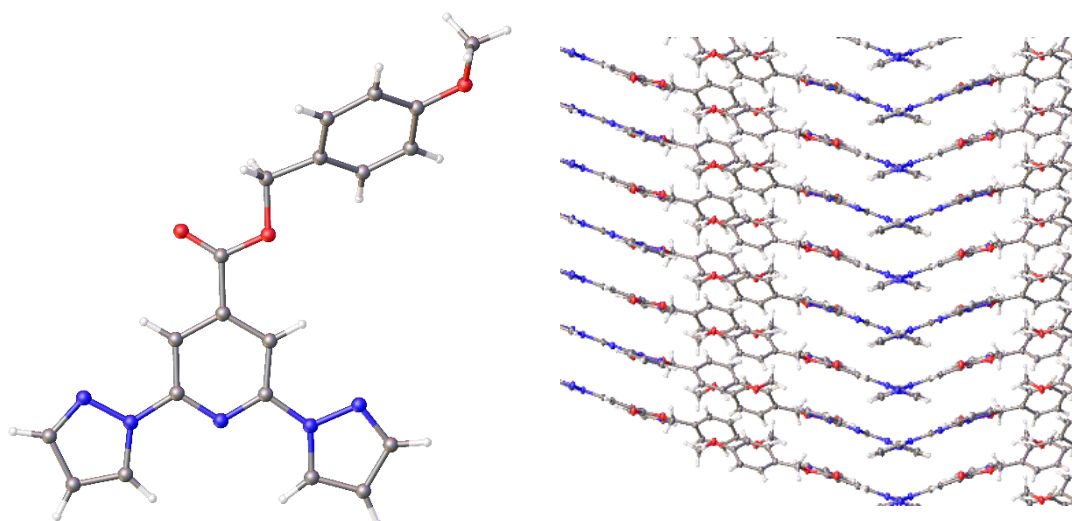


Fig. 2.17 Crystal structure of **L9** and its packing diagram from the view, parallel to the [010] vector

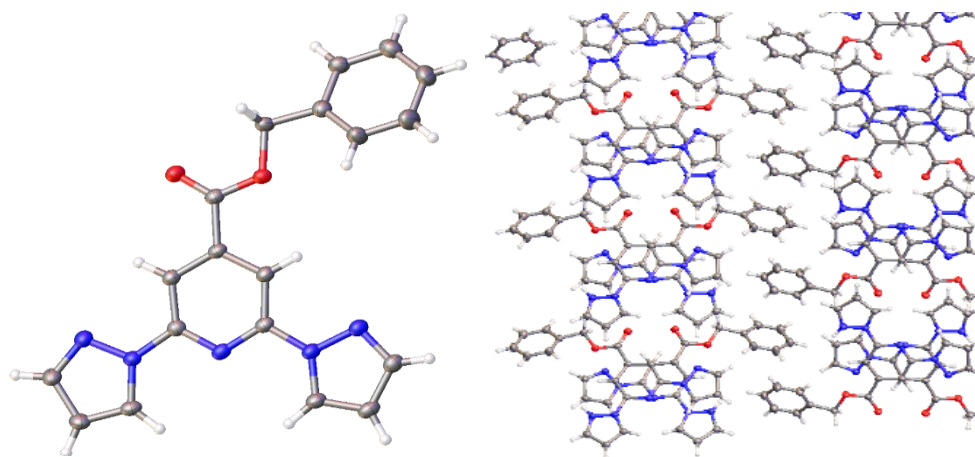


Fig. 2.18 Crystal structure of **L10** and its packing diagram from the view, parallel to the [100] vector

2.4.2 Crystal structures of iron complexes

[Fe(L3)₂][BF₄]₂, [Fe(L4)₂][BF₄]₂, [Fe(L5)₂][BF₄]₂, [Fe(L6)₂][BF₄]₂,

[Fe(L3)₂][BF₄]₂, [Fe(L4)₂][BF₄]₂, [Fe(L5)₂][BF₄]₂, and [Fe(L6)₂][BF₄]₂ were the first series of iron(II) complexes obtained during my PhD project, and because of that they were tested more for different crystallization solvents and techniques, which resulted in many different solvates, many of which were collected at few different temperatures to track the spin crossover process. This series has many crystal structures, and for convenience, they are all summarized in the table below (Table 2.1).

Crystallographic quality crystals of [Fe(L3)₂][BF₄]₂ were grown from three different solvents: acetone, MeCN, and MeNO₂. The crystals grown from acetone, contained in the asymmetric unit one iron complex molecule, two counteranions, one acetone, and two diethyl ether molecules. The structure grown from MeCN, had 2 MeCN and 3 water molecules and one iron complex molecule per asymmetric unit. A crystal structure for this compound was also collected at 300K, and the molecule remained LS at that temperature, but only one molecule of MeCN per iron complex molecule remained in the lattice. The crystals of [Fe(L3)₂][BF₄]₂ grown from MeNO₂ formed two polymorphs: the red crystals, and a small fraction of yellow crystals. The red polymorph was LS at 120K, so the crystal was heated to 290K, but it remained LS at this temperature. A crystal structure of the yellow polymorph was also collected, which showed that the iron(II) centre is HS in this molecule even at 120K. The two polymorphs, despite being grown from the same solvent and both having two MeNO₂ molecules per one iron complex molecule, have different colours, different unit cell parameters (Table 2.2), and completely different magnetic behaviour with temperature:

the red polymorph remains LS, even when heated to 290K, and the yellow polymorph stays HS even when cooled to 120K. Besides this, in the yellow polymorph molecules pack, so the iron complex molecules are located directly behind each other, while in the red polymorph every other molecule is shifted, which forms two co-parallel but offset rows (Fig. 2.19).

Table 2.1 XRD structures, collected for different solvates of [Fe(L3)₂][BF₄]₂, [Fe(L4)₂][BF₄]₂, [Fe(L5)₂][BF₄]₂, [Fe(L6)₂][BF₄]₂, [Fe(L8)₂][BF₄]₂, [Fe(L9)₂][BF₄]₂, and [Fe(L10)₂][BF₄]₂

* The highlighted solvates were also measured with the SQUID magnetometer

Ligand	Crystallization solvent	Iron Complex formula	Per asym. unit	Meas. at T, K
L3	Acetone	[Fe(L3) ₂][BF ₄] ₂ ·Me ₂ CO·2Et ₂ O	1	120
	MeCN	[Fe(L3) ₂][BF ₄] ₂ ·2MeCN·3H ₂ O	1	120, 300
	MeNO ₂ red polymorph*	[Fe(L3) ₂][BF ₄] ₂ ·2MeNO ₂	1	120, 290
	MeNO ₂ yellow polymorph	[Fe(L3) ₂][BF ₄] ₂ ·2MeNO ₂	1	120
L4	Acetone*	[Fe(L4) ₂][BF ₄] ₂	1	120, 293
	MeNO ₂	[Fe(L4) ₂][BF ₄] ₂	1	120
L5	Acetone*	[Fe(L5) ₂][BF ₄] ₂	2	120
L6	Acetone	[Fe(L6) ₂][BF ₄] ₂ ·Me ₂ CO	1	120
	MeCN	[Fe(L6) ₂][BF ₄] ₂ ·MeCN	2	120
	MeCN	[Fe(L6) ₂][BF ₄] ₂	1	121
	MeNO ₂ *	[Fe(L6) ₂][BF ₄] ₂ ·0.5H ₂ O	2	100, 250, 360
L8	MeCN	[Fe(L8) ₂][BF ₄] ₂ ·0.25MeCN	2	150
	Acetone*	[Fe(L8) ₂][BF ₄] ₂ ·Me ₂ CO·0.25H ₂ O	2	120
L9	MeCN*	[Fe(L9) ₂][BF ₄] ₂ ·1.5MeCN	2	150
	Acetone*	[Fe(L9) ₂][BF ₄] ₂ ·0.5Me ₂ CO	2	120
L10	MeCN*	[Fe(L10) ₂][BF ₄] ₂ ·1.5MeCN	2	150
	Acetone*	[Fe(L10) ₂][BF ₄] ₂ · ² / ₃ Me ₂ CO	3	120

Table 2.2 Comparison of the unit cells for the two polymorphs of $[\text{Fe}(\text{L3})_2][\text{BF}_4]_2 \cdot 2\text{MeNO}_2$

$[\text{Fe}(\text{L3})_2][\text{BF}_4]_2 \cdot 2\text{MeNO}_2$ polymorphs			
	Red		Yellow
Temperature/K	120.1(4)	Temperature/K	120.0(3)
Crystal system	triclinic	Crystal system	triclinic
Space group	P-1	Space group	P-1
a/Å	8.32214(15)	a/Å	11.3589(9)
b/Å	12.8301(2)	b/Å	13.2662(13)
c/Å	23.1768(6)	c/Å	17.5527(14)
α°	88.1141(17)	α°	67.653(8)
β°	80.2771(19)	β°	80.169(7)
γ°	89.5667(14)	γ°	78.448(8)
Volume/Å ³	2437.80(9)	Volume/Å ³	2383.7(4)
Z	2	Z	2

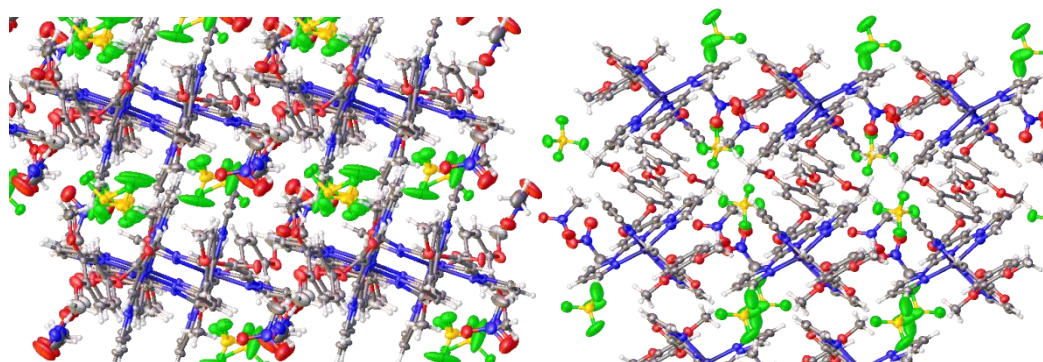


Fig. 2.19 Packing for the $[\text{Fe}(\text{L3})_2][\text{BF}_4]_2 \cdot 2\text{MeNO}_2$: red polymorph (left) and the yellow polymorph (right)

$[\text{Fe}(\text{L4})_2][\text{BF}_4]_2$ was crystallized from acetone and MeNO_2 , and in both cases the unit cell was the same (Table 2.3), so a complete dataset was collected only for the sample obtained from acetone (Fig. 2.12). There was no solvent in the crystal lattice, and as the iron was LS at 120K, another structure of the same iron complex was collected, this time at 293K, but at this temperature the iron centre remained LS.

There are no hydrogen bonding or π - π interactions in the crystal lattice of $[\text{Fe}(\text{L4})_2][\text{BF}_4]_2$, and the phenyl rings align, so they are not parallel to each other (Fig. 2.20).

For $[\text{Fe}(\text{L5})_2][\text{BF}_4]_2$ a crystal structure was collected only for the crystals grown from acetone. There was no solvent in the crystal lattice, and two iron complex molecules in the asymmetric unit. In the lattice there are hydrogen bonds between the para-OH hydrogen and the meta-OH oxygen from the

neighboring molecule, as well as between the para-OH hydrogen and BF₄ fluorine (Fig. 2.21).

Table 2.3 Comparison of the unit cells for [Fe(L4)₂][BF₄]₂ grown from different solvents

[Fe(L4) ₂][BF ₄] ₂	
Acetone	MeNO ₂
Temperature/K 120.0(3)	Temperature/K 119.99(10)
Crystal system monoclinic	Crystal system monoclinic
Space group I2/a	Space group I2/a
a/Å 27.5349(8)	a/Å 27.453(7)
b/Å 8.3035(2)	b/Å 8.294(3)
c/Å 35.3908(7)	c/Å 35.428(14)
α/° 90	α/° 90
β/° 99.537(2)	β/° 99.38(3)
γ/° 90	γ/° 90
Volume/Å ³ 7979.8(3)	Volume/Å ³ 7959(5)

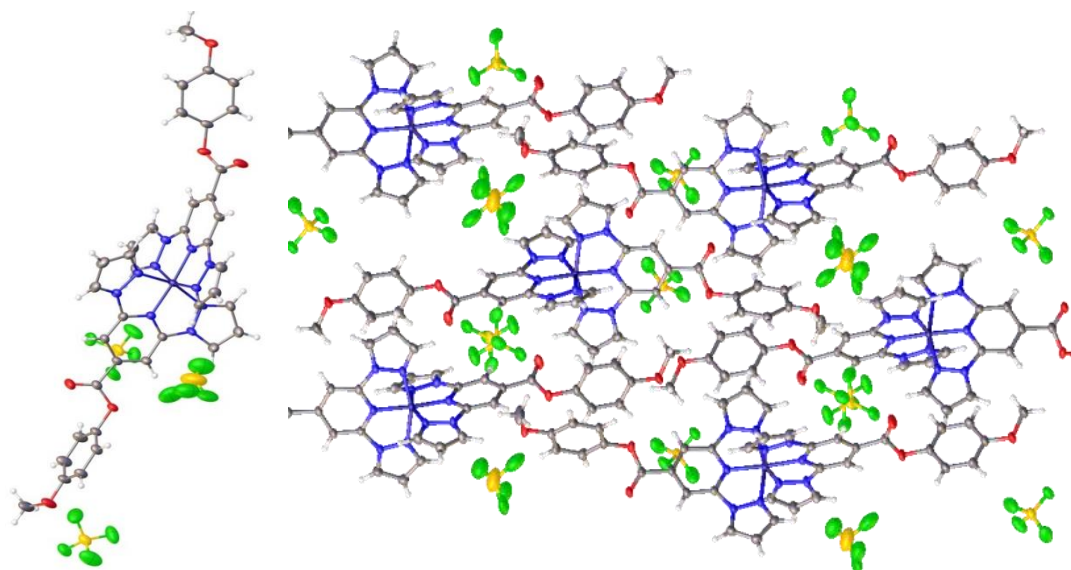


Fig. 2.20 Crystal structure of [Fe(L4)₂][BF₄]₂ at 120K, and its packing diagram from the view, parallel to the [010] vector

[Fe(L6)₂][BF₄]₂ was crystallized from acetone, MeCN, and MeNO₂. The crystals grown from acetone contained in the asymmetric unit one acetone and one iron complex molecule. For the crystals grown from MeCN there were two different crystal structures collected: one with no solvent in the lattice, and the other with two MeCN and two iron complex molecules in the asymmetric unit. The two structures had different unit cell parameters, but were both LS at 120K.

The crystals grown from MeNO₂ had one water molecule in the lattice per two iron complex molecules. The same crystal has been remeasured at 100K, 250K, and 360K, and the water molecule remained in the lattice at 100K and at 250K at full occupancy, but at 360K there was no solvent in the lattice. This water molecule was connected with two hydrogen bonds: water hydrogen to BF₄ fluorine, and water hydrogen to O3C oxygen. Besides this, there were other hydrogen bonds present: O3D hydrogen to O3C oxygen, and O3A hydrogen to F3 fluorine (Fig. 2.22).

The change in the average Fe-N bond length of [Fe(L6)₂][BF₄]₂·0.5H₂O when heated is too large to explain it by thermal expansion. Further investigation of this change and linking it with spin crossover can be found in the subchapter “Distortion parameters” below.

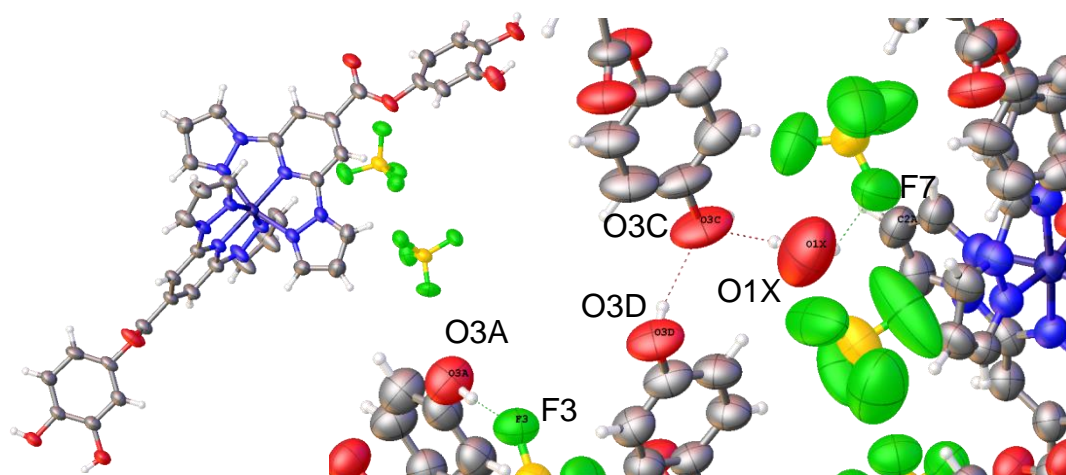


Fig. 2.21 Crystal structure of [Fe(L5)₂][BF₄]₂ at 120K, and its packing diagram from the view, parallel to the [100] vector

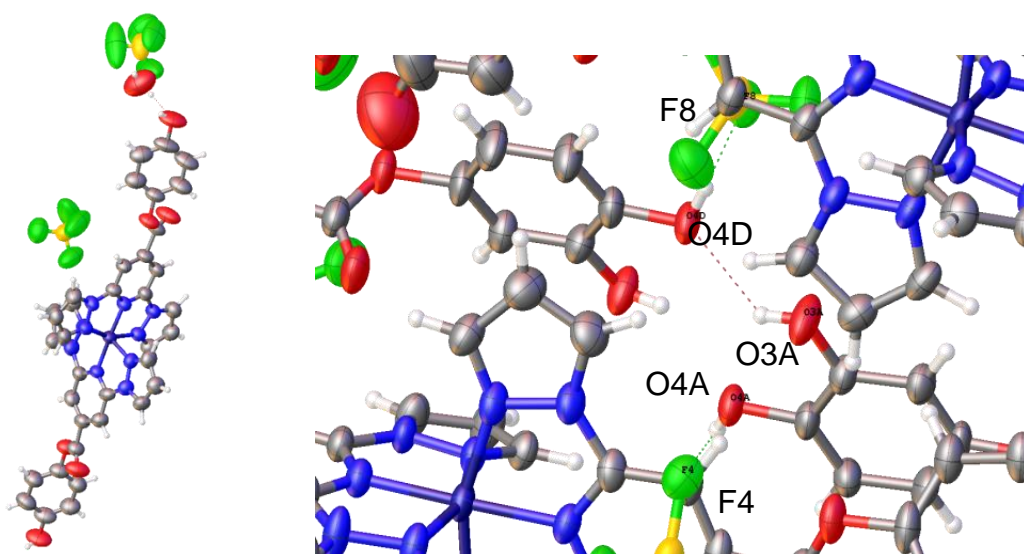


Fig. 2.22 Crystal structure of [Fe(L6)₂][BF₄]₂·0.5H₂O at 250K, and its packing diagram from the view, parallel to the [100] vector

[Fe(L8)₂][BF₄]₂, [Fe(L9)₂][BF₄]₂, and [Fe(L10)₂][BF₄]₂

It was relatively easy to obtain good quality crystals of the iron complexes [Fe(L8)₂][BF₄]₂, [Fe(L9)₂][BF₄]₂, and [Fe(L10)₂][BF₄]₂, so crystal structures were collected for all three iron complexes, for crystals grown from MeCN, and from acetone – 6 structures in total. The [Fe(L8)₂][BF₄]₂ crystals grown from acetone and MeCN have the same unit cell, while for the other two, [Fe(L9)₂][BF₄]₂ and [Fe(L10)₂][BF₄]₂, different solvents resulted in a different unit cell (Table 2.4). In all three cases the crystal structures of the MeCN solvates had much better quality, than crystals grown from acetone, and therefore the crystal structures of MeCN solvates will be discussed below.

[Fe(L8)₂][BF₄]₂·0.25MeCN has one half occupancy MeCN molecule per 2 iron complex molecules in the asymmetric unit (Fig. 2.23), while [Fe(L9)₂][BF₄]₂·1.5MeCN and [Fe(L10)₂][BF₄]₂·1.5MeCN have three. In [Fe(L9)₂][BF₄]₂·1.5MeCN, the MeCN molecules are located in the lattice in groups of two, packed head-to-tail (Fig. 2.24), while in [Fe(L8)₂][BF₄]₂·0.25MeCN and [Fe(L10)₂][BF₄]₂·1.5MeCN they are packed differently – further from each other, and in a less organized fashion.

[Fe(L8)₂][BF₄]₂·0.25MeCN and [Fe(L9)₂][BF₄]₂·1.5MeCN had no π-π stacking between the phenyl rings, as they were located too far from each other and were tilted from being parallel to each other. [Fe(L10)₂][BF₄]₂·1.5MeCN also had no π-π stacking, and the phenyl rings are much further from each other than in previous two cases, but the packing in general seems to be more tight and aligned (Fig. 2.25), which may explain the good cooperativity that causes abrupt spin crossover (Fig. 2.28).

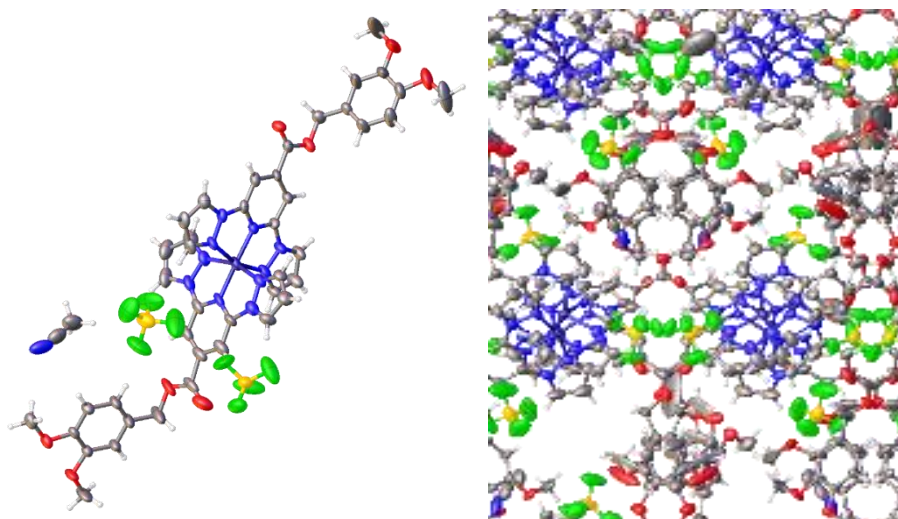


Fig. 2.23 Crystal structure of [Fe(L8)₂][BF₄]₂·0.25MeCN, and its packing diagram from the view, parallel to the [100] vector

Table 2.4 Comparison of the unit cells of [Fe(L8)₂][BF₄]₂, [Fe(L9)₂][BF₄]₂, and [Fe(L10)₂][BF₄]₂

	Acetone	MeCN
[Fe(L8) ₂][BF ₄] ₂	Crystal system orthorhombic Space group Pna2 ₁ a/Å 16.1790(10) b/Å 21.1621(11) c/Å 28.8196(8) α/° 90 β/° 90 γ/° 90 Volume/Å ³ 9867.3(8) Z 8	Crystal system orthorhombic Space group Pna2 ₁ a/Å 16.1146(5) b/Å 21.2398(8) c/Å 28.5755(10) α/° 90 β/° 90 γ/° 90 Volume/Å ³ 9780.6(6) Z 8
[Fe(L9) ₂][BF ₄] ₂	Crystal system orthorhombic Space group Pca2 ₁ a/Å 20.7502(16) b/Å 15.444(3) c/Å 28.842(7) α/° 90 β/° 90 γ/° 90 Volume/Å ³ 9243(3) Z 8	Crystal system monoclinic Space group P2 ₁ /c a/Å 27.4401(4) b/Å 16.5615(3) c/Å 20.5281(2) α/° 90 β/° 100.2570(10) γ/° 90 Volume/Å ³ 9179.9(2) Z 8
[Fe(L10) ₂][BF ₄] ₂	Crystal system monoclinic Space group P2 ₁ /c a/Å 14.6653(5) b/Å 46.894(2) c/Å 20.7067(6) α/° 90 β/° 105.985(3) γ/° 90 Volume/Å ³ 13689.7(9) Z 12	Crystal system triclinic Space group P-1 a/Å 13.8965(6) b/Å 17.0836(7) c/Å 20.8001(7) α/° 95.020(3) β/° 102.703(3) γ/° 113.133(4) Volume/Å ³ 4345.8(3) Z 4

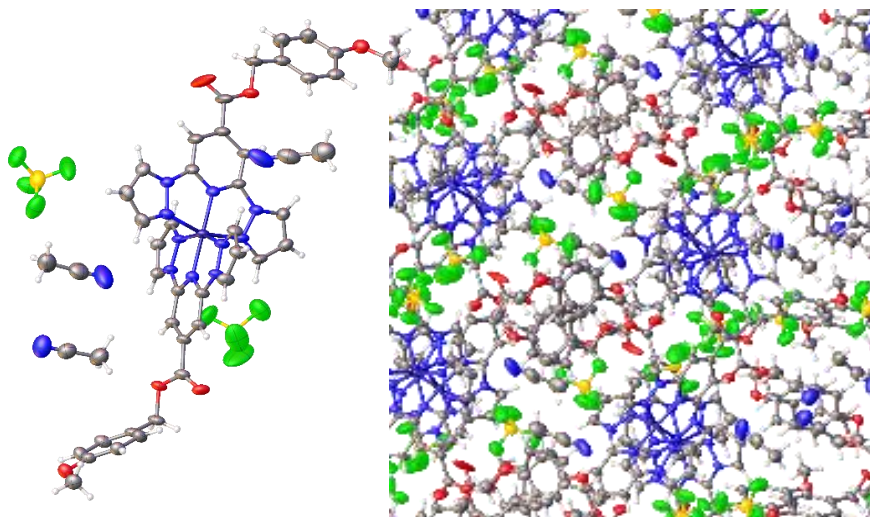


Fig. 2.24 Crystal structure of $[\text{Fe}(\text{L9})_2][\text{BF}_4]_2 \cdot 1.5\text{MeCN}$, and its packing diagram from the view, parallel to the $[010]$ vector

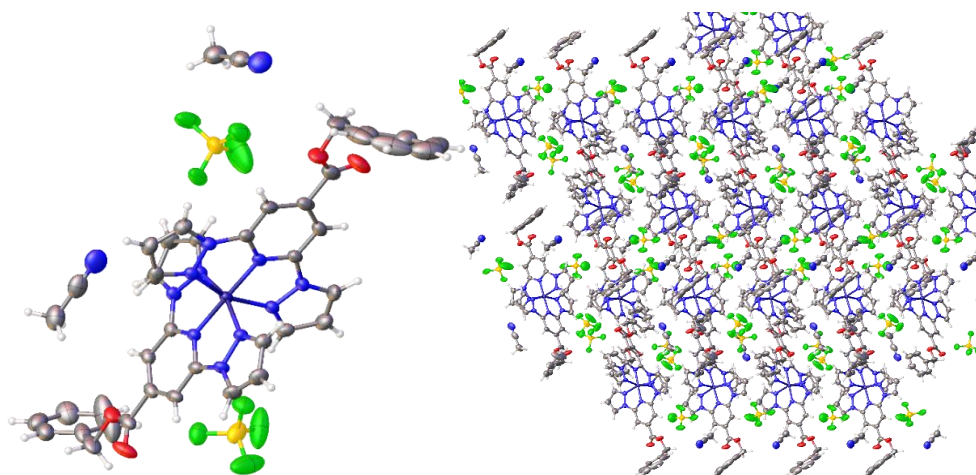


Fig. 2.25 Crystal structure of $[\text{Fe}(\text{L10})_2][\text{BF}_4]_2 \cdot 1.5\text{MeCN}$, and its packing diagram from the view, parallel to the $[100]$ vector

2.5 SQUID

2.5.1 $[\text{Fe}(\text{L3})_2][\text{BF}_4]_2$, $[\text{Fe}(\text{L4})_2][\text{BF}_4]_2$, $[\text{Fe}(\text{L5})_2][\text{BF}_4]_2$, and $[\text{Fe}(\text{L6})_2][\text{BF}_4]_2$

The magnetic behaviours of $[\text{Fe}(\text{L3})_2][\text{BF}_4]_2 \cdot 2\text{MeNO}_2$, $[\text{Fe}(\text{L4})_2][\text{BF}_4]_2$, $[\text{Fe}(\text{L5})_2][\text{BF}_4]_2$, and $[\text{Fe}(\text{L6})_2][\text{BF}_4]_2 \cdot 0.5\text{H}_2\text{O}$ were very similar to each other: they all remained LS between 5 and 300K, but started SCO at further heating, with $T_{1/2}$ beyond the measurement limit of the instrument, which is about 350K.

As the lattice solvent can affect the spin crossover in solid state,⁵ it would be useful to measure magnetic a SQUID curve for each solvate. However there was no possibility to measure all of them, due to the limited instrument time, and only one solvate of each ligand has been measured. However, for many

solvates crystal structures were collected at multiple temperatures, which also allows us to judge their spin-crossover behaviour (Table 2.1).

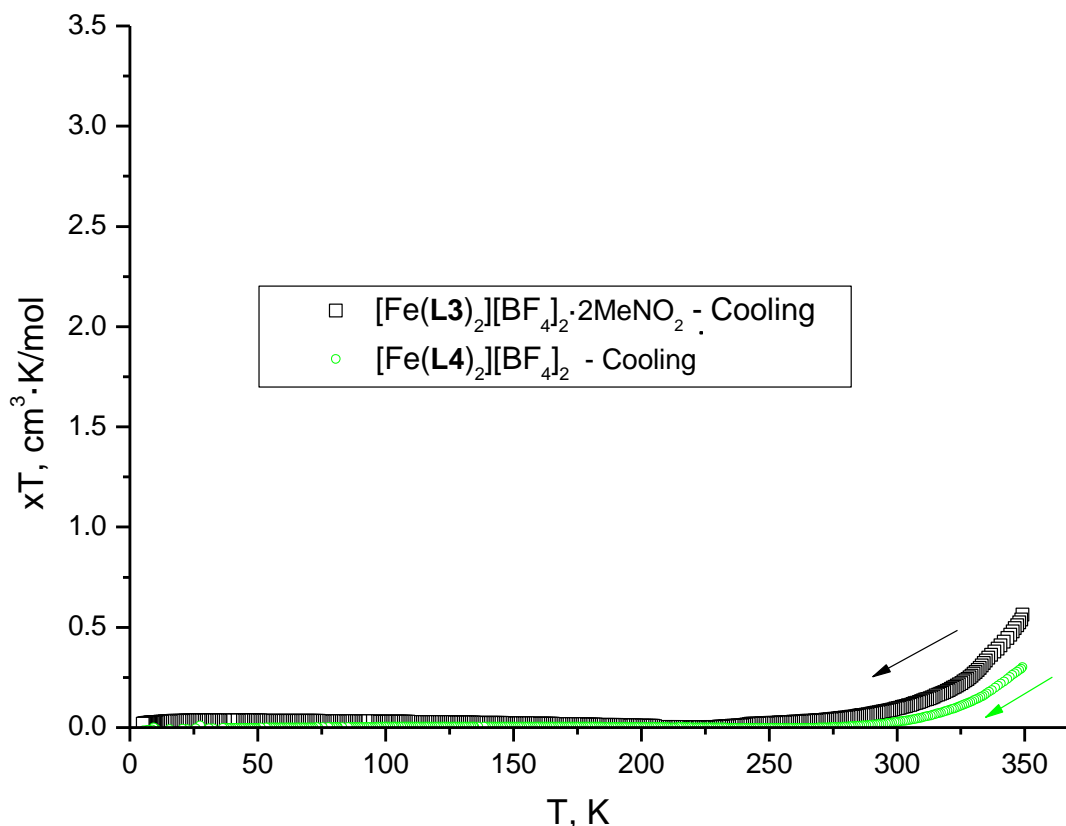


Fig. 2.26 Variable temperature magnetic susceptibility of $[\text{Fe}(\text{L3})_2][\text{BF}_4]_2 \cdot 2\text{MeNO}_2$ yellow polymorph, and $[\text{Fe}(\text{L4})_2][\text{BF}_4]_2$

As was mentioned above, $[\text{Fe}(\text{L3})_2][\text{BF}_4]_2 \cdot 2\text{MeNO}_2$ formed two polymorphs: the red and the yellow. The yellow polymorph stayed HS even at 120K, as can be seen from its crystal structure. The red polymorph, on the other hand, had a potential to switch from LS to HS when heated. The SQUID magnetic susceptibility measurements has shown that the red polymorph of $[\text{Fe}(\text{L3})_2][\text{BF}_4]_2 \cdot 2\text{MeNO}_2$ does partially switch to HS when heated to 350K, and goes back to LS after cooling to about 240K, however almost all sample is LS already below 300K. The $T_{1/2}$ lies beyond the measurement limit of this instrument of ca 350K (Fig. 2.26). $[\text{Fe}(\text{L4})_2][\text{BF}_4]_2$ is the $[\text{Fe}(\text{L4})_2][\text{BF}_4]_2$ crystallized from acetone, and as mentioned above, it has no lattice solvent, has shown similar magnetic behaviour to $[\text{Fe}(\text{L3})_2][\text{BF}_4]_2 \cdot 2\text{MeNO}_2$, but needed a slightly higher temperature to start switching to HS (Fig. 2.26).

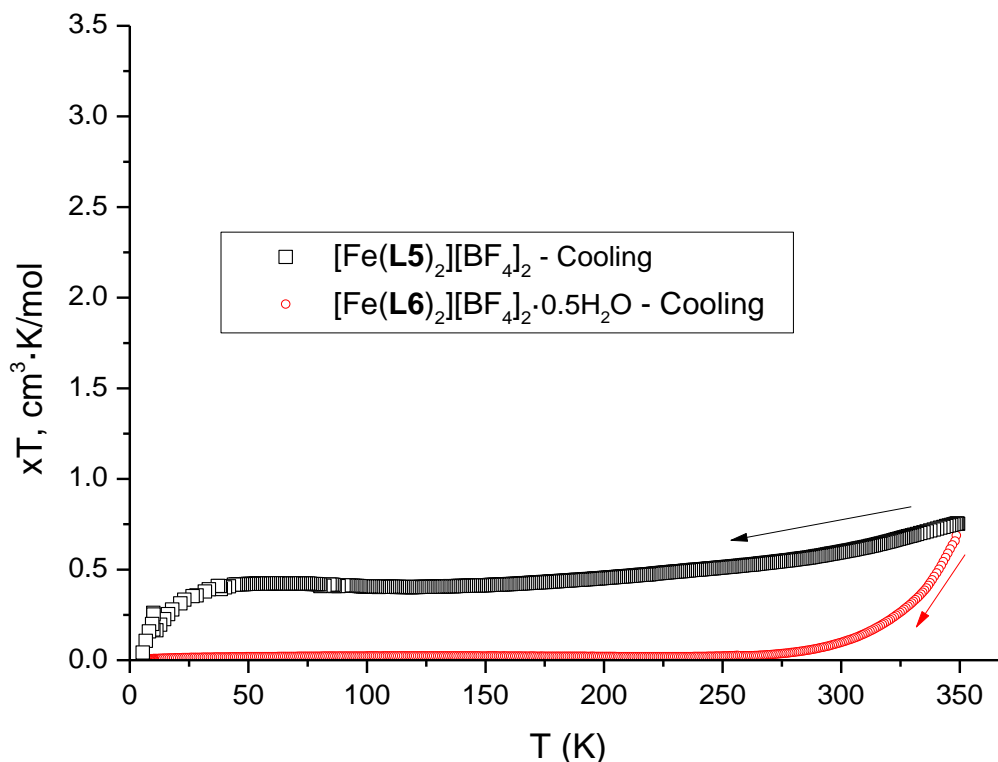


Fig. 2.27 Variable temperature magnetic susceptibility of $[\text{Fe}(\text{L5})_2][\text{BF}_4]_2$ and $[\text{Fe}(\text{L6})_2][\text{BF}_4]_2 \cdot 0.5\text{H}_2\text{O}$

$[\text{Fe}(\text{L5})_2][\text{BF}_4]_2$ likely consists of two phases: ca 14% of the fully HS part, and ca 86% of the LS phase, that undergoes very gradual SCO above 300K (Fig. 2.27). As the powder pattern of the bulk sample corresponds with the simulated from the crystal structure of the pure LS $[\text{Fe}(\text{L5})_2][\text{BF}_4]_2$ (Fig. 2.32), it can be concluded that the HS fraction in the SQUID sample of $[\text{Fe}(\text{L5})_2][\text{BF}_4]_2$ must either be not crystalline, or be a hydrate, that formed by absorbing the moisture from the air before the SQUID was measured.

$[\text{Fe}(\text{L6})_2][\text{BF}_4]_2 \cdot 0.5\text{H}_2\text{O}$ reached xT about $0.69 \text{ cm}^3 \cdot \text{mol}/\text{K}$, which is about 20% of the sample being HS at 350 K, and returned to fully LS after cooling to 275K (Fig. 2.27).

2.5.2 $[\text{Fe}(\text{L8})_2][\text{BF}_4]_2$, $[\text{Fe}(\text{L9})_2][\text{BF}_4]_2$, and $[\text{Fe}(\text{L10})_2][\text{BF}_4]_2$

For $[\text{Fe}(\text{L8})_2][\text{BF}_4]_2$, $[\text{Fe}(\text{L9})_2][\text{BF}_4]_2$, and $[\text{Fe}(\text{L10})_2][\text{BF}_4]_2$, the single crystals were grown from both acetone and MeCN, and magnetic susceptibility was measured by SQUID for all of them.

$[\text{Fe}(\text{L8})_2][\text{BF}_4]_2 \cdot \text{Me}_2\text{CO} \cdot 0.25\text{H}_2\text{O}$ has shown gradual spin crossover with hysteresis, $[\text{Fe}(\text{L9})_2][\text{BF}_4]_2 \cdot 0.5\text{Me}_2\text{CO}$ shown similar magnetic behaviour, but with smaller, hardly noticeable, hysteresis, and finally $[\text{Fe}(\text{L10})_2][\text{BF}_4]_2 \cdot \frac{2}{3}\text{Me}_2\text{CO}$ magnetic susceptibility vs temperature curve turned out to be the most promising – it showed an abrupt spin crossover from ca 233 to 300K,

with a small hysteresis with $T_{1/2}$ at 269K upon heating and $T_{1/2}$ at 278K upon cooling (Fig. 2.28).

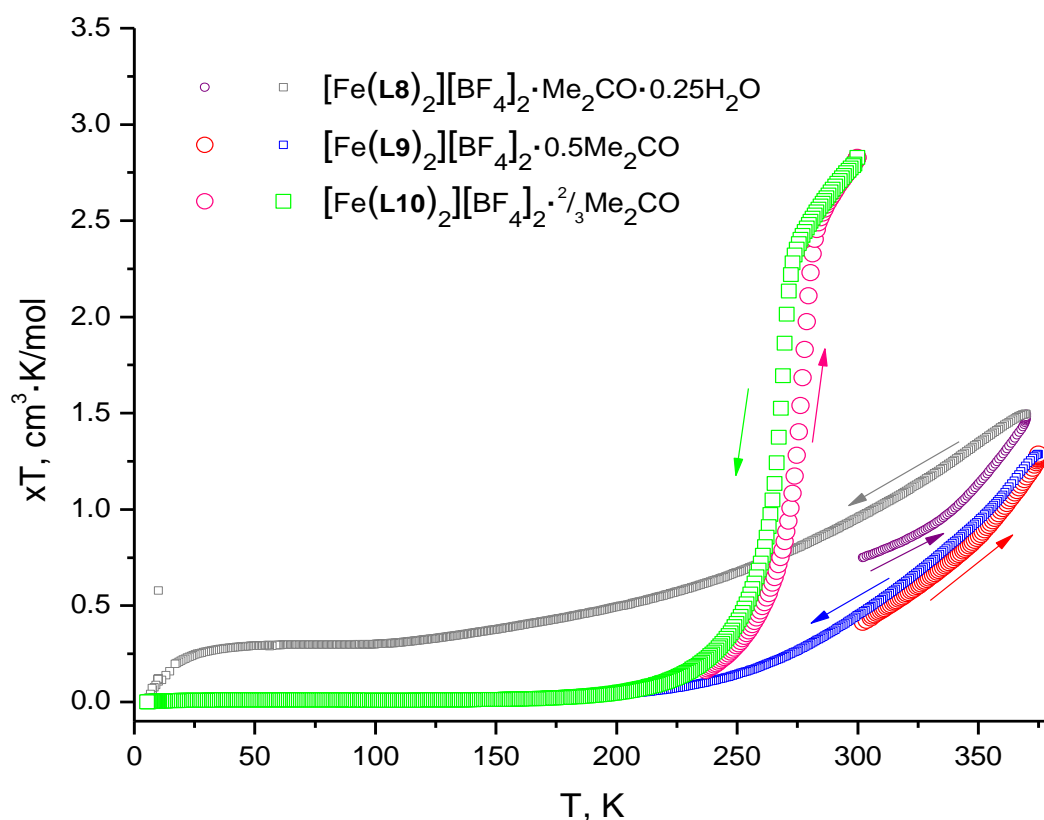


Fig. 2.28 Variable temperature magnetic susceptibility of $[\text{Fe}(\text{L}8)_2][\text{BF}_4]_2 \cdot \text{Me}_2\text{CO} \cdot 0.25\text{H}_2\text{O}$, $[\text{Fe}(\text{L}9)_2][\text{BF}_4]_2 \cdot 0.5\text{Me}_2\text{CO}$, and $[\text{Fe}(\text{L}10)_2][\text{BF}_4]_2 \cdot \frac{2}{3}\text{Me}_2\text{CO}$

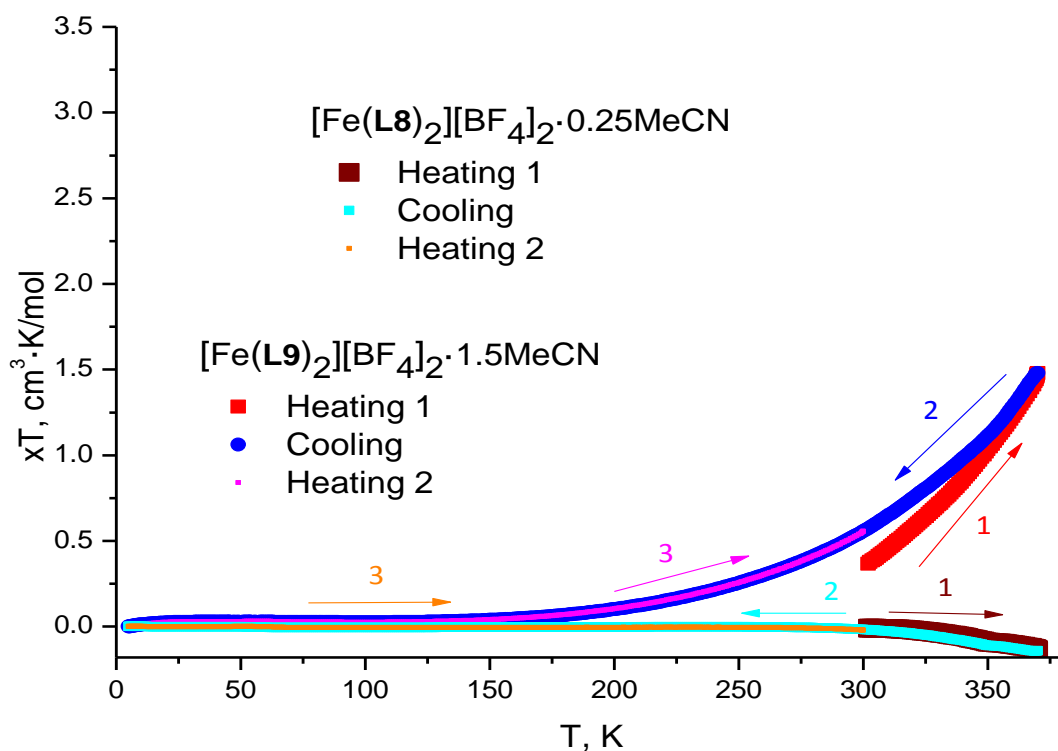


Fig. 2.29 Variable temperature magnetic susceptibility of $[\text{Fe}(\text{L}9)_2][\text{BF}_4]_2 \cdot 1.5\text{MeCN}$

[Fe(L8)₂][BF₄]₂ · 0.25MeCN, despite having the same unit cell (Table 2.4) as the acetone solvate [Fe(L8)₂][BF₄]₂ · Me₂CO · 0.25H₂O (Fig. 2.28), displayed different magnetic behaviour and remained low spin from 0 to 370 K (Fig. 2.29). [Fe(L9)₂][BF₄]₂ · 1.5MeCN, had a small hysteresis only during the first cycle, but upon second heating, the χT curve started following the cooling curve exactly. The T_{1/2} was ca 343K on heating, and 365K upon cooling, and heating 2 (Fig. 2.29). [Fe(L10)₂][BF₄]₂ · 1.5MeCN underwent a nice, abrupt SCO, similar to [Fe(L10)₂][BF₄]₂ · ²/₃Me₂CO, but at higher temperature, with T_{1/2} ca 363K upon cooling, and 358K upon heating (Fig. 2.30). There is almost a 100°C difference in T_{1/2} for [Fe(L10)₂][BF₄]₂ just because of the lattice solvent being MeCN or acetone. After undergoing two heating-cooling cycles, the [Fe(L10)₂][BF₄]₂ · 1.5MeCN sample didn't decompose and followed exactly the same line on the magnetic susceptibility graph (Fig. 2.30).

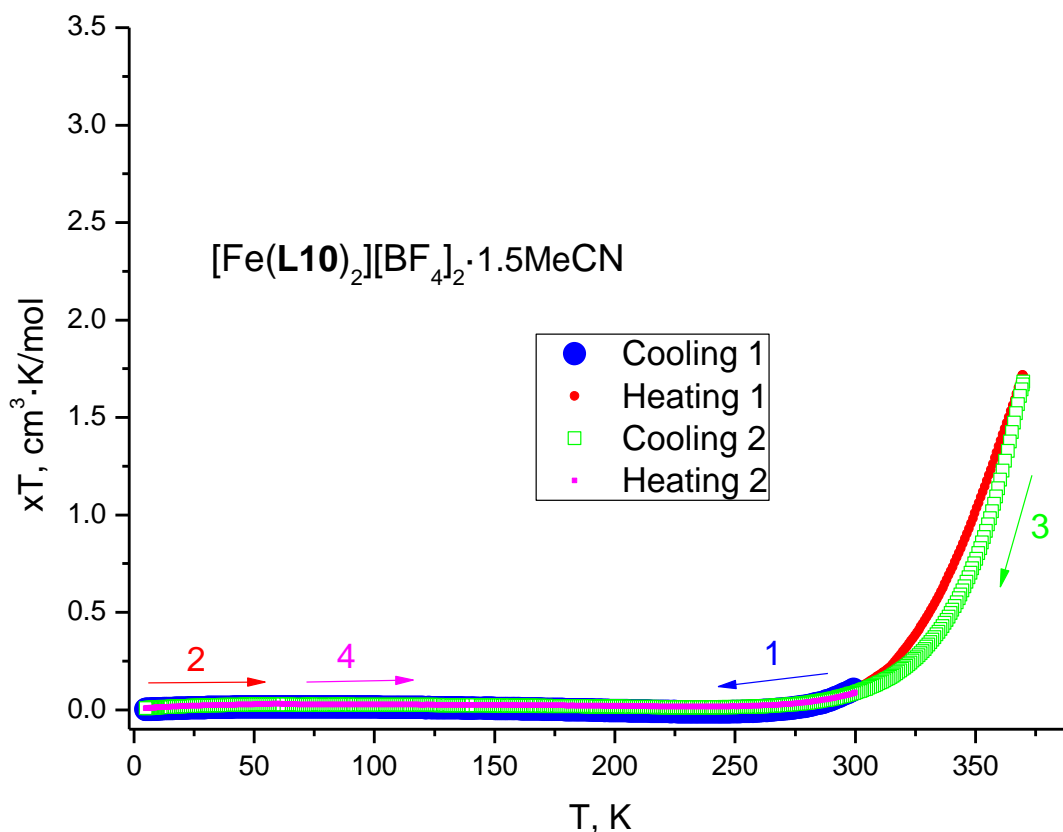


Fig. 2.30 Variable temperature magnetic susceptibility of [Fe(L10)₂][BF₄]₂ · 1.5MeCN

2.6 Distortion parameters for the XRD crystal structures

2.6.1 Introduction to distortion parameters

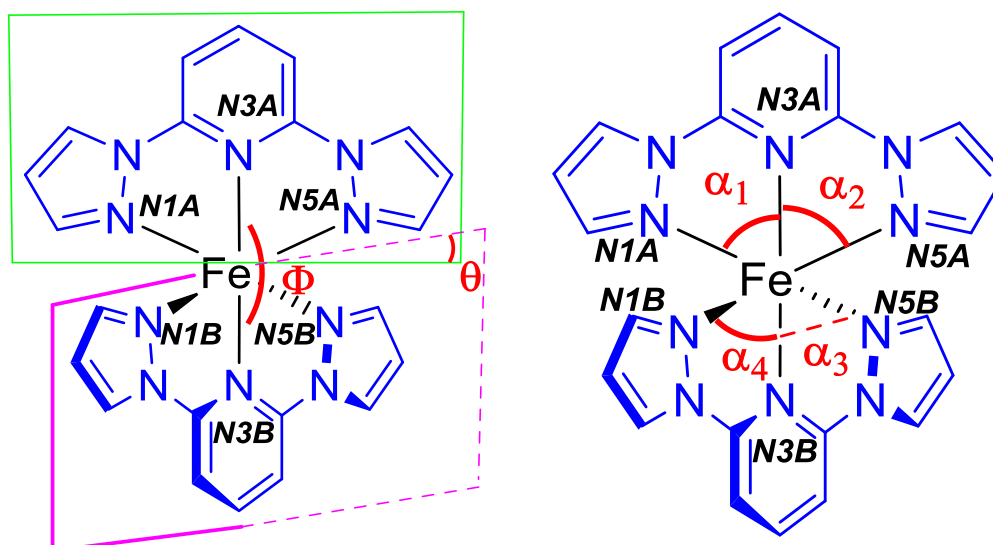


Fig. 2.31 Typical for crystal structures of bpp derivatives iron(II) complexes labelling of the Fe and N atoms at the bpp core, used in the distortion parameters calculations, and the angles used for distortion parameters calculation

The atoms in the crystal structures were all consistently labeled as shown on the Fig. 2.31. The distortion parameters were calculated using the methods, described by Cook *et al.*⁶ θ is the dihedral angle between the least squares planes of the two ligands, and it is usually ca 86.0-87.8° for HS, and ca 87.2-89.4° for LS bpp complexes.⁷ Φ is the N3A-Fe-N3B angle, which is usually around 167.8-169.5° for HS bpp complexes, and ca 174.3-174.5° for LS.⁷ α is the average of the four angles: N3B-Fe-N5B, N3B-Fe-N2B, N3A-Fe-N5A, and N3A-Fe-N2A, that for HS bpp iron complexes is between 73° and 74°, and 79.0-80.4° for LS.⁷ Σ measures the local angular distortions from octahedral geometry, and is calculated by this formula: $\Sigma = \sum_{i=1}^{12} |90 - \beta_i|$, where β_i are the 12 *cis*-N-Fe-N angles at the metal centre, and is usually 144-149° for HS, and 80-96° for LS.⁷ Besides these, one more distortion parameter has been calculated – V_{oct} , which is the volume of the octahedron, that has the vertices in the nitrogen atoms, that coordinate to the iron: N1A, N3A, N5A, N1B, N3B, N5B. V_{oct} is ca 9.4 Å³ for fully LS samples, and ca 12.4 Å³ for fully HS ones. Some distortion parameters are higher for LS state structures, and some for HS ones (Table 2.5). The distortion parameters of some crystal structures can deviate from the typical values, for example, most distorted known iron complex has $\theta = 59.84(3)^\circ$ and $\Phi = 154.52(14)^\circ$, which indicate HS state, but are far off from the typical

value range. The results of the distortion parameters calculations are summarized in the tables below (Tables 2.6-2.12).

Table 2.5 Typical values of the distortion parameters for iron(II) complexes of bpp derivatives^{6,7}

Distortion parameters	LS	HS	Perfect octahedron
α	79.0-80.4*	73-74	90
Σ	80-96	144-149	0
Φ	174.3-174.5	167.8-169.5	180
θ	87.2-89.4	86.0-87.8	90
V_{oct}	9.4	12.4	n/a

* The higher values for each distortion parameter are highlighted in grey

2.6.2 Distortion parameters for the structures, for which SQUID has been measured

For the $[\text{Fe}(\text{L3})_2][\text{BF}_4]_2$, $[\text{Fe}(\text{L4})_2][\text{BF}_4]_2$, $[\text{Fe}(\text{L5})_2][\text{BF}_4]_2$, and $[\text{Fe}(\text{L6})_2][\text{BF}_4]_2$ the distortion parameters were calculated for those solvates, for which SQUID data were measured (Table 2.1), in order to compare the results derived from both techniques.

For $[\text{Fe}(\text{L3})_2][\text{BF}_4]_2 \cdot 2\text{MeNO}_2$ it can be seen, that the average Fe-N bond length almost didn't change upon heating from 120K to 290K, as well as all the other distortion parameters (Table 2.8), which means that at 290K the iron centre is still LS, which agrees with the SQUID data (Fig. 2.31).

When heated from 120K to 293K, $[\text{Fe}(\text{L4})_2][\text{BF}_4]_2$ has shown a small decrease in the average Fe-N bond length, as well as in Φ (Table 2.8), which is rather unusual, and as this change is within the margin of error, it may be explained by an error of the bond length and angles determination, so we may conclude that the sample remained LS, and this result corresponds with the SQUID (Fig. 2.31).

The $[\text{Fe}(\text{L5})_2][\text{BF}_4]_2$ has two iron complex molecules in the asymmetric unit, which have slightly different distortion parameters, however both are LS (Table 2.9). There are no variable temperature crystal structures for this iron complex, but we know from SQUID that it remained LS up until 300K (Fig. 2.28).

Table 2.6 Percentage of [Fe(L6)₂][BF₄]₂·0.5H₂O switched to HS at different temperatures, based on average Fe-N bond length

	Average Fe-N bond length in Å, [Fe(L6) ₂][BF ₄] ₂ ·0.5H ₂ O						Fully HS Fe*
	100K		250K		360K		
	Fe1	Fe2	Fe1	Fe2	Fe1	Fe2	
	1.942	1.947	1.948	1.951	2.006	1.986	
Average	1.945		1.950		1.996		2.177
% HS**	0.0		2.2		22.2		100

* The reference fully HS distortion parameters were taken from the crystal structure of the yellow HS polymorph of [Fe(L3)₂][BF₄]₂·2MeNO₂, which corresponds with the previously reported data for HS iron(II) complexes with bpp derivatives⁶

** The percentage of the HS fraction in the sample was calculated by the formula: %HS = $\frac{X_T - X_{LS}}{X_{HS} - X_{LS}} \cdot 100\%$, where X is the parameter, which is used to calculate %HS, either Fe-N bond length or V_{oct}, X_T its value at the temperature T, and X_{HS} and X_{LS} are its values in a fully HS sample and fully LS sample correspondingly.

For [Fe(L6)₂][BF₄]₂·0.5H₂O there were crystal structures collected at three different temperatures. The mean Fe-N bond lengths for each temperature was averaged between the two molecules in the unit cell, and then these values were compared to the fully LS and full HS values. It was assumed that the sample is fully LS at 100K, as may be also seen from its SQUID, and the fully HS values were taken from the [Fe(L3)₂][BF₄]₂·2MeNO₂ sample that is HS at low temperatures (Table 2.12), and these data are consistent with the values for HS iron complexes in the paper by Cook *et al.*⁶ It turned out that the sample reached 2.2% HS at 250K, and 22.2% HS at 360K (Table 2.6), which is consistent with the SQUID data, which showed xT 0.688 cm³·K/mol, i.e. 20% HS at 350K (Fig 2.28). The same calculations based on the volume of the coordination octahedron gave very close values of the HS fraction percentage for each temperature (Table 2.7).

Table 2.7 Percentage of [Fe(L6)₂][BF₄]₂·0.5H₂O switched to HS at different temperatures, based on the volume of the coordination octahedron

	Average V _{oct} in Å ³ , for [Fe(L6) ₂][BF ₄] ₂ ·0.5H ₂ O						Fully HS Fe*
	100K		250K		360K		
	Fe1	Fe2	Fe1	Fe2	Fe1	Fe2	
	9.442	9.541	9.537	9.599	10.345	9.951	
Average	9.492		9.568		10.148		12.369
% HS**	0.0		2.7		22.8		100.0

Table 2.8 The distortion parameters of $[\text{Fe}(\text{L3})_2][\text{BF}_4]_2 \cdot 2\text{MeNO}_2$ and $[\text{Fe}(\text{L4})_2][\text{BF}_4]_2$

	$[\text{Fe}(\text{L3})_2][\text{BF}_4]_2 \cdot 2\text{MeNO}_2$		$[\text{Fe}(\text{L4})_2][\text{BF}_4]_2$	
	120K	290K	120K	293K
Fe1-N1A, Å	1.9832(18)	1.967(2)	1.979(3)	1.981(2)
Fe1-N1B, Å	1.9641(17)	1.951(2)	1.972(3)	1.969(2)
Fe1-N3A, Å	1.8908(16)	1.8914(18)	1.893(2)	1.892(2)
Fe1-N3B, Å	1.8908(16)	1.8914(18)	1.895(2)	1.896(2)
Fe1-N5A, Å	1.9491(18)	1.967(2)	1.952(3)	1.952(2)
Fe1-N5B, Å	1.965(17)	1.984(2)	1.964(3)	1.964(2)
Average, Å	1.94	1.94	1.94	1.94
α , °	80.34(7)	80.29(8)	80.35(11)	80.35(9)
Σ , °	84.52(7)	85.21(8)	86.05(11)	86.13(9)
Φ , °	174.36(7)	174.81(8)	174.83(11)	174.76(10)
θ , °	89.044	89.232	90.204	89.664
V_{oct} , Å ³	9.438	9.461	9.460	9.463

Table 2.9 The distortion parameters of the $[\text{Fe}(\text{L5})_2][\text{BF}_4]_2$ and $[\text{Fe}(\text{L6})_2][\text{BF}_4]_2 \cdot 0.5\text{H}_2\text{O}$

	$[\text{Fe}(\text{L5})_2][\text{BF}_4]_2$		$[\text{Fe}(\text{L6})_2][\text{BF}_4]_2 \cdot 0.5\text{H}_2\text{O}$	
	120K		100K	
	molecule 1*	molecule 2	molecule 1	molecule 2
Fe1-N1A, Å	1.990(4)	1.975(4)	1.996(4)	1.967(3)
Fe1-N1B, Å	1.971(4)	1.968(4)	1.955(4)	1.956(3)
Fe1-N3A, Å	1.895(3)	1.888(3)	1.889(3)	1.893(3)
Fe1-N3B, Å	1.896(3)	1.898(3)	1.895(3)	1.888(4)
Fe1-N5A, Å	1.956(4)	1.967(4)	1.952(3)	1.987(3)
Fe1-N5B, Å	1.965(4)	1.965(4)	1.963(4)	1.991(3)
Average, Å	1.94	1.94	1.94	1.95
α , °	80.31(15)	80.26(15)	80.02(15)	80.22(14)
Σ , °	89.06(15)	84.44(15)	86.68(15)	84.97(14)
Φ , °	177.00(15)	178.07(14)	175.18(14)	176.58(14)
θ , °	87.765	88.680	88.622	90.873
V_{oct} , Å ³	9.519	9.500	9.442	9.541

Table 2.10 The distortion parameters of $[\text{Fe}(\text{L6})_2][\text{BF}_4]_2 \cdot 0.5\text{H}_2\text{O}$

	$[\text{Fe}(\text{L6})_2][\text{BF}_4]_2 \cdot 0.5\text{H}_2\text{O}$			
	250K		360K	
	molecule 1	molecule 2	molecule 1	molecule 2
Fe1-N1A, Å	1.957(4)	1.982(4)	2.054(7)	1.998(7)
Fe1-N1B, Å	1.971(4)	1.965(4)	2.027(8)	2.033(8)
Fe1-N3A, Å	1.901(4)	1.897(3)	1.961(6)	1.925(8)
Fe1-N3B, Å	1.901(4)	1.898(3)	1.967(7)	1.951(8)
Fe1-N5A, Å	1.996(4)	1.979(4)	2.004(7)	1.993(8)
Fe1-N5B, Å	1.964(4)	1.985(4)	2.022(7)	2.014(10)
Average, Å	1.95	1.95	2.01	1.99
α , °	79.89(16.25)	80.17(14)	98.45(3)	78.08(3.75)
Σ , °	88.0(2)	79.97(14)	98.0(3)	105.0(3)
Φ , °	175.66(16)	177.24(14)	177.5(3)	173.4(3)
θ , °	89.056	90.735	90.596	88.876
V_{oct} , Å ³	9.537	9.599	10.345	9.951

At 150K $[\text{Fe}(\text{L9})_2][\text{BF}_4]_2 \cdot 1.5\text{MeCN}$ and $[\text{Fe}(\text{L10})_2][\text{BF}_4]_2 \cdot 1.5\text{MeCN}$ remained LS, judging by their distortion parameters (Table 2.11), which is in agreement with the SQUID magnetic measurement results (Fig. 2.29 and 2.31).

Table 2.11 The distortion parameters of the crystal structures $[\text{Fe}(\text{L8})_2][\text{BF}_4]_2 \cdot 0.5\text{MeCN}$, $[\text{Fe}(\text{L9})_2][\text{BF}_4]_2 \cdot 1.5\text{MeCN}$, and $[\text{Fe}(\text{L10})_2][\text{BF}_4]_2 \cdot 1.5\text{MeCN}$

	$[\text{Fe}(\text{L8})_2][\text{BF}_4]_2 \cdot \frac{1}{2}\text{MeCN}$		$[\text{Fe}(\text{L9})_2][\text{BF}_4]_2 \cdot 1.5\text{MeCN}$		$[\text{Fe}(\text{L10})_2][\text{BF}_4]_2 \cdot 1.5\text{MeCN}$	
	150K		150K		150K	
	mol. 1	mol. 2	mol. 1	mol. 2	mol. 1	mol. 2
Fe1-N1A	1.969(7)	1.981(8)	1.967(3)	1.966(3)	1.962(3)	1.953(3)
Fe1-N1B	1.954(8)	1.984(9)	1.976(3)	1.964(3)	1.956(3)	1.962(3)
Fe1-N3A	1.886(6)	1.889(7)	1.895(3)	1.891(3)	1.892(2)	1.891(2)
Fe1-N3B	1.886(7)	1.909(7)	1.890(3)	1.895(3)	1.893(2)	1.893(2)
Fe1-N5A	1.886(7)	1.961(8)	1.970(3)	1.977(3)	1.965(3)	1.953(3)
Fe1-N5B	1.886(7)	1.960(9)	1.965(3)	1.994(3)	1.956(3)	1.970(3)
Average	1.91	1.95	1.95	1.95	1.94	1.94
α	80.4(3)	80.5(3)	80.32(12)	80.13(12)	80.31(11)	80.33(11)
Σ	84.3(3)	82.1(3)	83.92(13)	90.49(12)	84.24(11)	83.88(11)
Φ	176.6(3)	173.6(3)	176.39(13)	175.92(12)	175.98(11)	178.44(11)
θ	88.518	89.174	90.267	87.104	88.727	91.562
V_{oct} , Å ³	9.459	9.486	9.499	9.534	9.399	9.406

2.6.3 Distortion parameters for the structures, for which SQUID has not been measured

Since time on the SQUID magnetometer was limited, magnetic data were measured only for one solvate of each iron complex. There are structures of some solvates, for which the crystal structures were collected at different temperatures in order to track spin crossover, but which were not measured with SQUID: $[\text{Fe}(\text{L3})_2][\text{BF}_4]_2 \cdot 2\text{MeCN} \cdot 3\text{H}_2\text{O}$ and the yellow polymorph of $[\text{Fe}(\text{L3})_2][\text{BF}_4]_2 \cdot 2\text{MeNO}_2$. It can be seen from the distortion parameters (Table 2.12), that the yellow polymorph of $[\text{Fe}(\text{L3})_2][\text{BF}_4]_2 \cdot 2\text{MeNO}_2$ is very different from the LS molecules, and must be fully HS, as its average Fe-N bond length corresponds with the previously reported values for HS Fe^{II} complexes of bpp derivatives^{6,7}. $[\text{Fe}(\text{L3})_2][\text{BF}_4]_2 \cdot 2\text{MeCN} \cdot 3\text{H}_2\text{O}$ seems to remain LS when heated from 120 K to 300 K, which is similar to the behaviour of the MeNO_2 solvate of the same iron complex (Fig. 2.31).

Table 2.12 The distortion parameters of the crystal structures of $[\text{Fe}(\text{L3})_2][\text{BF}_4]_2 \cdot 2\text{MeCN} \cdot 3\text{H}_2\text{O}$, and $[\text{Fe}(\text{L3})_2][\text{BF}_4]_2 \cdot 2\text{MeNO}_2$ yellow polymorph

	$[\text{Fe}(\text{L3})_2][\text{BF}_4]_2 \cdot 2\text{MeCN} \cdot 3\text{H}_2\text{O}$		$[\text{Fe}(\text{L3})_2][\text{BF}_4]_2 \cdot 2\text{MeNO}_2$
	120K	150K	120K, yellow polymorph
Fe1-N1A, Å	1.973(3)	1.957(8)	2.205(4)
Fe1-N1B, Å	1.971(3)	1.971(7)	2.203(4)
Fe1-N3A, Å	1.894(3)	1.88(6)	2.157(4)
Fe1-N3B, Å	1.897(3)	1.889(6)	2.144(3)
Fe1-N5A, Å	1.98(3)	1.961(7)	2.153(4)
Fe1-N5B, Å	1.976(3)	1.976(7)	2.200(4)
Average, Å	1.95	1.94	2.18
α , °	80.37(12)	80.15(3)	73.1(13)
Σ , °	85.24(12)	85.6(3)	158.76(13)
Φ , °	175.32(12)	176.7(3)	166.33(13)
θ , °	92.928	91.962	82.384
V_{oct} , Å ³	89.23	88.99	91.02

2.7 Powder Patterns

2.7.1 $[\text{Fe}(\text{L3})_2][\text{BF}_4]_2$, $[\text{Fe}(\text{L4})_2][\text{BF}_4]_2$, $[\text{Fe}(\text{L5})_2][\text{BF}_4]_2$, and $[\text{Fe}(\text{L6})_2][\text{BF}_4]_2$

The diffraction patterns were collected for the powders of $[\text{Fe}(\text{L3})_2][\text{BF}_4]_2 \cdot 2\text{MeNO}_2$, $[\text{Fe}(\text{L4})_2][\text{BF}_4]_2$, $[\text{Fe}(\text{L5})_2][\text{BF}_4]_2$, and $[\text{Fe}(\text{L6})_2][\text{BF}_4]_2 \cdot \text{Me}_2\text{CO}$, and plotted along with the powder patterns, simulated from the crystal structures for comparison (Fig. 2.32). The collected and simulated patterns roughly match each other, and all the powders are crystalline, $[\text{Fe}(\text{L3})_2][\text{BF}_4]_2 \cdot 2\text{MeNO}_2$ and $[\text{Fe}(\text{L4})_2][\text{BF}_4]_2$ are much more crystalline than $[\text{Fe}(\text{L5})_2][\text{BF}_4]_2$ and $[\text{Fe}(\text{L6})_2][\text{BF}_4]_2 \cdot \text{Me}_2\text{CO}$.

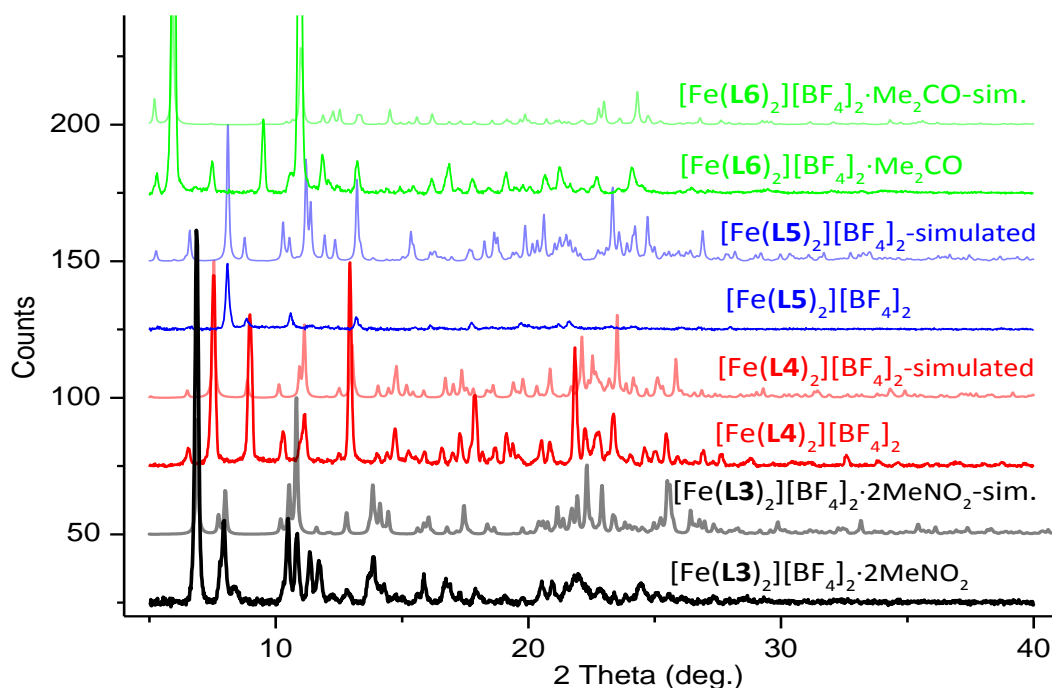


Fig. 2.32 Collected and simulated powder patterns of $[\text{Fe}(\text{L3})_2][\text{BF}_4]_2 \cdot 2\text{MeNO}_2$, $[\text{Fe}(\text{L4})_2][\text{BF}_4]_2$, $[\text{Fe}(\text{L5})_2][\text{BF}_4]_2$, and $[\text{Fe}(\text{L6})_2][\text{BF}_4]_2 \cdot \text{Me}_2\text{CO}$

2.7.2 $[\text{Fe}(\text{L7})_2][\text{BF}_4]_2$, $[\text{Fe}(\text{L8})_2][\text{BF}_4]_2$, and $[\text{Fe}(\text{L9})_2][\text{BF}_4]_2$

For $[\text{Fe}(\text{L7})_2][\text{BF}_4]_2$, $[\text{Fe}(\text{L8})_2][\text{BF}_4]_2$, and $[\text{Fe}(\text{L9})_2][\text{BF}_4]_2$, the powder patterns were collected for both, the crystals grown from acetone and from MeCN.

For the MeCN solvates, the powder patterns, which were simulated from the single crystal diffraction are quite different from the obtained from the powders (Fig. 2.33). The powders of $[\text{Fe}(\text{L8})_2][\text{BF}_4]_2 \cdot 0.25\text{MeCN}$, $[\text{Fe}(\text{L9})_2][\text{BF}_4]_2 \cdot 1.5\text{MeCN}$, and $[\text{Fe}(\text{L10})_2][\text{BF}_4]_2 \cdot 1.5\text{MeCN}$ were obtained from nice, big single crystals, so they must be clean and highly crystalline. The difference may be explained by the lattice solvent, which each of these structures has. The MeCN may be lost during the grinding of the crystals into powder.

For the acetone solvates, the simulated and obtained powder patterns were similar to each other for $[\text{Fe}(\text{L8})_2][\text{BF}_4]_2 \cdot \text{Me}_2\text{CO} \cdot 0.25\text{H}_2\text{O}$, but for $[\text{Fe}(\text{L9})_2][\text{BF}_4]_2 \cdot 0.5\text{Me}_2\text{CO}$ and $[\text{Fe}(\text{L10})_2][\text{BF}_4]_2 \cdot \frac{2}{3}\text{Me}_2\text{CO}$ they are quite different, which may be explained by the loss of the lattice solvent (Fig. 2.34).

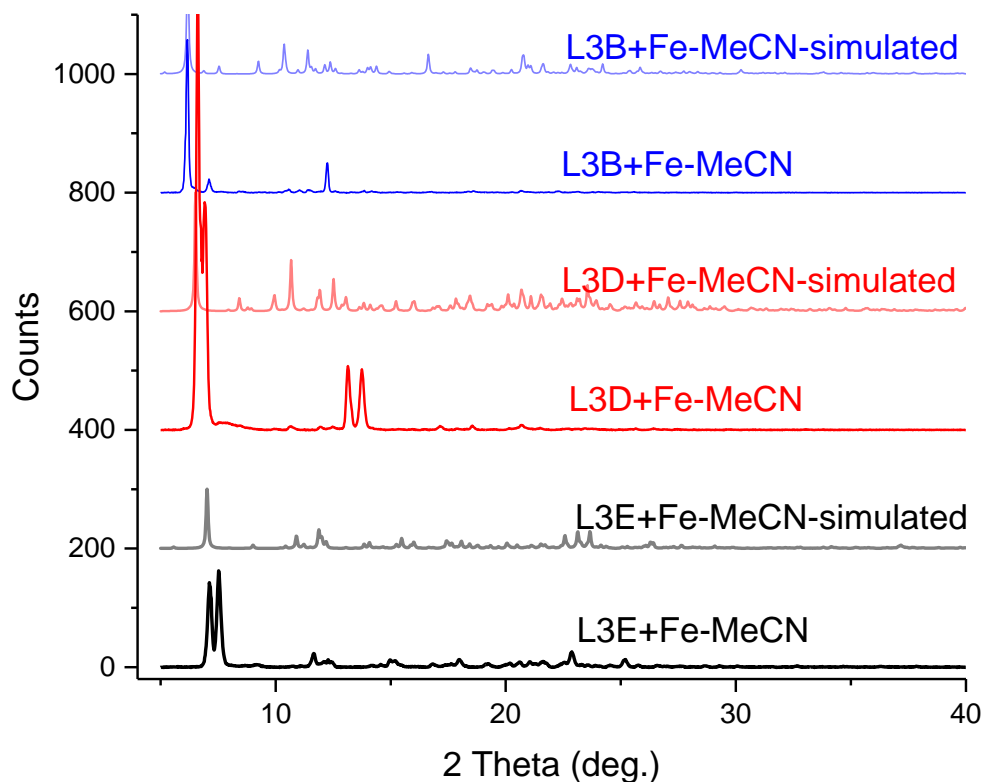


Fig. 2.33 Collected and simulated powder patterns of $[\text{Fe}(\text{L8})_2][\text{BF}_4]_2 \cdot 0.25\text{MeCN}$, $[\text{Fe}(\text{L9})_2][\text{BF}_4]_2 \cdot 1.5\text{MeCN}$, and $[\text{Fe}(\text{L10})_2][\text{BF}_4]_2 \cdot 1.5\text{MeCN}$

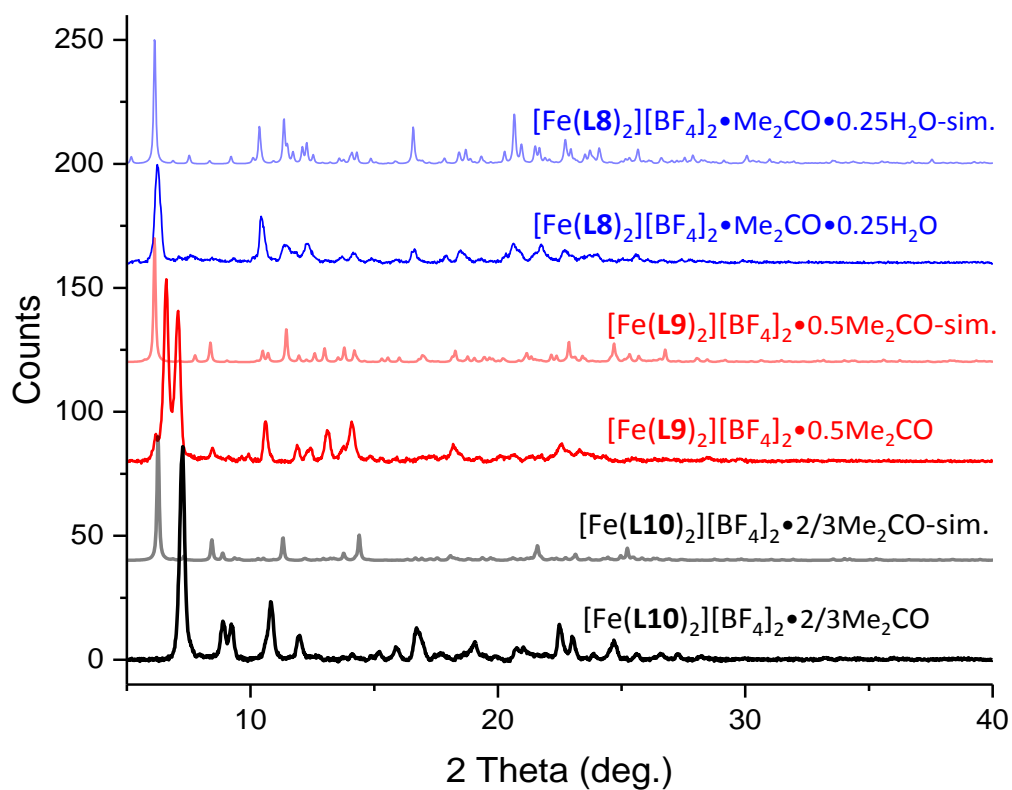


Fig. 2.34 Collected and simulated powder patterns of $[\text{Fe}(\text{L8})_2][\text{BF}_4]_2 \cdot \text{Me}_2\text{CO} \cdot 0.25\text{H}_2\text{O}$, $[\text{Fe}(\text{L9})_2][\text{BF}_4]_2 \cdot 0.5\text{Me}_2\text{CO}$, and $[\text{Fe}(\text{L10})_2][\text{BF}_4]_2 \cdot 2/3\text{Me}_2\text{CO}$

2.8 Evans method NMR

Spin crossover in solution for $[\text{Fe}(\text{L3})_2][\text{BF}_4]_2$, $[\text{Fe}(\text{L4})_2][\text{BF}_4]_2$, $[\text{Fe}(\text{L5})_2][\text{BF}_4]_2$, and $[\text{Fe}(\text{L6})_2][\text{BF}_4]_2$ was studied by Evans method NMR in MeCN-D₃. As expected, spin crossover in solution was much more gradual than in the solid state, as in solution the cooperativity decreases due to break up of the intermolecular interactions. All the iron complexes showed quite similar behaviour in solution. The $T_{1/2}$ was determined by measuring the temperature at which the sample reached $1.75 \text{ cm}^3 \cdot \text{K/mol}$, half the magnetic susceptibility of the full HS state. The results are shown in the table on the graph (Fig. 2.35).

There were no Evans method NMRs collected for the $[\text{Fe}(\text{L8})_2][\text{BF}_4]_2$, $[\text{Fe}(\text{L9})_2][\text{BF}_4]_2$, and $[\text{Fe}(\text{L10})_2][\text{BF}_4]_2$, as the variable temperature NMR probe at the School of Chemistry was broken. Quite likely they would look similar to the previous four samples, because changing the substituent at the ester bond seems to have a very weak effect on the magnetic behaviour in solutions for this series (Fig. 2.35).

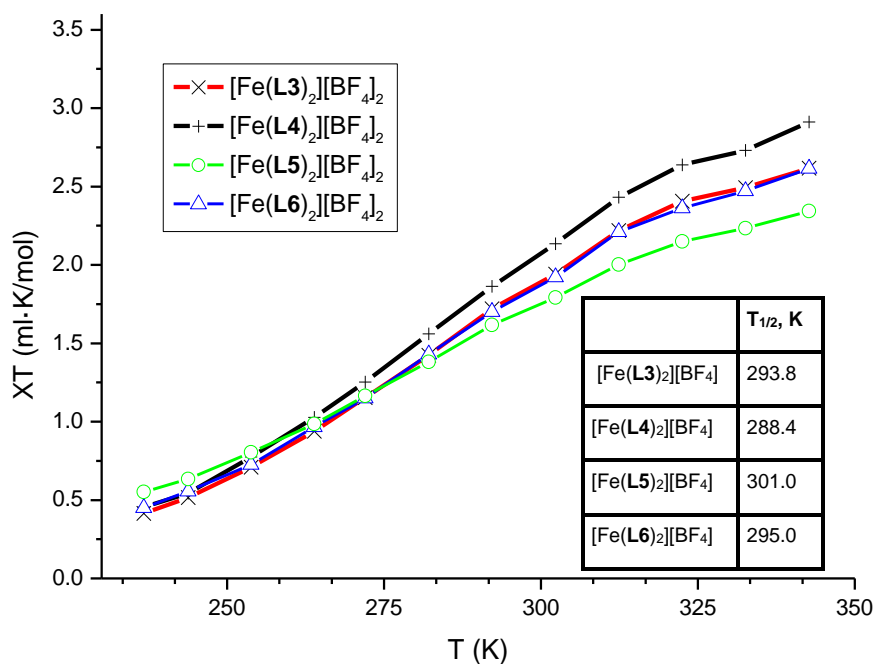


Fig. 2.35 Evans method NMR spectra of $[\text{Fe}(\text{L3})_2][\text{BF}_4]_2$, $[\text{Fe}(\text{L4})_2][\text{BF}_4]_2$, $[\text{Fe}(\text{L5})_2][\text{BF}_4]_2$, and $[\text{Fe}(\text{L6})_2][\text{BF}_4]_2$, measured in MeCN-D₃

2.9 Paramagnetic NMR

Paramagnetic NMR spectra were measured for each iron complex in this chapter. The spectra in the $[\text{Fe}(\text{L3})_2][\text{BF}_4]_2$, $[\text{Fe}(\text{L4})_2][\text{BF}_4]_2$, $[\text{Fe}(\text{L5})_2][\text{BF}_4]_2$, and $[\text{Fe}(\text{L6})_2][\text{BF}_4]_2$ series looked all almost identical, with two peaks close to each other, at around 40.5 and 39.6 ppm, a peak near 26.3 ppm, and a peak

at around 23.1 ppm, which all integrate in 1:1 ratio (Fig. 2.36). On expansion of the 0 to 7 ppm area the diamagnetically shifted peaks from the ligand are observed: 7.08 Ph H2, 3.88 (Ph H7), as well as the MeCN peak at 1.94.

For the $[\text{Fe}(\text{L8})_2][\text{BF}_4]_2$, $[\text{Fe}(\text{L9})_2][\text{BF}_4]_2$, and $[\text{Fe}(\text{L10})_2][\text{BF}_4]_2$ series, the paramagnetic NMRs were also almost identical between each other, but a bit less shifted downfield comparing to the previous series (Fig. 2.37), which means that at 300K in solution the fraction of the sample that is HS for $[\text{Fe}(\text{L8})_2][\text{BF}_4]_2$, $[\text{Fe}(\text{L9})_2][\text{BF}_4]_2$, and $[\text{Fe}(\text{L10})_2][\text{BF}_4]_2$ iron complexes is lower than for $[\text{Fe}(\text{L3})_2][\text{BF}_4]_2$, $[\text{Fe}(\text{L4})_2][\text{BF}_4]_2$, $[\text{Fe}(\text{L5})_2][\text{BF}_4]_2$, and $[\text{Fe}(\text{L6})_2][\text{BF}_4]_2$.

In the diamagnetic region of the $[\text{Fe}(\text{L8})_2][\text{BF}_4]_2$ spectrum were observed peaks from MeCN at 1.94, from acetone at 2.08, diamagnetically shifted peaks from the ligand at 5.86 Ph7, 2.86 Ph8,9, as well as a big TMS peak, because the solvent that was used for Evans method NMRs was prepared for Evans method NMR, and therefore contained TMS.

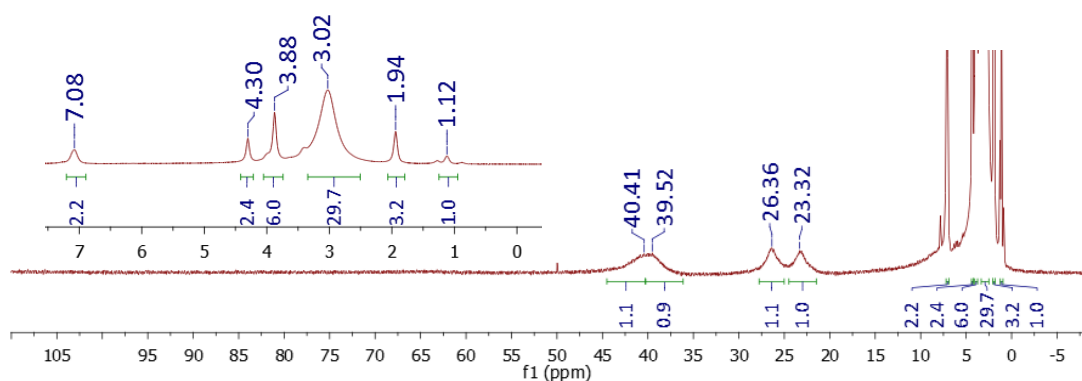


Fig. 2.36 Paramagnetic NMR of $[\text{Fe}(\text{L3})_2][\text{BF}_4]_2$, measured in MeCN-D3

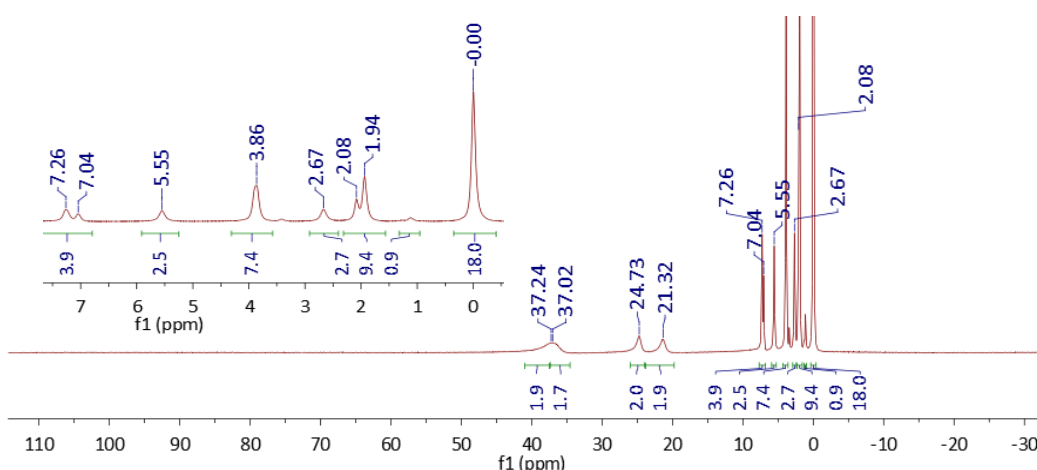


Fig. 2.37 Paramagnetic NMR of $[\text{Fe}(\text{L8})_2][\text{BF}_4]_2$, measured in MeCN-D3

2.10 Conclusions for Chapter 2

In this chapter are discussed the seven novel bpp carboxylate phenyl or benzyl ester ligands and their iron(II) complexes. Most of the iron complexes shown similar spin-crossover behaviour: they stayed low-spin below about 300K, and upon heating above this temperature exhibited gradual spin crossover, similarly to the previously reported iron complexes of bpp carboxylate esters.^{8,9,10,11} The exception is $[\text{Fe}(\mathbf{L10})_2][\text{BF}_4]_{2 \cdot 2/3}\text{Me}_2\text{CO}$, which exhibited abrupt SCO around 270K with a 9 K hysteresis. Also, noteworthy are the two polymorphs of $[\text{Fe}(\mathbf{L3})_2][\text{BF}_4]_{2 \cdot 2}\text{MeNO}_2$, which despite having the same counterion and lattice solvent, show completely different SCO behaviour: the yellow polymorph stayed HS above 120K, and the red polymorph exhibited typical for this series gradual SCO above 300K. Studying the polymorphism in SCO systems is important for understanding the contribution of structural factors to SCO.^{12,13} For this iron complexes family the separate crystallization of weakly distorted low-spin and strongly distorted high-spin polymorphs has only been observed once before, by Haryono et. al.¹⁴

All the phenyl ester ligands in this chapter have one ligand molecule per asymmetric unit, while the benzyl ester ligands, except **L9**, have two. The same tendency was observed for their iron complexes: all the iron complexes from the phenyl series have $Z' = 1$, except for $[\text{Fe}(\mathbf{L5})_2][\text{BF}_4]_2$, which has two; and for all the benzyl series iron complexes $Z' = 2$, except one solvate, $[\text{Fe}(\mathbf{L10})_2][\text{BF}_4]_{2 \cdot 2/3}\text{Me}_2\text{CO}$, with $Z' = 3$ (Table 2.1). This consistent pattern may be explained by the additional flexibility of benzyl comparing to phenyl substituent, due to the presents of the methylene group, which allows it to bend into different positions and therefore distort the symmetry. The iron complexes of these more flexible benzyl derivatives seems to have better cooperativity, as they showed more abrupt spin crossover (Fig. 2.28).¹⁵ The percentage of HS molecules calculated from the crystal structures' distortion parameters matched the magnetic behaviour observed by SQUID.

List of References

1. Beierlein, C.H. and Breit, B. Online Monitoring of Hydroformylation Intermediates by ESI-MS. *Organometallics*. **2010**, *29*, 2521–2532.
2. Kershaw Cook, L. J. PhD thesis, University of Leeds, **2014**.
3. Vermonden, T.; Branowska, D.; Marcelis, A.T.M.; Sudhölter, E.J.R. Synthesis of 4-functionalized terdentate pyridine-based ligands. *Tetrahedron*. **2003**, *59*, 5039–5045.
4. Galet, A.; Gaspar, A.B.; Muñoz, M.C.; and Real, J.A. Influence of the Counterion and the Solvent Molecules in the Spin Crossover System [Co(4-terpyridone)₂]Xp·nH₂O. *Inorg. Chem.* **2006**, *45* (11), 4413-4422.
5. Fumanal, M.; Jiménez-Grávalos, F.; Ribas-Arino, J. and Vela, S. Lattice-Solvent Effects in the Spin-Crossover of an Fe(II)-Based Material. The Key Role of Intermolecular Interactions between Solvent Molecules. *Inorg. Chem.* **2017**, *56*, 4474-4483.
6. Kershaw Cook, L.J.; Kulmaczewski, R.; Cespedes, O. and Halcrow, M.A. Different Spin-State Behaviors in Isostructural Solvates of a Molecular Iron(II) Complex. *Chem.: Eur. J.* **2016**, *22*(5), 1789-1799.
7. Halcrow, M. A. Iron(II) complexes of 2,6-di(pyrazol-1-yl)pyridines – a versatile system for spin-crossover research. *Coord. Chem. Rev.* **2009**, *253*, 2493–2514.
8. Bridonneau, N.; Rigamonti, L.; Poneti, G.; Pinkowicz, D.; Forni, A.; Cornia, A. Evidence of crystal packing effects in stabilizing high or low spin states of iron(II) complexes with functionalized 2,6-bis(pyrazol-1-yl)pyridine ligands. *Dalton Trans.* **2017**, *46*, 4075–4085.
9. García-López, V.; Palacios-Corella, M.; Abhervé, A.; Pellicer-Carreño, I.; Desplanches, C.; Clemente-León, M.; Coronado, E. Spin-crossover compounds based on iron(II) complexes of 2,6-bis(pyrazol-1-yl)pyridine (bpp) functionalized with carboxylic acid and ethyl carboxylic acid. *Dalton Trans.* **2018**, *47*, 16958–16968.
10. Galadzhun, I.; Kulmaczewski, R.; Cespedes, O.; Yamada, M.; Yoshinari, N.; Konno, T.; Halcrow, M. A. 2,6-Di(pyrazolyl)pyridine-4-carboxylate esters with alkyl chain substituents, and their iron(II) complexes. *Inorg. Chem.* **2018**, *57*, 13761–13771.

11. Kershaw Cook, L. J.; Kulmaczewski, R.; Mohammed, R.; Dudley, S.; Barrett, S. A.; Little, M. A.; Deeth, R. J.; Halcrow, M. A. A unified treatment of the relationship between ligand substituents and spin state in a family of iron(II) complexes. *Angew. Chem. Int. Ed.* **2016**, *55*, 4327–4331.
12. Tao, J.; Wei, R.-J.; Huang, R.-B.; Zheng, L.-S. Polymorphism in spin-crossover systems. *Chem. Soc. Rev.* **2012**, *41*, 703–737
13. Abhervé, A.; J. Recio-Carretero, M.; López-Jordà, M.; Clemente-Juan, J. M.; Canet-Ferrer, J.; Cantarero, A.; Clemente-León, M.; Coronado, E. Nonanuclear spin-crossover complex containing iron(II) and iron(III) based on a 2,6-bis(pyrazol-1-yl)pyridine ligand functionalized with a carboxylate group. *Inorg. Chem.* **2016**, *55*, 9361–9367.
14. Haryono, M.; Heinemann, F. W.; Petukhov, K.; Gieb, K.; Müller, P.; Grohmann, A. Parallel crystallization of a "static" and a spin-crossover polymorph of an iron(II) complex from the same solution. *Eur. J. Inorg. Chem.* **2009**, 2136–2143.
15. Galadzhun, I.; Kulmaczewski, R.; Halcrow, M.A. Five 2,6-Di(pyrazol-1-yl)pyridine-4-carboxylate Esters, and the Spin States of their Iron(II) Complexes. *Magnetochem.* **2019**, *5*, 9.

Chapter 3

Pyridine-substituted bis(pyrazol-1-yl)pyridine derivatives

with long alkyl chains, and their iron(II) complexes

3.1 Introduction

The aim of this PhD project is to obtain novel iron(II) complexes, which can both undergo spin crossover and form liquid crystalline phases. To achieve this, bpp, a core that is well-studied for spin crossover, was attached to the substituent groups that are likely to induce liquid crystallinity: long alkyl chains, phenyl rings and strongly polarizable groups. This chapter is about the bpp derivatives with substituents attached to the pyridine ring (Fig. 3.1), and their iron(II) complexes.

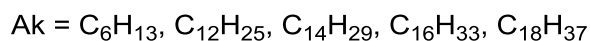
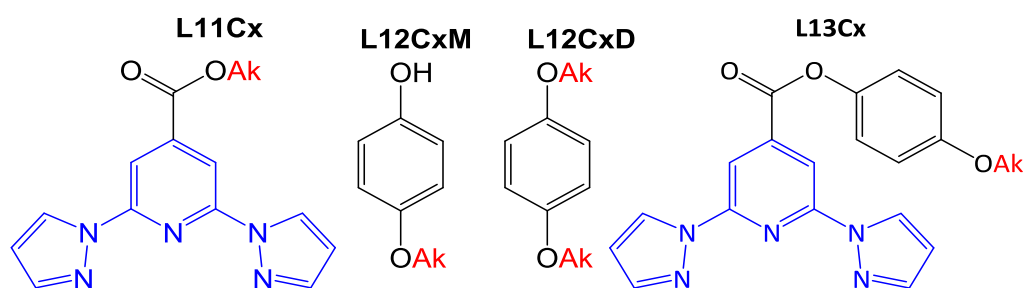


Fig. 3.1. The ligands, discussed in Chapter 3

3.2 Ligands synthesis

L2, the precursor for the synthesis of **L11Cx** and **L13Cx** ligand series, was obtained through a two-step synthesis described in Chapter 2.2.2.

3.2.1 L11Cx - alkyl (2,6-di-1H-pyrazol-1-yl)pyridine-4-carboxylates

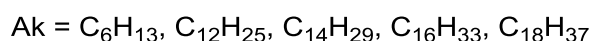
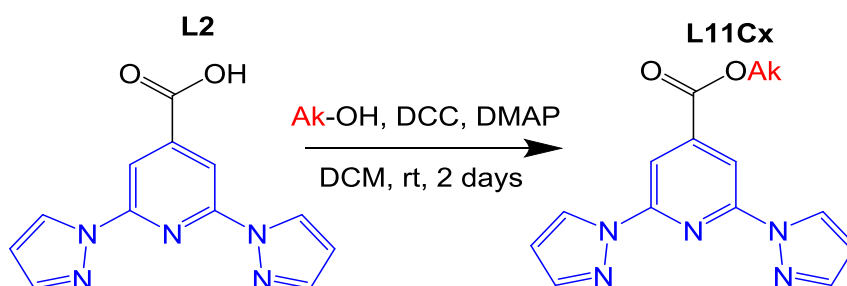


Fig. 3.2. Synthesis of **L11C6**, **L11C12**, **L11C14**, **L11C16**, and **L11C18**

Alkyl (2,6-di-1H-pyrazol-1-yl)pyridine-4-carboxylates were synthesized using DCC as a coupling agent (Fig. 3.2), as described by Vermonden *et al.*¹ During this reaction DCC turns into DCU, which is notoriously hard to remove. A few consecutive recrystallizations from boiling MeCN, during which the DCU stayed in the solution and the target product crystallized out,

allowed pure **L11C12-L11C18** to be obtained, but for the less hydrophobic shorter alkyl chain ligand **L11C6**, column chromatography was required. A crystal structure of a DCC intermediate was unintentionally collected (Fig. 3.12). ^1H NMR spectra of all the **L11Cx** ligands look very similar to each other, and differ by the integration of the 1.25 ppm peak, which comes from the overlapping of the C4 – Cn-1 alkyl chain hydrogens (Fig. 3.3). The labelling scheme for each chapter may be seen in the Chapter 6. The ^{13}C NMR spectra of this series also look almost the same, and differ just by the C4 – Cn-1 carbon peaks: for **L11C6** and **L11C12** the peak from each carbon can be clearly seen, and for longer alkyl chains, the peaks from all the carbons past 12 start overlapping (Fig. 3.4). For example, **L11C14** has only 12 alkyl carbon NMR peaks, and the signal at 29.8 ppm is much more intense, because the two missing peaks overlapped with it (Fig. 3.4).

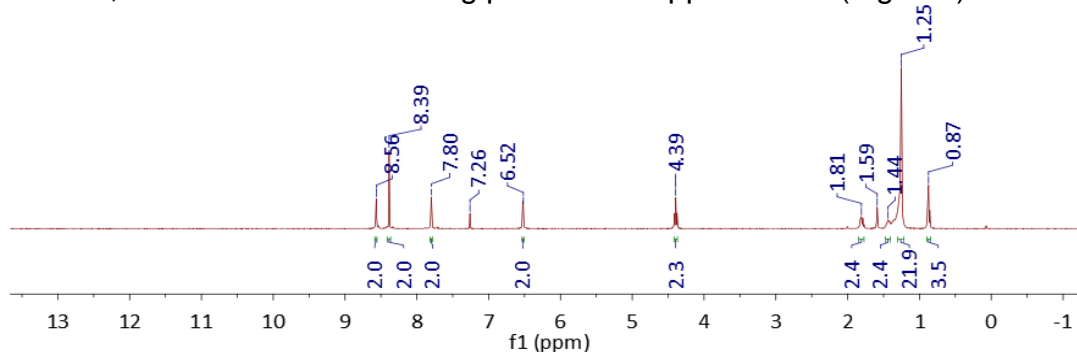


Fig. 3.3. ^1H NMR of **L11C14** in CDCl_3 , typical for all **L11Cx** ligands

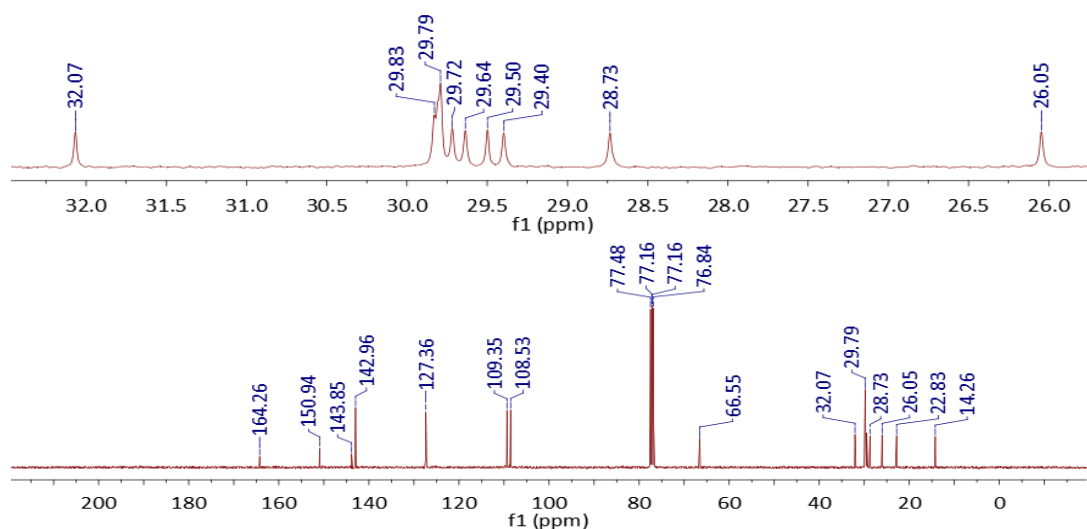


Fig. 3.4. ^{13}C NMR of **L11C14** in CDCl_3 : full view and an expansion

2.2.4 L12Cx - 4-alkoxyphenols

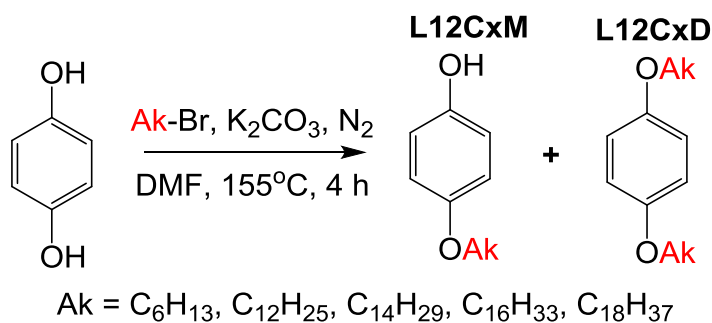


Fig. 3.5 Synthesis of **L12C6**, **L12C12**, **L12C14**, **L12C16**, and **L12C18**

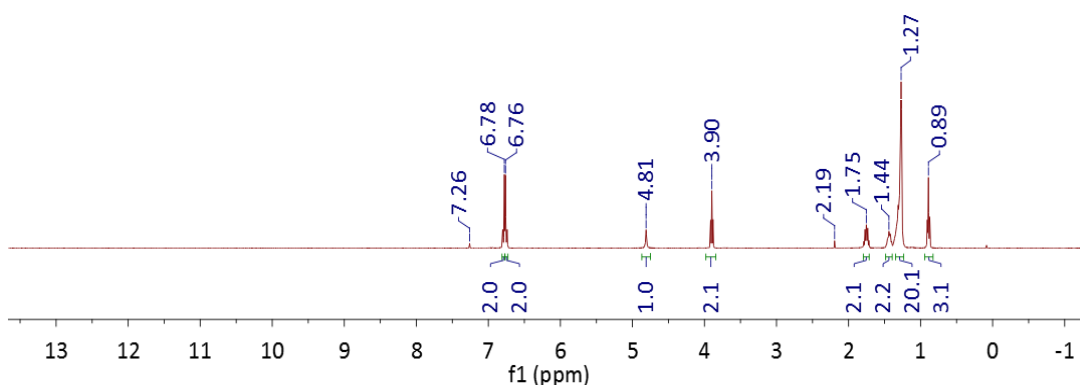


Fig. 3.6. ¹H NMR of **L12C14** in CDCl₃, typical for all **L12Cx** ligands

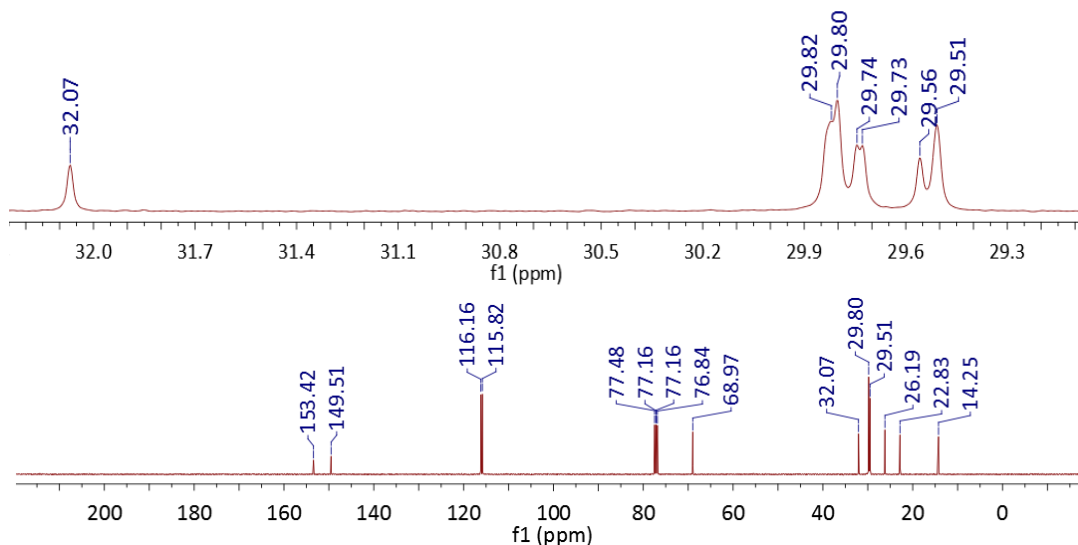


Fig. 3.7. ¹³C NMR of **L12C14** in CDCl₃: full view and an expansion

The **L12CxM** intermediate ligand series was obtained, so then they may be attached to **L2** to get the target **L13Cx** ligands. The synthesis of **L12Cx** was performed by the procedure reported by Borisov *et al.*² The target monosubstituted product was separated from the disubstituted product by extracting it with acetone. ¹H NMR spectra of all the ligands in these series differ from each other by the integration of the 1.27 ppm peak, depending on the number of carbons in the alkyl chain (Fig. 3.6). For the ¹³C NMR, up to

12 alkyl chain carbons' peaks were observed, and if there were more than 12 alkyl carbons, still only 12 peaks were observed, because the signals started to overlap (Fig. 3.7). As the result of obtaining the **L12CxM** ligands, the disubstituted by-products **L12CxD** were also isolated, and proven by analyses to be pure compounds (Chapter 6.3), but no practical use was found for them in this research.

2.2.5 L13Cx - 4-(alkyl)phenyl 2,6-di-1H-pyrazol-1-ylisonicotinates

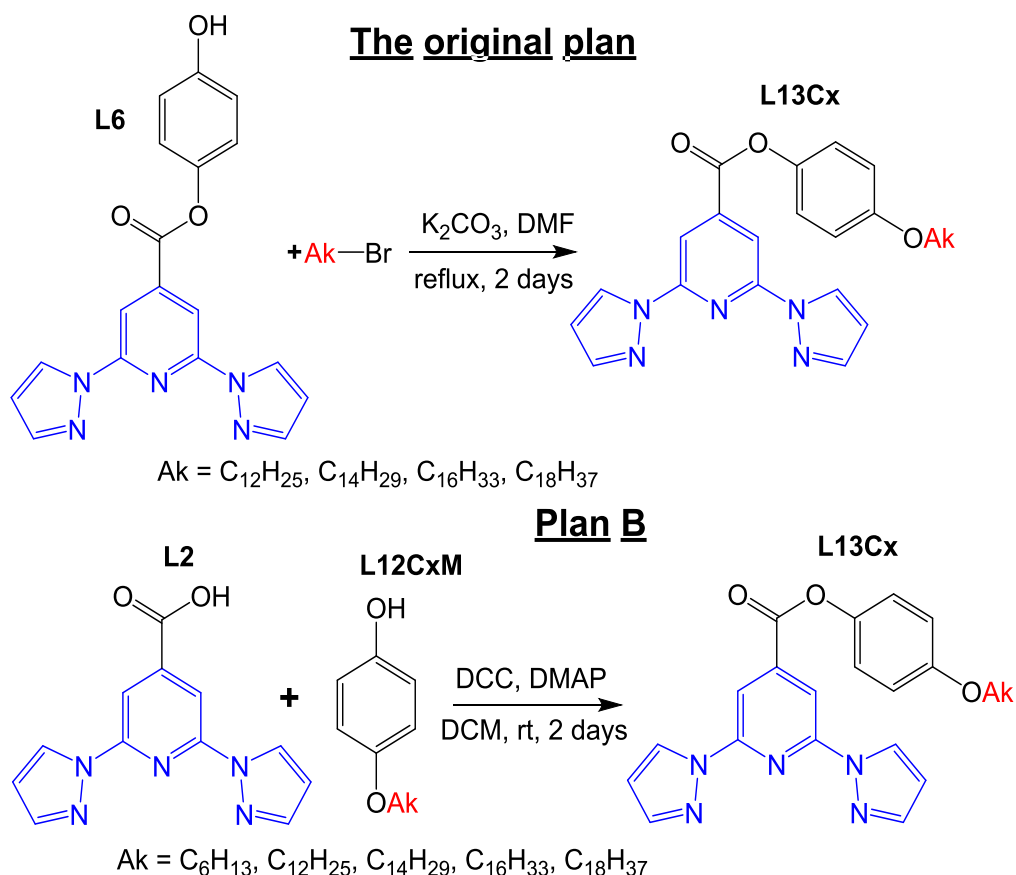


Fig. 3.8 Synthesis of 4-(alkyl)phenyl 2,6-di-1H-pyrazol-1-ylisonicotinates

The original plan was to attach a long alkyl chain to the **L5** and **L6** ligands (Fig. 3.8). However, this synthesis led to destruction of the ester bond and formation of an unexpected product **L7** (Fig. 2.7). To avoid this, another strategy was used to obtain the **L13Cx** ligands (Fig. 3.8).

As for the previous series in this chapter, ¹H NMR spectra of the **L13Cx** ligands differed from each other only by the integration of the 1.27 ppm alkyl peak (Fig. 3.9), and their ¹³C NMR alkyl peaks start overlapping after there more than 11 of them (Fig. 3.10).

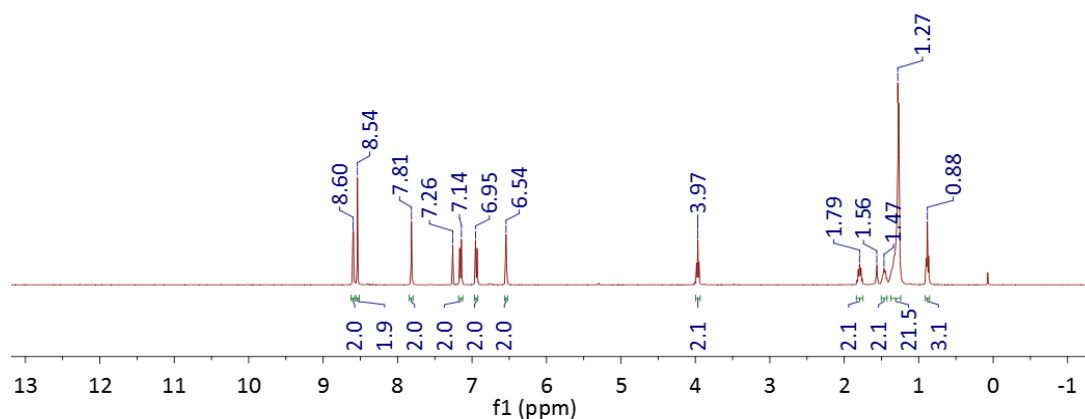


Fig. 3.9. ^1H NMR of **L13C14** in CDCl_3 , typical for all **L13Cx** ligands

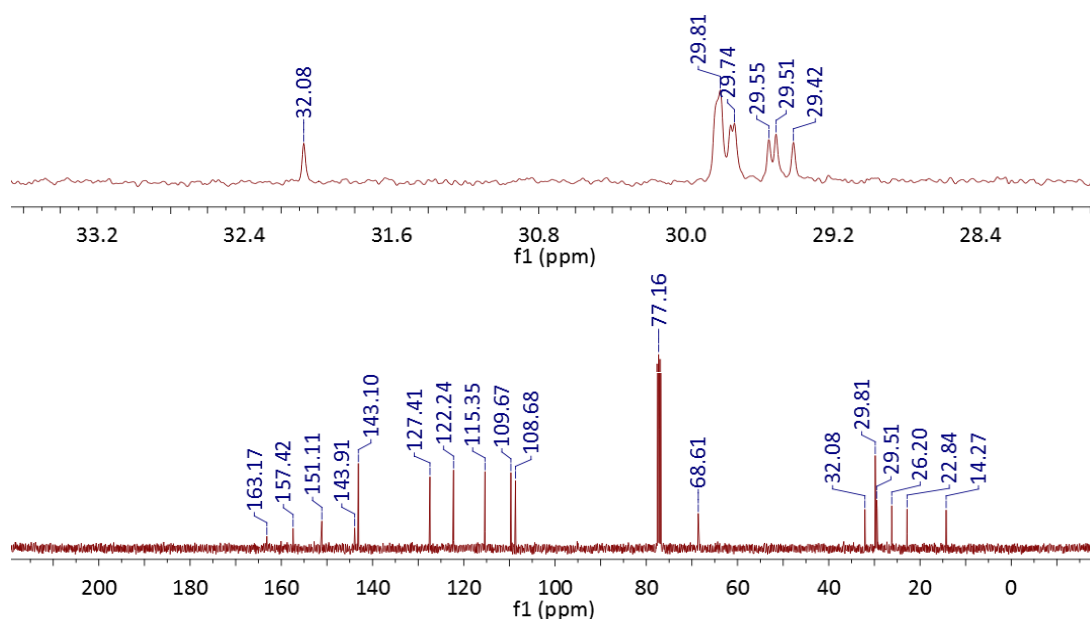


Fig. 3.10. ^{13}C NMR of **L13C14** in CDCl_3 : full view and an expansion

3.3 Iron(II) complex synthesis

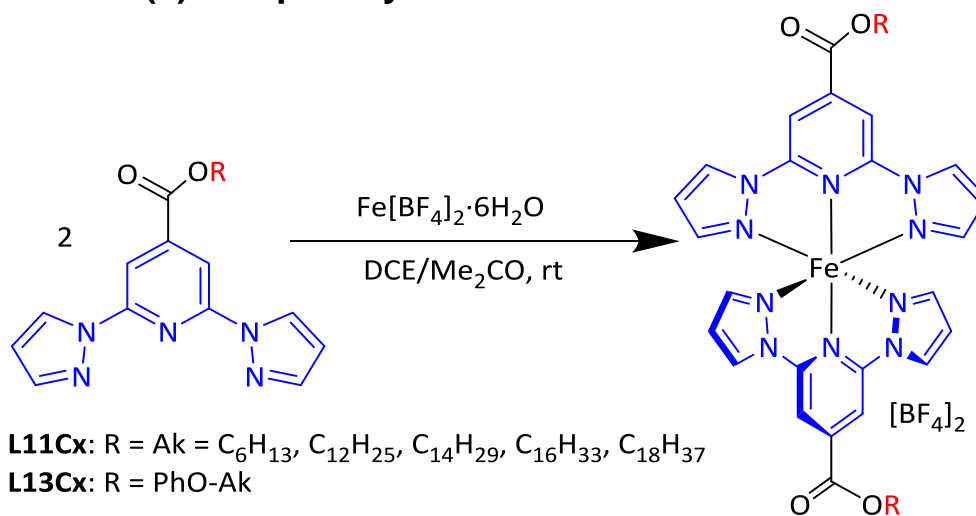


Fig. 3.11. General scheme for obtaining iron(II) complexes in Chapter 3

As the ligands in this chapter are quite hydrophobic, the usual solvents that are used for growing single crystals of iron complexes (MeCN, MeNO₂ and acetone) would not work in this case. Also, the antisolvents that are normally used for growing crystals by slow diffusion – diethyl ether or diisopropyl ether, would dissolve the iron complex and not induce the precipitation. After some trials, the best results were obtained in the following solvent system: the long alkyl chain ligand was dissolved in dichloroethane (DCE), Fe(BF₄)₂·6H₂O in acetone, and pentane was used as an antisolvent (Fig. 3.11). For more details and general procedure for growing single crystals for crystallography, please see the used techniques in the Experimental chapter (Chapter 6.1.2).

3.4 Crystal structures

Table 3.1 Crystal structures from Chapter 3

Formula	Per asym. unit	Formula	Per asym. unit
L11C12	1	[Fe(L11C6) ₂][BF ₄] ₂ ·2H ₂ O	1
L11C14	1	[Fe(L13C6) ₂][BF ₄] ₂ ·H ₂ O	1
L12C12M	2	[Fe(L13C14) ₂][BF ₄] ₂ ·2MeCN	1
L12C14M	2	[Fe(L13C16) ₂][BF ₄] ₂ ·H ₂ O	1
L13C12	1	DCC intermediate	1
L13C14	1		

In this chapter, the crystal structures were collected for at least one member of each ligand family, except for **L12CxD** ligands that have two long alkyl chains that disfavours single crystals formation, and also for each iron complex series (Table 3.1). None of the ligands had any solvent in their lattice, but all the iron complexes had some lattice solvent, usually water. Perhaps the non-polar long alkyl chains can hinder the escaping of the water molecules and trap them near the polar part of the iron complex molecule. Attempts were made to collect crystal structures for every ligand in this chapter, however data were successfully collected only for the ligands with twelve and fourteen carbon alkyl chains, which indicates that this chain length is optimal for crystallization of ligands, with six carbon being too short to form a strong bilayer, and sixteen and eighteen carbon chains being too long, bringing distortion into the crystal structure. In total for this chapter there were collected seven ligand and four iron complex crystal structures.

3.4.1 Crystal structures of the ligands

L11Cx

Crystals of **L11C6** did not diffract well, but among them there was a needle crystal that gave an unexpected structure of **DCC intermediate** (Fig. 3.12). Apparently **L2**, that was used as a starting material for obtaining **L11C6**, contained a trace of the monosubstituted product with one bromine atom not being replaced with a pyrazole ring. This compound formed an intermediate with DCC, which was then supposed to react with the long alkyl chain alcohol and emit DCU. However, instead it crystallized from the mixture at the intermediate stage. The molecules of the **DCC intermediate** pack in head-to-tail stacks, connected by hydrogen bonds between the N-H hydrogen and NC=O oxygen of the neighbouring molecule (Fig. 3.12).

The bpp fragments of the **L11C12** molecules pack on top of each other in stacks, and the alkyl chains from the neighbouring stacks interdigitate. The molecules in the adjacent stacks are related by 2_1 symmetry, so their alkyl chains point at different directions, which forms a V-shaped array (Fig. 3.13). A crystal structure of **L11C14** also has been collected. Its unit cell was very similar to **L11C12** (Table 3.2).

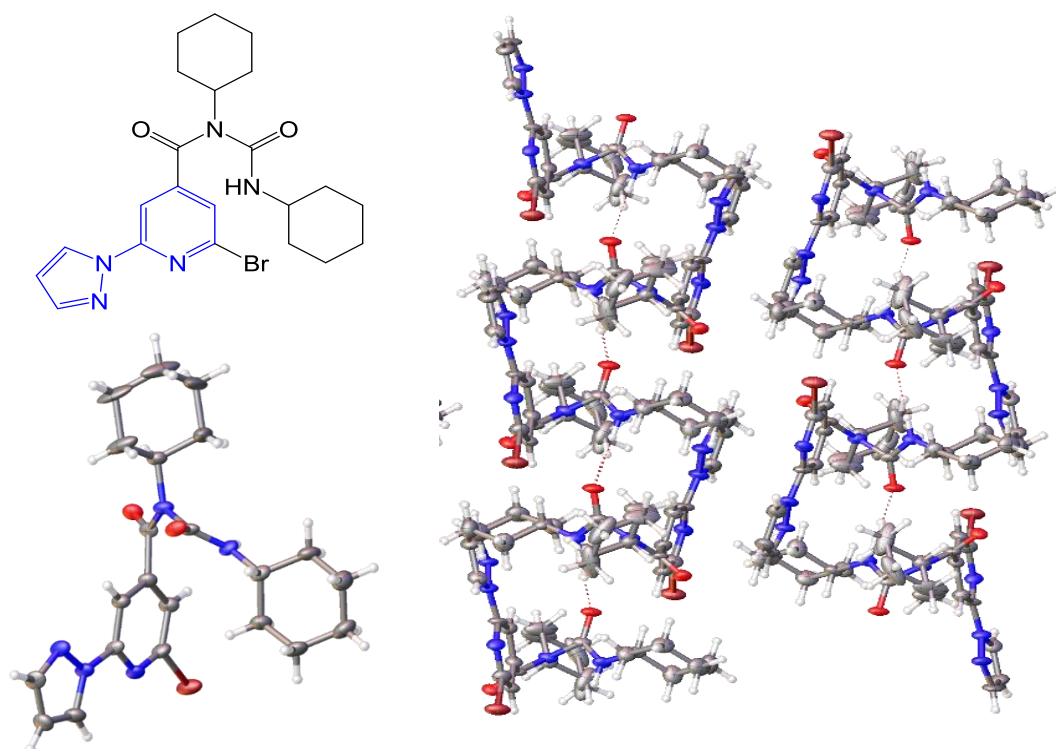


Fig. 3.12. Chemical formula, crystal structure, and packing diagram from the view, parallel to the [010] vector, for the **DCC intermediate**

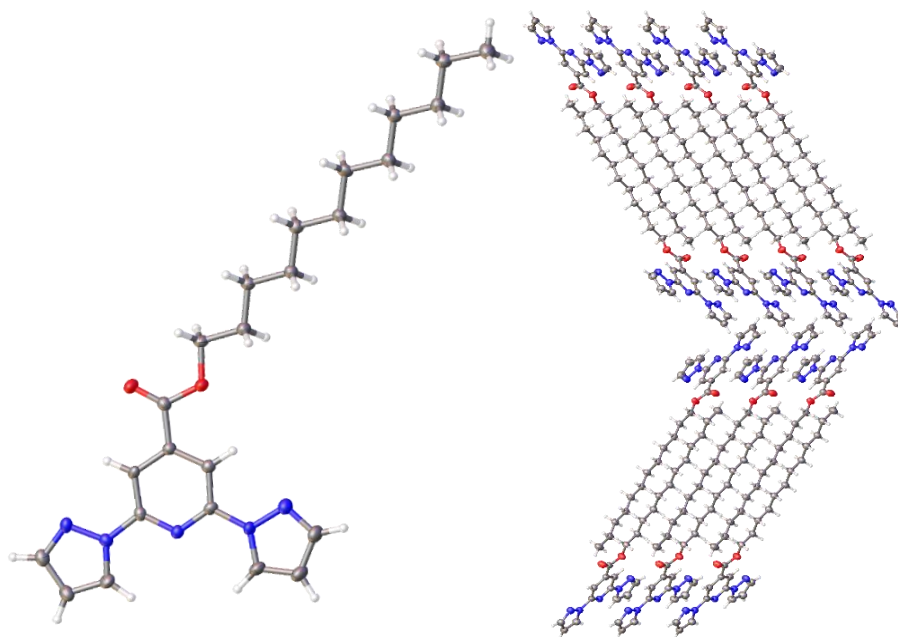


Fig. 3.13. Crystal structure of **L11C12** and its packing diagram from the view, parallel to the [010] vector

L12Cx

For the **L12Cx** series a crystal structures of **L12C12M** and **L12C14M** were collected, which have very similar unit cells (Table 3.2). There are two molecules of **L12C12M** in the unit cell. The phenyl rings are connected in parallel sheets by the hydrogen bonds between the OH hydrogen and the OH oxygen of the adjacent molecules (Fig. 3.13). The disubstituted products were hard to crystallize, so no crystal structures of them were collected.

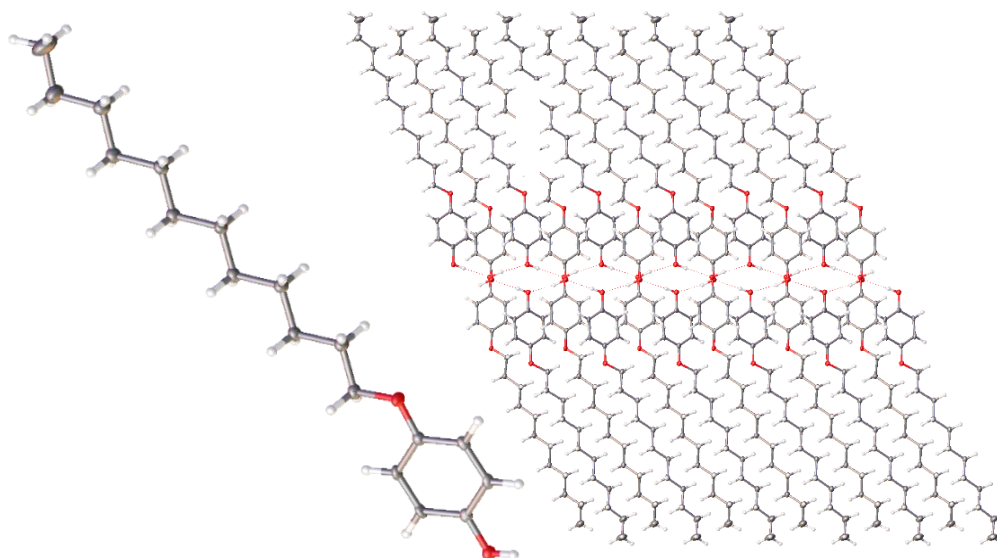


Fig. 3.14. Crystal structure of **L12C12M** and its packing diagram from the view, parallel to the [010] vector

Table 3.2 Unit cells of **L11C12**, **L11C14**, **L12C12M** and **L12C14M**

	L11C12	L11C14	L12C12M	L12C14M
Space group	P2 ₁ 2 ₁ 2 ₁	P2 ₁ 2 ₁ 2 ₁	P-1	P-1
a/Å	4.8180(4)	4.8622(4)	5.4266(2)	5.4604(11)
b/Å	8.9611(5)	8.9415(12)	7.2027(2)	7.2025(14)
c/Å	53.627(3)	57.636(6)	42.2414(14)	46.898(5)
α /°	90.00	90	88.093(3)	91.733(14)
β /°	90.00	90	86.332(3)	90.505(14)
γ /°	90.00	90	89.637(3)	90.417(16)
Volume/Å ³	2315.3(3)	2505.8(5)	1646.75(9)	1843.5(6)
Z'	1	1	2	2

L13Cx

L13C12 and **L13C14** had similar unit cells (Table 3.3) and the same packing of the molecules in the lattice. While **L11C12** ligand molecules are almost planar, in **L13C12** the bpp part of the molecule and the alkyl chain are in almost perpendicular planes, because of the additional flexibility added by the phenyl ring. **L13C12** forms V-shaped arrays, similarly to **L11C12**, but at a more obtuse angle (Fig. 3.15).

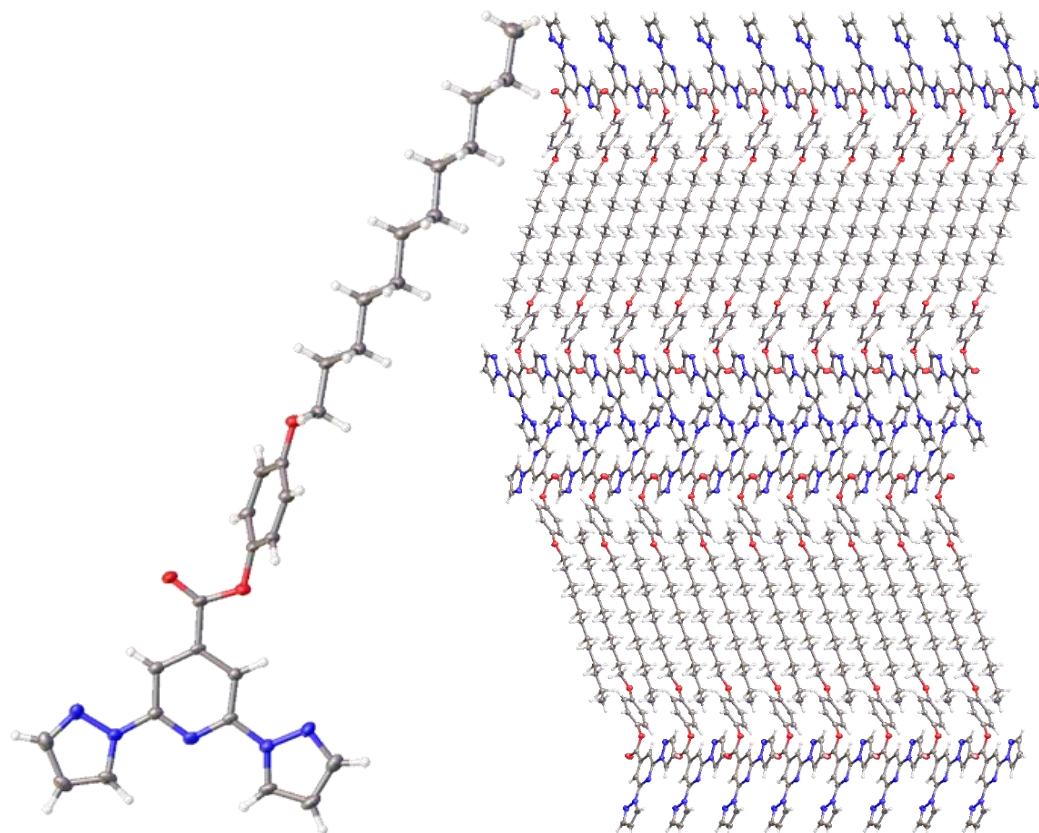
**Fig. 3.15.** Crystal structure of **L13C12** and its packing diagram from the view, parallel to the [001] vector

Table 3.3 Unit cells of **L13C12M** and **L13C14M**

	L13C12	L13C14
Space group	P2 ₁ /n	P2 ₁ /n
a/Å	4.09650(10)	4.12350(10)
b/Å	64.3183(13)	68.6353(8)
c/Å	10.3525(2)	10.32150(10)
α/°	90	90
β/°	96.694(2)	96.8220(10)
γ/°	90	90
Volume/Å ³	2709.08(10)	2900.48(8)
Z'	1	1

3.4.2 Crystal structures of iron complexes

[Fe(L11Cx)₂][BF₄]₂

The iron complexes from the [Fe(L11Cx)₂][BF₄]₂ series were very hard to crystallize, and a low quality crystal structure was collected only for [Fe(L11C6)₂][BF₄]₂ · 2H₂O. The molecules in this structure pack, so the counterions, the bpp parts of the molecules, and the lattice water molecules are located closely together in one layer, while the alkyl chains interdigitate with each other and form another layer, with much more free space inside it (Fig. 3.16).

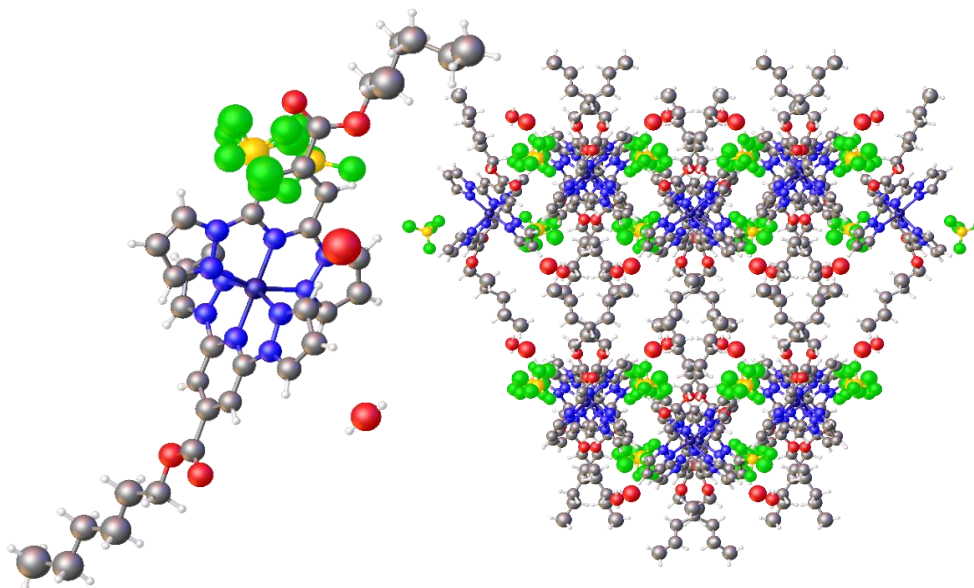


Fig. 3.16. Crystal structure of [Fe(L11C6)₂][BF₄]₂·2H₂O and its packing diagram from the view, parallel to the [001] vector

[Fe(L13Cx)₂][BF₄]₂

[Fe(L13Cx)₂][BF₄]₂ formed crystals more readily than [Fe(L11Cx)₂][BF₄]₂, so crystal structures were collected for [Fe(L13C6)₂][BF₄]₂·H₂O, [Fe(L13C14)₂][BF₄]₂·2MeCN, and [Fe(L13C16)₂][BF₄]₂·H₂O. The crystals of [Fe(L13C14)₂]

[BF₄]₂·2MeCN were grown in a NMR tube by **slow evaporation** from MeCN-D₃, and collected at the Diamond Light Source. The other two were grown by the conventional method of slow pentane diffusion. Unlike the ligands, iron complexes were reluctant to form crystals during slow evaporation, and usually decomposed, forming the ligand and Fe(BF₄)₂, so this was the only successful attempt out of many. Despite having long alkyl chains that may hinder crystal formation, [Fe(L13C16)₂][BF₄]₂·H₂O crystallized reproducibly and relatively easily, while shorter-chained [Fe(L13C6)₂][BF₄]₂·H₂O was crystallized only after multiple attempts. All three crystal structures of this series adopt triclinic space group P-1, but have different unit cell parameters (Table 3.4).

Table 3.4 Unit cells of [Fe(L11C6)₂][BF₄]₂·2H₂O, [Fe(L13C6)₂][BF₄]₂·H₂O, [Fe(L13C14)₂][BF₄]₂·2MeCN, and [Fe(L13C16)₂][BF₄]₂·H₂O

	[Fe(L11C6) ₂][BF ₄] ₂ ·2H ₂ O	[Fe(L13C6) ₂][BF ₄] ₂ ·H ₂ O	[Fe(L13C14) ₂][BF ₄] ₂ ·2MeCN	[Fe(L13C16) ₂][BF ₄] ₂ ·H ₂ O
Space group	P2 ₁ /c	P-1	P-1	P-1
a/Å	17.925(3)	10.3105(8)	14.31590(10)	13.2899(3)
b/Å	15.1997(15)	15.1489(10)	15.21930(10)	13.6465(4)
c/Å	20.4944(16)	16.7306(8)	16.7869(2)	19.4605(6)
α/°	90	89.136(5)	84.0090(10)	98.865(2)
β/°	101.974(12)	77.066(6)	89.7180(10)	91.201(2)
γ/°	90	82.387(6)	72.7220(10)	98.421(2)
Volume/Å ³	5462.2(12)	2524.2(3)	3472.07(6)	3446.19(17)
Z'	1	1	1	1

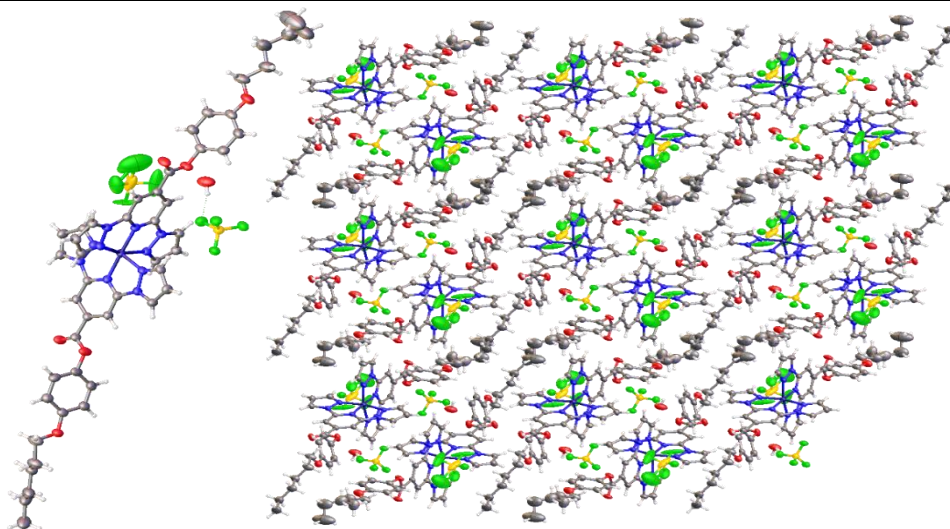


Fig. 3.17. Crystal structure of [Fe(L13C6)₂][BF₄]₂·H₂O and its packing diagram from the view, parallel to the [100] vector

Each of the crystal structures in this series had a lattice solvent. Water molecules formed hydrogen bonds between the H₂O hydrogen and BF₄ fluorine in both [Fe(L13C6)₂][BF₄]₂·H₂O (Fig. 3.17) and [Fe(L13C16)₂][BF₄]₂

$\cdot\text{H}_2\text{O}$ (Fig. 3.18), while MeCN molecules didn't form any hydrogen bonds in the crystal structure of $[\text{Fe}(\text{L13C14})_2][\text{BF}_4]_2 \cdot 2\text{MeCN}$ (Fig. 3.19). All three complexes were low spin, and it seems the hydrogen bonds in the lattice solvents didn't affect the iron centres substantially, as they were located too far from each other. There were no π - π interactions found in any of the three crystal structures.

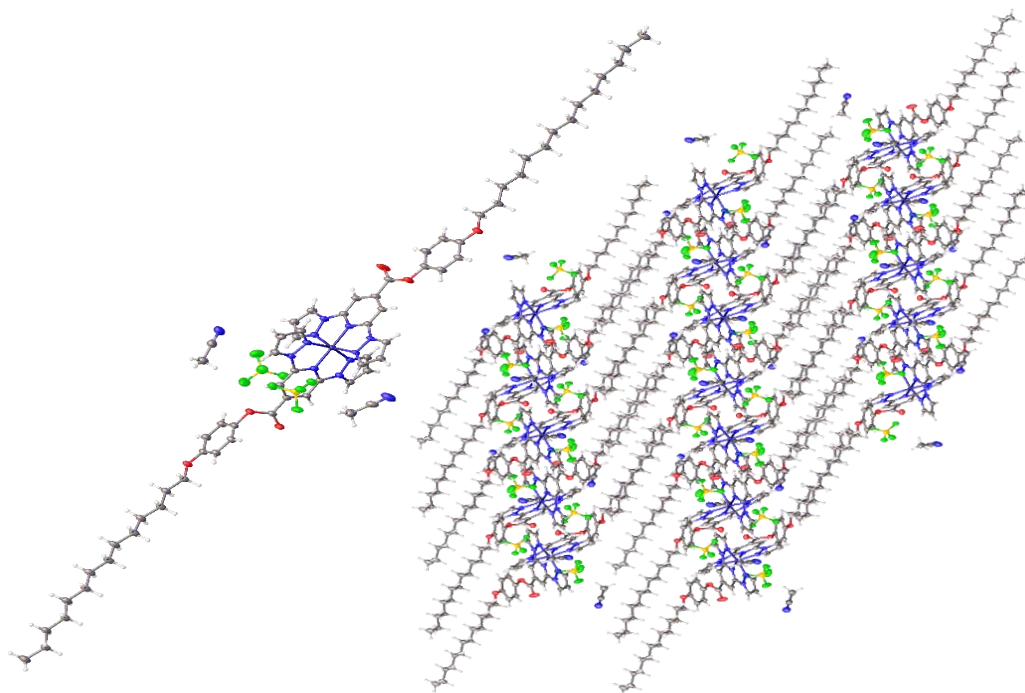


Fig. 3.18. Crystal structure of $[\text{Fe}(\text{L13C14})_2][\text{BF}_4]_2 \cdot 2\text{MeCN}$ and its packing diagram from the view, parallel to the [100] vector

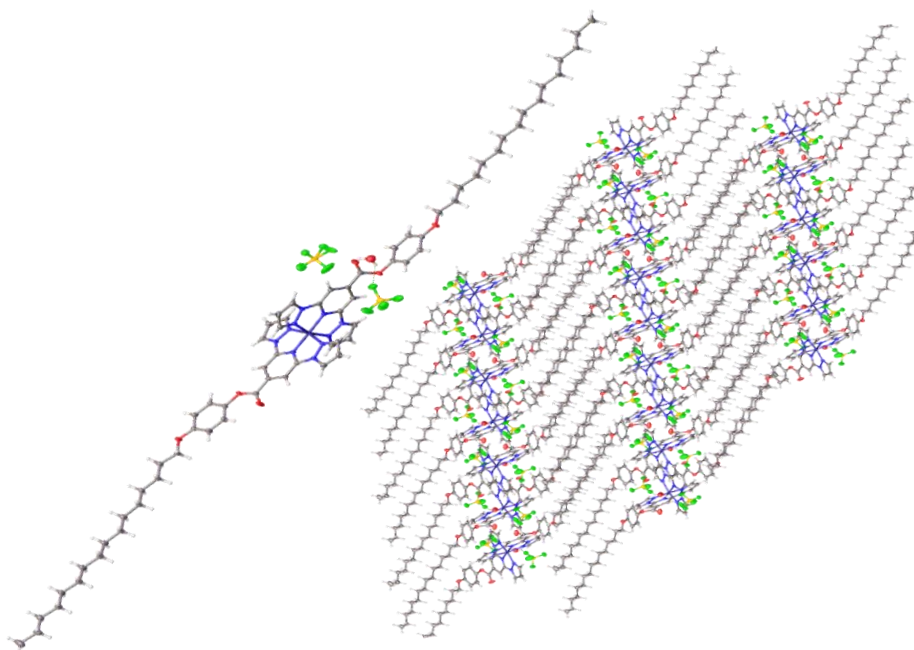


Fig. 3.19. Crystal structure of $[\text{Fe}(\text{L13C16})_2][\text{BF}_4] \cdot \text{H}_2\text{O}$ and its packing diagram from the view, parallel to the [010] vector

3.5 Distortion parameters

As can be seen from the distortion parameters, all the crystal structures of iron complexes in this chapter were LS (Table 3.5), which corresponds with their SQUID measurements at the given temperatures (Fig. 3.20, 3.23).

Table 3.5 The distortion parameters for the crystal structures of [Fe(L11C6)₂][BF₄]₂·2H₂O, [Fe(L13C6)₂][BF₄]₂·H₂O, [Fe(L13C14)₂][BF₄]₂·2MeCN, and [Fe(L13C16)₂][BF₄]₂·H₂O

	[Fe(L11C6) ₂] [BF ₄] ₂ ·2H ₂ O	[Fe(L13C6) ₂] [BF ₄] ₂ ·H ₂ O	[Fe(L13C14) ₂] [BF ₄] ₂ ·2MeCN	[Fe(L13C16) ₂] [BF ₄] ₂ ·H ₂ O
	120 K	120 K	293 K	120 K
Fe1-N1A, Å	1.967(15)	1.970(4)	1.9538(10)	1.9688(17)
Fe1-N1B, Å	1.950(15)	1.974(3)	1.9694(11)	1.9591(16)
Fe1-N3A, Å	1.884(13)	1.898(3)	1.8911(10)	1.8852(16)
Fe1-N3B, Å	1.892(14)	1.896(3)	1.8986(10)	1.8839(16)
Fe1-N5A, Å	1.981(13)	1.965(3)	1.9837(10)	1.9561(17)
Fe1-N5B, Å	1.967(13)	1.957(4)	1.9765(11)	1.9548(16)
Average, Å	1.94	1.94	1.95	1.94
α, °	80.05(6)	80.29(14)	80.10(4)	80.47(7)
Σ, °	86.7(6)	84.26(14)	87.45(4)	82.66(7)
Φ, °	178.5(6)	178.05(14)	175.39(4)	176.98(7)
θ, °	90.307	91.266	87.196	91.245
V _{oct} , Å ³	9.436	9.499	9.503	9.374

3.6 SQUID

3.6.1 [Fe(L11Cx)₂][BF₄]₂

All of the [Fe(L11Cx)₂][BF₄]₂ series members showed similar magnetic behaviour – they remained fully LS up to ca 340 K, but show a gradual switching above that temperature (Fig. 3.20), with a slight hysteresis for [Fe(L11C14)₂][BF₄]₂ (Fig. 3.21). Heating [Fe(L11C18)₂][BF₄]₂ to 170°C causes annealing, which makes some fraction of the sample permanently switch to HS (Fig. 3.22). Annealing was confirmed to take place for other

iron complexes in this series by DSC (Fig. 3.35) and powder patterns (Fig. 3.1).

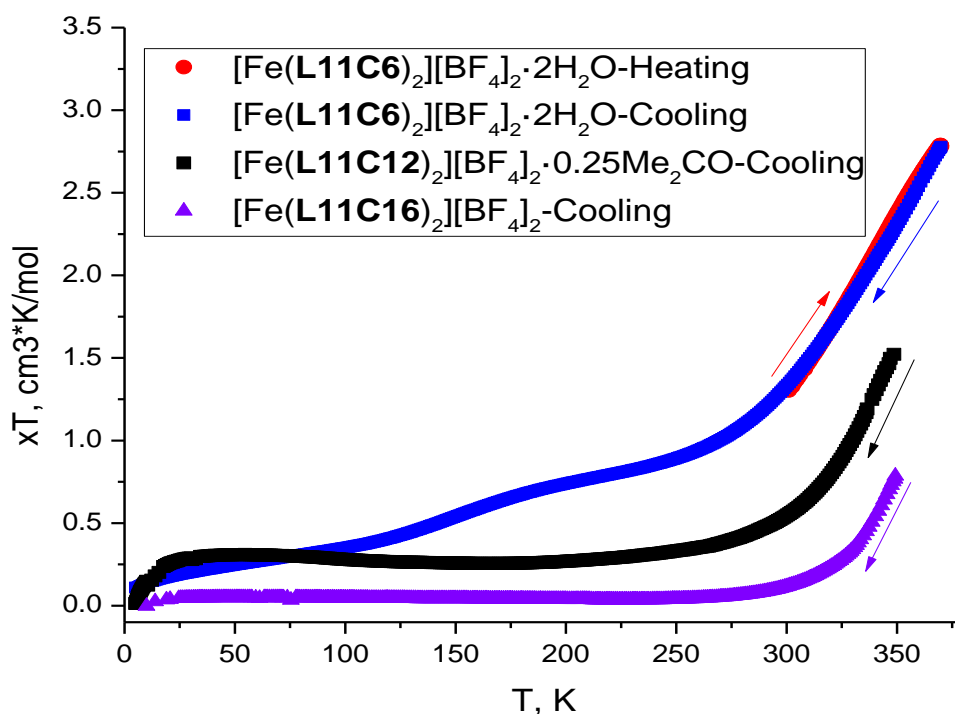


Fig. 3.20 Variable temperature magnetic susceptibility of $[\text{Fe}(\text{L11C6})_2][\text{BF}_4]_2 \cdot 2\text{H}_2\text{O}$, $[\text{Fe}(\text{L11C12})_2][\text{BF}_4]_2 \cdot 0.25\text{Me}_2\text{CO}$, and $[\text{Fe}(\text{L11C16})_2][\text{BF}_4]_2$

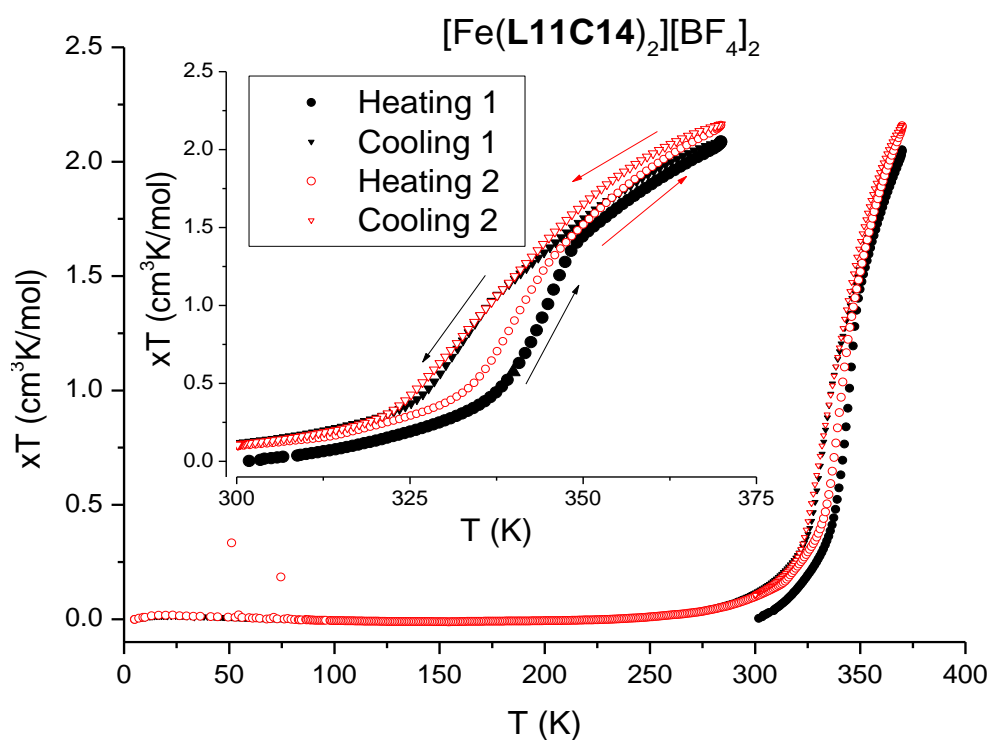


Fig. 3.21 Variable temperature magnetic susceptibility of $[\text{Fe}(\text{L11C14})_2][\text{BF}_4]_2$, showing hysteresis

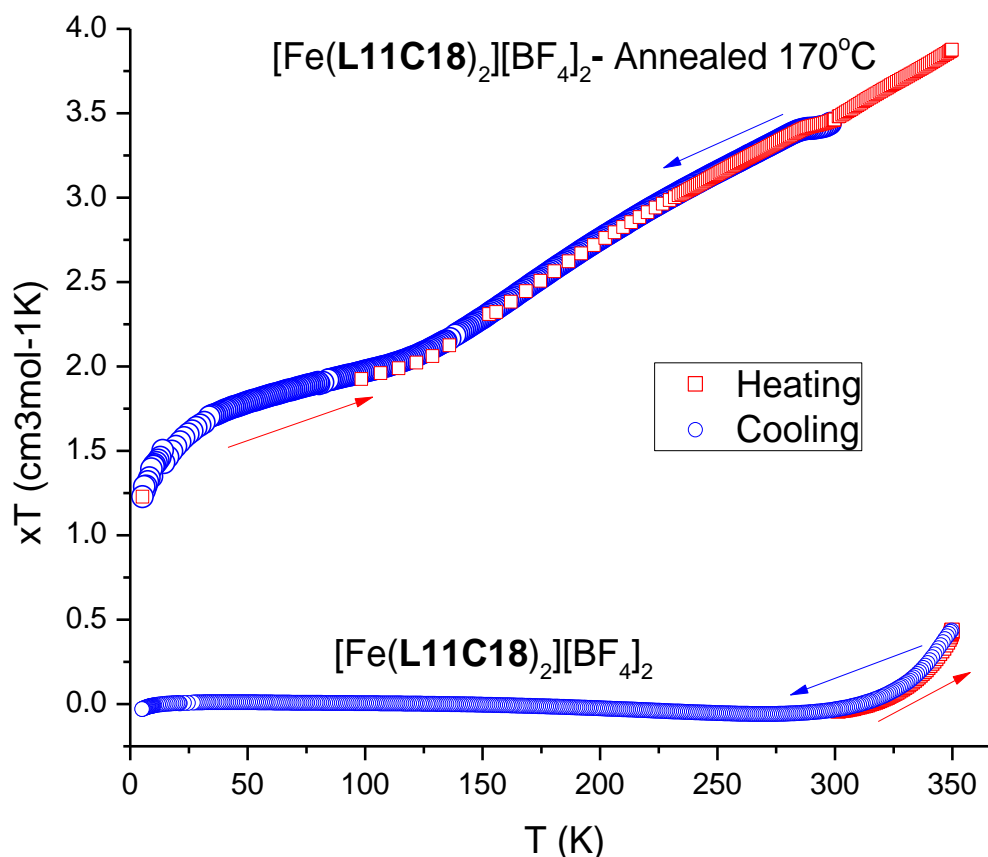


Fig. 3.22 Variable temperature magnetic susceptibility of [Fe(L11C18)₂][BF₄]₂: annealed at 170°C vs the fresh sample

3.5.2 [Fe(L13Cx)₂][BF₄]₂

The magnetic behaviour of the [Fe(L13Cx)₂][BF₄]₂ iron complexes was not as uniform as the one of [Fe(L11Cx)₂][BF₄]₂. Their powder patterns showed the same trend: similar powder patterns for all the [Fe(L11Cx)₂][BF₄]₂ series, and different powder patterns for each alkyl chain length [Fe(L13Cx)₂][BF₄]₂ iron complexes (Chapter 3.9). [Fe(L13C6)₂][BF₄]₂·H₂O and [Fe(L13C18)₂][BF₄]₂·1.6H₂O remained LS from 5 to 350 K (Fig. 3.23). [Fe(L13C14)₂][BF₄]₂·2MeCN showed some slight and gradual changes in the magnetic moment with temperature (Fig. 3.23). [Fe(L13C12)₂][BF₄]₂ showed some significant decrease in the magnetic moment upon cooling below 225 K, which may be explained by gradual spin crossover (Fig 3.23 purple and green dots). Another sample of the same iron complex has been measured, this time for three cycles (Fig 3.23 red, blue and magenta dots). Both times the magnetic moment followed roughly the same path, and the second heating cycle followed exactly the cooling cycle. This means that the SQUID measurements of [Fe(L13C12)₂][BF₄]₂ are reproducible, and showed gradual spin crossover with no hysteresis, probably in two steps with T_{1/2} at around 240 and 340K.

A sample of $[\text{Fe}(\text{L13C16})_2][\text{BF}_4]_2 \cdot 1.6\text{H}_2\text{O}$ was heated in the 170°C oil bath for a few minutes and allowed to cool to room temperature, after which measured at a SQUID magnetometer. The annealing changed the magnetic behaviour of the sample, so the main fraction of the sample remained HS from 5 to 370 K (Fig. 3.24).

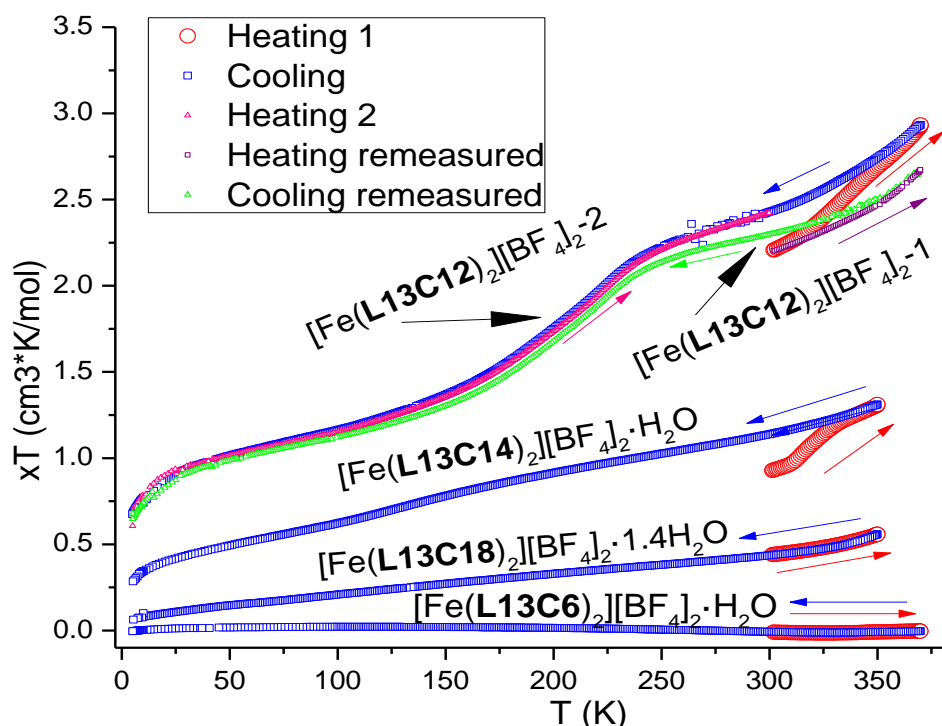


Fig. 3.23 Variable temperature magnetic susceptibility of $[\text{Fe}(\text{L13C6})_2][\text{BF}_4]_2 \cdot \text{H}_2\text{O}$, $[\text{Fe}(\text{L13C14})_2][\text{BF}_4]_2 \cdot \text{H}_2\text{O}$, $[\text{Fe}(\text{L13C18})_2][\text{BF}_4]_2 \cdot 1.4\text{H}_2\text{O}$, and the two measurements of $[\text{Fe}(\text{L13C12})_2][\text{BF}_4]_2$

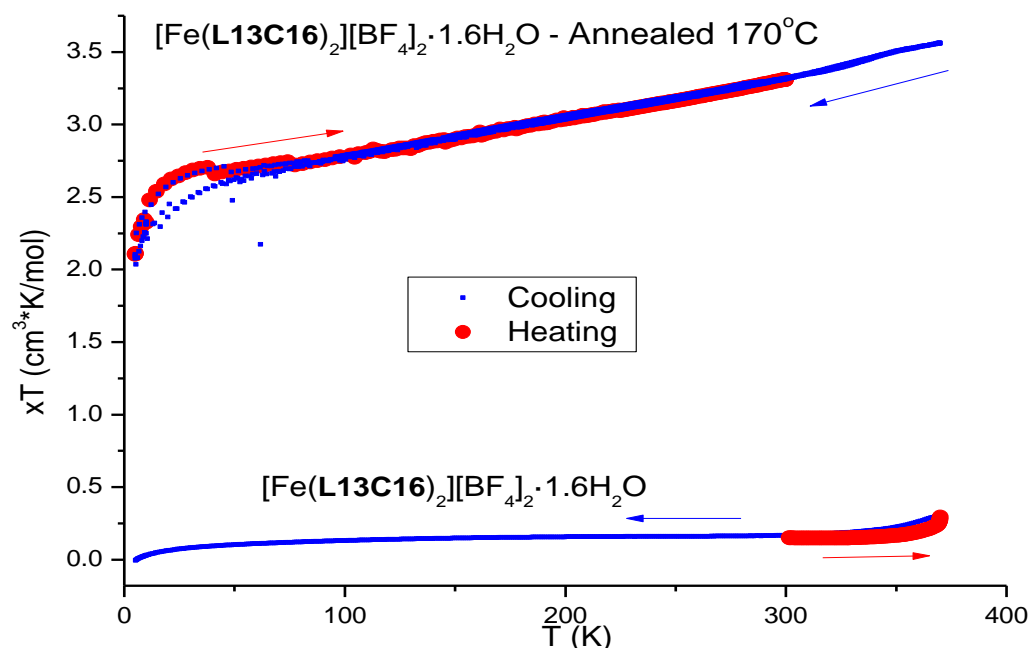


Fig. 3.24 Variable temperature magnetic susceptibility of $[\text{Fe}(\text{L13C16})_2][\text{BF}_4]_2 \cdot 1.6\text{H}_2\text{O}$: annealed at 170°C vs the fresh sample

3.7 DSC and TGA

3.7.1 Ligands

L11Cx

The DSC graphs of all the ligands in **L11Cx** series were pretty similar, with one peak on the first heating cycle, which corresponds with its manually measured melting point (see Chapter 6 for more details). The second heating cycle resembles the first one, but with the melting peak shifted down for about one degree (Fig. 3.25, 3.26). Unlike the other ligands in this series, **L11C18** shows one additional peak on the second heating cycle, ca 8 degrees below the main peak (Fig. 3.27). On the cooling cycle, the peak from the freezing back was observed on all the **L11Cx** series DSCs. In every case it was substantially below the melting point. This may be explained by the fact that forming crystals from liquid takes longer time than melting, which may cause a delay. The heating cycles were performed at 10°C per minute, and the cooling cycle was performed at 5°C per minute speed. Further details about DSC measurements can be seen at Chapter 6.1.4.

The **TGA** analyses of the **L11Cx** ligands all looked similar, with no signs of solvent loss. Decomposition started at 165-225°C depending on the alkyl chain length, with longer-chain ligands being more stable (Fig. 3.28).

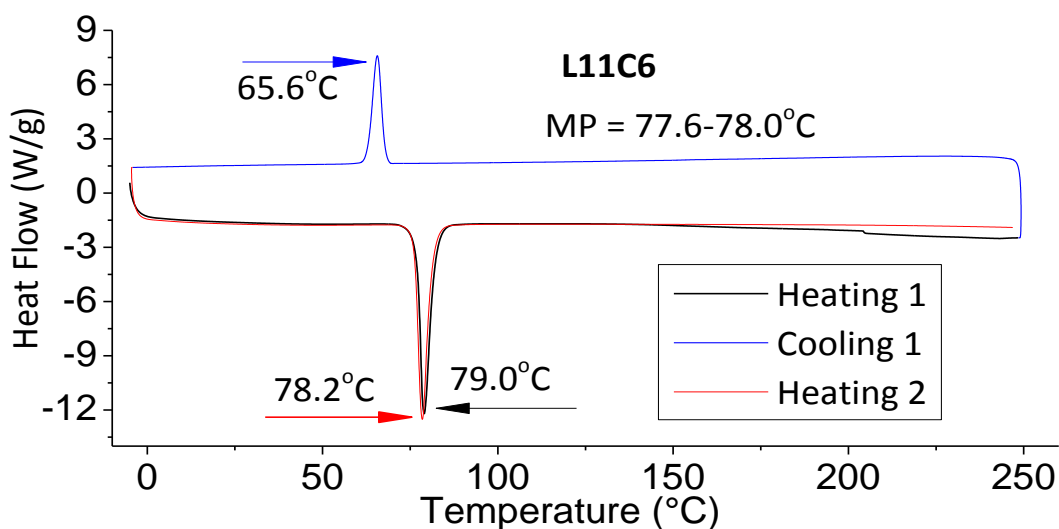


Fig. 3.25. DSC of L11C6

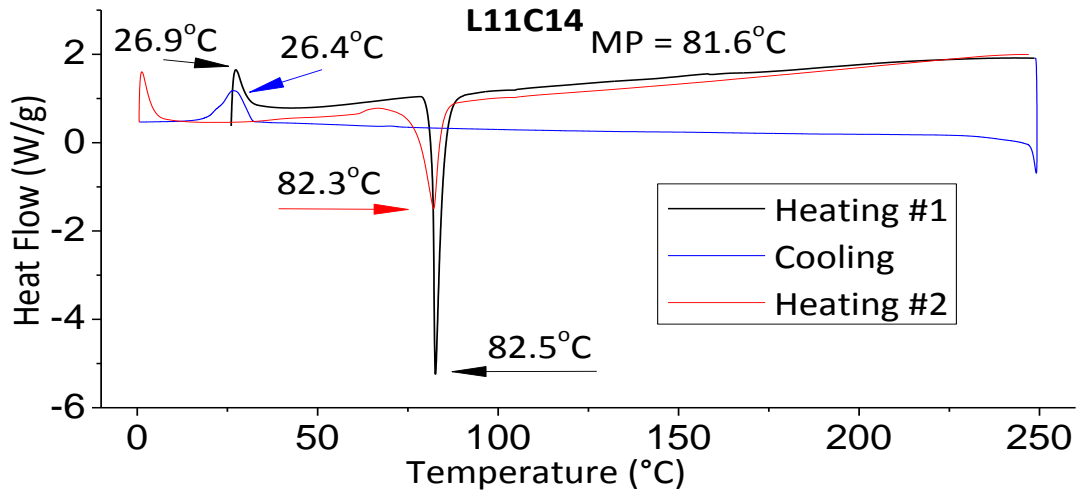


Fig. 3.26. DSC of L11C14

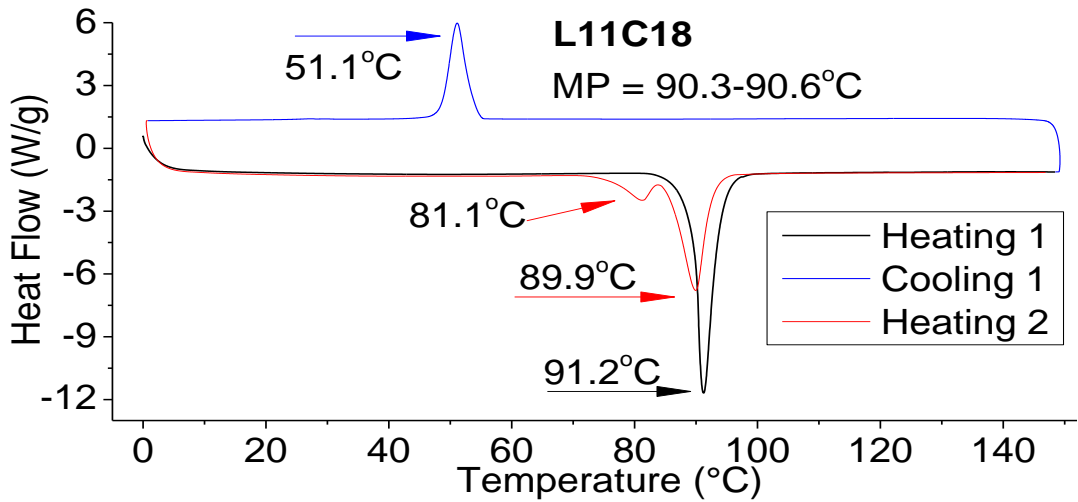


Fig. 3.27. DSC of L11C18

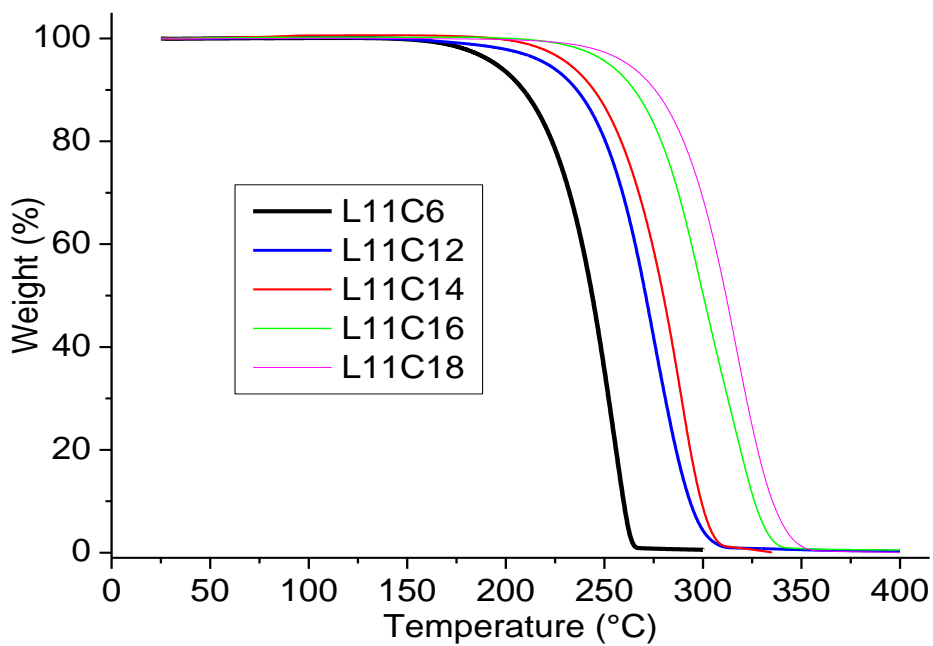


Fig. 3.28. TGA of L11C6, L11C12, L11C14, L11C16, and L11C18

L13Cx

The DSC analyses of **L13Cx** ligands were very similar to **L11Cx** series, but the peaks were sharper, and the peaks on the cooling mode were less downshifted. For the **L13Cx** ligands, only one peak was observed on each cycle, which corresponds with the melting points of the ligands, except **L13C12**, which on its cooling mode had some splitting of the main peak with 1.7°C difference between the two subpeaks, and one additional broad and very small peak at 108.7°C.

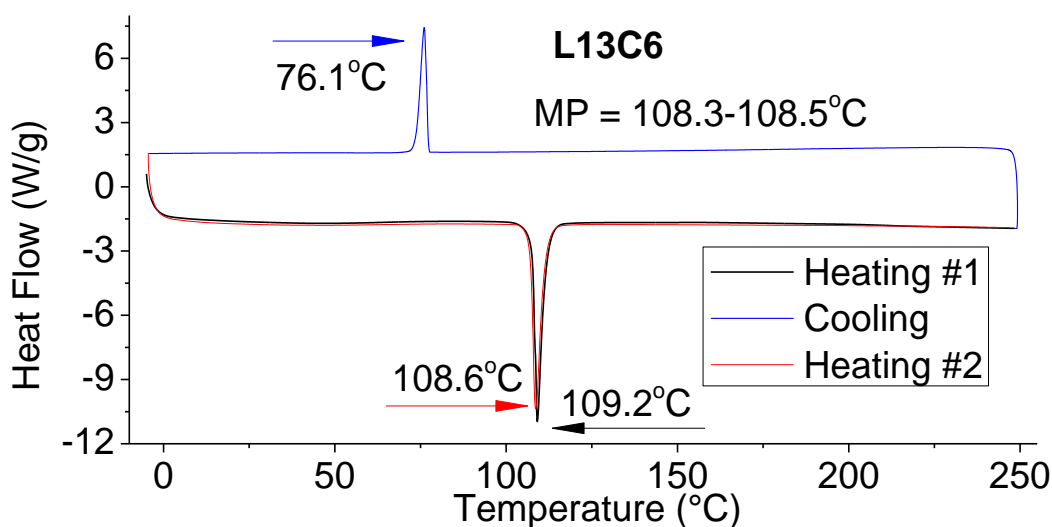


Fig. 3.29. DSC of **L13C6**, which is typical for the **L13Cx** series

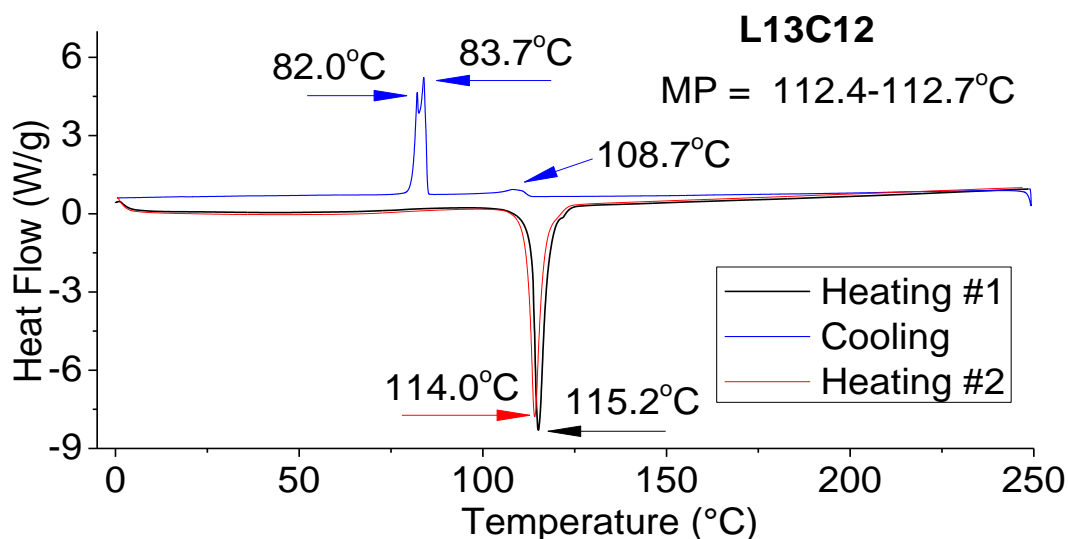


Fig. 3.30. DSC of **L13C12**, not similar to the other **L13Cx** ligands

For the TGAs of **L13Cx** series, unlike the **L11Cx** ligands, there was no direct correlation between the alkyl chain length and the temperature at which the ligand starts to decompose (Fig. 3.31). There were no signs of solvent loss on the TGAs.

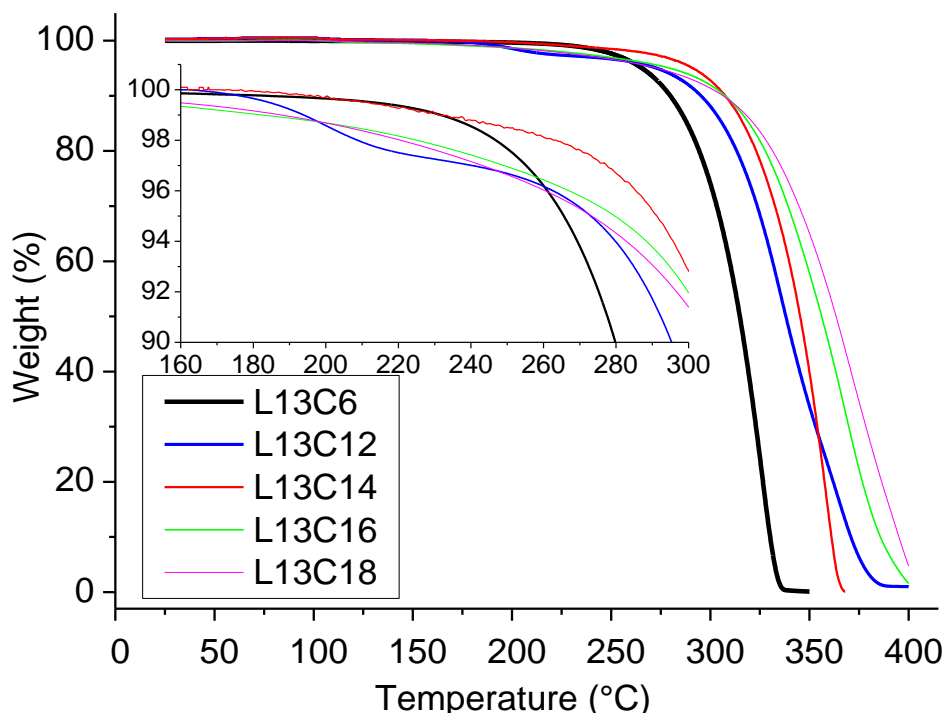


Fig. 3.31. TGA of **L13C6**, **L13C12**, **L13C14**, **L13C16**, and **L13C18**

3.7.2 Iron(II) complexes

The DSCs of the iron complexes had broader and less clear peaks, compared to the ligands. Some of the iron complexes shown peaks at the first heating cycle, and no peaks on the remaining two cycles, which means some irreversible changes happened in the sample upon heating to that temperature. In cases when this annealing was occurring, a fresh sample of the same compound was measured again at a lower maximum temperature to avoid the annealing. The annealing of the $[\text{Fe}(\text{L11Cx})_2][\text{BF}_4]_2$ and $[\text{Fe}(\text{L13Cx})_2][\text{BF}_4]_2$ series of iron complexes was studied also by SQUID, DSC, VT photographs and by powder patterns.

$[\text{Fe}(\text{L11Cx})_2][\text{BF}_4]_2$

TGAs of some of the $[\text{Fe}(\text{L11Cx})_2][\text{BF}_4]_2$ iron complexes showed presence of lattice solvent, and there are a few techniques that can help to identify them: TGA, DSC, microanalysis (which can be found in Chapter 6.3.4), and XRD. Sometimes these methods suggested different lattice solvents, so all the results were summarized all together in one table to compare them easily (Table 3.4).

$[\text{Fe}(\text{L11C16})_2][\text{BF}_4]_2$ was first measured by DSC from 0 to 250°C (Fig. 3.35), up to the same temperature for which the ligands were measured. Because some irreversible changes were observed, the same compound was re-measured with heating until 175°C, and annealing happened again. Running

a DSC from 0 to 110°C lead to absence of annealing, with the peaks on the heating 1 and heating 2 cycles matching each other (Fig. 3.36). There were two peaks on the cooling cycle, and one peak on each of the heating cycles at ca 92.5°C, or 366K, which may come from an SCO transition, as this temperature matches its expected $T_{1/2}$ (Fig. 3.20). The doubled peak on the cooling cycle does not come from a LC phase formation, as on the photos it may be seen that at that temperature the sample remains solid (Fig. 3.46). Therefore the origin of the second peak remains unknown. As the DSC showed no peaks from the solvent loss (Fig. 3.36), the TGA showed insignificant mass loss at 100°C (Fig. 3.38), and CHN showed no lattice solvent, the sample is likely to have no lattice solvent (Table 3.6).

Table 3.6 Assigning lattice solvents to $[\text{Fe}(\text{L11Cx})_2][\text{BF}_4]_2$ based on TGA, CHN and XRD

# of carbons	Mr, Da	Suspected lattice solvent	Solv, Mr, Da	Solvent loss, %		CHN	XRD
				Theoretical	Obs. at 100°C		
C6	908.24	2H ₂ O	36	3.81	3.68	0	2H ₂ O
C12	1076.55	0.25Me ₂ CO	14.52	1.33	1.09	0	-
C14	1132.66	-*	0*	0.00	0.5	0	-
C16	1188.77	-	0	0.00	0.24	0	-
C18	1244.87	-	0	0.00	0.53	3H ₂ O	-

* -- no measurement taken; 0 - no lattice solvent found

The DSC of $[\text{Fe}(\text{L11C6})_2][\text{BF}_4]_2$ was featureless (Fig. 3.32), which may be explained by its gradual SCO (Fig. 3.20), that produced a very broad and weak DSC peak. The crystal structure of this iron complex (Fig. 3.16) and its TGA (Fig. 3.38) suggest presence of two lattice water molecules, while the CHN shows no solvent (Table 3.4), which may be explained by escape of the lattice solvent during preparation of the CHN sample. Thus the final formula of this iron complex must be $[\text{Fe}(\text{L11C6})_2][\text{BF}_4]_2 \cdot 2\text{H}_2\text{O}$.

For $[\text{Fe}(\text{L11C12})_2][\text{BF}_4]_2$ there were two peaks on each cycle: at ca 44°C and 63°C, i.e. 317 and 336 K (Fig. 3.33). The second peak corresponds with $T_{1/2}$ of this iron complex (Fig. 3.20), while the first peaks on each heating cycle may come from escaping of the lattice solvent, which based on TGA and the escaping temperature from DSC must be 0.25Me₂CO.

The DSCs of both $[\text{Fe}(\text{L11C14})_2][\text{BF}_4]_2$ and $[\text{Fe}(\text{L11C18})_2][\text{BF}_4]_2$ had one peak on each cycle, which corresponded with their spin crossover $T_{1/2}$ of ca 350K or 77°C (Fig. 3.21), and at 95°C, i.e. 368 K (Fig. 3.37) respectively. Their TGAs suggest no lattice solvent present (Fig. 3.38).

The TGAs of the $[\text{Fe}(\text{L11Cx})_2][\text{BF}_4]_2$ iron complexes all looked similar, with a rapid drop in the mass at ca 300°C (Fig. 3.38). This means that the annealing, which happened to the iron complexes in this series between 100°C and 170°C, didn't cause a significant mass loss, but was likely associated with the alkyl chain orientation changes.

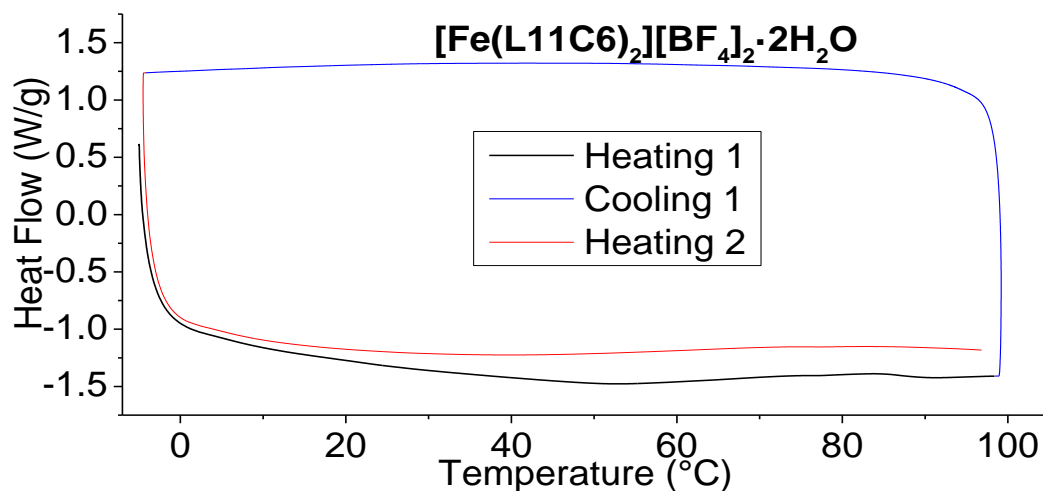


Fig. 3.32. DSC of $[\text{Fe}(\text{L11C6})_2][\text{BF}_4]_2 \cdot 2\text{H}_2\text{O}$

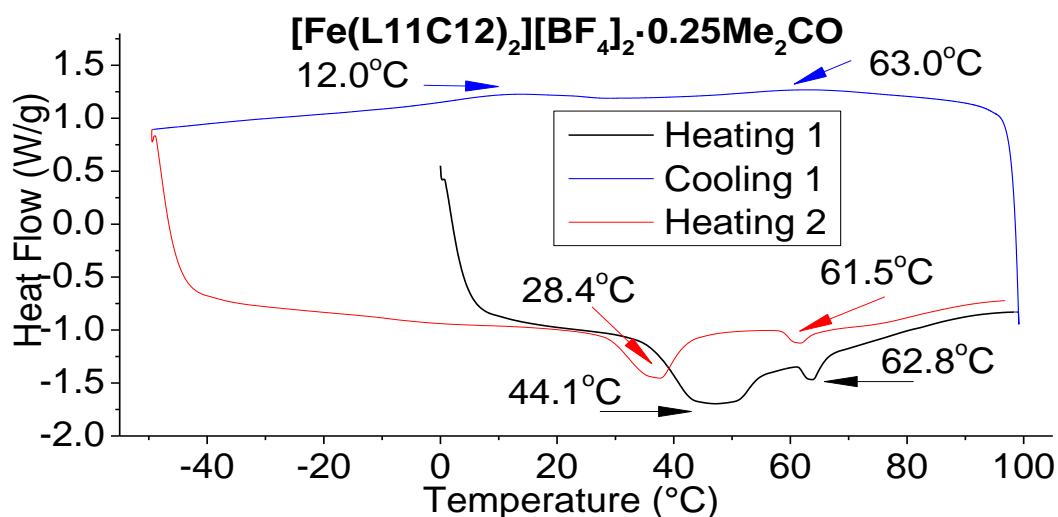


Fig. 3.33. DSC of $[\text{Fe}(\text{L11C12})_2][\text{BF}_4]_2 \cdot 0.25\text{Me}_2\text{CO}$

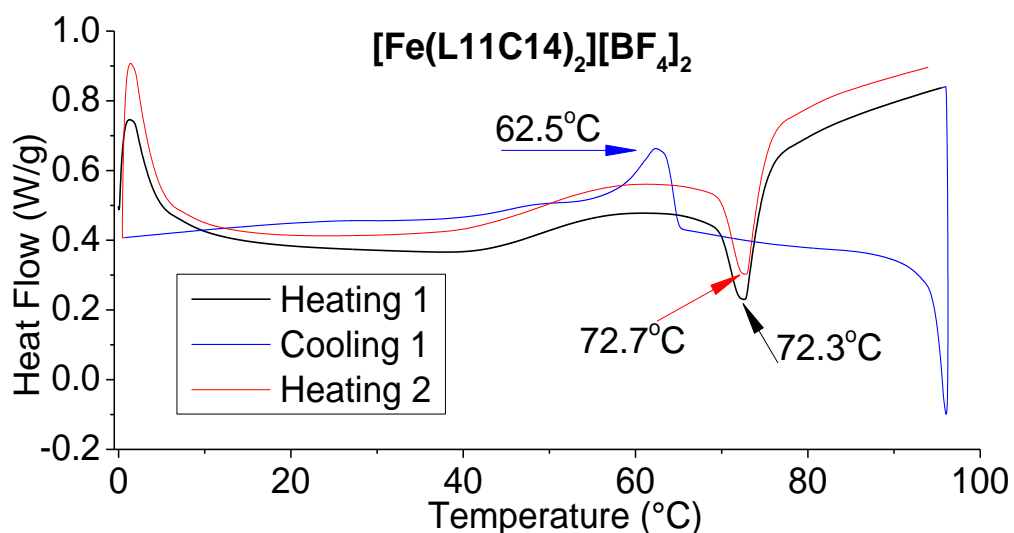


Fig. 3.34. DSC of [Fe(L11C14)₂][BF₄]₂

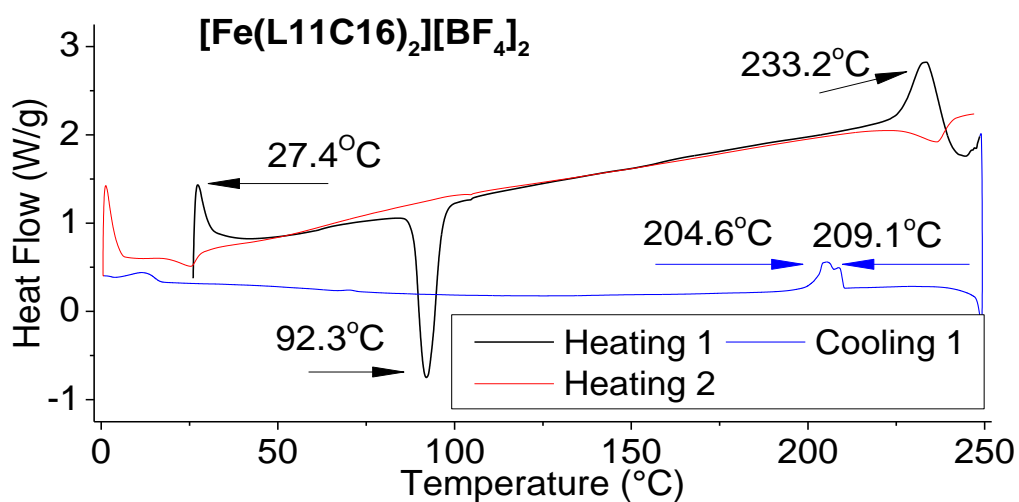


Fig. 3.35. DSC of [Fe(L11C16)₂][BF₄]₂, showing annealing

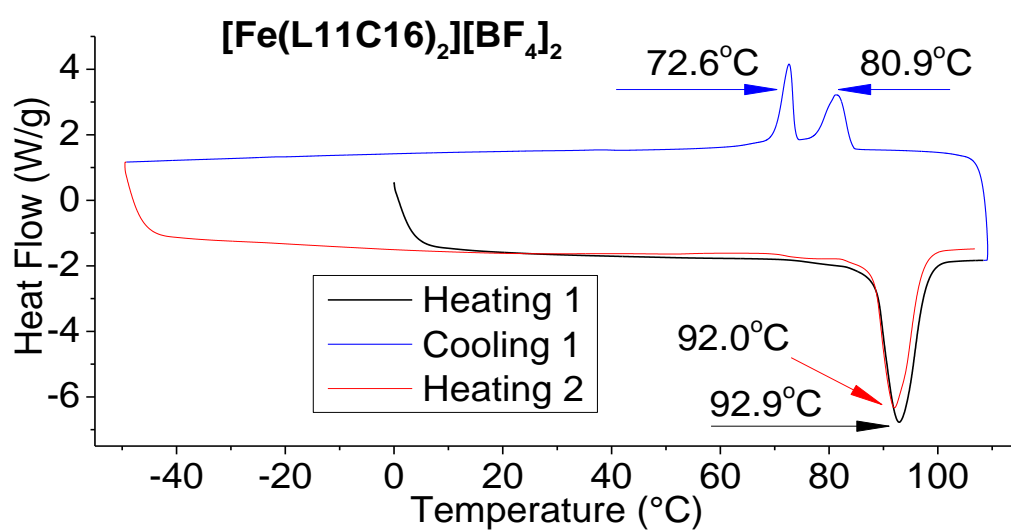


Fig. 3.36. DSC of [Fe(L11C16)₂][BF₄]₂

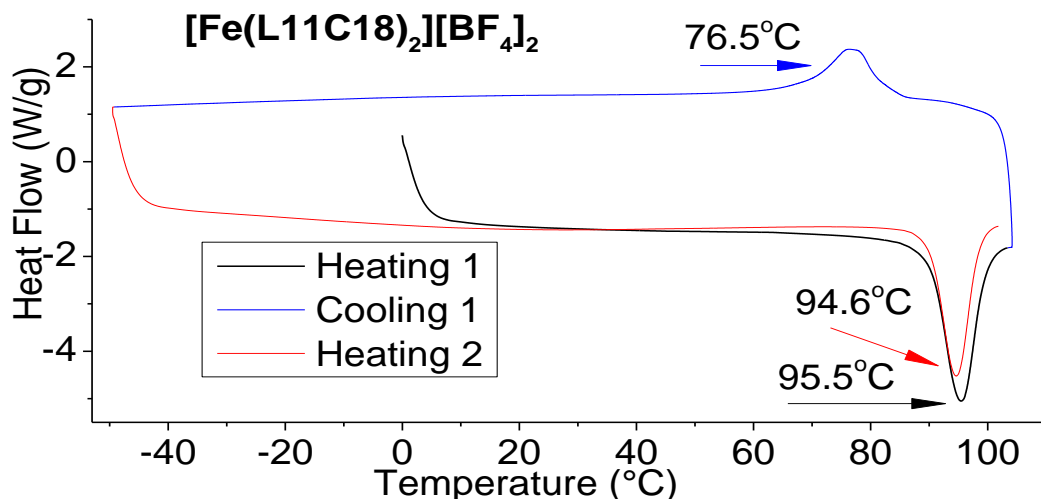


Fig. 3.37. DSC of $[\text{Fe}(\text{L11C18})_2][\text{BF}_4]_2$

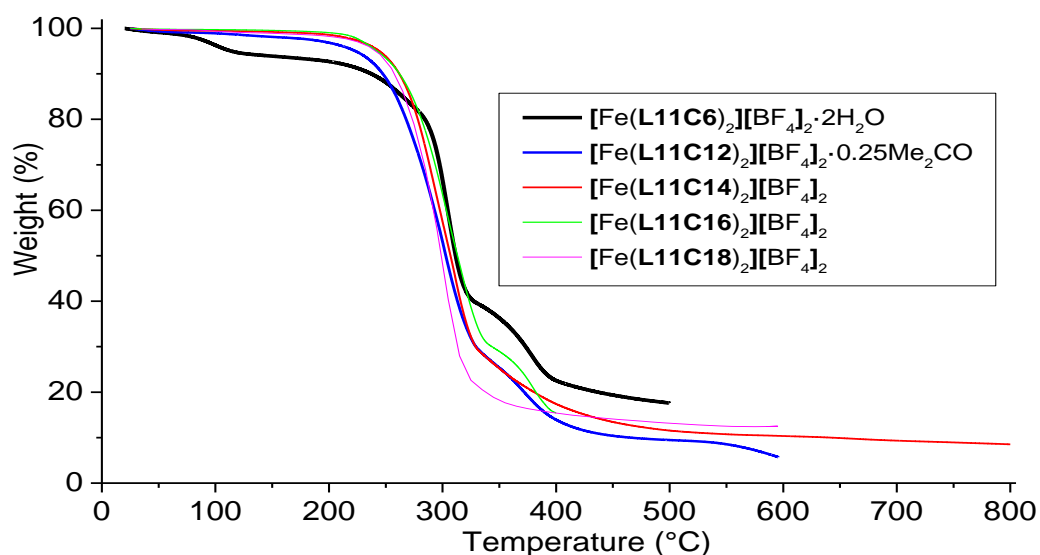


Fig. 3.38. TGA of $[\text{Fe}(\text{L11C6})_2][\text{BF}_4]_2 \cdot 2\text{H}_2\text{O}$, $[\text{Fe}(\text{L11C12})_2][\text{BF}_4]_2 \cdot 0.25\text{Me}_2\text{CO}$, $[\text{Fe}(\text{L11C14})_2][\text{BF}_4]_2$, $[\text{Fe}(\text{L11C16})_2][\text{BF}_4]_2$, and $[\text{Fe}(\text{L11C18})_2][\text{BF}_4]_2$

$[\text{Fe}(\text{L13Cx})_2][\text{BF}_4]_2$

On the TGA graphs of the $[\text{Fe}(\text{L13Cx})_2][\text{BF}_4]_2$ iron complexes we see that all of them undergo a rapid mass loss upon heating beyond ca 250°C (Fig. 3.44). Also, all of them except $[\text{Fe}(\text{L13C12})_2][\text{BF}_4]_2$, had a 1.37 – 2.15% mass loss at 100°C, which corresponds with the loss of lattice water (Table 3.7). For $[\text{Fe}(\text{L13C6})_2][\text{BF}_4]_2 \cdot \text{H}_2\text{O}$ and $[\text{Fe}(\text{L13C16})_2][\text{BF}_4]_2 \cdot \text{H}_2\text{O}$ there are also crystal structures available, showing lattice water molecules (Fig. 3.17, 3.19). The DCE molecules found in $[\text{Fe}(\text{L13C6})_2][\text{BF}_4]_2$ and $[\text{Fe}(\text{L13C12})_2][\text{BF}_4]_2$ by CHN can probably escape with time and be replaced by atmospheric water, which explains their DSC and TGA results.

Table 3.7 Assigning lattice solvents to $[\text{Fe}(\text{L13Cx})_2][\text{BF}_4]_2$ based on TGA, CHN and XRD

# of carbons	Mr, Da	Suspected lattice solvent	Solv. Mr, Da	Solvent loss, %		CHN	XRD
				Theoretical	Obs. at 100°C		
C6	1092.43	H ₂ O	18	1.62	1.61	DCE	H ₂ O
C12	1260.74	-*	0	0.00	0.24	0.5DCE	-
C14	1316.85	H ₂ O	18	1.35	1.37	0*	-
C16	1372.96	1.6 H ₂ O	28.8	2.05	2.15	0	H ₂ O
C18	1429.06	1.4 H ₂ O	25.2	1.73	1.72	0	-

* - - no measurement taken; 0 - no lattice solvent found

On the DSC graph of $[\text{Fe}(\text{L13C6})_2][\text{BF}_4]_2 \cdot \text{H}_2\text{O}$ there were no peaks observed on any of the three cycles, except two very small peaks during the first heating cycle, first of which is at 53°C, which is close to 56°C, the boiling point of acetone, and the second peak at 89.1°C may appear due to the loss of water (Fig. 3.39). This corresponds with the SQUID results (Fig. 3.23), which showed that the sample remained LS, which allows to make a conclusion that $T_{1/2}$ for this iron complex must lie beyond 180°C or 453 K.

The crystals of $[\text{Fe}(\text{L13C14})_2][\text{BF}_4]_2 \cdot 2\text{MeCN}$ were grown from MeCN-D₃ solution, and used only to collect the crystal structure, while the $[\text{Fe}(\text{L13C14})_2][\text{BF}_4]_2 \cdot \text{H}_2\text{O}$ sample was grown from acetone-DCE mixture, and was used for all the other measurements.

$[\text{Fe}(\text{L13C14})_2][\text{BF}_4]_2 \cdot \text{H}_2\text{O}$, $[\text{Fe}(\text{L13C16})_2][\text{BF}_4]_2 \cdot 1.6\text{H}_2\text{O}$, and $[\text{Fe}(\text{L13C18})_2][\text{BF}_4]_2 \cdot 1.4\text{H}_2\text{O}$ showed similar behaviour: there were two peaks on the first heating cycle, and no peaks on the consecutive ones. Unlike on the $[\text{Fe}(\text{L11Cx})_2][\text{BF}_4]_2$ graphs, for $[\text{Fe}(\text{L13Cx})_2][\text{BF}_4]_2$ the peaks were appearing at much higher temperatures, which made it impossible to lower the measurement temperature in order to avoid annealing. The first peaks on each of these graphs (Fig. 3.41, 3.42, 3.43) correspond with the loss of the lattice solvent, and the second peaks at 141.9°C, 134.8°C, and 126.0°C for the C12, C14 and C18 iron complexes respectively, most likely comes from a spin crossover transition, which matches with the observed SQUID curves, which show that the samples remained LS until the upper limit of the magnetometer of ca 360 K or 87°C (Fig. 3.23, 3.24). On the DSC graph for $[\text{Fe}(\text{L13C14})_2][\text{BF}_4]_2 \cdot \text{H}_2\text{O}$ the line is not horizontal, as in other DSC graphs, but is significantly tilted above ca 70°C. This process is observed on the both

heating cycles, and it indicates a very gradual release of thermal energy (Fig. 3.41). It may come from the increase in the entropy due to the long alkyl chains order loss. The other iron complexes from this series didn't show this behaviour at such low temperatures. A significant loss in crystallinity of $[\text{Fe}(\text{L13C14})_2][\text{BF}_4]_2 \cdot \text{H}_2\text{O}$ already at 100°C , that did not happen to any other iron complex in this chapter, was also observed in the powder pattern (Fig. 3.44).

$[\text{Fe}(\text{L13C12})_2][\text{BF}_4]_2$ stands out of this series, because unlike the others, this iron complex showed only one peak on its DSC graph, at ca 126°C or 399 K (Fig. 3.40), and also shown some switching on its SQUID curve (Fig. 3.23). This SQUID measurement was repeated, and twice the same result was obtained (Fig. 3.23), which means that probably this iron complex switches in two steps: firstly gradually at ca 250K or -23°C , which is below the DSC measurement, and secondly at ca 399 K or 126°C .

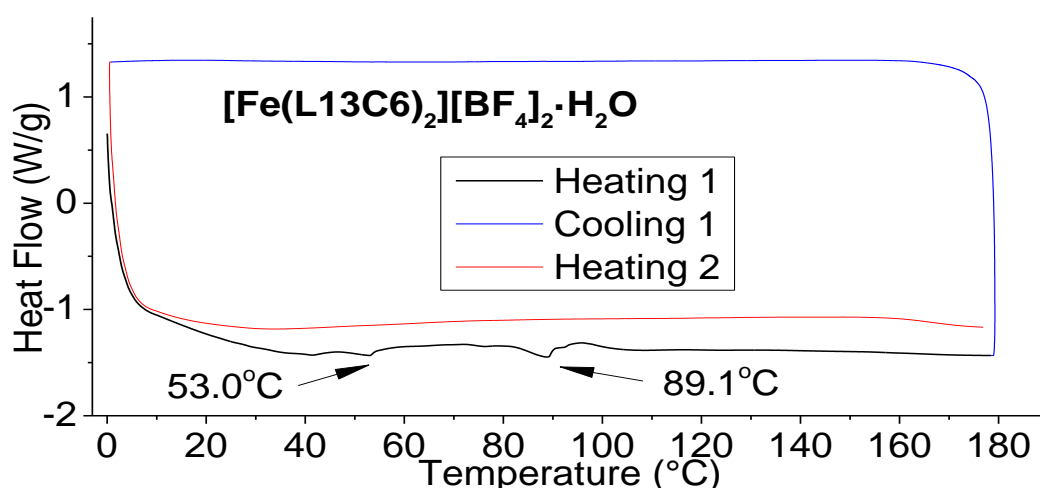


Fig. 3.39. DSC of $[\text{Fe}(\text{L13C6})_2][\text{BF}_4]_2 \cdot \text{H}_2\text{O}$

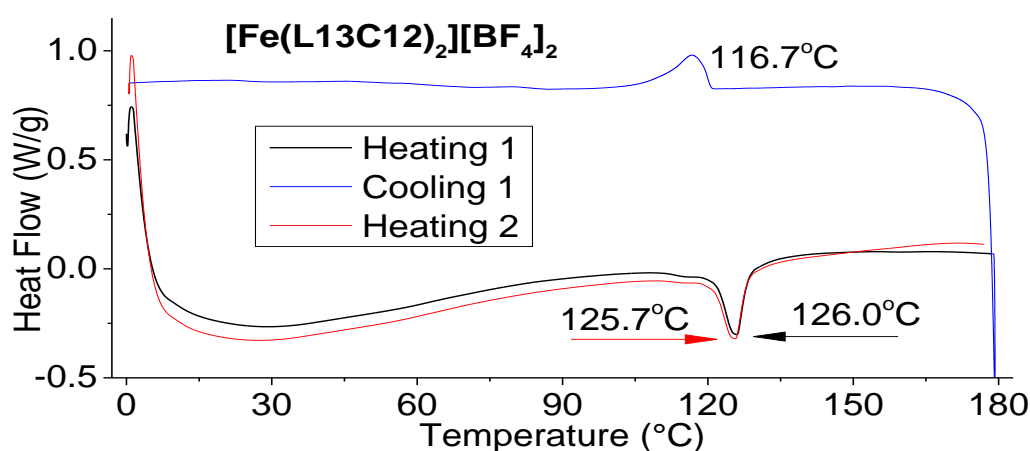


Fig. 3.40. DSC of $[\text{Fe}(\text{L13C12})_2][\text{BF}_4]_2$

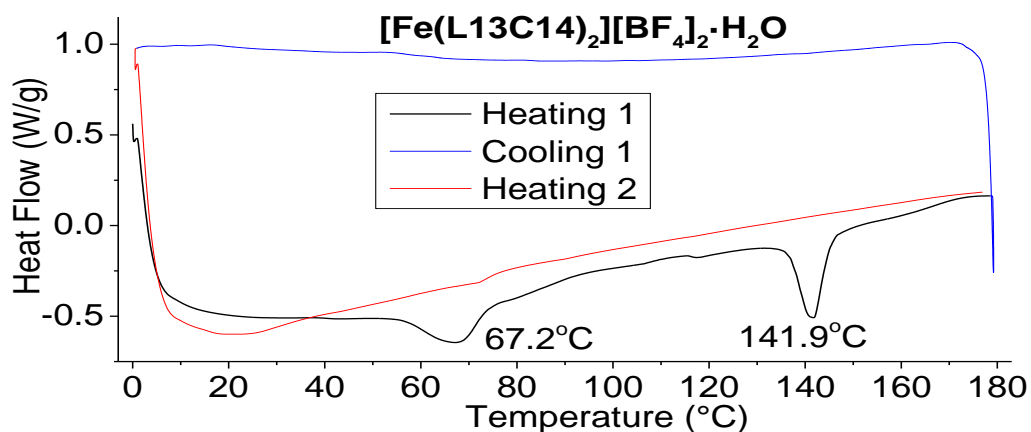


Fig. 3.41. DSC of [Fe(L13C14)₂][BF₄]₂·H₂O

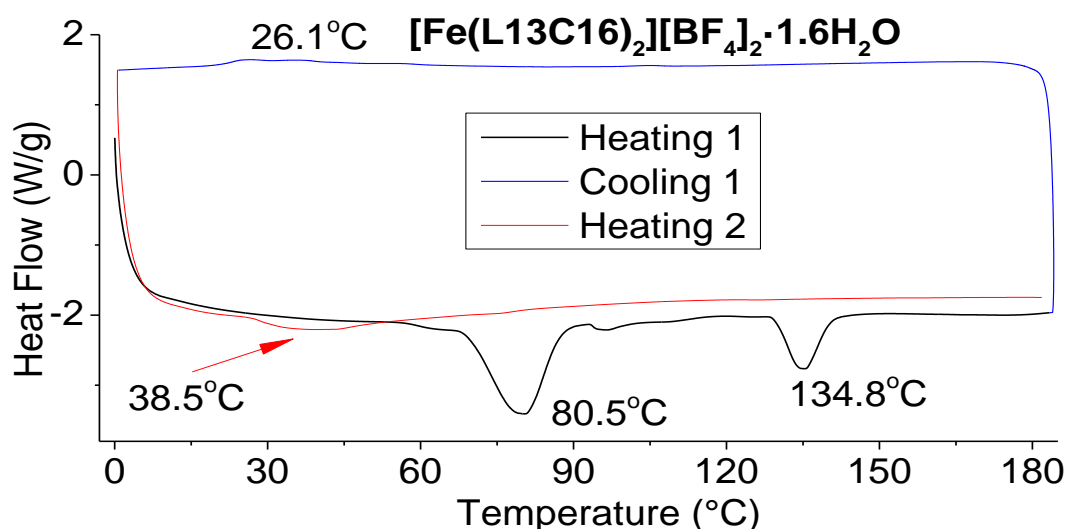


Fig. 3.42. DSC of [Fe(L13C16)₂][BF₄]₂·1.6H₂O

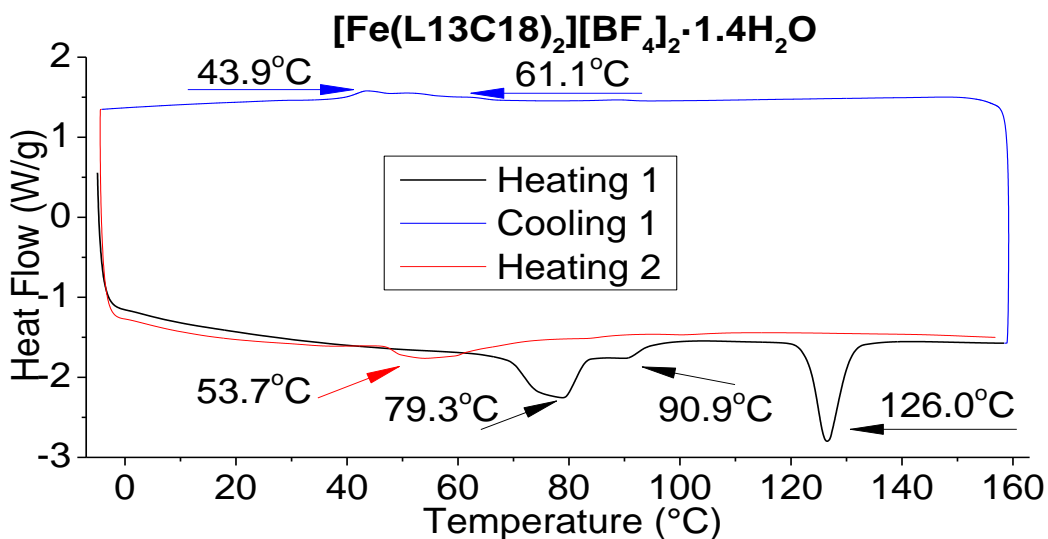


Fig. 3.43. DSC of [Fe(L13C18)₂][BF₄]₂·1.4H₂O

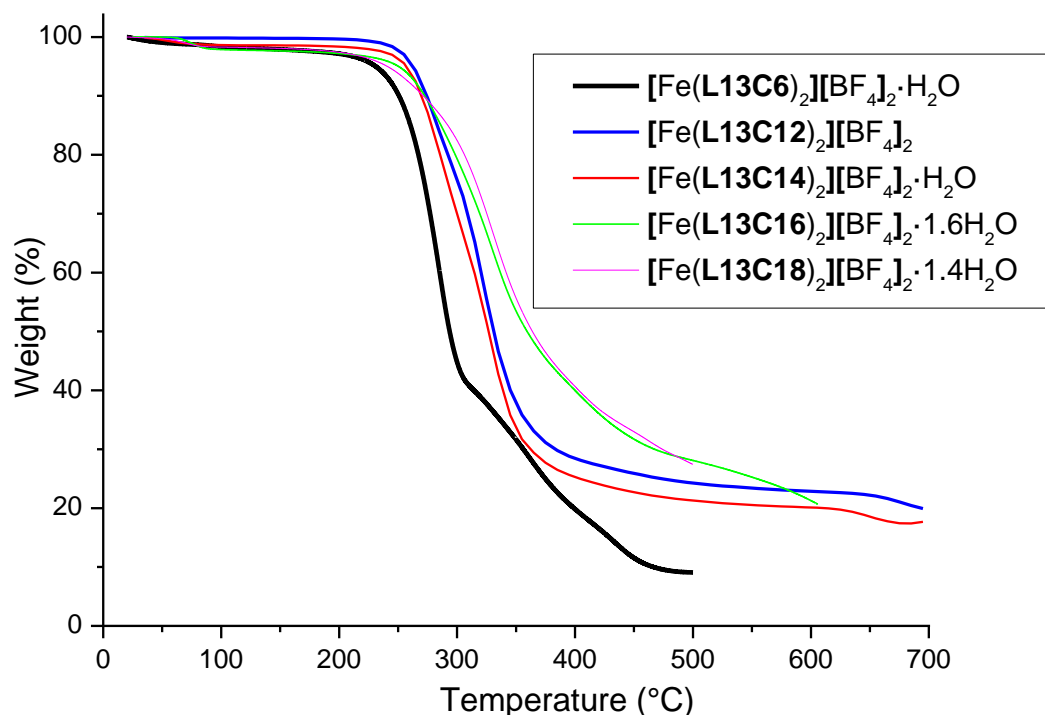


Fig. 3.44. TGA of $[\text{Fe}(\text{L13C6})_2][\text{BF}_4]_2 \cdot \text{H}_2\text{O}$, $[\text{Fe}(\text{L13C12})_2][\text{BF}_4]_2$, $[\text{Fe}(\text{L13C14})_2][\text{BF}_4]_2 \cdot \text{H}_2\text{O}$, $[\text{Fe}(\text{L13C16})_2][\text{BF}_4]_2 \cdot 1.6\text{H}_2\text{O}$, and $[\text{Fe}(\text{L13C18})_2][\text{BF}_4]_2 \cdot 1.4\text{H}_2\text{O}$

3.8 VT photographs

$[\text{Fe}(\text{L11C12})_2][\text{BF}_4]_2 \cdot 0.25\text{Me}_2\text{CO}$, $[\text{Fe}(\text{L13C14})_2][\text{BF}_4]_2 \cdot \text{H}_2\text{O}$, $[\text{Fe}(\text{L13C16})_2][\text{BF}_4]_2 \cdot 1.6\text{H}_2\text{O}$, and $[\text{Fe}(\text{L13C18})_2][\text{BF}_4]_2 \cdot 1.4\text{H}_2\text{O}$ show doubled DSC peaks, which most likely come from the lattice solvent, and $[\text{Fe}(\text{L11C16})_2][\text{BF}_4]_2$ shows a doubled peak of an unknown origin, so some of these cases may be signs of mesophase formation. Therefore, all the iron complexes from this chapter were tested for phase transitions by heating it on an oil bath and observing the colour and the consistency change by taking a photo every 20°C from room temperature to 170°C. Neither the $[\text{Fe}(\text{L11Cx})_2][\text{BF}_4]_2$ (Fig. 3.45), nor $[\text{Fe}(\text{L13Cx})_2][\text{BF}_4]_2$ (Fig. 3.46) iron complex series shown any sign of melting, although some colour changes from red to orange were observed, which indicates spin crossover on heating.

	Rt	40°C	60°C	80°C	100°C	100°C	120°C	140°C	160°C	170°C
[Fe(L13C6) ₂] [BF ₄] ₂ ·H ₂ O										
[Fe(L13C12) ₂] [BF ₄] ₂										
[Fe(L13C14) ₂] [BF ₄] ₂ ·2MeCN										
[Fe(L13C16) ₂] [BF ₄] ₂ ·H ₂ O										
[Fe(L13C18) ₂] [BF ₄] ₂										

Fig. 3.45. Changes in appearance of [Fe(L13Cx)₂][BF₄]₂ iron complexes series with heating from room temperature to 170°C

	Rt	40°C	60°C	80°C	100°C	100°C	120°C	140°C	160°C	170°C
[Fe(L11C6) ₂] [BF ₄] ₂ ·H ₂ O										
[Fe(L11C12) ₂] [BF ₄] ₂										
[Fe(L11C14) ₂] [BF ₄] ₂ ·2MeCN										
[Fe(L11C16) ₂] [BF ₄] ₂ ·H ₂ O										
[Fe(L11C18) ₂] [BF ₄] ₂										

Fig. 3.46. Changes in appearance of [Fe(L11Cx)₂][BF₄]₂ iron complexes series with heating from room temperature to 170°C

3.9 Powder patterns

3.9.1 Ligands

Powder patterns were collected for all the ligands in this chapter: **L11Cx**, **L12CxM**, **L12CxD**, and **L13Cx**, but only the powder patterns of the ligand series that are interesting for this research are discussed below, as they can form iron complexes: **L11Cx** and **L13Cx**. Available crystal structures were used to simulate powder patterns to compare them with the experimental data.

L11Cx

The ligands from the **L11Cx** series have similar powder patterns, with peaks at similar angles, but differing intensity proportions between them (Fig. 3.47). The **L11C6** sample was not very crystalline, but the observed peaks match the most intense peaks in the powder patterns of other ligands in this series. Data from **L11C12** and **L11C14** were an excellent match for their simulated powder patterns, showing those compounds are phase pure (Fig. 3.47).

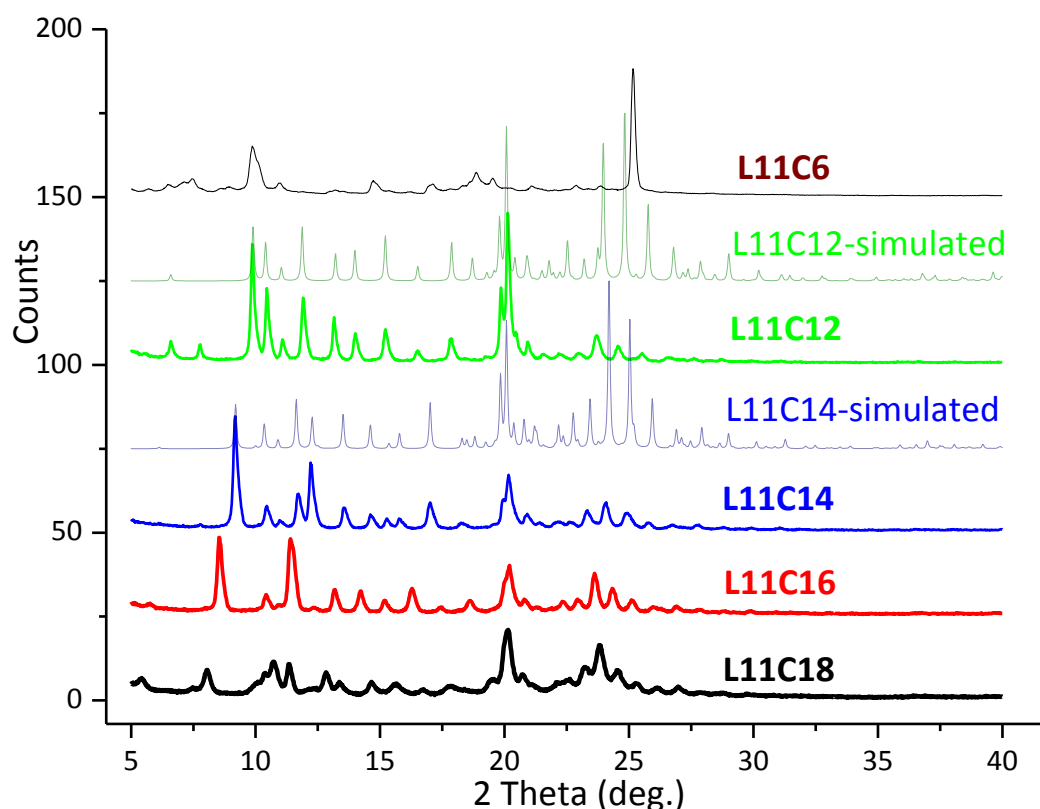


Fig. 3.47. Collected and simulated powder patterns of **L11Cx** ligands

The **L13Cx** series was more crystalline than **L11Cx**, and the powder patterns of all those ligands look similar to each other (Fig. 3.48). Again, the

powder patterns of **L13C12** and **L13C14** agree well with their simulated patterns (Fig. 3.48).

L13Cx

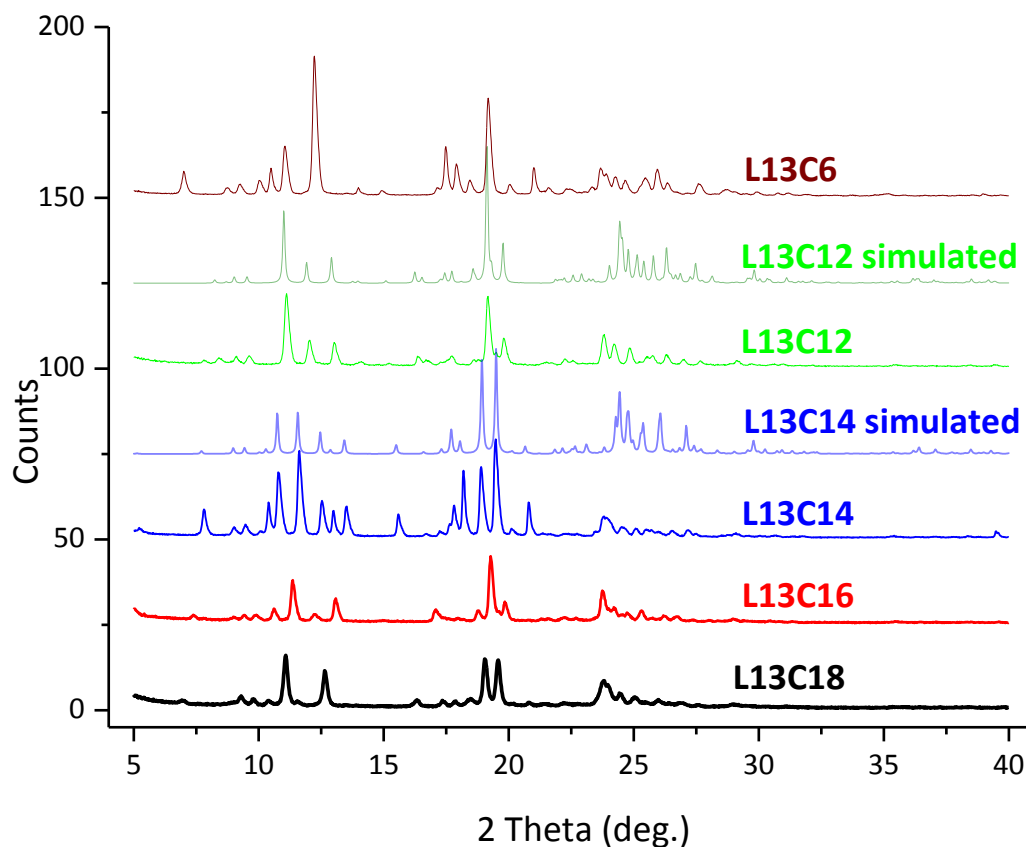


Fig. 3.48. Collected and simulated powder patterns of **L13Cx** ligands

3.9.2 Iron(II) complexes

DSC analyses for the $[\text{Fe}(\text{L11Cx})_2][\text{BF}_4]_2$ and $[\text{Fe}(\text{L13Cx})_2][\text{BF}_4]_2$ iron complex series shown some irreversible changes after heating to temperature between 100°C and 170°C. This effect was studied also by powder diffraction by comparing analyses collected at different temperatures: at room temperature, 100°C, and 170°C. A sample was heated to the corresponding temperature in a vial on an oil bath, kept at this temperature for about a minute, allowed to cool to room temperature, and then immediately measured. The same sample was reheated again, and used for all three measures. Collection of one powder pattern takes about half an hour, which hinder collecting analyses from more temperatures.

$[\text{Fe}(\text{L11Cx})_2][\text{BF}_4]_2$

The simulated powder pattern of $[\text{Fe}(\text{L11C6})_2][\text{BF}_4]_2 \cdot 2\text{H}_2\text{O}$ matches that obtained at room temperature (Fig. 3.49). The sample slightly lost its crystallinity upon heating to 100°C, as the peaks became weaker, while heating to 170°C led to annealing and almost complete loss of crystallinity

(Fig. 4.43). All the other samples in this series - $[\text{Fe}(\text{L11C12})_2][\text{BF}_4]_2 \cdot 0.25\text{Me}_2\text{CO}$, $[\text{Fe}(\text{L11C14})_2][\text{BF}_4]_2$, and $[\text{Fe}(\text{L11C16})_2][\text{BF}_4]_2$ and $[\text{Fe}(\text{L11C18})_2][\text{BF}_4]_2$, behaved similarly: heating to 100°C had almost no effect on their powder patterns, and heating to 170°C caused annealing (Fig. 3.49). The C12, C14 and C16 iron complexes after heating to 170°C underwent annealing with the main peaks remaining visible, while the C6 and C18 ones almost lost their crystallinity.

$[\text{Fe}(\text{L13Cx})_2][\text{BF}_4]_2$

The annealing effect for $[\text{Fe}(\text{L13Cx})_2][\text{BF}_4]_2$ (Fig. 3.50) was not as pronounced as for $[\text{Fe}(\text{L11Cx})_2][\text{BF}_4]_2$ (Fig. 4.43). Also, the powder patterns of $[\text{Fe}(\text{L13Cx})_2][\text{BF}_4]_2$ iron complexes were much less similar to each other, than $[\text{Fe}(\text{L11Cx})_2][\text{BF}_4]_2$ (Fig. 3.49, 3.50, and 3.51), which agrees with the obtained SQUID data, which show much more uniform behaviour for $[\text{Fe}(\text{L11Cx})_2][\text{BF}_4]_2$ (Fig. 3.20, 3.21 and 3.22), than for $[\text{Fe}(\text{L13Cx})_2][\text{BF}_4]_2$ (Fig. 3.23 and 3.24), and with the unit cells of the collected crystal structures (Table 3.3).

Upon heating to 100°C, significant changes were observed only for the **C14** iron complex. These results match its DSC measurements, which show some changes after heating above 70°C (Fig. 3.47). The **C18** iron complex also showed some annealing upon heating to 100°C (Fig. 3.51). This behaviour was not observed in the DSCs of any of the other iron complexes in this chapter. Heating to 170°C caused no significant loss in crystallinity for $[\text{Fe}(\text{L13C6})_2][\text{BF}_4]_2 \cdot \text{H}_2\text{O}$ and DSC of $[\text{Fe}(\text{L13C12})_2][\text{BF}_4]_2$, a strong annealing by DSC of $[\text{Fe}(\text{L13C14})_2][\text{BF}_4]_2 \cdot \text{H}_2\text{O}$ and $[\text{Fe}(\text{L13C18})_2][\text{BF}_4]_2 \cdot 1.4\text{H}_2\text{O}$, and a very strong annealing $[\text{Fe}(\text{L13C16})_2][\text{BF}_4]_2 \cdot 1.6\text{H}_2\text{O}$ (Fig. 3.50), which corresponds with the DSC results for these iron complexes: likely SCO above 180°C which didn't allow us to judge about the reversibility of the changes in $[\text{Fe}(\text{L13C6})_2][\text{BF}_4]_2 \cdot \text{H}_2\text{O}$ after heating (Fig. 3.39), no annealing observed for $[\text{Fe}(\text{L13C12})_2][\text{BF}_4]_2$ (Fig. 3.40), and irreversible changes upon heating for $[\text{Fe}(\text{L13C14})_2][\text{BF}_4]_2 \cdot \text{H}_2\text{O}$, $[\text{Fe}(\text{L13C16})_2][\text{BF}_4]_2 \cdot 1.6\text{H}_2\text{O}$, and $[\text{Fe}(\text{L13C18})_2][\text{BF}_4]_2 \cdot 1.4\text{H}_2\text{O}$ (Fig. 3.47, 3.48, and 3.49 correspondingly).

Even though $[\text{Fe}(\text{L13C6})_2][\text{BF}_4]_2 \cdot \text{H}_2\text{O}$ had low crystallinity, the observed peaks matched its simulated pattern (Fig. 3.50). The powder patterns of $[\text{Fe}(\text{L13C14})_2][\text{BF}_4]_2 \cdot \text{H}_2\text{O}$ don't quite match the pattern simulated from the crystal structure of $[\text{Fe}(\text{L13C14})_2][\text{BF}_4]_2 \cdot 2\text{MeCN}$, which means that the lattice solvent affected the unit cell in this case. For $[\text{Fe}(\text{L13C16})_2][\text{BF}_4]_2 \cdot 1.6\text{H}_2\text{O}$ the obtained powder pattern matched the simulation for $[\text{Fe}(\text{L13C16})_2][\text{BF}_4]_2 \cdot \text{H}_2\text{O}$.

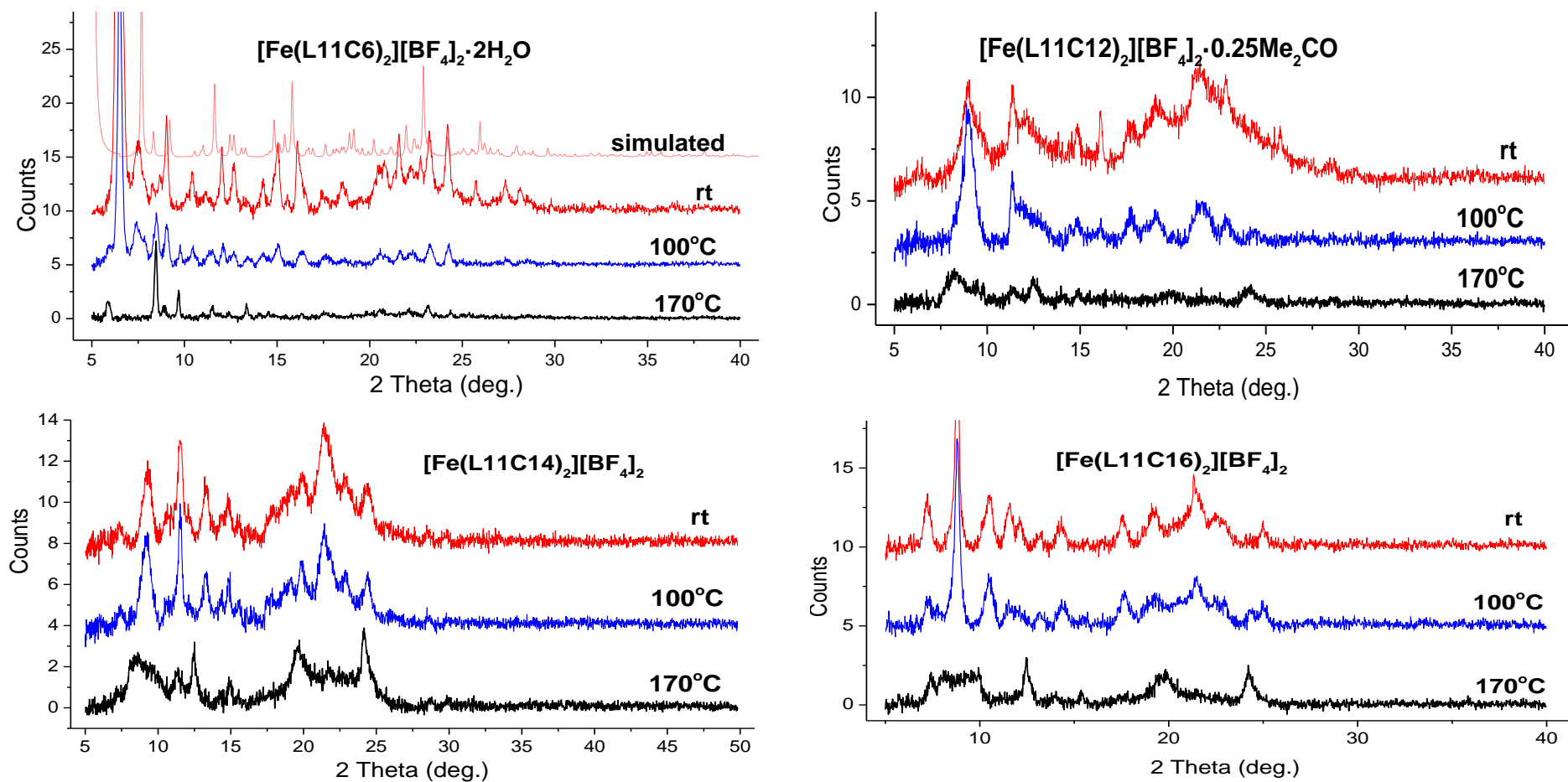


Fig. 3.49. Powder patterns of $[\text{Fe}(\text{L11C6})_2][\text{BF}_4]_2 \cdot 2\text{H}_2\text{O}$, $[\text{Fe}(\text{L11C12})_2][\text{BF}_4]_2 \cdot 0.25\text{Me}_2\text{CO}$, $[\text{Fe}(\text{L11C14})_2][\text{BF}_4]_2$, and $[\text{Fe}(\text{L11C16})_2][\text{BF}_4]_2$, collected at room temperature, 100°C, 170°C, and, where available, simulated powder patterns

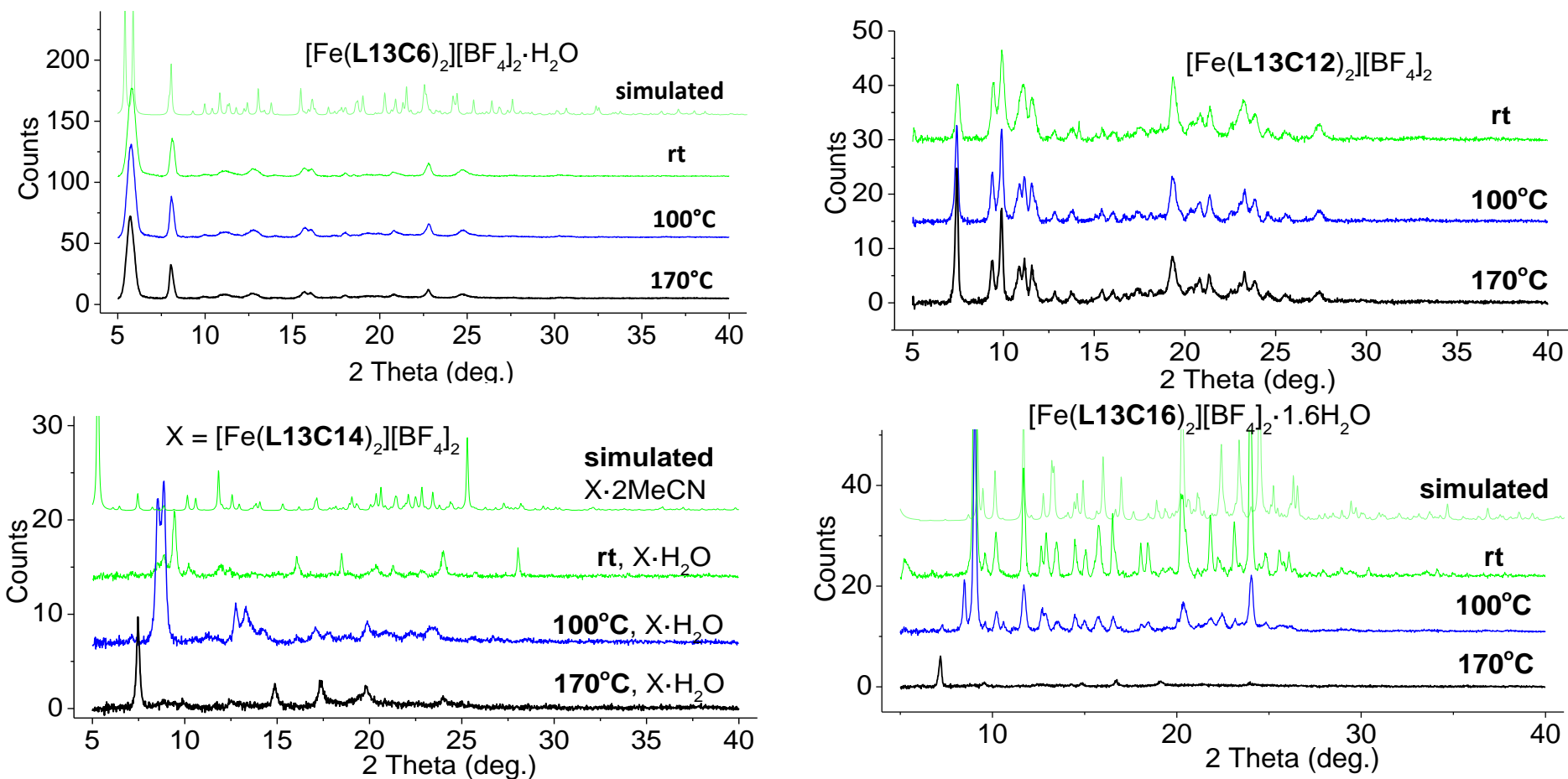


Fig. 3.50. Powder patterns of $[\text{Fe}(\text{L13C6})_2][\text{BF}_4]_2 \cdot \text{H}_2\text{O}$, $[\text{Fe}(\text{L13C12})_2][\text{BF}_4]_2$, $[\text{Fe}(\text{L13C14})_2][\text{BF}_4]_2 \cdot \text{H}_2\text{O}$, and $[\text{Fe}(\text{L13C16})_2][\text{BF}_4]_2 \cdot 1.6\text{H}_2\text{O}$, collected at room temperature, 100°C, 170°C, and, where available, simulated powder patterns

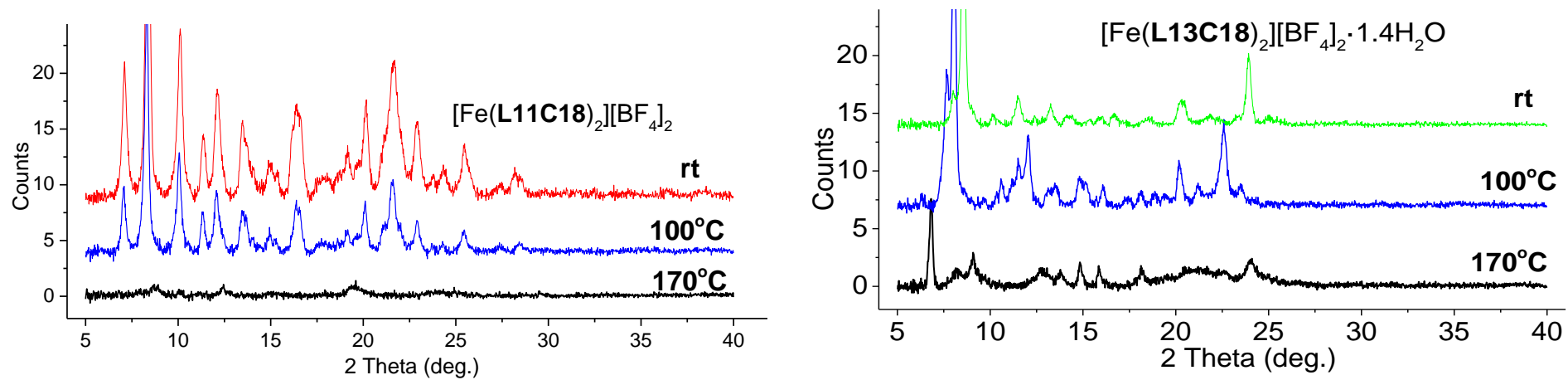


Fig. 3.51. Powder patterns of $[\text{Fe}(\text{L11C18})_2][\text{BF}_4]_2$, and $[\text{Fe}(\text{L13C18})_2][\text{BF}_4]_2 \cdot 1.4\text{H}_2\text{O}$ collected at room temperature, 100°C, and 170°C

3.10 Magnetic properties in solution

Evans method NMR

Magnetic properties in solution were studied by Evans method NMR in MeCN-D₃, and by paramagnetic NMR. Evans method NMR data were collected for one member of each iron complex series: for [Fe(L11C16)₂][BF₄]₂ and [Fe(L13C16)₂][BF₄]₂. Their solubility in MeCN-D₃ was not sufficient, and so the measurements failed due to a low concentration of the long alkyl sample, therefore series of Evans method NMRs were taken in MeCN-D₃:CDCl₃ 1:1 mixture in order to achieve a better solubility of ca 5.2 mg of the iron complex per 5 ml of solvent mixture, and to be able to measure at a high enough temperature below the boiling point. Both iron complexes show similar magnetic behaviour in solution (Fig. 3.52), which shows gradual switching with T_{1/2} at ca 290K for both. That is similar to the Evans method results for the iron complexes in the previous chapter (Chapter 2, Fig. 2.35).

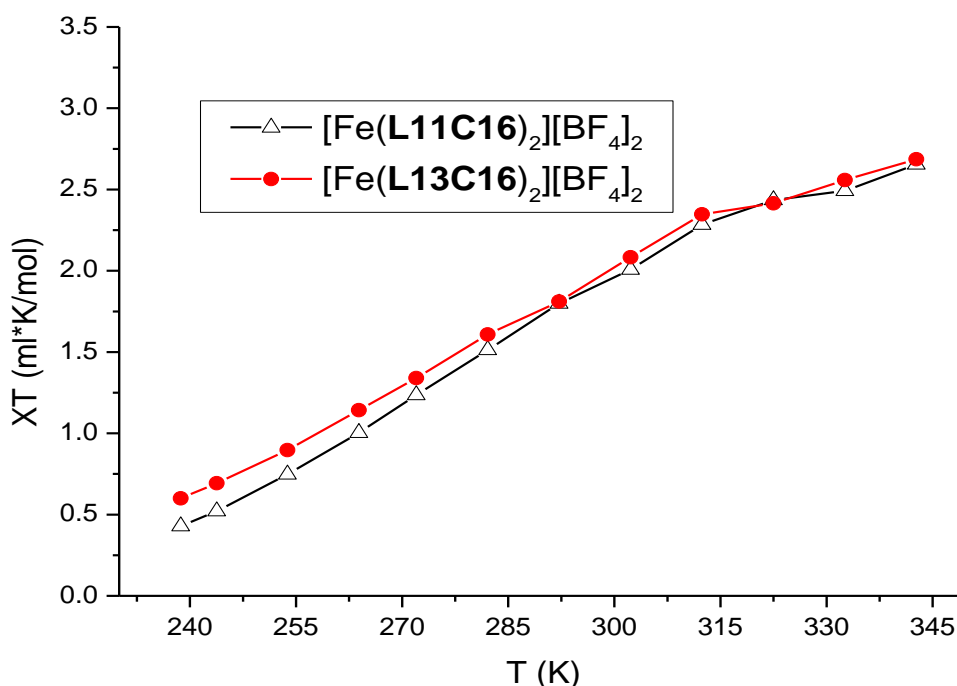


Fig. 3.52. Evans method NMRs of [Fe(L11C16)₂][BF₄]₂ and [Fe(L13C16)₂][BF₄]₂, measured in MeCN-D₃:CDCl₃ 1:1 mixture

Paramagnetic NMR

Paramagnetic NMR spectra of for [Fe(L11Cx)₂][BF₄]₂ all looked very similar. A typical NMR can be seen below (Fig. 3.53). The solubility of [Fe(L11C16)₂][BF₄]₂ in MeCN-D₃ was enough to run paramagnetic NMR, but for Evans method NMR a MeCN-D₃:CDCl₃ 1:1 mixture had to be used in

order to achieve acceptable solubility, as the Evans method NMR run in pure MeCN-D3 has failed. A paramagnetic NMR of $[\text{Fe}(\text{L11C18})_2][\text{BF}_4]_2$ was also measured in CDCl_3 and in this case no paramagnetically shifted peaks were observed.

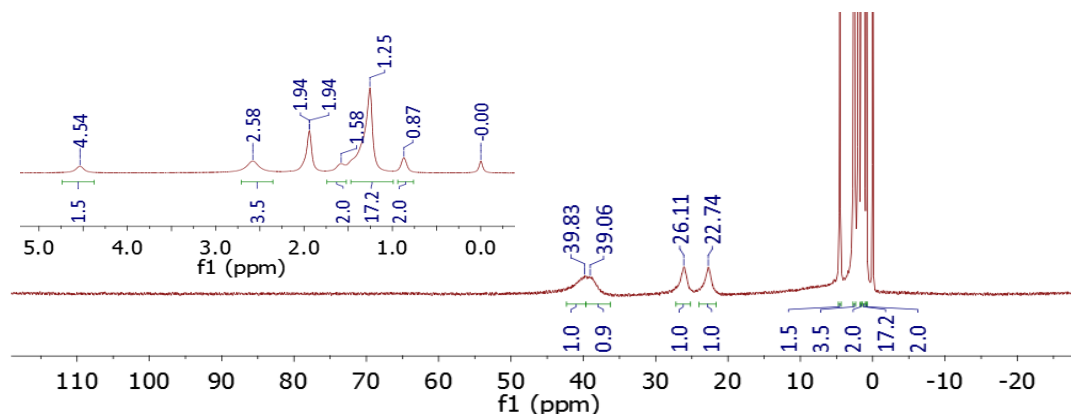


Fig. 3.53. Paramagnetic NMR of $[\text{Fe}(\text{L11C16})_2][\text{BF}_4]_2$, measured in MeCN-D3, typical for $[\text{Fe}(\text{L11Cx})_2][\text{BF}_4]_2$ series

The $[\text{Fe}(\text{L13Cx})_2][\text{BF}_4]_2$ iron complexes were all measured in MeCN-D3, and all their spectra looked almost the same (Fig. 3.54). Two unexpected extra peaks were observed at ca 66.19 and 63.23 ppm for the spectra measured in MeCN-D3, so the iron complexes were re-measured in a 1:1 MeCN-D3: CDCl_3 mixture, which resulted in spectra with no additional peaks. These also all looked almost identical (Fig. 3.55), except for $[\text{Fe}(\text{L13C12})_2][\text{BF}_4]_2$, whose paramagnetically shifted peaks were about 1-2 ppm shifted upfield, comparing to the other $[\text{Fe}(\text{L13Cx})_2][\text{BF}_4]_2$ iron complexes (Fig. 3.56). This difference cannot be corrected by referencing a different peak as a solvent, as each peak is shifted differently. Measurements in pure CDCl_3 were also done for the $[\text{Fe}(\text{L13C12})_2][\text{BF}_4]_2$, $[\text{Fe}(\text{L13C14})_2][\text{BF}_4]_2$, and $[\text{Fe}(\text{L13C18})_2][\text{BF}_4]_2$, and in each case no paramagnetically shifted peaks were observed.

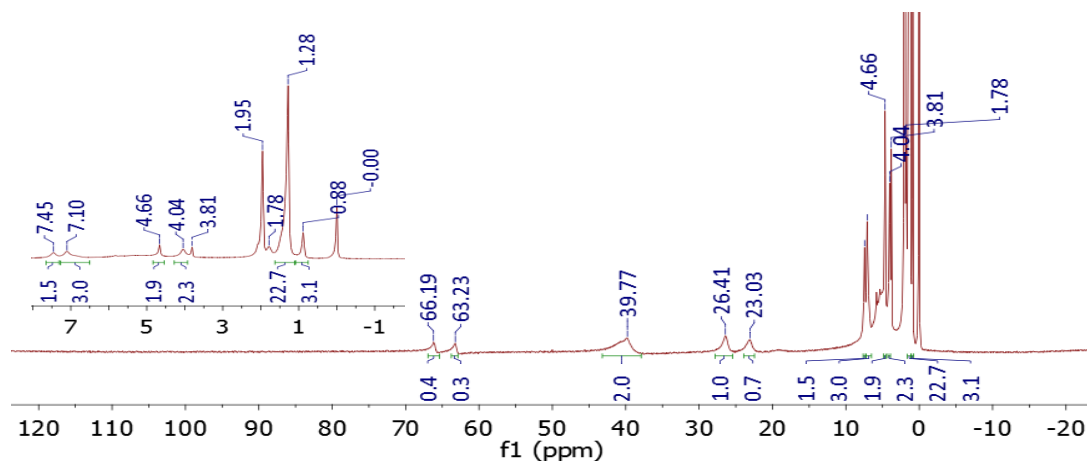


Fig. 3.54. Paramagnetic ^1H NMR of $[\text{Fe}(\text{L13C16})_2][\text{BF}_4]_2$, measured in MeCN-D3, typical for $[\text{Fe}(\text{L11Cx})_2][\text{BF}_4]_2$ series

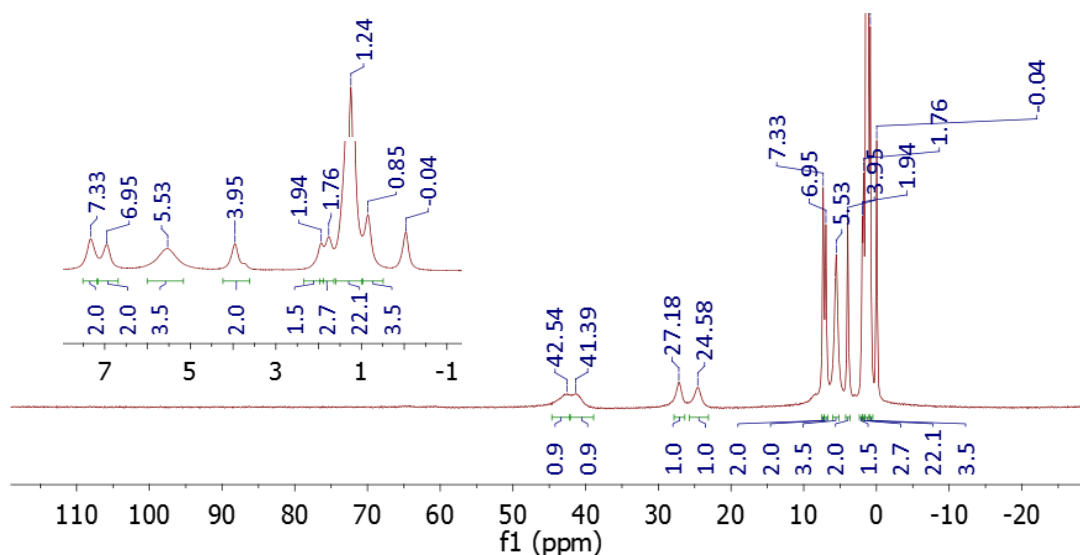


Fig. 3.55 Paramagnetic ^1H NMR of $[\text{Fe}(\text{L13C16})_2][\text{BF}_4]_2$, measured in MeCN-D $_3$:CDCl $_3$ 1:1 mixture, typical for $[\text{Fe}(\text{L13Cx})_2][\text{BF}_4]_2$ series

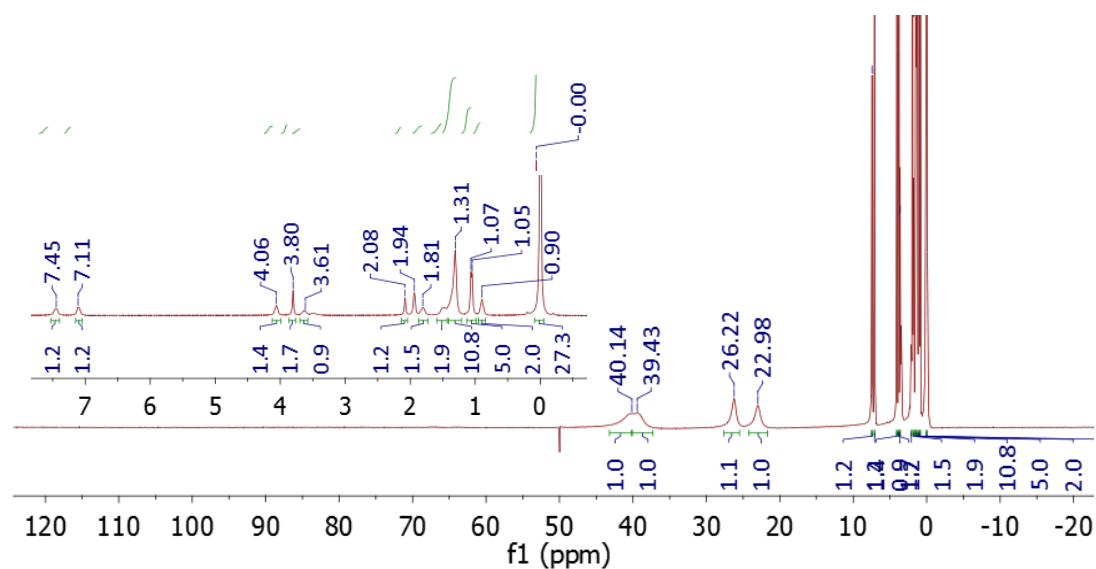


Fig. 3.56. Paramagnetic ^1H NMR of $[\text{Fe}(\text{L13C12})_2][\text{BF}_4]_2$, measured in MeCN-D $_3$:CDCl $_3$ 1:1 mixture

3.11 Conclusions

Two series of 2,6-bis(pyrazol-1-yl)pyridine-4-carboxylate esters with six, twelve, fourteen, sixteen and eighteen carbon chains were obtained, along with some intermediate ligands³. As the long alkyl chain ligands are nonpolar, a non-typical solvent system was used to obtain their iron complexes: a DCE-acetone mixture as a solvent, with pentane as an antisolvent. Despite their being hard to crystallize as single crystals, three crystal structures were collected for the iron complexes of 4-(alkyl)phenyl carboxylates $[\text{Fe}(\text{L13Cx})_2][\text{BF}_4]_2$, and one for the iron complex of alkyl carboxylate $[\text{Fe}(\text{L11C6})_2][\text{BF}_4]_2 \cdot 2\text{H}_2\text{O}$. Crystal structures were also obtained for some intermediate and long alkyl chain ligands.

In solution, judging by Evans method NMR^{4,5}, both series of iron complexes shown typical gradual spin-crossover, similar to the iron complexes of non-long-alkyl-chain 2,6-bis(pyrazol-1-yl)pyridine-4-carboxylate esters from Chapter 2,⁶ with $T_{1/2}$ at ca 290 K. The paramagnetic NMR spectra were almost identical for $[\text{Fe}(\text{L11Cx})_2][\text{BF}_4]_2$ iron complexes, and $[\text{Fe}(\text{L13Cx})_2][\text{BF}_4]_2$ iron complexes, showing four paramagnetically shifted peaks, which means that at 300K a significant fraction of these samples is HS. Based on these data it may be concluded, that the presence of long alkyl chains doesn't affect SCO in solution significantly for bpp esters.

In the solid state all the $[\text{Fe}(\text{L11Cx})_2][\text{BF}_4]_2$ iron complexes began switching to HS above 340°C, sometimes with a small hysteresis. $[\text{Fe}(\text{L13Cx})_2][\text{BF}_4]_2$ remained LS below the instrument's upper limit of 350 K, except for $[\text{Fe}(\text{L13C12})_2][\text{BF}_4]_2$, which shown gradual switching above 225 K. This SCO behaviour is similar to the iron complexes from the Chapter 2, and to other previously reported $[\text{Fe}(\text{bpp})_2]^{2+}$ derivatives with carboxy substituents on the pyridine ring.^{7,8,9} The results of the distortion parameter analysis from the available crystal structures corresponded to the SQUID results. Heating $[\text{Fe}(\text{L11C18})_2][\text{BF}_4]_2$ and $[\text{Fe}(\text{L13C16})_2][\text{BF}_4]_2 \cdot 1.6\text{H}_2\text{O}$ to 170°C caused annealing, with part of the sample becoming trapped in HS. The annealing effect was observed by powder diffraction and DSC, which revealed that annealing happens between 100°C and 170°C. The observed annealing may be explained by change in conformation of the long alkyl chains upon heating, which then freeze back in more disordered orientations, causing the changes to be irreversible. This behaviour is common for organic soft materials, and it is similar to a glass transition.^{10,11}

The $[\text{Fe}(\text{L11Cx})_2][\text{BF}_4]_2$ series was isostructural by powder diffraction, while $[\text{Fe}(\text{L13Cx})_2][\text{BF}_4]_2$ showed different structures and magnetic behaviour. On the DSC graphs SCO peaks, and sometimes lattice solvent loss peaks, were observed for the iron complexes, and only the melting peaks for the ligands. $[\text{Fe}(\text{L11C16})_2][\text{BF}_4]_2$ shown an unexpected doubling of the SCO peak on the cooling cycle. The TGAs showed decomposition after 200°C for **L11Cx**, 300°C for **L13Cx**, and 250°C, with small mass loss for escaping lattice solvent where applicable, for all the iron complexes in this chapter. All the $[\text{Fe}(\text{L13Cx})_2][\text{BF}_4]_2$ iron complexes except $[\text{Fe}(\text{L13C12})_2][\text{BF}_4]_2$ had water as lattice solvent, while all the $[\text{Fe}(\text{L11Cx})_2][\text{BF}_4]_2$ iron complexes, except $[\text{Fe}(\text{L13C6})_2][\text{BF}_4]_2 \cdot \text{H}_2\text{O}$ and $[\text{Fe}(\text{L13C12})_2][\text{BF}_4]_2$, had no lattice solvent. The lattice water can escape at around 340 K.^{12,13,14,15} Each of the iron complexes in this chapter was heated from room temperature to 170°C, and their photographs were taken every 20°C, which showed no mesophase formation or melting for any of them, only the colour change from red to orange due to spin crossover. Loss of crystallinity and changes in spin behaviour on heating, which is not related to melting or mesophase formation, has been reported previously.¹⁶⁻²²

List of References

1. Vermonden, T.; Branowska, D.; Marcelis, A.T.M.; Sudhölter, E.J.R. Synthesis of 4-functionalized terdentate pyridine-based ligands. *Tetrahedron*. **2003**, *59*, 5039–5045.
2. Borisov, A. V.; Korel'chuk, M. V.; Ageeva, E. S.; Galanin, N. E. and Shaposhnikov, G. P. Synthesis and spectral properties of lutetium complexes with unsymmetrical phthalocyanines and sandwich complexes based thereon containing tetraanthraquinonoporphyrine fragments. *Russ. J. Org. Chem.* **2014**, *50*, 986-992.
3. Galadzhun, I.; Kulmaczewski, R.; Cespedes, O.; Yamada, M.; Yoshinari, N.; Konno, T. and Halcrow, M.A. 2,6-Bis(pyrazol-1-yl)pyridine-4-carboxylate Esters with Alkyl Chain Substituents and Their Iron(II) Complexes. *Inorg. Chem.* **2018**, *57* (21), 13761-13771.
4. Evans, D. F. The Determination of the Paramagnetic Susceptibility of Substances in Solution by Nuclear Magnetic Resonance. *J. Chem. Soc.* **1959**, 2003–2005.
5. Schubert, E. M. Utilizing the Evans Method with a Superconducting NMR Spectrometer in the Undergraduate Laboratory. *J. Chem. Educ.* **1992**, *69*, 62.
6. Galadzhun, I.; Kulmaczewski, R. and Halcrow, M.A. Five 2,6-Di(pyrazol-1-yl)pyridine-4-carboxylate Esters, and the Spin States of their Iron(II) Complexes. *Magnetochem.* **2019**, *5*, 9.
7. Abhervé, A.; Clemente-León, M.; Coronado, E.; Gómez-García, C. J.; López-Jordà, M. A Spin-Crossover Complex Based on a 2,6-Bis(pyrazol-1-yl)pyridine (1-bpp) Ligand Functionalized with a Carboxylate Group. *Dalton Trans.* **2014**, *43*, 9406–9409.
8. Kershaw Cook, L. J.; Kulmaczewski, R.; Mohammed, R.; Dudley, S.; Barrett, S. A.; Little, M. A.; Deeth, R. J.; Halcrow, M. A. A Unified Treatment of the Relationship Between Ligand Substituents and Spin State in a Family of Iron(II) Complexes. *Angew. Chem. Int. Ed.* **2016**, *55*, 4327–4331.
9. Bridonneau, N.; Rigamonti, L.; Poneti, G.; Pinkowicz, D.; Forni, A.; Cornia, A. Evidence of Crystal Packing Effects in Stabilizing High or

- Low Spin States of Iron(II) Complexes with Functionalized 2,6-Bis(pyrazol-1-yl)pyridine Ligands. *Dalton Trans.* **2017**, *46*, 4075–4085.
10. McKenna, G. B.; Simon, S. L. Challenges in the Dynamics and Kinetics of Glass-Forming Polymers. *Macromolecules.* **2017**, *50*, 6333 – 6361.
 11. Zhang, W.; Zhao, F.; Liu, T.; Yuan, M.; Wang, Z.-M.; Gao, S. Spin Crossover in a Series of Iron(II) Complexes of 2-(2-Alkyl-2*H*-tetrazol-5-yl)-1,10-phenanthroline: Effects of Alkyl Side Chain, Solvent, and Anion. *Inorg. Chem.* **2007**, *46*, 2541–2555.
 12. Seredyuk, M.; Gaspar, A. B.; Ksenofontov, V.; Galyametdinov, Y.; Kusz, J.; Gütllich, P. Does the Solid-Liquid Crystal Phase Transition Provoke the Spin-State Change in Spin-Crossover Metallomesogens? *J. Am. Chem. Soc.* **2008**, *130*, 1431–1439.
 13. Sugiyarto, K. H.; Weitzner, K.; Craig, D. C.; Goodwin, H. A. Structural, Magnetic and Mössbauer Studies of Bis(2,6-bis(pyrazol-3-yl)pyridine)iron(II) Triflate and its Hydrates. *Aust. J. Chem.* **1997**, *50*, 869–873.
 14. Clemente-León, M.; Coronado, E.; Giménez-López, M. C.; Romero, F. M.; Asthana, S.; Desplanches, C.; Létard, J.-F. Structural, Thermal and Photomagnetic Properties of Spin Crossover $[\text{Fe}(\text{bpp})_2]^{2+}$ Salts Bearing $[\text{Cr}(\text{L})(\text{ox})_2]^-$ Anions. *Dalton Trans.* **2009**, 8087–8095.
 15. Bushuev, M. B.; Daletsky, V. A.; Pishchur, D. P.; Gatilov, Y. V.; Korolkov, I. V.; Nikolaenkova, E. B.; Krivopalov, V. P. Unprecedented Bistability Domain and Interplay Between Spin Crossover and Polymorphism in a Mononuclear Iron(II) Complex. *Dalton Trans.* **2014**, *43*, 3906–3910.
 16. Seredyuk, M.; Gaspar, A. B.; Ksenofontov, V.; Galyametdinov, Y.; Kusz, J.; Gütllich, P. Does the Solid-Liquid Crystal Phase Transition Provoke the Spin-State Change in Spin-Crossover Metallomesogens? *J. Am. Chem. Soc.* **2008**, *130*, 1431–1439.
 17. Seredyuk, M.; Gaspar, A. B.; Ksenofontov, V.; Galyametdinov, Y.; Kusz, J.; Gütllich, P. Iron(II) Metallomesogens Exhibiting Coupled Spin

- State and Liquid Crystal Phase Transitions near Room Temperature. *Adv. Funct. Mater.* **2008**, *18*, 2089–2101.
18. Seredyuk, M.; Muñoz, M. C.; Ksenofontov, V.; Gütllich, P.; Galyametdinov, Y.; Real, J. A. Spin Crossover Star-Shaped Metallomesogens of Iron(II). *Inorg. Chem.* **2014**, *53*, 8442–8454.
 19. Hayami, S.; Moriyama, R.; Shuto, A.; Maeda, Y.; Ohta, K.; Inoue, K. Spin Transition at the Mesophase Transition Temperature in a Cobalt(II) Compound with Branched Alkyl Chains. *Inorg. Chem.* **2007**, *46*, 7692–7694.
 20. Lee, Y. H.; Ohta, A.; Yamamoto, Y.; Komatsu, Y.; Kato, K.; Shimizu, T.; Shinoda, H.; Hayami, S. Iron(II) Spin Crossover Complexes with Branched Long Alkyl Chain. *Polyhedron.* **2011**, *30*, 3001–3005.
 21. Fujigaya, T.; Jiang, D.-L.; Aida, T. Switching of Spin States Triggered by a Phase Transition: Spin-Crossover Properties of Self-Assembled Iron(II) Complexes with Alkyl-Tethered Triazole Ligands. *J. Am. Chem. Soc.* **2003**, *125*, 14690–14691.
 22. Romero-Morcillo, T.; Seredyuk, M.; Muñoz, M. C.; Real, J. A. Meltable Spin Transition Molecular Materials with Tunable T_c and Hysteresis Loop Width. *Angew. Chem. Int. Ed.* **2015**, *54*, 14777–14781.

Chapter 4

Pyrazole-substituted bis(pyrazol-1-yl)pyridine derivatives

with long alkyl chains, and their iron(II) complexes

4.1 Introduction

In this chapter 1,4-bis[2,6-di(1H-pyrazole-1'-yl)pyridine derivatives with long alkyl chains at the 4-pyrazolyl position were obtained and studied, along with their iron(II) complexes. During these syntheses some intermediate ligands were obtained, and their iron(II) complexes with no long alkyl chains were also prepared and studied in cases when they were new (Fig. 4.1).

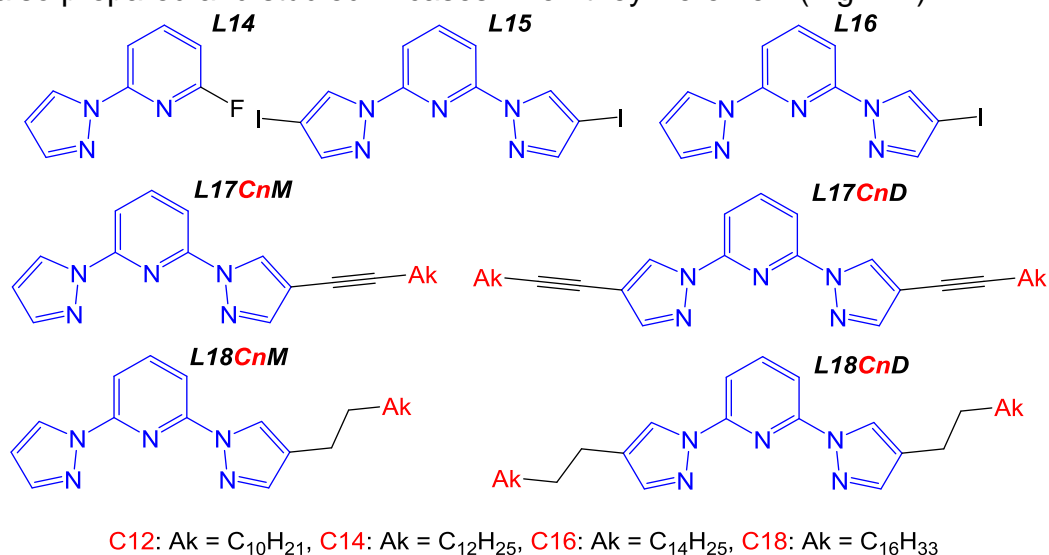


Fig. 4.1 The list of ligands discussed in Chapter 4

4.2 Ligands synthesis

4.2.1 L14, L15, L16 – the precursors

In order to obtain pyrazole-substituted bpps with long alkyl chains, first mono- and di- iodo bpps substituted at the pyrazolyl C4 position were obtained in large quantities, at about a 10 g scale. The di-iodo bpp **L15** was obtained in a single step (Fig. 4.2). This ligand has been reported before,¹ while the mono-iodo bpp **L16** is a novel compound. The **L16** synthesis required a two-step procedure with a column chromatography separation (Fig. 4.3, 4.4). The intermediate ligand in the **L16** synthesis, 2-fluoro-6-(1H-pyrazol-1-yl)pyridine **L14** (Fig. 4.3) was used also in other syntheses of various asymmetric ligands, which are discussed in Chapter 5. **L14**, besides being analysed by ¹H NMR and ¹³C NMR like all the other ligands, was also studied by ¹⁹F NMR, and this spectrum had only one peak as expected, at -68.27 ppm (Fig. 4.6). The ¹³C NMR of **L14** has an interesting feature – the peaks from certain carbon atoms are doubled, due to coupling with the fluorine atom (Fig. 4.5). More details on the assignment of these peaks may be found in Chapter 6.4.1.

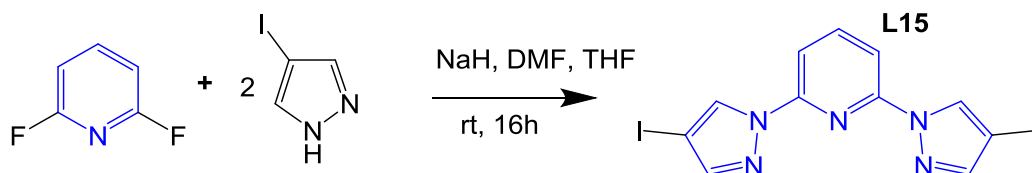


Fig. 4.2 Synthesis of 2,6-bis(4-iodo-1H-pyrazol-1-yl)pyridine **L15**

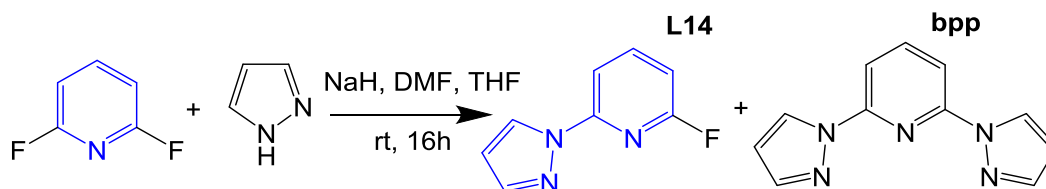


Fig. 4.3 Synthesis of 2-fluoro-6-(1H-pyrazol-1-yl)pyridine **L14**

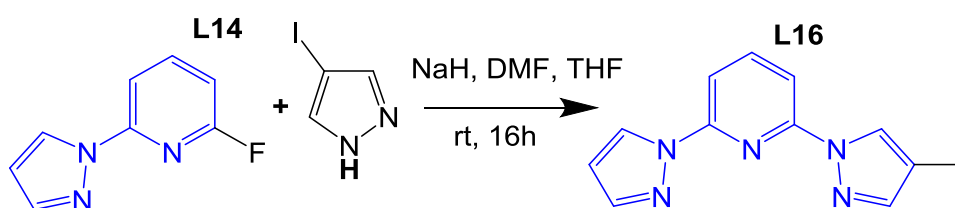


Fig. 4.4 Synthesis of 2-(3-iodo-1H-pyrazol-1-yl)-6-(1H-pyrazol-1-yl)pyridine **L16**

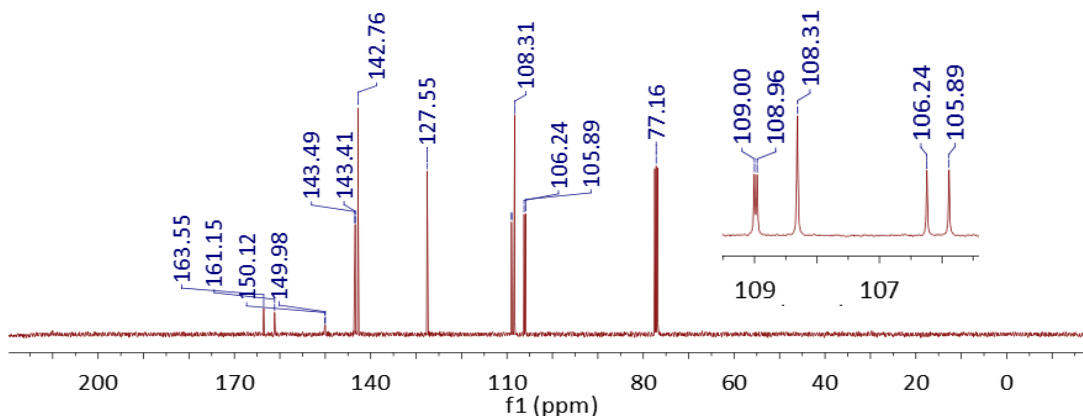


Fig. 4.5 ¹³C NMR of **L14** 2-fluoro-6-(1H-pyrazol-1-yl)pyridine, measured in CDCl₃, showing doubling of certain peaks

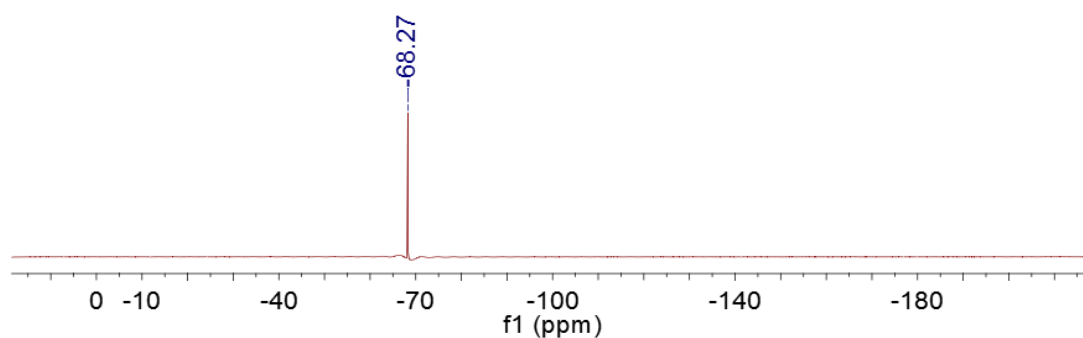


Fig. 4.6 ¹⁹F NMR of **L14** 2-fluoro-6-(1H-pyrazol-1-yl)pyridine, measured in CDCl₃

4.2.2 L17CxM – unsaturated mono-substituted ligands

2-(4-Alk-1-yn-1-yl-1H-pyrazol-1-yl)-6-(1H-pyrazol-1-yl)pyridines **L17CxM** were obtained using a procedure described in the literature² with some modifications (Fig. 4.7). The alkyne was added to the degassed reaction mixture, and the reaction was carried out under nitrogen at 80°C with monitoring by TLC, and took ca 2 days to complete. The initial purification was done by filtering the reaction mixture, as the palladium and copper catalysts are mostly insoluble in dioxane. The trimethylamine and excess alkyne were mostly removed under vacuum, together with the solvent. Recrystallization from boiling MeCN in all four cases afforded clean products, with yields 34-48%.

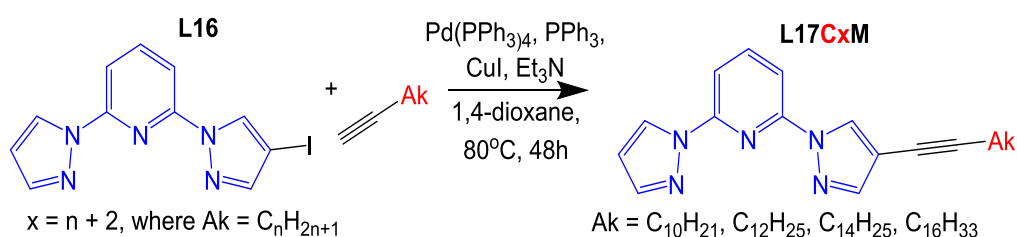


Fig. 4.7 Synthesis of **L17CxM** ligands

The ¹H NMR spectra of **L17CxM** ligands looked almost identical, and differed only in the integration of the 1.26 ppm peak (Fig. 4.8). The closely spaced peaks at 7.75 – 7.92 ppm were assigned using COSY NMR and NMRDB⁴ spectra simulation - see Chapter 6.4 for the assignment of each NMR peak. The ¹³C NMR spectra also looked almost identical, and for each ligand in this series there were twelve alkyne chain carbon NMR peaks present. For ligands with alkyne chains, longer than twelve carbon atoms, no additional peaks were observed. Instead the intensity of the peak at ca 29.8 ppm would increase, due to overlapping of the signals (Fig. 4.9). The carbon NMR peaks were assigned using HMQC NMR, except for the alkyne chain C5 – Cn-1 carbons, which were coupling with to same 1.26 ppm ¹H NMR peak. Therefore these seven signals were reported with no assignment to specific carbon atoms.

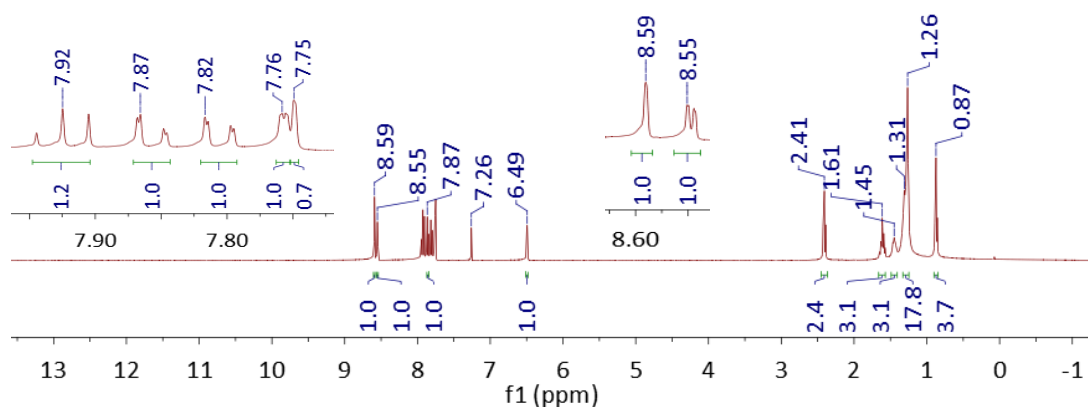


Fig. 4.8 ^1H NMR of **L17C14M** with expansion, measured in CDCl_3 , typical for **L17CxM** ligands series

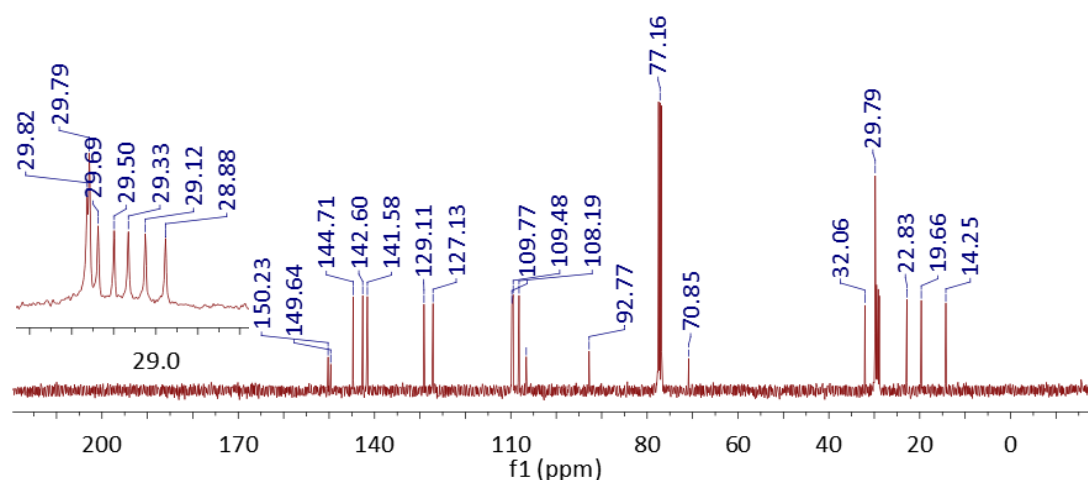


Fig. 4.9 ^{13}C NMR of **L17C14M** with expansion, measured in CDCl_3 , typical for **L17CxM** ligand series

4.2.3 L17Cx_D – unsaturated di-substituted ligands

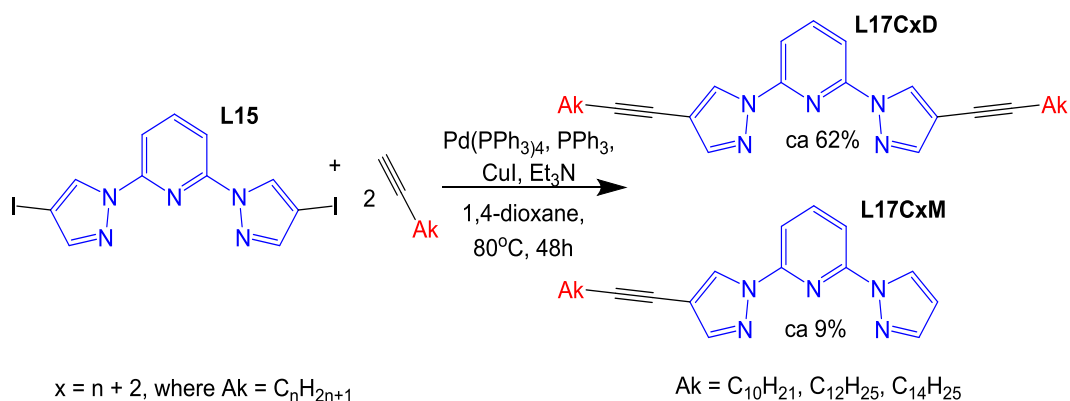


Fig. 4.10 Synthesis of **L17Cx_D** ligands

The **L17Cx_D** ligands were obtained using the same procedure as mentioned above for **L17CxM**. For the **L17C12D** synthesis the product mixture had to be separated by column chromatography and as well as the target disubstituted product at 62% yield, the monosubstituted product was also separated. About 9% of the starting material **L15** was converted into the

monosubstituted product. The starting material **L15** was proven to be clean by ^1H (Fig. 4.11) and ^{13}C NMR, and MS (Chapter 6.4). Therefore there must have been a side reaction, which caused substitution of one iodine by hydrogen (Fig. 4.10). The orange particles of the palladium catalyst passed through the column in small quantities and contaminated both the mono- and disubstituted fractions, which were additionally purified by recrystallization from ethyl acetate, so clean white crystalline powders of **L17C12D** and **L17C12M** were obtained. The consecutive ligands, **L17C14D** and **L17C16D**, were purified by multiple recrystallizations from ethyl acetate, which yielded clean white crystalline powders.

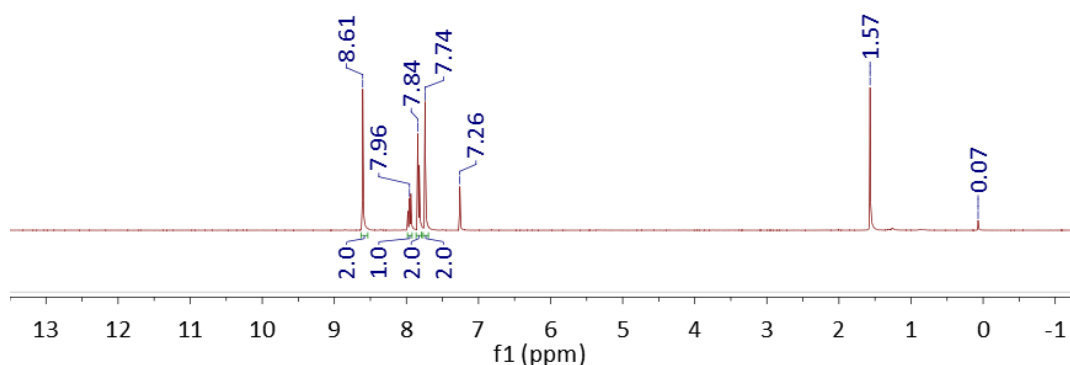


Fig. 4.11 ^1H NMR of **L15**, measured in CDCl_3

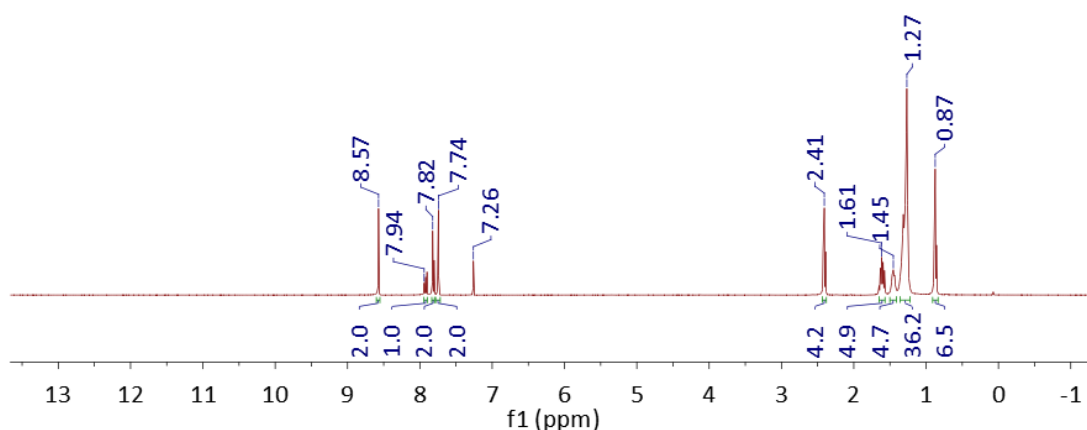


Fig. 4.12 ^1H NMR of **L17C14D** in CDCl_3 , typical for **L17CxD** ligand series

^1H NMR spectra of all three **L17CxD** ligands looked almost identical, and differ in the integration of the 1.27 ppm peak. The alkyne peaks appeared to have integrations slightly higher than expected, which is to be expected for taller peaks (Fig. 4.12). ^{13}C NMR **L17CxD** ligands also looked almost identical, and similarly as for the **L17CxM** series, since only twelve alkyne chain carbon peaks were observed for each ligand. With the increase of the alkyne chain length beyond twelve carbons, the peaks from the additional carbon atoms overlapped, so the peak at ca 29.8 ppm would increase for the longer-chained ligands (Fig. 4.13).

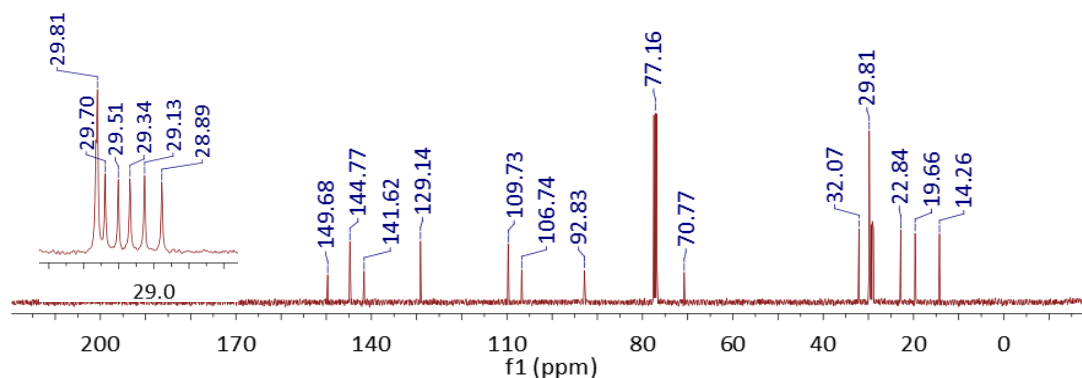


Fig. 4.13 ^{13}C NMR of **L17C14D** with expansion, measured in CDCl_3 , typical for **L17CxM** ligand series

4.2.4 L18CxM – saturated mono-substituted ligands

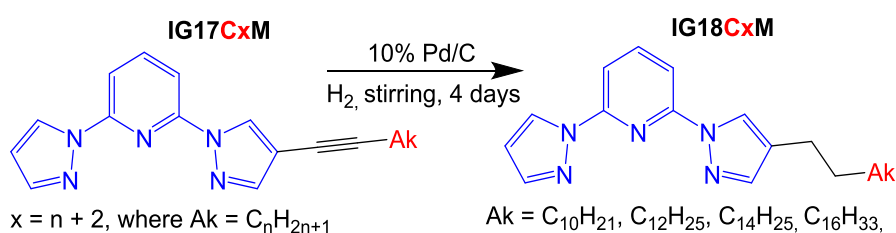


Fig. 4.14 Synthesis of **L18CxM** ligands

2-(4-Alk-1H-pyrazol-1-yl)-6-(1H-pyrazol-1-yl)pyridines **L18CxM** were obtained using a procedure described in the literature² with some modifications (Fig. 4.14) - see Chapter 6.4.5 for the full procedure, which gave the target products at 91 – 94% yields.

^1H and ^{13}C NMR spectra of all four **L18CxM** ligands looked identical. ^1H NMR spectra of **L18CxM** (Fig. 4.15) looked similar to the unsaturated ligands **L17CxM** (Fig. 4.7). The most affected by the saturation are the PzA hydrogen atoms. The signals from the alkyne chain Ak H3, H4, and H5 next to the triple bond hydrogens closely match alkyl chain Ak H1, H2, and H3 signals next to the pyrazole ring. The rest of the peaks were not significantly affected by the saturation. Although there is a 8.59 ppm peak present in both cases, it belongs to different hydrogen atoms and has different multiplicity (Table 4.1). The Py H3 and H5 signals are doublets of doublets, because in the aromatic system they couple not only with the immediate neighbour Py H4, but also with each other (Table 4.1). Some ambiguity remained about the Py H3 and H5 peaks, which were assigned using online NMR simulation NMRDB.³

Table 4.1 ^1H NMR spectra comparison for **L17C14M** and **L18C14M**

Assignment	L17C14M		L18C14M		Diff.
PzA H5	8.59	s	8.32	s	-0.27
PzB H5	8.55	dd	8.59	d	0.04
Py H4	7.92	t	7.90	t	-0.02
Py H3	7.87	dd	7.80	dd	-0.07
Py H5	7.82	dd	7.82	d	0
PzB H3	7.76	d	7.76	d	0
PzA H3	7.75	s	7.59	s	-0.16
PzB H4	6.49	dd	6.49	dd	0
Ak H3/ H1	2.41	t	2.55	t	0.14
Ak H4/ H2	1.61	p	1.64	p	0.03
Ak H5/ H3	1.45	p	1.35	h	-0.10
Ak H6-13/4-13	1.26	s	1.26	s	0
Ak H14	0.87	t	0.88	t	0.01

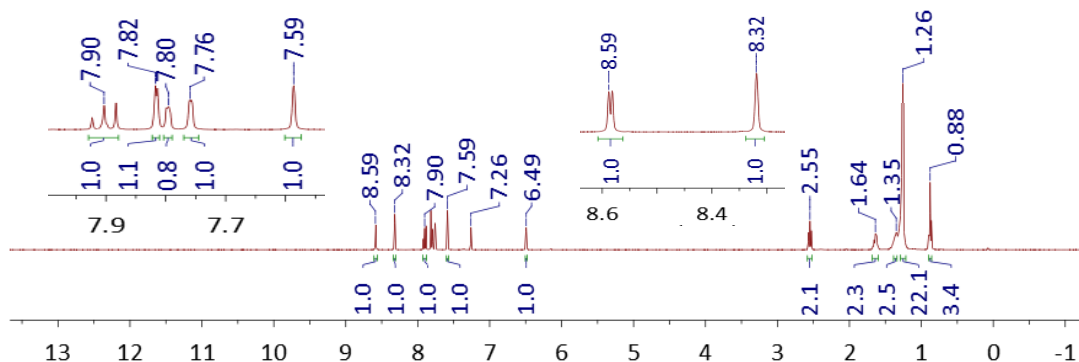
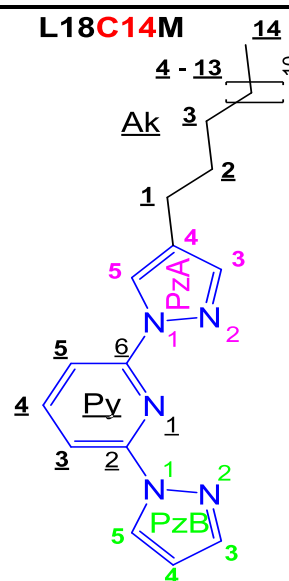


Fig. 4.15 ^1H NMR of **L18C14M** with expansions, measured in CDCl_3 , typical for **L18CxM** series

^{13}C NMR spectra of **L18CxM** (Fig. 4.16) were assigned using HMQC NMR. The assignments of the pairs of similar ^{13}C environments Py C3, Py C5, and Py C2, Py C6, were done by the best judgement from the mainly overlapping HMQC spots, as the NMRDB simulation was unable to distinguish them.

It can be seen from comparison of ^{13}C NMR spectra of the unsaturated **L17C14** and saturated **L18C14** ligands, that most affected by the saturation of the triple bond were the Ak C1, C2, and C3 atoms, and the neighbouring PzA C4. The other two carbons on the PzA ring, Pz C3 and C5 were also affected, while all the other atoms had almost the same chemical shifts for both structures (Table 4.2, and see Table 4.1 for the labelling scheme). On the ^{13}C NMR of the **L18CxM** series there were 10 alkyl chain peaks observed for each ligand, and the signals from the carbon atoms above this number were overlapping with each other at ca 29.8 ppm, increasing the intensity of that peak (Fig. 4.16). For the unsaturated ligands this

overlapping of the peaks occurred after 12 carbons in the alkyne chain (Fig. 4.9).

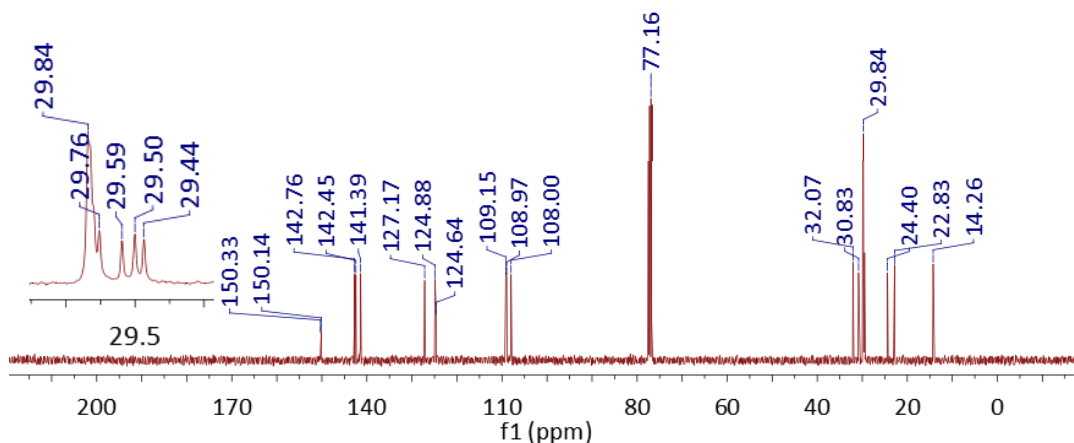


Fig. 4.16 ^{13}C NMR of **L18C14M** with expansion, measured in CDCl_3 , typical for **L18CxM** series

Table 4.2 ^{13}C NMR spectra comparison for **L17C14M** and **L18C14M**

Assign.	L17C14M	L18C14M	Diff.	Assign.	L17C14M	L18C14M	Diff.
Py C2	150.23	150.33	0.1	PzB C4	108.19	108.00	-0.19
Py C6	149.64	150.14	0.5	Ak C1	106.60	24.4	-82.2
PzA C3	144.71	142.76	-1.95	Ak C2	92.77	30.83	-61.94
PzB C3	142.6	142.45	-0.15	PzA C4	70.85	124.64	53.79
Py C4	141.58	141.39	-0.19	Ak C4	28.88	n/a	n/a
PzA C5	129.11	124.88	-4.23	Ak C3	19.66	29.5	9.84
PzB C5	127.13	127.17	0.04	Ak C5-13	7 pks	5 pks	n/a
Py C3	109.77	109.15	-0.62	Ak C14	14.25	14.26	0.01
Py C5	109.48	108.97	-0.51				

4.2.5 L18Cx_D – saturated di-substituted ligands

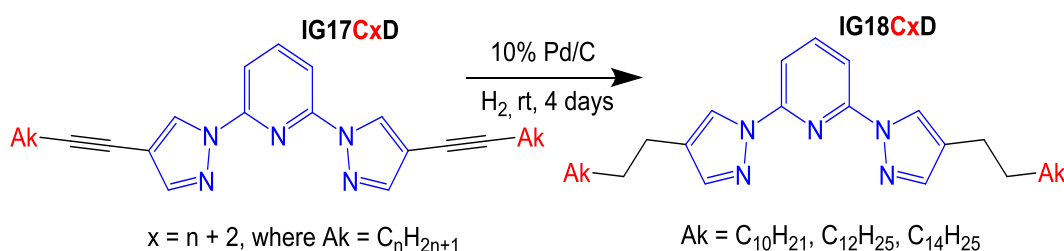


Fig. 4.18 Synthesis of **L18Cx_D** ligands

2-(4-Alk-1H-pyrazol-1-yl)-6-(1H-pyrazol-1-yl)pyridines **L18Cx_D** were obtained using the same procedure as for **L18Cx_M** ligands (Fig. 4.18), which resulted in lower yields than for **L18Cx_M** series: 61 – 91%. The disubstituted ligands **L18Cx_D** are more lipophilic than the monosubstituted **L18Cx_M**,

therefore less soluble in ethyl acetate, which makes them harder to separate from the catalyst, which resulted in lower yields.

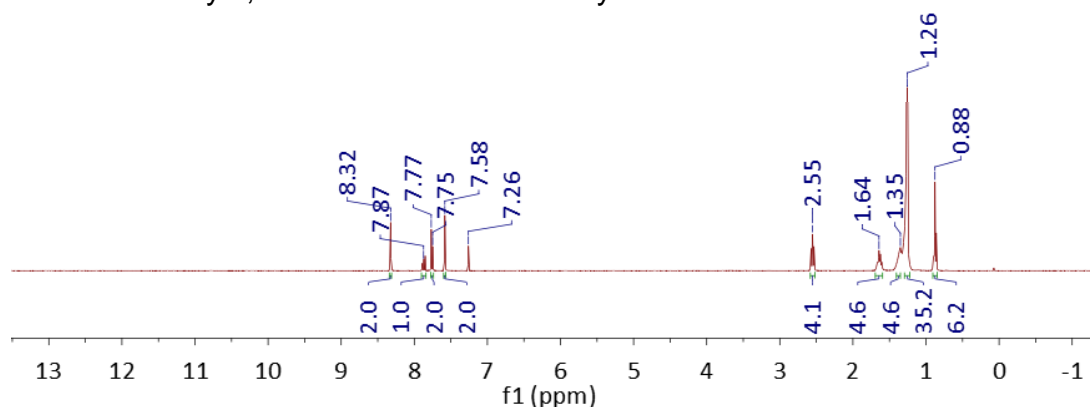


Fig. 4.19 ^1H NMR of **L18C14D** with expansions, measured in CDCl_3 , typical for **L18CxD** series

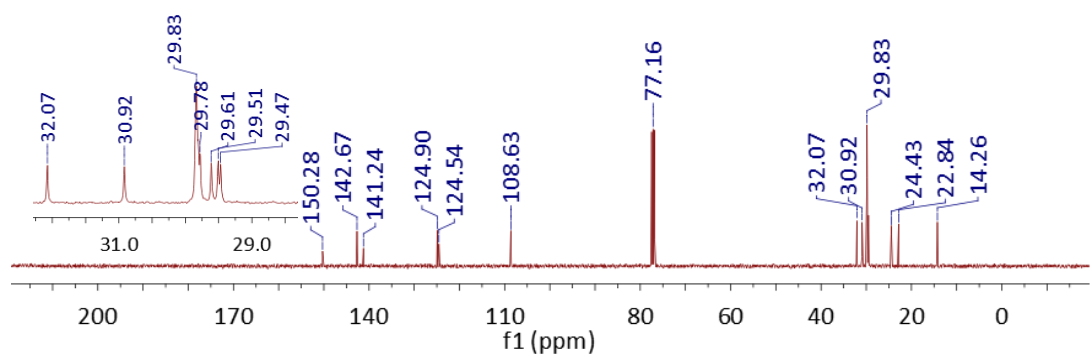


Fig. 4.20 ^{13}C NMR of **L18C14D** with expansion, measured in CDCl_3 , typical for **L18CxD** series

As for the previous ligand series, the ^1H and ^{13}C NMR spectra of the **L18CxM** ligands look almost identical. The ^1H NMR spectrum (Fig. 4.19) was assigned using COSY NMR. Each ^{13}C NMR in **L18CxD** series has 11 alkyl carbon peaks, and the signals from the rest of the alkyl carbons overlapped with each other, which made the peak at ca 29.8 ppm significantly taller (Fig. 4.20).

4.3 Iron(II) complex synthesis

Iron(II) complexes were obtained for all the ligands in this chapter, except for **L14**, which is not likely to form a SCO iron complex, and **L15**, whose iron complex has already been reported.¹

The iron complex of **L16** was obtained by dissolving both the ligand and the iron salt in MeCN, and using $i\text{Pr}_2\text{O}$ as antisolvent. For the unsaturated ligands **L17CxM** and **L17CxD**, DCM was used to dissolve the ligand and the iron salt, with $i\text{Pr}_2\text{O}$ as an antisolvent, and for the saturated ligands **L18CxM** and **L18CxD**, dichloroethane DCE was used to dissolve the ligand, acetone

was used to dissolve $\text{Fe}[\text{BF}_4]_2$, with pentane as an antisolvent (Fig. 4.21). Different solvent systems were used for different series, because the ligands had different solubilities, and it was hard to tune the system to give crystalline iron complex samples. Most of the obtained iron complexes were yellow plate microcrystals, with only $[\text{Fe}(\text{L16})_2][\text{BF}_4]$, $[\text{Fe}(\text{L17C12M})_2][\text{BF}_4]_2$, $[\text{Fe}(\text{L17C14M})_2][\text{BF}_4]_2$, $[\text{Fe}(\text{L17C16D})_2][\text{BF}_4]_2$ having a darker brown-orange colouration, which suggest that most of the iron complexes of pyrazole-substituted bpp in solid state are HS at room temperature.

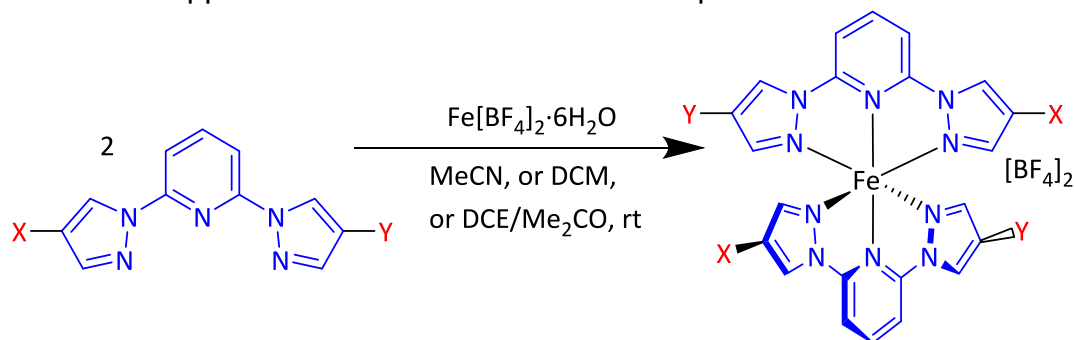


Fig. 4.21 General scheme for obtaining iron(II) complexes in Chapter 4

4.4 XRD Crystal Structures

4.4.1 Ligand crystal structures

Precursor ligands: L14, L15, L16

Crystal structures were collected for all three precursor ligands: **L14**, **L15**, and **L16**. **L14** initially was obtained by column chromatography as a clear oil, but after ca a week it started crystallization, and soon most of the sample transformed into large transparent prismatic crystals. **L15** readily formed transparent needle crystals, while for **L16** it was hard to obtain diffraction-quality crystals, so its XRD structure was collected at the Diamond Light Source.

L15 forms double layers of ligand molecules, with aromatic rings facing each other, and I atoms pointing out, with a quite long distance between iodine atoms i.e. between the two bilayers (Fig. 4.23). The molecules in the horizontal rows, adjacent to each other from the pyrazole rings, are not in one plane, and face each other at ca 90° angle, forming wedge-like grooves. The packing of **L16** is similar to the one of **L15**, but the bilayers are located closer together, because this time there is only one iodine atom per ligand molecule, so they can fit into the empty space, without repulsion by other iodine atoms (Fig. 4.24). **L14** molecules are arranged in the lattice even more closely together than **L16**. The **L14** packing consists of pairs of

molecules, facing each other with the pyridyl nitrogen and fluorine atom (Fig. 4.22), and these two molecules are in two planes, tilted at 67.5° angle relative each other. There were no hydrogen bonding or π - π interactions found in any of these three structures.

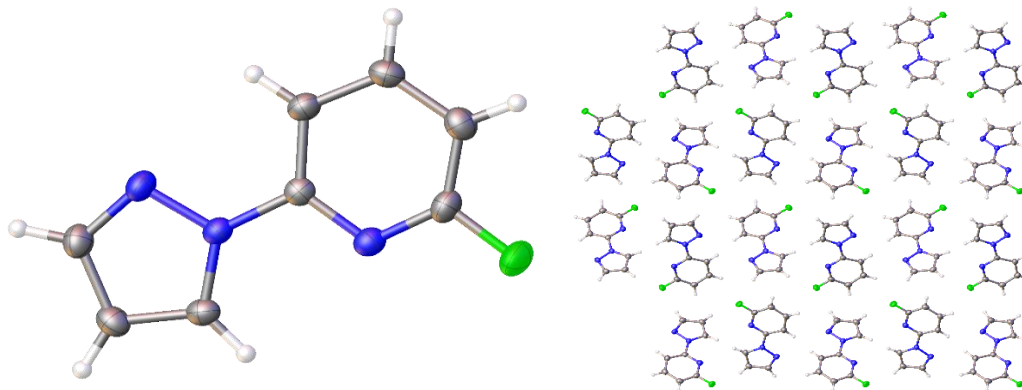


Fig. 4.22 Crystal structure of **L14** and its packing diagram from the view, parallel to the [100] vector

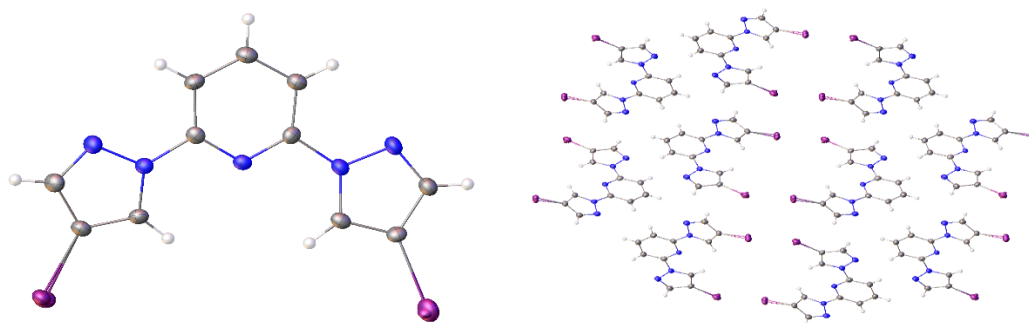


Fig. 4.23 Crystal structure of **L15** and its packing diagram from the view, parallel to the [010] vector

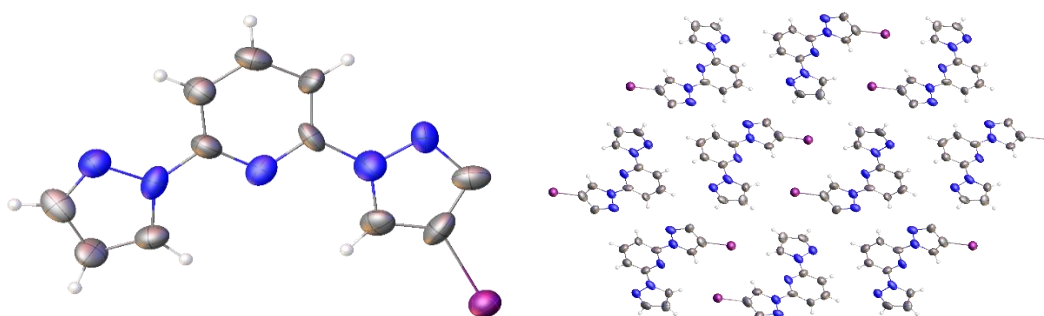


Fig. 4.24 Crystal structure of **L16** and its packing diagram from the view, parallel to the [010] vector

Unsaturated ligands: L17CxM and L17CxD

For the unsaturated long alkyne chain ligands the crystal structures were collected for **L17C12D**, **L17C16D**, and **L17C12M**. All of them had two molecules per unit cell ($Z = 2$), and one molecule per asymmetric unit ($Z' =$

1). For all the unsaturated ligands there was no interdigitation between the long alkyl chains.

The crystal structure of **L17C16D** was obtained from a crystal, which was accidentally grown during the attempt to obtain a mixed-ligand iron(II) complex between **L17C16D** and bpp. The unit cell parameters of **L17C12D** and **L17C16D** looked very similar (Table 4.3), and their molecules packed in the unit cell in the same way – the long alkyne chains are facing each other, and the bpp core of the molecules are stacked parallel to each other in layers (Fig. 4.25 and 4.26).

L17C12M had different unit cell parameters from the previous two structures (Table 4.3). The long alkyl chains are facing each other, forming bilayers (Fig. 4.27). At the edge of two bilayers, the two stacks of the aromatic part of the molecules are located close to each other. They are related by 2_1 symmetry, so the unsubstituted pyrazolyl rings can fit into the gaps between pyrazolyl rings in the adjacent stacks, which allows them to pack closely (Fig. 4.27).

Table 4.3 Unit cells of **L17C12D**, **L17C16D**, **L17C12M**, **L18C12M**, and **L18C14M**

	L17C12D	L17C16D	L17C12M	L18C12M	L18C14M
Temp., K	133.20(17)	150.00(10)	293(2)	293(2)	119.97(15)
Cr. sys.	monoclinic	monoclinic	monoclinic	triclinic	triclinic
Space gr.	Pc	Pc	P2 ₁	P-1	P-1
a, Å	5.45900(10)	5.4576(3)	5.3944(2)	5.38900(10)	5.4094(4)
b, Å	5.45440(10)	5.4477(3)	5.4384(2)	10.17380(10)	10.1832(6)
c, Å	52.5779(10)	65.309(2)	35.4153(14)	19.2473(3)	20.8390(15)
α, °	90	90	90	95.5290(10)	87.346(5)
β, °	91.576(2)	89.041(4)	90.989(3)	94.4050(10)	83.903(6)
γ, °	90	90	90	90.2580(10)	89.881(5)
V, Å³	1564.94(5)	1941.45(16)	1038.82(7)	1047.18(3)	1140.19(14)
Z	2	2	2	2	2

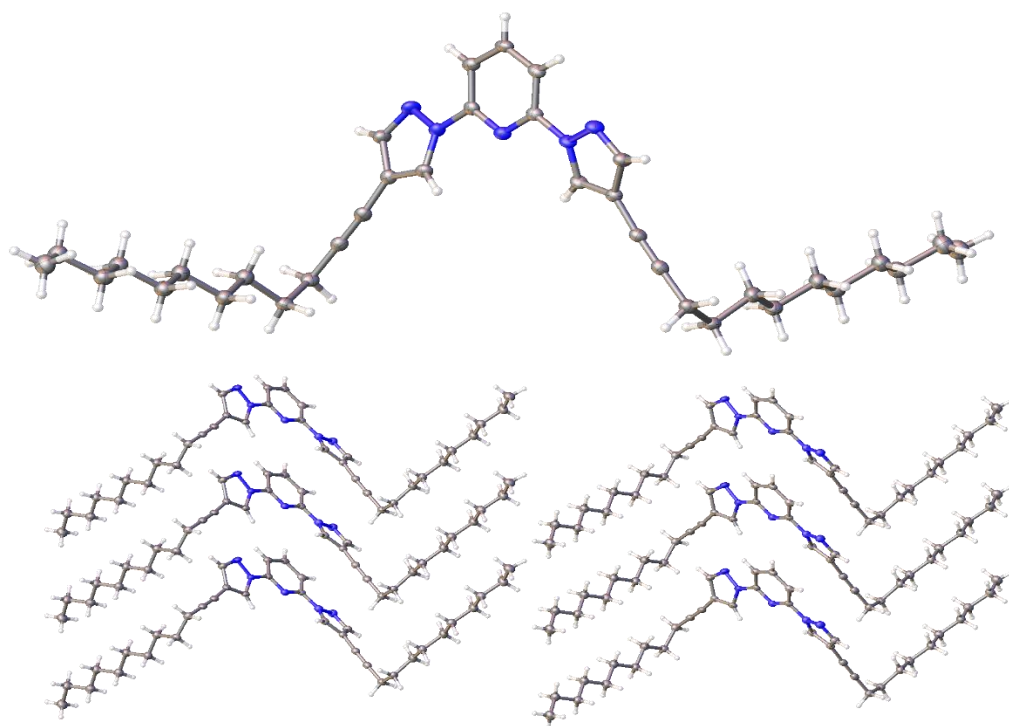


Fig. 4.25 Crystal structure of **L17C12D** and its packing diagram from the view, parallel to the [010] vector

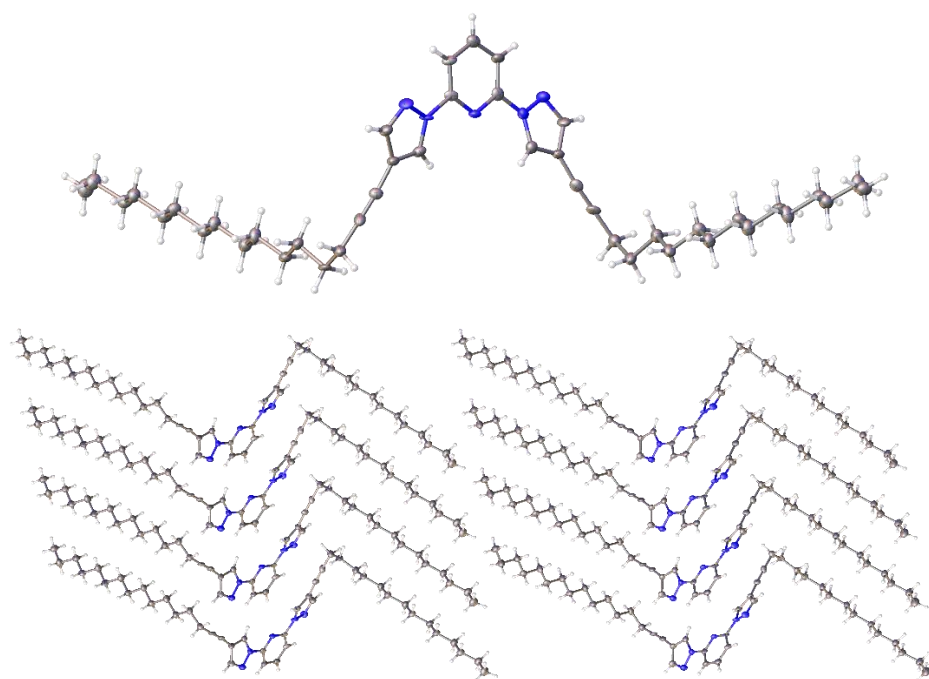


Fig. 4.26 Crystal structure of **L17C16D** and its packing diagram from the view, parallel to the [010] vector

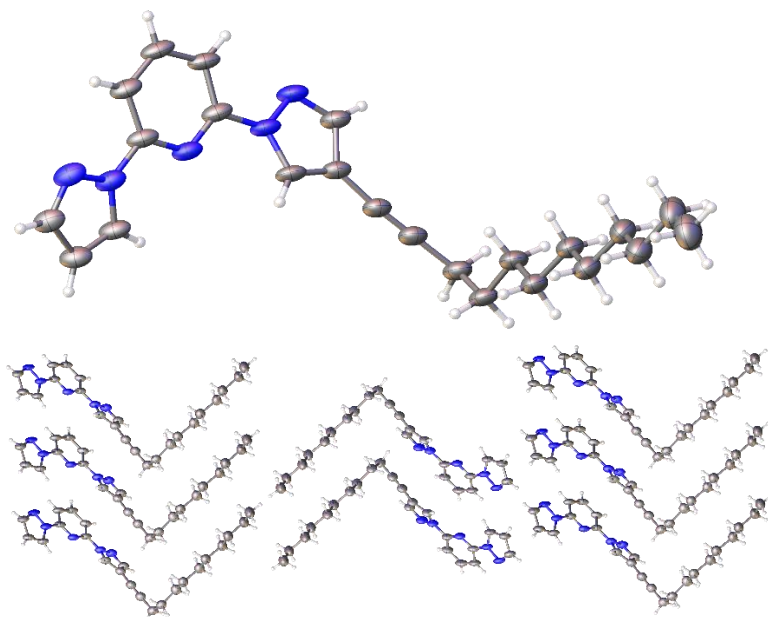


Fig. 4.27 Crystal structure of **L17C12M** and its packing diagram from the view, parallel to the [010] vector

Saturated ligands: L18CxM and L18CxD

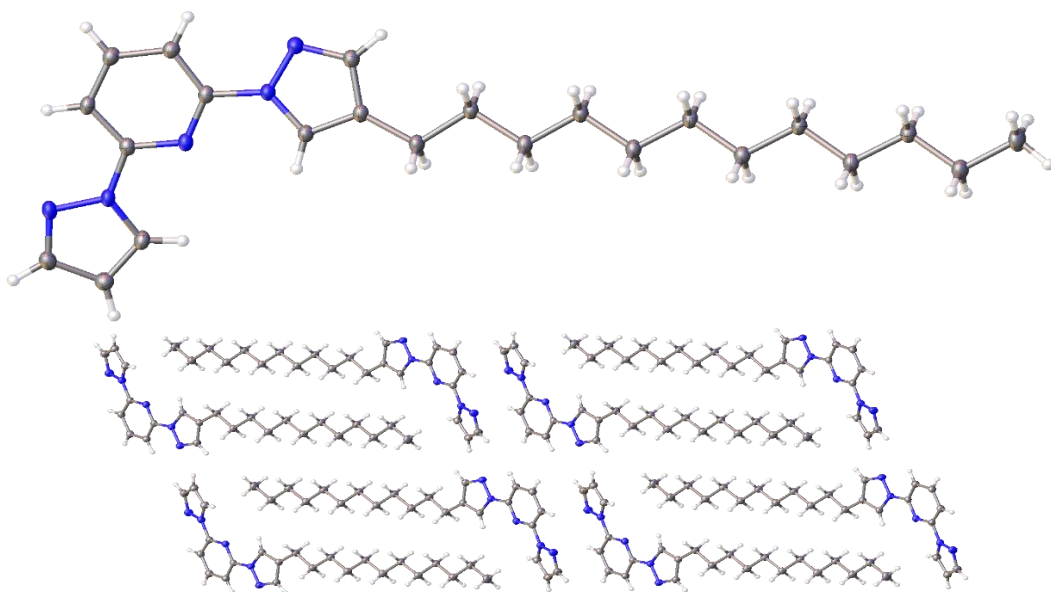


Fig. 4.28 Crystal structure of **L18C12M** and its packing diagram from the view, parallel to the [100] vector

The saturated ligands were harder to crystallize than the unsaturated ones, so the crystal structures were collected only for **L18C12M** and **L18C14M**. Saturated disubstituted ligands **L18CxD** were particularly reluctant to form crystals. For both **L18C12M** and **L18C14M** there were two molecules in the unit cell, and one in the asymmetric unit, i.e. $Z = 2$, and $Z' = 1$. All the available crystal structures of saturated ligands shown interdigitation of long alkyl chains, while all the unsaturated ligands had none. **L18C12M** and **L18C14M** have similar unit cell parameters (Table 4.3), and similar packing

of molecules in their unit cells (Fig. 4.28 and 4.29). Both of them form bilayers, where the molecules from the opposite sides of the bilayer are related by 2_1 symmetry. Because there is no rigid triple bond, the saturated ligands pack more tightly than the unsaturated ones. As for the saturated ligands the aromatic part of the molecule lies at a different angle to the alkyl chain, so both the pyrazolyl and pyridyl rings from the adjacent bilayers come close together (Fig. 4.28 and 4.29). There were no π - π interactions or hydrogen bonding found for the crystal structures of the ligands in this chapter, and also none of them contained lattice solvent.

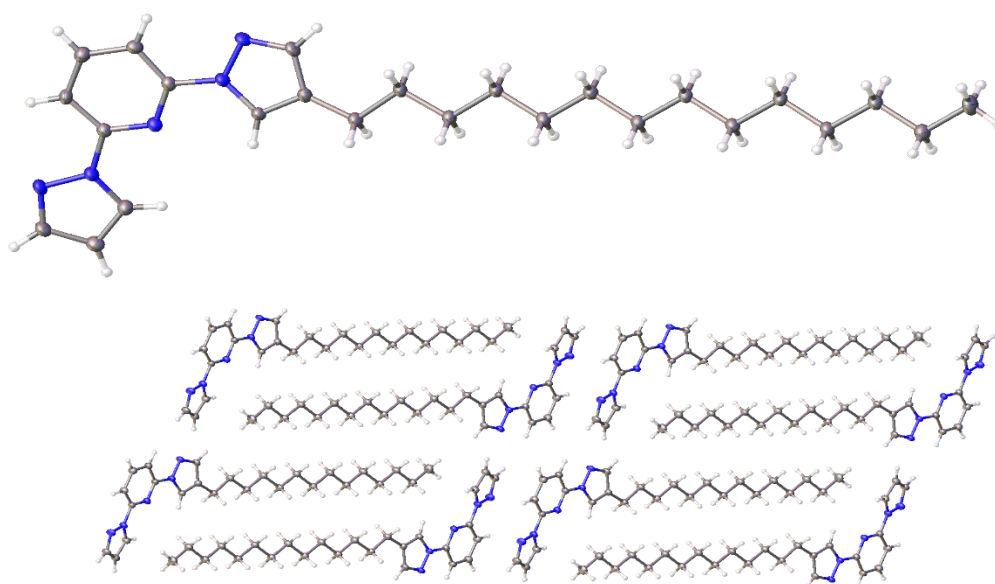


Fig. 4.29 Crystal structure of **L18C14M** and its packing diagram from the view, parallel to the [100] vector

4.4.2 Iron complex crystal structures

Iron complexes of precursor ligands:

The iron complexes of **L16** were surprisingly hard to crystallize. A crystal structure of $[\text{Fe}(\text{L16})_2][\text{BF}_4]_2$ was collected, but it was substantially disordered and hard to solve, although the main molecular backbone can still be seen. A crystal structure with another counterion, $[\text{Fe}(\text{L16})_2][\text{ClO}_4]_2 \cdot 2\text{MeCN}$ was also disordered, but finally solved (Fig. 4.30). All analyses were still collected for $[\text{Fe}(\text{L16})_2][\text{BF}_4]_2$ for consistency reasons, as all the iron complexes in this thesis had this counterion, and $[\text{Fe}(\text{L16})_2][\text{BF}_4]_2$ is a good quality crystalline sample. For $[\text{Fe}(\text{L16})_2][\text{ClO}_4]_2$ there were found: a weak hydrogen bond between a ClO_4^- oxygen and unsubstituted pyridyl hydrogen H3, and no π - π interactions (Fig. 4.30). It crystallized in P-1 space group, with $Z = 2$ and $Z' = 1$.

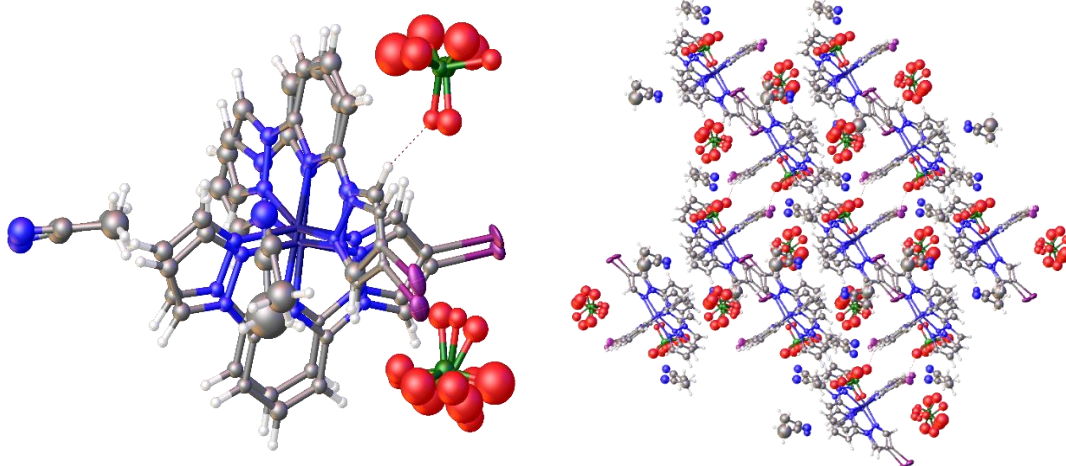


Fig. 4.30 Crystal structure of $[\text{Fe}(\text{L16})_2][\text{ClO}_4]_2 \cdot 2\text{MeCN}$, collected at 120K, and its packing diagram from the view, parallel to the $[010]$ vector

Iron complexes of long alkyl chain ligands: $\text{Fe}(\text{L17C18M})_2[\text{BF}_4]_2$, $[\text{Fe}(\text{L18C12M})_2][\text{BF}_4]_2$, $[\text{Fe}(\text{L18C16M})_2][\text{BF}_4]_2$, and $[\text{Fe}(\text{L18C18M})_2][\text{BF}_4]_2$

Out of all long alkyl chain iron complexes from this chapter, the iron complexes of monosubstituted saturated ligands **L18CxM** formed diffraction-quality crystals most readily, so the crystal structures were collected for three iron complexes from this series: $[\text{Fe}(\text{L18C12M})_2][\text{BF}_4]_2$, $[\text{Fe}(\text{L18C16M})_2][\text{BF}_4]_2$, and $[\text{Fe}(\text{L18C18M})_2][\text{BF}_4]_2$. Thanks to Diamond Light Source and efforts of Izar Capel an additional crystal structure was obtained from a small single crystal of the unsaturated iron complex $[\text{Fe}(\text{L17C18M})_2][\text{BF}_4]_2$. All four iron complexes, from which the crystal structures were collected, were obtained from DCE/acetone mixtures by slow pentane diffusion. All of them were pale-yellow plate crystals, and none of them contained lattice solvent. All four of these iron complexes had similar a and b unit cell dimensions (Table 4.4). All the saturated long alkyl chain iron complexes pack in the same way, forming bilayers of interdigitating long alkyl chains of molecules, which are related by 2_1 crystallographic symmetry. They only differ in the distance between the stacks of the aromatic parts of the molecules, which increases for longer alkyl chains (Fig. 4.32, 4.33, and 4.34).

The $[\text{Fe}(\text{L17C18M})_2][\text{BF}_4]_2$ molecules pack with interdigitation of the long alkyl chains (Fig. 4.31). At the same time, **L17C12M**, a ligand from the same series, had no interdigitation (Fig. 4.27).

All long alkyl chain iron complexes in this chapter pack with four molecules in the unit cell, and two molecules per asymmetric unit: $Z = 4$ and $Z' = 2$ (Table 4.4). No π - π interactions or hydrogen bonding were found for them.

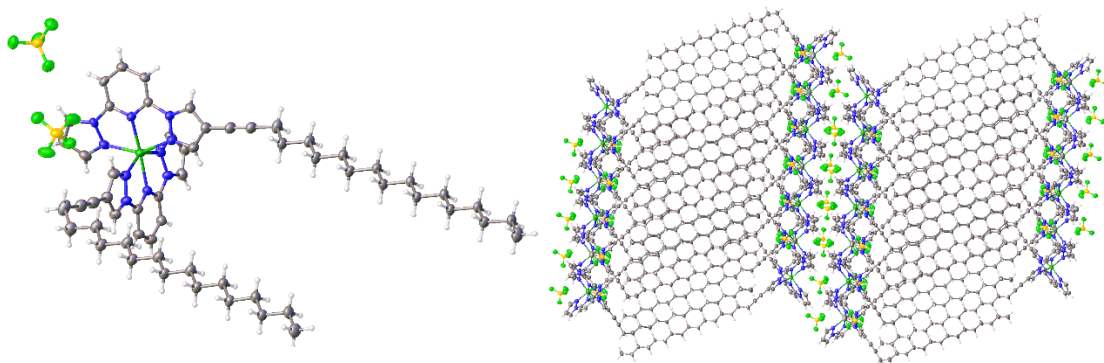


Fig. 4.31 Crystal structure of [Fe(L17C18M)₂][BF₄]₂, and its packing diagram from the view, parallel to the [010] vector

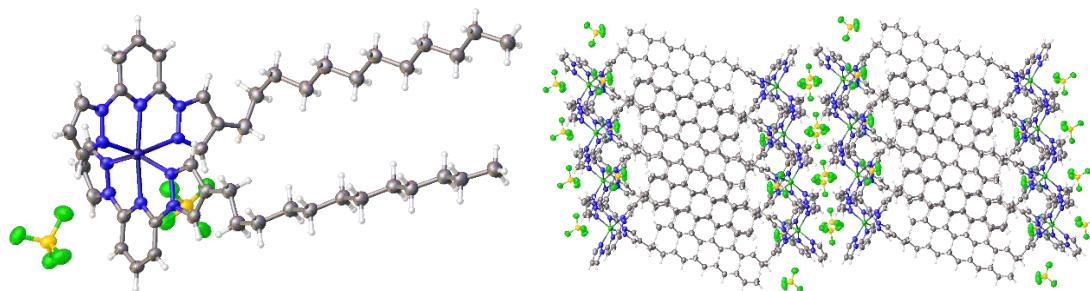


Fig. 4.32 Crystal structure of [Fe(L18C12M)₂][BF₄]₂, and its packing diagram from the view, parallel to the [010] vector

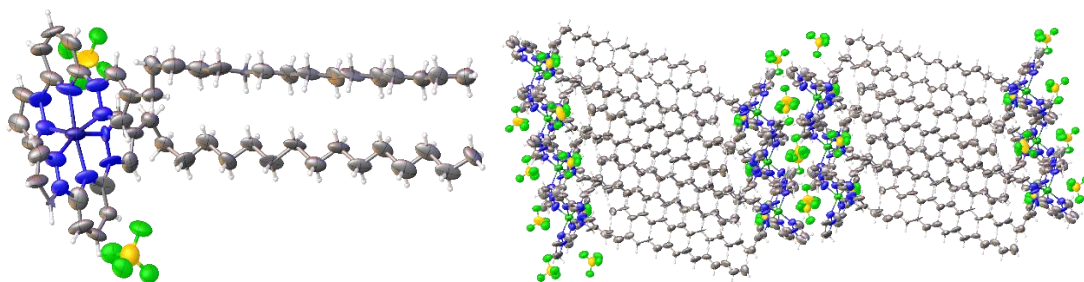


Fig. 4.33 Crystal structure of [Fe(L18C16M)₂][BF₄]₂, collected at 120K, and its packing diagram from the view, parallel to the [010] vector

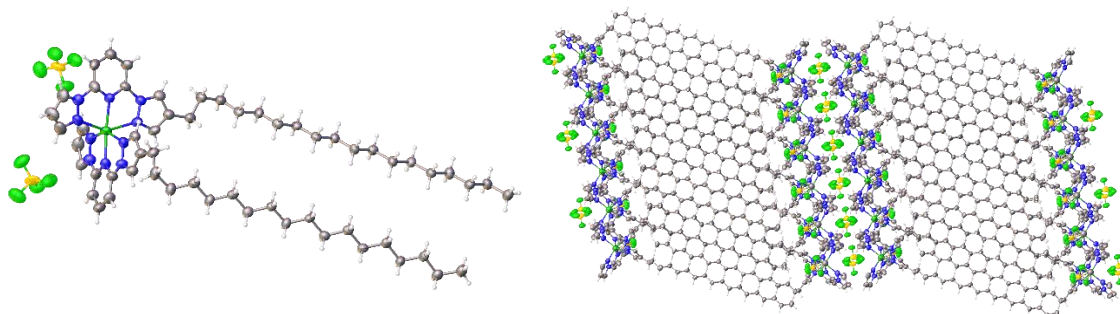


Fig. 4.34 Crystal structure of [Fe(L18C18M)₂][BF₄]₂, and its packing diagram from the view, parallel to the [010] vector

Table 4.4 Unit cells of [Fe(L17C18M)₂][BF₄]₂, [Fe(L18C12M)₂][BF₄]₂, [Fe(L18C16M)₂][BF₄]₂, and [Fe(L18C18M)₂][BF₄]₂

	[Fe(L17C18M) ₂][BF ₄] ₂	[Fe(L18C12M) ₂][BF ₄] ₂	[Fe(L18C16M) ₂][BF ₄] ₂		[Fe(L18C18M) ₂][BF ₄] ₂
Temp., K	293(2)	293(2)	119.99(16)	150.00(10)	293(2)
Cr. sys.	triclinic	triclinic	triclinic	triclinic	triclinic
Space gr.	P-1	P-1	P-1	P-1	P-1
a, Å	10.6801(2)	10.8827(4)	10.8707(15)	10.9510(14)	10.9192(5)
b, Å	15.2720(2)	15.2657(5)	15.1781(18)	15.0831(18)	15.1344(5)
c, Å	36.8778(5)	30.1249(11)	34.644(4)	34.713(4)	36.7856(17)
α, °	95.9150(10)	97.199(3)	83.813(10)	83.845(10)	84.117(4)
β, °	98.8820(10)	97.707(3)	82.791(10)	82.536(10)	85.034(4)
γ, °	89.9730(10)	90.123(3)	89.934(10)	89.868(10)	89.951(3)
V, Å³	5910.51(16)	4919.5(3)	5637.5(12)	5652.1(12)	6024.1(4)
Z	4	4	4	4	4

4.5 Distortion parameters

For all the long alkyl chain iron complexes in this chapter the volumes of the FeN_x octahedra around the iron atoms were around 12.40 Å³, which means that they were HS at the temperatures at which the crystal structures were collected (Table 4.5). It was unnecessary to calculate all the distortion parameters for them, except for [Fe(L18C16M)₂][BF₄]₂, which seemed to have some fraction of LS molecules in the sample (Table 4.5). Comparison of the distortion parameters for [Fe(L18C16M)₂][BF₄]₂ shows that there are more LS molecules in that sample at 150K than at 120K, which is unusual (Table 4.6). This effect may be explained by thermal spin trapping⁴.

Crystallographic data of the di-iodo bpp iron complex [Fe(L16)₂][BF₄]₂ were of a poor quality, but even for an incompletely solved structure it can be seen that the molecule is HS at 120 K (Table 4.5). The other structure of the same iron complex, but with a different counterion, [Fe(L16)₂][ClO₄]₂·2MeCN, was also disordered, but solved. The molecule was modelled with two intertwining molecule positions: A and B (Fig. 4.30). The distortion parameters from the two positions of the molecule were quite different from each other (Table 4.5), which may be explained by the disorder in the structure, but the average octahedral volume of 9.443 Å³, along with the rest of the distortion parameters, clearly indicates that the structure is LS. The

typical values of the distortion parameters for the high and low spin states can be found in the Table 2.5.

Table 4.5 Distortion parameters of the iron complexes from Chapter 4

	T, K		$V_{\text{oct}}, \text{\AA}^3$	
[Fe(L18C12M) ₂][BF ₄] ₂	293	Fe1	12.440	12.394
		Fe2	12.348	
[Fe(L18C16M) ₂][BF ₄] ₂	120	Fe1	11.938	11.807
		Fe2	11.675	
	150	Fe1	11.494	11.477
		Fe2	11.459	
[Fe(L18C18M) ₂][BF ₄] ₂	293	Fe1	12.145	12.144
		Fe2	12.142	
[Fe(L17C18M) ₂][BF ₄] ₂	293	Fe1	12.447	12.454
		Fe2	12.460	
[Fe(L16) ₂][ClO ₄] ₂ ·2MeCN	120.15	Fe1A	9.191	9.433
		Fe1B	9.674	
[Fe(L16) ₂][BF ₄] ₂	133.07	Fe1	12.128	11.770
		Fe2	11.811	
		Fe3	11.370	

Table 4.6 The distortion parameters for the crystal structures of [Fe(L16)₂][ClO₄]₂·2MeCN and [Fe(L18C16M)₂][BF₄]₂

	[Fe(L16) ₂][ClO ₄] ₂ ·2MeCN		[Fe(L18C16M) ₂][BF ₄] ₂			
	120.15 K		120 K		150 K	
	mol. A	mol. B	mol. 1	mol. 2	mol. 1	mol. 2
Fe1-N1A	1.971(14)	1.953(14)	2.108(17)	2.130(20)	2.104(14)	2.112(18)
Fe1-N1B	1.949(15)	1.988(14)	2.205(15)	2.158(15)	2.139(14)	2.112(14)
Fe1-N3A	1.875(14)	1.915(14)	2.078(14)	2.076(17)	2.058(10)	2.069(12)
Fe1-N3B	1.899(14)	1.872(13)	2.084(14)	2.140(16)	2.040(10)	2.068(10)
Fe1-N5A	1.866(17)	2.051(18)	2.214(19)	2.158(14)	2.119(10)	2.112(11)
Fe1-N5B	1.996(15)	1.94(14)	2.213(13)	2.129(15)	2.145(11)	2.11(8)
Average	1.93	1.95	2.15	2.13	2.10	2.10
α	79.5(6)	80.93(6)	73.4(7)	73.7(7)	75.2(4)	75.0(4)
Σ	93.0(6)	78.2(6)	159.3(7)	157.8(7)	137.0(4)	137.4(4)
Φ	179.0(6)	176.3(6)	171.9(6)	171.4(8)	173.8(4)	174.3(4)
θ	92.336	90.881	87.273	86.120	88.194	87.907
$V_{\text{oct}}, \text{\AA}^3$	9.191	9.674	11.938	11.675	11.494	11.459

4.6 Powder diffraction

4.6.1 Ligands

The powder patterns of the unsaturated monosubstituted ligands **L17CxM** roughly match each other. The pattern simulated from the only crystal structure collected from this series, **L17C12M**, also matches the collected powder pattern for that compound (Fig. 4.34). Similarly, for the unsaturated disubstituted ligands **L17CxD**, the powder patterns of a different alkyl chain length were similar to each other. The patterns, simulated from the crystal structures of **L17C12D** and **L17C16D**, matched the obtained powder patterns, but in the both cases the peaks at 15-30° were much more intense on the simulated powder patterns (Fig. 4.35). That probably arises from preferred orientation of the polycrystalline sample.

The saturated monosubstituted ligands **L18CxM** can be divided into two groups of ligands with similar powder patterns: **L18C12M** and **L18C14M** in the first group, and **L18C16M** and **L18C18M** in the second (Fig. 4.36). The simulated powder patterns of **L18C12M** and **L18C14M** matched the obtained ones. The powder patterns of saturated disubstituted ligands **L18CxD** were quite similar and with intense peaks, which shows good crystallinity of the samples (Fig. 4.37).

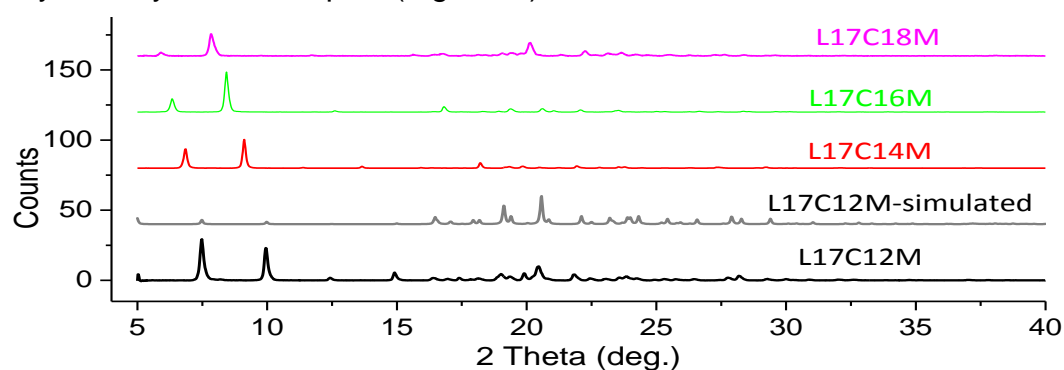


Fig. 4.34 Collected and simulated powder patterns of **L17CxM** ligands

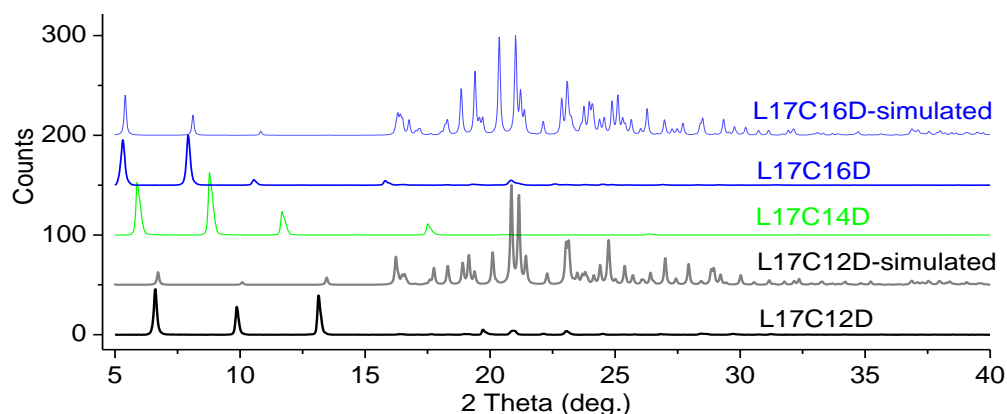


Fig. 4.35 Collected and simulated powder patterns of **L17CxD** ligands

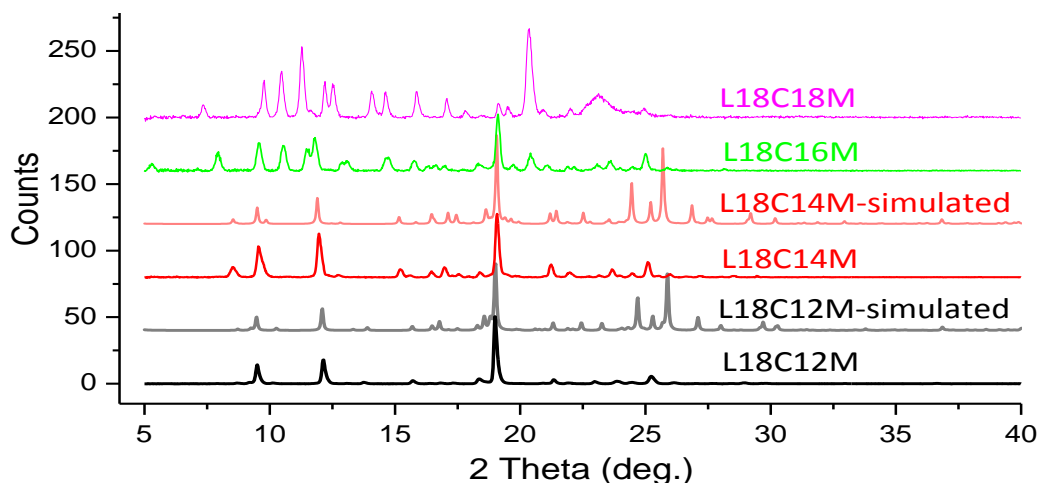


Fig. 4.36 Collected and simulated powder patterns of **L18CxM** ligands

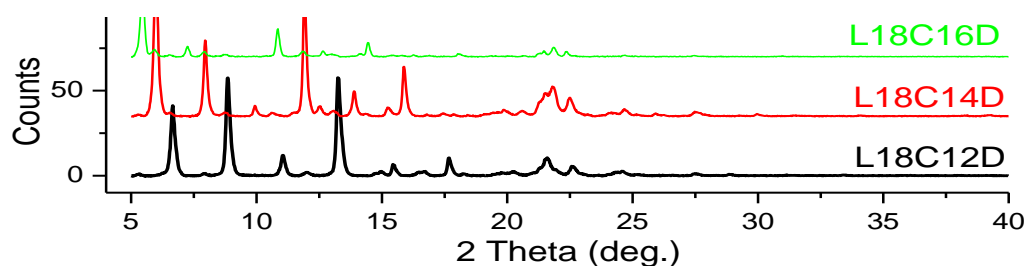


Fig. 4.37 Collected and simulated powder patterns of **L18CxD** ligands

4.6.2 Iron complexes

$[\text{Fe}(\text{L18C16M})_2][\text{BF}_4]_2$ and $[\text{Fe}(\text{L18C16M})_2][\text{ClO}_4]_2$ both had broad and noisy peaks on their powder patterns, which means they were not very crystalline (Fig. 4.38). The crystal structures of these two salts were disordered, and the powder patterns simulated from them poorly match the obtained powder patterns (Fig. 4.38). From these results it may be concluded that asymmetric ligands with heavy atoms like iodine and their iron complexes are reluctant to form crystals.

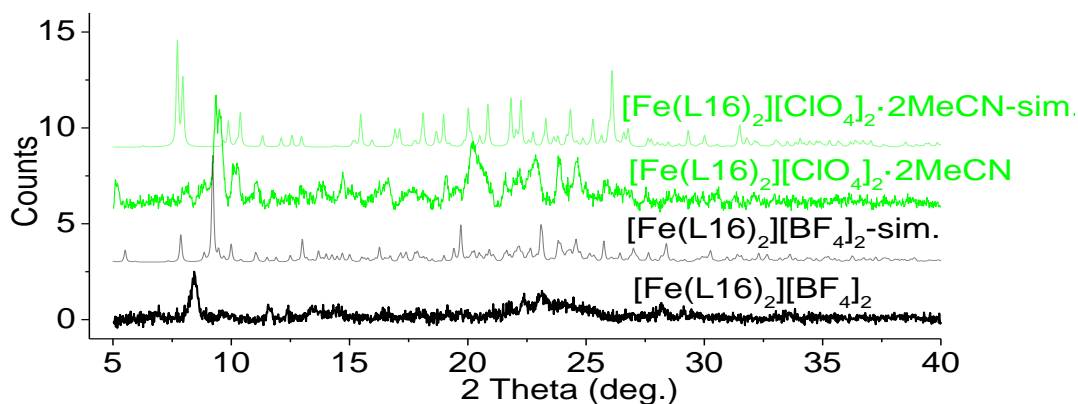


Fig. 4.38 Powder pattern of $[\text{Fe}(\text{L18C16M})_2][\text{BF}_4]_2$

All of the $[\text{Fe}(\text{L17CxM})_2][\text{BF}_4]_2$ iron complexes had two intense peaks near 10° , but otherwise their powder patterns looked different, which suggests

that they had different unit cells. There was only one crystal structure collected for this series, $[\text{Fe}(\text{L17C18M})_2][\text{BF}_4]_2$. For this structure the collected powder pattern matches the simulated one, but it also has an extra peak at ca 7° , which could mean that the sample had some additional crystalline phase in the sample. Out of this series, the powder pattern of $[\text{Fe}(\text{L17C16M})_2][\text{BF}_4]_2$ looks the most crystalline, and has the most intense peaks. The collected powder pattern of $[\text{Fe}(\text{L17C16M})_2][\text{BF}_4]_2$ also matches the simulated one for $[\text{Fe}(\text{L17C18M})_2][\text{BF}_4]_2$ very well. The peaks on both patterns appear in roughly the same places, but with different intensities (Fig. 4.39), which suggests that these two iron complexes must have very similar unit cells, with $[\text{Fe}(\text{L17C16M})_2][\text{BF}_4]_2$ being phase pure, and $[\text{Fe}(\text{L17C18M})_2][\text{BF}_4]_2$ having some other crystalline phase in the sample. $[\text{Fe}(\text{L17C12M})_2][\text{BF}_4]_2$ and $[\text{Fe}(\text{L17C14M})_2][\text{BF}_4]_2$ both have a broad peak at ca 18° , which must mean that both samples had some amorphous powder fraction (Fig. 4.39).

The powder patterns of $[\text{Fe}(\text{L17C12D})_2][\text{BF}_4]_2$ and $[\text{Fe}(\text{L17C14D})_2][\text{BF}_4]_2$ look similar, while the powder pattern of $[\text{Fe}(\text{L17C16D})_2][\text{BF}_4]_2$ had some features different from them (Fig. 4.40). There are no simulated powder patterns for this series to compare the measured patterns to.

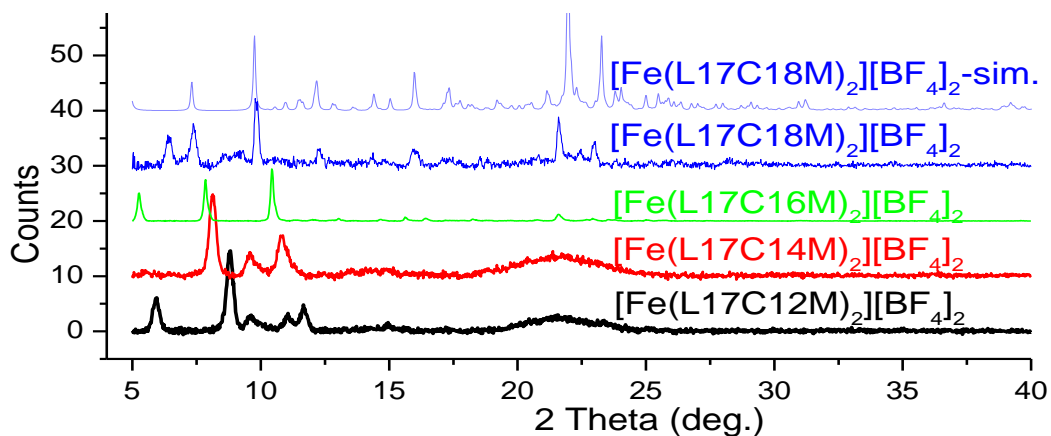


Fig. 4.39 Collected and simulated powder patterns of $[\text{Fe}(\text{L17CxM})_2][\text{BF}_4]_2$

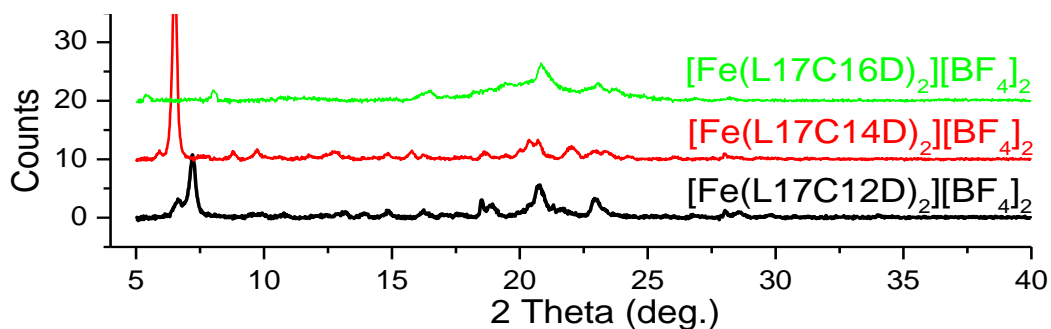


Fig. 4.40 Powder patterns of $[\text{Fe}(\text{L17CxD})_2][\text{BF}_4]_2$

The most crystal structures among all the iron complexes series in this chapter were collected for $[\text{Fe}(\text{L18CxM})_2][\text{BF}_4]_2$ series, and all the simulated patterns matched the measured ones (Fig. 4.41). The powder pattern of $[\text{Fe}(\text{L18C18M})_2][\text{BF}_4]_2$ and $[\text{Fe}(\text{L17C18M})_2][\text{BF}_4]_2$ resemble each other, which should be expected, as they have similar unit cell parameters (Table 4.4). The powder patterns of $[\text{Fe}(\text{L18C14M})_2][\text{BF}_4]_2$, $[\text{Fe}(\text{L18C16M})_2][\text{BF}_4]_2$, and $[\text{Fe}(\text{L18C18M})_2][\text{BF}_4]_2$ look very similar, while the pattern of $[\text{Fe}(\text{L18C12M})_2][\text{BF}_4]_2$ stands out of this group (Fig. 4.41), which is also true for its unit cell parameters (Table. 4.4).

The powder patterns of the $[\text{Fe}(\text{L18CxD})_2][\text{BF}_4]_2$ iron complexes are all similar to each other, and show a good crystallinity of the samples (Fig. 4.42).

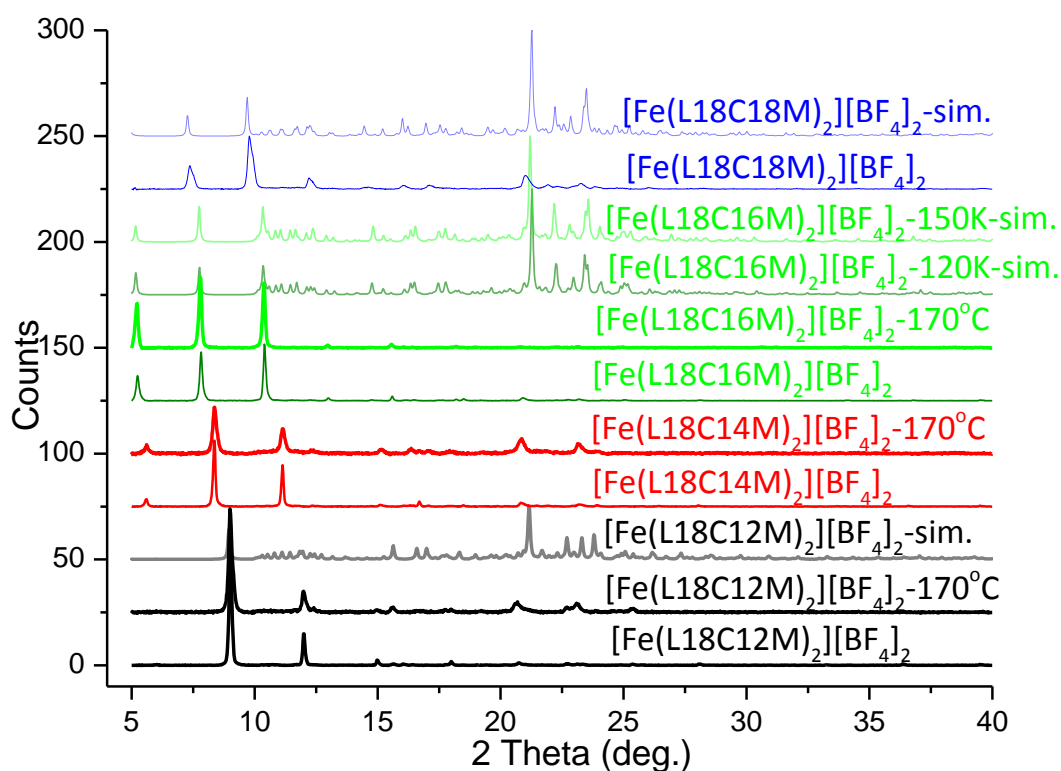


Fig. 4.41 Powder patterns of $[\text{Fe}(\text{L18CxM})_2][\text{BF}_4]_2$: fresh samples, annealed at 170°C , and simulated from crystal structures

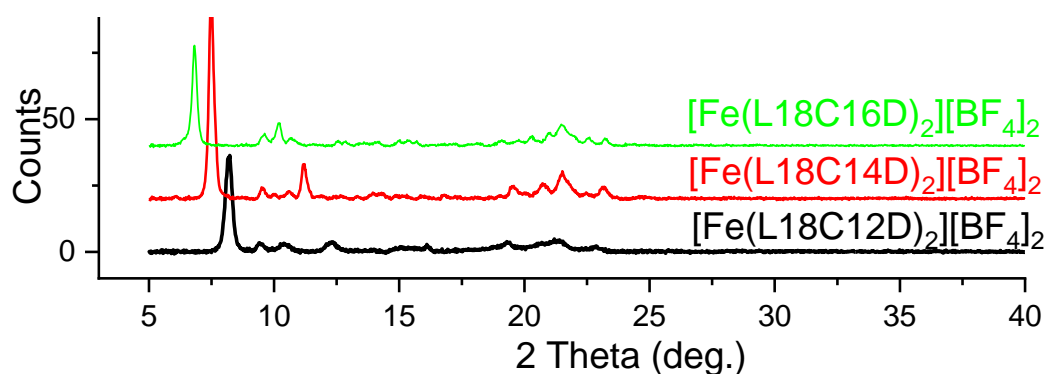


Fig. 4.42 Powder patterns of $[\text{Fe}(\text{L18CxD})_2][\text{BF}_4]_2$

4.7 SQUID

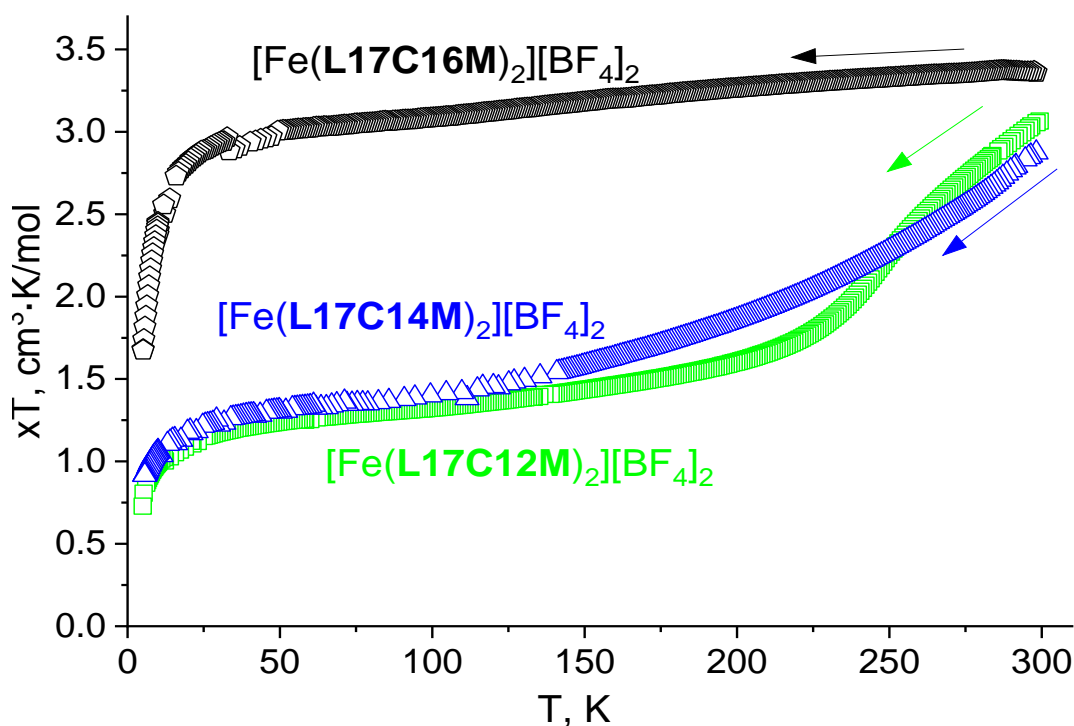


Fig. 4.43 SQUID magnetic susceptibility measurements for [Fe(L17C12M)₂][BF₄], [Fe(L17C14M)₂][BF₄], and [Fe(L17C16M)₂][BF₄]

Variable temperature magnetic susceptibilities were measured only for a cooling cycle for [Fe(L17C12M)₂][BF₄]₂, [Fe(L17C14M)₂][BF₄]₂, and [Fe(L17C16M)₂][BF₄]₂ (Fig. 4.43), and for three cycles for [Fe(L17C18M)₂][BF₄]₂ (Fig. 4.44). [Fe(L17C12M)₂][BF₄]₂ shows rather gradual SCO with HS trapping of some fraction of the sample. As the χT didn't go below ca 1.2 cm³·K/mol, it may be concluded that about 1.2/3.5 = 34% of the sample are trapped in HS. Therefore the $T_{1/2}$ shall be reached not at 1.75 cm³·K/mol, but at 1.2 + (3.5 - 1.2)/2 = 2.35 cm³·K/mol, which corresponds with 253 K. [Fe(L17C14M)₂][BF₄]₂ had much more gradual switching (Fig. 4.43), which makes it hard to determine its $T_{1/2}$ precisely, but from the DSC data for this compound it can be seen that its $T_{1/2}$ lays at about 24°C or 297 K (Fig. 4.65). [Fe(L17C16M)₂][BF₄]₂ remained HS between 300 K and 50 K (Fig. 4.43). [Fe(L17C18M)₂][BF₄]₂ shown a very gradual SCO with HS trapping of about 50% of the sample, as the SQUID curve reached only the χT of 1.75 cm³·K/mol before undergoing zero-field splitting (Fig. 4.44). The $T_{1/2}$ therefore should be measured at 1.75 + (3.5 - 1.75) = 2.625 cm³·K/mol, which corresponds with 239 K or -34°C, which is too low to see the corresponding peak on the DSC (Fig. 4.66).

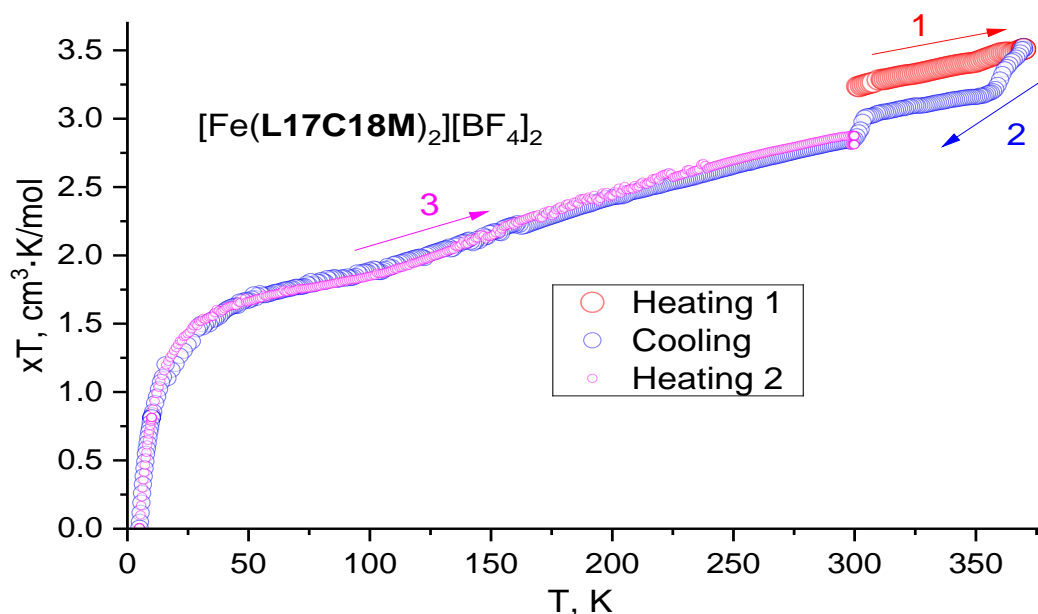


Fig. 4.44 SQUID magnetic susceptibility measurements for $[\text{Fe}(\text{L17C18M})_2][\text{BF}_4]_2$

$[\text{Fe}(\text{L17CxD})_2][\text{BF}_4]_2$

All the iron complexes from the $[\text{Fe}(\text{L17CxD})_2][\text{BF}_4]_2$ series shown similar magnetic behaviour, and remained HS from 300 K to 50 K with a decrease in the magnetic moment below 50 K due to zero-field splitting (Fig. 4.45).

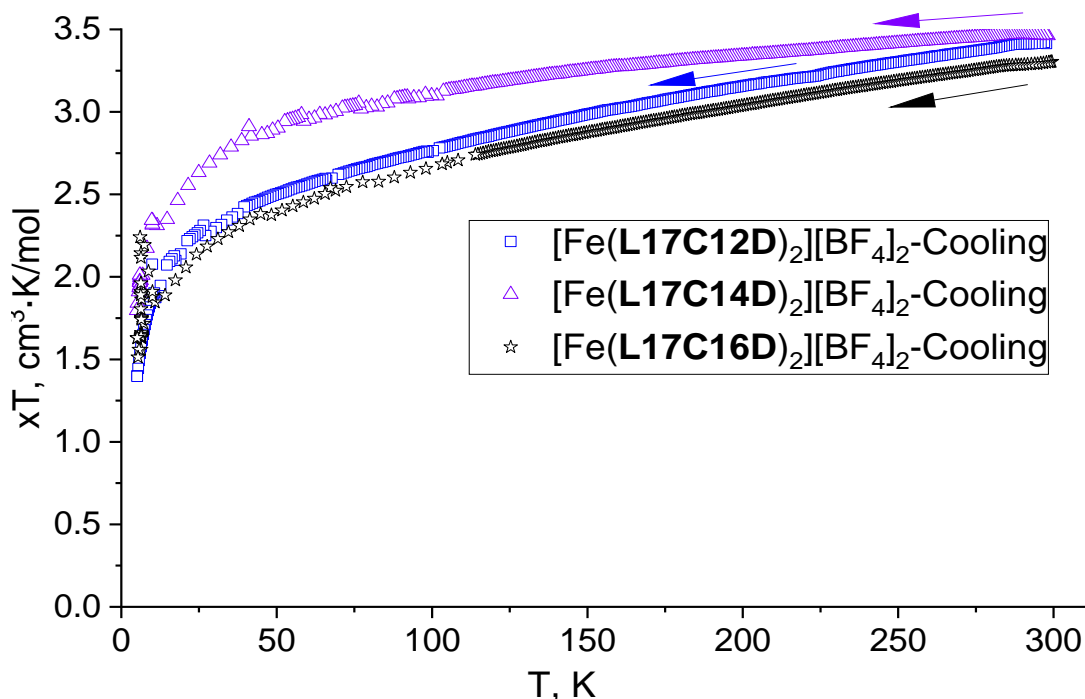


Fig. 4.45 SQUID magnetic susceptibility measurements for $[\text{Fe}(\text{L17CxD})_2][\text{BF}_4]_2$ iron complexes series

[Fe(L18CxM)₂][BF₄]₂

Out of all iron complexes in this chapter, the [Fe(L18CxM)₂][BF₄]₂ series formed crystallographic quality crystals the most readily. Besides this, they show some interesting SCO behaviour, so each compound from this series was measured over a few thermal cycles in the SQUID. All of them shown quite abrupt SCO with T_{1/2} at ca 155-160 K. Because of this, unlike the other iron complexes, [Fe(L18CxM)₂][BF₄]₂ series were also studied by Evans method NMR (Section 4.10) and variable temperature images (Section 4.9).

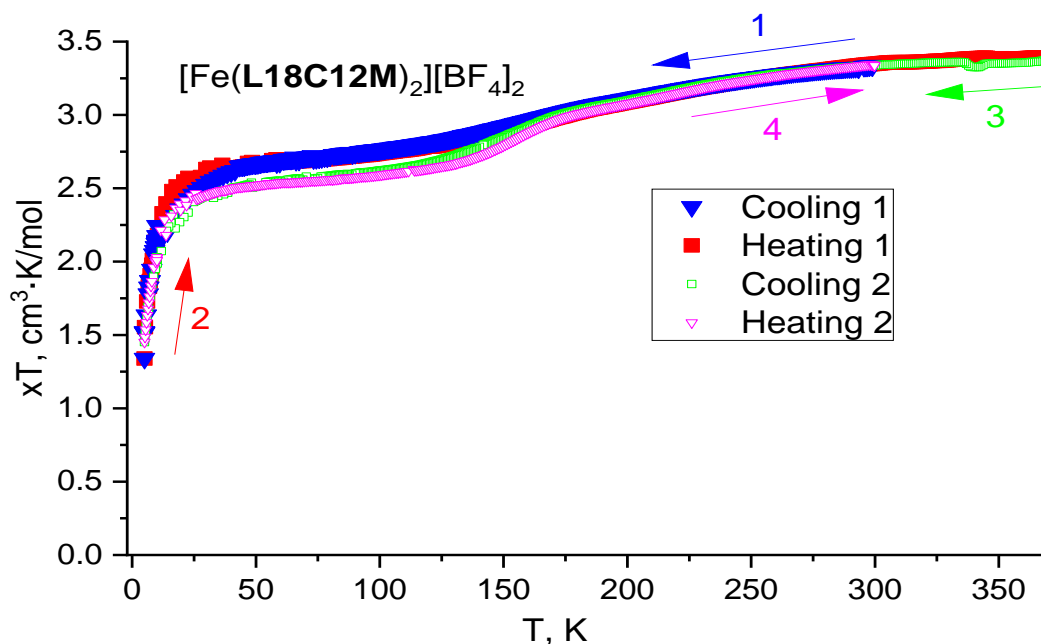


Fig. 4.46 SQUID magnetic susceptibility measurements for [Fe(L18C12M)₂][BF₄]₂

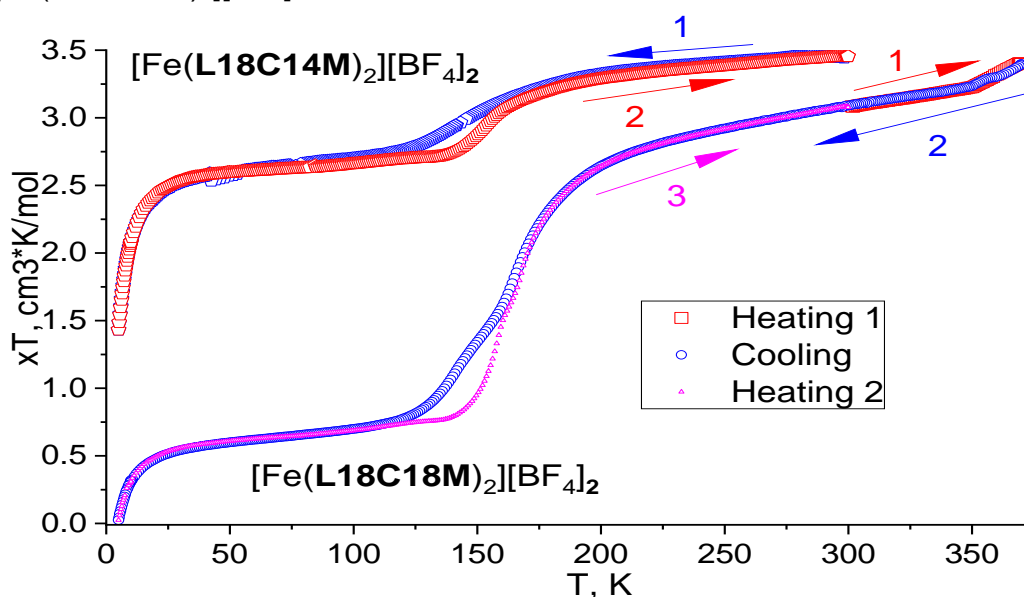


Fig. 4.47 SQUID magnetic susceptibility measurements for [Fe(L18C14M)₂][BF₄]₂ and [Fe(L18C18M)₂][BF₄]₂

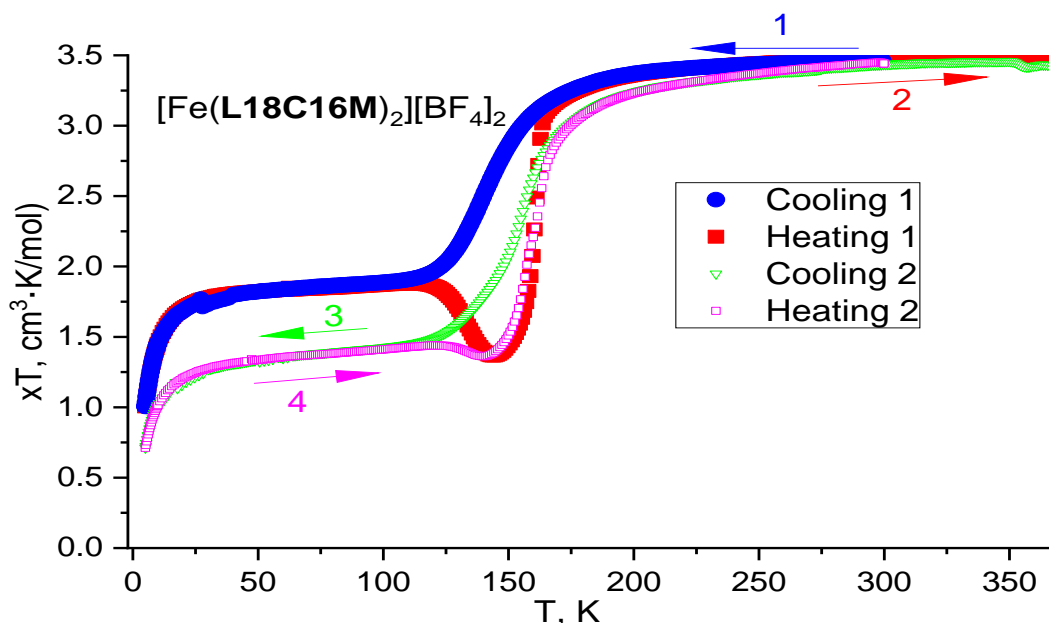


Fig. 4.48 SQUID magnetic susceptibility measurements for $[\text{Fe}(\text{L17C16M})_2][\text{BF}_4]_2$

$[\text{Fe}(\text{L18C12M})_2][\text{BF}_4]_2$ shows incomplete and gradual SCO between 125 and 250 K, with only ca 2/7 of the sample completely switching, as the magnetic moment only reached $2.5 \text{ cm}^3 \cdot \text{K/mol}$ (Fig. 4.46). There was no significant hysteresis observed, but heating the sample to 370 K or 97°C seems to decrease the number of the molecules trapped in the HS state, as the magnetic moment on both the cooling and the heating cycles 3 and 4, decreased by $0.15 \text{ cm}^3 \cdot \text{K/mol}$ over the 50-150 K temperature range. $[\text{Fe}(\text{L18C14M})_2][\text{BF}_4]_2$ shown similar magnetic behaviour: it also underwent an incomplete SCO only until ca $2.5 \text{ cm}^3 \cdot \text{K/mol}$, but this time the switching was more abrupt, from ca 127 to ca 170 K, and with about 16° hysteresis (Fig. 4.47). $[\text{Fe}(\text{L18C16M})_2][\text{BF}_4]_2$ reached the magnetic moment of only $1.75 \text{ cm}^3 \cdot \text{K/mol}$ upon cooling, which indicates that about half of the sample was trapped in the HS state. However upon heating, during cycle 2, the system gained enough energy to switch to the LS state, the magnetic moment started to decrease with the increase of the temperature, which is unusual (Fig. 4.48). This effect was also observed by comparing the crystal structures of $[\text{Fe}(\text{L18C16M})_2][\text{BF}_4]_2$, collected at 120 K and 150 K, which shown that the distortion parameters indicate the crystal being more LS at 150 K than at 120 K (Table 4.6). After the first two cycles the HS trapping became less pronounced, so cycle 3 reached lower χT values than cycle 1 (Fig. 4.48). $[\text{Fe}(\text{L18C18M})_2][\text{BF}_4]_2$ shows quite abrupt SCO from ca 138 K to ca 208 K, with about 14 K hysteresis. SCO for this sample seems to occur in two steps: from 138 to ca 208 K, and from ca 350 K and beyond 370 K (Fig. 4.47). The amount of the sample trapped in HS for this compound was

around 1/7 of the sample, as the magnetic moment didn't go below 0.5 cm³·K/mol, except for below 25 K due to zero-field splitting (Fig. 4.47). Heating the sample to 370 K seems to have no effect on the amount of the HS-trapped fraction, as each cycle followed the same path. Thus, all of the [Fe(L18CxM)₂][BF₄]₂ iron complexes shown similar magnetic behaviour, with HS trapping to a different extent.

[Fe(L18CxM)₂][BF₄]₂

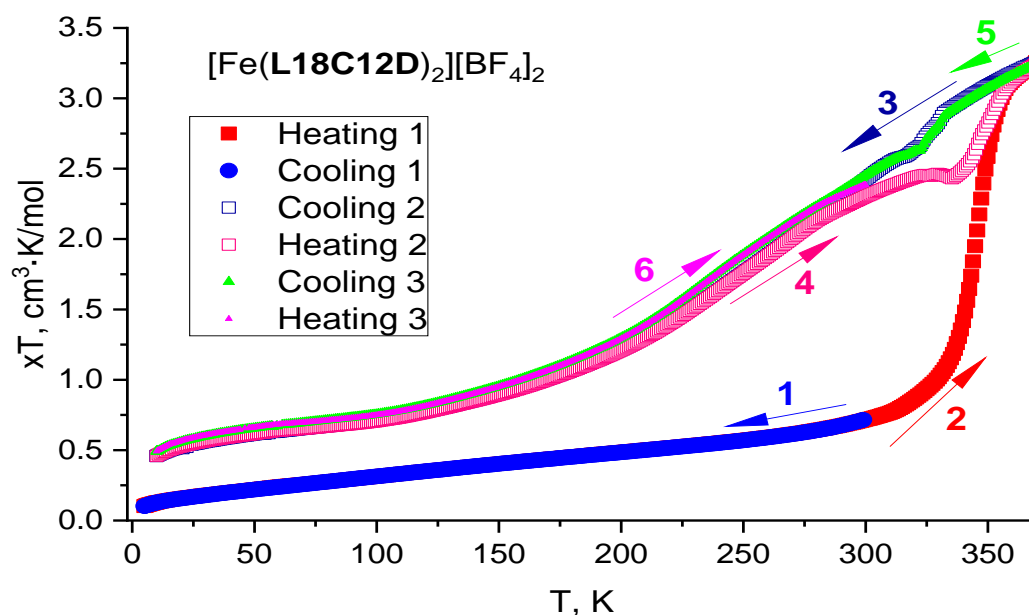


Fig. 4.49 SQUID magnetic susceptibility measurements for [Fe(L18C12D)₂][BF₄]₂

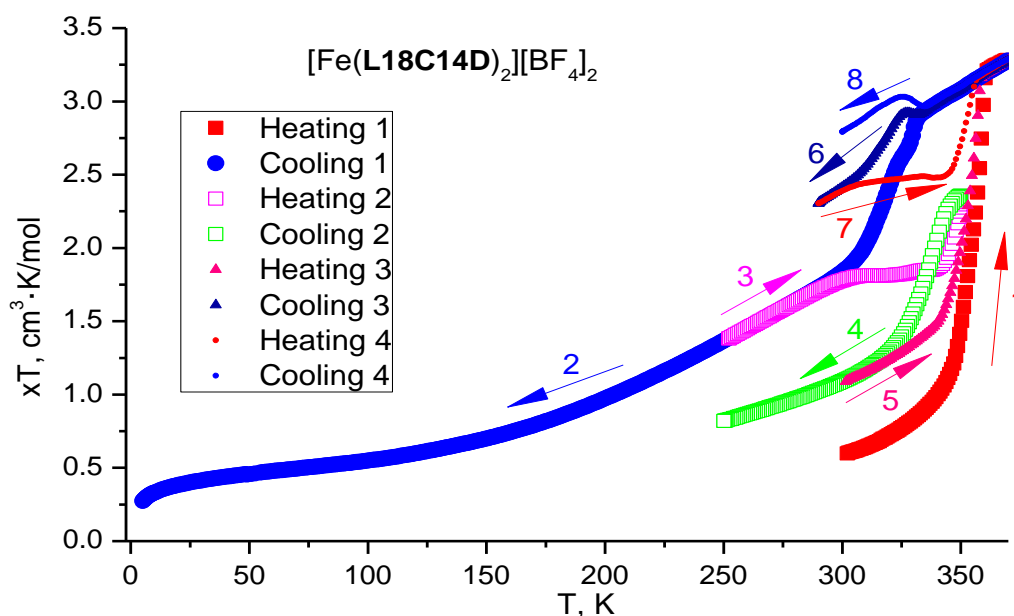


Fig. 4.50 SQUID magnetic susceptibility measurements for [Fe(L18C14D)₂][BF₄]₂

The $[\text{Fe}(\text{L18CxD})_2][\text{BF}_4]_2$ series shows interesting SCO magnetic behaviour, and some of these iron complexes were measured over multiple cycles in the SQUID. After the first two cycles, and heating to 370 K, $[\text{Fe}(\text{L18C12D})_2][\text{BF}_4]_2$ underwent some irreversible changes which increased the HS fraction of the sample (Fig. 4.49), and as at 5 K its magnetic moment is $0.5 \text{ cm}^3\cdot\text{K}/\text{mol}$, the HS trapped fraction must be ca 1/7 of the whole sample. Additional heating and cooling cycles didn't cause any further HS trapping, as cycle 3, 5, and 6 follow the same path. There was a small hysteresis observed after annealing, between cycles 4 and 5 (Fig. 4.49). This was not the case for $[\text{Fe}(\text{L18C14D})_2][\text{BF}_4]_2$, which shows a change in the HS trapped fraction after each heating to 370 K (Fig. 4.50). $[\text{Fe}(\text{L18C16D})_2][\text{BF}_4]_2$ behaved differently from the previous two samples, and remained LS from 0 K to 248 K, after which it started a gradual SCO, which reached only the magnetic moment of $0.50 \text{ cm}^3\cdot\text{K}/\text{mol}$ at 350 K (Fig. 4.51), which means that its $T_{1/2}$ must lie far beyond the upper limit of the SQUID.

$[\text{Fe}(\text{L16})_2][\text{BF}_4]_2$

$[\text{Fe}(\text{L16})_2][\text{BF}_4]_2$ shows a gradual SCO upon cooling (Fig. 4.51), which corresponds with its crystal structure data, which indicated that at 133 K the sample is mostly HS (Table 4.5).

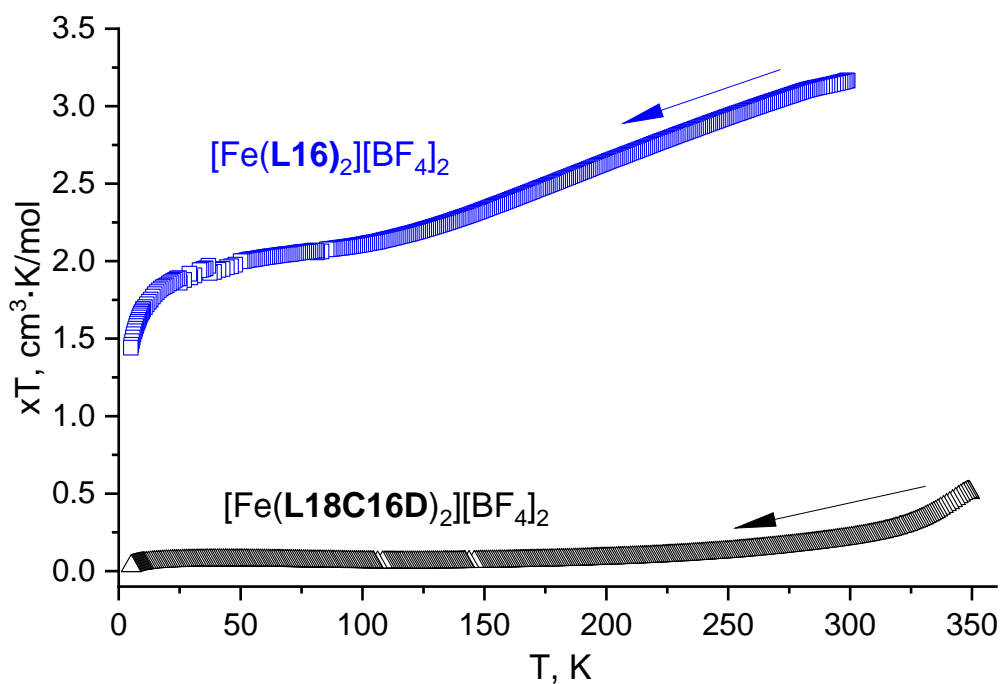


Fig. 4.51 SQUID magnetic susceptibility measurements for $[\text{Fe}(\text{L18C16D})_2][\text{BF}_4]_2$ and $[\text{Fe}(\text{L16})_2][\text{BF}_4]_2$

4.8 DSC

4.8.1 Ligands

L17CxM

The DSC of each **L17CxM** ligand had a peak that corresponds with its melting point. However, **L17C16M** and **L17C18M** had a small additional peak at about 20°C below the main peak on the first cooling cycle (Fig. 4.52). The DSC of **L17C14M** didn't have that additional peak, and also was missing the peak on the cooling cycle, likely because it lays below 0°C. **L17C12M** shows different DSC behaviour from the other members of this series, as it underwent some irreversible changes after heating to 175°C, so there were no peaks observed after the first heating cycle (Fig. 4.53).

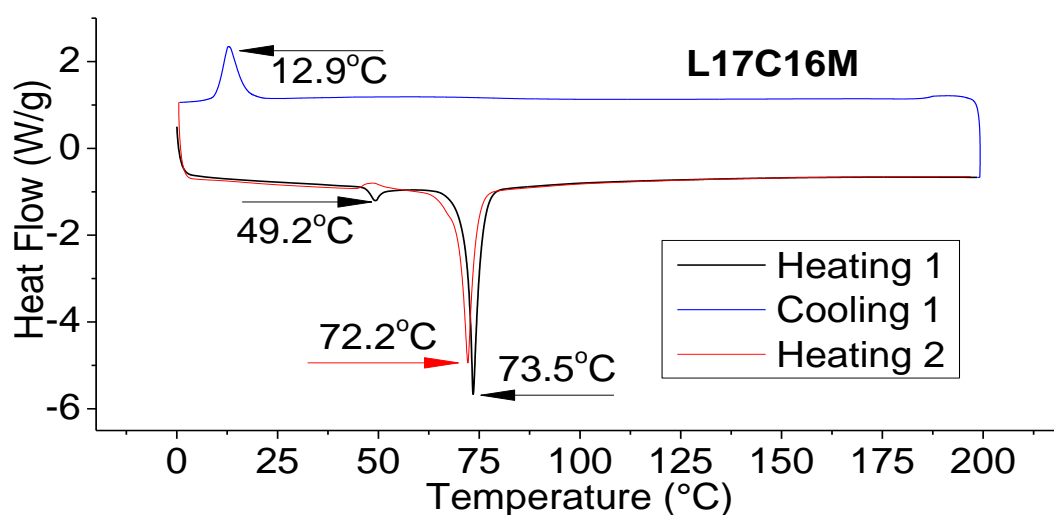


Fig. 4.52 DSC of **L17C16M**, typical for the **L17CxM** series

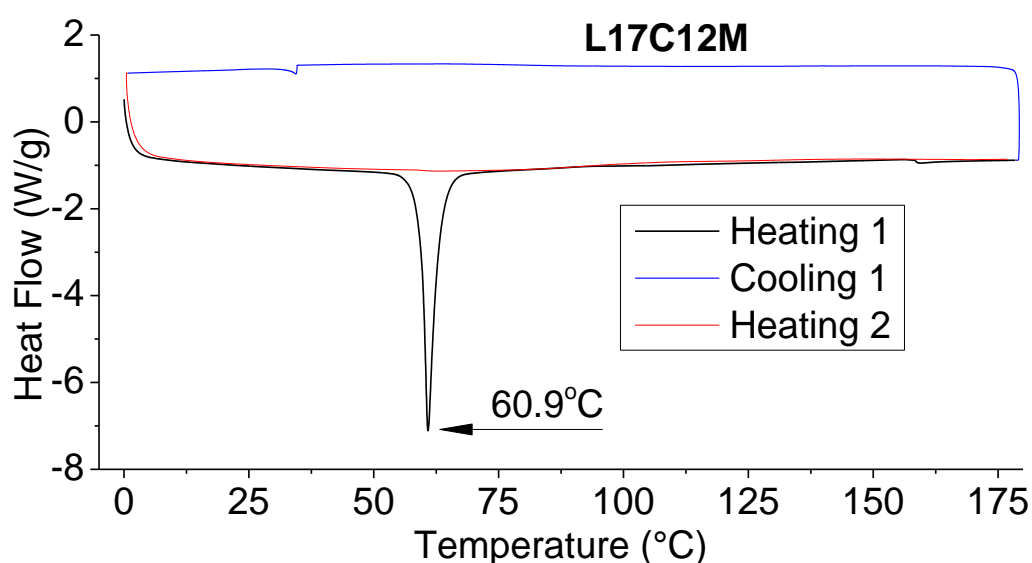


Fig. 4.53 DSC of **L17C12M**, different from the other **L17CxM** ligands

The ligands from the **L17CxM** series show the onset of mass loss by TGA above about 220°C, with the ligands with longer alkyl chains being more temperature resistant (Fig. 4.54).

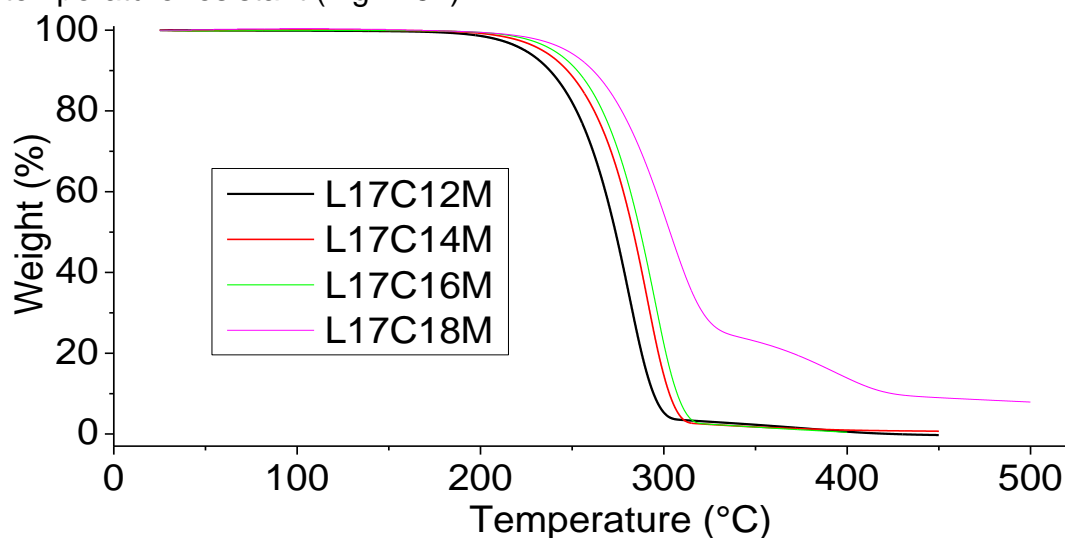


Fig. 4.54 TGA of the **L17CxM** ligand series

L17CxD

The DSCs of **L17C14D** and **L17C16D** all show the same features: a peak on each cycle, that corresponds with the ligand's melting point, and with the doubling of this peak on the cooling cycle, with 0.8-1.3° difference between the two parts of the peak (Fig. 4.55). **L17C12D** had the same features, but with no doubling of the peak on the cooling cycle. All the ligands from the **L17CxD** series start decomposing by TGA above 270°C, with the longer alkyl chain ligands being more thermally stable (Fig. 4.56).

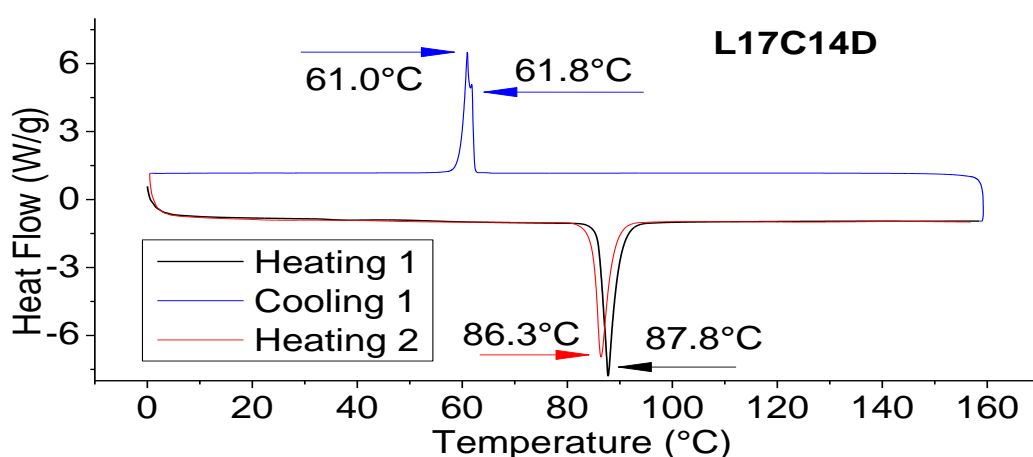


Fig. 4.55 DSC of the **L17C14D**, typical for the **L17CxD** series

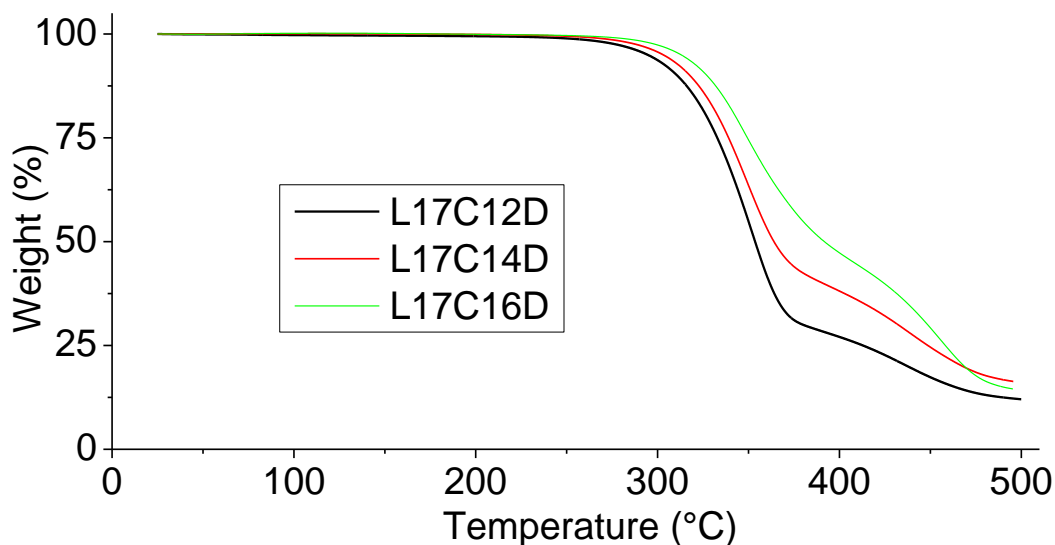


Fig. 4.56 TGA of the **L17CxM** ligand series

L18CxM

The DSCs of **L18C14M**, **L18C16M**, and **L18C18M** looked similar, showing only the one peak on each cycle, which corresponds with the melting point (Fig. 4.58), while **L18C12M** had some additional peak on the cooling cycle (Fig. 4.57).

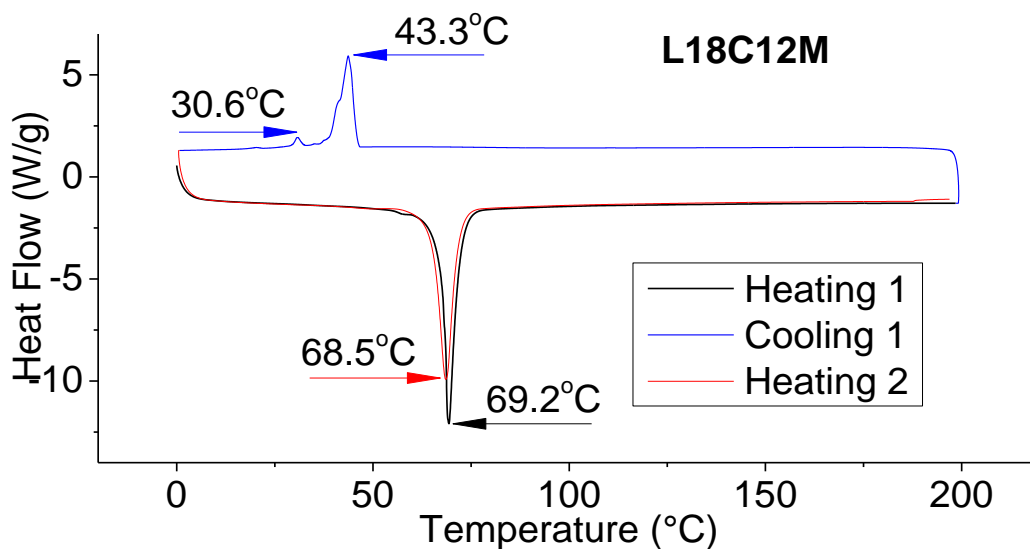


Fig. 4.57 DSC of **L18C12M**, different from the other **L18CxM** ligands

In the TGA all the **L18CxM** ligands behaved similarly, with mass loss starting above ca 220 °C, with a direct correlation between the alkyl chain length and the thermal stability of the ligand (Fig. 4.59).

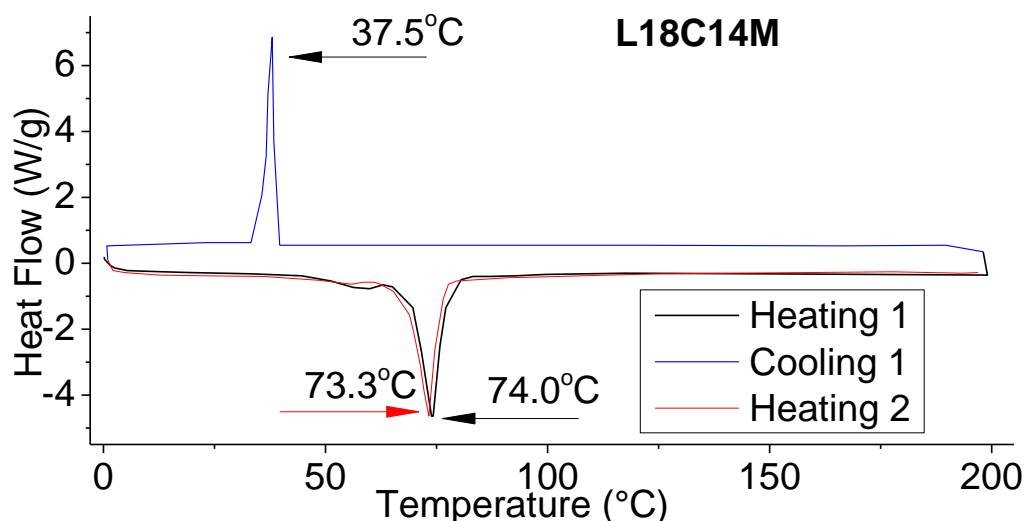


Fig. 4.58 DSC of **L18C14M**, typical for the **L18CxM** series

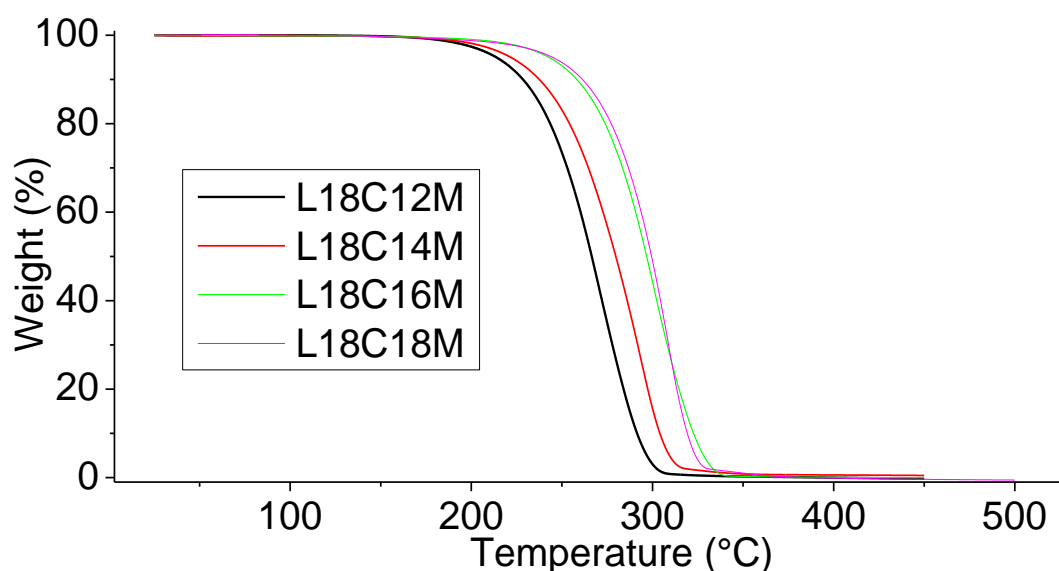


Fig. 4.59 TGA of the **L18CxM** ligand series

L18CxD

The DSCs of **L18CxD** ligands looked similar, showing a peak for melting of the ligand on each cycle. **L18C12D** and **L18C14D** also had a doubling of the peak on the cooling cycle, with a 9° and 3° difference between the peak parts correspondingly (Fig. 4.60), while **L18C16D** didn't have this feature on the cooling cycle. Also, there was annealing observed for **L18C12D**, when the sample was heated to 250°C , so after the first heating cycle there were no significant peaks observed on the consecutive cycles (Fig. 4.61), which is consistent with its TGA (Fig. 4.62). Please note, that for the **L11Cx** and **L13Cx** ligands from the previous chapter there was no annealing observed for the ligands upon heating to 250°C , only for the iron complexes (Chapter 3.7.1). The TGA shows that the **L18C12D** ligands are stable below about 170°C . Interestingly, unlike for the other ligand series, this one doesn't have

a direct correlation between the alkyl chain length and the ligand thermal stability (Fig. 4.62).

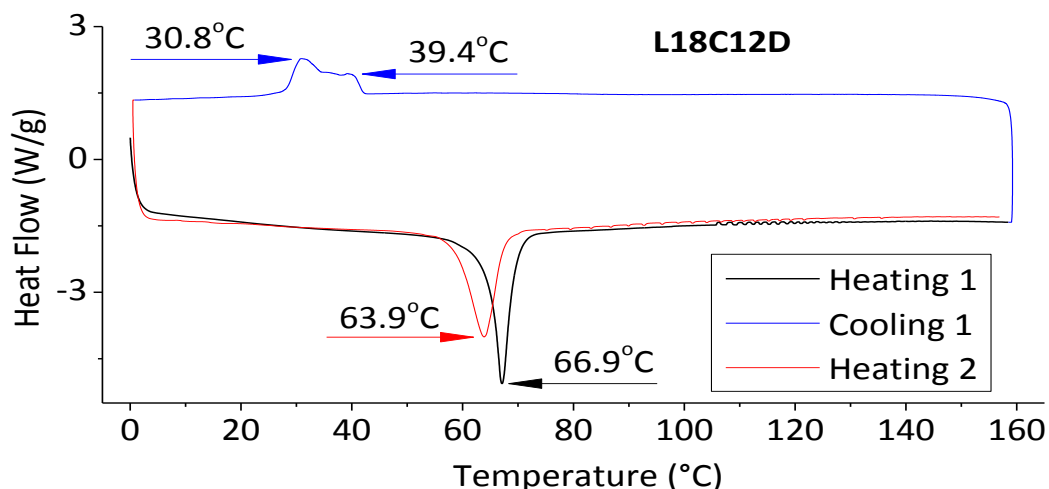


Fig. 4.60 DSC of L18C12D, typical for the L18Cx_D series

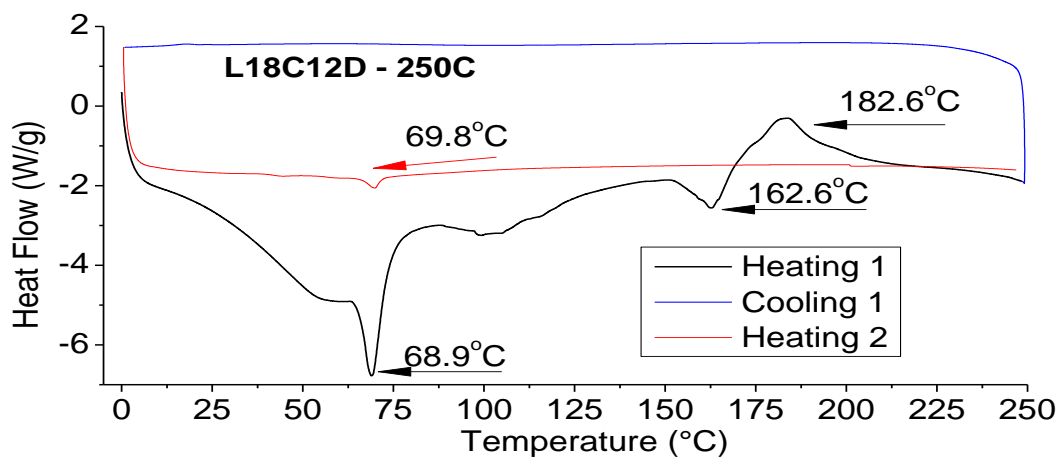


Fig. 4.61 DSC of L18C12D showing annealing upon heating above 250°C

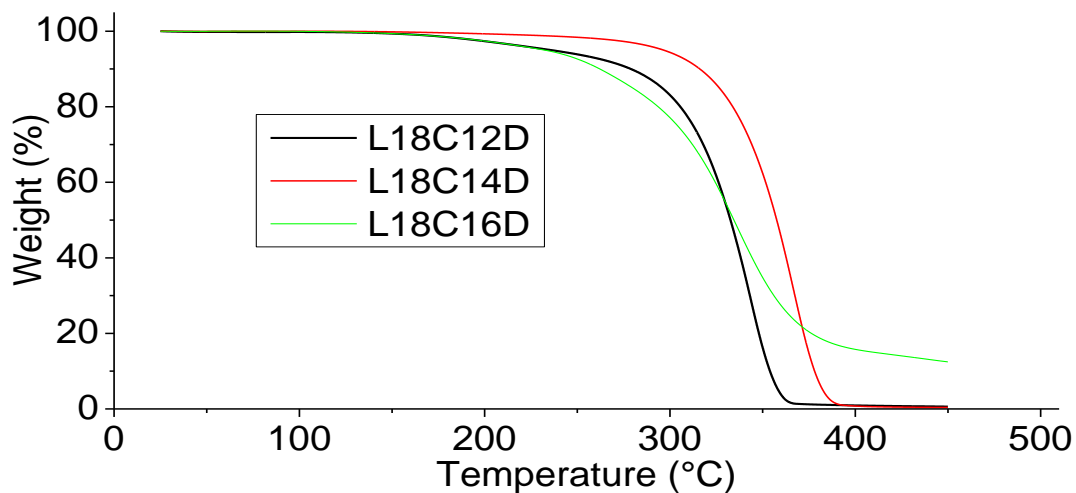


Fig. 4.62 TGA of the L18Cx_D ligand series

4.8.2 Iron complexes

[Fe(L17CxM)₂][BF₄]₂

For [Fe(L17C12M)₂][BF₄]₂ there were no DSC peaks observed on any of the cycles (Fig. 4.63), which may be explained by the fact that its T_{1/2} lays at ca 253 K or -20°C, below the measurement range of this DSC (Fig. 4.43). [Fe(L17C14M)₂][BF₄]₂ had one peak on each DSC cycle, which probably comes from the SCO transition (Fig. 4.43), which therefore had T_{1/2} at ca 24°C or 297°C (Fig. 4.64).

The DSC of Fe(L17C16M)₂][BF₄]₂ also had one peak on each cycle (Fig. 4.65), but at ca 60 K higher than [Fe(L17C14M)₂][BF₄]₂. On the other hand, the DSC peaks of [Fe(L17C18M)₂][BF₄]₂ appeared just at ca 2 K higher than for [Fe(L17C16M)₂][BF₄]₂. It appears that [Fe(L17C16M)₂][BF₄]₂ and [Fe(L17C18M)₂][BF₄]₂ are different from the previous two iron complexes. This suggestion can be also supported with the fact that they are isostructural (Table 4.43). As the SQUID graphs show that [Fe(L17C16M)₂][BF₄]₂ remained HS (Fig. 4.43), and [Fe(L17C16M)₂][BF₄]₂ underwent an extremely gradual SCO with T_{1/2} at ca -34°C (Fig. 4.44), the observed DSC couldn't come from a SCO transition. These peaks also did not come from melting of the corresponding ligands, which may be formed during decomposition of the iron complexes, as these ligands melt at significantly lower temperatures (Chapter 6.4.2). The observed DSC peaks may be caused by phase transitions.

On the TGA of [Fe(L17C18M)₂][BF₄]₂ there is some mass loss between 70°C and 120°C, which reached 5.2% at 120°C (Fig. 4.67), which corresponds with the loss of 3.5 water molecules per mole of the iron complex, and on its DSC there is a small broad peak at ca 120°C on the first heating cycle (Fig. 4.66), which probably comes from the same process. In the crystal structure of [Fe(L17C18M)₂][BF₄]₂, however, there was no lattice solvent present (Fig. 4.31). As the TGA was collected soon after obtaining the iron complex, and the crystal structure was collected about 3 months later, the lattice solvent might just evaporate from the sample. The rest of the compounds from this series were not losing any mass until about 225°C (Fig. 4.67).

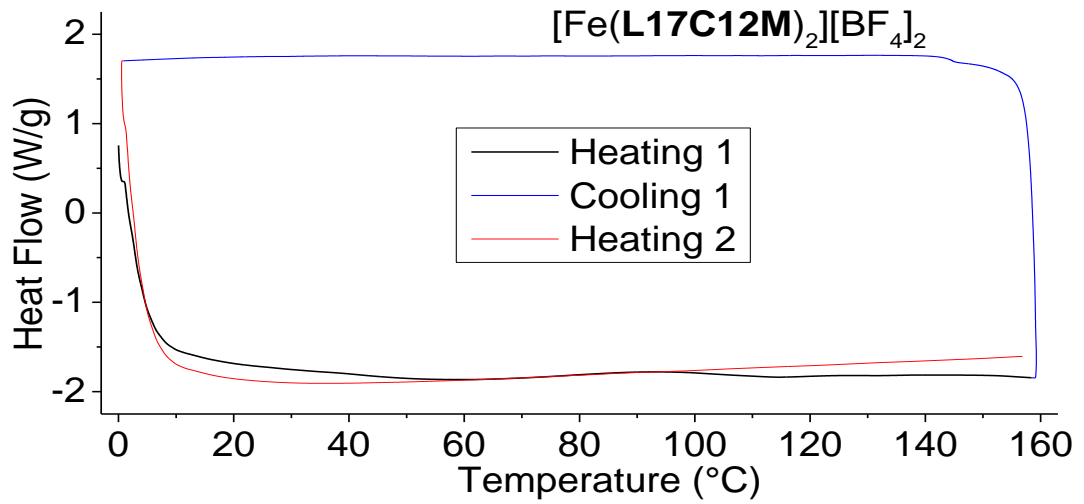


Fig. 4.63 DSC of $[\text{Fe}(\text{L17C12M})_2][\text{BF}_4]_2$

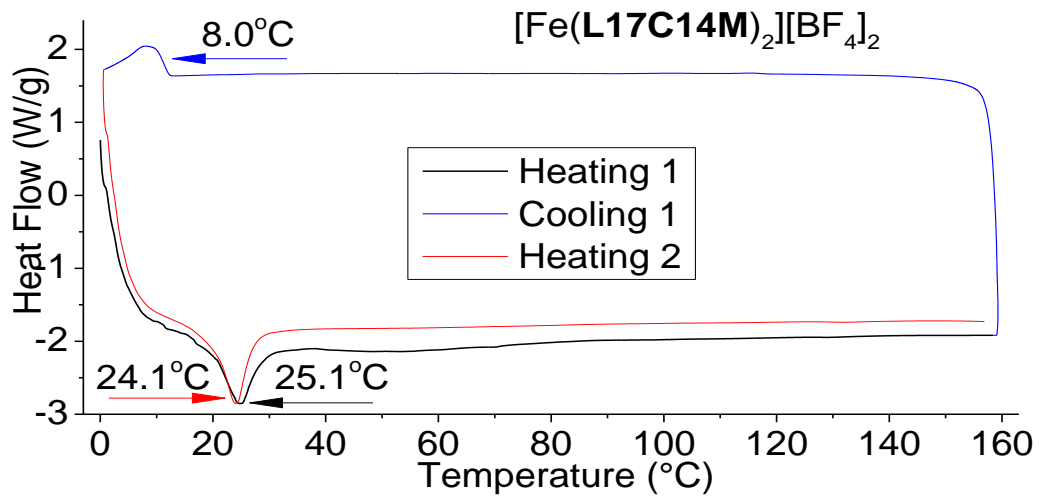


Fig. 4.64 DSC of $[\text{Fe}(\text{L17C14M})_2][\text{BF}_4]_2$

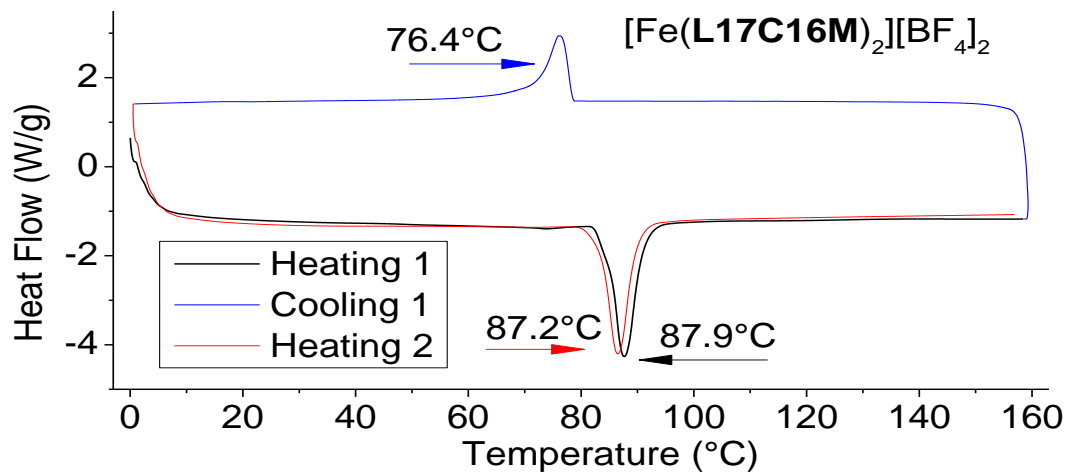


Fig. 4.65 DSC of $[\text{Fe}(\text{L17C16M})_2][\text{BF}_4]_2$

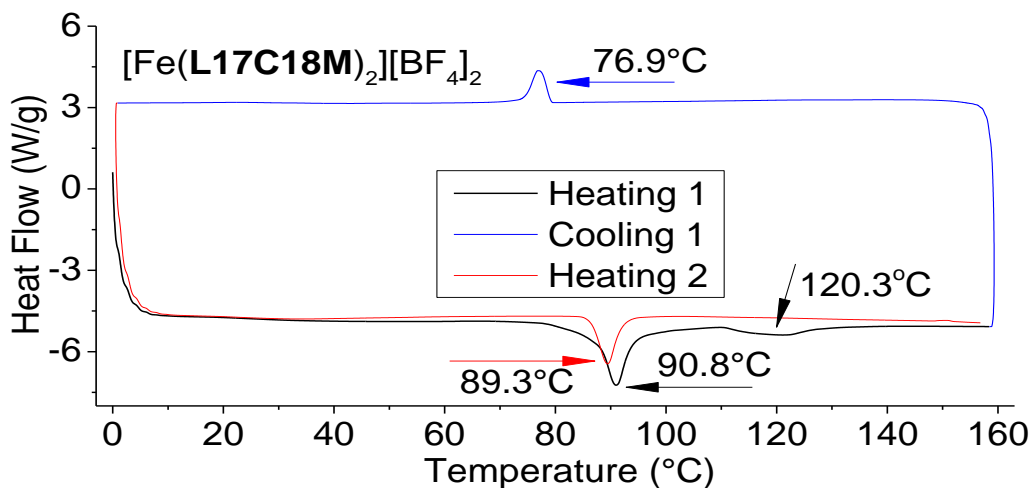


Fig. 4.66 DSC of $[\text{Fe}(\text{L17C18M})_2][\text{BF}_4]_2$

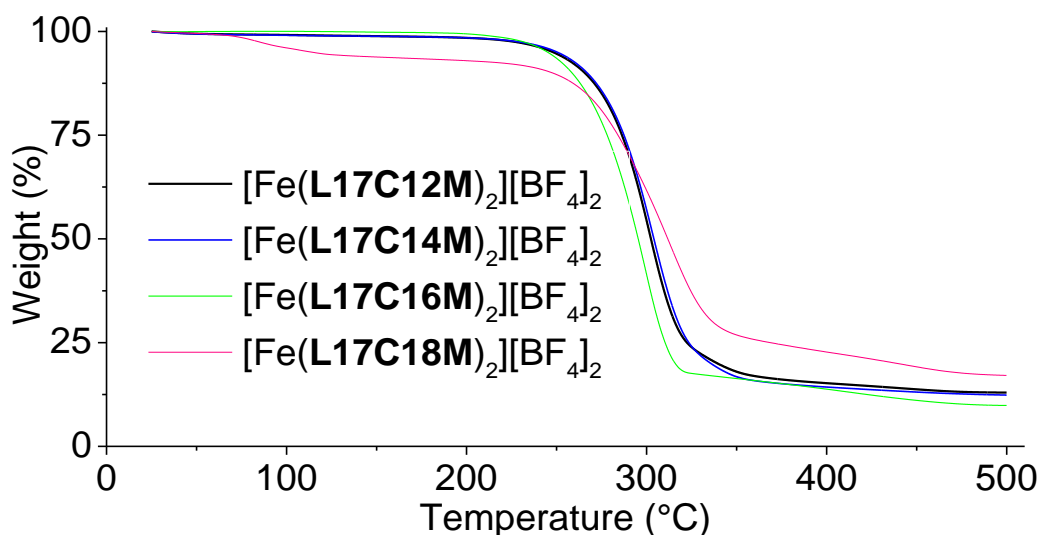


Fig. 4.67 TGA of the $[\text{Fe}(\text{L17CxM})_2][\text{BF}_4]_2$ series iron complexes

$[\text{Fe}(\text{L17CxD})_2][\text{BF}_4]_2$

Unlike other iron complexes series, $[\text{Fe}(\text{L17CxD})_2][\text{BF}_4]_2$ turned noticeably paler with time. The strongest effect was observed for $[\text{Fe}(\text{L17C12D})_2][\text{BF}_4]_2$. All three $[\text{Fe}(\text{L17CxD})_2][\text{BF}_4]_2$ iron complexes had one peak on each DSC cycle: $[\text{Fe}(\text{L17C12D})_2][\text{BF}_4]_2$ at ca 81°C or 354 K (Fig. 4.68), $[\text{Fe}(\text{L17C14D})_2][\text{BF}_4]_2$ at ca 62°C or 335 K (Fig. 4.69), and $[\text{Fe}(\text{L17C16D})_2][\text{BF}_4]_2$ at ca 95°C or 368 K. However, on their SQUID magnetic measurements there were no sign of SCO transition, as all three iron complexes remained HS (Fig. 4.45), therefore the observed DSC peaks must come from some other transitions. These iron complexes decompose at 265–280°C without melting, therefore the DSC peaks cannot come from melting of the sample. The melting points of the corresponding ligands: 80.9°C for **L17C12D**, 84.9–85.5°C for **L17C14D**, and 89.4–89.7°C for **L17C16D** (Chapter 6.4), closely match the observed peaks for these iron complexes, except $[\text{Fe}(\text{L17C14D})_2][\text{BF}_4]_2$.

Therefore, it may be concluded, that most likely all the $[\text{Fe}(\text{L17CxD})_2][\text{BF}_4]_2$ iron complexes were HS, but were not stable, and partially decomposed when stored. The formed ligand fraction gave a peak on the DSC. On the powder patterns of these iron complexes (Fig. 4.40) there are no significant peaks that may correspond with the ligands (Fig. 4.35), therefore the formed ligand fraction is either non-crystalline or very small.

$[\text{Fe}(\text{L17C12D})_2][\text{BF}_4]_2$ and $[\text{Fe}(\text{L17C14D})_2][\text{BF}_4]_2$ also had some additional very broad and small peaks solely on the first heating cycle, which must come from escaping lattice solvent. This mass loss is also visible on the TGA for these two iron complexes (Fig. 4.71), and $[\text{Fe}(\text{L17C16D})_2][\text{BF}_4]_2$ didn't have any signs of the lattice solvent loss neither on TGA, nor on DSC (Fig. 4.70).

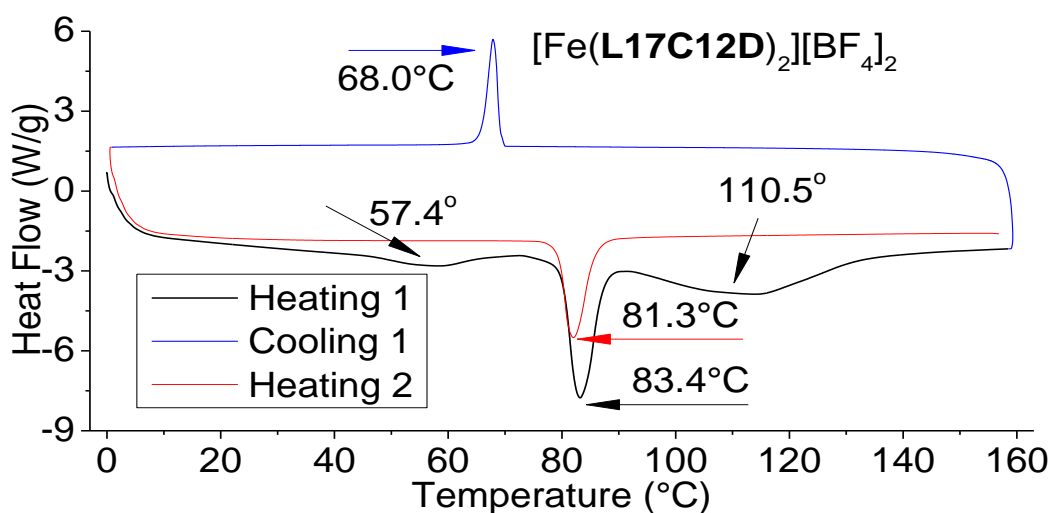


Fig. 4.68 DSC of $[\text{Fe}(\text{L17C12D})_2][\text{BF}_4]_2$

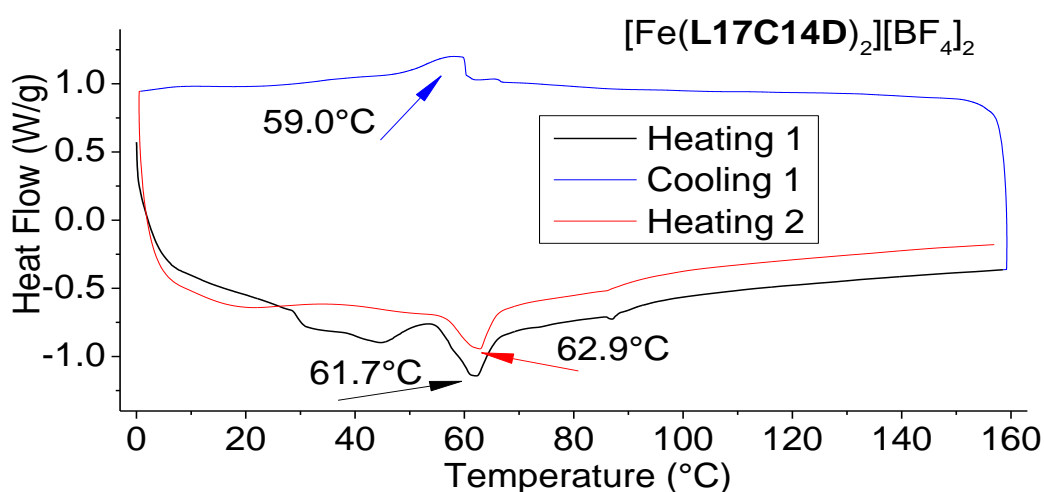


Fig. 4.69 DSC of $[\text{Fe}(\text{L17C14D})_2][\text{BF}_4]_2$

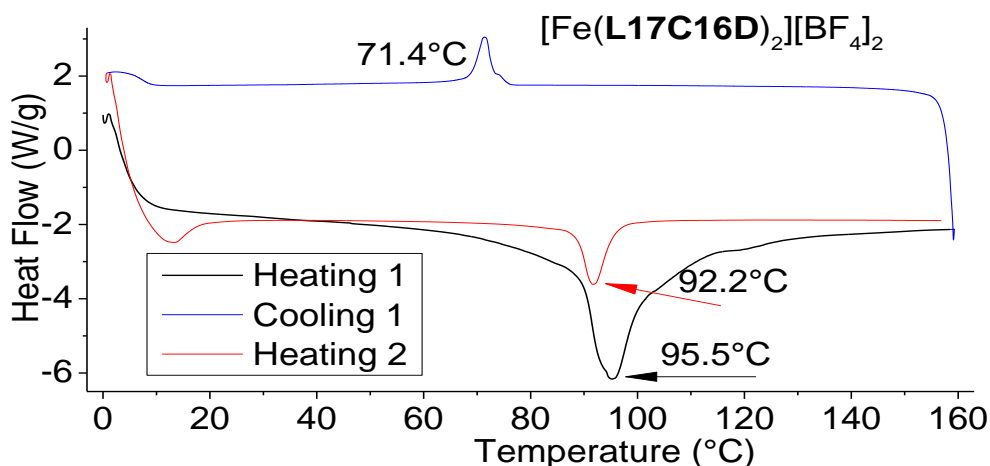


Fig. 4.70 DSC of $[\text{Fe}(\text{L17C16D})_2][\text{BF}_4]_2$

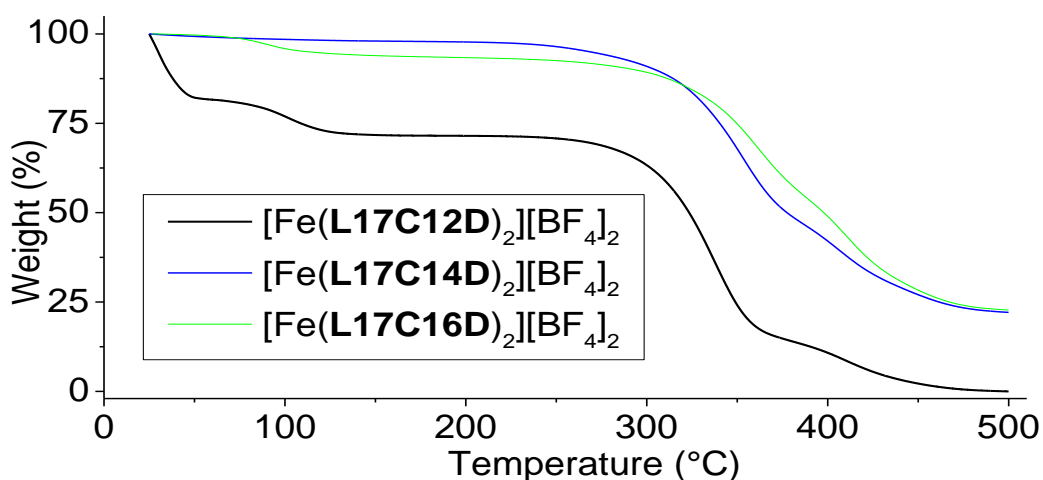


Fig. 4.71 TGA of the $[\text{Fe}(\text{L17CxM})_2][\text{BF}_4]_2$ series iron complexes

$[\text{Fe}(\text{L18CxM})_2][\text{BF}_4]_2$

Each iron complex from the $[\text{Fe}(\text{L18CxM})_2][\text{BF}_4]_2$ series has one peak on each DSC cycle (Fig. 4.72, 4.73, 4.74, and 4.75). These peaks cannot come from the SCO transition, as all the $[\text{Fe}(\text{L18CxM})_2][\text{BF}_4]_2$ iron complexes underwent SCO with $T_{1/2}$ at ca 160 K or -113°C (Fig. 4.47), which is below the minimum measurement temperature for the DSC machine of ca 200 K. They are also very different from the melting points of the corresponding ligands (Fig. 4.58), and therefore these DSC peaks must come from some other phase transitions, which take place for all the iron complexes in this series, and the temperature of this transition is higher for longer alkyl chain compounds. This transition might be a rearrangement of the long alkyl chains' position. $[\text{Fe}(\text{L17C16M})_2][\text{BF}_4]_2$ and $[\text{Fe}(\text{L17C18M})_2][\text{BF}_4]_2$ are both isostructural with $[\text{Fe}(\text{L18C18M})_2][\text{BF}_4]_2$, and unlike other iron complexes in the $[\text{Fe}(\text{L17CxM})_2][\text{BF}_4]_2$ series, they also show the DSC peaks, which may be explained by the long alkyl chains rearrangement (Fig. 4.65 and 4.66).

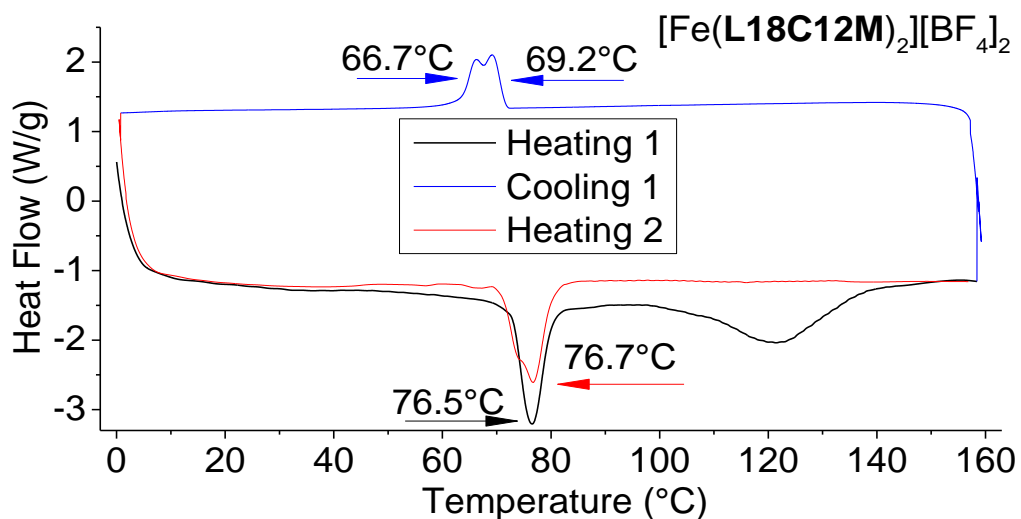


Fig. 4.72 DSC of [Fe(L18C12M)₂][BF₄]₂

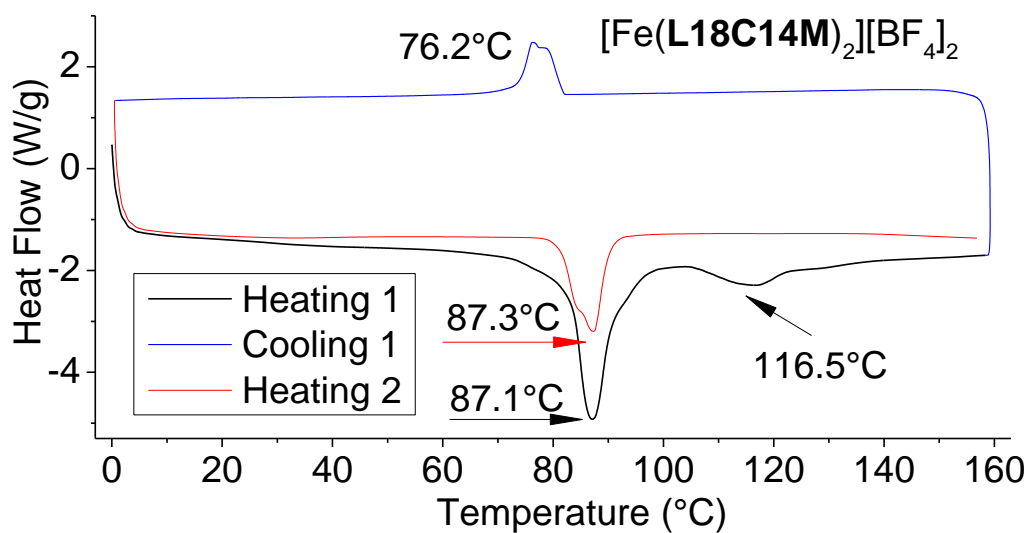


Fig. 4.73 DSC of [Fe(L18C14M)₂][BF₄]₂

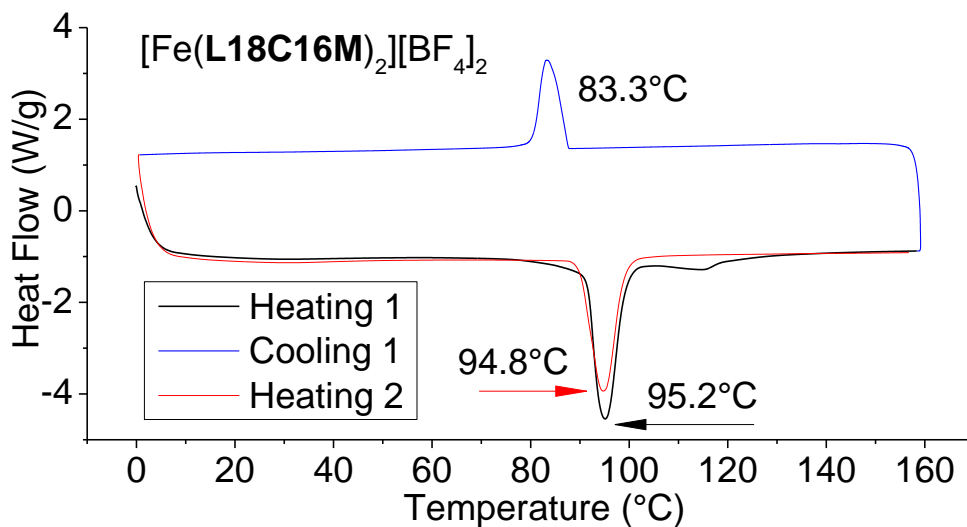


Fig. 4.74 DSC of [Fe(L18C16M)₂][BF₄]₂

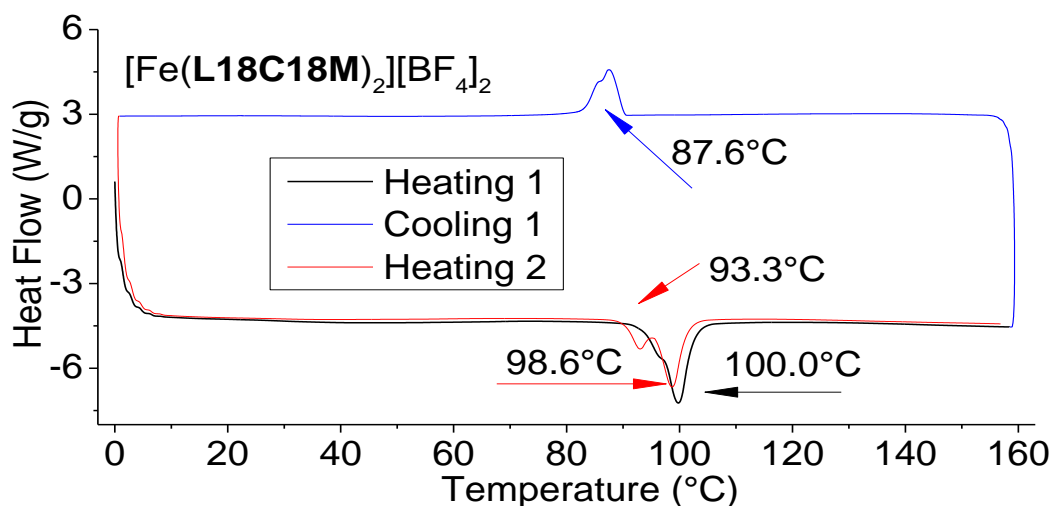


Fig. 4.75 DSC of $[\text{Fe}(\text{L18C18M})_2][\text{BF}_4]_2$

On the first heating cycle DSCs of $[\text{Fe}(\text{L18C12M})_2][\text{BF}_4]_2$ (Fig. 4.72) and $[\text{Fe}(\text{L18C14M})_2][\text{BF}_4]_2$ (Fig. 4.73) there are some broad and small peaks present, which must come from loss of the lattice solvent, probably water. For the same compounds there is some mass loss observed by TGA at ca 70°C and 94°C (Fig. 4.76).

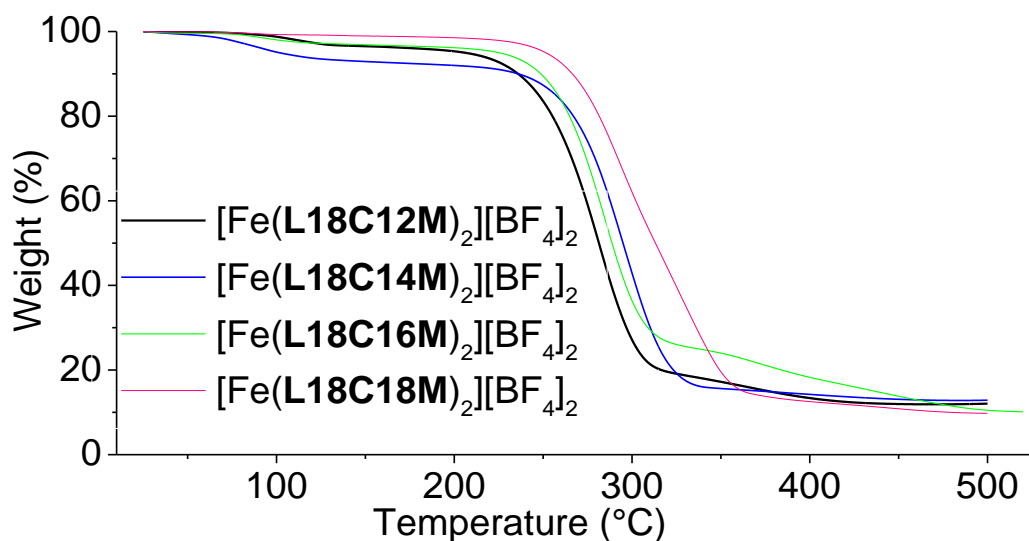


Fig. 4.76 TGA of the $[\text{Fe}(\text{L18CxM})_2][\text{BF}_4]_2$ series iron complexes

$[\text{Fe}(\text{L18CxD})_2][\text{BF}_4]_2$

All three $[\text{Fe}(\text{L18CxD})_2][\text{BF}_4]_2$ iron complexes had similar behaviour on DSC: one peak on the first heating cycle, and two peaks on the consecutive cycles (Fig. 4.77, 4.78, and 4.79). This behaviour correspond with their SQUID curves. $[\text{Fe}(\text{L18C12D})_2][\text{BF}_4]_2$ had one peak at 75°C (Fig. 4.77) or 348 K , which corresponds with its first two SQUID cycles (Fig. 4.49). Then some irreversible changes happen to the sample upon heating above 370 K , and the sample starts switching at a lower temperature on all the

consecutive cycles. The same effect can be observed for $[\text{Fe}(\text{L18C14D})_2][\text{BF}_4]_2$ (Fig. 4.78), which corresponds with the changes on its SQUID graph (Fig. 4.50). The same process can be observed on the DSC of $[\text{Fe}(\text{L18C16D})_2][\text{BF}_4]_2$, but its first peak appears at a higher temperature, ca 84°C or 357, which is above the measured SQUID values for this sample. However, it can be seen that the sample was starting switching to HS above ca 275 K, which shall reach its $T_{1/2}$ at ca 357 K (Fig. 4.51), judging by its DSC (Fig. 4.79) and comparing it to the other iron complexes from this series. In the TGA $[\text{Fe}(\text{L18C12D})_2][\text{BF}_4]_2$ lost ca 1.5% mass at 67°C, which must come from a lattice solvent, $[\text{Fe}(\text{L18C14D})_2][\text{BF}_4]_2$ lost ca 3% at 195°C, and finally all the iron complexes from this series started rapid mass loss at ca 275°C (Fig. 4.80).

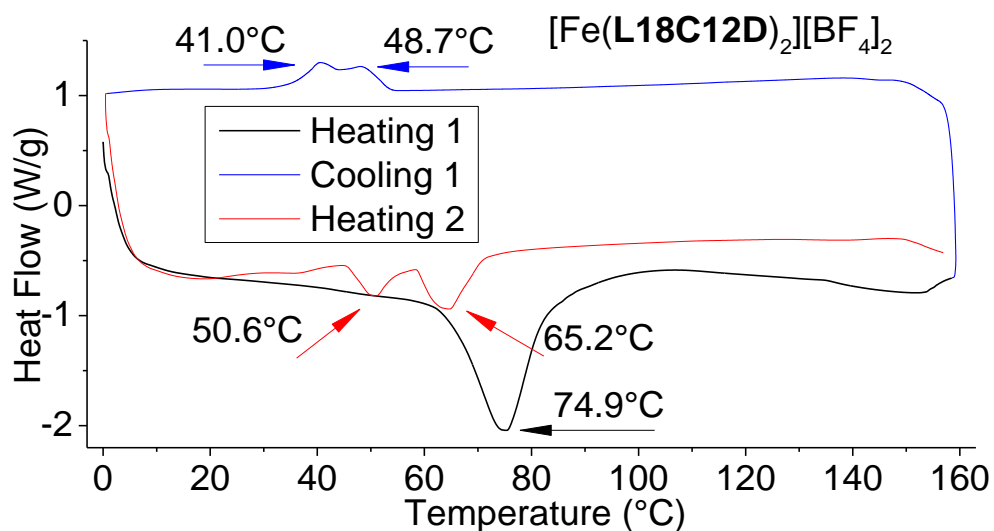


Fig. 4.77 DSC of $[\text{Fe}(\text{L18C12D})_2][\text{BF}_4]_2$

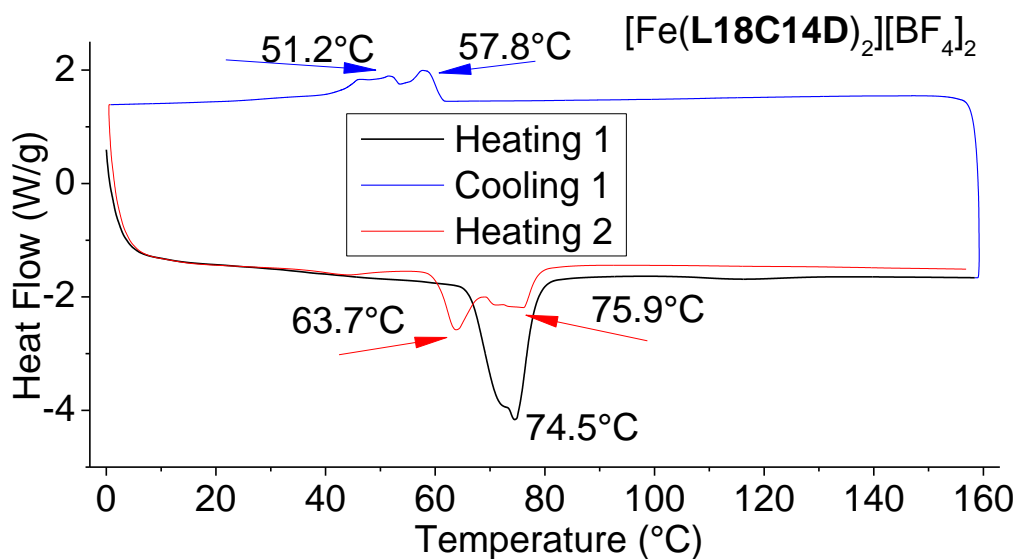


Fig. 4.78 DSC of $[\text{Fe}(\text{L18C14D})_2][\text{BF}_4]_2$

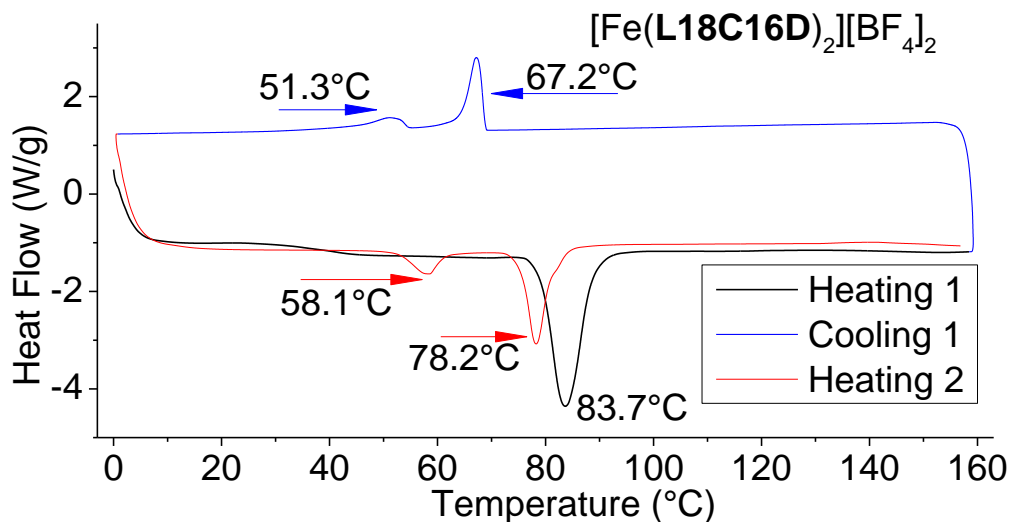


Fig. 4.79 DSC of $[\text{Fe}(\text{L18C16D})_2][\text{BF}_4]_2$

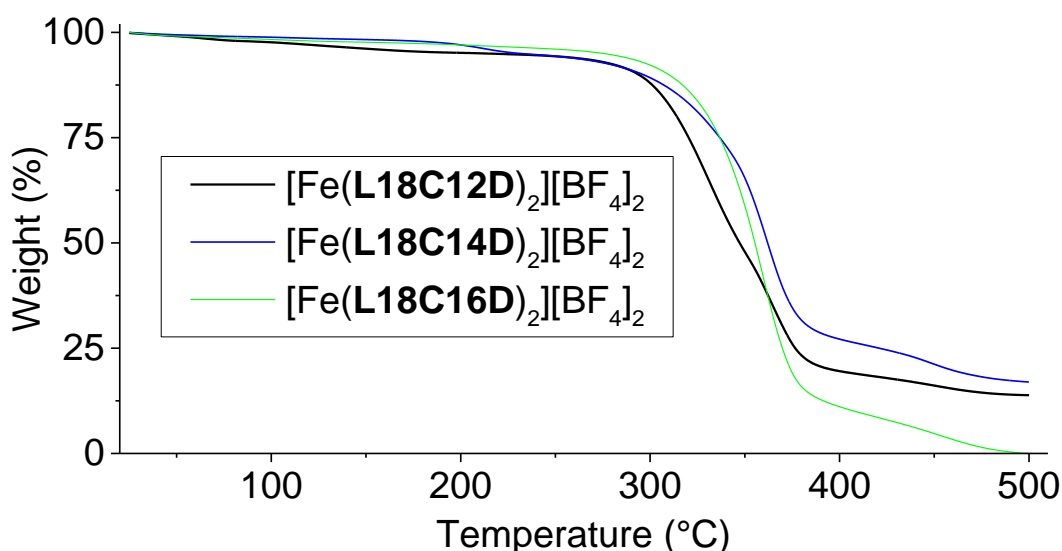


Fig. 4.80 TGA of the $[\text{Fe}(\text{L18CxD})_2][\text{BF}_4]_2$ series iron complexes

4.9 VT images

The iron complexes from the $[\text{Fe}(\text{L18CxM})_2][\text{BF}_4]_2$ series were heated in an oil bath, and photographed every 20 K, in order to track any phase changes, or a colour change, associated with spin crossover (Fig. 4.81). The same experiment was performed for different iron complexes in Chapter 3.8. All the $[\text{Fe}(\text{L18CxM})_2][\text{BF}_4]_2$ iron complexes were pale-yellow plate crystals, and didn't show any phase change all the way up to 170 $^{\circ}\text{C}$. Heating to 170 $^{\circ}\text{C}$ also didn't do any noticeable change to their powder patterns (Fig. 4.40). Between 140 $^{\circ}$ and 160 $^{\circ}\text{C}$ they all changed their colour to a darker yellow (Fig. 4.81).

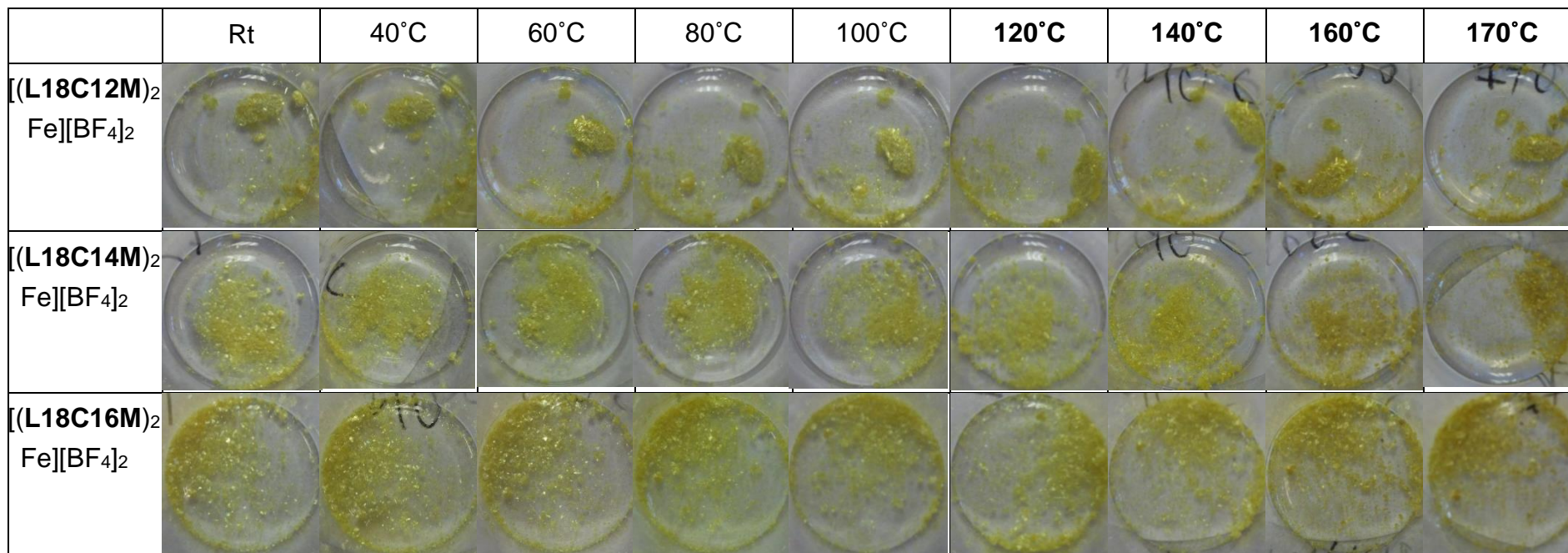


Fig. 4.81 The photographs of $[(L18CxM)_2Fe][BF_4]_2$ iron complexes, as they are being heated from room temperature to 170°C

4.10 Evans method NMR

Evans method NMR was measured only for one iron complex from this chapter, for $[\text{Fe}(\text{L18C16M})_2][\text{BF}_4]_2$. As expected, in solution it undergoes gradual SCO (Fig. 4.82). Unlike the pyridyl-substituted iron complexes from the previous chapters, which were undergoing SCO in solution with $T_{1/2}$ at ca 300K (Fig. 2.35 and 3.46), the pyrazolyl-substituted iron complex shows SCO with $T_{1/2}$ at 255K. Therefore it may be expected that the pyrazolyl-substituted bpp iron(II) complexes should also be HS at lower temperatures in solid state, as observed.

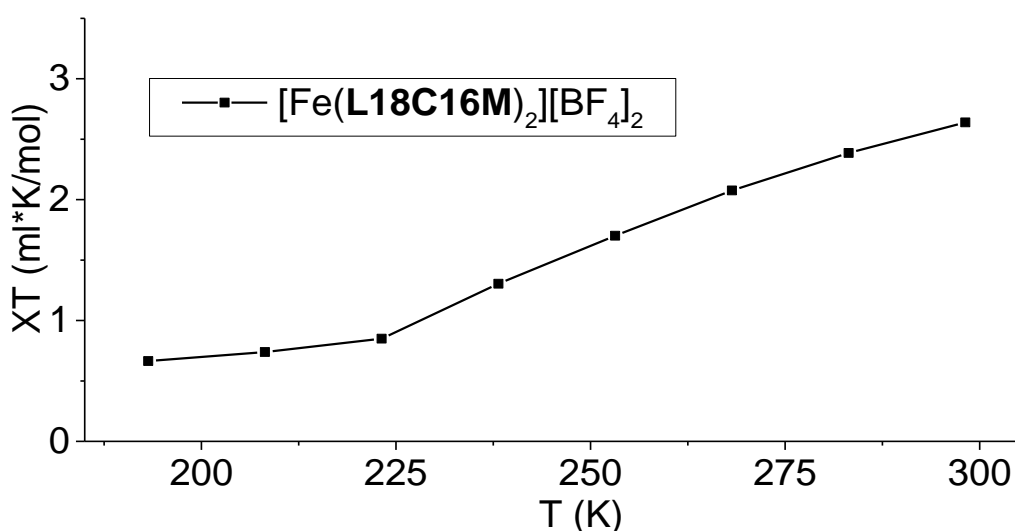


Fig. 4.82 Evans method NMR of $[\text{Fe}(\text{L18C16M})_2][\text{BF}_4]_2$, measured in $\text{Me}_2\text{CO}-\text{D}_6$

4.11 Paramagnetic NMR

Iron complexes of precursor ligands

As expected, the paramagnetic NMR spectra of $[\text{Fe}(\text{L16})_2][\text{BF}_4]_2$ and $[\text{Fe}(\text{L16})_2][\text{ClO}_4]_2$ looked identical (Fig. 4.83). The samples had poor solubility in chloroform, so the analyses were run in $\text{MeCN}-\text{D}_3$. The paramagnetically shifted peaks were assigned, and the full peaks assignment can be found in Chapter 6.4.6. The peaks that are closest to the iron centre are most shifted downfield. The least shifted peak, which is located at 1.1 ppm, belongs to the Py H4 hydrogen, the 57.8 ppm peak comes from the PzB H4 hydrogen, and the remaining peaks are assigned in pairs of barely distinguishable signals (Chapter 6.4.6). This peaks assignment is consistent with the results, obtained for similar bpp iron(II) complexes by L. Kershaw Cook in his PhD thesis⁵.

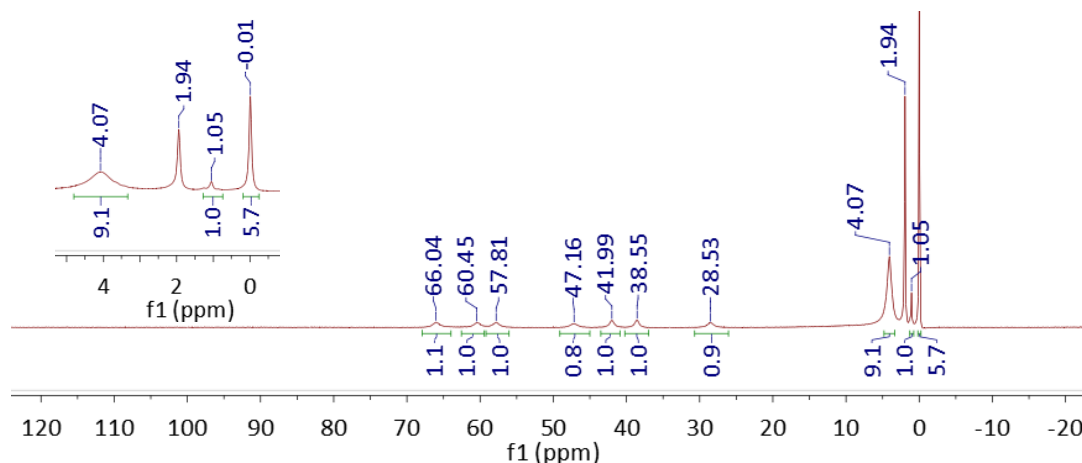


Fig. 4.83 Paramagnetic NMR of $[\text{Fe}(\text{L16})_2][\text{BF}_4]_2$, with extension, identical to $[\text{Fe}(\text{L16})_2][\text{ClO}_4]_2$, collected in MeCN-D3

$[\text{Fe}(\text{L17CxM})_2][\text{BF}_4]_2$

The iron complexes from the $[\text{Fe}(\text{L17CxM})_2][\text{BF}_4]_2$ series were both soluble in MeCN-D3 and in CDCl_3 , and the spectra collected in each of the solvents looked very similar, with slightly different chemical shift values. All the paramagnetic NMR spectra within the series looked identical (Fig. 4.84), and very similar to the spectrum of the asymmetric iron complex $[\text{Fe}(\text{L16})_2][\text{BF}_4]_2$ (Fig. 4.83).

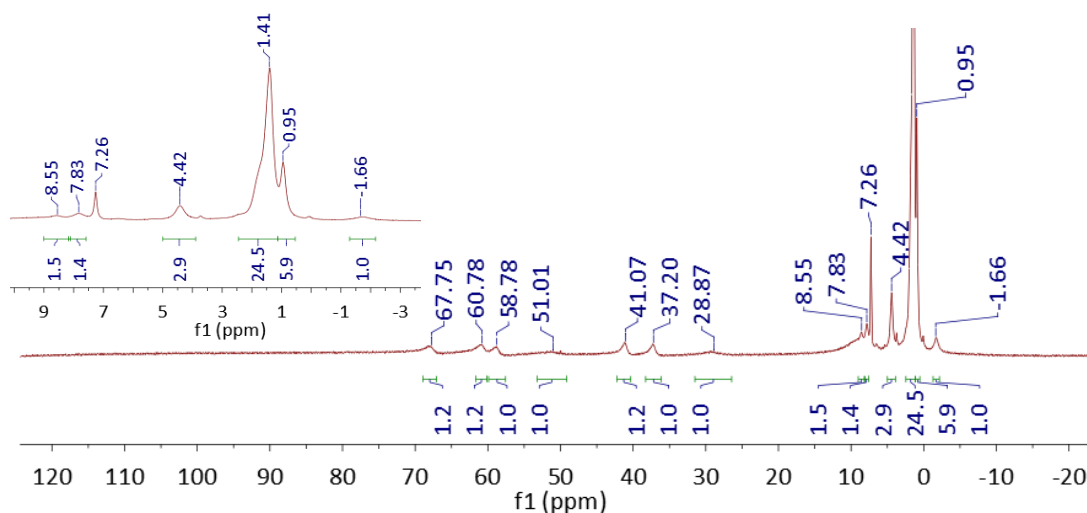


Fig. 4.84 Paramagnetic NMR of $[\text{Fe}(\text{L17C12M})_2][\text{BF}_4]_2$, with extension, typical for $[\text{Fe}(\text{L17CxM})_2][\text{BF}_4]_2$ series, collected in CDCl_3

$[\text{Fe}(\text{L17CxD})_2][\text{BF}_4]_2$

The $[\text{Fe}(\text{L17CxD})_2][\text{BF}_4]_2$ iron complexes had poor solubility in MeCN-D3, and their spectra were measured in a $\text{CDCl}_3/\text{MeCN-D3}$ 1:1 mixture. All of them looked identical, having four paramagnetically shifted peaks with 2:2:2:1 ratio (Fig. 4.85).

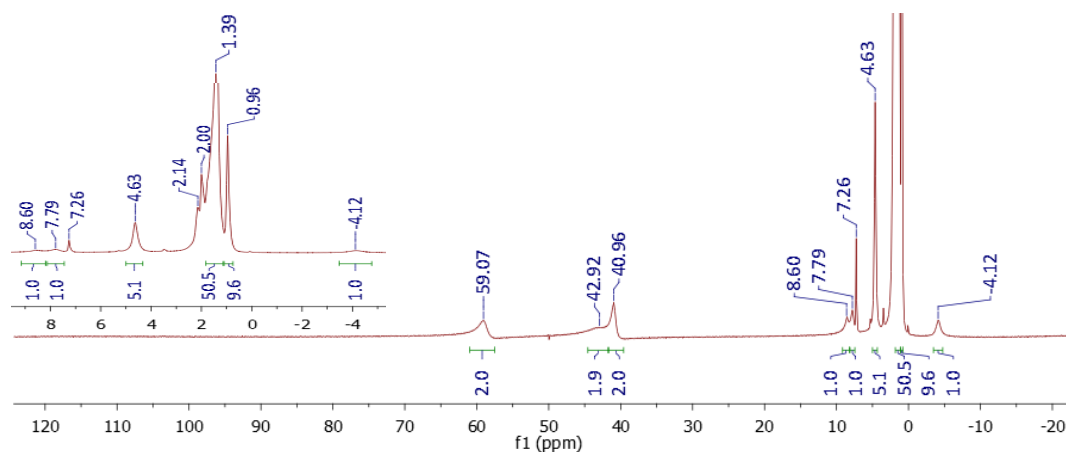


Fig. 4.85 Paramagnetic NMR of $[\text{Fe}(\text{L17C14D})_2][\text{BF}_4]_2$, with extension, typical for $[\text{Fe}(\text{L17CxM})_2][\text{BF}_4]_2$ series, collected in $\text{CDCl}_3/\text{MeCN-D}_3$ 1:1 mixture

$[\text{Fe}(\text{L18CxM})_2][\text{BF}_4]_2$

The paramagnetic NMR spectra of $[\text{Fe}(\text{L18CxM})_2][\text{BF}_4]_2$ series were measured in MeCN-D₃. All the paramagnetic spectra for this series looked identical, except for two weak additional peaks at 66.48 and 41.05 ppm, which integrated at 0.1-0.2 hydrogens, and were observed for $[\text{Fe}(\text{L18C14M})_2][\text{BF}_4]_2$ and $[\text{Fe}(\text{L18C16M})_2][\text{BF}_4]_2$, but not for $[\text{Fe}(\text{L18C12M})_2][\text{BF}_4]_2$. The paramagnetic spectra of this series and other asymmetric iron complexes resemble each other (Fig. 4.84), however for $[\text{Fe}(\text{L18CxM})_2][\text{BF}_4]_2$ some peaks were overlapping (Fig. 4.86). For example, the peak at 54.6 ppm must come from overlapping of either PzA H3 or PzB H3 signal with the PzB H4 peak. The $[\text{Fe}(\text{L18CxM})_2][\text{BF}_4]_2$ paramagnetic NMR spectra were assigned by comparing them with the spectra of the other asymmetric iron complexes, and by taking into account the peaks' integrations (Chapter 6.4.6).

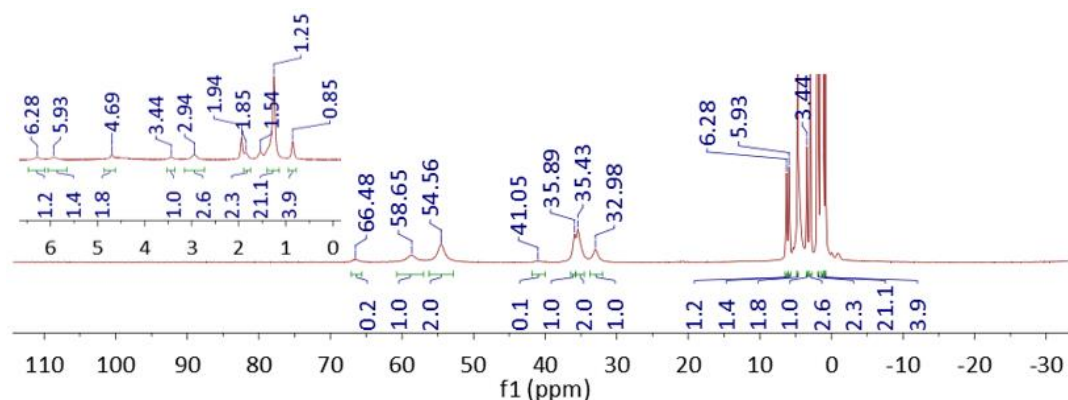


Fig. 4.86 Paramagnetic NMR of $[\text{Fe}(\text{L18C14M})_2][\text{BF}_4]_2$, with extension, typical for $[\text{Fe}(\text{L18CxM})_2][\text{BF}_4]_2$ series, collected in MeCN-D₃

[Fe(L18CxD)₂][BF₄]₂

The paramagnetic NMR spectra of the [Fe(L18CxD)₂][BF₄]₂ iron complexes were recorded in MeCN-D₃. As for the [Fe(L17CxD)₂][BF₄]₂ series, there were four paramagnetically shifted peaks, which integrate at a 2:2:2:1 ratio (Fig. 4.87), but are slightly less shifted downfield.

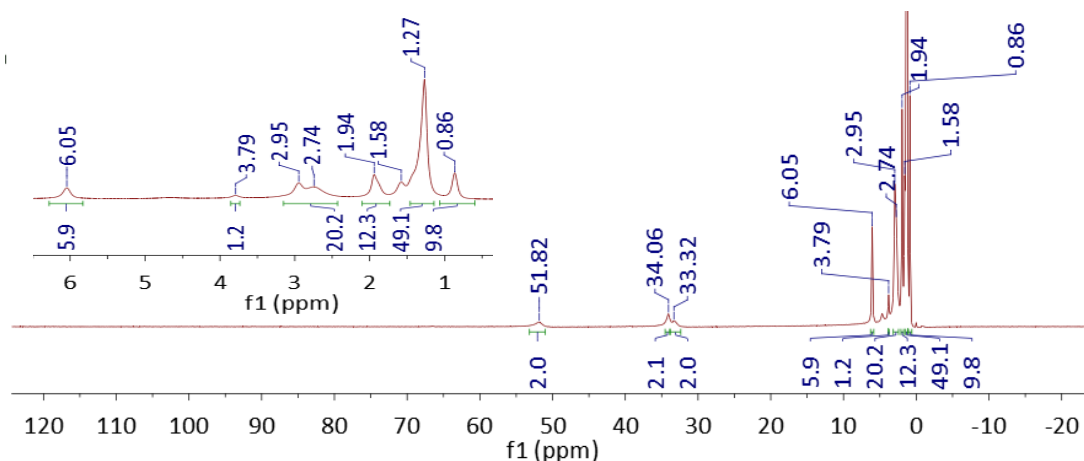


Fig. 4.87 Paramagnetic NMR of [Fe(L18C14D)₂][BF₄]₂, with extension, typical for [Fe(L18CxD)₂][BF₄]₂ series, collected in MeCN-D₃

4.12 Conclusions

Pyrazolyl-substituted 1,4-bis[2,6-di(1H-pyrazole-1'-yl)pyridine derivative ligands and their iron complexes were obtained, analysed, and discussed in this chapter. All the long alkyl chain ligands, and some of the precursor ligands with no long alkyl chains from this chapter are novel. There were four series of long alkyl chain ligands obtained: unsaturated monosubstituted **L17CxM**, unsaturated disubstituted **L17CxD**, saturated monosubstituted **L18CxM**, and saturated disubstituted **L18CxD**, with the twelve, fourteen, and sixteen-carbon chain ligands in each. The eighteen-carbon chain ligands were obtained only for **L17CxM** and **L18CxM** series.

All these iron complexes either remained HS from 300 to 3 K, or shown spin crossover. The [Fe(L17CxM)₂][BF₄]₂ iron complexes with twelve and fourteen carbon chains underwent a gradual SCO, with a part of the sample remaining HS, and this spin transition produced a peak on DSC. The iron complexes with sixteen and eighteen carbon chains were isostructural, and both underwent some possible phase transitions, which can be seen on their DSCs. The [Fe(L17CxD)₂][BF₄]₂ series iron complexes all remained HS, while the [Fe(L18CxM)₂][BF₄]₂ iron complexes underwent an interesting SCO switching with HS trapping and release, which caused unusual decrease of the magnetic moment upon heating. The same effect was

observed by Weihermüller for long alkyl chain ester iron complexes,⁶ and to a smaller extent by Lee for iron complexes with branched long alkyl chains.⁷ This effect was more pronounced for longer alkyl chain iron complexes, and was also tracked by XRD. The [Fe(**L18CxD**)₂][BF₄]₂ series underwent SCO with annealing after the first heating cycle on SQUID, and the same effect was also observed on its DSC.

Besides being isostructural, [Fe(**L17C18M**)₂][BF₄]₂ and [Fe(**L18C18M**)₂][BF₄]₂ undergo different SCO: [Fe(**L17C18M**)₂][BF₄]₂ switches very gradually, with T_{1/2} at ca 360 K, and no hysteresis, while [Fe(**L18C18M**)₂][BF₄]₂ undergoes a two-step SCO, with a quite abrupt SCO with T_{1/2} at ca 150 K, and an about 14 K hysteresis, along with a more gradual second step switching at ca 350 K.

In the solution the pyrazolyl-substituted iron complexes shown switching at ca 225 K, which is around 65 K lower than the pyridyl-substituted iron complexes from Chapters 2 and 3.

List of References

1. Pritchard, R.; Lazar, H.; Barrett, S.A.; Kilner, C.A.; Asthana, S.; Carbonera, C.; Letard, J.F. and Halcrow, M.A. Thermal and light-induced spin-transitions in iron(II) complexes of 2,6-bis(4-halopyrazolyl)pyridines: the influence of polymorphism on a spin-crossover compound. *Dalton Trans.* **2009**, 6656-6666.
2. Basak, S.; Hui, P.; Boodida, S. and Chandrasekar, R. Micropatterning of Metallopolymers: Syntheses of Back-to-Back Coupled Octylated 2,6-Bis(pyrazolyl)pyridine Ligands and Their Solution-Processable Coordination Polymers. *J. Org. Chem.* **2012**, *77*, 3620-3626.
3. NMR prediction tool online. <http://www.nmrdb.org>
4. Buchen, T.; Gütllich, P.; Sugiyarto, K. H.; Goodwin, and H. A. High-Spin \rightarrow Low-Spin Relaxation in $[\text{Fe}(\text{bpp})_2](\text{CF}_3\text{SO}_3)_2 \cdot \text{H}_2\text{O}$ after LIESST and Thermal Spin-State Trapping—Dynamics of Spin Transition Versus Dynamics of Phase Transition. *Chem. Eur. J.* **1996**, *2*, 1134-1138.
5. Kershaw Cook, L. J. Crystal Engineering and Bifunctionality in Spin-Crossover Materials. PhD Thesis. *University of Leeds.* **2014**.
6. Weihermüller, J.; Schlamp, S.; Dittrich, B. and Weber, B. Kinetic Trapping Effects in Amphiphilic Iron(II) Spin Crossover Compounds. *Inorg. Chem.* **2019**, *58*, 1278–1289.
7. Lee, Y.H.; Ohta, A.; Yamamoto, Y.; Komatsu, Y.; Kato, K.; Shimizu, T.; Shinoda, H.; Hayami, S. Iron(II) spin crossover complexes with branched long alkyl chain. *Polyhedron.* **2011**, *30*, 3001-3005.

Chapter 5

Asymmetric ligands with no long alkyl chains, and their iron(II) complexes

5.1 Introduction

In the previous chapter a series of asymmetric ligands was obtained: **L16**, **L17CxM**, and **L18CxM** (Fig. 4.1). Some of their Fe²⁺ complexes showed interesting SCO behaviour, such as thermal HS trapping, and many of them also readily formed crystallography quality single crystals. Therefore, research in this direction was continued, and attempts were made to obtain other asymmetric ligands. The starting material for these syntheses, 2-fluoro-6-(1*H*-pyrazol-1-yl)pyridine **L14**, was obtained previously in Chapter 4.2.1 (Fig. 4.3).

Chandrasekar *et al.* obtained three novel asymmetric ligands and their Fe²⁺ complexes, one of which shown an interesting SCO behaviour, with the switching around room temperature and a ca 10 K hysteresis (Fig. 5.1).¹ Similar novel asymmetric ligands with pyrazole and triazole rings were obtained and discussed in this chapter (Fig. 5.2).

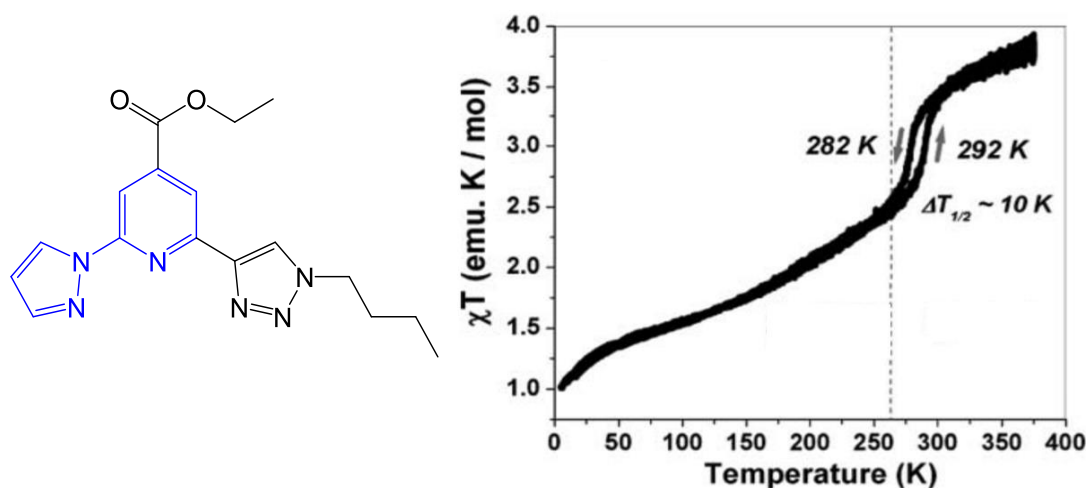


Fig. 5.1 An asymmetric ligand, obtained by Chandrasekar *et al.*, and its magnetic behaviour¹

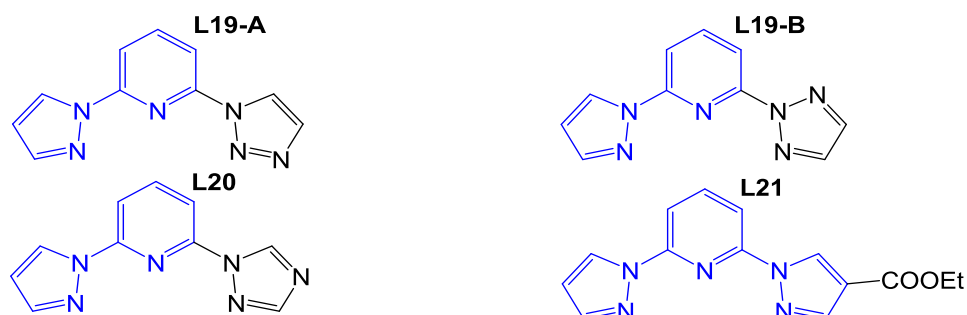


Fig. 5.2 List of the ligands discussed in Chapter 5

5.2 Ligand synthesis

L19 – Two isomers of 2-(1H-pyrazol-1-yl)-6-(1H-1,2,3-triazol-1-yl)pyridine

The reaction between 2-fluoro-6-(1H-pyrazol-1-yl)pyridine **L14** and 1H-1,2,3-triazole yielded the asymmetric ligand **L19** 2-(1H-pyrazol-1-yl)-6-(1H-1,2,3-triazol-1-yl)pyridine. The synthesis was carried out at 80°C while being monitored by TLC, and was complete after 3 days (Fig. 5.3).

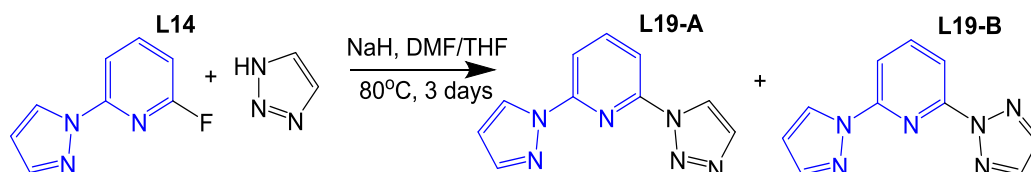


Fig. 5.3 Synthesis of 2-(1H-pyrazol-1-yl)-6-(1H-1,2,3-triazol-1-yl)pyridine **L19**

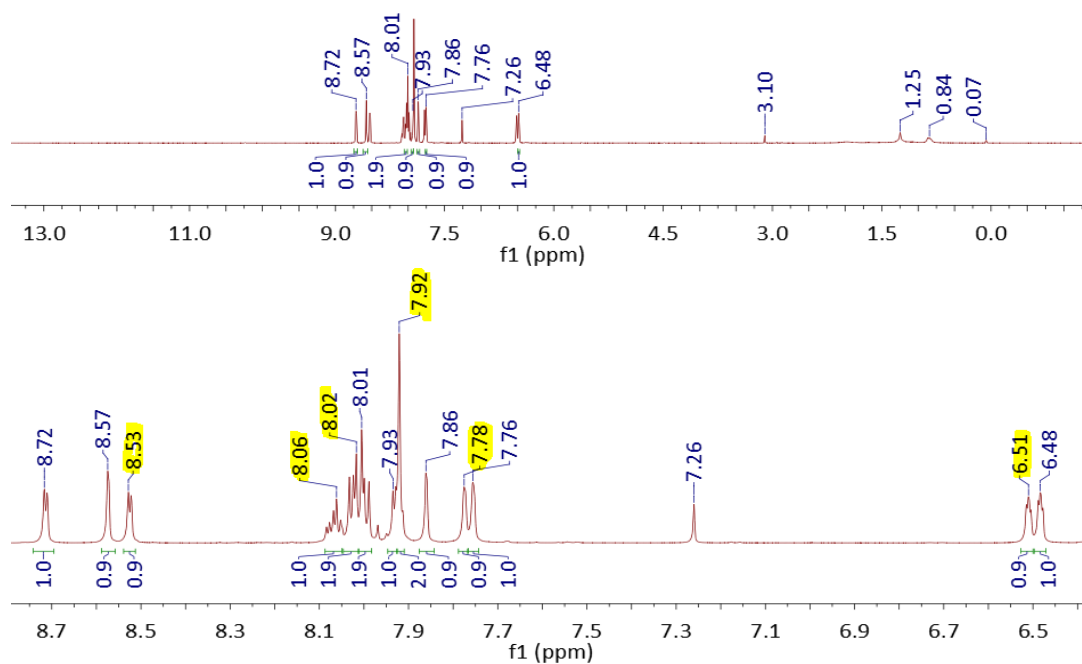


Fig. 5.4 ^1H NMR of the **L19-A** and **L19-B** 1:1 mixture with expansion, measured in CDCl_3 . The peaks from **L19-B** are highlighted in yellow.

Unfortunately 1H-1,2,3-triazole can undergo isomerization to 2H-1,2,3-triazole, which gave a 1:1 mixture of two isomers **L19-A** and **L19-B** (Fig. 5.3). In some cases it is possible to avoid isomerisation. For example, Wang *et al.* shown that it is possible to achieve selective N-2-substitution using direct alkylation without protecting groups for some 1,2,3-triazole derivatives, such as 4,5-dibromo-, 4-bromo-5-trimethylsilyl-, and 4,5-bis(trimethylsilyl)-1,2,3-triazoles.² Some of these derivatives might be used in the future work instead of plain 1,2,3-triazole, to avoid obtaining a mixture of isomers.

The ^1H NMR peaks were assigned to each isomer using COSY 2D NMR and NMRDB.³ The mass spectrum showed only a presence of $[\text{L}+\text{H}^+]$ and $[\text{L}+\text{Na}^+]$ ions, as the two isomers have the same molecular weight. This proves that a 1:1 mixture of two pure isomers was obtained.

It was not possible to separate the two isomers by chromatography, as their r_f values were very similar in hexane/ethylacetate or in DCM/MeOH eluent mixtures. Two recrystallizations from hexane/ CHCl_3 1:1 mixture afforded a 1:3 mixture of isomers, with isomer A being more soluble. The process was monitored by integration of the ^1H NMR peaks. The further recrystallizations were not performed.

L20 – 2-(1H-pyrazol-1-yl)-6-(1H -1,2,4-triazol-1-yl)pyridine

To avoid obtaining a mixture of isomers another, similar ligand was synthesized, but this time with 1H-1,2,4-triazole (Fig. 5.5) as there is no difference between the two isomers 1H-1,2,4-triazole and 2H-1,2,4-triazole.

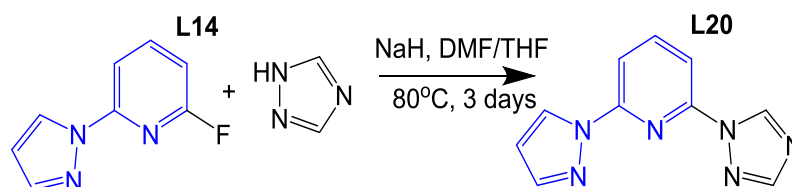


Fig. 5.5 Synthesis of 2-(1H-pyrazol-1-yl)-6-(1H -1,2,4-triazol-1-yl)pyridine L20

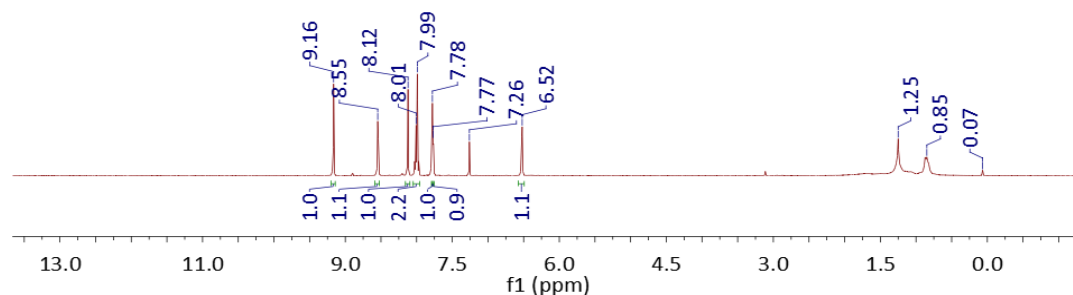


Fig. 5.6 ^1H NMR of L20 with expansion, measured in CDCl_3

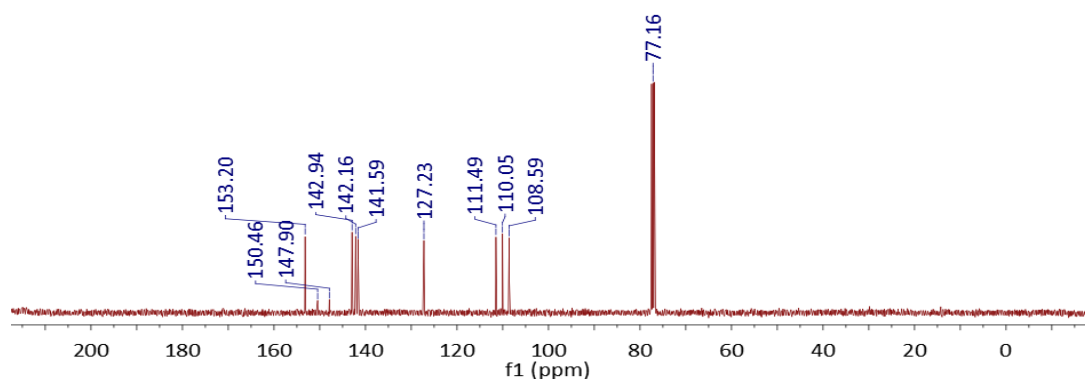


Fig. 5.7 ^{13}C NMR of L20 with expansion, measured in CDCl_3

The ^1H NMR of **L20** contained hexane, CHCl_3 , and TMS peaks. The Pz H3 peak at 7.78 ppm almost overlaps with the Py H4 signal at 7.77 ppm (Fig. 5.6). The peaks were assigned based on their multiplicity, chemical shifts, COSY NMR, and a NMRDB simulation.³ The ambiguity between the Py C3 and C5, and Py C2 and C6 peaks in the ^{13}C NMR spectrum of **L20** (Fig. 5.7) was resolved using an NMRDB³ simulation.

L21 – 2-(4-(Ethylcarboxy)pyrazol-1-yl)-6-(1H-pyrazol-1-yl)pyridine

Although a similar symmetrical ligand, 2,6-di[4-(ethylcarboxy)pyrazol-1-yl]pyridine, has been reported before by Halcrow *et al.*,⁴ the asymmetric bpp derivative with (ethylcarboxy)pyrazol-1-yl ligand hasn't been reported in the literature.⁵ It was obtained using the same procedure as for the other ligands from this series (Fig. 5.8). However the yield for **L21** was significantly lower, ca 53%. This may be because this ligand has a better solubility in hexane, so more of it was lost during the purification process.

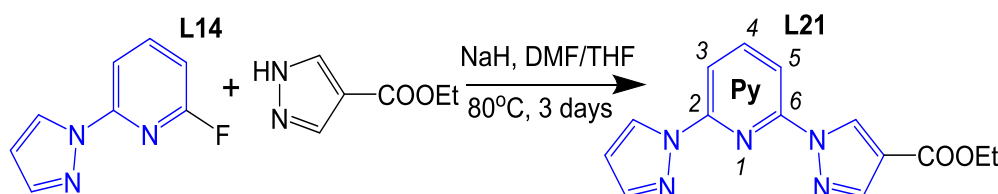


Fig. 5.8 Synthesis of 2-(4-(ethylcarboxy)pyrazol-1-yl)-6-(1H-pyrazol-1-yl)pyridine **L21**

The ^1H NMR peaks were assigned based on their multiplicity and using COSY NMR. The three pyridyl peaks have very similar chemical shifts (Fig. 5.9 - expansion).

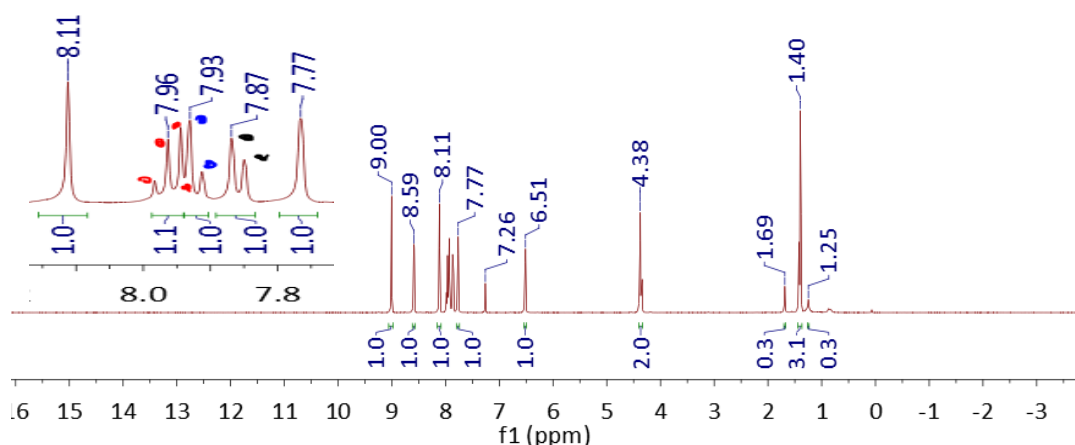


Fig. 5.9 ^1H NMR of **L21** with expansion, measured in CDCl_3 . The pyridine ring spiting signals are highlighted with dots for clarity: **Py H4** – red, **Py H3** – blue, **Py H5** – black.

The Py H4 peak (see Fig. 5.8 for the labelling) couples with two other signals and is doublet of doublets at 7.96 ppm. One of its splitting peaks overlaps

with the Py H3 signal, which is a doublet at 7.93 ppm. The Py H5 peak is also a doublet, at 7.78 ppm. The Py H4 and Py H3 peaks undergo a strong roofing towards each other.

The ^{13}C NMR for **L21** (Fig. 5.10) was assigned using HMQC NMR. The ambiguities between the Py C2 and C6, and Py C3 and C5 assignments were resolved using a NMRDB³ simulation.

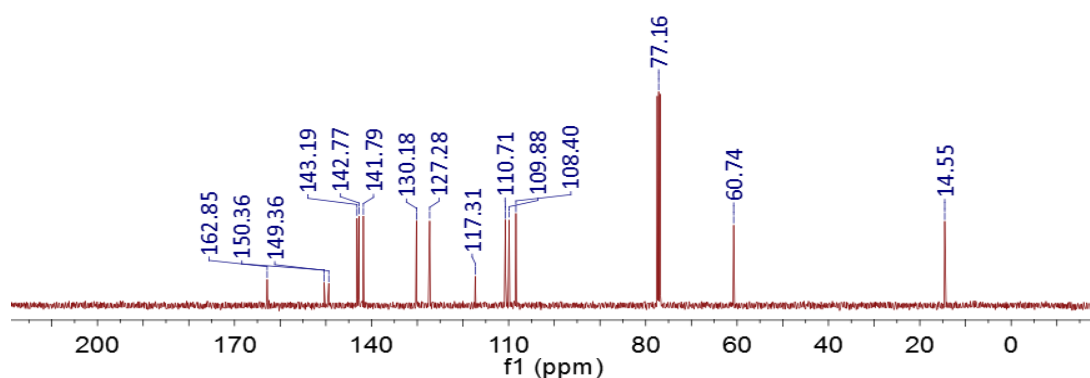


Fig. 5.10 ^{13}C NMR of **L21**, measured in CDCl_3

5.3 Iron complex synthesis

$[\text{Fe}(\text{L21})_2][\text{BF}_4]_2$

$[\text{Fe}(\text{L21})_2][\text{BF}_4]_2$ was obtained by a standard procedure for obtaining iron complexes, using acetone as a solvent, and diethyl ether as an antisolvent (Fig. 5.11). The crystallization from a concentrated solution yielded an oil precipitate, while more dilute solutions formed dark-yellow needle crystals which, however, were not big enough for crystallographic data collection.

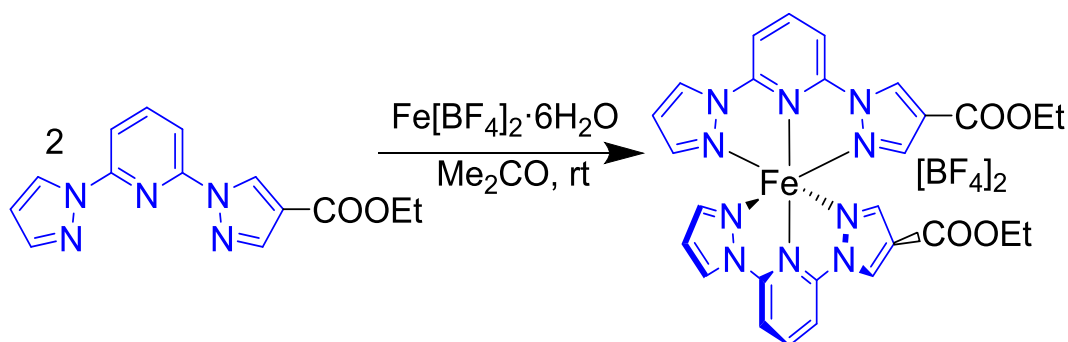


Fig. 5.11 Synthesis of $[\text{Fe}(\text{L21})_2][\text{BF}_4]_2$

$[\text{Fe}(\text{L20})_2][\text{Fe}(\text{L20})_2(\text{H}_2\text{O})_2][\text{BF}_4]_4 \cdot \text{MeNO}_2 \cdot \text{H}_2\text{O}$

The attempts to obtain an iron(II) complex with L20 led to formation of a coordination polymer $[\text{Fe}(\text{L20})_2][\text{Fe}(\text{L20})_2(\text{H}_2\text{O})_2][\text{BF}_4]_4 \cdot \text{MeNO}_2 \cdot \text{H}_2\text{O}$ (Fig. 5.12). Crystallization from MeCN led to a powder, while using MeNO_2 as a solvent led to formation of diffraction-quality crystals. Attempts to obtain an

iron complex with a NCS^- as a counterion, instead of BF_4^- , were unsuccessful. Therefore BF_4^- as a counterion, MeNO_2 as a solvent, and $i\text{Pr}_2\text{O}$ as an antisolvent was found to be the best system for obtaining iron complexes of **L20** as single crystals. Formation of the abovementioned coordination polymer is reproducible, and was repeated twice. More details on its structure can be found in the crystallography section of this chapter.

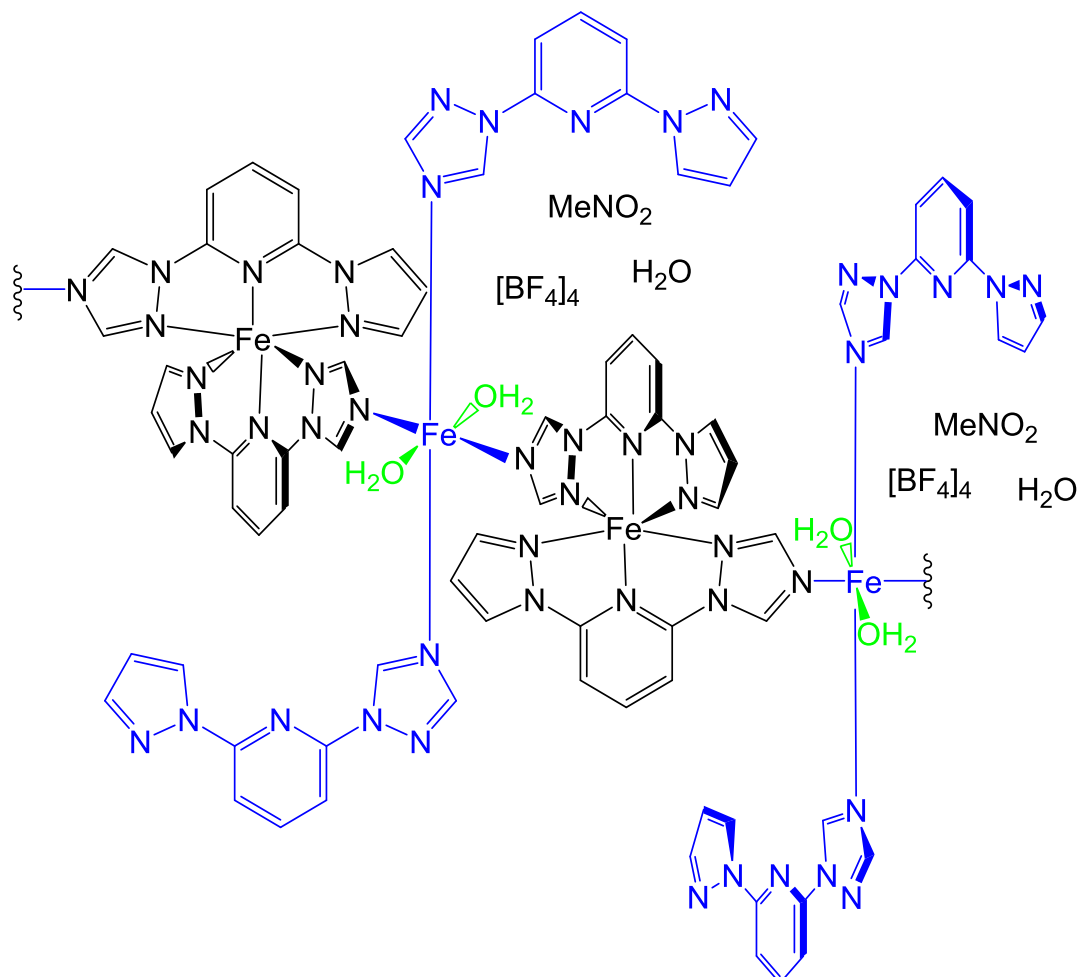


Fig. 5.12 The structure of the coordination polymer $[\text{Fe}(\text{L20})_2][\text{Fe}(\text{L20})_2(\text{H}_2\text{O})_2][\text{BF}_4]_4 \cdot \text{MeNO}_2 \cdot \text{H}_2\text{O}$

5.4 Paramagnetic NMR

$[\text{Fe}(\text{L21})_2][\text{BF}_4]_2$

Paramagnetic NMR of $[\text{Fe}(\text{L21})_2][\text{BF}_4]_2$ was very similar to the one for $[\text{Fe}(\text{L16})_2][\text{BF}_4]_2$ from the previous chapter (Chapter 4.11). The peak assignment can be seen in Chapter 6.5.5. The further the peak is located from the iron centre, the less shifted upfield its signal appears, with the least shifted Py H4 signal appearing at 1.11 ppm (Fig. 5.13 extension). All the paramagnetically shifted peaks integrate at 1:1 ratio. The ambiguity

between some pairs of peaks, such as PzA H3 and PzB H3, hasn't been resolved.

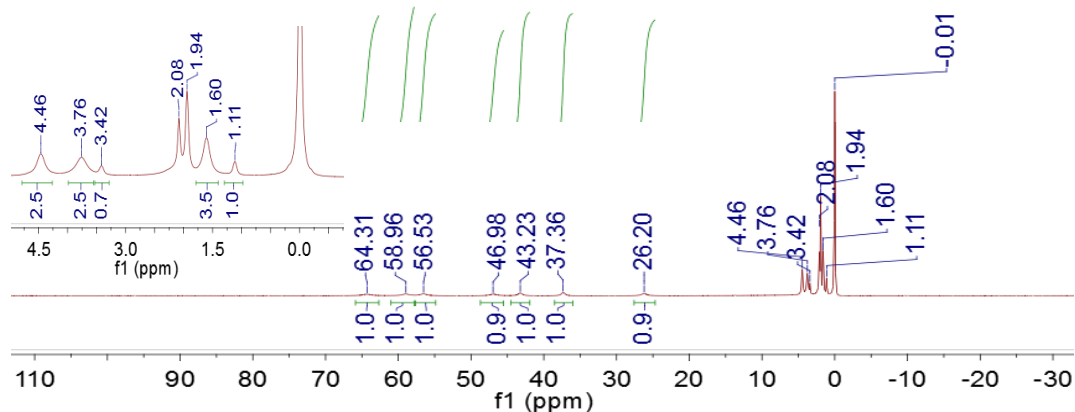


Fig. 5.13 Paramagnetic ¹H NMR of [Fe(L21)₂][BF₄]₂ with extension, measured in MeCN-D₃

5.5 XRD crystal structures and distortion parameters

Ligands

Both asymmetric triazole ligands readily crystallized as white needles, and their crystal structures were collected (Fig. 5.14 and 5.15). For **L19** only a crystal structure of one isomer was collected.

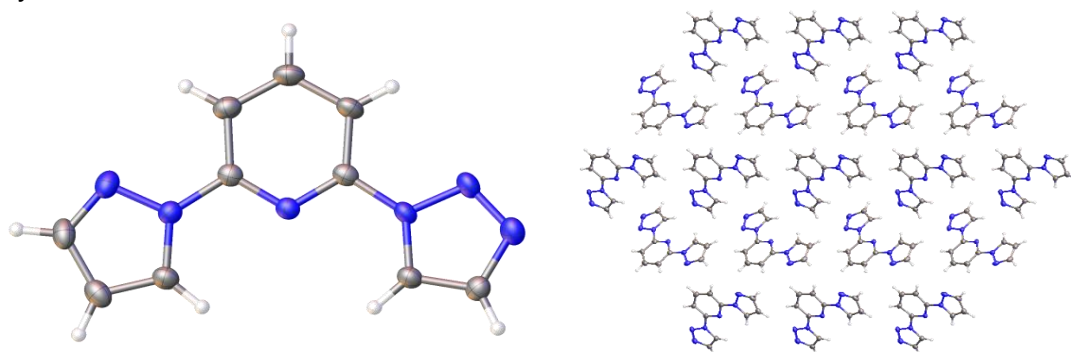


Fig. 5.14 Crystal structure of **L19**, and its packing diagram from the view, parallel to the [100] vector

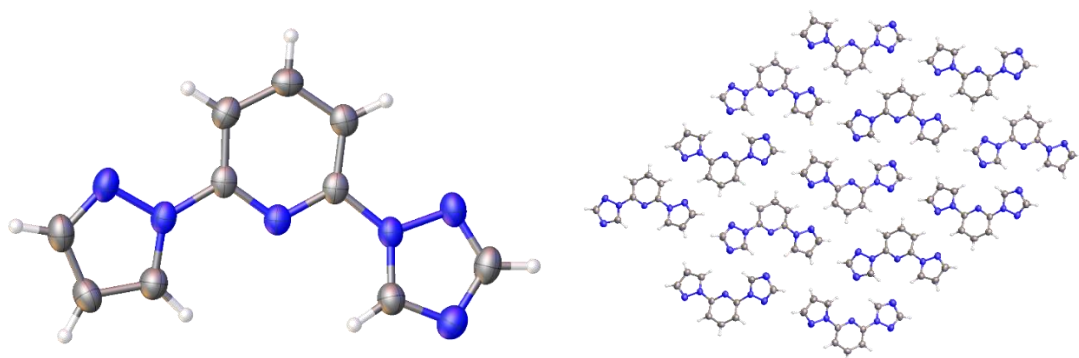


Fig. 5.15 Crystal structure of **L20**, and its packing diagram from the view, parallel to the [010] vector

The two ligands pack very differently: the **L19** molecules in the lattice are related by a 4-fold symmetry, while the **L20** – by a 2-fold symmetry. They have very different unit cell parameters, but similar unit cell volumes (Table 5.1).

Table 5.1 Unit cells of **L19** and **L20**

	L19	L20
Temperature/K	120.00(13)	150.01(10)
Crystal system	monoclinic	monoclinic
Space group	Cc	P2 ₁ /c
a/Å	4.54380(10)	12.5794(9)
b/Å	25.9740(7)	3.8549(3)
c/Å	8.5078(2)	20.4981(14)
α/°	90	90
β/°	99.788(3)	103.628(7)
γ/°	90	90
Volume/Å³	989.48(4)	966.01(12)
Z	4	4

Iron complexes

[Fe(L20)₂][Fe(L20)₂(H₂O)₂][BF₄]₄·MeNO₂·H₂O

The synthesis of coordination polymer [Fe(L20)₂][Fe(L20)₂(H₂O)₂][BF₄]₄·MeNO₂·H₂O is reproducible, and it was repeated twice. The product forms clusters of orangy-yellow prismatic crystals. A crystal structure from the first batch was collected at 150 K, and then a crystal from the second batch was used to obtain a series of complete crystal structure at different temperatures. For convenience, these five crystal structures will be referred as **S1-S5** further in the text (Table 5.2).

Table 5.2 Solvent content in crystal structures of [Fe(L20)₂][Fe(L20)₂(H₂O)₂][BF₄]₄·MeNO₂·nH₂O at different temperatures based on crystal structures

Code	Batch	Temp.	Formula*	Solvent content**
S1	1	150 K	C ₄₁ H ₄₁ B ₄ F ₁₆ Fe ₂ N ₂₅ O ₅	[Fe ¹ L ₂][Fe ² L ₂ (H ₂ O) ₂][BF ₄] ₄ ·MeNO ₂ ·H ₂ O
S2	2	150 K	C ₄₁ H ₄₃ B ₄ F ₁₆ Fe ₂ N ₂₅ O ₆	[Fe ¹ L ₂][Fe ² L ₂ (H ₂ O) ₂][BF ₄] ₄ ·MeNO ₂ ·2H ₂ O
S3	2	200 K	C ₄₁ H ₄₃ B ₄ F ₁₆ Fe ₂ N ₂₅ O ₆	[Fe ¹ L ₂][Fe ² L ₂ (H ₂ O) ₂][BF ₄] ₄ ·MeNO ₂ ·2H ₂ O
S4	2	250 K	C ₄₁ H ₄₁ B ₄ F ₁₆ Fe ₂ N ₂₅ O ₅	[Fe ¹ L ₂][Fe ² L ₂ (H ₂ O) ₂][BF ₄] ₄ ·MeNO ₂ ·H ₂ O
S5	2	290 K	C ₄₁ H ₄₁ B ₄ F ₁₆ Fe ₂ N ₂₅ O ₅	[Fe ¹ L ₂][Fe ² L ₂ (H ₂ O) ₂][BF ₄] ₄ ·MeNO ₂ ·H ₂ O

* The formula is calculated for one **segment** of the coordination polymer chain, which contains two asymmetric units.

** L = L20

The formulae in the Table 5.2 were calculated for a **segment** of the coordination polymer chain, spanning two asymmetric units, because that is the smallest segment that allows to obtain a whole number of each atom. There is some ambiguity for the structures **S1**, **S4** and **S5**, whether they

actually have one less lattice water molecule than the rest of the structures, or maybe they just appear to have half occupancy due to distortions in the structure.

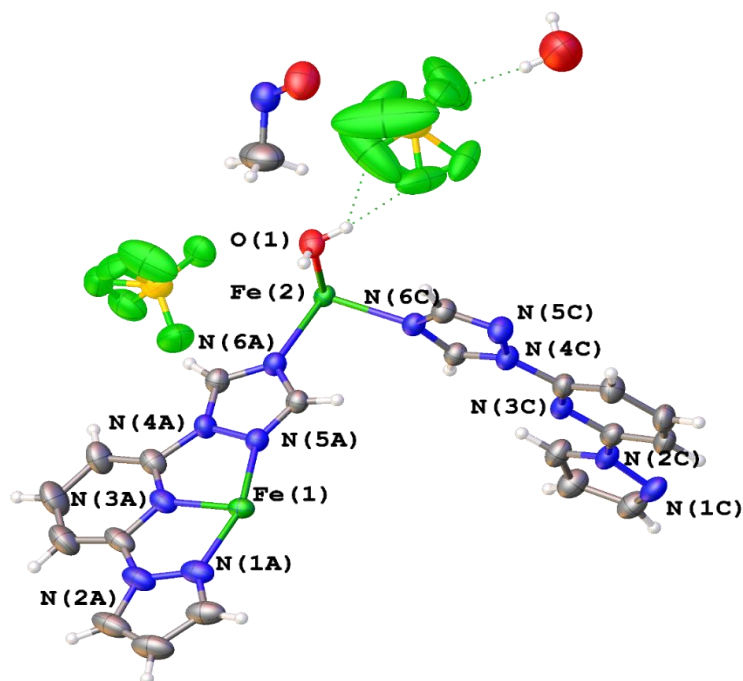


Fig. 5.16 Asymmetric unit of coordination polymer **S2** with labelling

The coordination polymer forms long parallel strains with a repeating pattern of two different iron centres: Fe1, which coordinates to N1, N3, and N5; and Fe2, which coordinates to N6A, N6B, and the two water molecules (Fig. 5.16).

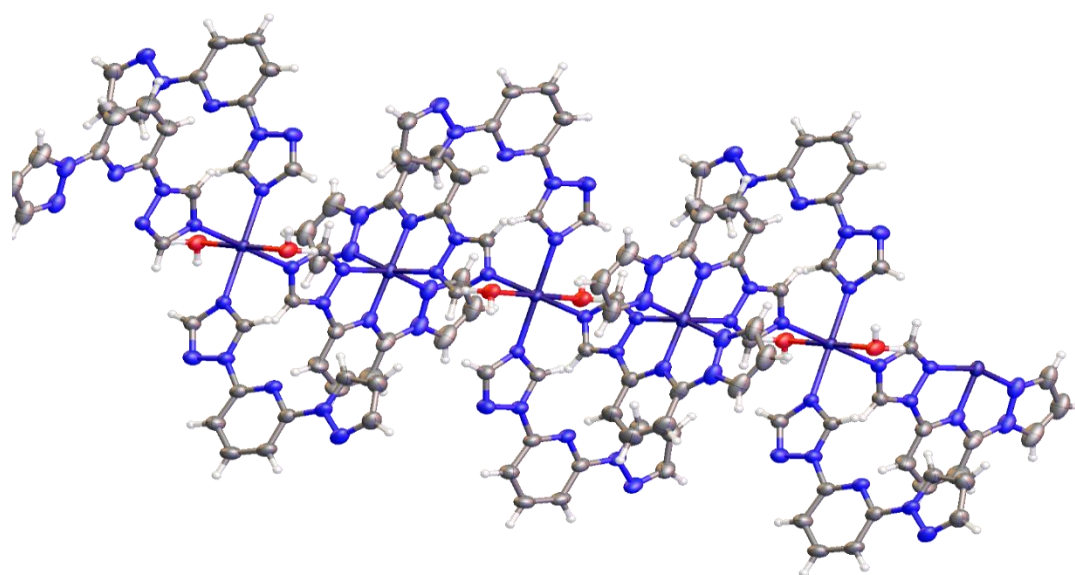


Fig. 5.17 Fragment of the crystal structure of coordination polymer **S2**, from the view parallel to the [010] vector. Counterions and lattice solvents are omitted for clarity.

Interestingly, the nitrogens on the triazole and pyrazole rings around Fe1 are pointing towards the iron centre, which is typical for iron complexes, while the ligand molecules around the Fe2 centre resemble the triazole and pyrazole rings orientation of a free ligand (Fig. 5.17).

In the crystal structures **S1-S5** there are two water molecules coordinating to the Fe2 centre, and also one lattice solvent water molecule for **S1** and **S5**, or two lattice solvent water molecules for **S2-S4**. All of structures **S1-S5** contain one MeNO₂ molecule per a segment (Table 5.2).

All five crystal structures had similar unit cell parameters (Table 5.3). The structures **S1** and **S2** were collected at the same temperature, but still have slightly different cell parameters, which may suggest that they do have different number of lattice water molecules.

Table 5.3 Unit cell parameters for five crystal structures of [Fe(L20)₂][Fe(L20)₂(H₂O)₂][BF₄]₄·MeNO₂·nH₂O

	S1	S2	S3	S4	S5
Temperature/K	150.00(10)	150.01(10)	200.00(10)	250.00(10)	289.97(10)
Crystal system	monoclinic	monoclinic	monoclinic	monoclinic	monoclinic
Space group	C2/c	C2/c	C2/c	C2/c	C2/c
a/Å	19.9215(6)	19.9190(3)	19.9235(5)	19.9189(6)	19.9010(5)
b/Å	15.5378(5)	15.3887(3)	15.5984(5)	15.8603(5)	15.9683(4)
c/Å	18.5292(6)	18.5909(3)	18.6533(4)	18.7484(4)	18.7282(6)
α/°	90	90	90	90	90
β/°	101.222(3)	101.152(2)	100.512(2)	99.528(2)	99.397(3)
γ/°	90	90	90	90	90
Volume/Å³	5625.8(3)	5591.02(17)	5699.7(3)	5841.3(3)	5871.7(3)
Z	4	4	4	4	4
Z'	0.5	0.5	0.5	0.5	0.5

Distortion Parameters

Based on the octahedral volume it may be concluded that the Fe2 centre remains HS from 150 to 290 K, while the Fe¹ centre undergoes SCO (Table 5.4). For bpp iron(II) complexes V_{oct} is ca 12.4 Å³ for HS, and ca 9.4 Å³ for LS (Chapter 2.51). Based on these values the percentage of HS molecules in the crystal at a given temperature was estimated (Table 5.4). Slightly different octahedral volume values should be expected for the Fe2 centre, which coordinates to two water molecules.

Table 5.4 Comparison of the octahedral volumes around the two iron centres in crystal structures of $[\text{Fe}(\text{L20})_2][\text{Fe}(\text{L20})_2(\text{H}_2\text{O})_2][\text{BF}_4]_4 \cdot \text{MeNO}_2 \cdot \text{H}_2\text{O}$ at different temperatures

	S1	S2	S3	S4	S5
Temperature, K	150	150	200	250	290
$V_{\text{oct}} \text{Fe1}, \text{\AA}^3$	10.102	9.764	10.502	12.109	12.236
$V_{\text{oct}} \text{Fe2}, \text{\AA}^3$	13.624	13.695	13.707	13.656	13.653
% HS Fe1	23	12	37	90	95

The same structures were analysed regarding the Fe-N bond lengths. The average Fe-N for Fe1 centre is expected to be 2.177 Å in HS, and 1.941 Å in LS (Chapter 2.51). Based on these expected values the percentage of HS molecules in the crystal at each temperature was estimated (Table 5.5), which roughly matched the results obtained by comparing the octahedral volumes (Fig. 5.4).

Table 5.5 Comparison of Fe-N bond lengths for the two iron centres in crystal structures of $[\text{Fe}(\text{L20})_2][\text{Fe}(\text{L20})_2(\text{H}_2\text{O})_2][\text{BF}_4]_4 \cdot \text{MeNO}_2 \cdot \text{H}_2\text{O}$ at different temperatures

	S1	S2	S3	S4	S5
T, K	150	150	200	250	290
Fe1-N1, Å	2.001(5)	1.977(3)	2.022(4)	2.137(6)	2.148(4)
Fe1-N3, Å	1.922(5)	1.900(3)	1.964(4)	2.077(6)	2.100(4)
Fe1-N5, Å	2.042(4)	2.016(3)	2.086(3)	2.200(4)	2.208(3)
Average	1.99	1.96	2.02	2.14	2.15
%HS	20	10	35	83	89
Fe2-O1, Å	2.096(4)	2.104(2)	2.102(3)	2.111(4)	2.112(3)
Fe2-N6A, Å	2.231(4)	2.234(2)	2.227(3)	2.218(4)	2.212(3)
Fe2-N6C, Å	2.186(4)	2.187(2)	2.191(3)	2.192(4)	2.193(3)

5.6 SQUID

[Fe(L20)₂][Fe(L20)₂(H₂O)₂][BF₄]₄·MeNO₂·H₂O

SQUID magnetic measurements for [Fe(L20)₂][Fe(L20)₂(H₂O)₂][BF₄]₄·MeNO₂·H₂O obtained from the first batch, the one that yielded the crystal structure **S1**, shown a gradual switching between 50 and 300 K, with no hysteresis (Fig. 5.18).

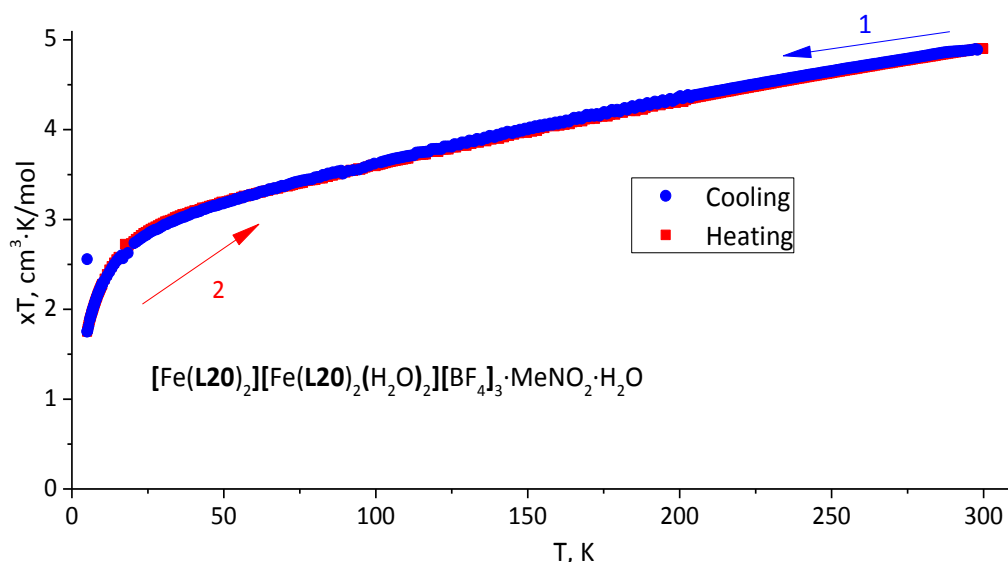


Fig. 5.18 SQUID magnetic susceptibility measurements a the coordination polymer [Fe(L20)₂][Fe(L20)₂(H₂O)₂][BF₄]₄·MeNO₂·H₂O

The magnetic moment changes from ca 3 to 4.9 $\text{cm}^3 \cdot \text{K} / \text{mol}$, which may mean that ca 15% of molecules in the Fe2 centre were switching from HS to LS below 150K, but remained fully HS above ca 150 K; and the Fe1 centre didn't switch fully to HS at 300 K. Based on the distortion parameters, at 290 K the Fe2 is expected to be fully HS, and the Fe1 shall be ca 90% HS, which would predict a magnetic moment of ca 6.65 $\text{cm}^3 \cdot \text{K} / \text{mol}$, and not 4.9 $\text{cm}^3 \cdot \text{K} / \text{mol}$, as was measured by SQUID. This difference may be explained by the fact that the variable temperature crystal structures were collected only for the crystal from the second batch **S2-5**, while the magnetic moment was measured for the sample from the first batch **S1**. Although the crystal structures produced from the two batches were very similar (Table 5.3), the sample from the first batch seems to have one less lattice water molecule (Table 5.2). This difference should be investigated further, and the magnetic moment of [Fe(L20)₂][Fe(L20)₂(H₂O)₂][BF₄]₄·MeNO₂·2H₂O should also be measured, if possible. In the literature there examples of a dramatic of the lattice solvent content on the magnetic properties. For example, Gutlich *et al.* obtained a series of SCO compounds (Fig. 5.19),⁴ one of which was crystallized with three, half, and no lattice water molecules. Each of these

has a different magnetic behaviour (Fig. 5.19), where Ak = C₁₆H₃₃ and A⁻ = Cl⁻ in all three cases, and S = 1 for **A**, S = 2 for **B**, and S = 0 for **C**.

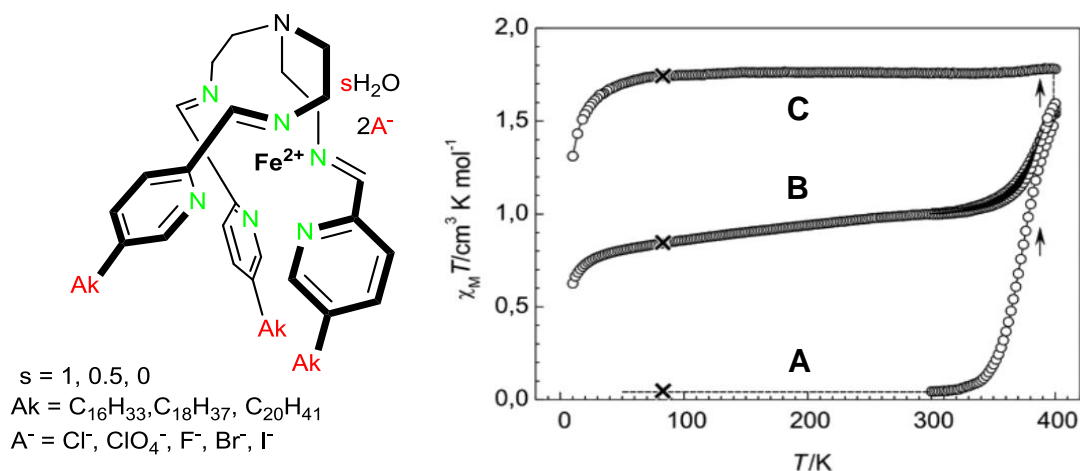


Fig. 5.19 Some of the long alkyl chain SCO complexes, obtained by Gutlich *et al.* and their magnetic behaviour⁴

[Fe(L21)₂][BF₄]₂

A symmetrical compound, 2,6-di(4-(ethylcarboxy)pyrazol-1-yl)-pyridine, similar to this asymmetric iron complex [Fe(L21)₂][BF₄]₂, has been reported by Halcrow *et al.* It stayed LS in solid state, and switched quite abruptly in solution, with T_{1/2} at ca 250 K.⁶ The asymmetric iron complex [Fe(L21)₂][BF₄]₂ hasn't been reported before.⁵ It shown a gradual SCO, with T_{1/2} at ca 200 K. Around 36% of the sample was trapped in HS, as the magnetic moment didn't go below ca 1.25 cm³·K/mol (Fig. 5.20). Therefore the T_{1/2} should match the xT = (3.5 - 1.25) + 1.25 = 2.375 cm³·K/mol, which gives a temperature of ca 200 K.

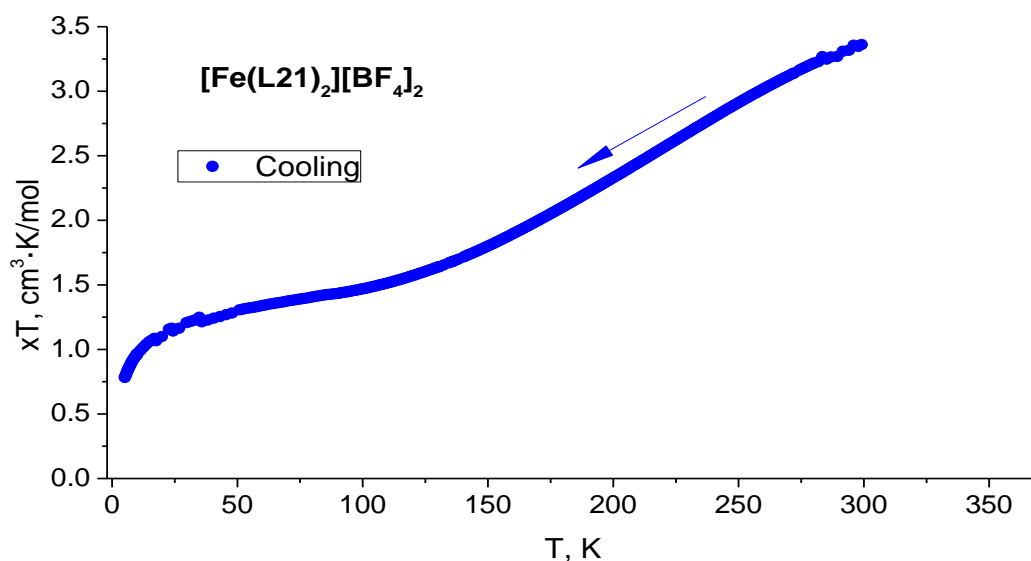


Fig. 5.20 SQUID magnetic susceptibility measurements for [Fe(L21)₂][BF₄]₂

5.7 Conclusions

In this chapter a series of novel asymmetric ligands, based on 2,6-bis(pyrazol-1-yl)pyridine was obtained and analysed. One of these ligands formed an interesting coordination polymer with Fe^{2+} , and five variable temperature crystal structures were collected for it. There are two different metal centres in the repeating chain of the coordination polymer, one of which undergoes a gradual SCO, and the other remains HS between 150 and 290 K. This structure can be crystallized with either one or two lattice water molecules, the effect of which should be further investigated, as there are examples in the literature of strong effect of the solvent content on the magnetic behaviour.^{6,7,8} Certain 1,2,3-triazole derivatives can be selectively N-alkylated.³ It would be good to test the synthesis of asymmetric ligands with them in the future work.

List of References

1. Chandrasekhar, N. and Chandrasekar, R. "Super hybrid tridentate ligands": 4-substituted-2-(1-butyl-1H-1,2,3-triazol-4-yl)-6-(1H-pyrazol-1-yl)pyridine ligands coordinated to Fe(II) ions display above room temperature spin transitions. *Dalton Trans.* **2010**, 39, 9872-9878.
2. Wang, X.-J.; Zhang, L.; Krishnamurthy, D.; Senanayake, C.H. and Wipf, P. General Solution to the Synthesis of N-2-Substituted 1,2,3-Triazoles. *Org. Lett.* **2010**, 12, 20, 4632-4635.
3. NMR prediction tool online. <http://www.nmrdb.org>
4. Pritchard, R.; Kilner, C.A.; Barrett, S.A. and Halcrow, M.A. Two new 4',4''-disubstituted dipyrazolylpyridine derivatives, and the structures and spin states of their iron(II) complexes. *Inorganica Chim. Acta.* **2009**, 362, 4365-4371.
5. *SciFinder*. Chemical Abstracts Service, accessed 24/4/2019 <https://scifinder.cas.org>
6. Seredyuk, M.; Gaspar, A. B.; Ksenofontov, V.; Galyametdinov, Y.; Kusz, J. and Gutlich, P. Does the Solid-Liquid Crystal Phase Transition Provoke the Spin-State Change in Spin-Crossover Metallomesogens? *J. Am. Chem. Soc.* **2008**, 130, 1431-1439.
7. Fumanal, M.; Jiménez-Grávalos, F.; Ribas-Arino, J. and Vela, S. Lattice-Solvent Effects in the Spin-Crossover of an Fe(II)-Based Material. The Key Role of Intermolecular Interactions between Solvent Molecules. *Inorg. Chem.* **2017**, 56(8), 4474-4483.
8. Galadzhun, I.; Kulmaczewski, R.; Halcrow, M.A. Five 2,6-Di(pyrazol-1-yl)pyridine-4-carboxylate Esters, and the Spin States of their Iron(II) Complexes. *Magnetochem.* **2019**, 5, 9.

Chapter 6

Experimental

6.1 General Experimental Considerations

6.1.1 Analytical techniques used

^1H NMR spectra were recorded at either 300 MHz on a *Bruker Ultrashield™ 300*, or at 400 MHz on a *Bruker Ascend™ 400* spectrometer at 298 ± 5 K. Evans method NMR spectra were measured at different temperatures. Chemical shifts were quoted in parts per million with respect to TMS or the respective residual solvent resonances. ^{13}C NMR spectra were run using broadband proton decoupling operating at 75 MHz, on a *Bruker Ascend™ 400* spectrometer, and quoted in parts per million with respect to the respective solvent resonances.

Electrospray ionization mass spectrometry (**ESI-MS**) spectra were obtained on an *Agilent Technologies 1200 Series* spectrometer, and on *Thermo Scientific Dionex UltiMate 3000*, from MeCN feed solution. **CHN** microanalyses were carried out either by the University of Leeds School of Chemistry microanalytical service, or by the London Metropolitan University microanalytical service. Infrared spectra **IR** were recorded on *Bruker Alpha Platinum - ATR* infrared spectrophotometer, with the samples being analyzed as solids. Melting points **MP** were determined on an *Electrothermal digital melting point apparatus* and on *Stuart SMP3* Melting Point Apparatus.

Differential Scanning Calorimetry **DSC** was run on a *TA instruments DSC Q20* analyser, and thermogravimetric analyses **TGA** using a *TA instruments TGA Q50* analyser. Both were performed at the University of Leeds by Dr A. Kazlauciuonas. Magnetic susceptibility measurements were performed by either Dr R. Kulmaczewski, Namrah Shahid, or Izar Capel Berdiell, on a *Quantum Design VSM SQUID* magnetometer at the School of Physics, University of Leeds, in an applied field of 5 000 G. A diamagnetic correction for each sample was estimated from Pascal's constants, and diamagnetic correction for the sample holder was measured and subtracted from the raw data. Variable temperature magnetic susceptibility measurements in solution were performed via **Evans method NMR** by Mr S. Barrett or Dr M. Howard on a *Bruker DRX 500* spectrometer at a frequency of 500.13 MHz. And a correction for the solvent density change with temperature were applied to the obtained data.

Powder X-ray Diffraction patterns **PXRD** were obtained at room temperature on a *Bruker D2 Phaser* machine, equipped with a *LynxEye* detector, using Long Fine Focused Cu radiation ($\lambda = 0.71073$). Data workup was done using *Bruker DIFFRAC Suite* software. X-ray Diffraction Crystal

Structures **XRD** were collected either on (i) Agilent SuperNova diffractometer, equipped with an Atlas CCD detector, and connected to an Oxford Cryosystem low temperature device, using monochromated Cu K α radiation ($\lambda = 1.54184 \text{ \AA}$) or Mo K α radiation ($\lambda = 0.7107 \text{ \AA}$), or (ii) Rigaku Saturn 724 CCD diffractometer, using synchrotron radiation from Diamond Light Source ($\lambda = 0.6889 \text{ \AA}$) and an Oxford Cryostream low temperature device.

Unless otherwise stated, the analyses were performed by the author of this thesis.

6.1.2 Obtaining single crystals for XRD crystallography

Single crystals for XRD crystallography in this thesis were obtained either by slow evaporation of the solvent from an NMR tube with a cap on – this technique has worked predominantly for ligands, – or by slow antisolvent diffusion, which works best for metal complexes. The obtained datasets were solved using the computer program ShelXT.¹

Growing single crystals by slow evaporation in an NMR tube

In order to grow single crystals in an NMR tube, ca 10 mg of the compound were dissolved in appropriate solvent, usually deuterated chloroform, and left for about a month with the cap on in a quiet place with no vibrations.

Growing single crystals by slow antisolvent diffusion

To grow single crystals by slow antisolvent diffusion, the metal complex was dissolved in an appropriate solvent, which was usually MeCN for compounds with no long alkyl chains, and a DCE/acetone mixture for compounds with long alkyl chains. This was placed in a vial, which is then inserted in a bigger jar containing some antisolvent, and sealed inside the jar using parafilm. The level of antisolvent should be lower than the solution level inside the vial. The more volatile antisolvent slowly diffuses from the jar into the vial, causing the metal complex to crystallize from the solution. Diisopropyl ether was found to be a good antisolvent for compounds with no long alkyl chains, while pentane showed good results for compounds with long alkyl chains.

6.1.3 Simulating powder patterns

The simulated powder patterns were obtained from the .res files of solved crystal structures, using the X-Seed software.²

6.1.4 Calculating $T_{1/2}$ from SQUID magnetic susceptibility graphs

$T_{1/2}$ is the temperature at which half of the molecules in the sample are HS, and half of them are LS. If spin crossover has a hysteresis, there going to be two $T_{1/2}$ values – one upon heating, and another one upon cooling. Many samples in this thesis have $T_{1/2}$ at the temperatures above the maximum temperature for the SQUID machine, which is ca 350K. In that case it is impossible to determine $T_{1/2}$ from the SQUID curve, which shows only beginning of the spin crossover. If switching on the SQUID curve goes from 0 to at least $1.75 \text{ cm}^3\text{K/mol}$, the $T_{1/2}$ may be determined by plotting the derivative of the SQUID curve, $d\chi T$ vs T . The maximum on this graph would be $T_{1/2}$.

In cases when a complete switching can be observed on the SQUID graph, $T_{1/2}$ may be determined directly by recording the temperature at which $\chi T = 1.75 \text{ cm}^3\text{K/mol}$, or a half of $3.5 \text{ cm}^3\text{K/mol}$ - the magnetic susceptibility of fully HS iron(II).

6.1.5 DSC measurements

As was mentioned above, DSC analyses were run by Dr A. Kazlauciusas at the University of Leeds. Each analysis was run according to the following protocol:

- 1: Equilibrate at T_{\min} , °C
- 2: Ramp $10.00^\circ\text{C}/\text{min}$ to T_{\max} , °C
- 3: Mark end of cycle 1
- 4: Ramp $5.00^\circ\text{C}/\text{min}$ to T_{\min} , °C
- 5: Mark end of cycle 2
- 6: Ramp $10.00^\circ\text{C}/\text{min}$ to T_{\max} , °C
- 7: Mark end of cycle 3

The T_{\min} and T_{\max} are the minimum and the maximum temperature, which depends on the sample, and may be seen on each individual DSC graph. As can be seen from the above protocol, the cooling cycle was performed at half the rate of the heating cycles.

6.1.6 Labelling schemes for NMR assignment for each chapter

For all the ligands in this thesis for ^1H and ^{13}C NMR assignment the atoms were consistently labelled as shown on the figures at the beginning of each section (Fig. 6.1 and 6.2). The labelling on the crystal structures is different,

as it is not possible to add long prefixes to atom numbering when processing the crystal structures in Olex.

6.2 Chapter 2 - Bis(pyrazol-1-yl)pyridine derivatives with no long alkyl chains, and their iron(II) complexes

The labelling scheme for this chapter is shown below, on the Fig. 6.1.

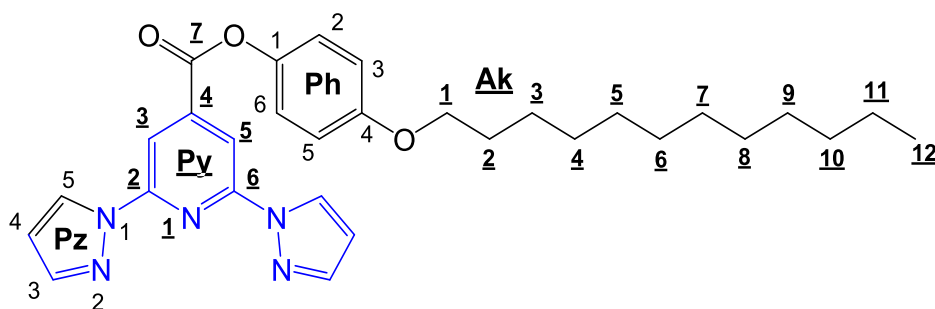
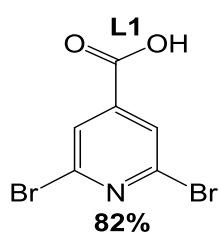


Fig. 6.1. Labelling scheme for Chapters 2 and 3

6.2.1 L1 - 2,6-dibromo pyridine-4-carboxylic acid



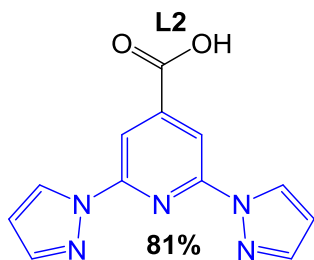
Citrazinic acid (4.725 g, 30.5 mmol, 1 eq.) was mixed with POBr₃ (26.250 g, 91.5 mmol, 3 eq.), and the flask was connected to a condenser, connected to a water bubbler, to absorb the emitted gases, and also to an empty safety bubbler, to prevent sucking water into the reaction mixture.

This was heated at 140°C for 24 hrs. After cooling to room temperature, the dark-brown mixture was quenched with deion. water (25 ml) (careful – strongly exothermic reaction), heated to reflux and cooled to rt again. The obtained precipitate was thoroughly washed with water. After desiccation 7.03 g (yield 82%) of the product was obtained as a cream-white powder.³

Notes: 1. The reaction mixture should be heated quickly, and water should be added fast enough so the water starts boiling, otherwise an insoluble glass-like solid will form on the bottom of the flask, which is extremely hard to remove.

Analyses: ¹H NMR (DMSO-D₆, 400.130 MHz, ppm): δ 7.99 (s, 2H, Py H3,5), ¹³C NMR (100.613 MHz, DMSO): δ 126.74 (Py C3,5), 140.80 (Py C4), 143.67 (Py C2,6), 163.52 (Py C7), **MS** (ESI) m/z: calc. for [C₆H₂Br₂NO₂]⁻: 279.8, found: 280.2, **MP**: 177.5 - 178°C (lit.¹ 173-175°C), **IR** (cm⁻¹): 1220 (Py C-H), 1236 (C-OH), 1730 (C=O), 2750-3100 broad (CO-H), **CHN**: calculated for C₆H₃Br₂NO₂: C 25.65, H 1.08, N 4.99%, found: C 25.40, H 1.00, N 4.90%.

6.2.2 L2 - 2,6-di(1H-pyrazole-1'-yl)pyridine-4-carboxylic acid



NaH, 60% dispersion in mineral oil (3.641 g, 90.59 mmol, 3.3 eq.) was stirred in diglyme (110 ml) for 30 mins, after which 1H-pyrazole (5.608 g, 82.35 mmol, 3 eq.) was carefully added to the suspension. After the H₂ has evolved completely and the reaction mixture become clear, 2,6-dibromo pyridine-4-carboxylic acid (7.71 g, 27.45

mmol, 1 eq.) was dropped into the flask, which then was connected to a condenser and heated at 130°C for 5 days.⁴

The cooled contents were poured onto water (500 cm³), and a crude beige solid was obtained through acidification to pH 3 with 4M HCl, and washed on a glass frit with acidified to pH 3 water.

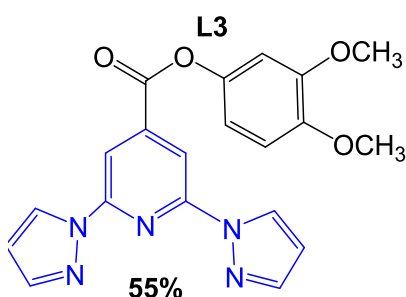
After thorough desiccation the beige solid was triturated in hexane, collected on a glass frit, and recrystallized from 5 ml of acetone. The obtained white powder was dried in the vacuum oven at 90°C for 24h, which yielded a clean final product (5.68 g, 81%).

Notes: It can be very hard to filter the water suspension of the product. It may be easier to filter the mixture before acidification, and then acidify the filtrate and filter it again.

Analyses: **¹H NMR** (DMSO-D₆, 400.130 MHz, ppm): δ 6.68 (dd, 2H, Pz H₄), 7.92 (d, 2H, Pz H₃), 8.18 (s, 2H, Py H_{3,5}), 9.00 (d, 2H, Pz H₅), **¹³C NMR** (100.613 MHz, DMSO, ppm): δ 108.06 (Py C_{3,5}), 108.83 (Pz C₄), 128.37 (Pz C₅), 143.16 (Pz C₃), 144.45 (Py C₄), 150.37 (Py C_{2,6}), 164.91 (Py C₇), **MS** (ESI) m/z: calc. for [C₁₂H₉N₅O₂ + H⁺]: 256.08, found: 255.5, calc. for [C₁₂H₉N₅O₂ + H⁺ + 2DMSO]: 412.1, found: 412.7, **MP:** 257°C dec., **IR** (cm⁻¹): 1210 (Py C-H), 1232 (C-OH), 1728 (C=O), 2300-3150 broad (CO-H), 1574 (Pz C=C and C=N), 1468,1445, 1399 (Pz ring).

6.2.3 L3 - 3,4-dimethoxyphenyl (2,6-di-1H-pyrazole-1-yl)pyridine-4-carboxylate

3,4-Dimethoxyphenyl (2,6-di-1H-pyrazole-1-yl)pyridine-4-carboxylate was



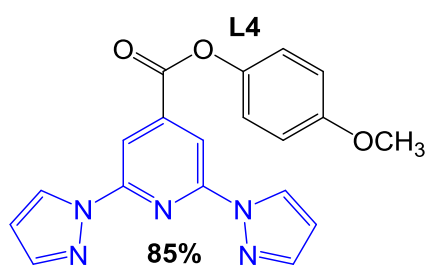
prepared using the following procedure:⁵

L2 2,6-Di(1H-pyrazole-1'-yl)pyridine-4-carboxylic acid (1.275 g, 5 mmol) was heated to reflux in thionyl chloride (10 ml) for 12 hrs. The coloured solution was dried *in vacuo* and the acid chloride was

redissolved in DMF (15 ml). 3,4-Dimethoxyphenol (0.77 g, 5 mmol) was dissolved in DMF (10 ml), and triethylamine (20 ml) was added into the solution, after which this mixture was added to the acid chloride at room temperature. The reaction mixture was stirred for 48 hrs, until a large quantity of precipitate formed. Then water (40 ml) was added to the stirring reaction mixture to remove the salts, which made the product to precipitate as a beige solid, which was then filtered off, washed with water, and desiccated, which yielded the product as a white powder (1.080 g, 55%).

Analyses: **¹H NMR** (DMSO-D₆, 400.130 MHz, ppm): δ 9.04 (d, 2H, Pz H₅), 8.31 (s, 2H, Py H_{3,5}), 7.94 (d, 2H, Pz H₃), 7.08 (d, 1H, Ph H₂), 7.03 (d, 1H, Ph H₅), 6.89 (dd, 1H, Ph H₆), 6.70 (dd, 2H, Pz H₄), 3.79 (s, 3H, Ph H₈), 3.77 (s, 3H, Ph H₇), **¹³C NMR** (100.613 MHz, DMSO, ppm): δ 162.69 (Py C₇), 150.50 (Py C_{2,6}), 149.27 (Ph C₁), 147.01 (Ph C₄), 143.77 (Py C₄), 143.40 (Pz C₃), 142.72 (Ph C₃), 128.52 (Pz C₅), 112.89 (Ph C₅), 111.81 (Ph C₆), 109.05 (Pz C₄), 108.20 (Py C_{3,5}), 106.29 (Ph C₂), 55.85 (Ph C₇), 55.77 (Ph C₈), **MS** (HR- ESI) m/z: calc. for [C₂₀H₁₇N₅O₄ + H⁺]: 392.1353, found: 392.1387, **MP**: 201-202°C, **IR** (cm⁻¹): 1188, 1179 (C-OR), 1748 (C=O), 1506 (Ph C-H), 2838 (Ph O-CH₃), 1574 (Pz C=C and C=N), 1462, 1446, 1392 (Pz ring), 1219 (Py C-H), **CHN**: calculated for C₂₀H₁₇N₅O₄: C 61.38, H 4.38, N 17.89%, found: C 61.80, H 4.20, N 18.80%.

6.2.4 L4 - 4-methoxyphenyl (2,6-di-1H-pyrazole-1-yl)pyridine-4-carboxylate



4-Methoxyphenyl (2,6-di-1H-pyrazole-1-yl)pyridine-4-carboxylate was prepared using the following procedure: **L2** 2,6-Di(1H-pyrazole-1'-yl)pyridine-4-carboxylic acid (3.00 g, 11.75 mmol, 1 eq.) was heated to reflux in thionyl chloride (70 ml, 29.2 eq.)

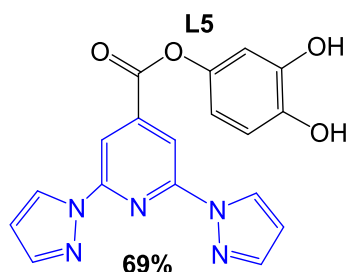
under nitrogen for 12 hrs. The obtained reddish-brown transparent solution was dried *in vacuo*, using an external liquid nitrogen trap to collect the thionyl chloride, and the obtained dark-brown solid was then heated for additional 15 mins at 70°C under vacuum, until the colour changed to light-yellow. It is important to remove all the thionyl chloride completely, otherwise the yield will be low and the product will be dirty. The obtained acid chloride was dissolved in dry THF (70 ml). 4-Methoxyphenol (1.459 g, 11.75 mmol, 1 eq.) was mixed with THF (10 ml) and triethylamine (9 ml), and the obtained transparent solution was added into the reaction mixture. The obtained pale-

brown mixture was stirred for 48 hrs, until a large quantity of the cream precipitate had been formed.

Water (40 ml) was added to the stirring reaction mixture to remove the salts, and the product was precipitated as a beige solid, filtered off and washed with water. After desiccation the pure product (3.618 g, 85%) was obtained as a white powder.

Analyses: $^1\text{H NMR}$ (DMSO- D_6 , 400.130 MHz, ppm): δ 9.06 (d, 2H, Pz H5), 8.31 (s, 2H, Py H3,5), 7.95 (s, 2H, Pz H3), 7.33 (d, 2H, Ph H2,6), 7.05 (d, 2H, Ph H3,5), 6.71 (t, 2H, Pz H4), 3.81 (s, 3H, Ph H7), $^{13}\text{C NMR}$ (100.613 MHz, DMSO, ppm): δ 162.7 (Py C7), 157.34 (Ph C4), 150.48 (Py C4), 143.62 (Ph C1), 143.38 (Pz C3), 142.66 (Py C2,6), 128.52 (Pz C5), 122.54 (Ph C2,6), 114.59 (Ph C3,5), 109.02 (Pz C4), 108.20 (Py C3,5), 55.47 (Ph C7), **MS** (HR- ESI) m/z: calc. for $[\text{C}_{19}\text{H}_{15}\text{N}_5\text{O}_3 + \text{Na}^+]$: 384.1073, found: 384.1085, **MP**: 196°C, **IR** (cm^{-1}): 1190, 1180 (C-OR), 1739 (C=O), 1507 (Ph C=C), 2835 (Ph O- CH_3), 1577 (Pz C=C and C=N), 1466, 1449, 1396 (Pz ring), 1227 (Py C-H)), **CHN**: Calculated for $\text{C}_{19}\text{H}_{15}\text{N}_5\text{O}_3 + 0.5 \text{H}_2\text{O}$: C 61.62, H 4.35, N 18.91 %, found: C 61.80, H 4.20, N 18.80 %.

6.2.5 L5 - 3,4-dihydroxyphenyl (2,6-di-1H-pyrazole-1-yl)pyridine-4-carboxylate



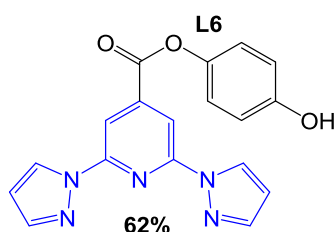
3,4-Dihydroxyphenyl (2,6-di-1H-pyrazole-1-yl)pyridine-4-carboxylate was prepared using the following procedure:⁴ **L3** 3,4-Dimethoxyphenyl (2,6-di-1H-pyrazole-1-yl)pyridine-4-carboxylate (1.564 g, 4 mmol, 1 eq.) was dissolved in dry DCM (40 ml) under nitrogen. The solution was

cooled in a mixture of cardice and acetone, and boron tribromide (4 ml, 42.15 mmol, 10.5 eq.) was added dropwise. The reaction mixture was stirring for 4 hrs at reflux under nitrogen using subaseal. The obtained orange solution was cooled in ice water and water (20 ml) was added dropwise, and two precipitates, white and red, were filtered, washed with water, dried on the filter and then washed with DCM and recrystallized from acetone. After this purification both red and white precipitates turned into a greyish-white powders, which were confirmed to be the same compound by $^1\text{H NMR}$. After desiccation, a greyish-white powder of the target product (1.009 g, 69%) was obtained.

Analyses: $^1\text{H NMR}$ (DMSO- D_6 , 400.130 MHz, ppm): δ 9.34 (s, 1H, Ph H7), 9.04 (d, 2H, Pz H5), 8.29 (s, 2H, Py H3,5), 7.95 (d, 2H, Pz H3), 6.82 (d, 1H, Ph H5), 6.77 (d, 1H, Ph H2), 6.71 (t, 2H, Pz H4), 6.64 (dd, 1H, Ph H6), ^{13}C

NMR (100.613 MHz, DMSO, ppm): δ 162.67 (Py C7), 150.46 (Py C2,6), 145.76 (Ph C1), 143.75 (Py C4), 143.39 (Pz C3,5), 142.79 (Ph C4), 142.44 (Ph C3), 128.52 (Pz C5), 115.32 (Ph C5), 111.61 (Ph C6), 109.29 (Ph C2), 109.04 (Pz C4), 108.18 (Py C3,5), **MS** (HR- ESI) m/z: calc. for [C₁₈H₁₃N₅O₄ + H⁺]: 364.0991, found: 364.1041, calc. for [C₁₈H₁₃N₅O₄ + Na⁺]: 386.0860, found: 386.0865, **MP**: 258°C, **IR** (cm⁻¹): 1194, 1184 (C-OR), 1738 (C=O), 2800-3300 broad (Ph O-H), 1517 (Ph C=C), 1575 (Pz C=C and C=N), 1463, 1446, 1399 (Pz ring), 1207 (Py C-H), **CHN**: calculated for C₁₈H₁₃N₅O₄: C 59.50, H 3.61, N 19.28%, found: C 59.37, H 3.75, N 19.11 %.

6.2.6 L6 - 4-hydroxyphenyl (2,6-di-1H-pyrazole-1-yl)pyridine-4-carboxylate

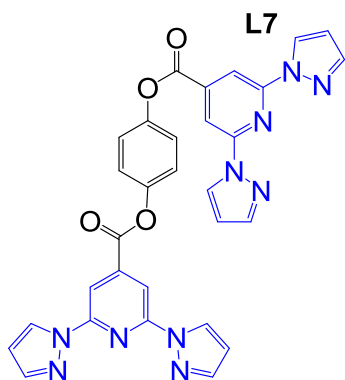


L6 3,4-Dihydroxyphenyl (2,6-di-1H-pyrazole-1-yl)pyridine-4-carboxylate was prepared from L4 by the procedure, described above for the L5 synthesis, using the following quantities: **L4** 4-methoxyphenyl (2,6-di-1H-pyrazole-1-yl)pyridine-

4-carboxylate 3.379 g (9.35 mmol, 1 eq), boron tribromide (5.32 ml, 14 g, 56.1 mmol, 6 eq), dry DCM (150 ml), which yielded the target product (2.025 g, 62 %) as white flakes.

Analyses: **¹H NMR** (DMSO-D₆, 400.130 MHz, ppm): δ 9.60 (br s, 1H, Ph H7), 9.03 (d, Pz 5), 8.29 (s, 2H, Py H3,5), 7.94 (s, 2H, Pz H3), 7.17 (d, 2H, Ph H2,6), 6.86 (d, 2H, Ph H3,5), 6.69 (t, 2H, Pz H4), **¹³C NMR** (100.613 MHz, DMSO, ppm): δ 162.79 (Py C7), 155.57 (Ph C4), 150.49 (Py C4), 143.39 (Ph C1), 142.42 (Pz C3), 142.74 (Py C2,6), 128.51 (Pz C5), 122.40 (Ph C2,6), 115.77 (Ph C3,5), 109.04 (Pz C4), 108.20 (Py C3,5), **MS** (HR-ESI) m/z: calc. for [C₁₈H₁₃N₅O₃ + Na⁺]: 370.0916, found: 370.0910, **MP**: 233-234°C, **IR** (cm⁻¹): 1188, 1180 (C-OR), 1750 (C=O), 3100-3300 broad (Ph O-H), 1509 (Ph C=C), 1574 (Pz C=C and C=N), 1465, 1443, 1395 (Pz ring), 1227 (Py C-H), **CHN**: calculated for C₁₈H₁₃N₅O₃: C 62.24, H 3.77, N 20.16%, found: C 62.14, H 3.58, N 19.95%.

6.2.7 L7 - 1,4-di(2,6-di(1H-pyrazol-1'-yl)pyridine-4-carboxy)benzene

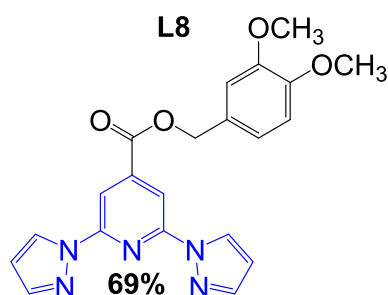


Attempts to attach a long alkyl chain to L6 led to formation of 1,4-di(2,6-di(1H-pyrazol-1'-yl)pyridine-4-carboxy)benzene. **L5** 4-hydroxy-phenyl(2,6-di-1H-pyrazole-1-yl)pyridine-4-carboxylate (63.6 mg, 0.18 mmol, 1 eq.) was dissolved in dry MeCN (15

ml), after which anhydrous K_2CO_3 (38 mg, 0.27 mmol, 1.5 eq.), a catalytic amount of KI, and 1-bromododecane (51 mg, 0.18 mmol, 1 eq.) in dry MeCN (5 ml) were added into the solution. The reaction mixture was stirred under nitrogen at 40°C for 16h, and then the cream coloured flakes were filtered off from the solution, washed with water and acetone, and dried.

Analyses: **MS** (HR- ESI) m/z: calc. for [L6+ Na⁺]: 370.0916, found: 370.0909; calc. for [L7 + H⁺]: 585.1748, found: 858.1759, calc. for [L7 + Na⁺]: 607.1567, found: 607.1578, calc. for [L7 + K⁺]: 623.1301, found: 623.1320, where L6 - C₁₈H₁₃N₅O₃, L7 - C₃₀H₂₀N₁₀O₄, **¹H NMR** (DMSO-D₆, 400.130 MHz, ppm): δ 9.05 (d, 2H, Pz H5), 8.89 (d, 2H, Pz H5'), 8.30 (s, 2H, Py H3,5), 8.13 (s, 2H, Py H3,5'), 7.95 (s, 2H, Pz H3), 7.85 (s, 2H, Pz H3'), 7.16 (d, 2H, Ph H2,6), 6.87 (d, 2H, Ph H3,5), 6.70 (t, 2H, Pz H4), 6.60 (t, 2H, Pz H4'). See Chapter 2.2.5 for more information.

6.2.8 L8 - 3,4-methoxybenzyl (2,6-di-1H-pyrazol-1-yl)pyridine-4-carboxylate



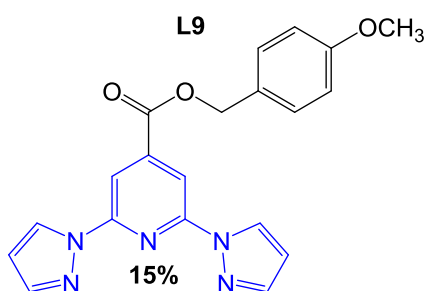
L8 was obtained according to the procedure, reported by Marcelis *et al.*⁵ with some modifications. A mixture of **L2** 2,6-di(1H-pyrazol-1'-yl)pyridine-4-carboxylic acid (1.100 g, 4.31 mmol, 1 eq), N,N-dicyclohexyl carbodiimide (DCC) (1.956 g, 9.482 mmol, 2.2 eq), 3,4-methoxybenzyl alcohol (0.725 g, 0.616

ml, 4.31 mmol, 1 eq), and a catalytic amount of dimethyl-aminopyridine (DMAP) (caution - very toxic) in DCM was stirred for 2 days under a CaCl₂ tube, the precipitate was filtered off, and the obtained golden-yellow filtrate was either concentrated under vacuum and recrystallized from boiling MeCN (20 ml), filtered off, washed with hexane and desiccated, which yielded a pure product as a white crystalline powder (1.200 g, 69%).

Analyses: **¹H NMR** (DMSO-D₆, 400.130 MHz, ppm): δ 8.96 (d, 2H, Pz H5), 8.13 (s, 2H, Py H3,5), 7.89 (d, 2H, Pz H3), 7.15 (d, 1H, Ph H2), 7.07 (dd, 1H, Ph H5), 7.01 (d, 1 H, Ph H6), 6.65 (dd, 2H, Pz H4), 5.35 (s, 2H, Ph H7), 3.79 (s, 3H, Ph H9), 3.78 (s, 3H, Ph H8), **¹³C NMR** (100.613 MHz, DMSO, ppm): δ 163.30 (Py C7), 150.35 (Ph C2,6), 149.11 (Ph C4), 148.70 (Ph C3), 142.95 (Ph C1), 143.21 (Pz C3), 128.36 (Pz C5), 127.44 (Py C4), 121.56 (Ph C5), 112.74 (Ph C2), 111.72 (Ph C6), 108.88 (Pz C4), 107.76 (Py C3,5), 67.70 (Ph C7), 55.50 (Ph C8,9), **MS** (HR- ESI) m/z: calc. for [C₂₁H₁₉N₅O₄ + H⁺]: 406.1510, found: 406.1507, calc. for [C₂₁H₁₉N₅O₄ + Na⁺]: 428.1329, found: 428.1335, calc. for [2 C₂₁H₁₉N₅O₄ + Na⁺]: 833.2766, found: 833.2764,

MP: 130.2-130.4°C, **IR** (cm⁻¹): 2826 (OCH₃), 1721 (C=O), 1575 (Pz C=C), 1459, 1446 (Ph OCHR-H), 1239, 1226, 1211 (C-OR), 1053, 1028 (RCH₂-OR), 757 (Py C-H).

6.2.9 L9 - 4-methoxybenzyl (2,6-di-1H-pyrazol-1-yl)pyridine-4-carboxylate

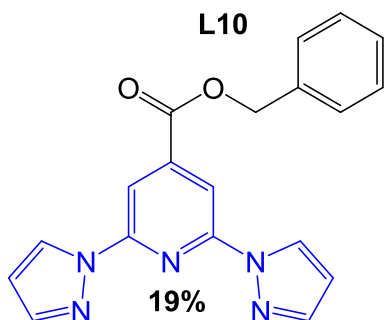


4-Methoxybenzyl (2,6-di-1H-pyrazol-1-yl)pyridine-4-carboxylate was prepared by the same procedure as for **L8**, using the following quantities: 2,6-di(1H-pyrazol-1'-yl)pyridine-4-carboxylic acid 1 g (3.918 mmol, 1 eq), 4-methoxybenzyl alcohol 541.3 mg (3.918 mmol, 1 eq), DCC 1.778 g

(8.620 mmol, 2.2 eq), and a pinch of DMAP as a catalyst. Recrystallization from MeCN didn't yield a pure compound, therefore the crude product was separated by column chromatography (hexane: ethyl acetate, 1:1, 1st spot) as a white crystalline powder (220 mg, 15%).

Analyses: **¹H NMR** (CDCl₃, 400.130 MHz, ppm): δ 8.55 (d, 2H, Pz H5), 8.38 (s, 2H, Py H3,5), 7.78 (d, 2H, Pz H3), 7.42 (d, 1H, Ph H2,6), 6.93 (d, 2H, Ph H3,5), 6.51 (dd, 2H, Pz H4), 5.37 (s, 2H, Ph H7), **¹³C NMR** (100.613 MHz, CDCl₃, ppm): δ 164.13 (Py C7), 160.10 (Ph C4), 150.92 (Py C4), 143.63 (Py C2,6), 142.96 (Pz C3), 130.75 (Ph 2,6), 127.41 (Ph C1), 127.35 (Pz C5), 114.24 (Ph C3,5), 109.40 (Py C3,5), 108.53 (Pz C4), 67.85 (Ph C7), 55.46 (Ph C8), **MS** (HR- ESI) m/z: calc. for [C₂₀H₁₇N₅O₃ + H⁺]: 376.1404, found: 376.1402, calc. for [C₂₀H₁₇N₅O₃ + Na⁺]: 398.1224, found: 398.1223, **MP:** 150.6-152.5°C, **IR** (cm⁻¹): 2850 (OCH₃), 1718 (C=O), 1575 (Pz C=C), 1463, 1448 (Ph OCHR-H), 1237, 1207 (C-OR), 1052, 1042 (RCH₂-OR), 753 (Py C-H).

6.2.10 L10 - benzyl (2,6-di-1H-pyrazol-1-yl)pyridine-4-carboxylate



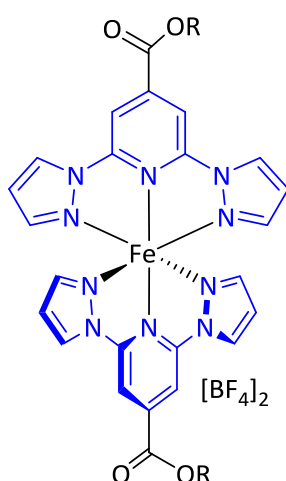
Benzyl (2,6-di-1H-pyrazol-1-yl)pyridine-4-carboxylate was prepared using the same procedure as for **L8**, with the following quantities: 2,6-di(1H-pyrazol-1'-yl)pyridine-4-carboxylic acid (1.000 g, 3.918 mmol, 1 eq), benzyl alcohol (424 mg, 3.918 mmol, 1 eq), DCC (1.778 g, 8.620 mmol, 2.2 eq), and a

pinch of DMAP as a catalyst. Recrystallization from MeCN and ethyl acetate yielded an almost pure compound, which was then purified by a short

column (hexane: ethyl acetate, 1:1, 1st spot) to yield white plate crystals (250 mg, 19%).

Analyses: **¹H NMR** (CDCl₃, 400.130 MHz, ppm): δ 8.56 (d, 2H, Pz H5), 8.41 (s, 2H, Py H3,5), 7.79 (d, 2H, Pz H4), 7.48 (dd, 1H, Ph H4), 7.47 (d, 2H, Ph H2,6), 7.39 (dd, 2H, Ph H3,5), 6.51 (t, 2H, Pz H4), 5.44 (s, 2H, Ph H7), **¹³C NMR** (100.613 MHz, CDCl₃, ppm): δ 164.08 (Py C7), 150.96 (Ph C4), 143.46 (Py C2,6), 142.99 (Pz C3), 135.26 (Ph C1), 128.86 (Ph C2,6), 128.81 (Ph C3,5), 127.36 (Pz C5), 109.40 (Py C3,5), 108.56 (Pz C4), 67.98 (Ph C7), **MS** (HR- ESI) m/z: calc. for [C₁₉H₁₅N₅O₂ + H⁺]: 346.1299, found: 346.1302, calc. for [C₁₉H₁₅N₅O₂ + Na⁺]: 368.1118, found: 368.1130, **MP**: 119.9-120.2°C, **IR** (cm⁻¹): 1727 (C=O), 1572 (Pz C=C), 1456, 1445 (Ph OCHR-H), 1237, 1207 (C-OR), 1064, 1048 (RCH₂-OR), 758 (Py C-H).

6.2.11 Iron(II) complexes from chapter 2



All the iron(II) complexes in Chapter 2 were obtained by this general procedure, adapted from the literature:⁴ The ligand (1 eq.) was dissolved in the appropriate solvent – either nitromethane, acetonitrile or acetone, and iron(II) tetrafluoroborate hexahydrate (0.5 eq.) was dissolved in the same solvent, with a gentle heating, if necessary. The two solutions were mixed at room temperature, which lead to instant formation of an intensively coloured solution, which, if necessary, was filtered through a pipette filter, then concentrated *in vacuo*. The isolated by filtration complex solution was

first tested by mixing a small amount of the solution with Et₂O, and if it induced the precipitation, the vials with the complex solution were set for ether diffusion crystallization. Sometimes diluting the complex solution a little led to growth of better quality crystals.

[Fe(L3)₂][BF₄]₂

3,4-Dimethoxyphenyl (2,6-di-1H-pyrazole-1-yl)pyridine-4-carboxylate iron(II) tetrafluoroborate was obtained according with the general procedure described above, using the following quantities: **L3** 3,4-dimethoxyphenyl (2,6-di-1H-pyrazole-1-yl)pyridine-4-carboxylate (39 mg, 0.100 mmol, 1eq), iron(II) tetrafluoroborate hexahydrate (17 mg, 0.050 mmol, 0.5 eq), MeNO₂ (7.5 ml), which yielded red crystals (32 mg, 63%), and a small quantity of yellow crystals, which were separated crystal-by-crystal using tweezers; single crystal XRD structures were collected for both red and yellow crystals,

which proved these two polymorphs to be have the same formula, but the red crystals to be LS at room temperature, and the yellow ones to be HS.

Analyses: **¹H NMR** (MeCN-D₃, 300.130 MHz, ppm): δ 40.41, 39.52, 26.36, 23.32 (Pz H₃, H₄, H₅, Py H_{3,5}), **MS** (HR - ESI) m/z: calc. for [C₂₀H₁₇N₅O₄+H⁺]: 392.1353, found: 392.1387, **IR** (cm⁻¹): 1186 (C-OR), 1744 (C=O), 970-1180 (B-F stretch), 521 (B-F deformation), 1509 (Ph C=C), 2831 (PhO-CH₃), 1577 (Pz C=C and C=N), 1461, 1440, 1407 (Pz ring), 1225 (Py C-H), **CHN**: calculated for C₄₀H₃₄N₁₀O₈Fe₁B₂F₈: C 47.46, H 3.39, N 13.84%, found: C 47.27, H 3.48, N 13.63%.

[Fe(L4)₂][BF₄]₂

4-Methoxyphenyl (2,6-di-1H-pyrazole-1-yl)pyridine-4-carboxylate iron(II) tetrafluoroborate was obtained according with the general procedure described above, using the following quantities: **L4** 4-methoxyphenyl (2,6-di-1H-pyrazole-1-yl)pyridine-4-carboxylate (65 mg, 0.180 mmol, 1eq), iron(II) tetrafluoroborate hexahydrate (30.36 mg, 0.090 mmol, 0.5 eq), Me₂CO, which yielded dark-red needle crystals (23 mg, 27%).

Analyses: **¹H NMR** (MeCN-D₃, 300.130 MHz, ppm): δ 40.38, 39.77, 26.22, 23.11 (Pz H₃, H₄, H₅, Py H_{3,5}), **MS** (HR- ESI) m/z: calc. for [C₁₉H₁₅N₅O₃+H⁺]: 362.1254, found: 362.1250, **IR** (cm⁻¹): 1187, 1168 (C-OR), 1744 (C=O), 960-1083(B-F stretch), 521 (B-F deformation), 1506 (Ph C=C), 2843 (PhO-CH₃), 1577 (Pz C=C and C=N), 1472, 1441, 1407 (Pz ring), 1223 (Py C-H), **CHN**: calculated for C₃₈H₃₀N₁₀O₆Fe₁B₂F₈: C 47.93, H 3.18, N 14.71, found: C 47.50, H 3.10, N 14.80%.

[Fe(L5)₂][BF₄]₂

3,4-Dihydroxyphenyl (2,6-di-1H-pyrazole-1-yl)pyridine-4-carboxylate iron(II) tetrafluoroborate was obtained according with the general procedure described above, using the following quantities: **L5** 3,4-Dihydroxyphenyl (2,6-di-1H-pyrazole-1-yl)pyridine-4-carboxylate (162 mg, 0.456 mmol, 1 eq), iron(II) tetrafluoroborate hexahydrate (75.3 mg, 0.223 mmol, 0.5 eq), Me₂CO, which yielded a dark-red crystalline powder (42 mg, 20%).

Analyses: **¹H NMR** (MeCN-D₃, 300.130 MHz, ppm): δ 40.32, 39.77, 26.01, 23.08 (Pz H₃, H₄, H₅, Py H_{3,5}), **MS** (HR-ESI) m/z: calc. for [C₁₈H₁₃N₅O₄+H⁺]: 364.1046, found: 364.1042, calc. for [C₁₈H₁₃N₅O₄+Na⁺]: 386.0866, found: 364.0860, **IR** (cm⁻¹): 1742 (C=O), 2800-3600 (PhO-H), 954-1144 (B-F stretch), ca. 520 (B-F deformation), 1498 (Ph C=C), 1575 (Pz C=C and C=N), 1461, 1440, 1407 (Pz ring), 1217 (Py C-H), **CHN**: calculated

for $C_{36}H_{26}N_{10}O_8Fe_1B_2F_8$: C 45.22, H 2.74, N 14.65%, found: C 45.19, H 2.52, N 14.72%.

[Fe(L6)₂][BF₄]₂

3,4-Dihydroxyphenyl (2,6-di-1H-pyrazole-1-yl)pyridine-4-carboxylate iron(II) tetrafluoroborate was obtained according with the general procedure described above, using the following quantities: **L6** 3,4-Dihydroxyphenyl (2,6-di-1H-pyrazole-1-yl)pyridine-4-carboxylate (150 mg, 0.431 mmol, 1 eq), iron(II) tetrafluoroborate hexahydrate (72.9 mg, 0.216 mmol, 0.5 eq), Me₂CO, which yielded thin red needle crystals (97 mg, 49%).

Analyses: **¹H NMR** (MeCN-D₃, 300.130 MHz, ppm): δ 40.74, 39.60, 26.39, 23.06 (Pz H₃, H₄, H₅, Py H_{3,5}), **MS** (HR-ESI) m/z: calc. for [C₁₈H₁₃N₅O₃+Na⁺]: 370.0911, found: 370.0925, **IR** (cm⁻¹): 1184, 1165 (C-OR), 1749 (C=O), 3100-3500 (PhO-H), 1050 very broad (B-F stretch), 517 (B-F deformation), 1509 (Ph C=C), 1574 (Pz C=C and C=N), 1472, 1442, 1409 (Pz ring), 1221 (Py C-H), **CHN**: calculated for C₃₆H₂₆N₁₀O₆Fe₁B₂F₈: C 46.79, H 2.84, N 15.16%, found: C 46.72, H 3.00, N 15.26%.

[Fe(L8)₂][BF₄]₂

3,4-Methoxybenzyl (2,6-di-1H-pyrazol-1-yl)pyridine-4-carboxylate iron(II) tetrafluoroborate was obtained according with the general procedure described above, using the following quantities: **L8** 3,4-methoxybenzyl (2,6-di-1H-pyrazol-1-yl)pyridine-4-carboxylate (200 mg, 0.493 mmol, 1eq), iron(II) tetrafluoroborate hexahydrate (93.1 mg, 0.247 mmol, 0.5 eq), acetone (ca 5.5 ml),), and Et₂O as antisolvent, which yielded the product as small red needle crystals (102 mg, 40%).

Analyses: **¹H NMR** (MeCN-D₃, 300.130 MHz, ppm): δ 37.24 ((Pz H₃), 37.02 (Pz H₄), 24.73 (Pz H₅), 21.32 (Py H_{3,5}), **MS** (HR- ESI) m/z: calc. for [C₂₁H₁₉N₅O₄ + H⁺]: 406.1510, found: 406.1514, calc. for [C₂₁H₁₉N₅O₄ + Na⁺]: 428.1329, found: 428.1332, calc. for [2 C₂₁H₁₉N₅O₄ + Na⁺]: 833.2766, found: 833.2767, **IR** (cm⁻¹): 2839 (OCH₃), 1731 (C=O), 1573 (Pz C=C), 1472, 1462 (Ph OCHR-H), 1247 (CO-R), 1052, 764 (B-F), **CHN**: calculated for C₄₂H₃₈N₁₀O₈Fe₁B₂F₈: C 48.49, H 3.68, N 13.46 %, found: C 48.36, H 3.72, N 13.33 %.

[Fe(L9)₂][BF₄]₂

4-Methoxybenzyl (2,6-di-1H-pyrazol-1-yl)pyridine-4-carboxylate iron(II) tetrafluoroborate was obtained according with the general procedure described above, using the following quantities: **L9** 4-methoxybenzyl (2,6-di-1H-

pyrazol-1-yl)pyridine-4-carboxylate (100 mg, 0.266 mmol, 1eq), iron(II) tetrafluoroborate hexahydrate (50.3 mg, 0.1332 mmol, 0.5 eq), acetone (ca 7.5 ml), and Et₂O as antisolvent, which yielded the product as big red scale-like crystals (104 mg, 40%).

Analyses: **¹H NMR** (MeCN-D₃, 600.2563 MHz, ppm): δ 40.11 (Pz H3), 38.26 (Pz H3), 24.89 (Pz H5), 21.38 (Py H3,5), **MS** (HR- ESI) m/z: calc. for [C₂₀H₁₇N₅O₃ + H⁺]: 376.1404, found: 376.1403, calc. for [C₂₀H₁₇N₅O₃ + Na⁺]: 398.1224, found: 398.1228, calc. for [2 C₂₀H₁₇N₅O₃ + Na⁺]: 773.2561, found: 773.2553, **IR** (cm⁻¹): 2937 (OCH₃), 1730 (C=O), 1573 (Pz C=C), 1472 (Ph OCHR-H), 1242 (CO-R), 1051, 764 (B-F), **CHN**: calculated for C₄₀H₃₄N₁₀O₆Fe₁B₂F₈: C 49.01, H 3.50, N 14.29 %, found: C 48.89, H 3.61, N 14.05 %.

[Fe(L10)₂][BF₄]₂

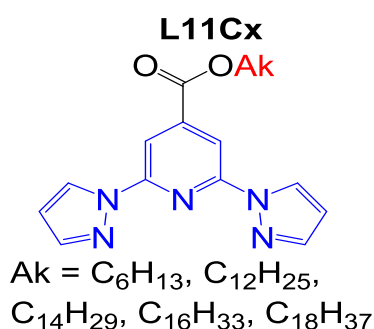
Benzyl (2,6-di-1H-pyrazol-1-yl)pyridine-4-carboxylate iron(II) tetrafluoroborate was obtained according with the general procedure described above, using the following quantities: **L10** benzyl (2,6-di-1H-pyrazol-1-yl)pyridine-4-carboxylate (100 mg, 0.266 mmol, 1eq), iron(II) tetrafluoroborate hexahydrate (54.7 mg, 0.145 mmol, 0.5 eq), acetone (ca 5.5 ml), and Et₂O as antisolvent, which yielded the iron complex as thick red plate crystals (96.5 mg, 36%).

Analyses: **¹H NMR** (MeCN-D₃, 600.2563 MHz, ppm): δ 36.85 (Pz H3), 35.41 (Pz H4), 23.66 (Pz H5), 20.20 (Py H3,5), **MS** (HR- ESI) m/z: calc. for [C₁₉H₁₅N₅O₂ + H⁺]: 346.1299, found: 346.1294, calc. for [C₁₉H₁₅N₅O₂ + Na⁺]: 368.1118, found: 368.1119, calc. for [2 C₁₉H₁₅N₅O₂ + Na⁺]: 713.2344, found: 713.2336, **IR** (cm⁻¹): 1729 (C=O), 1572 (Pz C=C), 1471 (Ph OCHR-H), 1243 (CO-R), 1050, 762 (B-F), **CHN**: calculated for C₃₈H₃₀N₁₀O₄Fe₁B₂F₈: C 49.60, H 3.29, N 15.22 %, found: C 49.45, H 3.17, N 15.08 %.

6.3 Chapter 3 - Pyridine-substituted bis(pyrazol-1-yl)pyridine derivatives with long alkyl chains, and their iron(II) complexes

The labelling scheme for this chapter is shown on the Fig. 6.1

6.3.1 L11Cx - alkyl (2,6-di-1H-pyrazol-1-yl)pyridine-4-carboxylates



Alkyl (2,6-di-1H-pyrazol-1-yl)pyridine-4-carboxylates were obtained using the procedure, described in literature,⁵ with some modifications. A mixture of L2 2,6-di(1H-pyrazol-1'-yl)pyridine-4-carboxylic acid (1 eq), N,N-dicyclohexyl carbodiimide (DCC) (2.2 eq), a long alkyl chain alcohol (1eq), and a catalytic amount of dimethylaminopyridine (DMAP)

/caution - very toxic/ in DCM was stirred for 2 days under a CaCl₂ tube, the precipitate was filtered off, and the obtained golden-yellow filtrate was either (i) concentrated under vacuum and separated by column chromatography (0.3% MeOH in DCM), the target product came out at *r_f* = 0.5, or (ii) recrystallized from boiling MeCN, washed with hexane and desiccated.

L11C6 - hexyl (2,6-di-1H-pyrazol-1-yl)pyridine-4-carboxylate

Hexyl (2,6-di-1H-pyrazol-1-yl)pyridine-4-carboxylate was prepared using the general procedure described above, using the following quantities: 2,6-di(1H-pyrazol-1'-yl)pyridine-4-carboxylic acid 2.036 g (7.97 mmol, 1 eq), hexanol 0.814 g (7.97 mmol, 1 eq), DCC 3.616 g (17.53 mmol, 2.2 eq), and a pinch of DMAP. The product was purified column chromatography (hexane: ethyl acetate, 4:1), and obtained as a white solid (1.249 g, 46%).

Analyses: ¹H NMR (CDCl₃, 400.130 MHz, ppm): δ 8.56 (d, 2 H, Pz H5), 8.38 (s, 2 H, Py H3,5), 7.79 (d, 2 H, Pz H3), 6.51 (dd, 2 H, Pz H4), 4.39 (t, 2 H Ak H1), 1.81 (p, 2H, Ak H2), 1.44 (p, 2 H, Ak H3), 1.35 (s, 4 H, Ak H4,5), 0.91 (t, 3H, Ak H6), ¹³C NMR (CDCl₃, 100.613 MHz, ppm): δ 164.24 (Py C7), 150.92 (Py C2,6), 143.82 (Py C4), 142.95 (Pz C3), 127.35 (Pz C5), 109.32 (Py C3,5), 108.52 (Pz C4), 66.52 (Ak C1), 31.56 (Ak C4), 28.69 (Ak C2), 25.71 (Ak C3), 22.66 (Ak C5), 14.13 (Ak C6), **MS** (HR-ESI) *m/z*: calc. for [C₁₈H₂₁N₅O₂+H⁺]: 340.1768, found: 340.1713, calc. for [C₁₈H₂₁N₅O₂+Na⁺]: 362.1587, found: 362.1512, **IR** (cm⁻¹): 2917, 2856 (CH₃, CH₂), 1724 (C=O), 1571 (Pz C=C, C=N), 1457, 1392 (Pz ring), 1240 (C-OR), 1039 (Py C=C-H), **MP**: 77.6-78.0°C, **CHN**: calculated for C₁₈H₂₁N₅O₂: C 63.70, H 6.24, N 20.64%, found: C 63.84, H 6.33, N 20.58%.

L11C12 - dodecyl (2,6-di-1H-pyrazol-1-yl)pyridine-4-carboxylate

Dodecyl (2,6-di-1H-pyrazol-1-yl)pyridine-4-carboxylate was prepared using the general procedure described above, using the following quantities: 2,6-di(1H-pyrazol-1'-yl)pyridine-4-carboxylic acid 0.26 g (1 mmol, 1 eq),

dodecanol 0.186 g (1 mmol, 1 eq), DCC 0.46 g (2.2 mmol, 2.2 eq), and a pinch of DMAP. The product was purified by recrystallization from MeCN, and collected as a white solid (0.228 g, 16%).

Analyses: $^1\text{H NMR}$ (CDCl_3 , 400.130 MHz, ppm): δ 8.58 (d, 2 H, Pz H5), 8.39 (s, 2 H, Py H3,5), 7.80 (d, 2 H, Pz H3), 6.53 (dd, 2 H, Pz H4), 4.40 (t, 2 H Ak H1), 1.81 (p, 2H, Ak H2), 1.44 (p, 2 H, Ak H3), 1.26 (s, 16 H, Ak H4-11), 0.87 (t, 3H, Ak H12), $^{13}\text{C NMR}$ (CDCl_3 , 100.613 MHz, ppm): δ 164.26 (Py C7), 150.94 (Py C2,6), 143.84 (Py C4), 142.96 (Pz C3), 127.36 (Pz C5), 109.35 (Py C3,5), 108.53 (Pz C4), 66.54 (Ak C1), 28.73 (Ak C2), 26.04 (Ak C3), 29.78, 29.76, 29.71, 29.63, 29.48, 29.39 (Ak C4-9), 32.05 (C10), 22.82 (Ak C11), 14.25 (Ak C12), **MS** (HR-ESI) m/z: calc. for $[\text{C}_{24}\text{H}_{33}\text{N}_5\text{O}_2+\text{H}^+]$: 424.2707, found: 424.2722, calc. for $[\text{C}_{24}\text{H}_{33}\text{N}_5\text{O}_2+\text{Na}^+]$: 446.2526, found: 446.2531, **IR** (cm^{-1}): 2912, 2848 (CH_3 , CH_2), 1728 ($\text{C}=\text{O}$), 1575 (Pz $\text{C}=\text{C}$, $\text{C}=\text{N}$), 1464. 1395 (Pz ring), 1243 ($\text{C}-\text{OR}$), 1039 (Py $\text{C}=\text{C}-\text{H}$), **MP**: 79.9°C, **CHN**: calculated for $\text{C}_{24}\text{H}_{33}\text{N}_5\text{O}_2$: C 68.06, H 7.85, N 16.53%, found: C 67.94, H 7.96, N 16.44%.

L11C14 - tetradecyl (2,6-di-1H-pyrazol-1-yl)pyridine-4-carboxylate

Tetradecyl (2,6-di-1H-pyrazol-1-yl)pyridine-4-carboxylate was prepared using the general procedure described above, using the following quantities: 2,6-di(1H-pyrazol-1'-yl)pyridine-4-carboxylic acid 0.800 g (3.1 mmol, 1 eq), tetradecanol 0.665 g (3.1 mmol, 1 eq), DCC 1.424 g (6.9 mmol, 2.2 eq), and a pinch of DMAP. The product was purified by recrystallization from MeCN, and collected as a white solid (0.225 g, 14%).

Analyses: $^1\text{H NMR}$ (CDCl_3 , 400.130 MHz, ppm): δ 8.57 (d, 2 H, Pz H5), 8.38 (s, 2 H, Py H3,5), 7.80 (d, 2 H, Pz H3), 6.52 (dd, 2 H, Pz H4), 4.39 (t, 2 H Ak H1), 1.81 (p, 2H, Ak H2), 1.44 (p, 2 H, Ak H3), 1.26 (s, 20 H, Ak H4-13), 0.87 (t, 3H, Ak H14), $^{13}\text{C NMR}$ (CDCl_3 , 100.613 MHz, ppm): δ 164.26 (Py C7), 150.94 (Py C2,6), 143.85 (Py C4), 142.96 (Pz C3), 127.36 (Pz C5), 109.35 (Py C3,5), 108.53 (Pz C4), 66.55 (Ak C1), 28.73 (Ak C2), 25.76 (Ak C3), 32.07, 29.83, 29.79, 29.72, 29.64, 29.50, 29.40 (Ak C4-13), 14.25 (Ak C14), **MS** (HR-ESI) m/z: calc. for $[\text{C}_{26}\text{H}_{37}\text{N}_5\text{O}_2+\text{H}^+]$: 452.3020, found: 452.3028, calc. for $[\text{C}_{26}\text{H}_{37}\text{N}_5\text{O}_2+\text{Na}^+]$: 474.2839, found: 474.2841, **IR** (cm^{-1}): 2914, 2849 (CH_3 , CH_2), 1728 ($\text{C}=\text{O}$), 1576 (Pz $\text{C}=\text{C}$, $\text{C}=\text{N}$), 1463. 1396 (Pz ring), 1241 ($\text{C}-\text{OR}$), 1039 (Py $\text{C}=\text{C}-\text{H}$), **MP**: 81.6°C, **CHN**: calculated for $\text{C}_{26}\text{H}_{37}\text{N}_5\text{O}_2$: C 69.15, H 8.26, N 15.51%, found: C 69.08, H 8.13, N 15.41%.

L11C16 - hexadecyl (2,6-di-1H-pyrazol-1-yl)pyridine-4-carboxylate

Hexadecyl (2,6-di-1H-pyrazol-1-yl)pyridine-4-carboxylate was prepared using the general procedure described above, using the following quantities: 2,6-di(1H-pyrazol-1'-yl)pyridine-4-carboxylic acid 0.831 g (3.1 mmol, 1 eq), hexadecanol 0.665 g (3.1 mmol, 1 eq), DCC 1.424 g (6.9 mmol, 2.2 eq), and a pinch of DMAP. The product was purified by recrystallization from MeCN, and collected as a white solid (0.810 g, 52%).

Analyses: $^1\text{H NMR}$ (CDCl_3 , 400.130 MHz, ppm): δ 8.57 (d, 2 H, Pz H5), 8.38 (s, 2 H, Py H3,5), 7.80 (d, 2 H, Pz H3), 6.52 (dd, 2 H, Pz H4), 4.39 (t, 2 H Ak H1), 1.81 (p, 2 H, Ak H2), 1.44 (p, 2 H, Ak H3), 1.26 (s, 24 H, Ak H4-15), 0.87 (t, 3 H, Ak H16), $^{13}\text{C NMR}$ (CDCl_3 , 100.613 MHz, ppm): δ 164.26 (Py C7), 150.94 (Py C2,6), 143.85 (Py C4), 142.96 (Pz C3), 127.36 (Pz C5), 109.35 (Py C3,5), 108.53 (Pz C4), 66.55 (Ak C1), 28.74 (Ak C2), 26.05 (Ak C3), 32.07, 29.84, 29.81, 29.72, 29.64, 29.50, 29.40, 22.84 (Ak C4-15), 14.26 (Ak C16), **MS** (HR-ESI) m/z: calc. for $[\text{C}_{28}\text{H}_{41}\text{N}_5\text{O}_2+\text{H}^+]$: 480.3333, found: 480.3337, calc. for $[\text{C}_{28}\text{H}_{41}\text{N}_5\text{O}_2+\text{Na}^+]$: 502.3152, found: 502.3152, **IR** (cm^{-1}): 2912, 2848 (CH_3 , CH_2), 1728 ($\text{C}=\text{O}$), 1575 (Pz $\text{C}=\text{C}$, $\text{C}=\text{N}$), 1464. 1395 (Pz ring), 1243 ($\text{C}-\text{OR}$), 1039 (Py $\text{C}=\text{C}-\text{H}$),), **MP**: 86.7°C, **CHN**: calculated for $\text{C}_{28}\text{H}_{41}\text{N}_5\text{O}_2$: C 70.11, H 8.62, N 14.60, found: C 69.95, H 8.57, N 14.48%.

L11C18 - octadecyl (2,6-di-1H-pyrazol-1-yl)pyridine-4-carboxylate

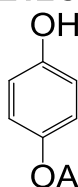
Octadecyl (2,6-di-1H-pyrazol-1-yl)pyridine-4-carboxylate was prepared using the general procedure described above, using the following quantities: 2,6-di(1H-pyrazol-1'-yl)pyridine-4-carboxylic acid 0.800 g (3.1 mmol, 1 eq), octadecanol 0.839 g (3.1 mmol, 1 eq), DCC 1.424 g (6.9 mmol, 2.2 eq), and a pinch of DMAP. The product was purified by recrystallization from MeCN, and collected as a white solid (0.800 g, 50%).

Analyses: $^1\text{H NMR}$ (CDCl_3 , 400.130 MHz, ppm): δ 8.57 (d, 2 H, Pz H5), 8.39 (s, 2 H, Py H3,5), 7.80 (d, 2 H, Pz H3), 6.52 (dd, 2 H, Pz H4), 4.39 (t, 2 H Ak H1), 1.81 (p, 2 H, Ak H2), 1.44 (p, 2 H, Ak H3), 1.26 (s, 28 H, Ak H4-17), 0.88 (t, 3 H, Ak H18), $^{13}\text{C NMR}$ (CDCl_3 , 100.613 MHz, ppm): δ 164.26 (Py C7), 150.94 (Py C2,6), 143.85 (Py C4), 142.96 (Pz C3), 127.36 (Pz C5), 109.35 (Py C3,5), 108.53 (Pz C4), 66.55 (Ak C1), 28.74 (Ak C2), 26.05 (Ak C3), 32.07, 29.84, 29.72, 29.64, 29.51, 29.40, 22.84 (Ak C4-17), 14.26 (Ak C18), **MS** (HR-ESI) m/z: calc. for $[\text{C}_{30}\text{H}_{45}\text{N}_5\text{O}_2+\text{H}^+]$: 508.3646, found: 508.3651, calc. for $[\text{C}_{30}\text{H}_{45}\text{N}_5\text{O}_2+\text{Na}^+]$: 530.3465, found: 530.3463, **IR** (cm^{-1}): 2912, 2848 (CH_3 , CH_2), 1728 ($\text{C}=\text{O}$), 1575 (Pz $\text{C}=\text{C}$, $\text{C}=\text{N}$), 1464. 1395 (Pz

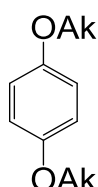
ring), 1243 (C-OR), 1039 (Py C=C-H), **MP**: 90.3-90.6°C, **CHN**: calculated for $C_{30}H_{45}N_5O_2 + 3 H_2O$: C 55.48, H 7.45, N 10.78%, found: C 55.19, H 7.64, N 10.86%.

6.3.2 L12CxM and L12CxD - 4-alkyloxyphenols and 1,4-bis(alkyloxy)benzenes

L12CxM



L12CxD



Alk = C_6H_{13} , $C_{12}H_{25}$,
 $C_{14}H_{29}$, $C_{16}H_{33}$, $C_{18}H_{37}$

4-Alkyloxyphenols and 1,4-bis(alkyloxy)benzenes were obtained using the procedure, described in literature⁶ with some modifications. A solution of the alkyl bromide (1 eq) and hydroquinone (5 eq) in DMF was flushed with nitrogen, after which K_2CO_3 (3 eq) was added, and the mixture was refluxed for 4 hours under an inert atmosphere.

After cooling to room temperature, the reaction mixture was poured into 350 mL of a 5% KOH solution. The precipitate was filtered off, washed with water until colourless filtrate starts coming out, then washed with 30 mL of 5% aqueous HCl and with water until pH 7.

The obtained white solid was washed with acetone, and the precipitate was dried, which resulted in a white powder of corresponding 1,4-bis(alkyloxy)benzene; while removing the solvent from the filtrate resulted in a white powder of 4-alkyloxyphenol.

L12C6

4-hexyloxyphenol **L12C6M** and 1,4-bis(hexyloxy)benzene **L12C6D** were prepared using the general procedure described above, using the following quantities: hydroquinone (10.2 g, 92.63 mmol, 5 eq), 1-bromohexane (3.058 g, 18.53 mmol, 1 eq), DMF 40 ml, and K_2CO_3 (7.683 g, 55.6 mmol, 3 eq). As the product mixture didn't precipitate from KOH solution, it was mixed with 15% HCl until the precipitate was formed, which then was filtered off, and separated by column chromatography (hexane: ethyl acetate, 4: 1), which yielded 1,4-bis(hexyloxy)benzene **L12C6D** (0.181 g, 7%), and 4-alkyloxyphenol **L12C6M** (1.641 g, 45.6%), both as white waxy solids.

Analyses: **L12C6M** 1H NMR ($CDCl_3$, 400.130 MHz, ppm): δ 6.78 (d, 2 H, Ph H_{2,6}), 6.76 (d, 2 H, Ph H_{3,5}), 4.82 (s, 1 H, Ph OH), 3.90 (t, 2 H, Alk H₁), 1.75 (p, 2 H, Alk H₂), 1.45 (p, 2 H, Alk H₃), 1.34 (s, 4 H, Alk H_{4,5}), 0.91 (t, 3 H, Alk H₆), ^{13}C NMR ($CDCl_3$, 100.613 MHz, ppm): δ 153.41 (Ph C₁), 149.51 (Ph C₄), 116.16 (Ph C_{2,6}), 115.83 (Ph C_{3,5}), 68.98 (Alk C₁), 31.74 (Alk C₄), 29.46 (Alk C₂), 25.85 (Alk C₃), 22.74 (Alk C₅), 14.16 (Alk C₆), **IR** (cm^{-1}):

3410.3 (PhO-H), 2931.2, 2869.7 (CH₃), 1511 (Ph C=C), 1231, (C-O stretch), 1034 (C-O), 822 (PhH-H), **MP**: 45.3-45.5°C.

L12C6D ¹H NMR (CDCl₃, 400.130 MHz, ppm): δ 6.83 (s, 4 H, Ph H_{2,3,5,6}), 3.90 (t, 4 H, Ak H₁), 1.75 (p, 4 H, Ak H₂), 1.45 (p, 4 H, Ak H₃), 1.34 (p, 8 H, Ak H_{4,5}), 0.89 (t, 6 H, Ak H₆), ¹³C NMR (CDCl₃, 100.613 MHz, ppm): δ 153.36 (Ph C_{1,4}), 115.56 (Ph C_{2,3,5,6}), 68.83 (Ak C₁), 31.77 (Ak C₄), 29.53 (Ak C₂), 22.85 (Ak C₅), 14.18 (Ak C₆), **MS** (HR-ESI) m/z: calc. for [C₁₈H₃₀O₂+H⁺]: 279.2319, found: 279.2314, **IR** (cm⁻¹): 2916, 2848 (CH₃), 1513 (Ph C=C), 1241, 1230 (C-O stretch), 1036, 1028 (C-O), 825 (PhH-H), **MP**: 43.8-44.3°C.

L12C12

4-Dodecyloxyphenol **L12C12M** and 1,4-bis (dodecyloxy)benzene **L12C12D** were prepared following the general procedure described above, using the following quantities: hydroquinone 11.045 g (100.3 mmols, 5 eq), 1-bromododecane 5 g (20.06 mmols, 1 eq), DMF 50 ml, and K₂CO₃ 8.32 g (60.18 mmols, 3 eq). The yield was 3.285 g (59%) for 4-dodecyloxyphenol and 0.654 g (15%) for 1,4-bis (dodecyloxy)benzene.

Analyses: **L12C12M** ¹H NMR (CDCl₃, 400.130 MHz, ppm): δ 6.78 (d, 2 H, Ph H_{2,6}), 6.76 (d, 2 H, Ph H_{3,5}), 4.76 (s, 1 H, Ph OH), 3.90 (t, 2 H, Ak H₁), 1.75 (p, 2 H, Ak H₂), 1.31 (p, 2 H, Ak H₃), 1.27 (s, 16 H, Ak H₄₋₁₁), 0.89 (t, 3 H, Ak H₁₂), ¹³C NMR (CDCl₃, 100.613 MHz, ppm): δ 153.44 (Ph C₁), 149.50 (Ph C₄), 116.15 (Ph C_{2,6}), 115.82 (Ph C_{3,5}), 68.96 (Ak C₁), 32.06 (Ak C₄), 29.75 (Ak C₂), 26.19 (Ak C₃), 29.80, 29.78, 29.74, 29.56, 29.51, 29.49 (Ak C₅₋₁₀), 22.83 (Ak C₁₁), 14.23 (Ak C₁₂), **MS** (HR-ESI) m/z: calc. for [C₁₈H₃₀O₂+H⁺]: 279.2319, found: 297.2317, **IR** (cm⁻¹): 3426 (PhO-H), 2915, 2850 (CH₃), 1514 (Ph C=C), 1237, 1038 (C-O stretch), 1038, 1047 (C-O), 820 (PhH-H), **MP**: 78.1°C, **CHN**: calculated for C₁₈H₃₀O₂: C 77.65, H 10.86%, found: C 77.58, H 10.79%.

L12C12D ¹H NMR (CDCl₃, 400.130 MHz, ppm): δ 6.82 (s, 4 H, Ph H_{2,3,5,6}), 3.90 (t, 4 H, Ak H₁), 1.76 (p, 4 H, Ak H₂), 1.45 (p, 4 H, Ak H₃), 1.31 (p, 4 H, Ak H₁₁), 1.28 (s, 28 H, Ak H₄₋₁₀), 0.89 (t, 6 H, Ak H₁₂), ¹³C NMR (CDCl₃, 100.613 MHz, ppm): δ 153.36 (Ph C_{1,4}), 115.54 (Ph C_{2,3,5,6}), 68.81 (Ak C₁), 32.08 (Ak C₄), 29.52 (Ak C₂), 26.22 (Ak C₃), 29.82, 29.79, 29.76, 29.58, 29.51 (Ak C₄₋₁₀), 22.84 (Ak C₁₁), 14.26 (Ak C₁₂), **MS** (HR-ESI) m/z: calc. for [C₃₀H₅₄O₂+H⁺]: 447.4197, found: 447.4192, **IR** (cm⁻¹): 2916, 2848 (CH₃), 1513 (Ph C=C), 1241, 1230 (C-O stretch), 1036, 1029 (C-O), 825 (PhH-H), **MP**: 74.7°C.

L12C14

4-Tetradecyloxyphenol and 1,4-bis (tetradecyloxy)benzene were prepared using the general procedure described above, using the following quantities: hydroquinone 9.91 g (90 mmols, 5 eq), 1-bromotetradecane 5 g (18 mmols, 1 eq), DMF 50 ml, and K₂CO₃ 7.463 g (54 mmols, 3 eq). The yield was 2.274 g (41%) for 4-tetradecyloxyphenol and 0.632 g (14%) for 1,4-bis (tetradecyloxy)benzene.

Analyses: **L12C14M** ¹H NMR (CDCl₃, 400.130 MHz, ppm): δ 6.78 (d, 2 H, Ph H_{2,6}), 6.76 (d, 2 H, Ph H_{3,5}), 4.81 (s, 1 H, Ph OH), 3.90 (t, 2 H, Ak H₁), 1.75 (p, 2 H, Ak H₂), 1.44 (p, 2 H, Ak H₃), 1.31 (p, 2 H, Ak H₁₃), 1.27 (s, 20 H, Ak H₄₋₁₂), 0.89 (t, 3H, Ak H₁₄), ¹³C NMR (CDCl₃, 100.613 MHz, ppm): δ 153.42 (Ph C₁), 149.51 (Ph C₄), 116.16 (Ph C_{2,6}), 115.82 (Ph C_{3,5}), 68.97 (Ak C₁), 29.75 (Ak C₂), 26.19 (Ak C₃), 32.07, 29.81, 29.80, 29.74, 29.73, 29.56, 29.51 (Ak C₄₋₁₂), 22.83 (Ak C₁₃), 14.25 (Ak C₁₄), **MS** (HR-ESI) m/z: calc. for [C₂₀H₃₄O₂+H⁺]: 307.2632, found: 307.2631, calc. for [2 C₂₀H₃₄O₂+H⁺]: 613.5190, found: 613.5194, **IR** (cm⁻¹): 3435 (PhO-H), 2915, 2848 (CH₃), 1515 (Ph C=C), 1370 (CH₃ C-H), 1241, 1230 (C-O stretch), 1036, 1029 (C-O), 820 (PhH-H), **MP**: 84.0 °C, **CHN**: calculated for C₂₀H₃₄O₂: C 78.38, H 11.18%, found: C 78.29, H 11.05%.

L12C14D ¹H NMR (CDCl₃, 400.130 MHz, ppm): δ 6.82 (s, 4 H, Ph H_{2,3,5,6}), 3.90 (t, 4 H, Ak H₁), 1.75 (p, 4 H, Ak H₂), 1.44 (p, 4 H, Ak H₃), 1.31 (p, 4 H, Ak H₁₃), 1.27 (s, 36 H, Ak H₄₋₁₂), 0.89 (t, 6 H, Ak H₁₄), ¹³C NMR (CDCl₃, 100.613 MHz, ppm): δ 153.36 (Ph C_{1,4}), 115.55 (Ph C_{2,3,5,6}), 68.33 (Ak C₁), 29.52 (Ak C₂), 26.22 (Ak C₃), 32.08 (Ak C₄), 29.81, 29.76, 29.75, 29.57, 29.52 (Ak C₅₋₁₂), 22.85 (Ak C₁₃), 14.26 (Ak C₁₄), **IR** (cm⁻¹): 2916, 2848 (CH₃), 1513 (Ph C=C), 1240, 1240 (C-O stretch), 1040, 1027 (C-O), 825 (PhH-H), **MP**: 80.1°C.

L12C16

4-hexadecyloxyphenol and 1,4-bis (hexadecyloxy)benzene were prepared using the general procedure described above, using the following quantities: hydroquinone 9.015 g (81.9 mmols, 5 eq), 1-bromododecane 5 g (16.4 mmols, 1 eq), DMF 50 ml, and K₂CO₃ 6.79 g (49.1 mmols, 3 eq). The yield was 3.729 g (68%) for 4-dodecyloxyphenol and 0.853 g (19%) for 1,4-bis (dodecyloxy)benzene.

Analyses: **L12C16M** ¹H NMR (CDCl₃, 400.130 MHz, ppm): δ 6.80 (d, 2 H, Ph H_{2,6}), 6.79 (d, 2 H, Ph H_{3,5}), 4.59 (s, 1 H, Ph OH), 3.90 (t, 2 H, Ak H₁), 1.77 (p, 2 H, Ak H₂), 1.44 (p, 2 H, Ak H₃), 1.27 (s, 24 H, Ak H₄₋₁₅), 0.89 (t,

3 H, Ak H16), **¹³C NMR** (CDCl₃, 100.613 MHz, ppm): δ 153.42 (Ph C1), 149.51 (Ph C4), 116.16 (Ph C2,6), 115.82 (Ph C3,5), 68.97 (Ak C1), 29.56 (Ak C2), 26.19 (Ak C3), 32.07, 29.81, 29.80, 29.74, 29.73, 29.56, 29.51 (Ak C4-14), 22.83 (Ak C15), 14.25 (Ak C16), **MS** (HR-ESI) m/z: calc. for [C₂₂H₃₈O₂ - H⁺]: 333.2794, found: 333.2797, calc. for [2 C₂₂H₃₈O₂ - H⁺]: 667.5665, found: 667.5668, **IR** (cm⁻¹): 3426 (PhO-H), 2915, 2850 (CH₃), 1514 (Ph C=C), 1370 (CH₃ C-H), 1241, 1230 (C-O stretch), 1036, 1029 (C-O), 820 (PhH-H), **MP**: 88.6°C, **CHN**: calculated for C₂₂H₃₈O₂: C 78.99, H 11.45%, found: C 79.01, H 11.49%.

L12C16D ¹H NMR (CDCl₃, 400.130 MHz, ppm): δ 6.82 (s, 4 H, Ph H2,3,5,6), 3.90 (t, 4 H, Ak H1), 1.75 (p, 4 H, Ak H2), 1.44 (p, 4 H, Ak H3), 1.31 (p, 4 H, Ak H15), 1.27 (s, 44 H, Ak H4-14), 0.89 (t, 6 H, Ak H16), **¹³C NMR** (CDCl₃, 100.613 MHz, ppm): δ 153.36 (Ph C1,4), 115.55 (Ph C2,3,5,6), 68.33 (Ak C1), 29.52 (Ak C2), 26.22 (Ak C3), 32.08, 29.81, 29.76, 29.57 (Ak C4-14), 22.85 (Ak C15), 14.26 (Ak C16), **IR** (cm⁻¹): 2916, 2848 (CH₃), 1515 (Ph C=C), 1243, 1231 (C-O strch.), 1039, 1030 (C-O), 824 (PhH-H), **MP**: 85.7°C.

L12C18

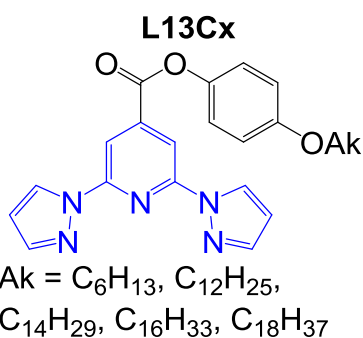
4-Octadecyloxyphenol and 1,4-bis (octadecyloxy)benzene were prepared using the general procedure described above, using the following quantities: hydroquinone 8.26 g (75 mmols, 5 eq), 1-bromododecane 5 g (15 mmols, 1 eq), DMF 50 ml, and K₂CO₃ 6.22 g (45 mmols, 3 eq). The yield was 3.569 g (65%) for 4-dodecyloxyphenol and 0.680 g (14%) for 1,4-bis (dodecyloxy)benzene.

Analyses: **L12C18M_1H NMR** (CDCl₃, 400.130 MHz, ppm): δ 6.77 (d, 2 H, Ph H2,6), 6.76 (d, 2 H, Ph H3,5), 4.49 (s, 1 H, Ph OH), 3.89 (t, 2 H, Ak H1), 1.75 (p, 2 H, Ak H2), 1.44 (p, 2 H, Ak H3), 1.26 (s, 28 H, Ak H4-17), 0.88 (t, 3 H, Ak H18), **¹³C NMR** (CDCl₃, 100.613 MHz, ppm): δ 153.52 (Ph C1), 149.46 (Ph C4), 116.13 (Ph C2,6), 115.78 (Ph C3,5), 68.91 (Ak C1), 32.08 (Ak C4), 29.57 (Ak C2), 26.20 (Ak C3), 29.85, 29.82, 29.75, 29.74, 29.57, 29.53, 29.52 (Ak C5-16), 22.84 (Ak C17), 14.26 (Ak C18), **MS** (HR-ESI) m/z: calc. for [C₂₄H₄₂O₂ - H⁺]: 361.3101, found: 361.3102, calc. for [2 C₂₄H₄₂O₂ - H⁺]: 723.6292, found: 723.6282, **IR** (cm⁻¹): 3432 (PhO-H), 2915, 2849 (CH₃), 1515 (Ph C=C), 1370 (CH₃ C-H), 1237, 1038 (C-O), 818 (PhH-H), **MP**: 92.4°C, **CHN**: calculated for C₂₄H₄₂O₂: C 79.50, H 11.68%, found: C 79.39, H 11.65%.

L12C18D ¹H NMR (CDCl₃, 400.130 MHz, ppm): δ 6.81 (s, 4 H, Ph H2,3,5,6), 3.89 (t, 4 H, Ak H1), 1.75 (p, 4 H, Ak H2), 1.44 (p, 4 H, Ak H3), 1.26 (s, 52 H,

Ak H4-17), 0.88 (t, 6 H, Ak H18), ^{13}C NMR (CDCl_3 , 100.613 MHz, ppm): δ 153.36 (Ph C1,4), 115.55 (Ph C2,3,5,6), 68.33 (Ak C1), 32.08 (Ak C4), 29.52 (Ak C2), 26.22 (Ak C3), 29.85, 29.76, 29.58, 29.52 (Ak C5-16), 22.85 (Ak C17), 14.26 (Ak C18), IR (cm^{-1}): 2915, 2847 (CH_3), 1516 (Ph C=C), 1241 (C-O stretch), 1038, 1026 (C-O), 823 (PhH-H), MP: 90.7°C.

6.3.3 L13Cx - 4-(alkyl)phenyl 2,6-di-1H-pyrazol-1-ylisonicotinates



4-(Alkyl)phenyl 2,6-di-1H-pyrazol-1-ylisonicotinates were obtained using the same protocol as for **L3** syntheses, described in literature,⁵ with some modifications. A mixture of **L2** 2,6-di(1H-pyrazol-1'-yl)pyridine-4-carboxylic acid (1 eq), N,N-dicyclohexyl carbodiimide (DCC) (2.2 eq), a long alkyl chain alcohol (1eq), and a catalytic amount of dimethylaminopyridine

(DMAP) /caution - very toxic/ in DCM was stirred for 2 days under a CaCl_2 tube, the precipitate was filtered of, and the solvent was removed under reduced pressure from the filtrate. After the obtained light-yellow oil crystallized, it was recrystallized from MeOH and desiccated.

L13C6

4-Hexyloxyphenyl (2,6-di-1H-pyrazol-1-yl)pyridine-4-carboxylate was prepared using the general procedure described above, using the following quantities: 2,6-di(1H-pyrazol-1'-yl)pyridine-4-carboxylic acid 1.839 g (7.21 mmol, 1 eq), 4-hexyloxyphenol 1.400 g (7.21 mmol, 1 eq), DCC 3.271 g (15.85 mmol, 2.2 eq), and a pinch of DMAP. Unlike other ligands in L9 series, L9C6 was hard to purify by recrystallization, so it was purified by column chromatography (hexane: ethyl acetate, 4:1) and additionally recrystallized from MeCN, which yielded clean product as a white crystalline solid (0.972 g, 31%).

Analyses: ^1H NMR (CDCl_3 , 400.130 MHz, ppm): δ 8.59 (d, 2 H, Pz H5), 8.53 (s, 2 H, Py H3,5), 7.81 (d, 2 H, Pz H3), 7.14 (Ph H2,6), 6.95 (Ph H3,5), 6.54 (dd, 2 H, Pz H4), 3.97 (t, 2 H Ak H1), 1.80 (p, 2 H, Ak H2), 1.47 (p, 2 H, Ak H3), 1.35 (s, 4 H, Ak H4,5), 0.92 (t, 3 H, Ak H6), ^{13}C NMR (CDCl_3 , 100.613 MHz, ppm): δ 163.14 (Py C7), 157.40 (Ph C1,4), 151.09 (Py C2,6), 143.09 (Py C4), 143.09 (Pz C3), 127.40 (Pz C5), 122.23 (Ph C2,6), 115.33 (Ph3,5), 109.64 (Py C3,5), 108.66 (Pz C4), 68.59 (Ak C1), 31.72 (Ak C4), 29.37 (Ak C2), 25.86 (Ak C3), 25.75 (Ak C5), 14.17 (Ak C6), **MS** (HR-ESI) m/z: calc. for $[\text{C}_{24}\text{H}_{25}\text{N}_5\text{O}_3 + \text{H}^+]$: 432.2030, found: 432.1951, calc. for $[\text{C}_{24}\text{H}_{25}\text{N}_5\text{O}_3 +$

Na⁺]: 454.1850, found: 454.1758, **IR** (cm⁻¹): 2940, 2847 (CH₃, CH₂), 1742(C=O), 1575 (Pz C=C, C=N), 1507 (Ph C=C), 1462, 1397 (Pz ring), 1227, 1201 (Ph-O-R), 1042 (Py C=C-H), 827 (PhH-H), 758 (Pz-Py N-C), **MP**: 108.3-108.5°C, **CHN**: calculated for C₂₄H₂₅N₅O₃: C 66.81, H 5.84, N 16.23, found: C 67.01, H 5.73, N 16.41%.

L13C12

4-(Dodecyl)phenyl 2,6-di-1H-pyrazol-1-ylisonicotinate was prepared using the general procedure described above, using the following quantities: 2,6-di(1H-pyrazol-1'-yl)pyridine-4-carboxylic acid 1.5 g (5.88 mmol, 1 eq), 4-dodecyloxyphenol 1.640 g (5.88 mmol, 1 eq), DCC 2.670 g (12.93 mmol, 2.2 eq), and a pinch of DMAP. The product was collected as a white crystalline solid (1.722 g, 57%).

Analyses: **¹H NMR** (CDCl₃, 400.130 MHz, ppm): δ 8.59 (d, 2 H, Pz H5), 8.53 (s, 2 H, Py H3,5), 7.81 (d, 2 H, Pz H3), 7.14 (Ph H2,6), 6.95 (Ph H3,5), 6.54 (dd, 2 H, Pz H4), 3.96 (t, 2 H Ak H1), 1.79 (p, 2 H, Ak H2), 1.47 (p, 2 H, Ak H3), 1.28 (s, 16 H, Ak H4-11), 0.89 (t, 3 H, Ak H12), **¹³C NMR** (CDCl₃, 100.613 MHz, ppm): δ 163.14 (Py C7), 157.40 (Ph C1,4), 151.08 (Py C2,6), 143.89 (Py C4), 143.08 (Pz C3), 127.39 (Pz C5), 122.22 (Ph C2,6), 115.33 (Ph3,5), 109.64 (Py C3,5), 108.66 (Pz C4), 68.59 (Ak C1), 29.40 (Ak C2), 26.18 (Ak C3), 32.06, 29.80, 29.78, 29.74, 29.73, 29.49, 29.54, 22.83 (Ak C4-11), 14.26 (Ak C12), **MS** (HR-ESI) m/z: calc. for [C₃₀H₃₇N₅O₃+H⁺]: 516.2969, found: 516.2971, **IR** (cm⁻¹): 2911, 2849 (CH₃, CH₂), 1742(C=O), 1575 (Pz C=C, C=N), 1506 (Ph C=C), 1464, 1395 (Pz ring), 1226, 1202 (Ph-O-R), 1042 (Py C=C-H), 826 (PhH-H), **MP**: 112.4-112.7°C, **CHN**: calculated for C₃₀H₃₇N₅O₃: C 69.88, H 7.23, N 13.58, found: C 69.69, H 7.35, N 13.51%.

L13C14

4-(Tetradecyl)phenyl 2,6-di-1H-pyrazol-1-ylisonicotinate was prepared using the general procedure described above, using the following quantities: 2,6-di(1H-pyrazol-1'-yl)pyridine-4-carboxylic acid 0.750 g (2.94 mmol, 1 eq), 4-tetradecyloxyphenol 0.900 g (2.94 mmol, 1 eq), DCC 1.330 g (6.45 mmol, 2.2 eq), and a pinch of DMAP. The product was collected as a white crystalline solid (0.979 g, 60%).

Analyses: **¹H NMR** (CDCl₃, 400.130 MHz, ppm): δ 8.59 (d, 2 H, Pz H5), 8.53 (s, 2 H, Py H3,5), 7.81 (d, 2 H, Pz H3), 7.14 (Ph H2,6), 6.95 (Ph H3,5), 6.54 (dd, 2 H, Pz H4), 3.96 (t, 2 H Ak H1), 1.79 (p, 2 H, Ak H2), 1.47 (p, 2 H, Ak H3), 1.28 (s, 20 H, Ak H4-13), 0.89 (t, 3 H, Ak H14), **¹³C NMR** (CDCl₃,

100.613 MHz, ppm): δ 163.14 (Py C7), 157.40 (Ph C1,4), 151.08 (Py C2,6), 143.89 (Py C4), 143.08 (Pz C3), 127.39 (Pz C5), 122.22 (Ph C2,6), 115.33 (Ph3,5), 109.64 (Py C3,5), 108.66 (Pz C4), 68.59 (Ak C1), 29.40 (Ak C2), 26.18 (Ak C3), 32.06, 29.80, 29.78, 29.74, 29.73, 29.49, 29.54, 22.83 (Ak C4-13), 14.26 (Ak C14), **MS** (HR-ESI) m/z : calc. for $[C_{32}H_{41}N_5O_3+H^+]$: 544.3282, found: 544.3438, **IR** (cm^{-1}): 2911, 2849 (CH₃, CH₂), 1742(C=O), 1575 (Pz C=C, C=N), 1506 (Ph C=C), 1464. 1395 (Pz ring), 1226, 1202 (Ph-O-R), 1042 (Py C=C-H), 826 (PhH-H), **MP**: 112.6-114.8°C, **CHN**: calculated for $C_{32}H_{41}N_5O_3$: C 70.69, H 7.60, N 12.88, found: C 70.75, H 7.66, N 12.89%.

L13C16

4-(Hexadecyl)phenyl 2,6-di-1H-pyrazol-1-ylisonicotinate was prepared using the general procedure described above, using the following quantities: 2,6-di(1H-pyrazol-1'-yl)pyridine-4-carboxylic acid 1.526 g (5.98 mmol, 1 eq), 4-hexadecyloxyphenol 2 g (5.98 mmol, 1 eq), DCC 2.714 g (13.15 mmol, 2.2 eq), and a pinch of DMAP. The product was collected as a white crystalline solid (0.477 g, 14%).

Analyses: **¹H NMR** (CDCl₃, 400.130 MHz, ppm): δ 8.59 (d, 2 H, Pz H5), 8.54 (s, 2 H, Py H3,5), 7.81 (d, 2 H, Pz H3), 7.14 (Ph H2,6), 6.95 (Ph H3,5), 6.54 (dd, 2 H, Pz H4), 3.97 (t, 2 H Ak H1), 1.79 (p, 2 H, Ak H2), 1.47 (p, 2 H, Ak H3), 1.27 (s, 24 H, Ak H4-15), 0.89 (t, 3 H, Ak H16), **¹³C NMR** (CDCl₃, 100.613 MHz, ppm): δ 163.14 (Py C7), 157.40 (Ph C1,4), 151.09 (Py C2,6), 143.90 (Py C4), 143.09 (Pz C3), 127.40 (Pz C5), 122.23 (Ph C2,6), 115.34 (Ph3,5), 109.65 (Py C3,5), 108.67 (Pz C4), 68.60 (Ak C1), 29.41 (Ak C2), 26.19 (Ak C3), 32.07, 29.85, 29.76, 29.74, 29.56, 29.51, 22.83 (Ak C4-13), 14.27 (Ak C14), **MS** (HR-ESI) m/z : calc. for $[C_{34}H_{45}N_5O_3+H^+]$: 572.3595, found: 572.3583, **IR** (cm^{-1}): 2911, 2849 (CH₃, CH₂), 1742(C=O), 1575 (Pz C=C, C=N), 1506 (Ph C=C), 1464. 1395 (Pz ring), 1226, 1202 (Ph-O-R), 1042 (Py C=C-H), 826 (PhH-H), **MP**: 112.4 – 112.7°C, **CHN**: calculated for $C_{34}H_{45}N_5O_3$: C 71.42, H 7.93, N 12.25, found: C 71.35, H 7.86, N 12.17%.

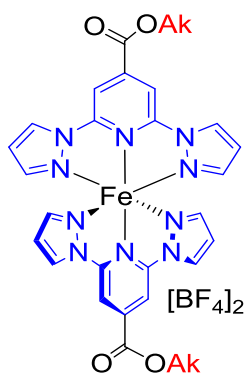
L13C18

4-(Octadecyl)phenyl 2,6-di-1H-pyrazol-1-ylisonicotinate was prepared using the general procedure described above, using the following quantities: 2,6-di(1H-pyrazol-1'-yl)pyridine-4-carboxylic acid 0.584 g (2.29 mmol, 1 eq), 4-octadecyloxyphenol 0.830 g (2.29 mmol, 1 eq), DCC 1.039 g (5.04 mmol, 2.2 eq), and a pinch of DMAP. The product was collected as a white crystalline solid (0.300 g, 22%).

Analyses: $^1\text{H NMR}$ (CDCl_3 , 400.130 MHz, ppm): δ 8.60 (d, 2 H, Pz H5), 8.54 (s, 2 H, Py H3,5), 7.81 (d, 2 H, Pz H3), 7.14 (Ph H2,6), 6.95 (Ph H3,5), 6.54 (dd, 2 H, Pz H4), 3.97 (t, 2 H Ak H1), 1.79 (p, 2 H, Ak H2), 1.47 (p, 2 H, Ak H3), 1.27 (s, 28 H, Ak H4-17), 0.89 (t, 3 H, Ak H18), $^{13}\text{C NMR}$ (CDCl_3 , 100.613 MHz, ppm): δ 163.14 (Py C7), 157.40 (Ph C1,4), 151.09 (Py C2,6), 143.90 (Py C4), 143.09 (Pz C3), 127.40 (Pz C5), 122.23 (Ph C2,6), 115.34 (Ph3,5), 109.65 (Py C3,5), 108.67 (Pz C4), 68.60 (Ak C1), 29.41 (Ak C2), 26.19 (Ak C3), 32.08, 29.85, 29.76, 29.74, 29.56, 29.51, 22.84 (Ak C4-17), 14.27 (Ak C18), **MS** (HR-ESI) m/z: calc. for $[\text{C}_{36}\text{H}_{49}\text{N}_5\text{O}_3+\text{H}^+]$: 600.3908, found: 600.3806, **IR** (cm^{-1}): 2911, 2849 (CH_3 , CH_2), 1742($\text{C}=\text{O}$), 1575 (Pz $\text{C}=\text{C}$, $\text{C}=\text{N}$), 1506 (Ph $\text{C}=\text{C}$), 1464, 1395 (Pz ring), 1226, 1202 (Ph-O-R), 1042 (Py $\text{C}=\text{C}-\text{H}$), 826 (PhH-H), **MP**: 115.7 – 116.1°C, **CHN**: calculated for $\text{C}_{36}\text{H}_{49}\text{N}_5\text{O}_3$: C 72.09, H 8.23, N 11.68, found: C 71.99, H 8.17, N 11.56%.

6.3.4 $[\text{Fe}(\text{L11Cx})_2][\text{BF}_4]_2$

The $[\text{Fe}(\text{L11Cx})_2][\text{BF}_4]_2$ iron(II) complexes were obtained by this general procedure, adapted from the literature:⁵ The ligand (1 eq.) was dissolved in either dichloroethane (DCE) or in DCM, and iron(II) tetrafluoroborate hexahydrate (0.5 eq.) was dissolved in acetone, with a gentle heating, if necessary. The two solutions were mixed at room temperature, which lead to instant formation of an intensively coloured solution, which, if necessary, was filtered through a pipette filter. The obtained complex solution was set for pentane diffusion crystallization.



Ak = C_6H_{13} , $\text{C}_{12}\text{H}_{25}$,
 $\text{C}_{14}\text{H}_{29}$, $\text{C}_{16}\text{H}_{33}$, $\text{C}_{18}\text{H}_{37}$

$[\text{Fe}(\text{L11C6})_2][\text{BF}_4]_2$

Hexyl(2,6-di-1H-pyrazol-1-yl)pyridine-4-carboxylate iron(II) tetrafluoroborate was obtained using the general procedure described above, using the following quantities: hexyl(2,6-di-1H-pyrazol-1-yl)pyridine-4-carboxylate (200 mg, 0.589 mmol, 1 eq), iron(II) tetrafluoroborate hexhydrate (111.2 mg, 0.295 mmol, 0.5 eq), which yielded dark-red crystals (199 mg, 74%).

Analyses: **paramagnetic** $^1\text{H NMR}$ ($\text{MeCN}-\text{D}_3$, 300 MHz, ppm): δ 39.56, 38.54, 25.88, 22.47 (Pz H3,4,5, Py H3,5), **MS** (HR-ESI) m/z: calc. for $[\text{C}_{18}\text{H}_{21}\text{N}_5\text{O}_2 + \text{H}^+]$: 340.1768, found: 340.1776, calc. for $[\text{C}_{18}\text{H}_{21}\text{N}_5\text{O}_2 + \text{Na}^+]$: 362.1587, found: 362.1595, **IR** (cm^{-1}): 2920, 2851 (CH_3 , CH_2), 1733 ($\text{C}=\text{O}$), 1575 (Pz $\text{C}=\text{C}$, $\text{C}=\text{N}$), 1471, 1408 (Pz ring), 1254 ($\text{C}-\text{OR}$), 1034 broad (B-F), 519.05 broad (B-F).

[Fe(L11C12)₂][BF₄]₂

Dodecyl(2,6-di-1H-pyrazol-1-yl)pyridine-4-carboxylate iron(II) tetrafluoroborate was obtained using the general procedure described above, using the following quantities: dodecyl(2,6-di-1H-pyrazol-1-yl)pyridine-4-carboxylate (150 mg, 0.35 mmol, 2 eq), iron(II) tetrafluoroborate hexhydrate (63 mg, 0.17 mmol, 1eq). The reagents were dissolved in DCM and Me₂CO, and crystallized by Et₂O diffusion, which yielded a dark-red powder (135 mg, 70%).

Analyses: **paramagnetic** ¹H NMR (MeCN-D₃, 300 MHz, ppm): δ 39.62, 38.95, 26.03, 22.60 (Pz H_{3,4,5}, Py H_{3,5}), **MS** (HR-ESI) m/z: calc. for [C₂₄H₃₃N₅O₂ + H⁺]: 424.2707, found: 424.2706, calc. for [C₂₄H₃₃N₅O₂ + Na⁺]: 446.2526, found: 446.2526, **IR** (cm⁻¹): 2920, 2851 (CH₃, CH₂), 1733 (C=O), 1575 (Pz C=C, C=N), 1471, 1408 (Pz ring), 1254 (C-OR), 1034 broad (B-F), 519.05 broad (B-F), **CHN**: calculated for [(C₂₄H₃₃N₅O₂)₂Fe][BF₄]₂: C 53.55, H 6.18, N 13.01%, found: C 53.38, H 6.33, N 12.94%.

[Fe(L11C14)₂][BF₄]₂

Tetradecyl(2,6-di-1H-pyrazol-1-yl)pyridine-4-carboxylate iron(II) tetrafluoroborate was obtained using the general procedure described above, using the following quantities: tetradecyl(2,6-di-1H-pyrazol-1-yl)pyridine-4-carboxylate (150 mg, 0.33 mmol, 2 eq), iron(II) tetrafluoroborate hexhydrate (67 mg, 0.18 mmol, 1eq). The reagents were dissolved in DCM and Me₂CO, and crystallized by Et₂O diffusion, which yielded a dark-red powder (107 mg, 55%).

Analyses: **paramagnetic** ¹H NMR (MeCN-D₃, 300 MHz, ppm): δ 39.60, 38.70, 25.93, 22.60 (Pz H_{3,4,5}, Py H_{3,5}), **MS** (HR-ESI) m/z: calc. for [C₂₆H₃₇N₅O₂ + H⁺]: 452.3020, found: 452.3018, calc. for [C₂₆H₃₇N₅O₂ + Na⁺]: 474.2839, found: 474.2840, **IR** (cm⁻¹): 2920, 2851 (CH₃, CH₂), 1733 (C=O), 1575 (Pz C=C, C=N), 1471, 1408 (Pz ring), 1254 (C-OR), 1034 broad (B-F), 519.05 broad (B-F), **CHN**: calculated for [(C₂₆H₃₇N₅O₂)₂Fe][BF₄]₂: C 55.14, H 6.58, N 12.37%, found: C 54.89, H 6.46, N 12.24%.

[Fe(L11C16)₂][BF₄]₂

Hexadecyl(2,6-di-1H-pyrazol-1-yl)pyridine-4-carboxylate iron(II) tetrafluoroborate was obtained using the general procedure described above, using the following quantities: hexadecyl(2,6-di-1H-pyrazol-1-yl)pyridine-4-carboxylate (150 mg, 0.312 mmol, 2 eq), iron(II) tetrafluoroborate hexhydrate (59 mg, 0.156 mmol, 1eq). The reagents were dissolved in DCM and Me₂CO, and crystallized by Et₂O diffusion, which yielded a dark red powder.

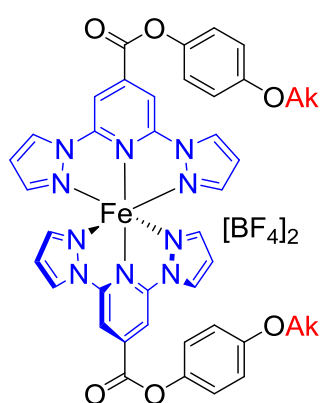
Analyses: **paramagnetic $^1\text{H NMR}$** (MeCN-D₃, 300 MHz, ppm): δ 39.83, 39.06, 26.11, 22.74 (Pz H_{3,4,5}, Py H_{3,5}), **MS** (HR-ESI) m/z : calc. for [C₂₈H₄₁N₅O₂ + H⁺]: 480.3333, found: 480.3333, calc. for [C₂₈H₄₁N₅O₂ + Na⁺]: 502.3152, found: 502.3153, **IR** (cm⁻¹): 2920, 2851 (CH₃, CH₂), 1733 (C=O), 1575 (Pz C=C, C=N), 1471, 1408 (Pz ring), 1254 (C-OR), 1034 broad (B-F), 519.05 broad (B-F), **CHN**: calculated for [(C₂₈H₄₁N₅O₂)₂Fe][BF₄]₂: C 56.58, H 6.95, N 11.78%, found: C 56.51, H 6.79, N 11.64%.

[Fe(L11C18)]₂[BF₄]₂·2.5H₂O

Octadecyl(2,6-di-1H-pyrazol-1-yl)pyridine-4-carboxylate iron(II) tetrafluoroborate was obtained using the general procedure described above, using the following quantities: octadecyl(2,6-di-1H-pyrazol-1-yl)pyridine-4-carboxylate (185 mg, 0.364 mmol, 1 eq), iron(II) tetrafluoroborate hexahydrate (68.8 mg, 0.182 mmol, 0.5 eq). The reagents were dissolved in DCE and Me₂CO, and crystallized by pentane diffusion, which yielded dark red crystals (91 mg, 40%).

Analyses: **paramagnetic $^1\text{H NMR}$** (MeCN-D₃, 300 MHz, ppm): δ 39.79, 39.06, 26.03, 22.67 (Pz H_{3,4,5}, Py H_{3,5}), **MS** (HR-ESI) m/z : calc. for [C₃₀H₄₅N₅O₂ + H⁺]: 508.3646, found: 508.3643, calc. for [C₃₀H₄₅N₅O₂ + Na⁺]: 530.3465, found: 530.3463, **IR** (cm⁻¹): 2920, 2851 (CH₃, CH₂), 1733 (C=O), 1575 (Pz C=C, C=N), 1471, 1408 (Pz ring), 1254 (C-OR), 1034 broad (B-F), 519.05 broad (B-F), **CHN**: calculated for [(C₃₀H₄₅N₅O₂)₂Fe][BF₄]₂·2.5 H₂O: C 55.87, H 7.42, N 10.86%, found: C 55.89, H 7.71, N 10.85%.

6.3.5 [Fe(L13Cx)]₂[BF₄]₂



Ak = C₆H₁₃, C₁₂H₂₅,
C₁₄H₂₉, C₁₆H₃₃, C₁₈H₃₇

The [Fe(L13Cx)]₂[BF₄]₂ iron(II) complexes were obtained using this general procedure: the ligand (1 eq.) was dissolved in dichloroethane (DCE), and iron(II) tetrafluoroborate hexahydrate (0.5 eq.) was dissolved in fresh, not moist acetone. The two solutions were mixed at room temperature, and the obtained deep red solution, if necessary, was filtered through a pipette filter. The solution was distributed into many vials and diluted to different concentrations by DCE-acetone mixture and set for a slow pentane diffusion crystallization. After many trials with the crystallization conditions single crystals were obtained.

[Fe(L13C6)₂][BF₄]₂

4-Hexyloxyphenyl (2,6-di-1H-pyrazol-1-yl)pyridine-4-carboxylate iron(II) tetrafluoroborate was obtained using the general procedure described above, using the following quantities: hexyloxyphenyl (2,6-di-1H-pyrazol-1-yl)pyridine-4-carboxylate (200 mg, 0.464 mmol, 1 eq), iron(II) tetrafluoroborate hexhydrate (87.5 mg, 0.232 mmol, 0.5 eq), which yielded a light red powder (139.5 mg, 55%).

Analyses: **paramagnetic ¹H NMR** (MeCN-D₃:CDCl₃ mixture, 300 MHz, ppm): δ 42.35, 41.25, 27.20, 24.13 (Pz H_{3,4,5}, Py H_{3,5}), **MS** (HR-ESI) m/z: calc. for [C₂₄H₂₅N₅O₃ + H⁺]: 432.2030, found: 432.2032, calc. for [C₂₄H₂₅N₅O₃ + Na⁺]: 454.1850, found: 454.1848, **IR** (cm⁻¹): 2922, 2850 (CH₃, CH₂), 1749, 1731 (C=O), 1571 (Pz C=C, C=N), 1504 (Ph C=C), 1470, 1408 (Pz ring), 1237, 1185 (Ph-O-R), 826 (PhH-H), 756 (Pz-Py N-C), 1030, 520 broad (B-F), **CHN**: calculated for [(C₂₄H₂₅N₅O₃)₂Fe][BF₄]₂·1DCE: C 50.40, H 4.57, N 11.76%, found: C 50.16, H 4.15, N 12.14%.

[Fe(L13C12)₂][BF₄]₂

4-Dodecyloxyphenyl (2,6-di-1H-pyrazol-1-yl)pyridine-4-carboxylate iron(II) tetrafluoroborate was obtained using the general procedure described above, using the following quantities: dodecyloxyphenyl (2,6-di-1H-pyrazol-1-yl)pyridine-4-carboxylate (200 mg, 0.400 mmol, 1 eq), iron(II) tetrafluoroborate hexhydrate (75.6 mg, 0.200 mmol, 0.5 eq), which yielded a dark red powder (131 mg, 53%).

Analyses: **paramagnetic ¹H NMR** (MeCN-D₃:CDCl₃ mixture, 300 MHz, ppm): δ 40.14, 39.43, 26.22, 22.98 (Pz H_{3,4,5}, Py H_{3,5}), **MS** (HR-ESI) m/z: calc. for [C₃₀H₃₇N₅O₃ + H⁺]: 516.2969, found: 516.2970, calc. for [C₃₀H₃₇N₅O₃ + Na⁺]: 538.2789, found: 538.2783, **IR** (cm⁻¹): 2922, 2852 (CH₃, CH₂), 1746(C=O), 1575 (Pz C=C, C=N), 1506 (Ph C=C), 1472, 1408 (Pz ring), 1235, 1186 (Ph-O-R), 826 (PhH-H), 756 (Pz-Py N-C), 1030, 520 broad (B-F), **CHN**: calculated for [(C₃₀H₃₇N₅O₃)₂Fe][BF₄]₂·0.5 DCE: C 55.92, H 5.85, N 10.69%, found: C 55.92, H 5.75, N 11.01%.

[Fe(L13C14)₂][BF₄]₂

4-Tetradecyloxyphenyl (2,6-di-1H-pyrazol-1-yl)pyridine-4-carboxylate iron(II) tetrafluoroborate was obtained using the general procedure described above, using the following quantities: tetradecyloxyphenyl (2,6-di-1H-pyrazol-1-yl)pyridine-4-carboxylate (200 mg, 0.379 mmol, 1 eq), iron(II) tetrafluoroborate hexhydrate (71.5 mg, 0.190 mmol, 0.5 eq), which yielded a light red powder (71 mg, 29%).

Analyses: **paramagnetic ^1H NMR** (MeCN-D₃:CDCl₃ mixture, 300 MHz, ppm): δ 42.55, 41.26, 27.17, 24.27 (Pz H_{3,4,5}, Py H_{3,5}), **MS** (HR-ESI) m/z: calc. for [C₃₂H₄₁N₅O₃ + H⁺]: 544.3282, found: 544.3284, calc. for [C₃₂H₄₁N₅O₃ + Na⁺]: 566.3102, found: 566.1442, **IR** (cm⁻¹): 2922, 2850 (CH₃, CH₂), 1749, 1731 (C=O), 1571 (Pz C=C, C=N), 1504 (Ph C=C), 1470, 1408 (Pz ring), 1237, 1185 (Ph-O-R), 826 (PhH-H), 756 (Pz-Py N-C), 1030, 520 broad (B-F), **CHN**: calculated for [(C₃₂H₄₁N₅O₃)₂Fe][BF₄]₂: C 58.37, H 6.28, N 10.64%, found: C 58.19, H 6.19, N 10.68%.

[Fe(L13C16)]₂[BF₄]₂

4-Hexadecyloxyphenyl (2,6-di-1H-pyrazol-1-yl)pyridine-4-carboxylate iron(II) tetrafluoroborate was obtained using the general procedure described above, using the following quantities: hexadecyloxyphenyl (2,6-di-1H-pyrazol-1-yl)pyridine-4-carboxylate (188.3 mg, 0.339 mmol, 1 eq), iron(II) tetrafluoroborate hexhydrate (63.9 mg, 0.169 mmol, 0.5 eq), which yielded a dark red powder (141 mg, 50%).

Analyses: **paramagnetic ^1H NMR** (MeCN-D₃:CDCl₃ mixture, 300 MHz, ppm): δ 42.54, 41.39, 27.18, 24.58 (Pz H_{3,4,5}, Py H_{3,5}), **MS** (HR-ESI) m/z: calc. for [C₃₄H₄₅N₅O₃ + H⁺]: 572.3595, found: 572.3595, calc. for [C₃₄H₄₅N₅O₃ + Na⁺]: 594.3415, found: 592.1604, **IR** (cm⁻¹): 2922, 2850 (CH₃, CH₂), 1749, 1731 (C=O), 1571 (Pz C=C, C=N), 1504 (Ph C=C), 1470, 1408 (Pz ring), 1237, 1185 (Ph-O-R), 826 (PhH-H), 756 (Pz-Py N-C), 1030, 520 broad (B-F), **CHN**: calculated for [(C₃₄H₄₅N₅O₃)₂Fe][BF₄]₂: C 59.49, H 6.61, N 10.20%, found: C 59.33, H 6.67, N 10.06%.

[Fe(L13C18)]₂[BF₄]₂

4-Octadecyloxyphenyl (2,6-di-1H-pyrazol-1-yl)pyridine-4-carboxylate iron(II) tetrafluoroborate was obtained using the general procedure described above, using the following quantities: octadecyloxyphenyl (2,6-di-1H-pyrazol-1-yl)pyridine-4-carboxylate (187.4 mg, 0.320 mmol, 1 eq), iron(II) tetrafluoroborate hexhydrate (60.6 mg, 0.160 mmol, 0.5 eq), which yielded a light red powder (133 mg, 59%).

Analyses: **paramagnetic ^1H NMR** (MeCN-D₃:CDCl₃ mixture, 300 MHz, ppm): δ 42.87, 41.28, 27.09, 24.67 (Pz H_{3,4,5}, Py H_{3,5}), **MS** (HR-ESI) m/z: calc. for [C₃₆H₄₉N₅O₃ + H⁺]: 600.3908, found: 600.3909, calc. for [C₃₆H₄₉N₅O₃ + Na⁺]: 622.3728, found: 622.3726, **IR** (cm⁻¹): 2922, 2850 (CH₃, CH₂), 1749, 1731 (C=O), 1571 (Pz C=C, C=N), 1504 (Ph C=C), 1470, 1408 (Pz ring), 1237, 1185 (Ph-O-R), 826 (PhH-H), 756 (Pz-Py N-C), 1030, 520

broad (B-F), **CHN**: calculated for $[(C_{36}H_{49}N_5O_3)_2Fe][BF_4]_2$: C 60.51, H 6.91, N 9.80%, found: C 60.51, H 6.99, N 9.83%.

6.4 Pyrazole-substituted bis(pyrazol-1-yl)pyridine derivatives with long alkyl chains, and their iron(II) complexes

The labelling scheme for this chapter is shown on the Fig. 6.2.

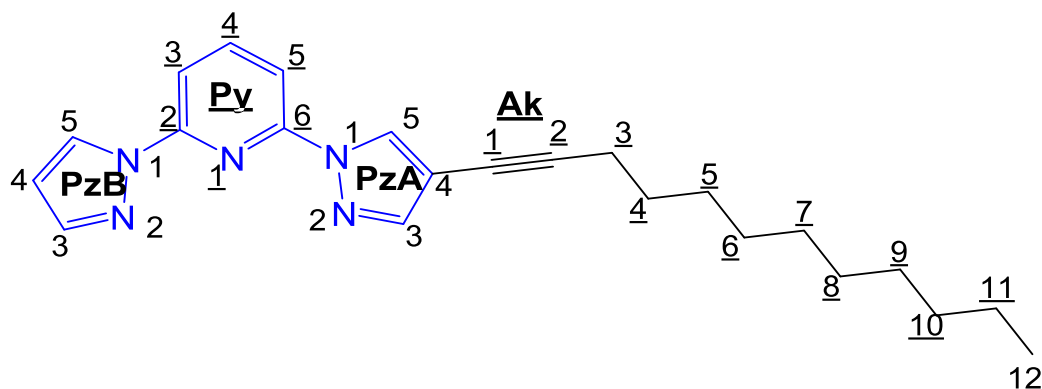
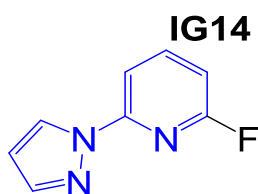


Fig. 6.2 Labelling Scheme for the ligands in the Chapters 4 and 5

6.4.1 L14, L15, L16 – the precursors

L14 - 2-Fluoro-6-(1*H*-pyrazol-1-yl)pyridine

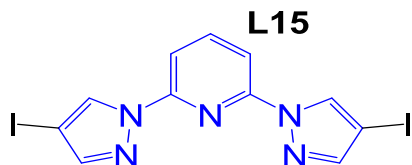


2-Fluoro-6-(1*H*-pyrazol-1-yl)pyridine was obtained using the procedure, described in literature,⁷ with some modifications: 1*H*-pyrazole 1.4 g (20 mmol, 1 eq) was dissolved in a DMF (20 ml) / THF (6 ml) solvent mixture, after which NaH 60% dispersion in mineral oil 0.8 g (20 mmols, 1 eq) was slowly added, and the reaction mixture was stirred for 10 minutes until hydrogen emission ceased. Then 2,6-difluoropyridine 1.9 ml (2.417 g, 21 mmol, 1.05 eq) was added in in one go, after which the reaction mixture was stirred for 20 h at room temperature, while being monitored by TLC. Water (250 ml) was then poured into the reaction mixture, which was extracted with Et₂O (50 ml x 5). The organic layer was washed with water, brine, dried with MgSO₄, after which the solvent was removed under reduced pressure, and the obtained yellowish oil was separated by column chromatography (1% MeOH in DCM, 2nd spot, *r_f* = 0.7). That yielded the target product as a slightly yellowish oil which crystallize very slowly into transparent prismatic crystals (1.135g, 34%).

Analyses: **¹H NMR** (CDCl₃, 400.130 MHz, ppm): δ 8.46 (d, 1 H, Pz H5), 7.87 (p, 1 H, Py H4), 7.84 (ddd, 1 H, Py H3) 7.72 (d, 1 H, Pz H3), 6.79 (ddd, 1 H,

Py H5), 6.45 (dd, 1 H, Pz H4), ^{13}C NMR (CDCl_3 , 100.613 MHz, ppm): δ 163.55, 161.15 (Py C7), 150.12, 149.98 (Py C2), 143.49, 143.41 (Py C4), 142.76 (Pz C3), 127.55 (Pz C5), 109.00, 108.96 (Pz C4), 108.31 (Py C3), 106.24, 105.89 (Py C5), ^{19}F NMR (CDCl_3 , 400.130 MHz, ppm): δ 68.27 (Py F6), **MS** (HR-ESI) m/z : calc. for $[\text{C}_8\text{H}_6\text{F}+\text{H}^+]$: 164.0619, found: 164.0610, calc. for $[\text{C}_8\text{H}_6\text{F}+\text{Na}^+]$: 186.0438, found: 186.0429, **IR** (cm^{-1}): 1606, 1586 (Py C=C in plane vibr.), 1461 (Py ring), 1237 (Ar-F), 754 (Py C-H), **MP**: ca 20°C.

L15 - 2,6-Bis(4-iodo-1H-pyrazol-1-yl)pyridine

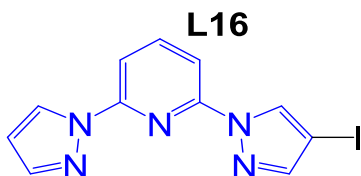


2,6-Bis(4-iodo-1H-pyrazol-1-yl)pyridine was obtained using the following procedure: 4-iodopyrazole 1 g (5.16 mmol, 2 eq) was dissolved in DMF (15 ml) and THF (5 ml)

solvent mixture, after which NaH 60% dispersion in mineral oil 0.258 g (6.45 mmols, 2.5 eq) was slowly added. The reaction mixture, was stirred for 1.5 h until clear solution formed, then 2,6-difluoro pyridine (0.23 ml, 0.297 g, 2.58 mmol, 1 eq) was added, after which the reaction mixture was stirred for 16 h at room temperature, while being monitored by TLC. Then water (180 ml) was slowly added into the reaction mixture, and the precipitate was filtered off, dried, and washed with hexane and desiccated. That yielded the target product as a white powder (0.807 g, 68%).

Analyses: ^1H NMR (CDCl_3 , 400.130 MHz, ppm): δ 8.61 (s, 2 H, Pz H5), 7.96 (dd, 1 H, Py H4), 7.84 (d, 2 H, Py H3,5), 7.74 (s, 2 H, Pz H3), ^{13}C NMR (CDCl_3 , 100.613 MHz, ppm): δ 149.30 (Py C2,6), 147.33 (Pz C3), 141.97 (Py C4), 131.70 (Pz C5), 109.66 (Py C3), 60.46 (Pz C4), **MS** (HR-ESI) m/z : calc. for $[\text{C}_{11}\text{H}_7\text{I}_2\text{N}_5+\text{H}^+]$: 463.8864, found: 463.8857, calc. for $[\text{C}_{11}\text{H}_7\text{I}_2\text{N}_5+\text{Na}^+]$: 485.8683, found: 485.8688, **IR** (cm^{-1}): 1609, 1585 (Py C=C in plane vibr.), 1466 (Py ring), 797 (Py 2,6-subst. C-H), 752 (Py C-H), 600 (C-I), **MP**: 177.8–178.5°C.

L16 - 2-(4-iodo-1H-pyrazol-1-yl)-6-(1H-pyrazol-1-yl)pyridine



2-(4-iodo-1H-pyrazol-1-yl)-6-(1H-pyrazol-1-yl)pyridine was obtained using the following procedure, similar to the one for **L14**. 4-iodopyrazole (3.24 g, 16.7 mmol, 1 eq) was

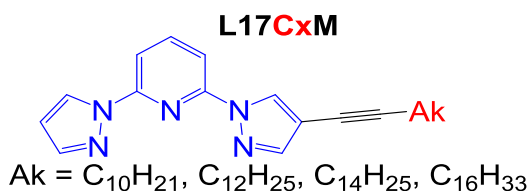
dissolved in DMF (17 ml) and THF (5 ml) solvent mixture, after which NaH 60% dispersion in mineral oil (0.703 g, 17.5 mmols, 1.05 eq) was slowly added. The reaction mixture was stirred until hydrogen emission ceased and a clear solution was formed. Then 2-fluoro-6-(1H-pyrazol-1-yl)pyridine (2.723 g, 16.7 mmol, 1 eq) was added, after which the reaction mixture was stirred

for 16 h at room temperature. Then water (200 ml) was poured into the reaction mixture, the precipitate was filtered off, dried, and washed with hexane and desiccated, which yielded the target product as a white powder (4.832g, 86%).

Analyses: $^1\text{H NMR}$ (CDCl_3 , 400.130 MHz, ppm): δ 8.61 (s, 1 H, PzA H5), 8.55 (d, 1 H, PzB H5), 7.94 (dd, 1 H, Py H4), 7.89 (dd, 1 H, Py H5), 7.79 (dd, 1 H, Py H3), 7.76 (d, 1 H, PzB H3), 7.73 (s, 1 H, PzA H3), 6.50 (dd, 1 H, PzB H4), $^{13}\text{C NMR}$ (CDCl_3 , 100.613 MHz, ppm): δ 150.20 (Py C6), 149.28 (Py C2), 147.16 (PzA C3), 142.69 (PzB C3), 141.74 (Py C4), 131.68 (PzA C5), 127.19 (PzB C5), 110.13 (Py C5), 109.02 (Py C3), 108.29 (PzB C4), 66.22 (PzA C4), **MS** (HR-ESI) m/z : calc. for $[\text{C}_{11}\text{H}_8\text{IN}_5+\text{H}^+]$: 337.9897, found: 337.9892, calc. for $[\text{C}_{11}\text{H}_8\text{IN}_5+\text{Na}^+]$: 359.9717, found: 359.9712, **IR** (cm^{-1}): 1608, 1585 (Py C=C in plane vibr.), 1468 (Py ring), 800 (Py 2,6-subst. C-H), 752 (Py C-H), 603 (C-I), **MP**: 141.9°C, **CHN**: calculated for $\text{C}_{11}\text{H}_8\text{N}_5\text{I}$: C 39.19, H 2.39, N 20.77 %, found: C 39.33, H 2.35, N 20.66 %.

6.4.2 L17CxM - 2-(4-alkyl-1-yn-1-yl-1H-pyrazol-1-yl)-6-(1H-pyrazol-1-yl)pyridines

L17C12M



2-(4-Dodec-1-yn-1-yl-1H-pyrazol-1-yl)-6-(1H-pyrazol-1-yl)pyridine was obtained using the procedure described in the literature,⁸ with some modifications. A mixture of 2-

(4-iodo-1H-pyrazol-1-yl)-6-(1H-pyrazol-1-yl)pyridine **L16** (1.2 g, 3.56 mmol, 1 eq), tetrakis(triphenylphosphine)-palladium(0) (0.123 g, 0.1 mmols, 0.03 eq), triphenylphosphine (0.149 g, 0.56 mmol, 0.16 eq), CuI (0.149 g, 0.78 mmol, 0.22 eq), Et₃N (15 ml), and anhydrous dioxane (7 ml) was placed in a Schlenk tube and degassed by bubbling nitrogen through for 2 h. 1-Dodecyne (1.141 ml, 0.887 g, 5.34 mmol, 1.5 eq) was then added, the reaction mixture was heated to 80°C and kept stirring at that temperature for 2 days, while being monitored by TLC. Later the reaction mixture was filtered, the solvent was removed from the filtrate, and recrystallization from MeCN resulted in a white powder of the target product (0.639 g, 48%).

Analyses: $^1\text{H NMR}$ (CDCl_3 , 400.130 MHz, ppm): δ 8.59 (s, 1 H, PzA H5), 8.55 (d, 1 H, PzB H5), 7.92 (t, 1 H, Py H4), 7.87 (dd, 1 H, Py H3), 7.82 (dd, 1 H, Py H5), 7.76 (d, 1 H, PzB H3), 7.75 (s, 1 H, PzA H3), 6.50 (dd, 1 H, PzB H4), 2.41 (t, 2 H, Ak H3), 1.61 (p, 2 H, Ak H4), 1.45 (s, 2 H, Ak H5), 1.28 (s, 12 H, Ak H6-11), 0.88 (t, 3 H, Ak H 12), $^{13}\text{C NMR}$ (CDCl_3 , 100.613 MHz,

ppm): δ 150.23 (Py C2), 149.65 (Py C6), 144.72 (PzA C3), 142.61 (PzB C3), 141.59 (Py C4), 129.12 (PzA C5), 127.14 (PzB C5), 109.78 (Py C3), 109.49 (Py C5), 108.20 (PzB C4), 106.61 (Ak C1), 92.78 (Ak C2), 70.85 (PzA C4), 28.88 (Ak C4), 19.66 (Ak C3), 32.05, 29.74, 29.69, 29.47, 29.32, 29.12, 22.83 (Ak C5-11), 14.25 (Ak C12), **MS** (HR-ESI) m/z: calc. for $[\text{C}_{23}\text{H}_{29}\text{N}_5+\text{H}^+]$: 376.2496, found: 376.2493, calc. for $[\text{C}_{23}\text{H}_{29}\text{N}_5+\text{Na}^+]$: 398.2315, found: 398.2319, calc. for $[2 \text{C}_{23}\text{H}_{29}\text{N}_5+\text{Na}^+]$: 773.4738, found: 773.4737, **IR** (cm^{-1}): 2915, 2847 (CH_3 , CH_2), 1602, 1582 (Pz C=N), 1465 (Py ring), 795 (Py C-H), **MP**: 58.1–58.5°C, **CHN**: calculated for $\text{C}_{23}\text{H}_{29}\text{N}_5$: C 73.57, H 7.78, N 18.65, found: C 73.60, H 7.75, N 18.47 %.

L17C14M

2-(4-Tetradec-1-yn-1-yl-1H-pyrazol-1-yl)-6-(1H-pyrazol-1-yl)pyridine was prepared using the same procedure as for **L17C12M**, using the following quantities: 2-(4-iodo-1H-pyrazol-1-yl)-6-(1H-pyrazol-1-yl)pyridine **L16** (1.448 g, 4.3 mmol, 1 eq), tetrakis(triphenylphosphine)palladium(0) (0.149 g, 0.13 mmols, 0.03 eq), triphenylphosphine (0.180 g, 0.69 mmol, 0.16 eq), CuI (0.180 g, 0.95 mmol, 0.22 eq), Et_3N (18 ml), and anhydrous dioxane (9 ml), and 1-tetradecyne (1.580 ml, 1.252 g, 6.4 mmol, 1.5 eq), which yielded white crystals of 2-(4-tetradec-1-yn-1-yl-1H-pyrazol-1-yl)-6-(1H-pyrazol-1-yl)pyridine (0.759 g, 44 %).

Analyses: **$^1\text{H NMR}$** (CDCl_3 , 400.130 MHz, ppm): δ 8.59 (s, 1 H, PzA H5), 8.55 (dd, 1 H, PzB H5), 7.92 (t, 1 H, Py H4), 7.87 (dd, 1 H, Py H3), 7.82 (dd, 1 H, Py H5), 7.76 (d, 1 H, PzB H3), 7.75 (s, 1 H, PzA H3), 6.49 (dd, 1 H, PzB H4), 2.41 (t, 2 H, Ak H3), 1.61 (p, 2 H, Ak H4), 1.45 (s, 2 H, Ak H5), 1.26 (s, 16 H, Ak H6-13), 0.87 (t, 3 H, Ak H14), **$^{13}\text{C NMR}$** (CDCl_3 , 100.613 MHz, ppm): δ 150.23 (Py C2), 149.64 (Py C6), 144.71 (PzA C3), 142.60 (PzB C3), 141.58 (Py C4), 129.11 (PzA C5), 127.13 (PzB C5), 109.77 (Py C3), 109.48 (Py C5), 108.19 (PzB C4), 106.60 (Ak C1), 92.78 (Ak C2), 70.85 (PzA C4), 28.88 (Ak C4), 19.66 (Ak C3), 32.06, 29.82, 29.79, 29.69, 29.50, 29.33, 29.12, 22.83 (Ak C5-13), 14.25 (Ak C14), **MS** (HR-ESI) m/z: calc. for $[\text{C}_{25}\text{H}_{33}\text{N}_5+\text{H}^+]$: 404.2809, found: 408.2803, calc. for $[\text{C}_{25}\text{H}_{33}\text{N}_5+\text{Na}^+]$: 426.2628, found: 426.2628, calc. for $[2 \text{C}_{25}\text{H}_{33}\text{N}_5+\text{Na}^+]$: 829.5364, found: 829.5364, **IR** (cm^{-1}): 2914, 2847 (CH_3 , CH_2), 1602, 1582 (Pz C=N), 1467 (Py ring), 795 (Py C-H), **MP**: 66.1–66.3, **CHN**: calculated for $\text{C}_{25}\text{H}_{33}\text{N}_5$: C 74.40, H 8.24, N 17.35, found: C 74.11, H 7.92, N 17.02 %.

L17C16M

2-(4-Hexadec-1-yn-1-yl-1H-pyrazol-1-yl)-6-(1H-pyrazol-1-yl)pyridine was prepared using the same procedure as for **L17C12M**, using the following quantities: 2-(4-iodo-1H-pyrazol-1-yl)-6-(1H-pyrazol-1-yl)pyridine **L16** (1.448 g, 4.3 mmol, 1 eq), tetrakis(triphenylphosphine)palladium(0) (0.149 g, 0.13 mmols, 0.03 eq), triphenylphosphine (0.180 g, 0.69 mmol, 0.16 eq), CuI (0.180 g, 0.95 mmol, 0.22 eq), Et₃N (18 ml), and anhydrous dioxane (9 ml), and 1-hexadecyne (1.80 ml, 1.433 g, 6.44 mmol, 1.5 eq), which yielded white crystals of 2-(4-hexadec-1-yn-1-yl-1H-pyrazol-1-yl)-6-(1H-pyrazol-1-yl)pyridine (0.780 g, 42 %).

Analyses: **¹H NMR** (CDCl₃, 400.130 MHz, ppm): δ 8.59 (s, 1 H, PzA H5), 8.55 (d, 1 H, PzB H5), 7.93 (t, 1 H, Py H4), 7.87 (dd, 1 H, Py H3), 7.82 (dd, 1 H, Py H5), 7.77 (d, 1 H, PzB H3), 7.75 (s, 1 H, PzA H3), 6.50 (dd, 1 H, PzB H4), 2.41 (t, 2 H, Ak H3), 1.61 (p, 2 H, Ak H4), 1.45 (s, 2 H, Ak H5), 1.28 (s, 20 H, Ak H6-15), 0.88 (t, 3 H, Ak H 16), **¹³C NMR** (CDCl₃, 100.613 MHz, ppm): δ 150.23 (Py C2), 149.65 (Py C6), 144.72 (PzA C3), 142.61 (PzB C3), 141.59 (Py C4), 129.12 (PzA C5), 127.14 (PzB C5), 109.78 (Py C3), 109.49 (Py C5), 108.20 (PzB C4), 106.61 (Ak C1), 92.78 (Ak C2), 70.85 (PzA C4), 28.88 (Ak C4), 19.66 (Ak C3), 32.05, 29.74, 29.69, 29.47, 29.32, 29.12, 22.83 (Ak C5-15), 14.25 (Ak C16), **MS** (HR-ESI) m/z: calc. for [C₂₇H₃₇N₅+H⁺]: 432.3122, found: 432.3122, calc. for [C₂₇H₃₇N₅+Na⁺]: 454.2941, found: 454.2936, calc. for [2 C₂₇H₃₇N₅+Na⁺]: 885.5990, found: 885.5986, **IR** (cm⁻¹): 2914, 2847 (CH₃, CH₂), 1602, 1583 (Pz C=N), 1469 (Py ring), 795 (Py C-H), **MP**: 68.8–71.0°C, **CHN**: calculated for C₂₇H₃₇N₅: C 75.13, H 8.64, N 16.23, found: C 75.08, H 8.83, N 15.97 %.

L17C18M

2-(4-Octadec-1-yn-1-yl-1H-pyrazol-1-yl)-6-(1H-pyrazol-1-yl)pyridine was prepared using the same procedure as for **L17C12M**, using the following quantities: 2-(4-iodo-1H-pyrazol-1-yl)-6-(1H-pyrazol-1-yl)pyridine **L16** (1.022 g, 3.032 mmol, 1 eq), tetrakis(triphenylphosphine)palladium(0) (0.105 g, 0.091 mmol, 0.03 eq), triphenylphosphine (0.127 g, 0.484 mmol, 0.16 eq), CuI (0.127 g, 0.667 mmol, 0.22 eq), Et₃N dried with KOH pellets (12 ml), anhydrous dioxane (6 ml), and 1-octadecyne (solid, 759 g, 3.032 mmol, 1 eq), which yielded white crystals of 2-(4-octadec-1-yn-1-yl-1H-pyrazol-1-yl)-6-(1H-pyrazol-1-yl)pyridine (0.574 g, 34%).

Analyses: **¹H NMR** (CDCl₃, 400.130 MHz, ppm): δ 8.60 (s, 1 H, PzA H5), 8.56 (d, 1 H, PzB H5), 7.93 (t, 1 H, Py H4), 7.87 (dd, 1 H, Py H3), 7.82 (dd, 1

H, Py H5), 7.76 (d, 1 H, PzB H3), 7.75 (s, 1 H, PzA H3), 6.50 (dd, 1 H, PzB H4), 2.41 (t, 2 H, Ak H3), 1.61 (p, 2 H, Ak H4), 1.45 (s, 2 H, Ak H5), 1.25 (s, 24 H, Ak H6-15), 0.88 (t, 3 H, Ak H 16), **¹³C NMR** (CDCl₃, 100.613 MHz, ppm): δ 150.23 (Py C2), 149.64 (Py C6), 144.72 (PzA C3), 142.62 (PzB C3), 141.60(Py C4), 129.12 (PzA C5), 127.14 (PzB C5), 109.78 (Py C3), 109.49 (Py C5), 108.21 (PzB C4), 106.59 (Ak C1), 92.78 (Ak C2), 70.83 (PzA C4), 28.88 (Ak C4), 19.66 (Ak C3), 32.07, 29.84, 29.69, 29.69, 29.51, 29.33, 29.13, 22.88 (Ak C5-15), 14.26 (Ak C16), **IR** (cm⁻¹): 2914, 2847 (CH₃, CH₂), 1602, 1583 (Pz C=N), 1469 (Py ring), 795 (Py C-H), **MP**: 75.3 – 75.6°C, **CHN**: calculated for C₂₉H₄₁N₅: C 75.77, H 8.99, N 15.24, found: C 75.49, H 8.86, N 15.06 %.

6.4.3 L17CxD - 2,6-bis(4-alk-1-yn-1-yl-1H-pyrazol-1-yl)pyridines

L17C12D



2,6-Bis(4-dodec-1-yn-1-yl-1H-pyrazol-1-yl)pyridine was obtained using the procedure described in the literature,⁸ with some modifications. A mixture of 2,6-

bis(4-iodo-1H-pyrazol-1-yl)pyridine **L15** (2 g, 4.3 mmol, 1 eq), tetrakis(triphenylphosphine)palladium(0) (0.250 g, 0.22 mmols, 0.05 eq), triphenylphosphine (0.1812 g, 6.9 mmol, 0.16 eq), CuI (0.181 g, 0.10 mmol, 0.22 eq), Et₃N (18 ml), and anhydrous dioxane (9 ml) was placed in a Schlenk tube and degassed by bubbling nitrogen through for 2 h. 1-Dodecyne (2.78 ml, 2.161 g, 13.0 mmol, 3 eq) was then added, the reaction mixture was heated to 80°C and kept stirring at that temperature for 2 days, while being monitored by TLC. The reaction mixture was filtered, the solvent was removed from the filtrate under reduced pressure, the crude mixture was separated by column chromatography (Hx/EtOAc, 12/1), and the obtained products were additionally recrystallized from EtOAc to remove the orange admixture of the palladium catalyst that passed through the column. This yielded the disubstituted product **IG17C12D** (spot #3, rf = 0.42, 1.454 g, 62 %), and monosubstituted product **IG17C12M** (spot #4, rf = 0.26, 0.147 g, 9 %), both as white powders.

Analyses: **¹H NMR** (CDCl₃, 400.130 MHz, ppm): δ 8.56 (s, 2 H, Pz H5), 7.90 (t, 1 H, Py H4), 7.81 (d, 2 H, Py H3,5) 7.73 (s, 2 H, Pz H3), 2.40 (t, 4 H, Ak H3), 1.61 (p, 4 H, Ak H4), 1.45 (s, 4 H, Ak H5), 1.28 (s, 24 H, Ak H6-11), 0.88 (t, 6 H, Ak H 12), **¹³C NMR** (CDCl₃, 100.613 MHz, ppm): δ 149.64 (Py C4), 144.73 (Pz C5), 141.56 (Py C4), 129.10 (Pz C3), 109.68 (Py C3,5),

106.73 (Ak C1), 92.78 (Ak C2), 70.77 (Pz C4), 28.88 (Ak C4), 19.64 (Ak C3), 32.05, 29.75, 29.68, 29.47, 29.33, 29.12, 22.82 (Ak C5-11), 14.24 (Ak C12), **MS** (HR-ESI) m/z: calc. for [C₃₅H₄₉N₅+H⁺]: 540.4061, found: 540.4058, calc. for [C₃₅H₄₉N₅+Na⁺]: 562.3880, found: 562.3876, **IR** (cm⁻¹): 2915, 2847 (CH₃, CH₂), 1598, 1587 (Pz C=N), 1463 (Py ring), 800 (Py C-H), **MP**: 80.9°C, **CHN**: calculated for C₃₅H₄₉N₅: C 77.88, H 9.15, N 12.97, found: C 77.66, H 9.26, N 13.11 %.

L17C14D

2,6-Bis(4-tetradec-1-yn-1-yl-1H-pyrazol-1-yl)pyridine was prepared using the same procedure as for **L13C12D**, using the following quantities: 2,6-bis(4-iodo-1H-pyrazol-1-yl)pyridine **L12** (2 g, 4.32 mmol, 1 eq), tetrakis(triphenylphosphine)palladium(0) (0.250 g, 0.22 mmols, 0.05 eq), triphenylphosphine (0.181 g, 6.9 mmol, 0.16 eq), CuI (0.181 g, 0.95 mmol, 0.22 eq), Et₃N (18 ml), and anhydrous dioxane (9 ml), and tetradecyne (3.19 ml, 2.519 g, 12.96 mmol, 3 eq). The product was purified by multiple recrystallizations from EtOAc. During the purification a spillage occurred, so the yield was lower than expected (0.589 g, 23%), and the product was obtained as white plate crystals.

Analyses: **¹H NMR** (CDCl₃, 400.130 MHz, ppm): δ 8.56 (s, 2 H, Pz H5), 7.90 (t, 1 H, Py H4), 7.81 (d, 2 H, Py H3,5) 7.73 (s, 2 H, Pz H3), 2.40 (t, 4 H, Ak H3), 1.61 (p, 4 H, Ak H4), 1.45 (s, 4 H, Ak H5), 1.28 (s, 32 H, Ak H6-13), 0.88 (t, 6 H, Ak H14), **¹³C NMR** (CDCl₃, 100.613 MHz, ppm): δ 148.64 (Py C4), 143.73 (Pz C5), 140.56 (Py C4), 128.10 (Pz C3), 108.68 (Py C3,5), 105.73 (Ak C1), 91.78 (Ak C2), 69.77 (Pz C4), 27.88 (Ak C4), 18.64 (Ak C3), 31.05, 28.75, 28.68, 28.47, 28.33, 28.12, 21.82 (Ak C5-13), 13.24 (Ak C14), **IR** (cm⁻¹): 2915, 2847 (CH₃, CH₂), 1598, 1582 (Pz C=N), 1463 (Py ring), 800 (Py C-H), **MP**: 84.9–85.5°C, **CHN**: calculated for C₃₉H₅₇N₅: C 78.61, H 9.64, N 11.75, found: C 78.70, H 9.52, N 11.82 %.

L17C16D

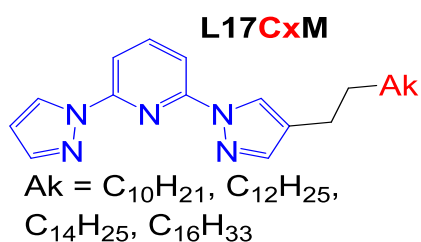
2,6-Bis(4-hexadec-1-yn-1-yl-1H-pyrazol-1-yl)pyridine was prepared using the same procedure as for **L13C12D**, using the following quantities: 2,6-bis(4-iodo-1H-pyrazol-1-yl)pyridine **L12** (2 g, 4.3 mmol, 1 eq), tetrakis(triphenylphosphine)palladium(0) (0.250 g, 0.22 mmols, 0.05 eq), triphenylphosphine (0.181 g, 6.9 mmol, 0.16 eq), CuI (0.181 g, 0.95 mmol, 0.22 eq), Et₃N (18 ml), and anhydrous dioxane (9 ml), and hexadecyne (3.63 ml, 2.891 g, 13.0 mmol, 3 eq). The product was purified by recrystallization from EtOAc,

instead of by column chromatography, which yielded the target product as a white crystalline powder (1.119 g, 40 %).

Analyses: $^1\text{H NMR}$ (CDCl_3 , 400.130 MHz, ppm): δ 8.56 (s, 2 H, Pz H5), 7.90 (t, 1 H, Py H4), 7.81 (d, 2 H, Py H3,5) 7.73 (s, 2 H, Pz H3), 2.40 (t, 4 H, Ak H3), 1.61 (p, 4 H, Ak H4), 1.45 (s, 4 H, Ak H5), 1.28 (s, 40 H, Ak H6-15), 0.88 (t, 6 H, Ak H16), $^{13}\text{C NMR}$ (CDCl_3 , 100.613 MHz, ppm): δ 148.64 (Py C4), 143.73 (Pz C5), 140.56 (Py C4), 128.10 (Pz C3), 108.68 (Py C3,5), 105.73 (Ak C1), 91.78 (Ak C2), 69.77 (Pz C4), 27.88 (Ak C4), 18.64 (Ak C3), 31.05, 28.75, 28.68, 28.47, 28.33, 28.12, 21.82 (Ak C5-15), 13.24 (Ak C16), **IR** (cm^{-1}): 2915, 2847 (CH_3 , CH_2), 1599, 1582 (Pz C=N), 1481, 1463 (Py ring), 800 (Py C-H), **MP**: 89.4–89.7°C, **CHN**: calculated for $\text{C}_{43}\text{H}_{65}\text{N}_5$: C 79.21, H 10.05, N 10.74, found: C 79.07, H 9.96, N 10.84 %.

6.4.4 L18CxM - 2-(4-alk-1H-pyrazol-1-yl)-6-(1H-pyrazol-1-yl)pyridines

L18C12M



2-(4-Dodec-1H-pyrazol-1-yl)-6-(1H-pyrazol-1-yl)pyridine was obtained using the same procedure as for **L14C12D**, using the following quantities: 2-(4-dodec-1-yn-1-yl)-1H-pyrazol-1-yl)-6-(1H-pyrazol-1-yl)pyridine **L13C12M** (0.350 g, 0.93 mmol, 1 eq), EtOAc

(152 ml), 10% Pd on activated carbon (0.272 g, 0.23 mmol, 0.25 eq), which yielded 2-(4-dodec-1H-pyrazol-1-yl)-6-(1H-pyrazol-1-yl)pyridine (0.320 g, 91%) as a white crystalline powder.

Analyses: $^1\text{H NMR}$ (CDCl_3 , 400.130 MHz, ppm): δ 8.59 (d, 1 H, PzB H5), 8.32 (s, 1 H, PzA H5), 7.90 (t, 1 H, Py H4), 7.82 (d, 1 H, Py H5), 7.80 (dd, 1 H, Py H3), 7.76 (d, 1 H, PzB H3), 7.59 (dd, 1 H, PzA H3), 6.49 (dd, 1H, PzB H4), 2.55 (t, 2 H, Ak H1), 1.64 (p, 2 H, Ak H2), 1.35 (p, 2 H, Ak H3), 1.28 (s, 16 H, Ak H4-11), 0.88 (t, 3 H, Ak H 12), $^{13}\text{C NMR}$ (CDCl_3 , 100.613 MHz, ppm): δ 150.30 (Py C6), 150.11 (Py C2), 142.73 (PzA C3), 142.42 (PzB C3), 141.36 (Py C4), 127.14 (PzB C5), 124.84 (PzA C5), 124.61 (PzA C4), 109.13 (Py C5), 108.94 (Py C3), 107.97 (PzB C4), 30.81 (Ak C2), 29.75 (Ak C3), 24.38 (Ak C1), 32.06, 29.58, 29.49, 29.43, 22.82 (Ak C4-11), 14.24 (Ak C12), **IR** (cm^{-1}): 2918, 2848 (CH_3 , CH_2), 1604, 1582 (Pz C=N), 1469 (Py ring), 799, 722 (Py C-H), **MP**: 66.3–66.7°C, **CHN**: calculated for $\text{C}_{23}\text{H}_{33}\text{N}_5$: C 72.78, H 8.76, N 18.45, found: C 72.72, H 8.87, N 18.33 %.

L18C14M

2-(4-Tetra-1H-pyrazol-1-yl)-6-(1H-pyrazol-1-yl)pyridine was obtained using the same procedure as for **L14C12D**, using the following quantities: 2-(4-tetradec-1-yn-1-yl-1H-pyrazol-1-yl)-6-(1H-pyrazol-1-yl)pyridine **L13C14M** (0.4 g, 0.99 mmol, 1 eq), EtOAc (162 ml), 10% Pd on activated carbon (0.288 g, 0.25 mmol, 0.25 eq), which yielded 2-(4-tetradec-1H-pyrazol-1-yl)-6-(1H-pyrazol-1-yl)pyridine (0.216 g, 54%) as a white powder.

Analyses: **¹H NMR** (CDCl₃, 400.130 MHz, ppm): δ 8.59 (d, 1 H, PzB H5), 8.32 (s, 1 H, PzA H5), 7.90 (t, 1 H, Py H4), 7.82 (d, 1 H, Py H5), 7.80 (dd, 1 H, Py H3), 7.76 (d, 1 H, PzB H3), 7.59 (dd, 1 H, PzA H3), 6.49 (dd, 1H, PzB H4), 2.55 (t, 2 H, Ak H1), 1.64 (p, 2 H, Ak H2), 1.35 (p, 2 H, Ak H3), 1.26 (s, 20 H, Ak H4-13), 0.88 (t, 3 H, Ak H 14), **¹³C NMR** (CDCl₃, 100.613 MHz, ppm): δ 150.33 (Py C2), 150.14 (Py C6), 142.76 (PzA C3), 142.45 (PzB C3), 141.39 (Py C4), 127.17 (PzB C5), 124.88 (PzA C5), 124.64 (PzA C4), 109.15 (Py C5), 108.97 (Py C3), 108.00 (PzB C4), 30.83 (Ak C2), 29.50 (Ak C3), 24.40 (Ak C1), 32.07, 29.76, 29.59, 29.44, 22.83 (Ak C4-13), 14.26 (Ak C14), **IR** (cm⁻¹): 2916, 2848 (CH₃, CH₂), 1604, 1582 (Pz C=N), 1470 (Py ring), 798, 772 (Py C-H), **MP:** 72.4–72.7°C, **CHN:** calculated for C₂₅H₃₇N₅: C 73.67, H 9.15, N 17.18, found: C 73.78, H 9.27, N 17.05 %.

L18C16M

2-(4-Hexadec-1H-pyrazol-1-yl)-6-(1H-pyrazol-1-yl)pyridine was obtained using the same procedure as for **L14C12D**, using the following quantities: 2-(4-hexadec-1-yn-1-yl-1H-pyrazol-1-yl)-6-(1H-pyrazol-1-yl)pyridine **L13C16M** (0.400 g, 0.93 mmol, 1 eq), EtOAc (151 ml), 10% Pd on activated carbon (0.270 g, 0.23 mmol, 0.25 eq), which yielded 2-(4-tetradec-1H-pyrazol-1-yl)-6-(1H-pyrazol-1-yl)pyridine (0.380 g, 94%) as a white powder.

Analyses: **¹H NMR** (CDCl₃, 400.130 MHz, ppm): δ 8.59 (d, 1 H, PzB H5), 8.32 (s, 1 H, PzA H5), 7.90 (t, 1 H, Py H4), 7.82 (d, 1 H, Py H5), 7.80 (dd, 1 H, Py H3), 7.76 (d, 1 H, PzB H3), 7.59 (dd, 1 H, PzA H3), 6.49 (dd, 1H, PzB H4), 2.55 (t, 2 H, Ak H1), 1.66 (p, 2 H, Ak H2), 1.35 (p, 2 H, Ak H3), 1.28 (s, 24 H, Ak H4-15), 0.88 (t, 3 H, Ak H 16), **¹³C NMR** (CDCl₃, 100.613 MHz, ppm): δ 150.30 (Py C6), 150.11 (Py C2), 142.73 (PzA C3), 142.42 (PzB C3), 141.36 (Py C4), 127.14 (PzB C5), 124.84 (PzA C5), 124.61 (PzA C4), 109.13 (Py C5), 108.94 (Py C3), 107.97 (PzB C4), 30.81 (Ak C2), 29.75 (Ak C3), 24.38 (Ak C1), 32.06, 29.58, 29.49, 29.43, 22.82 (Ak C4-15), 14.24 (Ak C16), **IR** (cm⁻¹): 2914, 2847 (CH₃, CH₂), 1609, 1582 (Pz C=N), 1474 (Py

ring), 798, 778 (Py C-H), **MP**: 78.6–78.9°C, **CHN**: calculated for C₂₇H₄₁N₅: C 74.44, H 9.49, N 16.08, found: C 74.52, H 9.57, N 15.87 %.

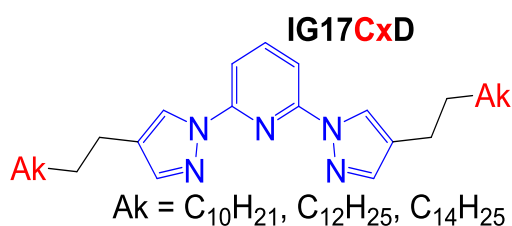
L18C18M

2-(4-Octadec-1H-pyrazol-1-yl)-6-(1H-pyrazol-1-yl)pyridine was obtained using the same procedure as for **L14C12D**, using the following quantities: 2-(4-octadec-1-yn-1-yl-1H-pyrazol-1-yl)-6-(1H-pyrazol-1-yl)pyridine **L13C18M** (0.200 g, 0.435 mmol, 1 eq), EtOAc (70 ml), 10% Pd on activated carbon (0.127 g, 0.1088 mmol, 0.25 eq), which yielded 2-(4-tetradec-1H-pyrazol-1-yl)-6-(1H-pyrazol-1-yl)pyridine (0.185 g, 92%) as a white powder.

Analyses: ¹H NMR (CDCl₃, 400.130 MHz, ppm): δ 8.59 (d, 1 H, PzB H5), 8.32 (s, 1 H, PzA H5), 7.91 (t, 1 H, Py H4), 7.91 (dd, 1 H, Py H3), 7.82 (d, 1 H, Py H5), 7.80 (dd, 1 H, Py H3), 7.76 (d, 1 H, PzB H3), 7.59 (dd, 1 H, PzA H3), 6.50 (dd, 1H, PzB H4), 2.55 (t, 2 H, Ak H1), 1.63 (p, 2 H, Ak H2), 1.34 (p, 2 H, Ak H3), 1.25 (s, 28 H, Ak H4-15), 0.88 (t, 3 H, Ak H 16), ¹³C NMR (CDCl₃, 100.613 MHz, ppm): δ 150.28 (Py C6), 150.10 (Py C2), 142.76 (PzA C3), 142.45 (PzB C3), 141.41 (Py C4), 127.17 (PzB C5), 124.88 (PzA C5), 124.63 (PzA C4), 109.13 (Py C5), 108.95 (Py C3), 108.01 (PzB C4), 30.83 (Ak C2), 29.77 (Ak C3), 24.39 (Ak C1), 32.08, 29.85, 29.77, 29.60, 29.51, 29.47, 22.85 (Ak C4-15), 14.28 (Ak C16), **IR** (cm⁻¹): 2914, 2847 (CH₃, CH₂), 1609, 1582 (Pz C=N), 1474 (Py ring), 798, 778 (Py C-H), **MP**: 81.4 – 81.9°C, **CHN**: calculated for C₂₉H₄₅N₅: C 75.12, H 9.78, N 15.10, found: C 75.06, H 9.56, N 14.93 %.

6.4.5 L18CxD - 2-(4-alk-1H-pyrazol-1-yl)-6-(1H-pyrazol-1-yl)pyridines

L18C12D



2-(4-dodec-1H-pyrazol-1-yl)-6-(1H-pyrazol-1-yl)pyridine was obtained using the procedure described in the literature,⁸ with some modifications.

2-(4-Dodec-1-yn-1-yl-1H-pyrazol-1-yl)-6-(1H-pyrazol-1-yl)pyridine **L13C12D** (0.243 g, 0.45 mmol, 1 eq) was dissolved in EtOAc (75 ml), degassed in a Schlenk tube by bubbling N₂ through the solution, after which 10% Pd on activated carbon (0.131 g, 0.11 mmol, 0.25 eq) was added in. Then the gas was thoroughly extracted from the Schlenk tube, until high vacuum was achieved and the solvent started boiling. H₂ gas was then added from a bladder via subaseal and a needle, and the extraction and filling with H₂ was repeated once more. The reaction

mixture was stirred for 4 days at room temperature, while being monitored by TLC, after which it was vacuum filtered through a Celite plug, the plug was washed with 120 ml of EtOAc. Solvent was removed under vacuum from the obtained filtrate, which afforded 2,6-bis(4-dodec-1H-pyrazol-1-yl)pyridine as a white crystalline powder (0.224 g, 91%).

Analyses: $^1\text{H NMR}$ (CDCl_3 , 400.130 MHz, ppm): δ 8.32 (s, 2 H, Pz H5), 7.87 (dd, 1 H, Py H4), 7.77 (dd, 2 H, Py H3,5), 7.59 (s, 2 H, Pz H3), 2.55 (t, 4 H, Ak H1), 1.64 (p, 4 H, Ak H2), 1.35 (p, 4 H, Ak H3), 1.26 (s, 32 H, Ak H4-11), 0.88 (t, 6 H, Ak H12), $^{13}\text{C NMR}$ (CDCl_3 , 100.613 MHz, ppm): δ 150.25 (Py C2,6), 142.66 (Pz C5), 141.27 (Py C4), 124.94 (Pz C4), 124.56 (Pz C3), 108.66 (Py C5,6), 30.91 (Ak C2), 29.46 (Ak C3), 24.42 (Ak C1), 32.06, 29.82, 29.79, 29.77, 29.60, 29.50, 29.46 (Ak C4-11), 14.25 (Ak C12), **MS** (HR-ESI) m/z : calc. for $[\text{C}_{35}\text{H}_{57}\text{N}_5+\text{H}^+]$: 548.4687, found: 548.4677, calc. for $[\text{C}_{35}\text{H}_{57}\text{N}_5+\text{Na}^+]$: 570.4506, found: 570.4490, **IR** (cm^{-1}): 2916, 2849 (CH_3 , CH_2), 1613, 1586 (Pz C=N), 1466 (Py ring), 800 (Py C-H), **MP**: 64.7–65.4°C, **CHN**: calculated for $\text{C}_{35}\text{H}_{57}\text{N}_5$: C 76.73, H 10.49, N 12.78, found: C 76.83, H 10.33, N 12.78 %.

L18C14D

2,6-Bis(4-tetradec-1H-pyrazol-1-yl)pyridine was prepared using the same procedure as for **L14C12D**, using the following quantities: 2-(4-tetradec-1-yn-1-yl-1H-pyrazol-1-yl)-6-(1H-pyrazol-1-yl)pyridine **L13C14D** (0.265 g, 0.45 mmol, 1 eq), EtOAc (75 ml + 100 ml for washing the Celite plug), 10% Pd on activated carbon (0.129 g, 0.11 mmol, 0.25 eq), which yielded 2,6-bis(4-tetradec-1H-pyrazol-1-yl)pyridine (0.189 g, 70%) as a white powder.

Analyses: $^1\text{H NMR}$ (CDCl_3 , 400.130 MHz, ppm): δ 8.32 (s, 2 H, Pz H5), 7.87 (dd, 1 H, Py H4), 7.77 (dd, 2 H, Py H3,5), 7.58 (s, 2 H, Pz H3), 2.55 (t, 4 H, Ak H1), 1.64 (p, 4 H, Ak H2), 1.35 (p, 4 H, Ak H3), 1.26 (s, 40 H, Ak H4-13), 0.88 (t, 6 H, Ak H14), $^{13}\text{C NMR}$ (CDCl_3 , 100.613 MHz, ppm): δ 150.25 (Py C2,6), 142.66 (Pz C5), 141.27 (Py C4), 124.94 (Pz C4), 124.56 (Pz C3), 108.66 (Py C5,6), 30.91 (Ak C2), 29.46 (Ak C3), 24.42 (Ak C1), 32.06, 29.82, 29.79, 29.77, 29.60, 29.50, 29.46 (Ak C4-13), 14.25 (Ak C14), **IR** (cm^{-1}): 2916, 2849 (CH_3 , CH_2), 1613, 1584 (Pz C=N), 1466 (Py ring), 800 (Py C-H), **MP**: 72.8–73.2°C, **CHN**: calculated for $\text{C}_{39}\text{H}_{65}\text{N}_5$: C 77.56, H 10.85, N 11.60, found: C 77.31, H 11.17, N 11.56 %.

L18C16D

2,6-bis(4-hexadec-1H-pyrazol-1-yl)pyridine was prepared using the same procedure as for **L14C12D**, using the following quantities: 2-(4-hexadec-1-

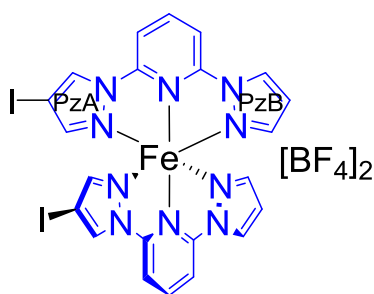
yn-1-yl-1H-pyrazol-1-yl)-6-(1H-pyrazol-1-yl)pyridine **L13C16D** (0.5 g, 0.84 mmol, 1 eq), EtOAc (137 ml + 200 ml for washing the Celite plug), 10% Pd on activated carbon (0.245 g, 0.21 mmol, 0.25 eq), which yielded 2,6-bis(4-tetradec-1H-pyrazol-1-yl)pyridine (0.339 g, 61%) as a white powder.

¹H NMR (CDCl₃, 400.130 MHz, ppm): δ 8.32 (s, 2 H, Pz H5), 7.87 (dd, 1 H, Py H4), 7.77 (dd, 2 H, Py H3,5), 7.59 (s, 2 H, Pz H3), 2.55 (t, 4 H, Ak H1), 1.64 (p, 4 H, Ak H2), 1.35 (p, 4 H, Ak H3), 1.26 (s, 48 H, Ak H4-15), 0.88 (t, 6 H, Ak H16), **¹³C NMR** (CDCl₃, 100.613 MHz, ppm): δ 150.25 (Py C2,6), 142.66 (Pz C5), 141.27 (Py C4), 124.94 (Pz C4), 124.56 (Pz C3), 108.66 (Py C5,6), 30.91 (Ak C2), 29.46 (Ak C3), 24.42 (Ak C1), 32.06, 29.82, 29.79, 29.77, 29.60, 29.50, 29.46 (Ak C4-15), 14.25 (Ak C16), **IR** (cm⁻¹): 2915, 2848 (CH₃, CH₂), 1613, 1586 (Pz C=N), 1466 (Py ring), 799 (Py C-H), **MP**: 75.2–75.9°C, **CHN**: calculated for C₄₃H₇₃N₅: C 78.24, H 11.15, N 10.61, found: C 78.15, H 11.26, N 10.44 %.

6.4.6 Iron(II) complexes

The [Fe(L17Cx)₂][BF₄]₂ iron(II) complexes were obtained by this general procedure, adapted from the literature:⁴ The ligand (1 eq.) was dissolved in either dichloroethane (DCE) or in DCM, and iron(II) tetrafluoroborate hexahydrate (0.5 eq.) was dissolved in acetone, with a gentle heating, if necessary. The two solutions were mixed at room temperature, which lead to instant formation of an intensively coloured solution, which, if necessary, was filtered through a pipette filter. The obtained complex solution was set for pentane diffusion crystallization.

[Fe(L16)₂][BF₄]₂



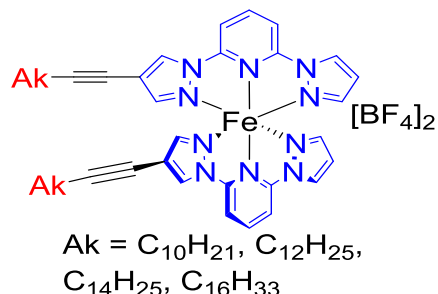
2-(4-Iodo-1H-pyrazol-1-yl)-6-(1H-pyrazol-1-yl)pyridine iron(II) tetrafluoro-borate was obtained by dissolving 2-(4-iodo-1H-pyrazol-1-yl)-6-(1H-pyrazol-1-yl)pyridine (133 mg, 0.390 mmol, 2 eq) and iron(II) tetrafluoroborate hexhydrate (74.5 mg, 0.20 mmol, 1eq) in MeCN. The two solutions were mixed, and the product was

crystallized by slow iPr₂O diffusion, which yielded a brown-orange powder (110 mg, 62%).

Analyses: **paramagnetic NMR** (MeCN-D₃, 300 MHz, ppm): δ 66.04, 60.45 (1 H PzA H3 and 1 H PzB H3), 57.81 (1 H, PzB H4), 47.16, 41.99 (1 H PzA H5 and 1H PzB H5), 38.55, 28.53 (1 H, Py H3 and 1 H, Py H5), 1.05 (Py H4), **IR** (cm⁻¹): 3128 (Py N-Fe), 1621, 1588 (Py C=C), 1472 (Py ring

substituted), 1032, 782 (B-F), 596 (C-I), **CHN**: calculated for $[(C_{11}H_8N_5)_2Fe][BF_4]_2$: C 29.24, H 1.78, N 15.50%, found: C 29.18, H 1.86, N 15.35%.

[Fe(L17CxM)₂][BF₄]₂



[Fe(L17C12M)₂][BF₄]₂

2-(4-Dodec-1-yn-1-yl-1H-pyrazol-1-yl)-6-(1H-pyrazol-1-yl)pyridine iron(II) tetrafluoroborate was obtained using the general procedure described above, using the following quantities: 2-(4-dodec-1-yn-1-yl-1H-pyrazol-1-yl)-6-(1H-pyrazol-1-yl)pyridine

(150 mg, 0.40 mmol, 2 eq), iron(II) tetrafluoroborate hexhydrate (75.4 mg, 0.20 mmol, 1eq). The reactants were dissolved in DCM, mixed, and the product was crystallized by *i*Pr₂O diffusion, which yielded a brown-orange powder (107 mg, 54%).

Analyses: **paramagnetic NMR** (CDCl₃, 300 MHz, ppm): δ 67.75, 60.78 (1 H, PzA H3 and 1 H, PzB H3), 58.78 (1 H, PzB H4), 51.01, 41.07 (1 H, PzA H5 and 1 H, PzB H5), 37.20, 28.87 (1 H, Py H3 and 1H, Py H5), -1.66 (1 H, py H4), **IR** (cm⁻¹): 3129 (Py N-Fe), 2923, 2853 (CH₃, CH₂), 2242 (C≡C), 1621, 1588 (Py C=C), 1476 (Py ring substituted), 1055, 784 (B-F), **CHN**: calculated for $[(C_{23}H_{29}N_5)_2Fe][BF_4]_2$: C 56.35, H 5.96, N 14.29%, found: C 56.18, H 6.12, N 14.16%.

[Fe(L17C14M)₂][BF₄]₂

2-(4-Tetra-1-yn-1-yl-1H-pyrazol-1-yl)-6-(1H-pyrazol-1-yl)pyridine iron(II) tetrafluoroborate was obtained using the general procedure described above, using the following quantities: 2-(4-tetradec-1-yn-1-yl-1H-pyrazol-1-yl)-6-(1H-pyrazol-1-yl)pyridine (150 mg, 0.37 mmol, 2 eq), iron(II) tetrafluoroborate hexhydrate (70.2 mg, 0.19 mmol, 1eq). The reactants were dissolved in DCM, mixed, and the product was crystallized by *i*Pr₂O diffusion, which yielded a brown-orange powder (94 mg, 48%).

Analyses: **paramagnetic NMR** (CDCl₃, 300 MHz, ppm): δ 67.72, 60.72 (1 H, PzA H3 and 1 H, PzB H3), 58.60 (1 H, PzB H4), 51.17, 41.01 (1 H, PzA H5 and 1 H, PzB H5), 37.13, 28.94 (1 H, Py H3 and 1H, Py H5), -1.82 (1 H, py H4), **IR** (cm⁻¹): 3129 (Py N-Fe), 2922, 2852 (CH₃, CH₂), 2244 (C≡C), 1621, 1588 (Py C=C), 1476 (Py ring substituted), 1056, 784 (B-F), **CHN**: calculated for $[(C_{25}H_{33}N_5)_2Fe][BF_4]_2 \cdot 2H_2O$: C 55.99, H 6.58, N 13.06%, found: C 56.08, H 6.28, N 13.19 %.

[Fe(L17C16M)₂][BF₄]₂

2-(4-Hexa-1-yn-1-yl-1H-pyrazol-1-yl)-6-(1H-pyrazol-1-yl)pyridine iron(II) tetrafluoroborate was obtained using the general procedure described above, using the following quantities: 2-(4-hexadec-1-yn-1-yl-1H-pyrazol-1-yl)-6-(1H-pyrazol-1-yl)pyridine (150 mg, 0.348 mmol, 2 eq), iron(II) tetrafluoroborate hexahydrate (65.6 mg, 0.174 mmol, 1eq). The reactants were dissolved in DCM, mixed, and the product was crystallized by iPr₂O diffusion, which yielded a yellow powder (63 mg, 37%).

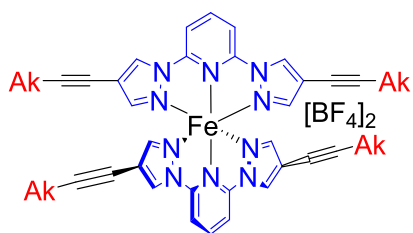
Analyses: **paramagnetic NMR** (CDCl₃, 300 MHz, ppm): δ 67.69, 60.76 (1 H, PzA H3 and 1 H, PzB H3), 58.65 (1 H, PzB H4), 50.86, 40.99 (1 H, PzA H5 and 1 H, PzB H5), 37.10, 29.20 (1 H, Py H3 and 1H, Py H5), -1.74 (1 H, py H4), **IR** (cm⁻¹): 3130 (Py N-Fe), 2916, 2850 (CH₃, CH₂), 2237 (C≡C), 1624, 1588 (Py C=C), 1480 (Py ring substituted), 1048, 784 (B-F), **CHN:** calculated for [(C₂₇H₃₇N₅)₂Fe][BF₄]₂: C 59.36, H 6.83, N 12.82%, found: C59.21 , H 6.75, N 12.73%.

[Fe(L17C18M)₂][BF₄]₂

2-(4-Octa-1-yn-1-yl-1H-pyrazol-1-yl)-6-(1H-pyrazol-1-yl)pyridine iron(II) tetrafluoroborate was obtained using the general procedure described above, using the following quantities: 2-(4-octadec-1-yn-1-yl-1H-pyrazol-1-yl)-6-(1H-pyrazol-1-yl)pyridine (75.5 mg, 0.163 mmol, 2 eq), iron(II) tetrafluoroborate hexahydrate (31 mg, 0.082 mmol, 1eq). The ligand was dissolved in DCE, and the iron salt was dissolved in acetone, the two solutions were mixed, and the obtained yellow solution was slowly precipitated by pentane diffusion, which yielded product as small yellow plate crystals (58 mg, 62%).

Analyses: **IR** (cm⁻¹): 3127 (Py N-Fe), 2916, 2849 (CH₃, CH₂), 2167 (C≡C), 1623, 1588 (Py C=C), 1479 (Py ring substituted), 1061, 784 (B-F).

[Fe(L17Cx_D)₂][BF₄]₂



Ak = C₁₀H₂₁, C₁₂H₂₅, C₁₄H₂₉

[Fe(L17C12D)₂][BF₄]₂

2,6-Bis(4-dodec-1-yn-1-yl-1H-pyrazol-1-yl)pyridine iron(II) tetrafluoroborate was obtained using the general procedure described above, using the following quantities: 2,6-bis(4-dodec-1-yn-1-yl-1H-pyrazol-1-yl)pyridine (142 mg, 0.26 mmol, 2 eq), iron(II) tetrafluoroborate hexahydrate (49.6 mg, 0.13 mmol, 1eq). The reagents were dissolved in

DCM, and crystallized by $i\text{Pr}_2\text{O}$ diffusion, which yielded a yellow powder (66 mg, 43%).

Analyses: **paramagnetic NMR** ($\text{CDCl}_3 + \text{MeCN-D}_3$, 300 MHz, ppm): δ 59.42 (2 H, Pz H3), 43.25 (2 H, Pz H5), 41.09 (2 H, Py H3,5), -3.77 (1 H, py H4), **IR** (cm^{-1}): 3203 (Py N-Fe), 2916, 2848 (CH_3 , CH_2), 2260 ($\text{C}\equiv\text{C}$), 1599, 1587 (Py $\text{C}=\text{C}$), 1479 (Py ring substituted), 1069, 779 (B-F), 800 (Py C-H).

[Fe(L17C14D)₂][BF₄]₂

2,6-Bis(4-tetradec-1-yn-1-yl-1H-pyrazol-1-yl)pyridine iron(II) tetrafluoroborate was obtained using the general procedure described above, using the following quantities: 2,6-bis(4-tetradec-1-yn-1-yl-1H-pyrazol-1-yl)pyridine (150 mg, 0.25 mmol, 2 eq), iron(II) tetrafluoroborate hexhydrate (47.5 mg, 0.126 mmol, 1eq). The reagents were dissolved in DCM, and crystallized by $i\text{Pr}_2\text{O}$ diffusion, which yielded a yellow powder (38 mg, 21%).

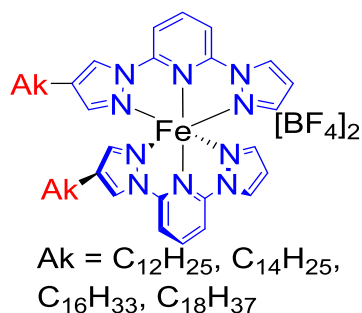
Analyses: **paramagnetic NMR** ($\text{CDCl}_3 + \text{MeCN-D}_3$, 300 MHz, ppm): δ 59.07 (2 H, Pz H3), 42.92 (2 H, Pz H5), 40.96 (2 H, Py H3,5), 7.79 (1 H, py H4), **IR** (cm^{-1}): 3146 (Py N-Fe), 2915, 2848 (CH_3 , CH_2), 2251 ($\text{C}\equiv\text{C}$), 1599, 1564 (Py $\text{C}=\text{C}$), 1477 (Py ring substituted), 1060, 779 (B-F), 800 (Py C-H), **CHN:** calculated for $[(\text{C}_{39}\text{H}_{57}\text{N}_5)_2\text{Fe}][\text{BF}_4]_2 \cdot 0.5 \text{ DCE}$: C 64.51, H 7.95, N 9.52%, found: C 64.59, H 7.66, N 9.48%.

[Fe(L17C16D)₂][BF₄]₂

2,6-Bis(4-hexadec-1-yn-1-yl-1H-pyrazol-1-yl)pyridine iron(II) tetrafluoroborate was obtained using the general procedure described above, using the following quantities: 2,6-bis(4-hexadec-1-yn-1-yl-1H-pyrazol-1-yl)pyridine (150 mg, 0.23 mmol, 2 eq), iron(II) tetrafluoroborate hexhydrate (43.4 mg, 0.120 mmol, 1eq). The reagents were dissolved in DCM, and crystallized by $i\text{Pr}_2\text{O}$ diffusion, which yielded a brown-orange powder (114 mg, 62%).

Analyses: **paramagnetic NMR** ($\text{CDCl}_3 + \text{MeCN-D}_3$, 300 MHz, ppm): δ 59.41 (2 H, Pz H3), 43.29 (2 H, Pz H5), 41.06 (2 H, Py H3,5), -3.66 (1 H, py H4), **IR** (cm^{-1}): 3125 (Py N-Fe), 2916, 2849 (CH_3 , CH_2), 2242 ($\text{C}\equiv\text{C}$), 1591, 1566 (Py $\text{C}=\text{C}$), 1477 (Py ring substituted), 1056, 791 (B-F), 800 (Py C-H), **CHN:** calculated for $[(\text{C}_{43}\text{H}_{65}\text{N}_5)_2\text{Fe}][\text{BF}_4]_2$: C 67.36, H 8.54, N 9.13%, found: C 67.43, H 8.50, N 9.05%.

[Fe(L18CxM)₂][BF₄]₂



[Fe(L18C12M)₂][BF₄]₂

2-(4-Dodec-1H-pyrazol-1-yl)-6-(1H-pyrazol-1-yl)pyridine iron(II) tetrafluoroborate was obtained using the general procedure described above, using the following quantities: 2-(4-dodec-1H-pyrazol-1-yl)-6-(1H-pyrazol-1-yl)pyridine (90.7 mg, 0.239 mmol, 2 eq), iron(II) tetrafluoroborate

hexhydrate (45.1 mg, 0.119 mmol, 1eq). The ligand was dissolved in DCE, and the iron salt was dissolved in acetone. The two solutions were mixed, and the bright red solution was slowly precipitated by pentane diffusion, which yielded the product as yellow plate crystals (82 mg, 69%).

Analyses: **paramagnetic NMR** (MeCN-D₃, 300 MHz, ppm): δ 58.81, 54.65 (3 H, PzA H₃, PzB H₃, PzB H₄), 35.94, 35.47, 33.00 (4H, PzA H₅, PzB H₅, Py 3,5), 3.45 (Py H₄), **MS** (HR-ESI) m/z: calc. for [C₂₃H₃₃N₅+H⁺]: 380.2809, found: 380.2809, calc. for [C₂₃H₃₃N₅+Na⁺]: 402.2628, found: 402.2631, calc. for [2 C₂₃H₃₃N₅+Na⁺]: 781.5364, found: 781.5367, **IR** (cm⁻¹): 3122 (Py N-Fe), 2917, 2850 (CH₃, CH₂), 1622, 1591 (Py C=C), 1481 (Py ring substituted), 1034, 789 (B-F), 801 (Py C-H).

[Fe(L18C14M)₂][BF₄]₂

2-(4-Tetradec-1H-pyrazol-1-yl)-6-(1H-pyrazol-1-yl)pyridine iron(II) tetrafluoroborate was obtained using the general procedure described above, using the following quantities: 2-(4-tetradec-1H-pyrazol-1-yl)-6-(1H-pyrazol-1-yl)pyridine (147 mg, 0.361 mmol, 2 eq), iron(II) tetrafluoroborate hexhydrate (68.1 mg, 0.180 mmol, 1eq). The ligand was dissolved in DCE, and the iron salt was dissolved in acetone. The two solutions were mixed, and the bright red solution was slowly precipitated by pentane diffusion, which yielded product as yellow plate crystals (155 mg, 82%).

Analyses: **paramagnetic NMR** (MeCN-D₃, 300 MHz, ppm): δ 58.65, 54.56 (3 H, PzA H₃, PzB H₃, PzB H₄), 35.89, 35.43, 32.98 (4H, PzA H₅, PzB H₅, Py 3,5), 3.44 (Py H₄), **MS** (HR-ESI) m/z: calc. for [C₂₅H₃₇N₅+H⁺]: 408.3122, found: 408.3124, calc. for [C₂₅H₃₇N₅+Na⁺]: 430.2941, found: 430.2940, calc. for [2 C₂₅H₃₇N₅+Na⁺]: 837.5990, found: 837.5991, **IR** (cm⁻¹): 3122 (Py N-Fe), 2916, 2850 (CH₃, CH₂), 1623, 1591 (Py C=C), 1481 (Py ring substituted), 1035, 789 (B-F), 801 (Py C-H).

[Fe(L18C16M)₂][BF₄]₂

2-(4-Hexadec-1H-pyrazol-1-yl)-6-(1H-pyrazol-1-yl)pyridine iron(II) tetrafluoroborate was obtained using the general procedure described above, using the

following quantities: 2-(4-hexadec-1H-pyrazol-1-yl)-6-(1H-pyrazol-1-yl)pyridine (186 mg, 0.427 mmol, 2 eq), iron(II) tetrafluoroborate hexhydrate (80.6 mg, 0.214 mmol, 1eq). The ligand was dissolved in DCE, and the iron salt was dissolved in acetone. The two solutions were mixed, and the obtained bright red solution was slowly precipitated by pentane diffusion, which yielded product as yellow plate crystals (194 mg, 83%).

Analyses: **paramagnetic NMR** (MeCN-D₃, 300 MHz, ppm): δ 58.64, 54.51 (3 H, PzA H₃, PzB H₃, PzB H₄), 35.89, 35.43, 33.03 (4H, PzA H₅, PzB H₅, Py 3,5), 3.43 (Py H₄), **MS** (HR-ESI) m/z: calc. for [C₂₇H₄₁N₅+H⁺]: 436.3435, found: 436.3435, calc. for [C₂₇H₄₁N₅+Na⁺]: 458.3254, found: 458.3258, calc. for [2 C₂₇H₄₁N₅ + Na⁺]: 893.6616, found: 893.6620, **IR** (cm⁻¹): 3122 (Py N-Fe), 2916, 2849 (CH₃, CH₂), 1622, 1591 (Py C=C), 1481 (Py ring substituted), 1035, 789 (B-F), 801 (Py C-H), **CHN**: calculated for [(C₃₇H₄₁N₅)₂Fe][BF₄]₂: C 58.92, H 7.51, N 12.72%, found: C 58.84, H 7.37, N 12.64%.

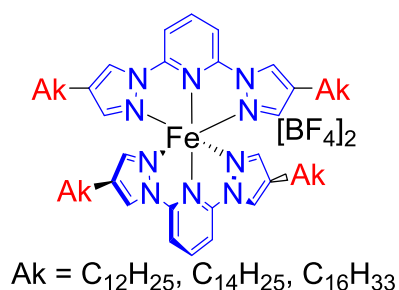
[Fe(L18C18M)₂][BF₄]₂

2-(4-Octadec-1H-pyrazol-1-yl)-6-(1H-pyrazol-1-yl)pyridine iron(II) tetrafluoroborate was obtained using the general procedure described above, using the following quantities: 2-(4-octadec-1H-pyrazol-1-yl)-6-(1H-pyrazol-1-yl)pyridine (77.5 mg, 0.167 mmol, 2 eq), iron(II) tetrafluoroborate hexhydrate (31.6 mg, 0.084 mmol, 1eq). The ligand was dissolved in DCE, and the iron salt was dissolved in acetone. The two solutions were mixed, and the obtained yellow solution was slowly precipitated by pentane diffusion, which yielded product as yellow plate crystals (71 mg, 73%).

Analyses: **IR** (cm⁻¹): 3122 (Py N-Fe), 2916, 2849 (CH₃, CH₂), 1623, 1590 (Py C=C), 1482 (Py ring substituted), 1047, 789 (B-F), 801 (Py C-H), **CHN**: calculated for [(C₂₉H₄₅N₅)₂Fe][BF₄]₂: C 60.22, H 7.84, N 12.11%, found: C 60.01, H 7.60, N 12.95 %.

[Fe(L18CxD)₂][BF₄]₂

[Fe(L18C12D)₂][BF₄]₂



2-(4-Dodec-1H-pyrazol-1-yl)-6-(1H-pyrazol-1-yl)pyridine iron(II) tetrafluoroborate was obtained using the general procedure described above, using the following quantities: 2-(4-dodec-1H-pyrazol-1-yl)-6-(1H-pyrazol-1-yl)pyridine (47.7 mg, 0.087 mmol, 2 eq), iron(II) tetrafluoroborate

hexhydrate (16.4 mg, 0.044 mmol, 1eq). The ligand was dissolved in DCE, and the iron salt was dissolved in acetone. The two solutions were mixed, and the obtained bright red solution was slowly precipitated by pentane diffusion, which yielded product as brown-red powder (30 mg, 52%).

Analyses: **paramagnetic NMR** (MeCN-D₃, 300 MHz, ppm): δ 50.98 (2H, Pz H₃), 33.60 (2H Pz H₅), 32.68 (2H, Py H_{3,5}), 3.94 (Py H₄), **MS** (HR-ESI) m/z: calc. for [C₃₅H₅₇N₅+H⁺]: 548.4687, found: 548.4685, calc. for [C₃₅H₅₇N₅+Na⁺]: 570.4506, found: 570.4505, **IR** (cm⁻¹): 3119 (Py N-Fe), 2917, 2850 (CH₃, CH₂), 1623, 1589 (Py C=C), 1489 (Py ring substituted), 1033, 787 (B-F), 804 (Py C-H), **CHN:** calculated for [(C₃₅H₅₇N₅)₂Fe][BF₄]₂: C 63.44, H 8.67, N 10.57%, found: C 63.29, H 8.53, N 10.47 %.

[Fe(L18C14D)₂][BF₄]₂

2,6-Bis(4-tetradec-1*H*-pyrazol-1-yl)pyridine iron(II) tetrafluoroborate was obtained using the general procedure described above, using the following quantities: 2,6-bis(4-tetradec-1*H*-pyrazol-1-yl)pyridine (100 mg, 0.166 mmol, 2 eq), iron(II) tetrafluoroborate hexhydrate (31.3 mg, 0.083 mmol, 1eq). The reagents were dissolved in DCM, and crystallized by pentane diffusion, which yielded a dark-yellow powder (63.5 mg, 53%).

Analyses: **paramagnetic NMR** (MeCN-D₃, 300 MHz, ppm): δ 51.82 (2H, Pz H₃), 34.06 (2H Pz H₅), 33.32 (2H, Py H_{3,5}), 3.79 (Py H₄), **IR** (cm⁻¹): 3117 (Py N-Fe), 2917, 2849 (CH₃, CH₂), 1623, 1588 (Py C=C), 1490 (Py ring substituted), 1032, 787 (B-F), 801 (Py C-H), **CHN:** calculated for [(C₃₉H₆₅N₅)₂Fe][BF₄]₂: C 65.18, H 9.12, N 9.74%, found: C 65.37, H 8.97, N 9.81%.

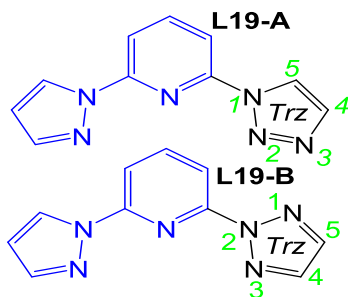
[Fe(L18C16D)₂][BF₄]₂

2,6-Bis(4-hexadec-1*H*-pyrazol-1-yl)pyridine iron(II) tetrafluoroborate was obtained using the general procedure described above, using the following quantities: 2,6-bis(4-hexadec-1*H*-pyrazol-1-yl)pyridine (100 mg, 0.151 mmol, 2 eq), iron(II) tetrafluoroborate hexhydrate (28.6 mg, 0.076 mmol, 1eq). The reagents were dissolved in DCM, and crystallized by pentane diffusion, which yielded a dark-yellow powder (71 mg, 60%).

Analyses: **paramagnetic NMR** (MeCN-D₃, 300 MHz, ppm): δ 51.87 (2H, Pz H₃), 34.06 (2H Pz H₅), 33.22 (2H, Py H_{3,5}), 3.78 (Py H₄), **IR** (cm⁻¹): 3117 (Py N-Fe), 2916, 2849 (CH₃, CH₂), 1623, 1588 (Py C=C), 1490 (Py ring substituted), 1055, 785 (B-F), 808 (Py C-H), **CHN:** calculated for [(C₄₃H₇₃N₅)₂Fe][BF₄]₂: C 66.66, H 9.50, N 9.04%, found: C 66.71, H 9.38, N 9.05%.

6.5 Asymmetric ligands with no long alkyl chains, and iron(II) complexes

6.5.1 L19 - 2-(1H-pyrazol-1-yl)-6-(1H-1,2,3-triazol-1-yl)pyridine



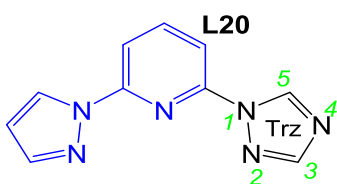
2-(1H-pyrazol-1-yl)-6-(1H-1,2,3-triazol-1-yl)pyridine **L19-A** and 2-(1H-pyrazol-1-yl)-6-(2H-1,2,3-triazol-1-yl)pyridine **L19-B** were obtained using the following procedure:⁶ NaH 60% dispersion in mineral oil (392 mg, 9.807 mmol, 1.6 eq) was added into a DMF (3 ml) / THF (6 ml) solvent mixture, after which 1,2,3-triazole (635 mg, 9.194

mmol, 1.5 eq) was slowly added, and the reaction mixture was then stirred for 30 minutes. **L14** 2-fluoro-6-(1H-pyrazol-1-yl)pyridine (1 g, 6.129 mmol, 1 eq) was then added. The reaction mixture was stirred at 80°C for 3 days under a CaCl₂ tube, and monitored by TLC. After cooling to room temperature, the reaction mixture was slowly mixed with water, and the obtained white precipitated was filtered off. This was thoroughly dried in a vacuum oven, triturated in hexane, filtered off, and desiccated again, which allowed the a 1:1 mixture of two isomers as a white powder (1.118 g, 86%).

The white powder turned out to be a mixture of two isomers, which have very small difference in *r_f* on TLC (ethyl acetate:hexane, 2:1). After two recrystallizations from hexane:chloroform 1:1 mixture, a 1:3 mixture of isomers was obtained from the original 1:1 mixture. The proportions were monitored by NMR integrations.

Analyses: **¹H NMR** (CDCl₃, 400.130 MHz, ppm): **L19-A**: δ 8.72 (d, 1 H, Pz H5), 8.57 (s, 1 H, Trz H5), 8.01 (m, 2 H, Py H3,5), 7.93 (m, 1 H, Py H4), 7.76 (d, 1 H, Pz H3), 6.48 (dd, 1 H, Pz H4); and **L19-B**: δ 8.53 (d, 1 H, Pz H5), 8.06 (m, 1 H, Py H4), 8.02 (m, 2 H, Py H3,5), 7.92 (s, 1 H, Trz H4,5), 7.78 (d, 1 H, Pz H3), 6.51 (dd, 1 H, Pz H4), **MS** (HR-ESI) *m/z*: calc. for [C₁₀H₈N₆+H⁺]: 213.0883, found: 213.1011, calc. for [C₁₀H₈N₆+Na⁺]: 235.0703, found: 235.0846.

6.5.2 L20 - 2-(1H-pyrazol-1-yl)-6-(1H-1,2,4-triazol-1-yl)pyridine

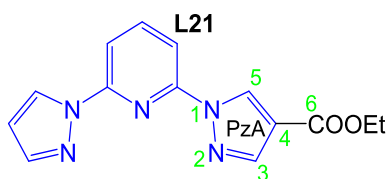


2-(1H-pyrazol-1-yl)-6-(1H-1,2,4-triazol-1-yl)pyridine **L20** was obtained using the same procedure as for **L19**, using the following quantities: NaH 60% dispersion in mineral oil (392 mg, 9.807 mmol, 1.6 eq), in DMF (3 ml), THF (6 ml), 1,2,4-triazole (635 mg, 9.194 mmol, 1.5 eq), and **L14** 2-fluoro-6-(1H-

pyrazol-1-yl)pyridine (1 g, 6.129 mmol, 1 eq), which afforded the target product as white powder (1.237 g, 95%).

Analyses: $^1\text{H NMR}$ (CDCl_3 , 400.130 MHz, ppm): δ 9.16 (s, 1 H, Trz H5), 8.55 (d, 1 H, Pz H5), 8.12 (s, 1 H, Trz H3), 8.01 (d, 1 H, Py H5), 7.99 (d, 1 H, Py H3), 7.78 (dt, 1 H, Pz H3), 7.77 (m, 1 H, Py H4), 6.52 (t, 1 H, Pz H4), $^{13}\text{C NMR}$ (CDCl_3 , 100.613 MHz, ppm): δ 153.20 (Trz C3), 150.46 (Py C6), 147.90 (Py C2), 142.94 (Pz C3), 142.16 (Trz C5), 141.59 (Py C4), 127.23 (Pz C5), 111.49 (Py C5), 110.05 (Py C3), 108.59 (Pz C4), **MS** (HR-ESI) m/z : calc. for $[\text{C}_{10}\text{H}_8\text{N}_6+\text{H}^+]$: 213.0883, found: 213.1019, calc. for $[\text{C}_{10}\text{H}_8\text{N}_6+\text{Na}^+]$: 235.0703, found: 235.0852, **IR** (cm^{-1}): 2922 (Py-H⁺), 1608, 1582 (Py C=C in plane vibr.), 1470 (Py ring 2-subst.), 1391 (C=N in-plane vibr.), **MP**: 163.3-164.0, **CHN**: calculated for $\text{C}_{10}\text{H}_8\text{N}_6$: C 56.60, H 3.80, N 39.60%, found: C 56.78, H 3.85, N 39.41%.

6.5.3 L21 - 2-(4-(ethylcarboxy)pyrazol-1-yl)-6-(1H-pyrazol-1-yl)pyridine

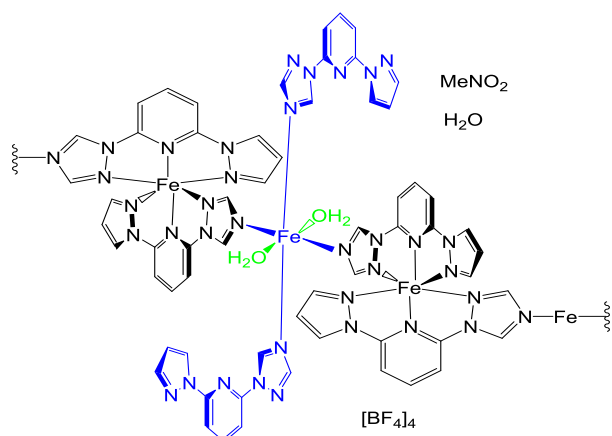


2-(4-(ethylcarboxy)pyrazol-1-yl)-6-(1H-pyrazol-1-yl)pyridine **L21** was obtained using the same procedure as for **L19**, with the following quantities: NaH 60% dispersion in mineral oil

(219 mg, 5.463 mmol, 1.1 eq), in DMF (2 ml), THF (5 ml), 4-(ethylcarboxy)pyrazole (731 mg, 5.215 mmol, 1.05 eq), and **L14** 2-fluoro-6-(1H-pyrazol-1-yl)pyridine (810 mg, 4.966 mmol, 1 eq), which afforded the target product as white powder (752 mg, 53%).

Analyses: $^1\text{H NMR}$ (CDCl_3 , 400.130 MHz, ppm): δ 9.00 (s, 1 H, PzA H5), 8.59 (d, 1 H, PzB H5), 8.11 (s, 1 H, PzA H3), 7.96 (dd, 1 H, Py H4), 7.93 (d, 1 H, Py H3), 7.87 (d, 1 H, Py H5), 7.77 (s, 1 H, PzB H3), 6.51 (t, 1 H, Pz H4), 4.38 (dd, 2 H, Ak H1), 1.25 (t, 3 H, Ak H2), $^{13}\text{C NMR}$ (CDCl_3 , 100.613 MHz, ppm): δ 162.85 (PzA C6), 150.36 (Py C6), 149.36 (Py C2), 143.19 (Pz A3), 142.77 (PzB C3), 141.79 (Py C4), 130.18 (PzA C5), 127.28 (PzB C5), 117.31 (PzA C4), 110.71 (Py C3), 109.88 (Py C5), 108.40 (PzB C4), 60.74 (Ak C1), 14.55 (Ak C2), **IR** (cm^{-1}): 2959, 2902 ($\text{CH}_2\text{-H}$), 1709 (ArC=O) 1607, 1584 (Py C=C in plane vibr.), 1472 (Py ring), 1247 (C-OC stretch), 762 (C-O-C deform.), **MP**: 123.2-123.4.

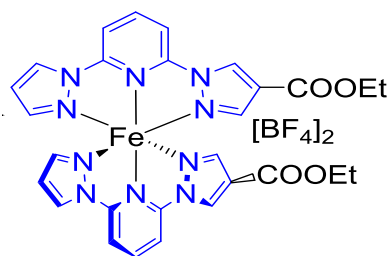
6.5.4 [Fe(L20)₂][Fe(L20)₂(H₂O)₂][BF₄]₄·MeNO₂·H₂O



The coordination polymer [Fe(L20)₂][Fe(L20)₂(H₂O)₂][BF₄]₄·MeNO₂·H₂O was obtained using the same procedure as for other iron complexes in previous chapter. **L20** 2-(1H-pyrazol-1-yl)-6-(1H-1,2,4-triazol-1-yl)pyridine (125 mg, 0.58 mmol, 2 eq) was dissolved in MeNO₂ and filtered through a cotton

pipette filter. Fe(BF₄)₂·6H₂O (99.5 mg, 0.295 mmol, 1 eq.) was also dissolved in MeNO₂ and filtered. The two solutions were mixed and the resulted yellow solution was set to form crystals by slow diisopropyl ether diffusion. The target product was obtained as clusters of pale-yellow prismatic crystals.

6.5.5 [Fe(L21)₂][BF₄]₂



2,6-di[4-(ethylcarboxy)pyrazol-1-yl]pyridine **L20** (200 mg, 0.706 mmol, 2 eq.) was dissolved in acetone (5 ml), and Fe(BF₄)₂·H₂O (133.3 mg, 0.353 mmol, 1 eq.) was also dissolved in acetone. The two solutions were mixed and left to form crystals under slow diethyl ether

diffusion, and after three days clusters of dark-yellow needle crystals (138 mg, 49%) were obtained.

Analyses: **paramagnetic NMR** (MeCN-D₃, 300 MHz, ppm): δ 64.31, 58.96 (1 H PzA H3 and 1 H PzB H3), 56.53 (1 H, PzB H4), 46.98, 43.23 (1 H PzA H5 and 1H PzB H5), 37.36, 26.20 (1 H, Py H3 and 1 H, Py H5), 1.11 (Py H4), **IR** (cm⁻¹): 3125 (Py N-Fe), 1715 (C=O), 1621, 1562 (Py C=C), 1478 (Py ring substituted), 1259 (COO-C), 1016, 763 (B-F).

List of References

1. Sheldrick, G. M. SHELXT - Integrated space-group and crystal-structure determination. *Acta Cryst.* **2015**, *A71*, 3-8.
2. Barbour, L. J. X-Seed—A Software Tool for Supramolecular Crystallography. *J. Supramol. Chem.* **2001**, *1*, 189-191.
3. Beierlein, C.H. and Breit, B. Online Monitoring of Hydroformylation Intermediates by ESI-MS. *Organometallics.* **2010**, *29*, 2521–2532.
4. Kershaw Cook, L. J. PhD thesis, University of Leeds, **2014**.
5. Vermonden, T.; Branowska, D.; Marcelis, A.T.M. and Sudhölter, E.J.R. Synthesis of 4-functionalized terdentate pyridine-based ligands. *Tetrahedron.* **2003**, *59*, 5039–5045.
6. Borisov, A. V.; Korel'chuk, M. V.; Ageeva, E. S.; Galanin, N. E. and Shaposhnikov, G. P. Synthesis and spectral properties of lutetium complexes with unsymmetrical phthalocyanines and sandwich complexes based thereon containing tetraanthraquinono-porphyrine fragments. *Russ. J. Org. Chem.* **2014**, *50*, 986-992.
7. Pritchard, R.; Lazar, H.; Barrett, S.A.; Kilner, C.A.; Asthana, S.; Carbonera, C.; Letard, J.F. and Halcrow, M.A. Thermal and light-induced spin-transitions in iron(II) complexes of 2,6-bis(4-halopyrazolyl)pyridines: the influence of polymorphism on a spin-crossover compound. *Dalton Trans.* **2009**, 6656-6666.
8. Basak, S.; Hui, P.; Boodida, S. and Chandrasekar, R. Micropatterning of Metallopolymers: Syntheses of Back-to-Back Coupled Octylated 2,6-Bis(pyrazolyl)pyridine Ligands and Their Solution-Processable Coordination Polymers. *J. Org. Chem.* **2012**, *77*, 3620-3626.

Appendix A

Crystallographic Tables

	L2	L3	L4	L6
Empirical formula	C ₁₂ H ₉ N ₅ O ₂	C ₂₀ H ₁₇ N ₅ O ₄	C ₁₉ H ₁₅ N ₅ O ₃	C ₁₈ H ₁₃ N ₅ O ₃
Formula weight	255.24	391.39	361.36	347.33
Temperature/K	275.56(10)	120.00(10)	119.99(10)	119.98(13)
Crystal system	orthorhombic	monoclinic	orthorhombic	orthorhombic
Space group	Pna2 ₁	P2 ₁ /c	Pna2 ₁	Pbca
a/Å	26.8599(13)	11.9677(2)	37.3393(10)	20.3048(5)
b/Å	10.9972(5)	20.7834(4)	11.6145(3)	7.14047(18)
c/Å	3.8386(2)	7.31376(14)	3.94390(10)	21.6604(5)
α/°	90	90	90	90
β/°	90	90.8996(17)	90	90
γ/°	90	90	90	90
Volume/Å ³	1133.86(10)	1818.93(6)	1710.38(8)	3140.45(13)
Z	4	4	4	8
D _{calc} /gcm ⁻³	1.495	1.429	1.403	1.469
μ/mm ⁻¹	0.902	0.855	0.817	0.867
F(000)	528.0	816.0	752.0	1440.0
Crystal size/mm ³	0.5501 × 0.0721 × 0.0300	0.475 × 0.077 × 0.06	0.607 × 0.101 × 0.067	0.744 × 0.131 × 0.105
Radiation λ/Å*	1.54184	1.54184	1.54184	1.54184
2θ range for data collection/°	6.582 to 134.052	7.388 to 147.696	7.972 to 147.96	8.164 to 148.12
Index ranges	-28 ≤ h ≤ 32, -13 ≤ k ≤ 13, -4 ≤ l ≤ 3	-14 ≤ h ≤ 13, -25 ≤ k ≤ 25, -8 ≤ l ≤ 5	-46 ≤ h ≤ 44, -14 ≤ k ≤ 10, -3 ≤ l ≤ 4	-25 ≤ h ≤ 23, -8 ≤ k ≤ 5, -26 ≤ l ≤ 25
Reflections collected	3505	7444	5988	11703
Independent reflections	1532 [R _{int} = 0.0341, R _σ = 0.0402]	3524 [R _{int} = 0.0256, R _σ = 0.0317]	2649 [R _{int} = 0.0529, R _σ = 0.0448]	3164 [R _{int} = 0.0342, R _σ = 0.0261]
Data/restraints/parameters	1532/1/173	3524/0/264	2649/1/245	3164/0/236
Goodness-of-fit on F ²	1.052	1.087	1.058	1.106
Final R indexes [I ≥ 2σ (I)]	R ₁ = 0.0387, wR ₂ = 0.0909	R ₁ = 0.0439, wR ₂ = 0.1373	R ₁ = 0.0516, wR ₂ = 0.1391	R ₁ = 0.0567, wR ₂ = 0.1717
Final R indexes [all data]	R ₁ = 0.0461, wR ₂ = 0.0948	R ₁ = 0.0519, wR ₂ = 0.1464	R ₁ = 0.0561, wR ₂ = 0.1427	R ₁ = 0.0656, wR ₂ = 0.1815
Largest diff. peak/hole / e Å ⁻³	0.18/-0.17	0.29/-0.20	0.33/-0.23	0.39/-0.40
Flack parameter	-0.6(4)	-	0.0(4)	-

* For **Cu** K_α, λ = 1.54184 Å; for **Mo** K_α, λ = 0.7107 Å; and for **synchrotron** radiation from Diamond Light Source λ = 0.6889 Å.

	L8-0.5MeCN	L9	L10	L7
Empirical formula	C ₂₂ H _{20.5} N _{5.5} O ₄	C ₂₀ H ₁₇ N ₅ O ₃	C ₁₉ H ₁₆ N ₅ O ₂	C ₃₀ H ₂₂ N ₁₀ O ₄
Formula weight	425.94	375.39	346.37	586.57
Temperature/K	293(2)	293(2)	293(2)	293(2)
Crystal system	monoclinic	orthorhombic	monoclinic	monoclinic
Space group	P2 ₁ /c	Pbca	Pc	P2 ₁ /n
a/Å	8.08190(10)	42.4145(3)	7.28330(10)	3.9643(4)
b/Å	65.5476(5)	11.44430(10)	7.72900(10)	32.442(3)
c/Å	7.60180(10)	7.20810(10)	29.9811(5)	10.7216(10)
α/°	90	90	90	90
β/°	91.0710(10)	90	92.9240(10)	92.221(8)
γ/°	90	90	90	90
Volume/Å ³	4026.34(8)	3498.84(6)	1685.52(4)	1377.9(2)
Z	8	8	4	2
D _{calc} /gcm ⁻³	1.405	1.425	1.365	1.414
μ/mm ⁻¹	0.094	0.094	0.087	0.821
F(000)	1784.0	1568.0	724.0	608.0
Crystal size/mm ³	300 × 20 × 180	0.14 × 0.04 × 0.02	0.14 × 0.09 × 0.01	0.19 × 0.07 × 0.02
Radiation λ/Å*	0.6889	0.6889	0.6889	1.54184
2θ range for data collection/°	1.204 to 71.944	1.862 to 71.838	2.636 to 71.734	8.692 to 124.792
Index ranges	-13 ≤ h ≤ 13, -107 ≤ k ≤ 111, -12 ≤ l ≤ 12	-68 ≤ h ≤ 71, -19 ≤ k ≤ 19, -12 ≤ l ≤ 12	-12 ≤ h ≤ 11, -13 ≤ k ≤ 13, -49 ≤ l ≤ 49	-4 ≤ h ≤ 3, -37 ≤ k ≤ 35, -12 ≤ l ≤ 11
Reflections collected	85158	69203	34739	8165
Independent reflections	19461 [R _{int} = 0.0660, R _σ = 0.0645]	8639 [R _{int} = 0.1162, R _σ = 0.0591]	15305 [R _{int} = 0.0962, R _σ = 0.1200]	2168 [R _{int} = 0.0812, R _σ = 0.0758]
Data/restraints/parameters	19461/0/573	8639/0/254	15305/2/469	2168/0/199
Goodness-of-fit on F ²	1.019	1.008	1.012	1.372
Final R indexes [I ≥ 2σ (I)]	R ₁ = 0.0704, wR ₂ = 0.1800	R ₁ = 0.0531, wR ₂ = 0.1544	R ₁ = 0.0694, wR ₂ = 0.1729	R ₁ = 0.1301, wR ₂ = 0.3628
Final R indexes [all data]	R ₁ = 0.0918, wR ₂ = 0.1864	R ₁ = 0.0688, wR ₂ = 0.1614	R ₁ = 0.1096, wR ₂ = 0.1895	R ₁ = 0.1737, wR ₂ = 0.3939
Largest diff. peak/hole / e Å ⁻³	0.61/-0.43	0.61/-0.30	0.47/-0.43	1.67/-0.51
Flack parameter	-	-	0.1(7)	-

* For **Cu** K_α, λ = 1.54184 Å; for **Mo** K_α, λ = 0.7107 Å; and for **synchrotron** radiation from Diamond Light Source λ = 0.6889 Å.

	[Fe(L3) ₂][BF ₄] ₂ ·2MeNO ₂ Red polymorph	[Fe(L3) ₂][BF ₄] ₂ ·2MeNO ₂ Yellow polymorph
Empirical formula	C ₄₂ H ₄₀ B ₂ F ₈ FeN ₁₂ O ₁₂	
Formula weight	1134.33	1106.89
Temperature/K	120.1(4)	290.00(10)
Crystal system	triclinic	triclinic
Space group	P-1	P-1
a/Å	8.32214(15)	8.3954(3)
b/Å	12.8301(2)	13.0340(3)
c/Å	23.1768(6)	23.1820(6)
α/°	88.1141(17)	88.817(2)
β/°	80.2771(19)	80.405(2)
γ/°	89.5667(14)	89.361(2)
Volume/Å ³	2437.80(9)	2500.62(12)
Z	2	2
D _{calc} /gcm ⁻³	1.545	1.470
μ/mm ⁻¹	3.412	3.299
F(000)	1160.0	1128.0
Crystal size/mm ³	0.2303 × 0.16 × 0.0973	0.2608 × 0.1415 × 0.0806
Radiation λ/Å*	1.54184	1.54184
2θ range for data collection/°	7.744 to 148.714	6.784 to 147.558°
Index ranges	-10 ≤ h ≤ 10, -16 ≤ k ≤ 15, -28 ≤ l ≤ 28	-9 ≤ h ≤ 10, -16 ≤ k ≤ 14, -28 ≤ l ≤ 28
Reflections collected	42425	22937
Independent reflections	9493 [R _{int} = 0.0340, R _σ = 0.0273]	9469 [R(int) = 0.0250]
Data/restraints /parameters	9493/0/700	9469/115/719
Goodness-of-fit on F ²	1.079	1.033
Final R indexes [I ≥ 2σ (I)]	R ₁ = 0.0454, wR ₂ = 0.1232	R ₁ = 0.0492, wR ₂ = 0.1458
Final R indexes [all data]	R ₁ = 0.0470, wR ₂ = 0.1246	R ₁ = 0.0537, wR ₂ = 0.1513
Largest diff. peak/hole / e Å ⁻³	1.03/-0.92	0.61/-0.39
Flack parameter	-	-

* For **Cu** K_α, λ = 1.54184 Å; for **Mo** K_α, λ = 0.7107 Å; and for **synchrotron** radiation from Diamond Light Source λ = 0.6889 Å.

	[Fe(L3) ₂][BF ₄] ₂ ·2MeCN·3H ₂ O	[Fe(L3) ₂][BF ₄] ₂ ·2MeCN	[Fe(L3) ₂][BF ₄] ₂ ·Me ₂ CO·2Et ₂ O
Empirical formula	C ₄₄ H ₄₇ B ₂ F ₈ FeN ₁₂ O ₁₁	C ₄₄ H ₄₁ B ₂ F ₈ FeN ₁₂ O ₈	C ₄₇ H ₅₁ B ₂ F ₈ FeN ₁₀ O ₁₀
Formula weight	1149.40	1074.83	1145.44
Temperature/K	120.4(9)	300.01(10)	120.4(9)
Crystal system	triclinic	triclinic	triclinic
Space group	P-1	P-1	P-1
a/Å	11.8763(5)	12.0097(11)	11.4869(3)
b/Å	13.7050(6)	13.5397(8)	13.1875(4)
c/Å	16.5211(7)	16.3744(14)	19.8174(8)
α/°	81.690(4)	81.295(6)	103.178(3)
β/°	86.566(4)	84.017(7)	99.818(3)
γ/°	67.594(4)	70.585(7)	97.119(2)
Volume/Å ³	2459.9(2)	2478.1(4)	2838.37(17)
Z	2	2	2
D _{calc} /gcm ⁻³	1.552	1.440	1.340
μ/mm ⁻¹	3.372	3.259	2.896
F(000)	1182.0	1100.0	1182.0
Crystal size/mm ³	0.1081 × 0.0873 × 0.0504	0.183 × 0.0919 × 0.0633	0.639 × 0.199 × 0.104
Radiation λ/Å*	1.54184	1.54184	1.54184
2θ range for data collection/°	7.038 to 147.484	6.976 to 112.332	7.352 to 147.934
Index ranges	-12 ≤ h ≤ 14, -15 ≤ k ≤ 17, -20 ≤ l ≤ 20	-10 ≤ h ≤ 12, -13 ≤ k ≤ 14, -15 ≤ l ≤ 17	-14 ≤ h ≤ 14, -12 ≤ k ≤ 15, -24 ≤ l ≤ 24
Reflections collected	18471	12783	39100
Independent reflections	9264 [R _{int} = 0.0409, R _σ = 0.0524]	6158 [R _{int} = 0.0761, R _σ = 0.0946]	10915 [R _{int} = 0.0364, R _σ = 0.0305]
Data/restraints /parameters	9264/0/718	6158/0/682	10915/0/766
Goodness-of-fit on F ²	1.034	1.019	1.073
Final R indexes [I ≥ 2σ (I)]	R ₁ = 0.0657, wR ₂ = 0.1757	R ₁ = 0.0972, wR ₂ = 0.2603	R ₁ = 0.0812, wR ₂ = 0.2435
Final R indexes [all data]	R ₁ = 0.0789, wR ₂ = 0.1902	R ₁ = 0.1643, wR ₂ = 0.3193	R ₁ = 0.0855, wR ₂ = 0.2476
Largest diff. peak/hole / e Å ⁻³	1.00/-0.53	0.55/-0.45	1.44/-1.19
Flack parameter	-	-	-

* For **Cu** K_α, λ = 1.54184 Å; for **Mo** K_α, λ = 0.7107 Å; and for **synchrotron** radiation from Diamond Light Source λ = 0.6889 Å.

	[Fe(L4) ₂][BF ₄] ₂	[Fe(L5) ₂][BF ₄] ₂	
Empirical formula	C ₃₈ H ₃₀ B ₂ F ₈ FeN ₁₀ O ₆	C ₃₈ H ₃₀ B ₂ F ₈ FeN ₁₀ O ₆	C ₃₆ H ₂₅ B ₂ F ₈ FeN ₁₀ O ₈
Formula weight	952.19	952.19	955.13
Temperature/K	120.0(3)	293(2)	120.1(4)
Crystal system	monoclinic	monoclinic	triclinic
Space group	I2/a	I2/a	P-1
a/Å	27.5349(8)	35.3876(9)	8.6669(3)
b/Å	8.3035(2)	8.3029(2)	16.8340(6)
c/Å	35.3908(7)	27.5431(11)	27.0836(10)
α/°	90	90	85.116(3)
β/°	99.537(2)	99.546(3)	82.527(3)
γ/°	90	90	87.474(3)
Volume/Å ³	7979.8(3)	7980.6(4)	3901.5(2)
Z	8	8	4
D _{calc} /gcm ⁻³	1.585	1.585	1.626
μ/mm ⁻¹	3.916	3.915	4.048
F(000)	3872.0	3872.0	1932.0
Crystal size/mm ³	0.295 × 0.026 × 0.02	0.291 × 0.089 × 0.041	0.25 × 0.028 × 0.019
Radiation λ/Å*	1.54184	1.54184	1.54184
2θ range for data collection/°	6.51 to 147.628	6.508 to 147.606	5.992 to 149.102
Index ranges	-28 ≤ h ≤ 33, -10 ≤ k ≤ 9, -43 ≤ l ≤ 42	-43 ≤ h ≤ 42, -9 ≤ k ≤ 10, -28 ≤ l ≤ 33	-10 ≤ h ≤ 10, -21 ≤ k ≤ 21, -29 ≤ l ≤ 33
Reflections collected	17646	17633	59588
Independent reflections	7630 [R _{int} = 0.0349, R _σ = 0.0462]	7631 [R _{int} = 0.0377, R _σ = 0.0501]	15162 [R _{int} = 0.0738, R _σ = 0.0609]
Data/restraints /parameters	7630/68/629	7631/0/626	15162/199/1261
Goodness-of-fit on F ²	1.026	1.011	1.014
Final R indexes [I ≥ 2σ (I)]	R ₁ = 0.0560, wR ₂ = 0.1388	R ₁ = 0.0479, wR ₂ = 0.1088	R ₁ = 0.0726, wR ₂ = 0.1938
Final R indexes [all data]	R ₁ = 0.0731, wR ₂ = 0.1509	R ₁ = 0.0656, wR ₂ = 0.1196	R ₁ = 0.1025, wR ₂ = 0.2202
Largest diff. peak/hole / e Å ⁻³	1.67/-1.34	0.86/-0.48	1.21/-0.51
Flack parameter	-	-	-

* For **Cu** K_α, λ = 1.54184 Å; for **Mo** K_α, λ = 0.7107 Å; and for **synchrotron** radiation from Diamond Light Source λ = 0.6889 Å.

	[Fe(L6) ₂][BF ₄] ₂ ·Me ₂ CO	[Fe(L6) ₂][BF ₄] ₂ ·MeCN	[Fe(L6) ₂][BF ₄] ₂
Empirical formula	C ₃₉ H ₃₂ B ₂ F ₈ FeN ₁₀ O ₇	C ₃₈ H ₂₉ B ₂ F ₈ FeN ₁₁ O ₆	C ₃₆ H ₂₆ B ₂ F ₈ FeN ₁₀ O ₆
Formula weight	982.21	965.19	924.14
Temperature/K	120.00(13)	120.00(13)	121(1)
Crystal system	monoclinic	triclinic	triclinic
Space group	P2 ₁ /c	P-1	P-1
a/Å	8.0143(5)	13.5568(3)	9.0387(6)
b/Å	16.4857(9)	17.3525(5)	12.6099(7)
c/Å	33.9358(12)	17.6675(6)	17.0032(6)
α/°	90	84.906(3)	77.368(4)
β/°	90.566(4)	82.515(2)	85.039(4)
γ/°	90	78.283(2)	83.273(5)
Volume/Å ³	4483.4(4)	4026.6(2)	1874.34(18)
Z	4	4	2
D _{calc} /gcm ⁻³	1.455	1.592	1.637
μ/mm ⁻¹	3.520	3.897	4.148
F(000)	2000.0	1960.0	936.0
Crystal size/mm ³	0.128 × 0.052 × 0.029	0.83 × 0.69 × 0.215	0.14 × 0.08 × 0.05
Radiation λ/Å*	1.54184	1.54184	1.54184
2θ range for data collection/°	7.476 to 146.966	6.704 to 148.842	7.222 to 158.47°
Index ranges	-9 ≤ h ≤ 8, -20 ≤ k ≤ 16, -40 ≤ l ≤ 42	-16 ≤ h ≤ 16, -21 ≤ k ≤ 21, -21 ≤ l ≤ 18	-11 ≤ h ≤ 10, -15 ≤ k ≤ 14, -21 ≤ l ≤ 20
Reflections collected	20551	62738	13156
Independent reflections	8615 [R _{int} = 0.0823, R _σ = 0.1027]	15485 [R _{int} = 0.0993, R _σ = 0.0726]	7069 [R(int) = 0.0806]
Data/restraints /parameters	8615/0/608	15485/0/1195	7069/0/604
Goodness-of-fit on F ²	1.633	1.033	1.478
Final R indexes [I ≥ 2σ (I)]	R ₁ = 0.1565, wR ₂ = 0.4374	R ₁ = 0.0726, wR ₂ = 0.1768	R ₁ = 0.1171, wR ₂ = 0.3451
Final R indexes [all data]	R ₁ = 0.1874, wR ₂ = 0.4527	R ₁ = 0.0965, wR ₂ = 0.1940	R ₁ = 0.1660, wR ₂ = 0.4190
Largest diff. peak/hole / e Å ⁻³	1.58/-0.98	0.92/-1.01	1.23/-2.16
Flack parameter	-	-	-

* For **Cu** K_α, λ = 1.54184 Å; for **Mo** K_α, λ = 0.7107 Å; and for **synchrotron** radiation from Diamond Light Source λ = 0.6889 Å.

	[Fe(L6) ₂][BF ₄] ₂ ·0.5H ₂ O		
Empirical formula	C ₁₄₄ H ₁₀₈ B ₈ F ₃₂ Fe ₄ N _{39.5} O ₂₈	C ₃₆ H _{27.5} B ₂ F ₈ FeN ₁₀ O _{6.5}	C ₇₂ H ₅₅ B ₂ F ₁₇ Fe ₂ N ₂₀ O ₁₂
Formula weight	3757.57	933.65	1848.68
Temperature/K	100	250	360
Crystal system	triclinic	triclinic	triclinic
Space group	P-1	P-1	P-1
a/Å	11.9000(8)	11.9795(8)	11.950(3)
b/Å	16.6124(11)	16.8209(12)	16.952(5)
c/Å	20.8569(13)	21.0000(12)	21.191(5)
α/°	99.288(6)	99.507(6)	100.78(2)
β/°	99.125(6)	98.595(6)	97.96(2)
γ/°	100.889(6)	100.802(6)	100.51(2)
Volume/Å ³	3919.0(5)	4027.8(5)	4079.6(18)
Z	1	4	2
D _{calc} /gcm ⁻³	1.592	1.540	1.505
μ/mm ⁻¹	0.450	0.437	0.432
F(000)	1904.0	1894.0	1876.0
Crystal size/mm ³			
Radiation λ/Å*	0.6889	0.6889	0.6889
2θ range for data collection/°	2.468 to 72.558°	2.438 to 72.456°	1.928 to 40.296
Index ranges	-20 ≤ h ≤ 19, -27 ≤ k ≤ 27, -35 ≤ l ≤ 35	-20 ≤ h ≤ 20, -27 ≤ k ≤ 28, -35 ≤ l ≤ 35	-11 ≤ h ≤ 11, -16 ≤ k ≤ 16, -21 ≤ l ≤ 21
Reflections collected	84122	85877	33743
Independent reflections	35855[R(int) = 0.1366]	36744[R(int) = 0.1231]	8519 [R _{int} = 0.0964, R _σ = 0.0728]
Data/restraints/parameters	35855/0/1163	36744/0/1151	8519/0/1130
Goodness-of-fit on F ²	0.880	0.902	1.115
Final R indexes [I ≥ 2σ(I)]	R ₁ = 0.1199, wR ₂ = 0.2915	R ₁ = 0.1219, wR ₂ = 0.3119	R ₁ = 0.0991, wR ₂ = 0.2757
Final R indexes [all data]	R ₁ = 0.2558, wR ₂ = 0.3795	R ₁ = 0.2846, wR ₂ = 0.4116	R ₁ = 0.1356, wR ₂ = 0.3163
Largest diff. peak/hole / e Å ⁻³	3.79/-0.80	2.73/-0.54	1.05/-0.30
Flack parameter	-	-	-

* For **Cu** K_α, λ = 1.54184 Å; for **Mo** K_α, λ = 0.7107 Å; and for **synchrotron** radiation from Diamond Light Source λ = 0.6889 Å.

	[Fe(L8) ₂][BF ₄] ₂ ·0.25MeCN	[Fe(L8) ₂][BF ₄] ₂ ·Me ₂ CO·0.25H ₂ O	[Fe(L9) ₂][BF ₄] ₂ ·1.5MeCN	[Fe(L9) ₂][BF ₄] ₂ ·0.5Me ₂ CO
Empirical formula	C ₄₂ H _{38.75} B ₂ F ₈ FeN _{10.25} O ₈	C ₄₅ H _{44.5} B ₂ F ₈ Fe N ₁₀ O _{9.25}	C ₄₃ H _{38.75} B ₂ F ₈ FeN _{11.5} O ₆	C _{41.5} H _{32.5} B ₂ F ₈ FeN ₁₀ O _{6.5}
Formula weight	1044.55	1102.87	1042.07	1004.74
Temperature/K	150.00(10)	119.99(13)	150.01(10)	120.2(5)
Crystal system	orthorhombic	orthorhombic	monoclinic	orthorhombic
Space group	Pna2 ₁	Pna2 ₁	P2 ₁ /c	Pca2 ₁
a/Å	16.1146(5)	16.1790(10)	27.4401(4)	20.7502(16)
b/Å	21.2398(8)	21.1621(11)	16.5615(3)	15.444(3)
c/Å	28.5755(10)	28.8196(8)	20.5281(2)	28.842(7)
α/°	90	90	90	90
β/°	90	90	100.2570(10)	90
γ/°	90	90	90	90
Volume/Å ³	9780.6(6)	9867.3(8)	9179.9(2)	9243(3)
Z	8	8	8	8
D _{calc} /gcm ⁻³	1.419	1.485	1.508	1.444
μ/mm ⁻¹	0.399	3.298	3.466	3.421
F(000)	4276.0	4532.0	4266.0	4092.0
Crystal size/mm ³	0.453 × 0.283 × 0.198	0.156 × 0.067 × 0.065	1.006 × 0.316 × 0.202	
Radiation λ/Å*	0.71073	1.54184	1.54184	1.54184
2θ range for data collection/°	6.874 to 59.436	6.878 to 147.934	7.298 to 149.53	7.136 to 150.934
Index ranges	-17 ≤ h ≤ 21, -20 ≤ k ≤ 29, -35 ≤ l ≤ 36	-19 ≤ h ≤ 16, - 26 ≤ k ≤ 25, - 35 ≤ l ≤ 35	-34 ≤ h ≤ 34, -18 ≤ k ≤ 15, -25 ≤ l ≤ 25	-25 ≤ h ≤ 16, -18 ≤ k ≤ 12, -31 ≤ l ≤ 31
Reflections collected	39370	42450	77067	21769
Independent reflections	19974 [R _{int} = 0.0316, R _σ = 0.0537]	16737 [R _{int} = 0.1478, R _σ = 0.1585]	17912 [R _{int} = 0.0514, R _σ = 0.0428]	12614[R(int) = 0.1603]
Data/restraints/parameters	19974/1/131 5	16737/1/1378	17912/0/132 2	12614/1/128 7
Goodness-of-fit on F ²	1.074	1.018	1.043	1.003
Final R indexes [I ≥ 2σ(I)]	R ₁ = 0.0887, wR ₂ = 0.2313	R ₁ = 0.0935, wR ₂ = 0.2141	R ₁ = 0.0710, wR ₂ = 0.1901	R ₁ = 0.1027, wR ₂ = 0.2232
Final R indexes [all data]	R ₁ = 0.1160, wR ₂ = 0.2524	R ₁ = 0.1663, wR ₂ = 0.2677	R ₁ = 0.0804, wR ₂ = 0.1977	R ₁ = 0.2260, wR ₂ = 0.2906
Largest diff. peak/hole / e Å ⁻³	0.76/-0.47	0.77/-0.76	0.96/-0.56	0.69/-0.51
Flack parameter	0.284(6)	0.396(7)	-	0.062(15)

* For **Cu** K_α, λ = 1.54184 Å; for **Mo** K_α, λ = 0.7107 Å; and for **synchrotron** radiation from Diamond Light Source λ = 0.6889 Å.

	[Fe(L10) ₂][BF ₄] ₂ ·1.5 MeCN	[Fe(L10) ₂][BF ₄] ₂ · ² / ₃ Me ₂ CO	DCC intermediate
Empirical formula	C ₄₁ H _{34.5} B ₂ F ₈ FeN _{11.5} O ₄	B _{1.666667} C _{38.166667} F _{6.666667} FeN ₁₀ O _{5.333333} H _{0.083333}	C ₂₂ H ₂₈ BrN ₅ O ₂
Formula weight	981.77	884.43	474.40
Temperature/K	150.01(10)	120.3(7)	120.0(2)
Crystal system	triclinic	monoclinic	monoclinic
Space group	P-1	P2 ₁ /c	P2 ₁ /n
a/Å	13.8965(6)	14.6653(5)	11.7221(9)
b/Å	17.0836(7)	46.894(2)	9.7208(7)
c/Å	20.8001(7)	20.7067(6)	19.502(3)
α/°	95.020(3)	90	90
β/°	102.703(3)	105.985(3)	92.979(10)
γ/°	113.133(4)	90	90
Volume/Å ³	4345.8(3)	13689.7(9)	2219.2(4)
Z	4	12	4
D _{calc} /gcm ⁻³	1.501	1.287	1.420
μ/mm ⁻¹	0.438	3.346	2.752
F(000)	2004.0	5233.0	984.0
Crystal size/mm ³	0.838 × 0.421 × 0.298	0.22 × 0.09 × 0.05	0.34 × 0.06 × 0.04
Radiation λ/Å*	0.71073	1.54184	1.54184
2θ range for data collection/°	6.456 to 59.394	7.19 to 147.028°	8.608 to 146.98
Index ranges	-19 ≤ h ≤ 19, -17 ≤ k ≤ 21, -27 ≤ l ≤ 27	-13 ≤ h ≤ 18, -47 ≤ k ≤ 57, -25 ≤ l ≤ 21	-14 ≤ h ≤ 13, -11 ≤ k ≤ 8, -21 ≤ l ≤ 23
Reflections collected	46531	56114	8398
Independent reflections	20799 [R _{int} = 0.0369, R _σ = 0.0658]	26692 [R(int) = 0.1034]	4326 [R _{int} = 0.0944, R _σ = 0.1249]
Data/restraints/parameters	20799/0/1219	26692/0/1701	4326/0/271
Goodness-of-fit on F ²	1.037	1.655	1.109
Final R indexes [I >= 2σ (I)]	R ₁ = 0.0700, wR ₂ = 0.1622	R ₁ = 0.1490, wR ₂ = 0.3503	R ₁ = 0.1041, wR ₂ = 0.2754
Final R indexes [all data]	R ₁ = 0.1101, wR ₂ = 0.1865	R ₁ = 0.2367, wR ₂ = 0.3924	R ₁ = 0.1355, wR ₂ = 0.2956
Largest diff. peak/hole / e Å ⁻³	1.02/-0.49	4.57/-0.68	2.17/-1.49
Flack parameter	-	-	-

* For **Cu** K_α, λ = 1.54184 Å; for **Mo** K_α, λ = 0.7107 Å; and for **synchrotron** radiation from Diamond Light Source λ = 0.6889 Å.

	L11C12	L11C14	L12C12	L12C14
Empirical formula	C ₂₄ H ₃₄ N ₅ O ₂	C ₂₆ H ₃₇ N ₅ O ₂	C ₁₈ H ₃₀ O ₂	C ₂₀ H ₃₄ O ₂
Formula weight	424.56	451.60	278.42	172.20
Temperature/K	119.97(17)	120.0(2)	120.00(11)	119.97(15)
Crystal system	orthorhombic	orthorhombic	triclinic	triclinic
Space group	P2 ₁ 2 ₁ 2 ₁	P2 ₁ 2 ₁ 2 ₁	P-1	P-1
a/Å	4.8145(2)	4.8622(4)	5.4266(2)	5.4604(11)
b/Å	8.9592(9)	8.9415(12)	7.2027(2)	7.2025(14)
c/Å	53.565(2)	57.636(6)	42.2414(14)	46.898(5)
α/°	90	90	88.093(3)	91.733(14)
β/°	90	90	86.332(3)	90.505(14)
γ/°	90	90	89.637(3)	90.417(16)
Volume/Å ³	2310.5(3)	2505.8(5)	1646.75(9)	1843.5(6)
Z	4	4	4	4
D _{calc} /gcm ⁻³	1.221	1.197	1.123	1.241
μ/mm ⁻¹	0.632	0.612	0.071	0.639
F(000)	916.0	976.0	616.0	728.0
Crystal size/mm ³	0.0836 × 0.0626 × 0.0518	0.25 × 0.07 × 0.03	0.467 × 0.381 × 0.113	0.1312 × 0.0618 × 0.0482
Radiation λ/Å*	1.54184	1.54184	0.71073	1.54184
2θ range for data collection/°	6.6 to 134.146	6.134 to 145.502	6.75 to 57.51	7.544 to 152.632
Index ranges	-5 ≤ h ≤ 4, -10 ≤ k ≤ 6, -63 ≤ l ≤ 55	-5 ≤ h ≤ 5, - 10 ≤ k ≤ 11, - 68 ≤ l ≤ 71	-7 ≤ h ≤ 4, - 8 ≤ k ≤ 9, - 35 ≤ l ≤ 57	-5 ≤ h ≤ 6, - 8 ≤ k ≤ 8, - 58 ≤ l ≤ 56
Reflections collected	5413	8856	7545	13844
Independent reflections	3740 [R _{int} = 0.0686, R _σ = 0.1068]	4508 [R _{int} = 0.1396, R _σ = 0.1440]	6137 [R _{int} = 0.0162, R _σ = 0.0446]	6108 [R _{int} = 0.2165, R _σ = 0.2060]
Data/restraints/parameters	3740/0/281	4508/0/299	6137/0/371	6108/0/177
Goodness-of-fit on F ²	1.113	1.039	1.083	1.310
Final R indexes [I ≥ 2σ (I)]	R ₁ = 0.1069, wR ₂ = 0.2369	R ₁ = 0.1082, wR ₂ = 0.2721	R ₁ = 0.0794, wR ₂ = 0.1885	R ₁ = 0.1960, wR ₂ = 0.4119
Final R indexes [all data]	R ₁ = 0.1461, wR ₂ = 0.2613	R ₁ = 0.1624, wR ₂ = 0.3261	R ₁ = 0.0955, wR ₂ = 0.1980	R ₁ = 0.3419, wR ₂ = 0.5108
Largest diff. peak/hole / e Å ⁻³	0.42/-0.39	0.67/-0.36	0.33/-0.29	0.70/-0.47
Flack parameter	-0.6(9)	0.5	-	-

* For **Cu** K_α, λ = 1.54184 Å; for **Mo** K_α, λ = 0.7107 Å; and for **synchrotron** radiation from Diamond Light Source λ = 0.6889 Å.

	L13C12	L13C14	[Fe(L11C6)₂][BF₄] ·2H₂O
Empirical formula	C ₃₀ H ₃₇ N ₅ O ₃	C ₃₂ H ₄₁ N ₅ O ₃	C _{32.5} H ₃₇ B ₂ F ₈ FeN ₁₀ O ₆
Formula weight	515.64	543.70	893.19
Temperature/K	120.01(13)	293(2)	120.15
Crystal system	monoclinic	monoclinic	monoclinic
Space group	P2 ₁ /n	P2 ₁ /n	P2 ₁ /c
a/Å	4.09650(10)	4.12350(10)	17.925(3)
b/Å	64.3183(13)	68.6353(8)	15.1997(15)
c/Å	10.3525(2)	10.32150(10)	20.4944(16)
α/°	90	90	90
β/°	96.694(2)	96.8220(10)	101.974(12)
γ/°	90	90	90
Volume/Å ³	2709.08(10)	2900.48(8)	5462.2(12)
Z	4	4	4
D _{calc} /gcm ⁻³	1.264	1.245	1.086
μ/mm ⁻¹	0.664	0.077	2.824
F(000)	1104.0	1168.0	1832.0
Crystal size/mm ³	0.573 × 0.095 × 0.075	0.14 × 0.01 × 0.005	0.56 × 0.37 × 0.16
Radiation λ/Å*	1.54184	0.6889	1.54184
2θ range for data collection/°	8.248 to 148.296	1.15 to 72.082	7.298 to 149.056
Index ranges	-4 ≤ h ≤ 4, -76 ≤ k ≤ 80, -12 ≤ l ≤ 12	-7 ≤ h ≤ 6, -115 ≤ k ≤ 116, -17 ≤ l ≤ 17	-17 ≤ h ≤ 22, -15 ≤ k ≤ 18, -25 ≤ l ≤ 22
Reflections collected	17853	62461	21577
Independent reflections	5403 [R _{int} = 0.0701, R _σ = 0.0599]	14043 [R _{int} = 0.0936, R _σ = 0.0965]	10751 [R _{int} = 0.1117, R _σ = 0.1569]
Data/restraints/parameters	5403/0/344	14043/0/362	10751/31/279
Goodness-of-fit on F ²	1.114	0.894	1.654
Final R indexes [I ≥ 2σ (I)]	R ₁ = 0.1194, wR ₂ = 0.2678	R ₁ = 0.0567, wR ₂ = 0.1374	R ₁ = 0.2698, wR ₂ = 0.5751
Final R indexes [all data]	R ₁ = 0.1284, wR ₂ = 0.2714	R ₁ = 0.1076, wR ₂ = 0.1542	R ₁ = 0.3721, wR ₂ = 0.6385
Largest diff. peak/hole / e Å ⁻³	0.40/-0.39	0.39/-0.41	3.27/-1.70
Flack parameter	-	-	-

* For **Cu** K_α, λ = 1.54184 Å; for **Mo** K_α, λ = 0.7107 Å; and for **synchrotron** radiation from Diamond Light Source λ = 0.6889 Å.

	[Fe(L13C6) ₂][BF ₄] ₂ ·H ₂ O	[Fe(L13C14) ₂][BF ₄] ₂ ·2MeCN	[Fe(L13C16) ₂][BF ₄] ₂ ·H ₂ O
Empirical formula	C ₄₈ H ₅₂ B ₂ F ₈ FeN ₁₀ O ₇	C ₆₈ H ₈₈ B ₂ F ₈ FeN ₁₂ O ₆	C ₆₈ H ₉₂ B ₂ F ₈ FeN ₁₀ O ₇
Formula weight	1110.46	1398.97	1390.98
Temperature/K	119.99(14)	293(2)	120.01(10)
Crystal system	triclinic	triclinic	triclinic
Space group	P-1	P-1	P-1
a/Å	10.3105(8)	14.31590(10)	13.2899(3)
b/Å	15.1489(10)	15.21930(10)	13.6465(4)
c/Å	16.7306(8)	16.7869(2)	19.4605(6)
α/°	89.136(5)	84.0090(10)	98.865(2)
β/°	77.066(6)	89.7180(10)	91.201(2)
γ/°	82.387(6)	72.7220(10)	98.421(2)
Volume/Å ³	2524.2(3)	3472.07(6)	3446.19(17)
Z	2	2	2
D _{calc} /gcm ⁻³	1.461	1.338	1.340
μ/mm ⁻¹	3.191	0.294	0.301
F(000)	1148.0	1472.0	1468.0
Crystal size/mm ³	0.426 × 0.047 × 0.028	0.125 × 0.045 × 0.02	0.5509 × 0.3449 × 0.2437
Radiation λ/Å*	1.54184	0.6889	0.71073
2θ range for data collection/°	7.944 to 147.374	2.732 to 71.914	5.384 to 59.242
Index ranges	-12 ≤ h ≤ 8, -18 ≤ k ≤ 18, -20 ≤ l ≤ 20	-23 ≤ h ≤ 23, -24 ≤ k ≤ 25, -27 ≤ l ≤ 27	-18 ≤ h ≤ 18, -18 ≤ k ≤ 18, -27 ≤ l ≤ 26
Reflections collected	21098	74716	51002
Independent reflections	9509 [R _{int} = 0.0536, R _σ = 0.0696]	31297 [R _{int} = 0.0507, R _σ = 0.0722]	16785 [R _{int} = 0.0483, R _σ = 0.0617]
Data/restraints/parameters	9509/0/699	31297/0/878	16785/0/879
Goodness-of-fit on F ²	1.015	0.955	1.023
Final R indexes [I ≥ 2σ (I)]	R ₁ = 0.0753, wR ₂ = 0.1993	R ₁ = 0.0506, wR ₂ = 0.1313	R ₁ = 0.0531, wR ₂ = 0.1115
Final R indexes [all data]	R ₁ = 0.0947, wR ₂ = 0.2176	R ₁ = 0.0877, wR ₂ = 0.1442	R ₁ = 0.0790, wR ₂ = 0.1247
Largest diff. peak/hole / e Å ⁻³	1.08/-0.58	0.95/-0.56	0.88/-0.53
Flack parameter	-	-	-

* For **Cu** K_α, λ = 1.54184 Å; for **Mo** K_α, λ = 0.7107 Å; and for **synchrotron** radiation from Diamond Light Source λ = 0.6889 Å.

	L14	L15	L16
Empirical formula	C ₈ H ₆ FN ₃	C ₁₁ H ₇ I ₂ N ₅	C ₁₁ H ₇ IN ₅
Formula weight	163.16	463.02	336.12
Temperature/K	120.01(10)	119.98(14)	293(2)
Crystal system	orthorhombic	monoclinic	monoclinic
Space group	P2 ₁ 2 ₁ 2 ₁	C2/c	P2 ₁ /n
a/Å	4.03930(10)	33.3176(8)	16.2454(15)
b/Å	11.2187(4)	4.63510(10)	4.3868(4)
c/Å	16.2922(4)	17.8226(4)	17.3002(17)
α/°	90	90	90
β/°	90	101.956(2)	109.873(8)
γ/°	90	90	90
Volume/Å ³	738.29(4)	2692.64(11)	1159.5(2)
Z	4	8	4
D _{calc} /gcm ⁻³	1.468	2.284	1.925
μ/mm ⁻¹	0.943	36.621	2.544
F(000)	336.0	1712.0	644.0
Crystal size/mm ³	0.465 × 0.201 × 0.145	0.404 × 0.079 × 0.079	0.34 × 0.12 × 0.08
Radiation λ/Å*	1.54184	1.54184	0.6889
2θ range for data collection/°	9.572 to 147.32	10.146 to 147.966	2.882 to 72.49
Index ranges	-2 ≤ h ≤ 4, -10 ≤ k ≤ 13, -19 ≤ l ≤ 17	-40 ≤ h ≤ 40, -4 ≤ k ≤ 5, -20 ≤ l ≤ 22	-27 ≤ h ≤ 20, -7 ≤ k ≤ 6, -27 ≤ l ≤ 20
Reflections collected	1712	9566	10728
Independent reflections	1212 [R _{int} = 0.0130, R _σ = 0.0191]	2678 [R _{int} = 0.0280, R _σ = 0.0210]	4721 [R _{int} = 0.4031, R _σ = 0.9116]
Data/restraints/parameters	1212/0/109	2678/0/181	4721/0/154
Goodness-of-fit on F ²	1.092	1.064	0.741
Final R indexes [I ≥ 2σ (I)]	R ₁ = 0.0261, wR ₂ = 0.0708	R ₁ = 0.0262, wR ₂ = 0.0713	R ₁ = 0.1170, wR ₂ = 0.2254
Final R indexes [all data]	R ₁ = 0.0275, wR ₂ = 0.0721	R ₁ = 0.0297, wR ₂ = 0.0745	R ₁ = 0.4538, wR ₂ = 0.3605
Largest diff. peak/hole / e Å ⁻³	0.14/-0.13	0.95/-0.89	1.93/-1.02
Flack parameter	0.04(10)	-	-

* For **Cu** K_α, λ = 1.54184 Å; for **Mo** K_α, λ = 0.7107 Å; and for **synchrotron** radiation from Diamond Light Source λ = 0.6889 Å.

	L17C12D	L17C16D	L17C12M
Empirical formula	C ₃₅ H ₄₉ N ₅	C ₄₃ H ₆₅ N ₅	C ₂₃ H ₂₉ N ₅
Formula weight	539.79	652.00	375.51
Temperature/K	133.20(17)	150.00(10)	293(2)
Crystal system	monoclinic	monoclinic	monoclinic
Space group	Pc	Pc	P2 ₁
a/Å	5.45900(10)	5.4576(3)	5.3944(2)
b/Å	5.45440(10)	5.4477(3)	5.4384(2)
c/Å	52.5779(10)	65.309(2)	35.4153(14)
α/°	90	90	90
β/°	91.576(2)	89.041(4)	90.989(3)
γ/°	90	90	90
Volume/Å ³	1564.94(5)	1941.45(16)	1038.82(7)
Z	2	2	2
D _{calc} /gcm ⁻³	1.146	1.115	1.200
μ/mm ⁻¹	0.517	0.492	0.069
F(000)	588.0	716.0	404.0
Crystal size/mm ³	0.01 × 0.003 × 0.003	0.39 × 0.19 × 0.09	0.06 × 0.03 × 0.01
Radiation λ/Å*	1.54184	1.54184	0.6889
2θ range for data collection/°	6.728 to 148.496°	8.124 to 140.704	2.23 to 71.702
Index ranges	-6 ≤ h ≤ 5, -6 ≤ k ≤ 6, -62 ≤ l ≤ 65	-6 ≤ h ≤ 6, -6 ≤ k ≤ 5, -79 ≤ l ≤ 73	-9 ≤ h ≤ 9, -9 ≤ k ≤ 9, -57 ≤ l ≤ 59
Reflections collected	6835	8193	22143
Independent reflections	4262 [R(int) = 0.0206]	5116 [R _{int} = 0.0380, R _σ = 0.0415]	9487 [R _{int} = 0.0999, R _σ = 0.1543]
Data/restraints/parameters	4262/2/363	5116/2/435	9487/1/254
Goodness-of-fit on F ²	1.134	1.136	0.951
Final R indexes [I ≥ 2σ (I)]	R ₁ = 0.0452, wR ₂ = 0.1183	R ₁ = 0.0893, wR ₂ = 0.2239	R ₁ = 0.0979, wR ₂ = 0.2415
Final R indexes [all data]	R ₁ = 0.0463, wR ₂ = 0.1190	R ₁ = 0.0910, wR ₂ = 0.2246	R ₁ = 0.1787, wR ₂ = 0.2817
Largest diff. peak/hole / e Å ⁻³	0.23/-0.20	0.43/-0.40	0.48/-0.30
Flack parameter	-0.1(4)	0.5	-0.7(10)

* For **Cu** K_α, λ = 1.54184 Å; for **Mo** K_α, λ = 0.7107 Å; and for **synchrotron** radiation from Diamond Light Source λ = 0.6889 Å.

	L18C12M	L18C14M	[Fe(L17C18M) ₂][BF ₄] ₂
Empirical formula	C ₂₃ H ₃₃ N ₅	C ₂₅ H ₃₇ N ₅	C ₅₉ H ₈₃ B ₂ F ₈ FeN ₁₀
Formula weight	379.54	407.59	1161.82
Temperature/K	293(2)	119.97(15)	293(2)
Crystal system	triclinic	triclinic	triclinic
Space group	P-1	P-1	P-1
a/Å	5.38900(10)	5.4094(4)	10.6801(2)
b/Å	10.17380(10)	10.1832(6)	15.2720(2)
c/Å	19.2473(3)	20.8390(15)	36.8778(5)
α/°	95.5290(10)	87.346(5)	95.9150(10)
β/°	94.4050(10)	83.903(6)	98.8820(10)
γ/°	90.2580(10)	89.881(5)	89.9730(10)
Volume/Å ³	1047.18(3)	1140.19(14)	5910.51(16)
Z	2	2	4
D _{calc} /gcm ⁻³	1.204	1.187	1.306
μ/mm ⁻¹	0.069	0.550	0.304
F(000)	412.0	444.0	2460.0
Crystal size/mm ³	0.18 × 0.08 × 0.01	0.437 × 0.069 × 0.047	
Radiation λ/Å*	0.6889	1.54184	0.6889
2θ range for data collection/°	2.066 to 71.318	8.544 to 147.594	1.09 to 72.56
Index ranges	-8 ≤ h ≤ 8, -12 ≤ k ≤ 17, -32 ≤ l ≤ 32	-6 ≤ h ≤ 4, -11 ≤ k ≤ 12, -25 ≤ l ≤ 23	-16 ≤ h ≤ 17, -25 ≤ k ≤ 25, -44 ≤ l ≤ 59
Reflections collected	15704	9977	96928
Independent reflections	8473 [R _{int} = 0.0678, R _σ = 0.1196]	4286 [R _{int} = 0.0373, R _σ = 0.0409]	50251 [R _{int} = 0.0848, R _σ = 0.2469]
Data/restraints/parameters	8473/0/254	4286/0/272	50251/0/1445
Goodness-of-fit on F ²	0.976	1.054	0.827
Final R indexes [I > 2σ (I)]	R ₁ = 0.0573, wR ₂ = 0.1643	R ₁ = 0.0592, wR ₂ = 0.1664	R ₁ = 0.0966, wR ₂ = 0.2318
Final R indexes [all data]	R ₁ = 0.0875, wR ₂ = 0.2100	R ₁ = 0.0721, wR ₂ = 0.1778	R ₁ = 0.2592, wR ₂ = 0.2844
Largest diff. peak/hole / e Å ⁻³	0.53/-0.45	0.30/-0.36	1.56/-0.87
Flack parameter	-	-	-

* For **Cu** K_α, λ = 1.54184 Å; for **Mo** K_α, λ = 0.7107 Å; and for **synchrotron** radiation from Diamond Light Source λ = 0.6889 Å.

	[Fe(L18C12M) ₂] [BF ₄] ₂	[Fe(L18C16M) ₂] [BF ₄] ₂	[Fe(L18C16M) ₂][BF ₄] ₂
Empirical formula	C ₄₆ H ₆₆ B ₂ F ₈ FeN ₁₀	C ₅₄ H ₈₇ B ₂ F ₈ FeN ₁₀	C ₅₄ H ₈₂ B ₂ F ₈ FeN ₁₀
Formula weight	988.55	1105.80	1100.76
Temperature/K	293(2)	119.99(16)	150.00(10)
Crystal system	triclinic	triclinic	triclinic
Space group	P-1	P-1	P-1
a/Å	10.8827(4)	10.8707(15)	10.9510(14)
b/Å	15.2657(5)	15.1781(18)	15.0831(18)
c/Å	30.1249(11)	34.644(4)	34.713(4)
α/°	97.199(3)	83.813(10)	83.845(10)
β/°	97.707(3)	82.791(10)	82.536(10)
γ/°	90.123(3)	89.934(10)	89.868(10)
Volume/Å ³	4919.5(3)	5637.5(12)	5652.1(12)
Z	4	4	4
D _{calc} /gcm ⁻³	1.335	1.303	1.294
μ/mm ⁻¹	0.353	2.747	2.739
F(000)	2080.0	2356.0	2336.0
Crystal size/mm ³	0.07 × 0.02 × 0.005	0.374 × 0.076 × 0.042	0.36 × 0.074 × 0.038
Radiation λ/Å*	0.6889	1.54184	1.54184
2θ range for data collection/°	1.332 to 72.184	7.762 to 155.296°	7.408 to 149.32
Index ranges	-18 ≤ h ≤ 17, -25 ≤ k ≤ 25, -49 ≤ l ≤ 51	-13 ≤ h ≤ 13, -18 ≤ k ≤ 13, -38 ≤ l ≤ 42	-13 ≤ h ≤ 9, -18 ≤ k ≤ 18, -43 ≤ l ≤ 42
Reflections collected	108366	51522	49647
Independent reflections	44891 [R _{int} = 0.2684, R _σ = 0.4271]	21509[R(int) = 0.3165]	21302 [R _{int} = 0.2087, R _σ = 0.2635]
Data/restraints/parameters	44891/0/1211	21509/0/1345	21302/0/1355
Goodness-of-fit on F ²	0.736	0.956	1.017
Final R indexes [I ≥ 2σ (I)]	R ₁ = 0.0935, wR ₂ = 0.1971	R ₁ = 0.2089, wR ₂ = 0.3894	R ₁ = 0.1356, wR ₂ = 0.2986
Final R indexes [all data]	R ₁ = 0.3426, wR ₂ = 0.2910	R ₁ = 0.4108, wR ₂ = 0.5292	R ₁ = 0.3040, wR ₂ = 0.4196
Largest diff. peak/hole / e Å ⁻³	0.97/-0.66	0.75/-0.90	0.68/-0.87
Flack parameter	-	-	-

* For **Cu** K_α, λ = 1.54184 Å; for **Mo** K_α, λ = 0.7107 Å; and for **synchrotron** radiation from Diamond Light Source λ = 0.6889 Å.

	[Fe(L18C18M) ₂][BF ₄] ₂	L19	L20
Empirical formula	C ₅₉ H ₉₁ B ₂ F ₈ FeN ₁₀	C ₁₀ H ₈ N ₆	C ₁₀ H ₈ N ₆
Formula weight	1169.88	212.22	212.22
Temperature/K	293(2)	120.00(13)	150.01(10)
Crystal system	triclinic	monoclinic	monoclinic
Space group	P-1	Cc	P2 ₁ /c
a/Å	10.9192(5)	4.54380(10)	12.5794(9)
b/Å	15.1344(5)	25.9740(7)	3.8549(3)
c/Å	36.7856(17)	8.5078(2)	20.4981(14)
α/°	84.117(4)	90	90
β/°	85.034(4)	99.788(3)	103.628(7)
γ/°	89.951(3)	90	90
Volume/Å ³	6024.1(4)	989.48(4)	966.01(12)
Z	4	4	4
D _{calc} /gcm ⁻³	1.290	1.425	1.459
μ/mm ⁻¹	0.298	0.785	0.804
F(000)	2492.0	440.0	440.0
Crystal size/mm ³		0.483 × 0.122 × 0.056	0.37 × 0.074 × 0.046
Radiation λ/Å*	0.6889	1.54184	1.54184
2θ range for data collection/°	2.166 to 71.964	12.566 to 147.176	7.23 to 148.47
Index ranges	-18 ≤ h ≤ 17, -25 ≤ k ≤ 23, -60 ≤ l ≤ 45	-5 ≤ h ≤ 4, -32 ≤ k ≤ 32, -7 ≤ l ≤ 10	-15 ≤ h ≤ 15, -4 ≤ k ≤ 4, -25 ≤ l ≤ 25
Reflections collected	94542	3732	4625
Independent reflections	49978 [R _{int} = 0.2155, R _σ = 0.3853]	1315 [R _{int} = 0.0291, R _σ = 0.0300]	1948 [R _{int} = 0.0334, R _σ = 0.0388]
Data/restraints/parameters	49978/0/1435	1315/2/145	1948/0/145
Goodness-of-fit on F ²	1.045	1.092	1.159
Final R indexes [I ≥ 2σ(I)]	R ₁ = 0.1969, wR ₂ = 0.4609	R ₁ = 0.0329, wR ₂ = 0.0865	R ₁ = 0.0538, wR ₂ = 0.1321
Final R indexes [all data]	R ₁ = 0.4213, wR ₂ = 0.5521	R ₁ = 0.0337, wR ₂ = 0.0870	R ₁ = 0.0702, wR ₂ = 0.1407
Largest diff. peak/hole / e Å ⁻³	1.95/-1.09	0.16/-0.26	0.31/-0.18
Flack parameter	-	0.8(3)	-

* For **Cu** K_α, λ = 1.54184 Å; for **Mo** K_α, λ = 0.7107 Å; and for **synchrotron** radiation from Diamond Light Source λ = 0.6889 Å.

Code	Batch	Formula*	Solvent content**
S1	1	C ₄₁ H ₄₁ B ₄ F ₁₆ Fe ₂ N ₂₅ O ₅	[Fe ¹ L ₂][Fe ² L ₂ (H ₂ O) ₂][BF ₄] ₄ ·MeNO ₂ ·H ₂ O
S2	2	C ₄₁ H ₄₃ B ₄ F ₁₆ Fe ₂ N ₂₅ O ₆	[Fe ¹ L ₂][Fe ² L ₂ (H ₂ O) ₂][BF ₄] ₄ ·MeNO ₂ ·2H ₂ O
S3	2	C ₄₁ H ₄₃ B ₄ F ₁₆ Fe ₂ N ₂₅ O ₆	[Fe ¹ L ₂][Fe ² L ₂ (H ₂ O) ₂][BF ₄] ₄ ·MeNO ₂ ·2H ₂ O
S4	2	C ₄₁ H ₄₁ B ₄ F ₁₆ Fe ₂ N ₂₅ O ₅	[Fe ¹ L ₂][Fe ² L ₂ (H ₂ O) ₂][BF ₄] ₄ ·MeNO ₂ ·H ₂ O
S5	2	C ₄₁ H ₄₁ B ₄ F ₁₆ Fe ₂ N ₂₅ O ₅	[Fe ¹ L ₂][Fe ² L ₂ (H ₂ O) ₂][BF ₄] ₄ ·MeNO ₂ ·H ₂ O

	S1	S2	S3
Empirical formula	C ₄₁ H ₄₁ B ₄ F ₁₆ Fe ₂ N ₂₅ O ₅	C ₄₁ H ₄₃ B ₄ F ₁₆ Fe ₂ N ₂₅ O ₆	C ₄₁ H ₄₃ B ₄ F ₁₆ Fe ₂ N ₂₅ O ₆
Formula weight	1422.93	1440.94	1440.94
Temperature/K	150.00(10)	150.01(10)	200.00(10)
Crystal system	monoclinic	monoclinic	monoclinic
Space group	C2/c	C2/c	C2/c
a/Å	19.9215(6)	19.9190(3)	19.9235(5)
b/Å	15.5378(5)	15.3887(3)	15.5984(5)
c/Å	18.5292(6)	18.5909(3)	18.6533(4)
α/°	90	90	90
β/°	101.222(3)	101.152(2)	100.512(2)
γ/°	90	90	90
Volume/Å ³	5625.8(3)	5591.02(17)	5699.7(3)
Z	4	4	4
D _{calc} /gcm ⁻³	1.680	1.712	1.679
μ/mm ⁻¹	5.240	5.294	5.193
F(000)	2872.0	2912.0	2912.0
Crystal size/mm ³	0.656 × 0.589 × 0.407	1.045 × 0.384 × 0.263	0.895 × 0.326 × 0.277
Radiation λ/Å*	1.54184	1.54184	1.54184
2θ range for data collection/°	7.268 to 148.018	7.312 to 148.16	7.244 to 147.44
Index ranges	-24 ≤ h ≤ 24, -19 ≤ k ≤ 18, -22 ≤ l ≤ 19	-22 ≤ h ≤ 24, -18 ≤ k ≤ 18, -22 ≤ l ≤ 21	-21 ≤ h ≤ 24, -19 ≤ k ≤ 14, -23 ≤ l ≤ 23
Reflections collected	17923	19986	19798
Independent reflections	5558 [R _{int} = 0.0604, R _σ = 0.0483]	5616 [R _{int} = 0.0330, R _σ = 0.0284]	5714 [R _{int} = 0.0412, R _σ = 0.0345]
Data/restraints/parameters	5558/0/450	5616/0/477	5714/0/450
Goodness-of-fit on F ²	1.049	1.046	1.036
Final R indexes [I > 2σ (I)]	R ₁ = 0.1006, wR ₂ = 0.2697	R ₁ = 0.0585, wR ₂ = 0.1610	R ₁ = 0.0869, wR ₂ = 0.2467
Final R indexes [all data]	R ₁ = 0.1040, wR ₂ = 0.2731	R ₁ = 0.0604, wR ₂ = 0.1627	R ₁ = 0.0899, wR ₂ = 0.2507
Largest diff. peak/hole / e Å ⁻³	0.75/-0.92	0.69/-0.84	0.89/-0.77
Flack parameter	-	-	-

* For **Cu** K_α, λ = 1.54184 Å; for **Mo** K_α, λ = 0.7107 Å; and for **synchrotron** radiation from Diamond Light Source λ = 0.6889 Å.

	S4	S5
Empirical formula	C ₄₁ H ₄₁ B ₄ F ₁₆ Fe ₂ N ₂₅ O ₅	C ₄₁ H ₄₁ B ₄ F ₁₆ Fe ₂ N ₂₅ O ₅
Formula weight	1422.93	1422.93
Temperature/K	250.00(10)	289.97(10)
Crystal system	monoclinic	monoclinic
Space group	C2/c	C2/c
a/Å	19.9189(6)	19.9010(5)
b/Å	15.8603(5)	15.9683(4)
c/Å	18.7484(4)	18.7282(6)
α/°	90	90
β/°	99.528(2)	99.397(3)
γ/°	90	90
Volume/Å ³	5841.3(3)	5871.7(3)
Z	4	4
D _{calc} /gcm ⁻³	1.618	1.610
μ/mm ⁻¹	5.046	5.020
F(000)	2872.0	2872.0
Crystal size/mm ³	0.918 × 0.389 × 0.232	0.888 × 0.38 × 0.309
Radiation λ/Å*	1.54184	1.54184
2θ range for data collection/°	8.19 to 147.2	8.174 to 147.738
Index ranges	-24 ≤ h ≤ 22, -17 ≤ k ≤ 19, -23 ≤ l ≤ 22	-24 ≤ h ≤ 24, -18 ≤ k ≤ 19, -23 ≤ l ≤ 20
Reflections collected	11206	19128
Independent reflections	5722 [R _{int} = 0.0521, R _σ = 0.0651]	5822 [R _{int} = 0.0451, R _σ = 0.0429]
Data/restraints/parameters	5722/0/462	5822/0/450
Goodness-of-fit on F ²	1.014	1.033
Final R indexes [I ≥ 2σ (I)]	R ₁ = 0.0820, wR ₂ = 0.2085	R ₁ = 0.0800, wR ₂ = 0.2247
Final R indexes [all data]	R ₁ = 0.1205, wR ₂ = 0.2362	R ₁ = 0.0867, wR ₂ = 0.2349
Largest diff. peak/hole / e Å ⁻³	0.62/-0.46	0.70/-0.56
Flack parameter	-	-

* For **Cu** K_α, λ = 1.54184 Å; for **Mo** K_α, λ = 0.7107 Å; and for **synchrotron** radiation from Diamond Light Source λ = 0.6889 Å.